S

de Saint-Venant, Adhémar-Jean-Claude Barré

James Casey[1] and Annie Ruimi[2]
[1]Department of Mechanical Engineering, University of California, Berkeley, CA, USA
[2]Mechanical Engineering Program, Texas A&M University at Qatar, Doha, Qatar

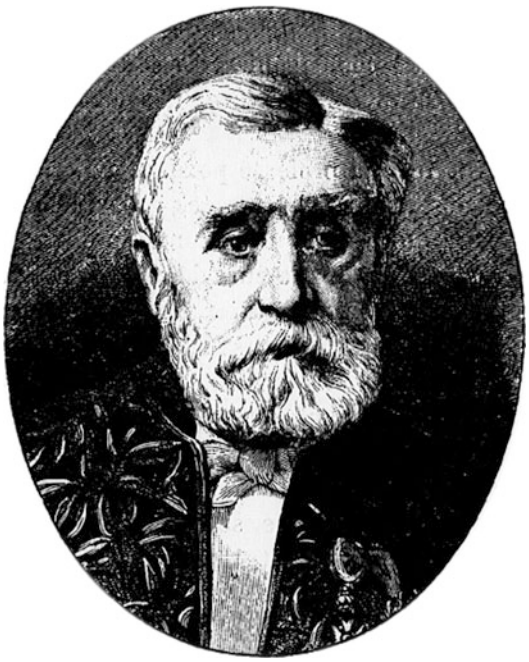

Adhémar-Jean-Claude Barré de Saint-Venant

Adhémar-Jean-Claude Barré de Saint-Venant (*August 23, 1797, Château de Fortoiseau, Villiers-en-Bière, Seine-et-Marne, France; †January 6, 1886, Villeporcher, France) was a civil engineer, scholar and educator, and an eminent elastician. He made fundamental contributions to mechanics, most notably to linear elasticity, but also to fluid mechanics and plasticity. (This entry is based on an article by Casey and Kaplan (1997), where additional references to primary and secondary sources may be found.)

Biographical Information, Education, and Career

Saint-Venant was born into a monarchist, Catholic family shortly after the French Revolution. Mathematically gifted, he was admitted to the École Polytechnique in 1813, but was forced to leave as a result of political disturbances in 1814. He found a position as an engineer's assistant in the Service des Poudres et Salpêtres (i.e., gunpowder). In 1823, he resumed studies at the École des Ponts et Chaussées, where he came under the influence of Claude-Louis Navier. After graduating at the head of his class in 1825, he worked for many years as a civil engineer.

In 1837, when Gaspard Coriolis was not well enough to lecture, Saint-Venant substituted for him at the École des Ponts et Chaussées

H. Altenbach, A. Öchsner (eds.), *Encyclopedia of Continuum Mechanics*,
https://doi.org/10.1007/978-3-662-55771-6

and delivered a landmark course of lectures on elasticity, which have been preserved in lithographic form (Saint-Venant 1837–38; Todhunter and Pearson 1886: Articles 1561–1577). In this year also, Saint-Venant married Julie Rohault de Fleury; the couple had six children. To supplement his income, Saint-Venant worked for some time with the city of Paris on public thoroughfares.

Also proficient in fluid mechanics, Saint-Venant sought to improve agricultural conditions in the Sologne, a poor region lying to the south of Paris. In 1850, he was appointed to the Chair in Rural Engineering at the newly founded Institut National Agronomique de Versailles. There, he lectured on geometry, mechanics, and agricultural hydraulics until 1852. In 1857, the Saint-Venant family moved to a château at Villeporcher (near Vendôme).

During the 1840s, original scientific work by Saint-Venant, particularly on theoretical elasticity, began to appear. His monumental contributions on elastic torsion and flexure followed in the 1850s.

Saint-Venant sought to consolidate the advances he had made in elasticity by working them into a major revision (Navier 1864) of the textbook of his beloved teacher. With the addition of extensive notes and appendices, as well as a superb historical introduction, the size of the original increased by about 1000 pages! Appendix III of the new edition contains a masterly presentation of the theory of linear elasticity and includes the recently discovered equations of compatibility.

In the late 1860s, Saint-Venant became aware of the pioneering experiments of Henri Tresca on the behavior of ductile materials beyond the elastic range. He encouraged Tresca to publish his results, with carefully drawn diagrams, and he developed a theory to describe these materials.

Saint-Venant's last great contribution to elasticity was the translation and revision of Alfred Clebsch's treatise on elasticity, originally published in German in 1861. By making generalizations, commentaries, additions, and corrections, the value of the original edition was greatly increased. The *Annotated Clebsch,* as it became known, is about three times the size of the first edition and quickly became the standard treatise on elasticity in the late nineteenth century.

In personality, Saint-Venant was known for his integrity, independence, generosity, and good wit. He held conservative religious and political beliefs. He continued to work up to his final days. He died surrounded by his large family of children and grandchildren. His wife had passed away less than a year before.

Notable among Saint-Venant's disciples were Joseph Boussinesq, Maurice Levy, and Alfred Flamant.

Scientific Accomplishments

Saint-Venant learned theoretical elasticity directly from its founder Claude-Louis Navier, benefiting greatly also from the work of Augustin Cauchy and Siméon-Denis Poisson. He advanced Navier's intellectual program, which aimed to build a rational theory that would enable structural engineering calculations to be performed with confidence.

In the mid-1840s, Saint-Venant wrote a number of papers on elastic beams and rods, through which he became aware of the shortcomings of existing theories of torsion and flexure. Pursuing the torsion problem unrelentingly, he finally came to realize the necessity of cross-sectional warping. His investigations culminated in the epoch-making memoir of 13 June 1853 (Saint-Venant 1856a), 328 pages long. In it, adept use is made of his clever semi-inverse method. Also, we find Saint-Venant's celebrated principle, which may be stated as: statically equivalent distributions of loads on the ends of a beam in torsion or flexure will give rise to strain fields (and stress fields) that differ little from each other sufficiently far away from the ends. This powerful, if somewhat imprecise, principle extends the range of applicability of exact solutions to practical situations in which the distribution of loads is not known in detail. The memoir of 1853 also contains many splendid illustrations which have become part of the permanent literature on elasticity. The flexure

problem is elaborated upon in a second classic memoir (Saint-Venant 1856b). Once again, Saint-Venant was able to establish which parts of the older theories are compatible with the equations of elasticity.

Detailed accounts of Saint-Venant's prodigious works are given in Todhunter and Pearson (1886, 1887) and his most important contributions to elasticity are included in the standard textbooks (see especially Love (1927), including the informative *Historical Introduction*).

The governing equations for viscous fluids were obtained first by Navier in the 1820s, using a complicated molecular argument. While Saint-Venant was a supporter of molecular models, he also understood the value of the continuum approach. In a beautiful short paper (Saint-Venant 1843), he derived the constitutive equations for viscous fluids by starting with the assumption that the shearing component of surface traction vanishes for the direction in which there is no sliding. This was two years before the classic paper by George Gabriel Stokes. Lamb (1932, p. 577) and Truesdell and Toupin (1960, p. 716) give credit to both Saint-Venant and Stokes. The history of the discovery of the Navier-Stokes equations, to which Cauchy and Poisson also contributed, is recounted by Darrigol (2005, Chap. 3).

In Paris, during the period 1864–1872, Henri Édouard Tresca single-handedly initiated the field of plasticity with extensive experiments involving punching and extrusion of a variety of solids using a hydraulic press. He concluded that under sufficiently high applied pressure, solids flow in "the manner of fluids." He determined that a solid will yield once the maximum shear stress reaches a characteristic value for the material. An excellent summary of Tresca's work may be found in Bell (1973, pp. 427–449).

Saint-Venant fully appreciated the scientific value of Tresca's investigations and set himself the task of creating an idealized theory that would model the observed behavior. On March 7, 1870, he proposed a novel theory for "this new species of hydro-dynamics" (Saint-Venant 1870). At first, he called the subject *hydrostéréodynamique* (solid hydrodynamics) but soon settled on the better name *plasticodynamique*. The salient assumptions of Saint-Venant's constitutive theory are: (a) Tresca's yield criterion; (b) plastic incompressibility; and most significantly, (c) the direction for which the shearing stress is a maximum is the same as the direction for which the sliding is a maximum. On June 20, 1870, Saint-Venant's disciple, Maurice Levy, extended Saint-Venant's theory to three-dimensional flows (Levy 1870). Much later (in 1913), Richard von Mises proposed a similar theory having a mathematically simpler yield criterion. The St. Venant-Levy-Mises theory of plasticity is useful when elastic strains can be neglected in comparison with plastic strains, for example in metal forming processes.

Mention should also be made of work by Saint-Venant in the 1840s on the differential geometry of space curves and on an early vectorial system.

Honors and Awards

Saint-Venant was awarded a medal in 1849 by the Société d'Agriculture for his contributions to agricultural hydraulics. He was elected to the Mechanics Section of the Académie des Sciences in 1868.

Cross-References

- Cauchy, Augustin Louis
- History of Plasticity
- Levy, Maurice
- Love, Augustus Edward Hough
- von Mises, Richard
- Poisson, Siméon Denis
- Stokes, George Gabriel

References

Bell J (1973) The experimental foundations of solid mechanics. In: Flügge S, Truesdell C (eds) Handbuch der physik, vol VIa/1, Mechanics of solids I. Springer, Berlin, pp 1–778

Casey J, Kaplan A (1997) Adhémar-Jean-Claude Barré de Saint-Venant. Math Mech Solids 2:371–378
Clebsch RFA (1883) Théorie de l'élasticité des corps solides, traduite par MM. Barré de Saint-Venant et Flamant, avec des notes étendues de M. de Saint-Venant. Dunod, Paris
Darrigol O (2005) Worlds of flow: a history of hydrodynamics from the Bernoullis to Prandtl. University Press, Oxford
Lamb Sir H (1932) Hydrodynamics, 6th edn. University Press, Cambridge
Levy M (1870) Mémoire sur les équations générales des mouvements intérieurs des corps solides ductiles au delà des limites où l'élasticité pourrait les ramener à leur premier état (Extrait). C R Acad Sci Paris 70:1323–1325 [Reprinted (1871) J Math Pures Appl 16:369–372]
Love AEH (1927) A treatise on the mathematical theory of elasticity, 4th edn. University Press, Cambridge
Navier CLMH (1864) Résumé des leçons données à l'École des Ponts et Chaussées sur l'application de la mécanique à l'établissement des constructions et des machines, première section: de la résistance des corps solides (troisième édition), avec des notes et appendices par M. Barré de Saint-Venant, tome première, fascicule 1. Dunod, Paris
Saint-Venant AJC Barré de (1837–38) Leçons de mécanique appliquée faites par intérim. École des Ponts et Chaussées, Paris
Saint-Venant AJC Barré de (1843) Note à joindre au mémoire sur la dynamique des fluides, présenté le 14 Avril 1834. C R Acad Sci Paris 17:1240–1243
Saint-Venant AJC Barré de (1856a) Mémoire sur la torsion des prismes, avec des considérations sur leur flexion ainsi que sur l'équilibre intérieur des solides élastiques en général, et des formules pratiques pour le calcul de leur résistance à divers efforts s'exerçant simultanément. Mém Divers Savants Acad Sci Paris 14:233–560 [Printed as a separate publication in 1855, Imprimerie Impériale, Paris]
Saint-Venant AJC Barré de (1856b) Mémoire sur la flexure des prismes, sur les glissements transversaux et longitudinaux qui l'accompagnent lorsqu'elle ne s'opère pas uniformément ou en arc de cercle, et sur la forme courbe affectée alors pas leurs sections transversales primitivement planes. J Math Pures Appl (Sér 2) 1:89–189
Saint-Venant AJC Barré de (1870) Sur l'établissement des équations des mouvements intérieurs opérés dans les corps solides ductiles au delà des limites où l'élasticité pourrait les ramener à leur premier état. C R Acad Sci Paris 70:473–480 [Reprinted (1871) J Math Pures Appl 16:308–316]
Todhunter I, Pearson K (1886) A history of the theory of elasticity and of the strength of materials from Galilei to Lord Kelvin, vol I. University Press, Cambridge
Todhunter I, Pearson K (1887) A history of the theory of elasticity and of the strength of materials from Galilei to the present time, vol II. University Press, Cambridge
Truesdell C, Toupin R (1960) The classical field theories (with an appendix on tensor fields by Ericksen JL). In: Flügge S (ed) Handbuch der physik, vol III/1, Principles of classical mechanics and field theories. Springer, Berlin, pp 226–858

SAW (Surface Acoustic Waves)

▸ Surface Waves

Scaling Function in Mechanics of Random Materials

Shivakumar I. Ranganathan[1] and Muhammad Ridwan Murshed[2]
[1]Department of Mechanical Engineering, Virginia Polytechnic Institute and State University, Northern Virginia Center, Falls Church, VA, USA
[2]Department of Mechanical Engineering, Rowan University, Glassboro, NJ, USA

Synonyms

Composite materials; Dimensionless numbers; Homogenization; Mesoscale

Definition

The concept of a dimensionless scaling function is introduced and its role is discussed in the context of multiscale mechanics of random composites. The proposed scaling function stems from the scalar contraction of the ensemble averaged tensors obtained using Dirichlet and Neumann type boundary conditions. In its most generic form, the scaling function depends upon the phase contrast, volume fraction, material anisotropy, and mesoscale. The scaling function essentially quantifies the departure of a random medium from a homogeneous continuum.

Introduction

Recent advances in computational mechanics have dramatically changed the landscape of engineering and science. The primary driving force is due to a rapid decrease in the computational cost which is estimated as a billion-fold reduction during the last 40 years (Belytschko et al. 2007). In particular, computational mechanics has led to technological advancements in several areas including manufacturing, medicine, communication, defense, as well as to improved understanding of natural phenomena such as the movement of tectonic plates, and astrophysics of black holes (Oden et al. 2003).

A fertile ground of research within computational mechanics is the multiscale modeling of advanced functional materials (for instance, enhanced fracture toughness Murshed et al. 2016, superior thermoelasticity Huang et al. 2016). A versatile approach in multiscale modeling stems from the use of Hill-Mandel homogenization condition (Hill 1963 and Mandel 1966) in which rigorous scale-dependent bounds are obtained by setting up and solving Dirichlet and Neumann type boundary value problems. Such a methodology has been successfully employed over the past several decades within the context of elasticity (Murshed and Ranganathan 2017a; Raghavan and Ranganathan 2014; Ranganathan and Ostoja-Starzewski 2009, 2008c), thermal conductivity (Dalaq and Ranganathan 2015; Dalaq et al. 2013; Ranganathan and Ostoja-Starzewski 2008a), electrical conductivity (Raghavan et al. 2015), thermoelasticity (Ostoja-Starzewski et al. 2015; Khisaeva and Ostoja-Starzewski 2006; Ostoja-Starzewski 2006), flow in porous media (Ostoja-Starzewski et al. 2007; Du and Ostoja-Starzewski 2006), fracture and damage phenomena in random microstructures (Ostoja-Starzewski 2007), and nonlinear elastic and inelastic materials (Ostoja-Starzewski et al. 2016; Ostoja-Starzewski and Ranganathan 2013; Ranganathan and Ostoja-Starzewski 2008b). Within this framework, the notion of a scaling function is introduced that is analogous to the definition of dimensionless numbers that are widely used in several fields including fluid mechanics (White 2003), electromagnetism (Kuneš 2012), astrophysics (Shore 2012), medicine (Splinter 2010; Ranganathan et al. 2010a,b), and pharmacy (Gorb et al. 2014). Recently, a combination of dimensionless numbers such as nondimensional heat input, Peclet number (ratio of convective to diffusive transport Donea and Huerta 2003), Marangoni number (ratio of surface tension force to viscous force Panigrahi 2016), and Fourier number (ratio of heat transfer by conduction to rate of energy stored Huebner et al. 2008) was used to analyze the structure-property relationship of 3D printed materials (see Mukherjee et al. 2017). The scaling function by definition quantifies the departure of a random medium from a homogeneous continuum.

In the subsequent sections, a functional form for the scaling function will be introduced that is applicable to a wide range of composite materials (two-phase checkerboards, two-phase correlated microstructures, and 3D polycrystals).

Notion of a Scaling Function

The functional form of the scaling function depends upon the specific microstructure under investigation. Within the scope of this research, four microstructures are considered – (i) uncorrelated random checkerboard (see Fig. 1a), (ii) correlated two-phase microstructure (see Fig. 1b), (iii) two-phase viscoelastic composite (see Fig. 1c), and (iv) random polycrystal (see Fig. 1d). In order to identify the specific form of the functions f_1 to f_4, a methodology based on the Hill-Mandel homogenization condition is employed (see Fig. 1). In this approach, the microstructures are subjected to Dirichlet and Neumann type boundary conditions that result in rigorous scale-dependent bounds with increasing mesoscales (δ, see section "Effect of Mesoscale, δ, on Scaling Function"). For a given realization, $\omega(\in \Omega)$, the Dirichlet boundary condition results in a mesoscale random stiffness tensor $C_\delta^d(\omega)$, and the Neumann boundary condition results in a mesoscale random compliance tensor $S_\delta^n(\omega)$ for linear elastic

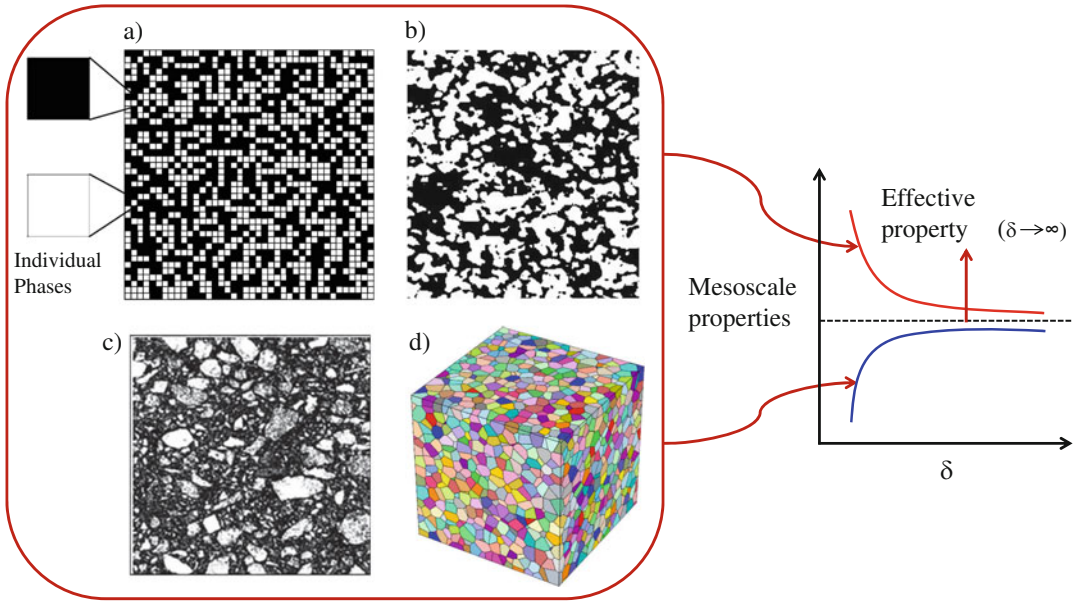

Fig. 1 Homogenization Methodology: (**a**) Checkerboard microstructure in thermal conductivity (Dalaq and Ranganathan 2015; Dalaq et al. 2013), elasticity (Raghavan and Ranganathan 2014) and electrical conductivity (Raghavan et al. 2015); (**b**) two-phase (Al_2O_3-Ni) microstructure in thermal conductivity (Kale et al. 2015); (**c**) microstructure of a viscoelastic material (mixture of asphalt and concrete) (Zhang and Ostoja-Starzewski 2016); (**d**) polycrystal in 3D elasticity (color represents random orientation of each grain) (Murshed and Ranganathan 2017b; Quey et al. 2011)

materials. In the context of heat or electrical conductivity, $C_\delta^d(\omega)\,[S_\delta^n(\omega)]$ represents the second-rank conductivity [resistivity] tensors, and for viscoelastic materials, they represent the complex modulus [compliance] tensors, respectively. These tensors are inverse of each other in the limit $\delta \to \infty$. The scaling function in its most generic form is defined as follows:

$$f = \left\langle \mathbf{C}_\delta^d \right\rangle : \langle \mathbf{S}_\delta^n \rangle - \left\langle \mathbf{C}_\infty^d \right\rangle : \langle \mathbf{S}_\infty^n \rangle, \qquad (1)$$

where the operators : and $\langle \bullet \rangle$ indicate tensor contraction and ensemble averaging over the realization space, respectively. It turns out that Eq. (1) takes the following generic form for all microstructures investigated:

$$f = c f_1(k) f_2(v_f) f_3(A) f_4(\delta), \qquad (2)$$

where c is a constant, k is phase contrast, v_f is volume fraction, A is an anisotropy measure, and δ is mesoscale. In the subsequent sections, the functional form of each of the terms appearing in Eq. (2) will be discussed.

Effect of Phase Contrast, k, on Scaling Function

The phase contrast (k) quantifies the mismatch in the material properties of a composite material. For a 2D microstructure, $k = \frac{c_1}{c_2}$, where c_1 and c_2 correspond to the conductivities (thermal or electrical conductivity) for phase 1 and phase 2, respectively. For 3D polycrystals with uniaxial thermal character, $k = \frac{c_1}{c_3}$, where c_1 and c_3 correspond to ratio of the two independent principal conductivities of the single crystal. The dependence of scaling function on the contrast can now be expressed as follows:

$$f_1(k) = \left(\sqrt{k} - \frac{1}{\sqrt{k}}\right)^2. \qquad (3)$$

Figure 2 illustrates the phase contrasts ($k = 0.01, 0.1, 1, 10, 100$) for two-phase checkerboards, two-phase correlated microstructures,

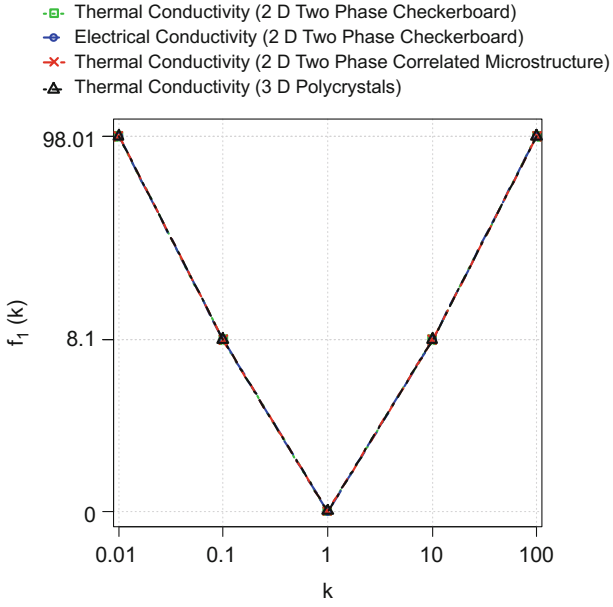

Fig. 2 $f_1(k)$ vs. Phase Contrast, k in (i) 2D Two Phase Checkerboard (Thermal Conductivity Dalaq et al. 2013 and Electrical Conductivity Raghavan et al. 2015); (ii) 2D Two Phase Correlated Microstructure (Thermal Conductivity Kale et al. 2015); (iii) 3D Polycrystals (Thermal Conductivity Ranganathan and Ostoja-Starzewski 2008a)

and 3D polycrystals. It is evident that the phase contrast has the same effect on scaling function for all applications. Also, scaling function does not distinguish between k and k^{-1}, and, therefore, microstructures with phase contrasts k or k^{-1} scale identically.

Effect of Volume Fraction, v_f, on Scaling Function

In this section, the effect of volume fraction, v_f (amount of phase 1 in the entire volume), on the scaling function is examined. Clearly, the volume fraction always ranges between zero and one ($0 \leq v_f \leq 1$), with the limiting values representing a homogeneous material. The following is the dependence of scaling function on the volume fraction:

$$f_2(v_f) = v_f(1 - v_f). \tag{4}$$

Figure 3 illustrates the effect of volume fraction on $f_2(v_f)$ for a two-phase checkerboard in electrical conductivity. It is clear that the scaling function value is largest [$f_2(v_f) = 0.25$] at $v_f = 0.5$. This is due to the fact that at 50% volume fraction, level of heterogeneity is largest in a given microstructure (see Raghavan et al. 2015).

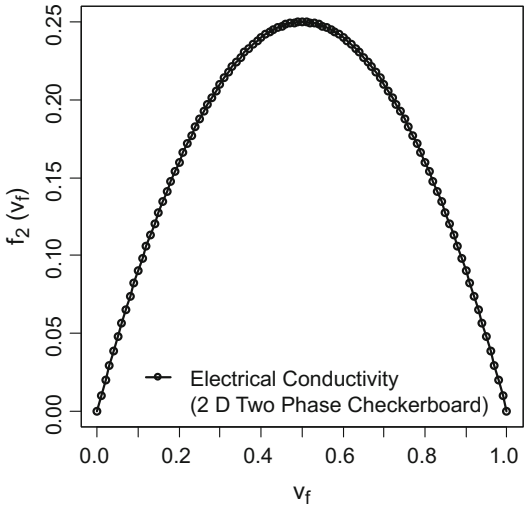

Fig. 3 $f_2(v_f)$ vs. Volume Fraction, v_f in Electrical Conductivity (Raghavan et al. 2015)

Effect of an Anisotropy Measure, A, on Scaling Function

Material anisotropy of the microstructure plays an important role in the definition of the scaling function. The effect of anisotropy, A, on the scaling function depends upon the specific microstructure under investigation. For single-phase 3D polycrystals, this dependance is as follows:

S

$$f_3(A) = A^U = 5\frac{G^V}{G^R} + \frac{K^V}{K^R} - 6, \tag{5}$$

where A^U is the universal anisotropy index (Ranganathan and Ostoja-Starzewski 2008d), G is shear modulus, K is bulk modulus, V is Voigt estimate (Voigt 1928), and R is Reuss estimate (Reuss 1929). Along similar lines, for 2D two-phase elastic microstructures, $f_3(A)$ takes the following form (see Raghavan and Ranganathan 2014):

$$f_3(A) = 2\frac{G^V}{G^R} + \frac{K^V}{K^R} - 3. \tag{6}$$

More recently, (Zhang and Ostoja-Starzewski 2016) examined the scaling of 2D viscoelastic composites and proposed the following form for $f_3(A)$:

$$f_3(A) = 2\mu_{2D}^{*V}(\gamma)J_{2D}^{*R}(\gamma) + k_{2D}^{*V}(\gamma)L_{2D}^{*R}(\gamma) - 3, \tag{7}$$

where γ is the frequency, μ_{2D}^* is the relaxation shear modulus, J_{2D}^* is the complex shear compliance, k_{2D}^* is the relaxation bulk modulus, and L_{2D}^* is the complex bulk compliance.

Effect of Mesoscale, δ, on Scaling Function

The mesoscale (δ) can be defined as (see Ranganathan and Ostoja-Starzewski 2008c)

$$\delta = \frac{l}{d}, \tag{8}$$

where l is the length scale of observation (domain size) and d is the characteristic length scale (e.g., the grain size). For 3D polycrystals, $\delta = (N_G)^{1/3}$. Under limiting values of the mesoscale, δ, the scaling function takes an exact form:

$$f_4(\delta = \infty) = 0. \tag{9}$$

In addition, the following rigorous bounds on scaling function can be established at finite mesoscales:

$$f_4(\delta = \infty) \le f_4(\delta') \le f_4(\delta) \le f_4(\delta = 1)\ \forall 1 \le \delta \le \delta' \le \infty. \tag{10}$$

Extensive numerical simulations on a variety of composite materials by several authors (see Raghavan et al. 2015; Dalaq et al. 2013; Kale et al. 2015; Ranganathan and Ostoja-Starzewski 2008a; Raghavan and Ranganathan 2014; Ranganathan and Ostoja-Starzewski 2008c; Murshed and Ranganathan 2017b; Zhang and Ostoja-Starzewski 2016) resulted in the following empirical forms for the function $f_4(\delta)$:

$$f_4(\delta) = \exp[B(\delta - 1)^C], \tag{11a}$$

$$f_4(\delta) = \delta^D, \tag{11b}$$

$$f_4(\delta) = \frac{e}{\left(f + \frac{\delta}{\lambda}\right)^n}, \tag{11c}$$

where B, C, D, e, f, λ, and n are arbitrary constants relevant to the specific microstructure being investigated and is discussed in the following section (see Fig. 4).

Application Problems

In this section, the functional form of the scaling function is summarized for a variety of applications. These include conductivity in 2D two-phase random and correlated microstructures, conductivity in 3D polycrystals, elasticity in 2D two-phase checkerboards, elasticity in 3D polycrystals, and viscoelasticity in 2D two-phase checkerboards.

Conductivity in 2D Two-Phase Microstructures

Consider 2D two-phase microstructures either conducting heat (or electricity) as illustrated in Fig. 1a, b. One of the microstructures is a random checkerboard, and the other is a Gaussian-correlated microstructure. In order to establish the functional form of the scaling function, they were subjected to temperature (electric field) and heat flux (current density) boundary conditions. The boundary value problems were then set up and solved over several realizations to extract the mesoscale random conductivity and resistivity tensors. The procedure was repeated for a variety of material combinations, and, subsequently, Eq. (1) was used to establish the following form of the scaling function (see Raghavan et al. 2015; Dalaq et al. 2013; Kale et al. 2015):

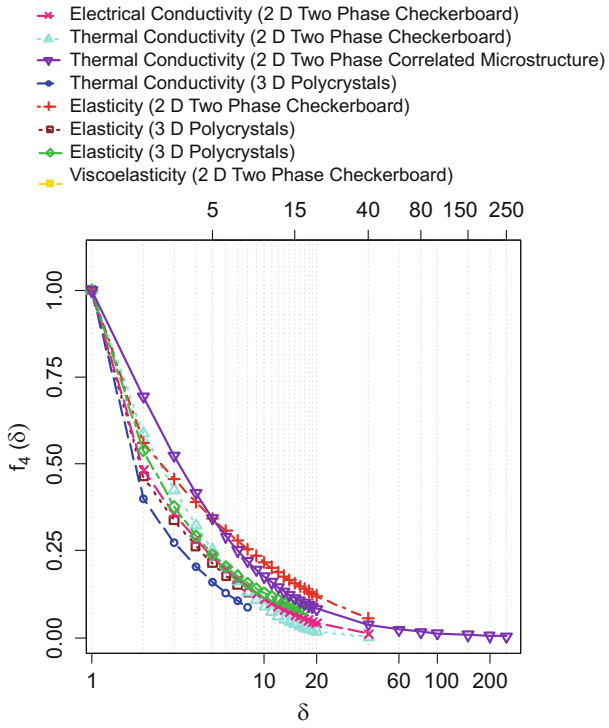

Fig. 4 $f_4(\delta)$ vs. Mesoscale, δ for several applications: (**a**) Electrical Conductivity (2D Two Phase Checkerboard) (Raghavan et al. 2015); (**b**) Thermal Conductivity (2D Two Phase Checkerboard) (Dalaq et al. 2013); (**c**) Thermal Conductivity (2D Two Phase Correlated Microstructure) (Kale et al. 2015); (**d**) Thermal Conductivity (3D Polycrystals) (Ranganathan and Ostoja-Starzewski 2008a); (**e**) Elasticity (2D Two Phase Checkerboard) (Raghavan and Ranganathan 2014); (**f**) Elasticity (3D Polycrystals) (Ranganathan and Ostoja-Starzewski 2008c); (**g**) Elasticity (3D Polycrystals) (Murshed and Ranganathan 2017b); (**h**) Viscoelasticity (2D Two Phase Checkerboard) (Zhang and Ostoja-Starzewski 2016)

$$f = cf_1(k)f_2(v_f)f_3(A)f_4(\delta), \tag{12a}$$

and

$$\begin{aligned} c &= 2, \\ f_1(k) &= \left(\sqrt{k} - \frac{1}{\sqrt{k}}\right)^2, \\ f_2(v_f) &= v_f(1 - v_f), \\ f_3(A) &= 1, \\ f_4(\delta) &= \exp[B(\delta - 1)^C] \\ &\quad \text{(random microstructure)}, \\ f_4(\delta) &= \frac{e}{\left(f + \frac{\delta}{\lambda}\right)^n} \\ &\quad \text{(correlated microstructure)}. \end{aligned} \tag{12b}$$

(Dalaq et al. 2013) studied random checkerboards at 50% volume fractions and empirically determined the constants B and C to be -0.53 and 0.69, respectively. In a subsequent study, (Raghavan et al. 2015) accounted for all volume fractions and proposed $B = -0.73$ and $C = 0.5$. In a more recent study, (Kale et al. 2015) analyzed a correlated microstructure and obtained the following constants $e = 3.7$, $f = 1.9$, $\lambda = 1$, and $n = 1.23$.

Conductivity in 3D Polycrystals

The microstructure used for determining thermal conductivity in 3D polycrystals is similar to Fig. 1d, albeit with cubic-shaped grains. By applying temperature and heat flux boundary conditions on the polycrystal, and by employing

a similar procedure as described in section "Conductivity in 2D Two-Phase Microstructures", results in the functional form for the scaling function (Ranganathan and Ostoja-Starzewski 2008a):

$$f = cf_1(k)f_2(v_f)f_3(A)f_4(\delta), \tag{13a}$$

and

$$\begin{aligned} c &= \frac{2}{3}, \\ f_1(k) &= \left(\sqrt{k} - \frac{1}{\sqrt{k}}\right)^2, \\ f_2(v_f) &= 1, \\ f_3(A) &= 1, \\ f_4(\delta) &= \exp[-0.91(\delta - 1)^{0.50}]. \end{aligned} \tag{13b}$$

Elasticity in 2D Two-Phase Checkerboards

A two-phase random checkerboard is illustrated in Fig. 1a. Much of the numerical procedure remains the same as described in section "Conductivity in 2D Two-Phase Microstructures". The main difference is that the temperature and heat flux boundary conditions are replaced with the displacement and traction boundary conditions, respectively. The resulting mesoscale random stiffness and compliance tensors turn out to be tensors of rank four unlike the second-rank conductivity (or resistivity) tensor. Based on extensive numerical simulations, the scaling function takes the following form (see Raghavan and Ranganathan 2014):

$$f = cf_1(k)f_2(v_f)f_3(A)f_4(\delta), \tag{14a}$$

and

$$\begin{aligned} c &= 1, \\ f_1(k) &= 1, \\ f_2(v_f) &= 1, \\ f_3(A) &= 2\frac{G^V}{G^R} + \frac{K^V}{K^R} - 3, \\ f_4(\delta) &= \exp[-0.58(\delta - 1)^{0.44}]. \end{aligned} \tag{14b}$$

Elasticity in 3D Polycrystals

Consider 3D random polycrystals as shown in Fig. 1d. Microstructures using Voronoi tessellations were generated in the software Neper (Quey et al. 2011) by (Murshed and Ranganathan 2017b), whereas (Ranganathan and Ostoja-Starzewski 2008c) considered cubic-shaped grains. Employing a similar procedure as described in Section "Elasticity in 2D Two-Phase Checkerboards" results in the following form for the scaling function:

$$f = cf_1(k)f_2(v_f)f_3(A)f_4(\delta), \tag{15a}$$

and

$$\begin{aligned} c &= 1, \\ f_1(k) &= 1, \\ f_2(v_f) &= 1, \\ f_3(A) = A^U &= 5\frac{G^V}{G^R} + \frac{K^V}{K^R} - 6, \\ f_4(\delta) &= \exp[-0.77(\delta - 1)^{0.50}], \\ f_4(\delta) &= \delta^{-0.89}. \end{aligned} \tag{15b}$$

A stretched exponential form was obtained for $f_4(\delta)$ by (Ranganathan and Ostoja-Starzewski 2008c) who considered only crystals belonging to cubic symmetry. However, (Murshed and Ranganathan 2017b) conducted simulations on all crystal classes (from cubic to triclinic) and proposed a power law relation for $f_4(\delta)$.

Viscoelasticity in 2D Two-Phase Checkerboards

The viscoelastic composite material considered is shown in Fig. 1c. These microstructures were subjected to displacement and traction boundary conditions. Subsequently, the boundary value problems were set up and solved over several realizations in order to extract the mesoscale random complex modulus and complex compliance tensors. The following form of the scaling function was then determined (Zhang and Ostoja-Starzewski 2016):

$$f = cf_1(k)f_2(v_f)f_3(A)f_4(\delta), \tag{16a}$$

and

$$\begin{aligned} c &= 1, \\ f_1(k) &= 1, \\ f_2(v_f) &= 1, \\ f_3(A) &= f_3(A) = 2\mu_{2D}^{*V}(\gamma)J_{2D}^{*R}(\gamma) \\ &\quad + k_{2D}^{*V}(\gamma)L_{2D}^{*R}(\gamma) - 3, \\ f_4(\delta) &= \exp[-0.45(\delta - 1)^{0.66}]. \end{aligned} \tag{16b}$$

The scaling functions for all the materials considered are summarized in Fig. 4. Clearly, it can be seen that the scaling function approaches zero with increasing mesoscales.

Conclusion

Dimensionless numbers play an important role in a variety of problems in physics and engineering. In this context, the concept of a scaling function is introduced, and its generic form is proposed based on the studies of a variety of composite materials. The extent of heterogeneity (phase contrast, volume fraction) and anisotropy in the microstructure contributes significantly to the scaling function. The scaling function also strongly depends on the mesoscale, with good curve-fitting models obtained on the basis of extensive numerical simulations. In essence, the scaling function quantifies the departure of a random medium from a homogeneous continuum.

References

Belytschko T, Hughes T, Patankar N, Herakovich C, Bakis C (2007) Research directions in computational and composite mechanics. A report of the United States National Committee on theoretical and applied mechanics

Dalaq AS, Ranganathan SI (2015) Invariants of mesoscale thermal conductivity and resistivity tensors in random checkerboards. Eng Comput 32(6):1601–1618

Dalaq AS, Ranganathan SI, Ostoja-Starzewski M (2013) Scaling function in conductivity of planar random checkerboards. Comput Mater Sci 79:252–261

Donea J, Huerta A (2003) Finite element methods for flow problems. Wiley, Chichester

Du X, Ostoja-Starzewski M (2006) On the size of representative volume element for darcy law in random media. In: Proceedings of the royal society of London A: mathematical, physical and engineering sciences, The Royal Society, vol 462, pp 2949–2963

Gorb L, Kuz'min V, Muratov E (2014) Application of computational techniques in pharmacy and medicine, vol 17. Springer, Dordrecht

Hill R (1963) Elastic properties of reinforced solids: some theoretical principles. J Mech Phys Solids 11(5): 357–372

Huang YG, Shiota Y, Wu MY, Su SQ, Yao ZS, Kang S, Kanegawa S, Li GL, Wu SQ, Kamachi T et al (2016) Superior thermoelasticity and shape-memory nanopores in a porous supramolecular organic framework. Nat Commun 7:11564

Huebner KH, Dewhirst DL, Smith DE, Byrom TG (2008) The finite element method for engineers. Wiley, Hoboken

Kale S, Saharan A, Koric S, Ostoja-Starzewski M (2015) Scaling and bounds in thermal conductivity of planar gaussian correlated microstructures. J Appl Phys 117(10):104301

Khisaeva Z, Ostoja-Starzewski M (2006) Mesoscale bounds in finite elasticity and thermoelasticity of random composites. In: Proceedings of the royal society of London A: mathematical, physical and engineering sciences, The Royal Society, vol 462, pp 1167–1180

Kuneš J (2012) Dimensionless physical quantities in science and engineering. Elsevier, London

Mandel J (1966) Contribution théorique à létude de lécrouissage et des lois de lécoulement plastique. In: Görtler H (ed) Applied mechanics. Springer, Berlin/Heidelberg, pp 502–509

Mukherjee T, Manvatkar V, De A, DebRoy T (2017) Dimensionless numbers in additive manufacturing. J Appl Phys 121(6):064904

Murshed MR, Ranganathan SI (2017a) Hill–Mandel condition and bounds on lower symmetry elastic crystals. Mech Res Commun 81:7–10

Murshed MR, Ranganathan SI (2017b) Scaling laws in elastic polycrystals with individual grains belonging to any crystal class. Acta Mechanica 228(4):1525–1539

Murshed MR, Ranganathan SI, Abed FH (2016) Design maps for fracture resistant functionally graded materials. Eur J Mech A Solids 58:31–41

Oden JT, Belytschko T, Babuska I, Hughes T (2003) Research directions in computational mechanics. Comput Methods Appl Mech Eng 192(7):913–922

Ostoja-Starzewski M (2006) Material spatial randomness: from statistical to representative volume element. Probab Eng Mech 21(2):112–132

Ostoja-Starzewski M (2007) Microstructural randomness and scaling in mechanics of materials. CRC Press, Boca Raton

Ostoja-Starzewski M, Ranganathan SI (2013) Scaling and homogenization in spatially random composites. In: Mantič V (ed) Mathematical methods and models in composites. Imperial College Press, London, pp 61–101
Ostoja-Starzewski M, Du X, Khisaeva Z, Li W (2007) Comparisons of the size of the representative volume element in elastic, plastic, thermoelastic, and permeable random microstructures. Int J Multiscale Comput Eng 5(2):73–82
Ostoja-Starzewski M, Costa L, Ranganathan SI (2015) Scale-dependent homogenization of random hyperbolic thermoelastic solids. J Elast 118(2):243–250
Ostoja-Starzewski M, Kale S, Karimi P, Malyarenko A, Raghavan B, Ranganathan SI, Zhang J (2016) Chapter two-scaling to RVE in random media. Adv Appl Mech 49:111–211
Panigrahi PK (2016) Transport phenomena in microfluidic systems. Wiley, Singapore
Quey R, Dawson P, Barbe F (2011) Large-scale 3D random polycrystals for the finite element method: generation, meshing and remeshing. Comput Methods Appl Mech Eng 200(17):1729–1745
Raghavan BV, Ranganathan SI (2014) Bounds and scaling laws at finite scales in planar elasticity. Acta Mechanica 225(11):3007–3022
Raghavan BV, Ranganathan SI, Ostoja-Starzewski M (2015) Electrical properties of random checkerboards at finite scales. AIP Adv 5(1):017131
Ranganathan SI, Ostoja-Starzewski M (2008a) Mesoscale conductivity and scaling function in aggregates of cubic, trigonal, hexagonal, and tetragonal crystals. Phys Rev B 77(21):214308
Ranganathan SI, Ostoja-Starzewski M (2008b) Scale-dependent homogenization of inelastic random polycrystals. J Appl Mech 75(5):051008
Ranganathan SI, Ostoja-Starzewski M (2008c) Scaling function, anisotropy and the size of RVE in elastic random polycrystals. J Mech Phys Solids 56(9):2773–2791
Ranganathan SI, Ostoja-Starzewski M (2008d) Universal elastic anisotropy index. Phys Rev Lett 101(5):055504
Ranganathan SI, Ostoja-Starzewski M (2009) Towards scaling laws in random polycrystals. Int J Eng Sci 47(11):1322–1330
Ranganathan SI, Decuzzi P, Wheeler LT, Ferrari M (2010a) Geometrical anisotropy in biphase particle reinforced composites. J Appl Mech 77(4):041017
Ranganathan SI, Yoon DM, Henslee AM, Nair MB, Smid C, Kasper FK, Tasciotti E, Mikos AG, Decuzzi P, Ferrari M (2010b) Shaping the micromechanical behavior of multi-phase composites for bone tissue engineering. Acta Biomaterialia 6(9):3448–3456
Reuss A (1929) Berechnung der fließgrenze von mischkristallen auf grund der plastizitätsbedingung für einkristalle. ZAMM-Journal of Applied Mathematics and Mechanics/Zeitschrift für Angewandte Mathematik und Mechanik 9(1):49–58
Shore SN (2012) An introduction to astrophysical hydrodynamics. Academic, San Diego
Splinter R (2010) Handbook of physics in medicine and biology. CRC Press, Boca Raton
Voigt W (1928) Lehrbuch der Kristallphysik (mit Ausschluss der Kristalloptik). Teubner, Leipzig
White FM (2003) Fluid mechanics. McGraw-Hill, New York
Zhang J, Ostoja-Starzewski M (2016) Frequency-dependent scaling from mesoscale to macroscale in viscoelastic random composites. In: Proceedings of the royal society of London A: mathematical, physical and engineering sciences, The Royal Society, vol 472

Search Algorithms; Contact Search Algorithms

▸ Discrete Element and Particle Methods

Second Gradient Continua

▸ Higher Gradient Theories and Their Foundations

Second Law of Thermodynamics

▸ Truesdell's and Zhilin's Approaches: Derivation of Constitutive Equations

Second Sound

▸ Entropy Principle Exploited by Lagrange Multipliers
▸ Nonlocal Transport Equations for Small Systems and Fast Processes

Self-Similarity Problems in Nonlinear Elastic Media

Anatoliy A. Burenin[1], Dmitrii A. Potianikhin[2], and Marina V. Shitikova[3,4]
[1]Institute of Machinery and Metallurgy, Far-Eastern Branch of Russian Academy of Sciences, Komsomolsk-na-Amure, Russia
[2]Komsomolsk-na-Amure State University, Komsomolsk-na-Amare, Russia
[3]Research Center on Dynamics of Solids and Structures, Voronezh State Technical University, Voronezh, Russia
[4]Research Center for Wave Dynamics of Solids and Structures, Voronezh State Technical University, Voronezh, Russia

Synonyms

Nonlinear dynamic problems enabling self-similar solutions

Definition

The solution of equations or a set of equations is called self-similar if independent variables enter in it in the form of some combination called the self-similar variable. In mechanics, self-similar motion remains mechanically similar to itself under changes of one or several parameters which determine this motion.

By a shock wave we mean a special moving surface, on which the condition of continuity is satisfied, but at least one first derivative of the displacements with respect to time or spatial coordinate (and, therefore, velocity, density, stress) has a discontinuity of the first order.

Introduction

Solutions of self-similar problems (Sedov 1993) constitute an essential part of the theory of gas dynamics (Cherny 1988). They are used to construct the algorithms of numerical calculations of transient gas-dynamic flows (Kulikovskii et al. 2001) and, in particular, algorithms for extracting velocity discontinuities (Godunov et al. 1976). In nonlinear mechanics of deformable bodies, their direct use for such purposes has not been achieved. It is connected with the fact that in deformable bodies, along with the volume strains, as in gas dynamics, there also exist strains of the shape change. Consequently, the discontinuity surfaces presented as elements of solutions for such problems turn out to be combined (Godunov et al. 1976; Burenin and Chernyshov 1978), and that is why solutions of self-similar problems (for example, the problem of discontinuity decay (Godunov et al. 1976)), which are necessary for numerical calculation methods, turned out to be difficult to obtain. However, being asymptotic to a certain degree, quasi-stationary self-similar solutions (except for their independent value) allow one in some cases to evaluate the qualitative features of the dynamics of deformation and thereby to facilitate the correct formulation of the corresponding boundary problems of nonstationary and shock deformation. Advanced mechanics has a sufficiently large set of self-similar solutions to problems of the dynamics of deformable solids, namely, in nonlinear dynamic theory of elasticity (Kulikovskii and Sveshnikova 1985; Burenin and Lapygin 1986; Agapov et al. 1990; Dudko and Potyanikhin 2008; Burenin et al. 2013; Potianikhin and Dudko 2014) and theory of plasticity (Bleich and Nelson 1966; Baskakov 1982). In the present entry, only elastic self-similar solutions are considered. The laws of propagation of the bulk strains in elastic bodies are in line with those in gas dynamics, and thus have been studied in more detail. Therefore, the laws of propagation of the strains of shape change along the solids will be considered below. In order to exclude in such a propagation, the mutual influence of volume strains and strains of shape change, the simplest self-similar problem of plane waves in an incompressible elastic medium will be analyzed first, and then the peculiarities of the solutions of plane self-similar problems in a compressible elastic medium will be evaluated.

The System of Model Relationships

In the Cartesian rectangular system of Euler spatial coordinates x_i, the dynamics of an elastic compressible medium in the adiabatic approximation is described by the equations

$$\sigma_{ij} = \frac{\rho}{\rho_0}\frac{\partial W}{\partial d_{ik}}\left(\delta_{kj} - 2d_{kj}\right), d_{ij} = \frac{1}{2}\left(u_{i,j} + u_{j,i} - u_{k,i}u_{k,j}\right), \sigma_{ij,j} = \rho\frac{d^2u_i}{dt^2},$$
$$\upsilon_i = \frac{du_i}{dt} = \frac{\partial u_i}{\partial t} + \upsilon_j u_{i,j}, \frac{\rho}{\rho_0} = \left(1 - 2I_1 + 2I_1^2 - 2I_2 - \frac{4}{3}I_1^3 + 4I_1I_2 - \frac{8}{3}I_3\right),$$
$$I_1 = d_{jj},\ I_2 = d_{ij}d_{ji},\ I_3 = d_{ij}d_{jk}d_{ki}. \tag{1}$$

where u_i and υ_i are components of the displacement and velocity vectors, respectively, σ_{ij} and d_{ij} are components of the stress and Almansi strain tensors, respectively, ρ and ρ_0 is the density in the current and free state, respectively.

The set of Eq. (1) is closed one if the elastic potential $W = W(d_{ij})$ (the internal energy divided by ρ_0) will be defined in the deformation region and the functions entering in Eq. (1) are differentiable.

For the compressible elastic medium, the elastic potential could be represented by expanding in series the components of the strain tensor in the vicinity of the free state. The potential of an isotropic material depends on the invariants of the strain tensor

$$W = \frac{\lambda}{2}I_1 + \mu I_2 + \kappa I_1 I_2 + \chi I_1^3 + \eta I_3 + \ldots \tag{2}$$

where the coefficients of expansion λ and μ are the Lame parameters, and κ, χ, η are elastic moduli of the third order.

In the case of an incompressible isotropic elastic medium, when $\rho \equiv \rho_0$, the potential W and the Murnaghan formula (the first relationship of Eq. (1)) could be rewritten in the form

$$\sigma_{ij} = \frac{\partial W}{\partial d_{ik}}\left(\delta_{kj} - 2d_{kj}\right) - p\delta_{ij},$$
$$W = (a - \mu)\, I_1 + aI_2 + bI_1^2 - \kappa I_1 I_2 - \theta I_1^3 + cI_1^4 + dI_2^2 + kI_1^2 I_2 + \ldots. \tag{3}$$

where p is an unknown additional pressure, and a, b, κ, θ, c, d, k are elastic constants of the higher order.

On possible surfaces of discontinuities Σ, the dynamic conditions of compatibility are fulfilled

$$\left[\sigma_{ij}\right]\nu_j = \rho^+\left(\upsilon_j^+\nu_j - G\right)\left[\upsilon_i\right],$$
$$\left[\rho\left(\upsilon_j\nu_j - G\right)\right] = 0. \tag{4}$$

In Eq. (4), square brackets denote the discontinuity in the parameter on the surface of the discontinuity $[f] = f^+ - f^-$, ν_j are components of the unit normal to Σ, G is the velocity of moving Σ, signs « + » and « − » denote the magnitudes of the function f immediately ahead of and behind the wave surface, respectively.

The consequence of the second law of thermodynamics for shock waves in an elastic medium is the thermodynamic condition for the compatibility of discontinuities (Burenin and Chernyshov 1978)

$$\sigma_{ij}^+\left[\upsilon_i\right]\nu_j - \frac{1}{2}\rho\left(\upsilon_j^+\nu_j - G\right)\left[\upsilon_j\right]\left[\upsilon_j\right] + \frac{\rho}{\rho_0}\left(\upsilon_j^+\nu_j - G\right)[W] \geq 0. \tag{5}$$

It is an analogue of the Zemplén theorem in gas dynamics about the impossibility of the existence of shock unloading waves.

Plane One-Dimensional Shock Waves in an Incompressible Medium

Shock Wave Velocities

Consider the propagation of waves in an incompressible elastic medium. In the simplest one-dimensional case, from Eqs. (3) and (4) it follows

$$\sigma_{11} = -p - \sum_{k=1}^{\infty} \beta_k m^k, \quad \sigma_{i1} = u_{i,1} \sum_{k=0}^{\infty} \gamma_k m^k$$
$$(i = 2, 3), \quad m = u_{2,1}^2 + u_{3,1}^2,$$
$$\beta_1 = \mu + a, \quad \gamma_0 = \mu, \quad \gamma_1 = a + b + d + \kappa, \ldots \tag{6}$$

$$[\sigma_{11}] = 0, \quad [\sigma_{i1}] = -\rho^+ G [\upsilon_i],$$
$$[\upsilon_i] = -G\tau_i, \quad \tau_i = [u_{i,1}], \quad [\upsilon_1] = 0. \tag{7}$$

The first equality in Eq. (7) provides the basis for calculating $[p]$ on Σ using the found values of τ_2 and τ_3, and the second equality in Eq. (7) with due account for Eq. (6) leads to the set of equations

$$\tau_i \sum_{k=0}^{\infty} \gamma_k m^k + (u_{i,1} - \tau_i)[m] \sum_{k=1}^{\infty} \gamma_k$$
$$\times \sum_{n=1}^{k} (-1)^n C_k^n m^{k-n} [m]^{n-1} = \rho^+ G^2 \tau_i. \tag{8}$$

The deformed state $u_{i,1} = u_{i,1}^+$ is considered to be known. Then Eq. (8) represents a system of two equations for three unknowns: G, τ_2, and τ_3. Multiplying the first of them ($i = 2$) by τ_3, the second ($i = 3$) by τ_2 and then subtracting one from the other, the solvability condition with respect to τ_2 and τ_3 could be obtained

$$\left(\tau_3 (u_{2,1} - \tau_2) - \tau_2 (u_{3,1} - \tau_3)\right)[m] = 0. \tag{9}$$

Consequently, the plane of discontinuities Σ in τ_2 and τ_3 exists only under condition (9). Let it holds for $[m] \neq 0$. In this case, the plane $\Sigma = \Sigma_1$ occurs to be plane-polarized, on which

$$\frac{u_{3,1}}{u_{2,1}} = \frac{u_{3,1}^+}{u_{2,1}^+} = \frac{u_{3,1}^-}{u_{2,1}^-} = \frac{\tau_3}{\tau_2},$$
$$G = G_1 = \left\{ \rho^{-1} \sum_{k=0}^{\infty} \gamma_k m^k + (\rho\tau_2)^{-1} (u_{i,1} - \tau_i) \right.$$
$$\left. \times [m] \sum_{k=1}^{\infty} \gamma_k \sum_{n=1}^{k} (-1)^n C_k^n m^{k-n} [m]^{n-1} \right\}^{1/2}. \tag{10}$$

Thus, when $u_{2,1} = u_{2,1}^+ \neq 0$ and $u_{3,1} = u_{3,1}^+ = 0$, what could be always easily achieved by an appropriate choice of the coordinate system, then $\tau_2 \neq 0$ and $\tau_3 = 0$ on the plane-polarized discontinuity.

In the case under consideration, on the plane of discontinuities Σ_1 from Eq. (5) at $u_{3,1} = 0$, it follows that

$$\sum_{k=2}^{\infty} \sum_{n=3}^{2k} \left(\frac{n}{3} - 1\right) \frac{2k!(-1)^n}{n!\,(2k-n)!} u_{2,1}^{2k-n} \tau_2^n \geq 0. \tag{11}$$

A sufficient condition for satisfying Eq. (11) is the requirement for $u_{2,1}\tau_2 \leq 0$, i.e., plane-polarized planes of discontinuities, resulting in the further development of preliminary shear deformations, are possible, while unloading planes of discontinuities are thermodynamically impossible.

The second case of satisfying condition (9) is connected with the equality $[m] = 0$. On such a plane of discontinuity $\Sigma = \Sigma_2$, the intensity of the preliminary shear m remains unchanged, but only its direction changes. The plane Σ_2 propagates with the velocity

$$G = G_2 = \left\{ \rho^{-1} \sum_{k=0}^{\infty} \gamma_k m^k \right\}^{1/2}. \tag{12}$$

This plane of discontinuity is an isentropic one. The inequality (Eq. 5) on the surface Σ_2 turns into the identity. Comparison of G_2 with G_1 shows that Σ_1 always precedes Σ_2.

The Problem of the Shear of the Half-Pace Boundary

The aforesaid allows one to formulate and to obtain a solution of the problem of the shock deformation of an incompressible elastic half-space $x_1 > 0$. Assume that the preliminary strains within the half-space are constant and are given by the values of the dependent variables: $u_{2,1} = s_{20}$, $u_{3,1} = s_{30}$, $p = p_0$, and $m_0 = s_{20}^2 + s_{30}^2$. At the moment of time $t = 0$, they change on the boundary plane abruptly up

to the values $u_{2,1}(0,t) = s_{22}$, $u_{3,1}(0,t) = s_{32}$, and $m_2(0,t) = s_{22}^2 + s_{32}^2$, resulting in the corresponding changes of the stresses on the boundary plane $x_1 = 0$. To follow the propagation of the given boundary shock perturbation on the half-space $x_1 > 0$, it is convenient to introduce the following variables: $\xi = x_1/ct$, $u(\xi) = u_2/ct$, $\upsilon(\xi) = u_3/ct$, where $c^2 = \mu/\rho$. Following the equation of motion (1) and considering Eq. (6) yield

$$\begin{cases} A_1 u'' + B\upsilon'' = 0, \\ Bu'' + A_2\upsilon'' = 0; \end{cases} \tag{13}$$

where $A_1 = -\rho c^2\xi^2 + \sum_{k=0}^{\infty} \gamma_k m^k + 2(u')^2 \sum_{k=1}^{\infty} k m^{k-1}$, $A_2 = -\rho c^2\xi^2 + \sum_{k=0}^{\infty} \gamma_k m^k + 2(\upsilon')^2 \sum_{k=1}^{\infty} k m^{k-1}$, and a prime denotes the derivative of the functions with respect to ξ.

The shear intensity m is now a function only of the self-similar variable ξ, since $m = (u')^2 + (\upsilon')^2$. The set of Eq. (13) admits a trivial solution $u' = s_2 = \text{const}$ and $\upsilon' = s_2 = \text{const}$, when its determinant is nonzero. Nontrivial solution of Eq. (13) is possible only under the condition of $A_1A_2 - B^2 = 0$. Direct verification shows that this condition is satisfied if ξ and m are coupled by the relationship

$$\xi^2 = 1 + \left(\rho c^2\right)^{-1} \sum_{k=1}^{\infty} \gamma_k (1 + 2k) m^k. \tag{14}$$

Substituting Eq. (14) into Eq. (13) leads to the relationship $u'/\upsilon' = u_{3,1}/u_{2,1}$, which means that within the domain of a nontrivial solution, the direction of the preliminary shear does not change. Consequently, Eq. (14) is satisfied in the region of a simple Riemann wave, completely corresponding to the plane-polarized shock wave Σ_1. The ahead ξ^+ and back ξ^- fronts of the simple wave are the acceleration discontinuity planes (weak waves), and the variable m decreases in the region of such a simple wave, which corresponds to the relationships characteristic to the gas dynamics.

The boundary impact, resulting in the further development of the shear strains, propagates in an incompressible elastic medium in the form of the shock wave of loading Σ_1, while when it leads to the decrease in the shear strains, the simple wave, bounded by the planes ξ^+ and ξ^-, is generated.

The determinant of the system of Eq. (13) is also equal to zero at

$$\xi^2 = 1 + \left(\rho c^2\right)^{-1} \sum_{k=1}^{\infty} \gamma_k m^k. \tag{15}$$

However, substituting Eq. (15) in Eq. (13) leads to only one magnitude of $\xi = \xi_n$, at which the deformed state could change. Comparison of Eq. (15) with Eq. (12) shows that this corresponds to the plane of discontinuity Σ_2. Thus, the simple wave does not correspond to Σ_2, that is, the direction of the pre-shear could only change abruptly on the plane of discontinuity Σ_2, in so doing $\xi_n < \xi^-$. Consequently, Σ_2 moves more slowly than the back front of the simple wave. Thus, at $m_2 > m_0$, the solution is constructed using two shock waves Σ_1 and Σ_2. The shock wave Σ_1 governs the deformed state: $u_{2,1} = s_{21}$; $u_{3,1} = s_{31}$; $s_{21}^2 + s_{31}^2 = m_2$; $s_{21}/s_{31} = s_{20}/s_{30}$. On the plane of discontinuity Σ_2: $\tau_2 = s_{21} - s_{22} \neq 0$; $\tau_3 = s_{31} - s_{32} \neq 0$, but at the same time $[m] = 0$, i.e., $m^+ = m^- = m_2$. When $m_2 < m_0$, the shock wave Σ_1 should be replaced by the simple wave, on which the variable m varies from the magnitude m_0 to the magnitude m_2. On the plane of discontinuity Σ_2, following the simple wave, the variation of the deformation parameters $u_{2,1} = s_{21}$, $u_{3,1} = s_{31}$ takes place behind the simple wave front, such that $u_{2,1} = s_{22}$ and $u_{3,1} = s_{32}$. Thus, the construction of a closed solution is completed. In case of refusal from the requirement of incompressibility of the medium, the solution of the problem becomes more complicated. Either a quasi-longitudinal shock wave is added under loadings resulting in further compression, or the corresponding simple wave. The plane of discontinuity corresponding to Σ_1 is quasi-transverse one with $[u_{1,1}] \neq 0$, while in the case of the simple wave the values of $u_{1,1}(\xi)$ are changed, and only the discontinuity surface Σ_2 does not lose its properties.

Plane Self-Similar Problems

Problem Formulation

Under the conditions of the plane deformed state, self-similar problems of the nonlinear dynamic theory of elasticity have been considered repeatedly (Burenin and Lapygin 1986; Agapov et al. 1990; Dudko and Potyanikhin 2008; Burenin et al. 2013; Potianikhin and Dudko 2014). As an example, the solution of one of them (Dudko and Potyanikhin 2008) will be considered below in more detail.

Let the plane shock wave Σ_1 (ν_i is the normal to the wave surface) propagate in an undeformed medium and fall at an angle $\beta_1 < 90°$ to the rigidly fixed boundary of the elastic half-space L.

In the chosen rectangular Cartesian coordinate system, the displacement vector is parallel to the coordinate plane Ox_1x_2:

$$u_1 = u_1(x_1, x_2, x_3), \quad u_2 = u_2(x_1, x_2, x_3), \quad u_3 \equiv 0.$$

If the wave intensity $\tau_1 = [u_{\nu,\nu}]$ and, consequently, its velocity G_1 are constant, then the wave pattern consisting of the incident and reflected waves will be unchanged, i.e., it will move parallel to itself with the velocity $S = G_1/\sin\beta_1$ in the x_2-axis direction. This means that the motion of a continuous medium is self-similar, and all parameters of the stress-strain state depend only on the parameter connected with the angle between the boundary plane L and the plane intersecting the x_3-axis. Choosing the variable $\xi = (x_2 - St)/x_1$ as such a parameter, nonzero components of the displacement vector could be represented in the form

$$u_1 = x_1 \cdot F(\xi), \quad u_2 = x_1 \cdot \Phi(\xi). \tag{16}$$

Substituting Eq. (16) in the equation of motion (1) leads to a homogeneous system of ordinary differential equations

$$\begin{cases} A \cdot F''(\xi) + B \cdot \Phi''(\xi) = 0, \\ C \cdot F''(\xi) + D \cdot \Phi''(\xi) = 0, \end{cases} \tag{17}$$

where A, B, C, and D depends on ξ, F, Φ, F', Φ', and elastic moduli of the medium.

The nontrivial solution of Eq. (17) depends on the condition

$$AD - BC = 0. \tag{18}$$

If Eq. (18) is satisfied at a certain value of $\xi = \xi^*$, then the solution corresponds to a shock wave. If Eq. (18) is satisfied within the interval $\xi \in [\xi^+, \xi^-]$, then the solution corresponds to the Riemann wave, and ξ^+ and ξ^- define the position of its ahead and back fronts, respectively.

In the regions of the trivial solution

$$F(\xi) = a\xi + b, \quad \Phi(\xi) = e\xi + f, \quad u_{1,1} = b,$$
$$u_{1,2} = a, \quad u_{2,1} = f, \quad u_{2,2} = e,$$
$$\upsilon_1 = \frac{-Sa}{(1-b)(1-e) - af},$$
$$\upsilon_2 = \frac{-S(e - be + af)}{(1-b)(1-e) - af},$$
$$\frac{\rho}{\rho_0} = (1-b)(1-e) - af,$$
$$d_{11} = b - \frac{1}{2}\left(b^2 + f^2\right), \; d_{12} = \frac{1}{2}(a + f - ab - ef),$$
$$d_{22} = e - \frac{1}{2}\left(a^2 + e^2\right). \tag{19}$$

stresses are expressed in terms of constants of integration a, b, f and e in a more complex way. The region of constant parameters of the stress-strain state of the medium corresponds to the trivial solution.

The consequence of using the system of Eq. (1) (obtained under the assumption of the adiabatic nature of the deformation process) is the non-uniqueness of the problem solution. It turns out that, from a mathematical point of view, different wave patterns could correspond to the same boundary conditions (Fig. 1). One of the ways to define the unique physically correct solution is the simultaneous solution of the problem for all possible statements and their subsequent comparison using two criteria: the thermodynamic compatibility condition (5) and the evolutionary condition of the shock waves.

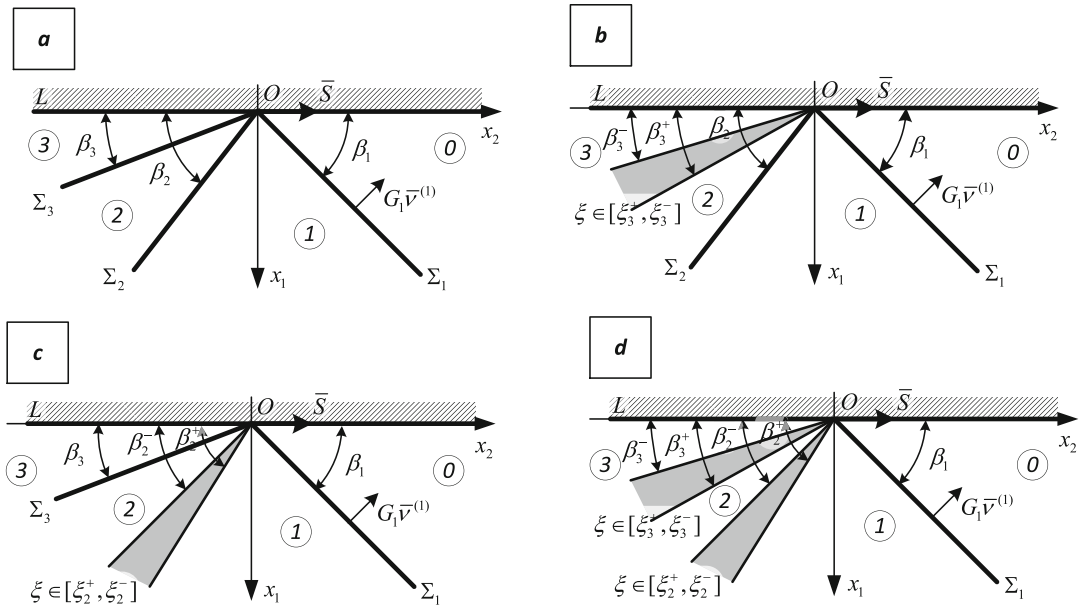

Fig. 1 Mathematically possible wave patterns of reflection of a plane longitudinal shock wave from the rigid boundary of an elastic half-space

The Solution of the Boundary Problem

In zone 1 between the wave Σ_1 and the first of the reflected surfaces, according to the conditions for compatibility of discontinuities

$$a_1 = f_1 = \tau_1 \sin\beta_1 \cos\beta_1, \quad b_1 = \tau_1 \cos^2\beta_1,$$
$$e_1 = \tau_1 \sin^2\beta_1. \tag{20}$$

Hereinafter, the subscript of the integration constants a, b, e, f corresponds to the numbering of the regions in Fig. 1.

The ahead reflected front is either the quasi-longitudinal shock wave Σ_2, the position of which is defined by the value $\xi_2 = -\mathrm{ctg}\beta_2$ (Fig. 1a, b), or the Riemann simple wave $\xi \in [\xi_2^+, \xi_2^-]$ (Fig. 1c, d), making the main contribution to the change in volume strains. Further, after the first wave, either the quasi-transverse shock wave Σ_3 could propagate, corresponding to the value $\xi_3 = -\mathrm{ctg}\beta_3$ (Fig. 1a, c), or centered simple wave $\xi \in [\xi_3^+, \xi_3^-]$ (Fig. 1r, b, d), influencing mainly the produced shear.

Assume that a wave pattern is realized with the shock wave Σ_2 and the Riemann wave $\xi \in [\xi_3^+, \xi_3^-]$.

In order to define all the parameters of the stress-strain state on the shock wave, the continuity of displacements and the fulfillment of the dynamic compatibility conditions (4) should be required:

$$[u_1]|_{\Sigma_2} = 0, \quad [u_2]|_{\Sigma_2} = 0,$$
$$\left[\sigma_{ij}\right]\big|_{\Sigma_2} \nu_j = \rho^+ \left(\upsilon_j^+ \nu_j - G\right) [\upsilon_i]|_{\Sigma_2} = 0,$$
$$i = 1, 2. \tag{21}$$

The solution in the area of the simple wave is constructed by integrating over a self-similar parameter ξ of the set of ordinary differential equations consisting of condition (18) and one of the equalities (Eq. 17):

$$\begin{cases} A\left(\xi, F, \Phi, F', \Phi'\right) \cdot F''(\xi) + B\left(\xi, F, \Phi, F', \Phi'\right) \\ \quad \cdot \Phi''(\xi) = 0, \\ A\left(\xi, F, \Phi, F', \Phi'\right) \cdot D\left(\xi, F, \Phi, F', \Phi'\right) \\ \quad - B\left(\xi, F, \Phi, F', \Phi'\right) \cdot C\left(\xi, F, \Phi, F', \Phi'\right) = 0, \end{cases} \tag{22}$$

The set of Eq. (22) in terms of unknown functions $F(\xi)$ and $\Phi(\xi)$ could not be reduced to the normal

form. For its numerical integration, it is proposed to use an implicit finite-difference scheme with a three-point template with a constant step h. The segment $\xi \in \left[\xi_3^+,\ \xi_3^-\right]$ is divided into n equal parts by points $\xi_{(i)}$, $i = 0 \ldots n$, therefore $F_{(i)}$ and $\Phi_{(i)}$ are values of functions $F(\xi)$ and $\Phi(\xi)$ in the corresponding nodes.

Derivatives of the functions in the internal (i) nodes and boundary points (0) and (n) are defined, respectively, as follows

$$
\begin{aligned}
F'_{(i)} &= \frac{F_{(i+1)} - F_{(i-1)}}{2h}, \\
F''_{(i)} &= \frac{F_{(i+1)} - 2F_{(i)} + F_{(i-1)}}{h^2}, \\
\Phi'_{(i)} &= \frac{\Phi_{(i+1)} - \Phi_{(i-1)}}{2h}, \\
\Phi''_{(i)} &= \frac{\Phi_{(i+1)} - 2\Phi_{(i)} + \Phi_{(i-1)}}{h^2}; \\
F'_{(0)} &= \frac{-3F_{(0)} + 4F_{(1)} - F_{(2)}}{2h}, \\
F'_{(n)} &= \frac{3F_{(n)} - 4F_{(n-1)} + F_{(n-2)}}{2h}, \\
\Phi'_{(0)} &= \frac{-3\Phi_{(0)} + 4\Phi_{(1)} - \Phi_{(2)}}{2h}, \\
\Phi'_{(n)} &= \frac{3\Phi_{(n)} - 4\Phi_{(n-1)} + \Phi_{(n-2)}}{2h}.
\end{aligned}
\tag{23}
$$

At the node $\xi_{(0)} = \xi_3^+$ (at the ahead front of the Riemann wave), $F_{(0)} = a_2\xi_3^+ + b_2$, $\Phi_{(0)} = e_2\xi_3^+ + f_2$, $F'_{(0)} = a_2$, $\Phi'_{(0)} = e_2$, and at the node $\xi_{(n)} = \xi_3^-$ (at the back front), $F_{(n)} = a_3\xi_3^- + b_3$, $\Phi_{(n)} = e_3\xi_3^- + f_3$, $F'_{(n)} = a_3$, $\Phi'_{(n)} = e_3$.

To close the set of equations, the condition of the fixed boundary $[u_1]|_L = [u_2]|_L = 0$ should be used.

Solutions with other wave patterns could be constructed similarly. Having obtained all the mathematically possible solutions of the boundary value problem (four in the general case), the comparison of them with each other should be carried out, with checking two criteria to be satisfied.

First, on each shock wave, the fulfillment of the thermodynamic compatibility condition (5) should be checked. If relation (5) is not satisfied at a certain formulation, then such problem statement should be excluded from the number of possible solutions.

Another limitation on the existence of shock waves is the evolutionary condition.

If as the result of comparing the two solutions, it turns out that the shock wave front occupies an intermediate position inside the fan of the simple wave, then the shock wave is considered to be nonevolutionary, and further the solution with the Riemann wave should be chosen.

In the conventional hydrodynamics, the requirement for the evolutionary nature of shock waves does not lead to any additional limitations in comparison with the condition of the entropy increase: the shock waves assumed by the Zemplén theorem are automatically evolutionary waves (Landau and Lifshitz 1987). For a nonlinearly elastic medium, in the general case, this is not true (Kulikovskii and Sveshnikova 1998). However, for the considered five-constant model of an elastic medium in this and a number of other plane self-similar problems (Dudko and Potyanikhin 2008; Burenin et al. 2013; Potyanikhin and Dudko 2014), the condition of thermodynamic compatibility and the evolutionary condition are equivalent.

As an example, consider a nonlinear elastic medium with the following dimensionless constants: $\lambda/(\lambda + 2\mu) = 0.4$, $\mu/(\lambda + 2\mu) = 0.3$, $\kappa/(\lambda + 2\mu) = -1$, $\chi/(\lambda + 2\mu) = -1.5$, and $\eta/(\lambda + 2\mu) = -2$. Then the values of the parameters of the incident wave could vary in the intervals $0 < \beta_1 \le 80°$, $0.001 \le \tau_1 \le 0.03$. A series of computational experiments allows one to propose that the wave patterns shown in Fig. 1a, c do not occur. The distribution of the stress-strain state parameters typical for a wave pattern with the reflected quasi-longitudinal shock wave Σ_2 and the centered wave $\xi \in \left[\xi_3^+,\ \xi_3^-\right]$ (Fig. 1b) is obtained at $\beta_1 = 30°$ and $\tau_1 = 0.02$ and is shown in Fig. 2.

The quasi-longitudinal shock wave Σ_2 leads to a further compression of the medium. The simple wave, on the contrary, expands the medium ($\rho_{(3)} < \rho_{(2)}$), reducing the level of the

S

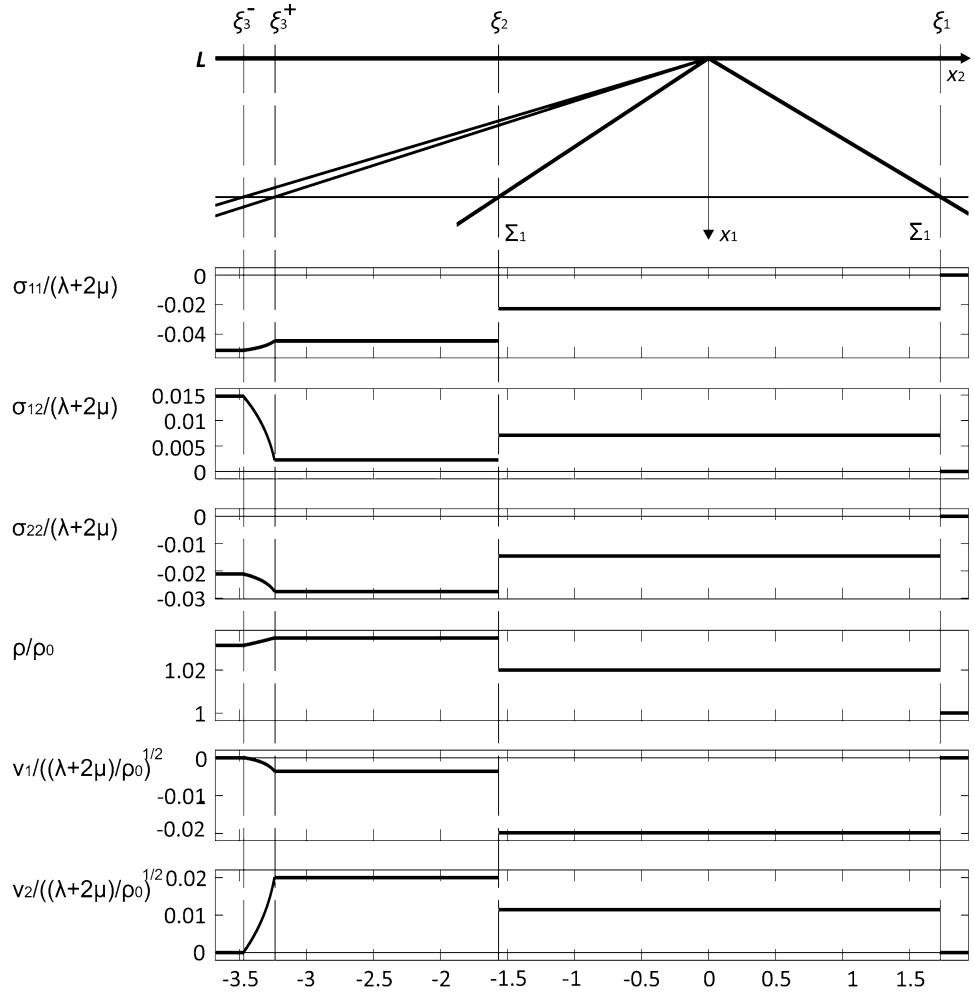

Fig. 2 Stress-strain state corresponding to a wave pattern with a reflected quasi-longitudinal shock wave and Riemann wave

volume strains. There exists some critical angle of incidence β_1^*, depending on τ_1. At $\beta_1 > \beta_1^*$, the quasi-longitudinal shock wave Σ_2 transforms into the simple wave $\xi \in \left[\xi_2^+, \xi_2^-\right]$, i.e., the wave pattern shown in Fig. 1, d is realized. The limit values β_1^* increase with the increase in the wave intensity: at $\tau_1 = 0.01$, $\beta_1^* = 64.54°$, and at $\tau_1 = 0.02$, $\beta_1^* = 65.70°$. On both simple waves, the level of the volume strains decreases ($\rho_{(3)} < \rho_{(2)} < \rho_{(1)}$). For each magnitude τ_1 of the intensity, there exists also a limiting value of the angle of incidence, above which the formulation of the problem in the self-similar formulation becomes impossible.

Cross-References

▸ Ray Expansion Theory

References

Agapov IE, Belogortsev AM, Burenin AA, Rezunov AV (1990) A self-similar problem dealing with the one-dimensional collision of two half spaces of a nonlinear-elastic material. J Appl Mech Tech Phys 30(6):976–980

Baskakov VA (1982) Plastic deformation of a medium upon the interaction of shear shock waves. J Appl Mech Tech Phys 23(2):278–284

Bleich HH, Nelson I (1966) Plane waves in an elastic-plastic half-space due to combined surface pressure and shear. J Appl Mech 33(1):149–158

Burenin AA, Chernyshov AD (1978) Shock waves in an isotropic elastic space. J Appl Math Mech 42(4):758–765
Burenin AA, Lapygin VV (1986) Reflection of a plane longitudinal shock wave of constant intensity from a plane rigid boundary with a nonlinear elastic medium. J Appl Mech Tech Phys 26(5):717–721
Burenin AA, Dudko OV, Potianikhin DA (2013) On the collision of two elastic solids with plane boundaries. Comp Continuum Mech 6(2):157–167
Cherny GG (1988) Gas dynamics. Nauka, Moscow (in Russian)
Dudko OV, Potyanikhin DA (2008) A self-similar problem of nonlinear dynamic elasticity theory concerning the interaction between a longitudinal shock wave and a rigidly clamped boundary. Comp Continuum Mech 1(2):27–37
Godunov SK, Zabrodin AV, Ivanov MI, Kraiko AN, Prokopov GP (1976) Numerical solution of multidimensional problems of gas dynamics. Nauka, Moscow (in Russian)
Kulikovskii AG, Sveshnikova EI (1985) A self-similar problem on the action of a sudden load on the boundary of an elastic half-space. J Appl Math Mech 49(2):214–220
Kulikovskii AG, Sveshnikova EI (1998) Nonlinear waves in elastic media. Moskovskii Litsei, Moscow (in Russian)
Kulikovskii AG, Pogorelov NV, Semenov AY (2001) Mathematical aspects of numerical solution of hyperbolic systems. Chapman & Hall/CRC, London/Boca Raton
Landau LD, Lifshitz EM (1987) Fluid mechanics. Butterworth-Heinemann, Amsterdam
Potianikhin DA, Dudko OV (2014) Self-similar reflection of longitudinal shock wave from free boundary in elastic medium. Adv Mater Res 1040:652–657
Sedov LI (1993) Similarity and dimensional methods in mechanics. CRC Press, Boca Raton

Sensitivity

▸ Sensitivity Analysis in Structural and Multidisciplinary Problems

Sensitivity Analysis

▸ Topology Optimization Based on Explicit Geometry Description

Sensitivity Analysis in Structural and Multidisciplinary Problems

Tomasz Lekszycki[1] and Fabio Di Cosmo[2]
[1]Faculty of Production Engineering, Warsaw University of Technology, Warszawa, Poland
[2]International Research Center M&MoCS, University of L'Aquila, L'Aquila, Italy

Synonyms

Functional derivative; Sensitivity; Variational derivative

Definition

This entry is an introduction to sensitivity analysis and some applications in different topics related to continuum mechanics. Two main approaches, the direct method and the adjoint system one, are presented for both discrete and continuous design parameters. The theoretical investigation is supported by some illustrative examples in order to make more clear the analysis. Some notes on second-order sensitivity analysis are also included.

Introduction

Many continuous systems are characterized by parameters, the values of which deeply affect their resulting mechanical behaviors under different conditions. Therefore, in a smart design procedure, it is very important to fix these values in order to fit a certain desired behavior or at least to investigate what are the effects connected to these modifications. Such a study is called sensitivity analysis: One is considering some objective functions which refer to selected properties of the system under investigation, and sensitivity analysis provides information about their dependence on the design parameters. The aim of this entry is to show how to extract this information:

Firstly the focus will be on continuous design parameters bringing the so-called variational sensitivity analysis, and then the discussion will move to discrete sensitivity analysis, which is a very general case since finite element analysis always provides discrete systems described in terms of stiffness matrices and nodal vectors. In both situations two approaches will be discussed: the direct method and the adjoint system one. The choice between the two usually depends on the ratio of the number of design parameters to the number of objective functions, as it will be shown in the next sections. In order to make more concrete the theoretical discussion, an example coming from structural mechanics will be presented and studied in detail. However, already from these few lines, it is clear that sensitivity analysis can find interesting applications in any field, especially when one is interested in realizing a certain production process and reducing the associated costs. It plays also an important role in formulation of optimization problems; see, e.g., Lekszycki (2018). The main part of the text will be dedicated to the so-called first-order sensitivity analysis. However, a short digression on second-order sensitivity analysis will also be developed: such a study can be useful when more accuracy is required or when the effect of small changes of optimal values is investigated. For the sake of compactness, a selection of the topics related to sensitivity analysis has been performed, and for more details, the interested reader can refer, for instance, to the books (Haftka and Gürdal 2012; Choi and Kim 2006a), which have been the main sources of this entry.

Variational Sensitivity Analysis

As a starting point let $\mathscr{B}_0$ be the reference configuration of a continuous body, described as a compact domain of a three-dimensional Euclidean affine space $\mathscr{E}^3$, with boundary $\partial\mathscr{B}_0 = \Omega_0$. From a kinematical point of view, the placement of the body is represented by the field $\chi : \mathscr{B}_0 \to \mathscr{B} \subset \mathscr{E}^3$, which, for the sake of simplicity, will be supposed twice differentiable. Its mechanical behavior is described as a Cauchy continuum governed, therefore, by the balance equations for mass and momentum (this is just a simplified assumption, since one could consider also higher gradient models, i.e., models in which the energy could depend also on higher gradient of the placement field and not only on its first gradient dell'Isola et al. (2018)). In particular, if one is interested in the equilibrium configurations of the system, they are solutions of the following equation:

$$\nabla\sigma + \mathbf{f} = 0 \tag{1}$$

subject to the boundary conditions:

$$\mathbf{u} = \mathbf{u}_0 \quad \text{on } \Omega_1 \tag{2}$$

$$\mathbf{t} = \sigma \cdot \mathbf{n}_0 = \mathbf{t}^{(e)} \quad \text{on } \Omega_2, \tag{3}$$

where Ω_1 is the part of the boundary where the displacement field, $\mathbf{u}(\mathbf{X}) = \chi(\mathbf{X}) - \mathbf{X}$, is prescribed, whereas Ω_2 is the region of the boundary where the external traction is assigned, and $\Omega_0 = \Omega_1 + \Omega_2$. Here $\mathbf{X}$ denotes the coordinate of a material particle in the reference configuration $\mathscr{B}_0$, and $\mathbf{n}_0$ is the normal vector to the surface Ω_0. In order to explain how the procedure progresses, the relationship between the Green strain tensor E and the displacement vector $\mathbf{u}$ is linearized, that is, $\mathsf{E} = \frac{1}{2}\left((\nabla\mathbf{u})^T + \nabla\mathbf{u}\right)$, so that the previous equation can be written according to the principle of virtual work as follows:

$$\langle \delta\mathsf{E}, \sigma \rangle_{\mathscr{B}_0} = \langle \delta\mathbf{u}, \mathbf{f} \rangle_{\mathscr{B}_0} + \left\langle \mathbf{t}^{(e)}, \delta\mathbf{u} \right\rangle_{\Omega_0}. \tag{4}$$

Here and in the rest of the entry, the brackets $\langle \cdot, \cdot \rangle_{\cdot}$ denote the product between the argument fields integrated over the domain specified by the subscript.

At this point a useful digression can be inserted. Indeed, a wider class of phenomena can be described by means of a linear differential operator L, whose action on the displacement field $\mathbf{u}$ will be denoted by $L(\mathbf{u})$. Therefore, one could replace Eq. 1 by the expression:

$$L(\mathbf{u}) = -\mathbf{f}. \tag{5}$$

Multiplying the above equation by $\delta\mathbf{u}$, which is any kinematically admissible variation of the field $\mathbf{u}$, and integrating over the domain $\mathscr{B}_0$, one obtains the following chain of results:

$$\begin{aligned}&\langle L(\mathbf{u}), \delta\mathbf{u}\rangle_{\mathscr{B}_0} = \langle -\mathbf{f}, \delta\mathbf{u}\rangle_{\mathscr{B}_0}\\ &\left\langle \mathbf{u}, L^a(\delta\mathbf{u})\right\rangle_{\mathscr{B}_0} - \left\langle B(\mathbf{u}), B^a(\delta\mathbf{u})\right\rangle_{\Omega_0}\\ &\qquad = \langle -\mathbf{f}, \delta\mathbf{u}\rangle_{\mathscr{B}_0}\ ,\end{aligned}$$

where L^a represents the adjoint differential operator associated with L and the chosen scalar product. The linear operators B and B^a are defined on the boundary of the body $\mathscr{B}_0$, and they have been obtained after integration by parts. A closer look at the boundary term permits to write it as follows:

$$\begin{aligned}\left\langle B(\mathbf{u}), B^a(\delta\mathbf{u})\right\rangle_{\Omega_0} &= \left\langle B(\mathbf{u}), B^a(\delta\mathbf{u})\right\rangle_{\Omega_1}\\ &\quad + \left\langle B(\mathbf{u}), B^a(\delta\mathbf{u})\right\rangle_{\Omega_2}. \quad (6)\end{aligned}$$

The first term of the right-hand side vanishes because of the imposed boundary conditions on the displacement field, whereas the second term represents the work done by the external traction on the admissible variation $\delta\mathbf{u}$ along the surface Ω_2.

In the case of a linear elastic body, it is possible to write:

$$\begin{aligned}&\langle \nabla\cdot\sigma, \delta\mathbf{u}\rangle_{\mathscr{B}_0} = \langle -\mathbf{f}, \delta\mathbf{u}\rangle_{\mathscr{B}_0}\\ &\left\langle \sigma, \frac{1}{2}\left(\nabla\delta\mathbf{u} + (\nabla\delta\mathbf{u})^T\right)\right\rangle_{\mathscr{B}_0} - \langle \sigma\cdot\mathbf{n}_0, \delta\mathbf{u}\rangle_{\Omega_2}\\ &\qquad = \langle \mathbf{f}, \delta\mathbf{u}\rangle_{\mathscr{B}_0}\\ &\langle \sigma, \delta\mathsf{E}\rangle_{\mathscr{B}_0} = \left\langle \mathbf{t}^{(e)}, \delta\mathbf{u}\right\rangle_{\Omega_2} + \langle \mathbf{f}, \delta\mathbf{u}\rangle_{\mathscr{B}_0}\ ,\end{aligned}$$

which coincides with Eq. (4).

In a big class of sensitivity analysis problems, one is interested in the dependence of a set of objective functionals, K_j, which describe some properties of the body under investigation, with respect to design variables, which in this section will be described as continuous fields $b_p(\cdot)$ (the terms design variables or parameters refer to all the variables which characterize the configurations of the continuous systems and can be modified during the process). From a mathematical point of view, this dependence is quantitatively expressed by means of the first Gateaux derivative of the functionals K_j with respect to design parameters, i.e.:

$$\frac{\delta K_j}{\delta b_p} = \frac{d}{d\epsilon} Kj\left(b_p + \epsilon\delta b_p\right)|_{\epsilon=0}\ .$$

These quantities are usually called first-order sensitivities. For the sake of simplicity, the case of a single objective functional, K, will be analyzed in the rest of the entry. In particular this functional is written as the sum of four terms:

$$\begin{aligned}K = &\int_{\mathscr{B}_0} g_0(\sigma, b_p)dV + \int_{\mathscr{B}_0} g_1(\mathbf{u}, b_p)dV\\ &+ \int_{\partial\mathscr{B}_0^E} g_2(\mathbf{t})d\Sigma + \int_{\partial\mathscr{B}_0^N} g_3(\mathbf{u})d\Sigma, \quad (7)\end{aligned}$$

where the dependence on the design variables $b_p(\cdot)$ is both explicit, in g_0 and g_1, and implicit through the displacement and the stress fields. In order to compute the sensitivity of this functional, there are two approaches which can be adopted: the direct method and the adjoint system one.

Direct Method for Sensitivity Analysis

The direct method for computing first-order design sensitivity is the most intuitive one since it involves the direct evaluation of the sensitivity of the stress and displacement fields. Indeed, assuming that the functions g_0, g_1, g_2, g_3 are all differentiable with respect to their arguments, the first derivative of the functional (7) can be expressed as follows:

$$\begin{aligned}\frac{\delta K}{\delta b_p} = &\int_{\mathscr{B}_0}\left(\frac{\partial g_0}{\partial\sigma}\frac{\delta\sigma}{\delta b_p} + \frac{\partial g_0}{\partial b_p}\right)dV +\\ &+ \int_{\mathscr{B}_0}\left(\frac{\partial g_1}{\partial\mathbf{u}}\frac{\delta\mathbf{u}}{\delta b_p} + \frac{\partial g_1}{\partial b_p}\right)dV + \quad (8)\\ &+ \int_{\partial\mathscr{B}_0^E}\left(\frac{\partial g_2}{\partial\mathbf{t}}\frac{\delta\mathbf{t}}{\delta b_p}\right)d\Sigma +\\ &+ \int_{\partial\mathscr{B}_0^N}\left(\frac{\partial g_3}{\partial\mathbf{u}}\frac{\delta\mathbf{u}}{\delta b_p}\right)d\Sigma. \quad (9)\end{aligned}$$

It can be immediately noticed that, in order to obtain the final result, one needs to know the sensitivities $\frac{\delta \mathbf{u}}{\delta b_p}$ and $\frac{\delta \sigma}{\delta b_p}$. Differentiation of the equilibrium equation (1) with respect to the design variables leads to the following equation for the unknown sensitivity of the stress field:

$$\left\langle \delta \mathsf{E}, \frac{\delta \sigma}{\delta b_p} \right\rangle_{\mathscr{B}_0} = 0. \tag{10}$$

The additional information about the relationship between stress and displacement is given by the constitutive relations and their differentiation with respect to the design variables. In the case of linear elasticity, for instance, one has that:

$$\sigma = C : \mathsf{E}, \tag{11}$$

where C is the elasticity tensor and the symbol: denotes the double contraction between tensors. Therefore, the derivative of the stress tensor can be written as follows:

$$\frac{\delta \sigma}{\delta b_p} = C : \nabla \frac{\delta \mathbf{u}}{\delta b_p} + \frac{\delta C}{\delta b_p} : \mathsf{E}. \tag{12}$$

Substituting Eq. 12 into Eq. 10, one can obtain an equation for the unknown sensitivity $\frac{\delta \mathbf{u}}{\delta b_p}$ which is similar to Eq. 4. The boundary conditions, instead, become:

$$\frac{\delta \mathbf{t}}{\delta b_p} = \frac{\delta \sigma}{\delta b_p} \cdot \mathbf{n} = 0 \quad \text{on } \Omega_2 \tag{13}$$

$$\frac{\delta \mathbf{u}}{\delta b_p} = 0 \quad \text{on } \Omega_1. \tag{14}$$

However, due to the differentiation of the constitutive relationship, some additional terms, which can be interpreted as mechanical loads, have been produced. Eventually it is possible to write the following equations:

$$\begin{aligned} &\left\langle \delta \mathbf{u}, \nabla \left(C : \nabla \frac{\delta \mathbf{u}}{\delta b_p} \right) \right\rangle_{\mathscr{B}_0} - \left\langle \delta \mathbf{u}, \left(C : \nabla \frac{\delta \mathbf{u}}{\delta b_p} \right) \cdot \mathbf{n}_0 \right\rangle_{\Omega_2} \\ &= \left\langle \delta \mathbf{u}, -\nabla \cdot \left(\frac{\delta C}{\delta b_p} : \mathsf{E} \right) \right\rangle_{\mathscr{B}_0} + \left\langle \delta \mathbf{u}, \left(\frac{\delta C}{\delta b_p} : \mathsf{E} \right) \cdot \mathbf{n}_0 \right\rangle_{\Omega_2}, \end{aligned} \tag{15}$$

where the right-hand side contains terms which can be interpreted as additional loads.

By solving these equations, the final expression for the first-order sensitivity of the objective functional K can be eventually computed. However, despite its simplicity, this method requires the solutions of P additional equations, where P is the number of design variables. Consequently its cost increases as this number grows up.

Adjoint System Method for Sensitivity Analysis

The main idea underlying the adjoint system method for the computation of sensitivity of objective functionals consists in expressing the variation of the considered functionals in terms of two families of fields, one referring to a primary continuous system and the other to a fictitious adjoint system. The additional fields for the adjoint system are introduced as Lagrange multipliers (see dell'Isola and Di Cosmo 2018 for an introduction to this method), in an extended objective functional which will include also balance equations and constitutive relations as constraints. In order to make a more direct comparison with the method outlined in the previous subsection, the main focus of the following discussion will be on a continuous body described as a linear elastic material, obeying the equations earlier introduced (see Eqs. 1, 2, 3, and 11). In addition to the aforementioned sources, the interested reader can refer also to Dems and Mroz (1983) and Tortorelli and Michaleris (1994).

Let H be the following extended functional:

$$H = K + \left\langle \mathsf{E}^a, (\sigma - C : \mathsf{E}) \right\rangle_{\mathscr{B}_0} + \left\langle \sigma^a, (\mathsf{E} - \nabla \mathbf{u}) \right\rangle_{\mathscr{B}_0} - \frac{1}{2} \left\langle \sigma, \left(\nabla \mathbf{u}^a + \left(\nabla \mathbf{u}^a \right)^T \right) \right\rangle_{\mathscr{B}_0} + \left\langle \mathbf{f}, \mathbf{u}^a \right\rangle_{\mathscr{B}_0} + \int_{\partial \mathscr{B}_0} \mathbf{t} \cdot \mathbf{u}^a d\Sigma,$$

where the fields with the additional index $(\cdot)^a$ are the fields referring to the adjoint structure and they are independent of the fields without this index, which refer to the primary structure. Therefore, the variation of this functional with respect to design variables gives the following result:

$$\begin{aligned} \frac{\delta H}{\delta b_p} = \int_{\mathscr{B}_0} \Bigg[& \left(\frac{\partial g_0}{\partial \sigma} + \mathsf{E}^a - \frac{1}{2} \left(\nabla \mathbf{u}^a + \left(\nabla \mathbf{u}^a \right)^T \right) \right) \frac{\delta \sigma}{\delta b_p} + \left(\sigma^a - C : \mathsf{E}^a \right) \\ & + \left(\nabla \sigma^a + \frac{\partial g_1}{\partial \mathbf{u}} \right) \frac{\delta u}{\delta b_p} + \mathsf{E}^a : \frac{\partial C}{\partial b_p} : \mathsf{E} + \left(\frac{\partial g_0}{\partial b_p} + \frac{\partial g_1}{\partial b_p} \right) \Bigg] dV \\ & + \int_{\partial \mathscr{B}_0^E} \frac{\delta \mathbf{t}}{\delta b_p} \left(\mathbf{u}^a - \frac{\partial g_2}{\partial \mathbf{t}} \right) d\Sigma + \int_{\partial \mathscr{B}_0^N} \frac{\delta \mathbf{u}}{\delta b_p} \left(\frac{\partial g_3}{\partial \mathbf{u}} - n \cdot \sigma^a \right) d\Sigma \\ & + \int_{\mathscr{B}_0} \left[\frac{\delta \sigma^a}{\delta b_p} \left(E - \frac{1}{2} \left(\nabla \mathbf{u} + (\nabla \mathbf{u})^T \right) \right) + \frac{\delta \mathsf{E}^a}{\delta b_p} (\sigma - C : \mathsf{E}) + \frac{\delta \mathbf{u}^a}{\delta b_p} (\nabla \sigma + \mathbf{f}) \right] dV. \end{aligned} \tag{16}$$

If the primary fields satisfy the equations for the equilibrium of the elastic body, the last line in the above variation can be eliminated. On the other hand, it is possible to choose the adjoint fields such that they satisfy the following system of equations:

$$\begin{aligned} \mathsf{E}^a &= \frac{\partial g_0}{\partial \sigma} - \frac{1}{2} \left(\nabla \mathbf{u}^a + \left(\nabla \mathbf{u}^a \right)^T \right) \\ \sigma^a &= C : \mathsf{E}^a \\ \nabla \sigma^a + \frac{\partial g_1}{\partial \mathbf{u}} &= 0 \\ n \cdot \sigma^a = \frac{\partial g_3}{\partial \mathbf{u}} & \quad \text{on } \partial \mathscr{B}_0^N \\ \mathbf{u}^a = \frac{\partial g_2}{\partial \mathbf{t}} & \quad \text{on } \partial \mathscr{B}_0^E. \end{aligned}$$

It can be immediately noticed that $\frac{\partial g_0}{\partial \sigma}$ plays the role of an initial strain, whereas $\frac{\partial g_3}{\partial \mathbf{u}}$ and $\frac{\partial g_2}{\partial \mathbf{t}}$ provide the two boundary conditions for the adjoint structure.

Inserting the two solutions of the primary and adjoint problems in the expression of the sensitivity, one obtains the final result:

$$\begin{aligned} \frac{\delta H}{\delta b_p} &= \frac{\delta K}{\delta b_p} \\ &= \int_{\mathscr{B}_0} \left[\mathsf{E}^a : \frac{\partial C}{\partial b_p} : \mathsf{E} + \left(\frac{\partial g_0}{\partial b_p} + \frac{\partial g_1}{\partial b_p} \right) \right] dV, \end{aligned} \tag{17}$$

where all the quantities inside the square brackets are known. It is clear from the above discussion that for every additional objective functional one obtains an additional adjoint system. Therefore the number of additional solutions to find increases with the number of objective functionals, whereas the cost of the direct method increases with the number of design variables. Therefore, the choice between the two methods depends on the ratio of the number of objective functionals to the number of design variables.

Discrete Sensitivity Analysis

Many problems in continuum mechanics require the introduction of discretizations and the use of numerical approximation techniques in order to find a solution. If before the recent advances in computer technology these methods were rarely used and other scheme of approximation were widely spread, nowadays numerical methods and discretized systems are strictly connected to the world of continuum mechanics, and computational mechanics is an extremely active research field (see, for instance, Kaessmair and Steinmann 2018; Turco et al. 2016). Finite element methods (see de Borst 2018), in particular, have become a tool which is implemented in all the softwares which are used for solving mechanical problems. Therefore, discrete sensitivity analysis involves many nontrivial situations, being the proper approach after discretization techniques have been applied. Furthermore discrete sensitivity analysis can be helpful to understand how the change of some parameters in a mathematical model could affect a chosen response functional: Such a study is, actually, fundamental to fit the constitutive parameters of suitable mathematical models. Additional references regarding this topic are, for instance, the papers (Van Keulen et al. 2005; Adelman and Haftka 1986).

After applying discretization techniques, the equilibrium equation can be rewritten in terms of the nodal displacement vector $\mathbf{u}$ as follows:

$$\mathsf{K}\mathbf{u} = \mathbf{f}, \tag{18}$$

where K is the stiffness matrix and $\mathbf{f}$ is a vector load. Let $G(\mathbf{u}, \mathbf{b})$ be the objective function for the considered problem. The sensitivity of G with respect to the design variables $\mathbf{b}$ is made up of two terms, the explicit dependence on the variables and the one implicitly contained in the nodal vector $\mathbf{u}$. In formulas one can write:

$$\frac{dG}{db_p} = \frac{\partial G}{\partial b_p} + \frac{\partial G}{\partial \mathbf{u}} \frac{d\mathbf{u}}{db_p}. \tag{19}$$

In order to evaluate the sensitivity of the objective function, the sensitivity $\frac{d\mathbf{u}}{db_p}$ of the nodal vector is required. Also for the discrete analysis, this quantity can be computed using two different approaches, the direct method and the adjoint one.

Direct Method for Discrete Sensitivity Analysis

Differentiating the equilibrium condition Eq. 18 with respect to the design variables, one obtains the following equation:

$$\mathsf{K}\frac{d\mathbf{u}}{db_p} = -\frac{d\mathsf{K}}{db_p}\mathbf{u} + \frac{d\mathbf{f}}{db_p}. \tag{20}$$

If K is invertible (this is true when K is positive definite), the solution to this problem can be easily written as follows:

$$\frac{d\mathbf{u}}{db_p} = \mathsf{K}^{-1}\left(\frac{d\mathbf{f}}{db_p} - \frac{d\mathsf{K}}{db_p}\mathbf{u}\right). \tag{21}$$

Finally, by replacing this expression in Eq. 19, one obtains the following expression for the sensitivity analysis of the function G:

$$\frac{dG}{db_p} = \frac{\partial G}{\partial b_p} + \frac{\partial G}{\partial \mathbf{u}}\mathsf{K}^{-1}\left(\frac{d\mathbf{f}}{db_p} - \frac{d\mathsf{K}}{db_p}\mathbf{u}\right). \tag{22}$$

This very simple method only requires the invertibility of the stiffness matrix (a condition which is ensured in finite element analysis) and the computation of the derivatives of K and G. In particular, these derivatives could be efficiently computed also by means of finite difference methods (this approach is called *semi-analytical method* for sensitivity analysis). However, such an approximation suffers from accuracy problems as several authors have illustrated in the literature. These accuracy problems, in particular, becomes more evident in beam or plate theory, where the error in the semi-analytical method increases as the mesh becomes more refined (Cheng and Olhoff 1993; Pedersen et al. 1989).

Adjoint Method for Discrete Sensitivity Analysis

The adjoint method for the computation of sensitivity $\frac{dG}{db_p}$ is based on the introduction of an

additional field, which plays the role of the displacement nodal vector of an adjoint system. An equilibrium equation is derived for this adjoint response vector, the solution of which will be used for the evaluation of the sensitivity $\frac{dG}{db_p}$.

Let H be the extended function:

$$H = G - \lambda^T(\mathsf{K}\mathbf{u} - \mathbf{f}), \tag{23}$$

where λ is a Lagrange multiplier introduced for the equilibrium constraint. The derivative with respect to the design variables of this extended function will be written as follows:

$$\frac{dH}{db_p} = \frac{\partial G}{\partial b_p} + \frac{\partial G}{\partial \mathbf{u}}\frac{d\mathbf{u}}{db_p} - \frac{d\lambda^T}{db_p}(\mathsf{K}\mathbf{u} - \mathbf{f}) - \lambda^T\left(\mathsf{K}\frac{d\mathbf{u}}{db_p} + \frac{d\mathsf{K}}{db_p}\mathbf{u} - \frac{d\mathbf{f}}{db_p}\right) \tag{24}$$

The nodal vector $\mathbf{u}$ ca be chosen to satisfy the equilibrium condition in Eq. 18, whereas the Lagrange multiplier can be selected in order to eliminate the coefficient of the sensitivity $\frac{d\mathbf{u}}{db_p}$, which means:

$$\mathsf{K}\lambda = \frac{\partial G}{\partial \mathbf{u}}. \tag{25}$$

According to this choice, the following result becomes a straightforward consequence:

$$\frac{dH}{db_p} = \frac{dG}{db_p} = \frac{\partial G}{\partial b_p} - \lambda^T\left(\frac{d\mathsf{K}}{db_p}\mathbf{u} - \frac{d\mathbf{f}}{db_p}\right). \tag{26}$$

It is worth remarking once more that this sensitivity is expressed only in terms of the vectors $\mathbf{u}$ and λ, which can be interpreted, from a mechanical point of view, as nodal vectors of the primary and the adjoint systems.

Nonlinear Sensitivity Analysis

The last part of this section will be devoted to a short digression about sensitivity analysis for nonlinear equilibrium equations (more details can be found in Choi and Kim 2006b; Haftka and Mroz 1986; Mróz and Piekarski 1998; Cardoso and Arora 1988, for instance). In nonlinear mechanical problems, the equilibrium condition can be expressed as follows:

$$q(\mathbf{u}, \mathbf{b}) = \mu\mathbf{f}(\mathbf{b}), \tag{27}$$

where q is the nonlinear internal force, $\mathbf{f}$ is the external load, and μ is a scale parameter which is explicitly used to take into account for the whole loading process, starting at zero load. The objective function remains $G(\mathbf{u}, \mathbf{b})$ and the corresponding sensitivity is written in Eq. 19. In order to evaluate the quantity $\frac{d\mathbf{u}}{db_p}$, one can differentiate Eq. 27 with respect to the design variables, obtaining the following equation:

$$\mathsf{J}\frac{d\mathbf{u}}{db_p} = \mu\frac{d\mathbf{f}}{db_p} - \frac{\partial q}{\partial b_p}, \tag{28}$$

where the tangent stiffness matrix is

$$\mathsf{J} = \frac{\partial q}{\partial \mathbf{u}}.$$

Efficient approximation for the solution $\mathbf{u}$ and the tangent stiffness J can be computed by means of Newton's iterative methods (see Haftka and Gürdal 2012). Therefore one gets:

$$\frac{d\mathbf{u}}{db_p} = \mathsf{J}^{-1}\left(\mu\frac{d\mathbf{f}}{db_p} - \frac{\partial q}{\partial b_p}\right), \tag{29}$$

and this expression can be replaced in Eq. 19 to obtain the final expression:

$$\frac{dG}{db_p} = \frac{\partial G}{\partial b_p} + \frac{\partial G}{\partial \mathbf{u}}\mathsf{J}^{-1}\left(\mu\frac{d\mathbf{f}}{db_p} - \frac{\partial q}{\partial b_p}\right). \tag{30}$$

Concerning the adjoint method, it proceeds as in the previous section, but replacing the stiffness K with the tangent stiffness J. In particular one obtains the following expression:

$$\frac{dG}{db_p} = \frac{\partial G}{\partial b_p} + \lambda^T\left(\mu\frac{d\mathbf{f}}{db_p} - \frac{\partial q}{\partial b_p}\right), \tag{31}$$

where the vector λ is solution of the adjoint linear problem:

$$\mathsf{J}^T\lambda = \frac{\partial G}{\partial \mathbf{u}}.$$

Example: A Vibrating Beam with an Elastic Foundation

In order to show how the procedure can be implemented, an easy example will be investigated in this section. The system under investigation is a linear Euler-Bernoulli beam, clamped at the left end, over a spring foundation under a cyclic load. The equation of motion for the system is:

$$\left[EJy''\right]'' + K(x)y + A\rho\ddot{y} = F_0 e^{i\omega t}, \qquad (32)$$

where $y(x,t)$ is the vertical displacement of the beam. In this example the beam will be a steel beam, so that E and ρ are the Young modulus and the density of steel, respectively. The cross section of the beam is a square with side $a_c = 2\,\text{cm}$ and area $A = 4\,\text{cm}^2$, whereas its length is $L = 2\,\text{m}$. $K(x) = \frac{K_0 x(L-x)}{L^2}$ is the nonuniform stiffness of the spring foundation, with $K_0 = 1\text{e}^6 \frac{\text{N}}{\text{m}^2}$. The amplitude of the load is $F_0 = 10\text{N}$, and its frequency is $\nu = \frac{\omega}{2\pi} = 40\,\text{Hz}$.

The time dependence in the problem can be factorized choosing a solution in the form:

$$y(x,t) = u(x)\text{e}^{i\omega t}, \qquad (33)$$

which gives the following equation for the amplitude $u(x)$:

$$\frac{d^2}{dx^2}\left[EJ\frac{d^2u}{dx^2}\right] + K(x)u - A\rho\omega^2 u = F_0. \quad (34)$$

Let the objective functional be $G = u(s) = \int_0^L \delta(x-s)u(x)dx$ the displacement of the material particle occupying the position $x = s$ in the reference configuration, which is the interval $[0, L]$, and let the design variable be the value of the stiffness $K(x)$ at the point $x = s_0$.

The sensitivity of the functional G with respect to the design variable will be computed using the adjoint method, in order to show the mechanical realization of the adjoint system. Therefore, let H be the extended functional:

$$H = \int_0^L \delta(x-s)u(x)dx - \int_0^L v^a(x)\left(\frac{d^2}{dx^2}\left[EJ\frac{d^2u}{dx^2}\right] + K(x)u - A\rho\omega^2 u - F_0\right),$$

where the boundary term is not included since the adjoint field $v^a(\cdot)$ will satisfy the same boundary conditions as the primary field (even if, in more general situations, the boundary conditions could be different). By performing the variation with respect to the design variable and imposing the constraint in Eq. 34 one gets that the sensitivity $\frac{\delta H}{\delta K(s_0)} = \frac{\delta G}{\delta K(s_0)}$ can be written as follows:

$$\begin{aligned}\frac{\delta H}{\delta K(s_0)} = \int_0^L \Bigg(&\frac{d^2}{dx^2}\left[EJ\frac{d^2v^a}{dx^2}\right] + \\ &+ K(x)v^a - A\rho\omega^2 v^a - \\ &- \delta(x-s)\Bigg)\frac{\delta u}{\delta K(x_0)}dx + \\ &+ u(s_0)v^a(s_0). \end{aligned} \qquad (35)$$

By choosing as adjoint field $v^a(\cdot)$ the solution of the equation:

$$\frac{d^2}{dx^2}\left[EJ\frac{d^2v^a}{dx^2}\right] + K(x)v^a - A\rho\omega^2 v^a = \delta(x-s), \qquad (36)$$

the sensitivity of the objective functional has the following expression:

$$\frac{\delta G}{\delta K(s_0)} = u(s_0)v^a(s_0), \qquad (37)$$

which is written only in terms of the primary and adjoint displacement fields. Let us notice that, in this situation, the adjoint system is again a clamped beam with the same features of the primary one but the load is different: It is a unit dead load at the material point, which in the reference configuration occupies the position $x = s$, which is also the material point involved in the definition of the objective functional $G = u(s)$.

The numerical implementation of the problem has been performed using the weak form package

of the software *Comsol Multiphysics*®, which uses standard finite element methods for solving the problem. Both the primary and the adjoint solutions, $u(\cdot)$ and $v^a(\cdot)$, respectively, have been computed, and the results have been plotted in Figs. 1 and 2. A parametric study has been computed, where both the positions s and s_0 have been varied.

In particular the chart plotted in Fig. 1 shows the value of the sensitivity as a function of the position s_0 for different values of the parameter s in the objective functional. Instead, the diagram in Fig. 2 presents the maximal and minimal values of the sensitivity over the set of possible s_0 as a function of the position s. One can notice that the values of the sensitivity are higher, in absolute value, when s is closer to the right end of the beam, whereas a second lower peak can be observed between the left end and the middle point of the beam. From this example, it is also possible to notice that sensitivity analysis is important also from another point of view: It can be used to obtain the direction of maximal growth, providing useful information for optimization algorithms.

Second-Order Sensitivity Analysis

Under some circumstances, for instance, when one is interested in the sensitivity of an optimal solution, the information coming from the first-order sensitivity analysis is not sufficient, and it is needed the knowledge of second-order derivatives of the objective functional G. In this section the discussion will focus on discrete system, the variational approach being an immediate generalization (the interested reader can refer to Dems and Mroz 1985). The two approaches, the direct method and the adjoint one, are still available, but the adjoint method usually requires a less number of solutions to compute.

Let the discrete system be described by the nodal displacement vector $\mathbf{u}$ obeying the equilibrium condition:

$$\mathsf{K}\mathbf{u} = \mathbf{f}. \tag{38}$$

The objective function is $G(\mathbf{u}, \mathbf{b})$ and its second derivative can be easily computed:

$$\frac{d^2G}{db_p db_r} = \frac{\partial^2 G}{\partial b_p \partial b_r} + \frac{\partial^2 G}{\partial u_j \partial b_r}\frac{du_j}{db_p} + \frac{\partial^2 G}{\partial u_j \partial b_p}\frac{du_j}{db_r} + \\ + \frac{\partial^2 G}{\partial u_j \partial u_l}\frac{du_j}{db_p}\frac{du_l}{db_r} + \frac{\partial G}{\partial u_j}\frac{d^2 u_j}{db_r db_p}. \tag{39}$$

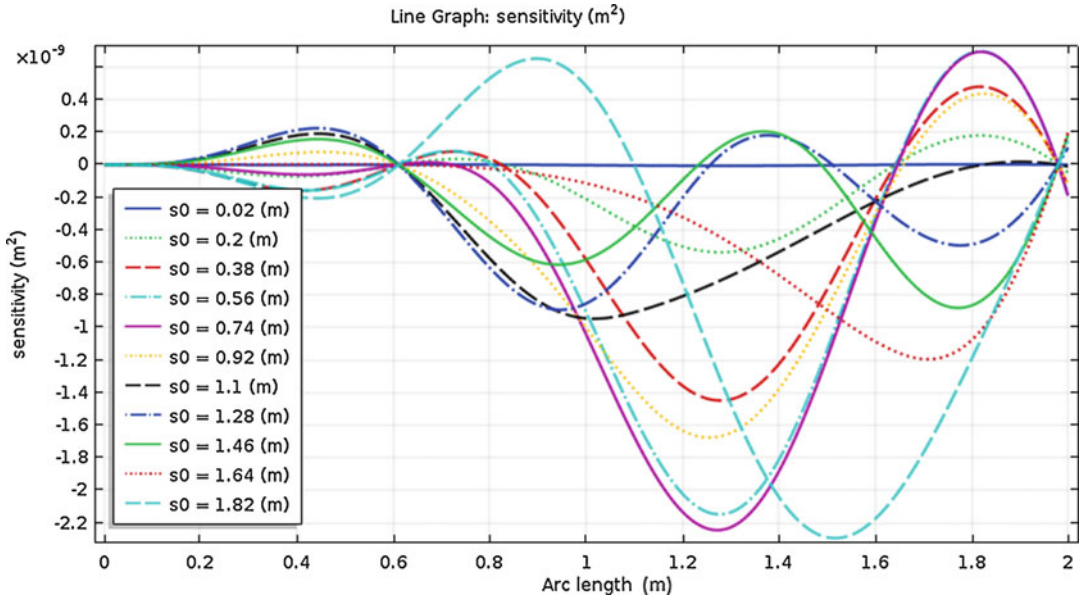

Fig. 1 Plot of the sensitivity $\frac{\delta G}{\delta K(s_0)}$ for some values of the parameter s and with s_0 ranging from $s_0 = 0.1$ to $s_0 = 1.99$ m

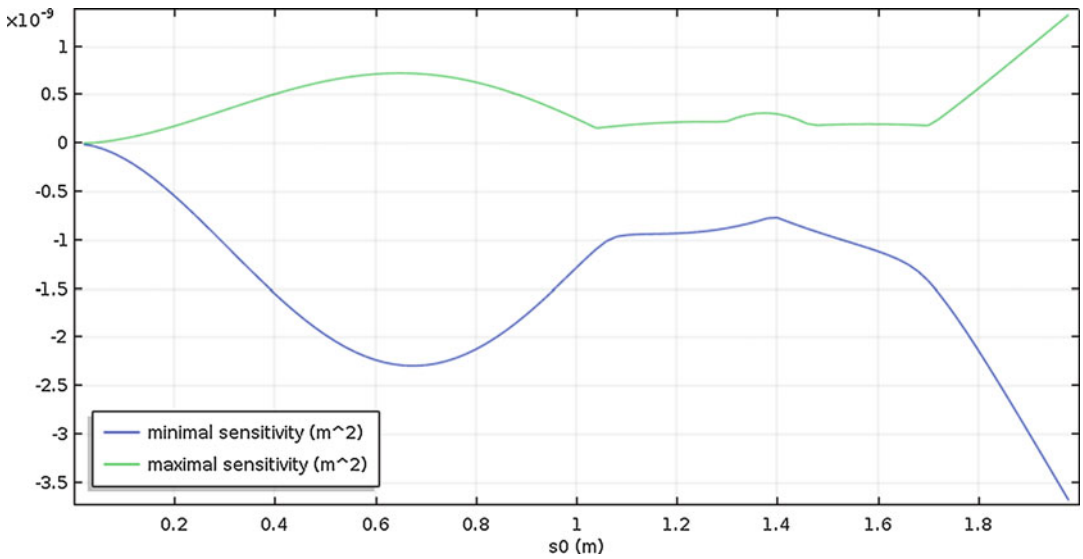

Fig. 2 Plot of the maximal and minimal values of the sensitivity $\frac{\delta G}{\delta K(s_0)}$ as the parameters s varies from $s = 0.1$ to $s = 1.99$ m

This expression involves the unknown second-order sensitivities $\frac{d^2u_j}{db_r db_p}$ which can be computed by deriving twice the equilibrium condition:

$$\mathsf{K}\frac{d\mathbf{u}}{db_p db_r} = \frac{\partial^2 \mathbf{f}}{\partial b_p \partial b_r} + \frac{\partial \mathsf{K}}{\partial b_p}\frac{d\mathbf{u}}{db_r} + \frac{\partial \mathsf{K}}{\partial b_r}\frac{d\mathbf{u}}{db_p} + \\ + \frac{\partial^2 \mathsf{K}}{\partial b_p \partial b_r}\mathbf{u}. \tag{40}$$

If the matrix K is invertible, it is straightforward to find the expression for the unknown $\frac{d^2\mathbf{u}}{db_p db_r}$, and consequently a simple replacement of the solution in Eq. 39 provides the desired expression for the second-order sensitivity of the function G. Despite its simplicity, this method is numerically costly since it grows quadratically in the number of design variables.

A more efficient approach in this case is the hybrid direct-adjoint method. Starting from the expression of the first-order sensitivity analysis:

$$\frac{dG}{db_p} = \frac{\partial G}{\partial b_p} - \lambda^T\left(\frac{d\mathsf{K}}{db_p}\mathbf{u} - \frac{d\mathbf{f}}{db_p}\right), \tag{41}$$

and differentiating again with respect to the design variables, one obtains the following expression for the second-order sensitivity analysis:

$$\frac{d^2G}{db_p db_r} = \frac{\partial^2 G}{\partial b_p \partial b_r} + \frac{\partial G}{\partial b_p \partial u_j}\frac{du_j}{db_r} \\ - \frac{d\lambda^T}{db_r}\left(\frac{\partial \mathsf{K}}{\partial b_p}\mathbf{u} - \frac{d\mathbf{f}}{db_p}\right) + \\ - \lambda^T\left(\frac{\partial \mathsf{K}}{\partial b_p}\frac{d\mathbf{u}}{db_r} + \frac{\partial^2 \mathsf{K}}{\partial b_p \partial b_r}\mathbf{u} \right. \\ \left. - \frac{\partial^2 \mathbf{f}}{\partial b_p \partial b_r}\right).$$

By deriving Eq. 25 with respect to the design variables, one obtains the following equation:

$$\mathsf{K}\frac{d\lambda_j}{db_r} = \frac{\partial^2 G}{\partial u_j \partial u_k}\frac{du_k}{db_r} - \frac{\partial \mathsf{K}_{jl}}{\partial b_r}\lambda_l, \tag{42}$$

which can be replaced in the expression of the second-order sensitivity analysis to write the final result:

$$\frac{d^2G}{db_p db_r} = \frac{\partial^2 G}{\partial b_p \partial b_r} + \frac{\partial G}{\partial b_p \partial u_j}\frac{du_j}{db_r} - \\ - \frac{du_j}{db_r}\frac{\partial^2 G}{\partial u_j \partial u_k}\frac{du_k}{db_p} +$$

$$-\lambda^T\left(\frac{\partial \mathsf{K}}{\partial b_p}\frac{d\mathbf{u}}{db_r}+\frac{\partial \mathsf{K}}{\partial b_r}\frac{d\mathbf{u}}{db_p}+\frac{\partial^2 \mathsf{K}}{\partial b_p \partial b_r}\mathbf{u}-\frac{\partial^2 \mathbf{f}}{\partial b_p \partial b_r}\right).$$

If the sensitivities $\frac{d\mathbf{u}}{db_p}$ are computed by the direct method, all the quantities that appear in the right-hand side of the above expression are known, and this result requires to find P solution of the direct method (where P is the number of design variables) and the adjoint field λ. Therefore, this method is more advantageous with respect to the direct one from the point of view of numerical implementation.

Concluding Remarks

The main aim of this entry is to provide an introduction to the methods of sensitivity analysis for mechanical problems. This introduction, of course, cannot be considered exhaustive since some topics have not been investigated and other ones have been only marginally approached. Therefore, some remarks are required in order to conclude this work.

First of all, even if the entry focused on elasticity, multidisciplinary problems can be treated as well. In particular, many authors extended the methods presented in this entry to coupled systems, like thermoelastic or thermoplastic (see Dems 1987, 1986; Dems and Mroz 1987), or to biological systems (see Coelho et al. 2011), or to thermofluids (see Tortorelli et al. 1991; Smith et al. 1998a). For instance, dealing with solid-acoustic interaction phenomena, it is relevant to study the sensitivity of functionals, like natural frequencies, eigenvectors and amplitudes, or, when the domain is unbounded, energy flux and directivity of the radiation. Indeed, these characteristics of the acoustic vibrations are extremely important in order to study wave propagation or to reduce vibrations of systems (see Christensen et al. 1998a,b).

Another interesting application of sensitivity analysis to multidisciplinary topics is related to the work by Smith et al. In some papers, indeed, sensitivity analysis has been applied to the study of extrusion of melt polymers (see Smith et al. 1998b,c). The motion of the melt polymer is modeled according to Hele-Shaw flow model, and sensitivity analysis is applied to functional like the inlet pressure or the exit velocity, parameters which deeply affect the cost and the quality of the extrusion process.

Even if some topics should need more details, like nonlinear sensitivity analysis and second-order variations, an entire chapter of sensitivity analysis, which is shape sensitivity analysis, has not been discussed, and, consequently, some remarks concerning this field will be added in this concluding section. In shape sensitivity analysis, one is interested in the dependence of objective functionals on the variation of shape of the body which constitutes the system. The main tool that is used to evaluate this variation is the so-called material derivative: Under a shape variation, the particles of the body are transported along a flow, which is parameterized by a time-like parameter τ. The total derivative of a physical quantity ψ with respect to this parameter, computed considering the point x as a material particle moving along the aforementioned flow, is the material derivative $\frac{d\psi}{d\tau}=\frac{\partial\psi}{\partial\tau}+\frac{dx^j}{d\tau}\frac{\partial\psi}{\partial x^j}$, where $\frac{dx^j}{d\tau}$ play the role of generalized velocity fields. Replacing the derivative with respect to design variable with the material derivative abovementioned, one can generalize direct and adjoint methods to this more complex situation. Material derivatives of volume and surface elements can be computed, producing additional terms which involve, for instance, the mean curvature of the boundary. Such a method has been widely studied in literature (see Dems and Mroz 1984; Choi and Kim 2006a), and interesting applications to multiphase problems have been also considered.

Cross-References

- Direct Method of Calculus of Variations in Elasticity
- Variational Methods in Structural Optimization

References

Adelman HM, Haftka RT (1986) Sensitivity analysis of discrete structural systems. AIAA J 24(5): 823–832

Cardoso J, Arora J (1988) Variational method for design sensitivity analysis in nonlinear structural mechanics. AIAA J 26(5):595–603

Cheng G, Olhoff N (1993) Rigid body motion test against error in semi-analytical sensitivity analysis. Comput Struct 46(3):515–527

Choi K, Kim N (2006a) Structural sensitivity analysis and optimization 1: linear systems. Springer Science & Business Media, New York

Choi K, Kim N (2006b) Structural sensitivity analysis and optimization 2: nonlinear systems and applications. Springer Science & Business Media, New York

Christensen S, Sorokin S, Olhoff N (1998a) On analysis and optimization in structural acoustics part I: problem formulation and solution techniques. Struct Optim 16(2–3):83–95

Christensen S, Sorokin S, Olhoff N (1998b) On analysis and optimization in structural acoustics part II: exemplifications for axisymmetric structures. Struct Optim 16(2–3):96–107

Coelho P, Fernandes P, Rodrigues H (2011) Multiscale modeling of bone tissue with surface and permeability control. J Biomech 44(2):321–329

de Borst R (2018) Finite element methods. In: Altenbach H, Öchsner A (eds) Encyclopedia of continuum mechanics. Springer, Berlin/Heidelberg, pp 1–8

dell'Isola F, Di Cosmo F (2018) Lagrange multipliers in infinite-dimensional systems, methods of. In: Altenbach H, Öchsner A (eds) Encyclopedia of continuum mechanics. Springer, Berlin/Heidelberg, pp 1–9

dell'Isola F, Seppecher P, Corte AD (2018) Higher gradient theories and their foundations. In: Altenbach H, Öchsner A (eds) Encyclopedia of continuum mechanics. Springer, Berlin/Heidelberg, pp 1–10

Dems K (1986) Sensitivity analysis in thermal problems I: variation of material parameters within a fixed domain. J Therm Stresses 9(4):303–324

Dems K (1987) Sensitivity analysis in thermal problems II: structure shape variation. J Therm Stresses 10(1):1–16

Dems K, Mroz Z (1983) Variational approach by means of adjoint systems to structural optimization and sensitivity analysis I: variation of material parameters within fixed domain. Int J Solids Struct 19(8):677–692

Dems K, Mroz Z (1984) Variational approach by means of adjoint systems to structural optimization and sensitivity analysis II: structure shape variation. Int J Solids Struct 20(6):527–552

Dems K, Mroz Z (1985) Variational approach to first-and second-order sensitivity analysis of elastic structures. Int J Numer Methods Eng 21(4):637–661

Dems K, Mroz Z (1987) Variational approach to sensitivity analysis in thermoelasticity. J Therm Stresses 10(4):283–306

Haftka R, Gürdal Z (2012) Elements of structural optimization, vol 11. Springer Science & Business Media, Dordrecht

Haftka R, Mroz Z (1986) First-and second-order sensitivity analysis of linear and nonlinearstructures. AIAA J 24(7):1187–1192

Kaessmair S, Steinmann P (2018) Computational mechanics of generalized continua. In: Altenbach H, Öchsner A (eds) Encyclopedia of continuum mechanics. Springer, Berlin/Heidelberg, pp 1–13

Lekszycki T (2018) Variational methods in optimization of structures, Methods of. Springer, Berlin/Heidelberg, pp 1–9

Mróz Z, Piekarski J (1998) Sensitivity analysis and optimal design of non-linear structures. Int J Numer Methods Eng 42(7):1231–1262

Pedersen P, Cheng G, Rasmussen J (1989) On accuracy problems for semi-analytical sensitivity analyses. J Struct Mech 17(3):373–384

Smith D, Tortorelli D, Tucker III C (1998a) Analysis and sensitivity analysis for polymer injection and compression molding. Comput Methods Appl Mech Eng 167(3–4):325–344

Smith D, Tortorelli D, Tucker III C (1998b) Optimal design for polymer extrusion. Part I: sensitivity analysis for nonlinear steady-state systems. Comput Methods Appl Mech Eng 167(3–4):283–302

Smith D, Tortorelli D, Tucker III C (1998c) Optimal design for polymer extrusion. Part II: sensitivity analysis for weakly-coupled nonlinear steady-state systems. Comput Methods Appl Mech Eng 167(3–4):303–323

Tortorelli D, Michaleris P (1994) Design sensitivity analysis: overview and review. Inverse Prob Eng 1(1): 71–105

Tortorelli D, Subramani G, Lu S, Haber R (1991) Sensitivity analysis for coupled thermoelastic systems. Int J Solids Struct 27(12):1477–1497

Turco E, dell Isola F, Cazzani A, Rizzi N (2016) Hencky-type discrete model for pantographic structures: numerical comparison with second gradient continuum models. Zeitschrift für angewandte Mathematik und Physik 67(4):85

Van Keulen F, Haftka R, Kim N (2005) Review of options for structural design sensitivity analysis. Part 1: linear systems. Comput Methods Appl Mech Eng 194: 3213–3243

Series Expansion

▸ Higher Order Theory of Micropolar Curved Rods

Serrations

▸ Avalanches in Solids

Seven- and Twelve-Parameter Shell Finite Element Models

▸ Laminated Composite Elastic Shells, Nonlinear Theory

SH Surface Waves in Solids with Surface Stresses

▸ Anti-plane Surface Waves in Materials with Surface Energy

Shakedown and Plastic Collapse in Plane Stress Problems

Duc-Chinh Pham[1], Canh-Van Le[2], and Trung-Dung Tran[3]
[1]VAST – Institute of Mechanics, Ba dinh, Hanoi, Vietnam
[2]Department of Civil Engineering, International University – VNU HCMC, Ho Chi Minh City, Vietnam
[3]Faculty of Construction and Electricity, Ho Chi Minh City Open University, Ho Chi Minh City, Vietnam

Synonyms

Adaptation (Shakedown)

Definition

Shakedown theory defines the load limits and respective collapse deformation modes for elastic plastic structures under loading cycles. A structure made of elastic plastic material under loading, after an initial stage of possible limited plastic deformation (of finite total plastic dissipation), may eventually shake down to some residual stress state, from which it subsequently responds elastically (hence safely) to the external agencies. Otherwise, the structure is considered as having failed, because of the instantaneous plastic collapse (corresponding to the maximal static load bearing capacity of the structure), or the plastic deformation would accumulate unrestrictively over loading cycles (the mode is called the ratchetting or incremental collapse one), or the plastic deformation should be bounded but vary cyclically and unceasingly (fatigue, cyclic, rotating plasticity, or alternating plasticity collapse).

In principle shakedown incremental checking for a structure can be performed for any sophisticated elastic plastic material model in small or large deformations, following a particular loading history. Powerful shakedown theorems can be constructed for certain classes of elastic plastic materials (Koiter 1963; Pham 2003, 2007, 2008, 2017). The essential advantage of the theorems is their path independence: the theorems determine the time-independent boundary in the loading space, under which a structure is safe regardless of particular loading histories, while the structure fails if the boundary is allowed to be violated unrestrictively. There is a singular point in the theorems because most usual yield conditions, including the Mises and Tresca ones, in the general case do not restrict the hydrostatic stress, while the plastic strain is restricted to be deviatoric, which requires special treatments. However, for many practical thin structures, including the plane stress ones, there is no kinematic restriction in a thickness direction for the hydrostatic stress to build up unrestrictively, and the singularity problem disappears.

Like the plastic limit theorems (the limiting case of the shakedown ones), the shakedown static and kinematic theorems are stated as the nonlinear optimization problems. Second-order cone programming techniques are especially effective in solving the elastic plastic plane stress problems.

Limited Kinematic Hardening Plasticity Theory

Basic assumptions of classical phenomenological plasticity theory and plastic limit and shakedown theorems include the small deformation, the plastic incompressibility, the similarity of the yield stresses in tension and compression, and the rate independence of the plastic stress-strain response ones.

Let $\boldsymbol{\sigma}$, $\boldsymbol{\varepsilon}^p$, $\mathbf{e}^p$ be the real stress, plastic strain, and plastic strain rate tensors and $\boldsymbol{\sigma}^*$ be any allowable stress state (i.e., that within the elastic domain inside the yield surface). The plastic deformation is supposed to follow Hill's principle of maximal dissipation (Koiter 1963; König 1987; Pham 2017).

Maximal Dissipation Hypothesis

$$(\boldsymbol{\sigma} - \boldsymbol{\sigma}^*) : \mathbf{e}^p \geq 0 \quad \text{or} \quad (\boldsymbol{\sigma} - \boldsymbol{\sigma}^*) : d\boldsymbol{\varepsilon}^p \geq 0, \tag{1}$$

which implies normality rule (or associated flow law) for the plastic strain rate and convexity of the yield surface. Stronger Drucker postulate, which implies Hill principle and requires additionally the material to be stable (softening is not allowed, in particular $d\boldsymbol{\sigma} : d\boldsymbol{\varepsilon}^p \geq 0$), can also be assumed.

The general limited kinematic hardening plasticity (the two-yield surface model) is considered, which involves the classical elastic perfectly plasticity as a limiting case. The particular hardening law relating the back stress $\boldsymbol{\alpha}$ to the corresponding plastic deformation $\boldsymbol{\varepsilon}_\alpha^p$ is generally nonlinear and plastic deformation path dependent and needs not to be specified, but the imposing hypotheses on the two-surface plastic hardening are stated as follows (needed for the construction of path-independent shakedown theorems). A representative material element in homogeneous stress-strain state is considered. The size of the yield surface Γ_α, which envelopes the elastic domain $\mathcal{Y}_\alpha$ centered at the (deviatoric) back stress $\boldsymbol{\alpha}$ in the stress space, is determined by the initial yield stress σ_Y^i, in particular for Mises material

$$\|\bar{\boldsymbol{\sigma}} - \boldsymbol{\alpha}\|_\sigma^2 = \frac{3}{2}(\bar{\boldsymbol{\sigma}} - \boldsymbol{\alpha}) : (\bar{\boldsymbol{\sigma}} - \boldsymbol{\alpha}) = (\sigma_Y^i)^2 , \tag{2}$$

where $\bar{\boldsymbol{\sigma}}$ denotes the deviatoric part of the stress tensor $\boldsymbol{\sigma}$. The elasticity domain $\mathcal{Y}_\alpha$ bounded by surface Γ_α is translated in the stress space following its center $\boldsymbol{\alpha}$ without changing size and form. However, the hardening is supported to be limited, and the set of all allowable stresses is restricted by the unmovable ultimate yield surface Γ_u, which encompasses the respective ultimate domain $\mathcal{Y}_u$ and is defined by the ultimate yield stress σ_Y^u, using the Mises criterium

$$\|\bar{\boldsymbol{\sigma}}\|_\sigma^2 = \frac{3}{2}\bar{\boldsymbol{\sigma}} : \bar{\boldsymbol{\sigma}} = (\sigma_Y^u)^2. \tag{3}$$

A picture of the yield surfaces for the material element (under homogeneous stress-strain state) in the deviatoric stress coordinates $\bar{\sigma}_{ij}$ is presented in Fig. 1a, with the origin of the coordinates being the center of the ultimate yield hypersphere $\mathcal{Y}_u$. Since the stress $\boldsymbol{\sigma}$ is bounded by the ultimate surface Γ_u, the domain $\mathcal{Y}_\alpha$ containing the recent state $\boldsymbol{\sigma}$ with back stress at the center cannot lie entirely outside the domain $\mathcal{Y}_u$, and the back stress is automatically bounded above, at most by the surface $\Gamma_{0\alpha}$, as can be seen in Fig. 1a.

The usual normality yield rule is assumed on both yield surfaces Γ_α and Γ_u, but they do not act simultaneously. When the two criteria attained simultaneously (the stress state is on both yield surfaces), the material yields according to that corresponding to the ultimate yield surface. The total plastic strain rate $\mathbf{e}^p$ and plastic strain $\boldsymbol{\varepsilon}^p$ are composed of those two components:

$$\mathbf{e}^p = \mathbf{e}_\alpha^p + \mathbf{e}_u^p, \quad \boldsymbol{\varepsilon}^p = \boldsymbol{\varepsilon}_\alpha^p + \boldsymbol{\varepsilon}_u^p. \tag{4}$$

Strictly Stable Hardening Hypothesis (Pham 2017)

$$d\boldsymbol{\alpha} : d\boldsymbol{\varepsilon}_\alpha^p \geq h_0 d\boldsymbol{\varepsilon}_\alpha^p : d\boldsymbol{\varepsilon}_\alpha^p, \tag{5}$$

where h_0 is some nonvanishing positive value. The condition indicates that the bending angle

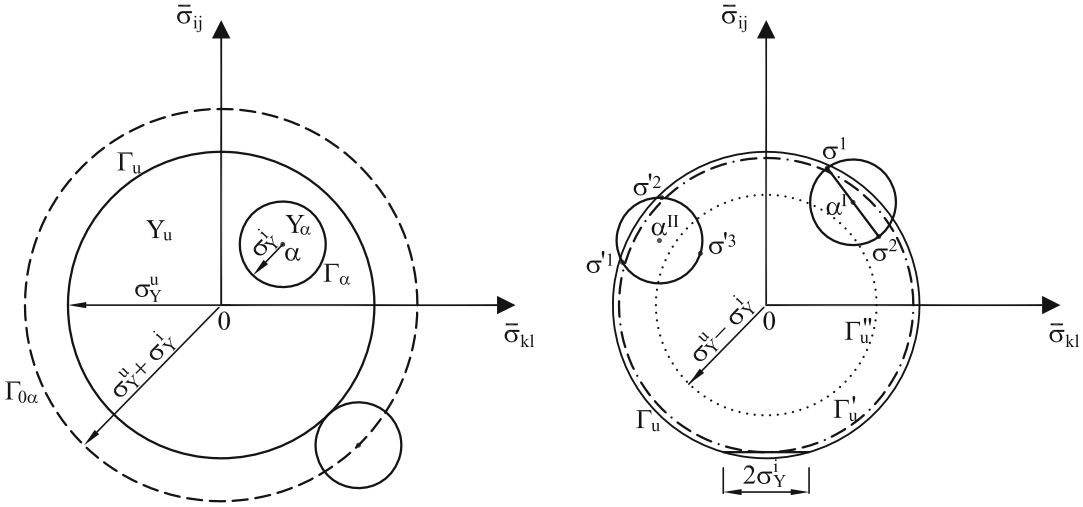

Fig. 1 Yield surfaces in the deviatoric stress coordinates: Γ_u – the ultimate yield surface; Γ_α – the moving inner yield surface centered at $\boldsymbol{\alpha}$ (or $\boldsymbol{\alpha}^I, \boldsymbol{\alpha}^{II}$); $\Gamma_{0\alpha}, \Gamma_u', \Gamma_u''$ – the possible limiting surfaces for the back stress $\boldsymbol{\alpha}$; $\boldsymbol{\sigma}^1, \boldsymbol{\sigma}^2$, or $\boldsymbol{\sigma}'^1, \boldsymbol{\sigma}'^2, \boldsymbol{\sigma}'^3$ – some stress picks on the inner yield surfaces

of the hardening curve against the horizontal strain coordinate (of the strain-stress system of coordinates) in an uniaxial experiment should always be larger than a finite positive value. The hypothesis, together with the two-surface hardening model, implies the upper bound limitation of $\boldsymbol{\varepsilon}_\alpha^p$ (Pham 2017). It is clear that the strict stability here requires more than that of Drucker stability; however, it applies only to $\boldsymbol{\varepsilon}_\alpha^p$, not to $\boldsymbol{\varepsilon}_u^p$ and hence $\boldsymbol{\varepsilon}^p$ generally. Alternatively, the assumption (5) could also be substituted by

$$d\boldsymbol{\sigma} : d\boldsymbol{\varepsilon}_\alpha^p \geq h_0 d\boldsymbol{\varepsilon}_\alpha^p : d\boldsymbol{\varepsilon}_\alpha^p. \tag{6}$$

Positive hysteresis hypothesis (Pham 2007, 2017): For any closed cycle of plastic deformation $\boldsymbol{\varepsilon}_\alpha^p$ [over a period $0 \leq t \leq \theta$, $\boldsymbol{\varepsilon}_\alpha^p(0) = \boldsymbol{\varepsilon}_\alpha^p(\theta)$]

$$\oint \boldsymbol{\alpha} : d\boldsymbol{\varepsilon}_\alpha^p = \int_0^\theta \boldsymbol{\alpha} : \mathbf{e}_\alpha^p dt \geq 0. \tag{7}$$

Note that, generally, it is not required that $\boldsymbol{\alpha}(0) = \boldsymbol{\alpha}(\theta)$. Condition (7) implicates that the loading-unloading cycle should mostly follow clockwise direction along the hysteresis loop, but not anti-clockwise. Instead of (7), it might also be presumed, instead, that

$$\oint \boldsymbol{\sigma} : d\boldsymbol{\varepsilon}_\alpha^p \geq 0. \tag{8}$$

In an uniaxial reversed loading experiment, the Bauschinger effect is observed with perfect elastic behavior intervals (centered at the respective back stress $\boldsymbol{\alpha}$) between the loading and unloading yield points of the size $2\sigma_Y^i$, which shall be referred to as the Bauschinger diameter. For the full meaning of the two-yield surface hardening model, the following crucial assumptions are assumed (Pham 2017).

Multiaxial Bauschinger hypothesis 1: The Bauschinger diameter keeps the same constant value $2\sigma_Y^i$ for reversal loading in any loading direction at any place within the ultimate hypersphere $\mathcal{Y}_u$ of the two-surface hardening assumption.

The translation of the hypersphere $\mathcal{Y}_\alpha$ of Bauschinger diameter $2\sigma_Y^i$ following its center $\boldsymbol{\alpha}$ without changing size and form in the stress space has been assumed for the kinematic hardening

plasticity generally, and this assumption should allow broad possible back stresses $\boldsymbol{\alpha}$:

Multiaxial Bauschinger hypothesis 2: All the back stresses $\boldsymbol{\alpha}$ centered between any two admissible stresses $\boldsymbol{\sigma}^1, \boldsymbol{\sigma}^2$ distanced at Bauschinger diameter $2\sigma_Y^i$ within the ultimate hypersphere $\mathcal{Y}_u$ are admissible. Moreover, any back stress center $\boldsymbol{\alpha}$ of a hypersphere $\mathcal{Y}_\alpha$ uniquely enclosing the cycle stress picks $\boldsymbol{\sigma}'^1, \boldsymbol{\sigma}'^2, \boldsymbol{\sigma}'^3, \ldots$ of a loading process, which belong to $\mathcal{Y}_u$, is admissible. The back stress $\boldsymbol{\alpha}$, if originally positioned otherwise, should converge toward that central point, as the stress cycles are repeated.

Two examples of admissible back stress centers $\boldsymbol{\alpha}^I$ and $\boldsymbol{\alpha}^{II}$ with respective hyperspheres $\mathcal{Y}_\alpha$ are given in Fig. 1b, which may be not enveloped by Γ_u, and illustrate the hypothesis.

The reasonable set $\mathcal{B}$ of possible back stresses $\boldsymbol{\alpha}$, which is – at least – bounded by $\Gamma_{0\alpha}$ (see Fig. 1a), might be the domain enveloped by the set of all possible midpoints of the chords with Bauschinger size $2\sigma_Y^i$ of the ultimate yield surface Γ_u, which is presented as the surface Γ_u' just inside Γ_u in Fig. 1b. The finite set $\mathcal{B}$ need not to be specified in proving the path-independent shakedown theorems.

Shakedown Theorems and Plastic Collapse Modes

Let $\boldsymbol{\sigma}^e(\mathbf{x}, t)$ denote the fictitious elastic stress response of the body V (under the assumption of its perfectly elastic behaviour) to external agencies over a period of time ($\mathbf{x} \in V,\ t \in [0, T]$), called a loading history. The actions of all kinds of external agencies upon V can be expressed explicitly through $\boldsymbol{\sigma}^e$. At every point $\mathbf{x} \in V$, the elastic stress response $\boldsymbol{\sigma}^e(\mathbf{x}, t)$ is confined to a bounded time-independent domain with prescribed limits in the stress space, called a local loading domain $\mathcal{L}_x$. As a field over V, $\boldsymbol{\sigma}^e(\mathbf{x}, t)$ belongs to the time-independent global loading domain $\mathcal{L}$:

$$\mathcal{L} = \{\boldsymbol{\sigma}^e \mid \boldsymbol{\sigma}^e(\mathbf{x}, t) \in \mathcal{L}_x,\ \mathbf{x} \in V,\ t \in [0, T]\}. \tag{9}$$

In the spirit of shakedown theorems, the bounded loading domain $\mathcal{L}$, instead of a particular loading history $\boldsymbol{\sigma}^e(\mathbf{x}, t)$, is given a priori. Shakedown of a body in $\mathcal{L}$ means it shakes down for all possible loading histories $\boldsymbol{\sigma}^e(\mathbf{x}, t) \in \mathcal{L}$.

Let k_s denote the shakedown safety factor: at $k_s > 1$ the structure will shake down, while it will not at $k_s < 1$, and $k_s = 1$ defines the boundary of the shakedown domain.

Shakedown static theorem (Pham 2007, 2017)

$$k_s = \min\{\bar{U}, \bar{C}\}, \tag{10}$$

where

$$\bar{U} = \sup_{\boldsymbol{\rho} \in \mathcal{R}} \{\, k \mid k(\boldsymbol{\rho} + \boldsymbol{\sigma}^e) \in \mathcal{Y}_u,\ \forall \boldsymbol{\sigma}^e \in \mathcal{L}\}, \tag{11}$$

$$\bar{C} = \sup_{\boldsymbol{\rho}'} \{\, k \mid k(\boldsymbol{\rho}' + \boldsymbol{\sigma}^e) \in \mathcal{Y}_i,\ \forall \boldsymbol{\sigma}^e \in \mathcal{L}\}, \tag{12}$$

$\mathcal{R}$ is the set of admissible time-independent self-equilibrated residual stress fields $\boldsymbol{\rho}(\mathbf{x})$ that satisfy homogeneous equilibrium equations on V; $\boldsymbol{\rho}'$ is a time-independent stress field that is not requied to be self-equilibrated; $\mathcal{Y}_u$ designates the elastic domain in the stress space that is bounded by the yield surface determined by the ultimate yield stress σ_Y^u, while $\mathcal{Y}_i$ is the respective domain bounded by the yield surface determined by the initial yield stress σ_Y^i.

In the case $\sigma_Y^i = \sigma_Y^u = \sigma_Y$, statement (11) leads to the classical shakedown static theorem for perfectly plastic body: at $\bar{U} > 1$ (safe), sum of the time-independent residual stress $\boldsymbol{\rho}$ and the elastic stress $\boldsymbol{\sigma}^e$ over the whole body is in a safe state defined by the yield surface $\mathcal{Y}_u$, while at $\bar{U} < 1$ (unsafe) no such residual stress should exist. Statement (12) verifies just the possibility of the bounded cyclic plasticity mode determined by the yield stress σ_Y^i: if the range of the varying part of the stress $\boldsymbol{\sigma}^e$ (from the static part $\boldsymbol{\rho}'$) everywhere inside the body should be smaller than the size of the yield surface $\mathcal{Y}_i$ (safe with respect to the mode) or not (unsafe).

In plane stress problems, it is presumed that $\sigma_{33} = \sigma_{31} = \sigma_{32} = 0$, and subsequently $\varepsilon_{31} = \varepsilon_{32} = 0$; also $\sigma^e_{33} = \sigma^e_{31} = \sigma^e_{32} = 0$. The plastic incompressibility implies $\varepsilon^p_{33} = -\varepsilon^p_{11} - \varepsilon^p_{22}$. The yield condition (3) has the particular expression for Mises material

$$\sigma^2_{11} + \sigma^2_{22} - \sigma_{11}\sigma_{22} + 3\sigma^2_{12} = (\sigma^u_Y)^2, \quad (13)$$

(it is obvious that all the components of the stresses are bounded by the yield condition in the case – in contrast with the general three-dimensional case where the hydrostatic stress is unlimited by Mises yield condition), while the dissipation function has the particular expression for Mises material

$$D(\mathbf{e}^p) = \boldsymbol{\sigma}^e : \mathbf{e}^p = \sqrt{2/3}\sigma_Y(\mathbf{e}^p : \mathbf{e}^p)^{1/2}$$
$$= \frac{2}{\sqrt{3}}\sigma_Y[(e^p_{11})^2 + (e^p_{22})^2$$
$$+ e^p_{11}e^p_{22} + e^p_{12}e^p_{12}]^{1/2}, \quad (14)$$

which is clearly a positive quadratic form of the two-dimensional plastic strain rate components that is needed for application of second-order cone programming techniques to solve the optimization problem based on the kinematic theorem that followed.

Shakedown kinematic theorem (Pham 2007, 2017)

$$k_s^{-1} = \max\{U, C\}, \quad (15)$$

where

$$U = \sup_{\mathbf{e}^p \in \mathcal{A}; \boldsymbol{\sigma}^e \in \mathcal{L}} \frac{\int_0^T dt \int_V \boldsymbol{\sigma}^e : \mathbf{e}^p dV}{\int_0^T dt \int_V D_u(\mathbf{e}^p) dV}, \quad (16)$$

$$C = \sup_{\mathbf{x} \in V; \boldsymbol{\sigma}^e \in \mathcal{L}; \hat{\mathbf{e}}^p; \boldsymbol{\rho}'} \frac{(\boldsymbol{\sigma}^e + \boldsymbol{\rho}') : \hat{\mathbf{e}}^p}{D_i(\hat{\mathbf{e}}^p)}, \quad (17)$$

$\mathcal{A}$ is the set of compatible-end-cycle plastic strain rate fields $\mathbf{e}^p$ over the time cycles $0 \le t \le T$:

$$\mathcal{A} = \{\mathbf{e}^p \mid \boldsymbol{\varepsilon}^p = \int_0^T \mathbf{e}^p dt \in \mathcal{C}\}; \quad (18)$$

$\mathcal{C}$ is the set of compatible plastic strain increment fields on V; $\hat{\mathbf{e}}^p$ and $\boldsymbol{\rho}'$ are plastic strain rate and time-independent stress fields that are not required to satisfy any compatibility and equilibrium constraints, respectively; $D_u(\mathbf{e}^p)$ and $D_i(\mathbf{e}^p)$ are the dissipation functions with σ^u_Y and σ^i_Y taking the places of σ_Y, respectively.

In the case $\sigma^i_Y = \sigma^u_Y = \sigma_Y$, statement (16) leads to the classical shakedown kinematic theorem for perfectly plastic body: at $U < 1$ (safe), the internal plastic dissipation capacity of the body is greater than the possible mechanical work of the external agencies, while at $U > 1$ (unsafe), the reverse is true. Statement (17) verifies just the possibility of the bounded cyclic plasticity mode determined by the yield stress σ^i_Y: if the range of the varying part of the stress $\boldsymbol{\sigma}^e$ around the static part $\boldsymbol{\rho}'$ everywhere inside the body should be smaller than the size of the yield surface $\mathcal{Y}_i$ (safe with respect to the mode) or not (unsafe).

In summary, statements (11) and (16) are identical to those of the shakedown static and kinematic theorems for elastic perfectly plastic material with the (ultimate) yield stress σ^u_Y, while statements (12) or (17) are just expressions of the bounded cyclic plasticity mode determined by the (initial) yield stress σ^i_Y. In contrast to the global mode (11) involving the self-equilibrated residual stress field $\boldsymbol{\rho}$ over V [or (16) involving the end-cycle-compatible plastic strain rate field $\mathbf{e}^p$ over V], the mode (12) [or (17)] is local and can be checked at every point $\mathbf{x} \in V$ separately. At $\bar{U} > \bar{C}$ of criterion (10) [or $U < C$ of criterion (15)], the nonshakedown collapse mode is cyclic plasticity; otherwise the incremental plasticity collapse mode prevails.

For applications, the following reduced kinematic theorem is useful (Pham and Stumpf 1994; Pham 2003, 2008)

Reduced kinematic theorem

$$k_s^{-1} \geq \hat{k}_s^{-1} = \max\{I, A\}, \tag{19}$$

$$I = \sup_{\boldsymbol{\sigma}^e \in \mathcal{L}; \boldsymbol{\varepsilon}^p \in \mathcal{C}} \frac{\int_V \max_{t_x} [\boldsymbol{\sigma}^e(\mathbf{x}, t_x) : \boldsymbol{\varepsilon}^p(\mathbf{x})] dV}{\int_V D_u(\boldsymbol{\varepsilon}^p) dV}, \tag{20}$$

where

$$A = \sup_{\mathbf{x} \in V; \boldsymbol{\sigma}^e \in \mathcal{L}; \hat{\boldsymbol{\varepsilon}}^p; t_1, t_2} \frac{[\boldsymbol{\sigma}^e(\mathbf{x}, t_1) - \boldsymbol{\sigma}^e(\mathbf{x}, t_2)] : \hat{\boldsymbol{\varepsilon}}^p(\mathbf{x})}{2D_i(\hat{\boldsymbol{\varepsilon}}^p)}, \tag{21}$$

the latest problem (21) can be solved explicitly for Mises material ($\bar{\sigma}^e$ is the deviatoric part of σ^e):

$$A = \max_{\mathbf{x} \in V; t, t'; \boldsymbol{\sigma}^e \in \mathcal{L}} \frac{\sqrt{[\bar{\boldsymbol{\sigma}}^e(\mathbf{x}, t) - \bar{\boldsymbol{\sigma}}^e(\mathbf{x}, t')] : [\bar{\boldsymbol{\sigma}}^e(\mathbf{x}, t) - \bar{\boldsymbol{\sigma}}^e(\mathbf{x}, t')]}}{2\sqrt{\frac{2}{3}}\sigma_Y^i}. \tag{22}$$

The reduced kinematic theorem (19), (20), (21), and (22) is simpler than the kinematic theorem (15), (16), and (17). In particular, as the incremental collapse criterion (20) is compared to the criterion (16), the incremental collapse mode (20) does not involve time integrals and has the expression almost as simple as that of the respective plastic limit kinematic theorem, with only the difference that the underintegral maximum operation over time parameter t is taken at every point $\mathbf{x} \in V$ separately, which makes the incremental collapse criterion (20) more conservative than the plastic limit one (Pham and Stumpf 1994; Pham 2003). Hence available kinematic methods of plastic limit analysis can be modified to be used to solve problem (20). Meanwhile, the simple expression (21) or solution (22), measuring the size of change of the stresses in alternating directions against the diameter of the yield surface, indicates the alternating plasticity collapse mode. For a broad class of practical problems, where the components of plastic deformations at every point inside a structure should change proportionally during loading cycles, the exact equality $k_s = \hat{k}_s$ has been proved. Generally $\hat{k}_s$ is expected to provide a very good upper bound estimate, if not the exact value, of k_s. Indeed, $k_s = \hat{k}_s$ for most practical examples considered. Still, certain sophisticated structure and loading program have been constructed in Le et al. (2016) to exhibit the strict inequalities $k_s < \hat{k}_s$ and $A > C$, though the differences are small. The question if $k_s^{-1} = \max\{I, C\}$ still remains an open problem.

Examples of Application

Besides the semi-analytical solutions of shakedown problems for certain simple structures (König 1987; Pham and Stumpf 1994; Pham 2014, etc.), numerical finite element method has been developed to solve certain, mostly two-dimensional plane stress, plastic limit and shakedown problems (Belytschko 1972; Weichert and Gross-Weege 1988; Gross-Weege 1997; Zhang et al. 2002; Zhang and Raad 2002; Garcea et al. 2005; Tran et al. 2010; Nguyen-Xuan et al. 2012, etc.).

For engineering applications, the shakedown theorems for elastic perfectly plastic structures (11) and (16) lead to the finite element large-scale nonlinear convex optimization problems with large numbers of variables and constraints. Direct iterative optimization algorithms have been developed to provide solution of such the nonlinear programming, where the primal-dual interior-point method (Andersen et al. 2001, 2003) has

been found to be especially efficient and robust. The algorithm has been extended to both static and kinematic shakedown analysis problems (Vu et al. 2004; Bisbos et al. 2005; Makrodimopoulos 2006; Weichert and Simon 2012; Simon 2013; Tran et al. 2014; Le et al. 2016).

An effective approach has been developed to solve numerically the incremental plasticity collapse mode (20) in Tran et al. (2014) and Le et al. (2016), though a general appropriate direct algorithm of solution is still awaited.

The local bounded cyclic mode (12) of the static theorem has a form of the smallest enclosing ball problem (Cheng et al. 2006; Nam et al. 2012), for which majorization-minimization principle and Nesterov smooth algorithm can be applied. The algorithm has been implemented successfully for shakedown analysis in Le et al. (2016).

Example 1 (Square plate with a circular hole (Tran et al. 2014)) The first example deals with a square plate with central circular hole, which is subjected to quasi-static biaxial uniform loads (Fig. 2)

$$0.4p_1 \le p_1' \le p_1, \quad 0.4p_2 \le p_2' \le p_2. \quad (23)$$

Due to symmetry, only the upper-right quarter of the plate is modeled, and symmetry conditions are enforced on the left and bottom edges. The input data was assumed as follows: $E = 2.1 \times 10^5$. MPa, $\nu = 0.3$, $L = 10$ m, $D/L = 0.2$, and $\sigma_Y = 200.$ MPa. $\sigma_Y^u = \sigma_Y^i = \sigma_Y$ is assumed, which corresponds to the elastic-perfectly plastic case. Graphics of the collapse curves are presented in Fig. 3. As p_1/σ_Y increases from 0.4, the nonshakedown mode switches from the incremental plasticity collapse mode to the alternating plasticity one and vice versa, at certain values of the external load limits; the incremental plasticity collapse curve $I = 1$ of Eq. (20) does not coincide with the plastic limit ones. The lower envelope of the incremental plasticity collapse $I = 1$ of Eq. (20) and alternating plasticity collapse $A = 1$ of Eq. (22) curves agrees with the result $k_s = U = 1$ of direct application of Koiter's theorem (16), using FEM-DUAL method of Vu et al. (2004). In the case of hardening plasticity material, the alternating plasticity collapse curve should be lowered according to the relation σ_Y^i/σ_Y (assuming $\sigma_Y^u = \sigma_Y$). Numerical application of the static theorem (10) yields the same results as those of the kinematic theorem (15) (Le et al. 2016).

Example 2 (Grooved rectangular plate (Tran et al. 2014)) A grooved rectangular plate subjected to in-plane tension p_N, and bending p_M, as shown in Fig. 4, is considered. The load domain is given by

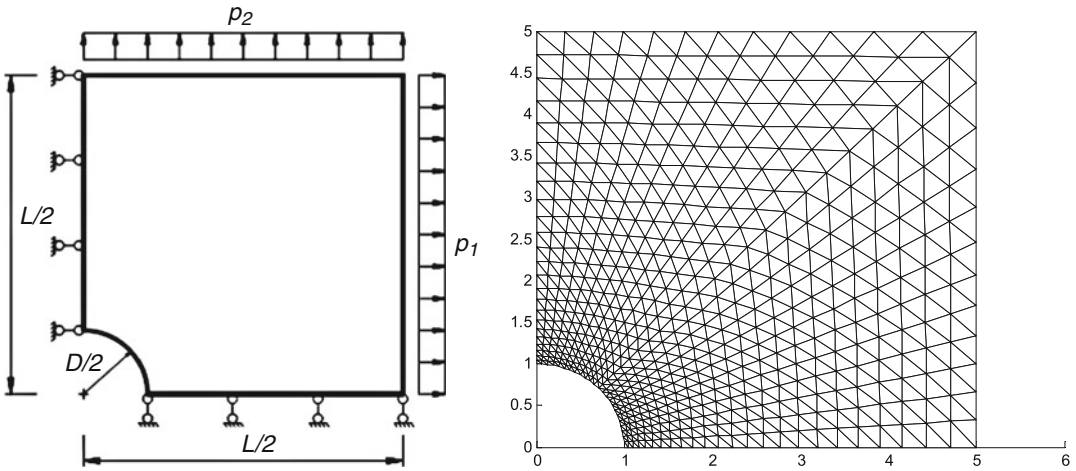

Fig. 2 The upper-right quarter of the square plate with a circular hole subjected to quasi-static biaxial uniform loads, and a finite element mesh

S

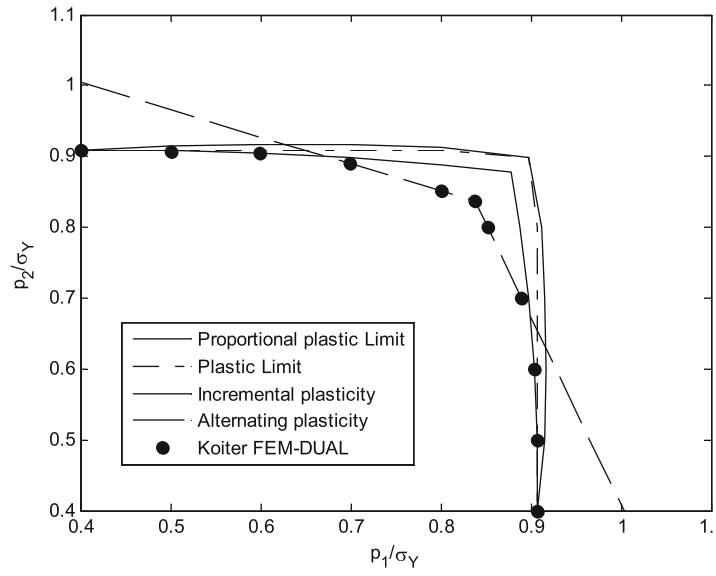

Fig. 3 The incremental plasticity collapse curve $I = 1$, alternating plasticity collapse curve $A = 1$, proportional plastic limit curve, plastic limit curve, and nonshakedown curve using FEM-DUAL method, for the square plate with a circular hole subjected to biaxial uniform loads $0.4p_1 \le p_1' \le p_1,\ 0.4p_2 \le p_2' \le p_2$

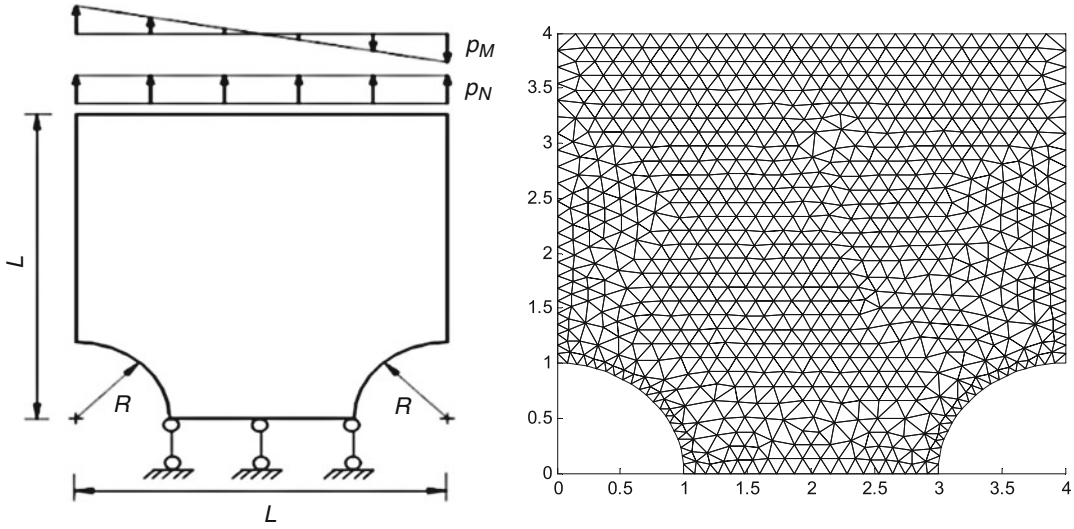

Fig. 4 A grooved rectangular plate subjected to varying tension and bending and a finite element mesh

$$0.035p_N \le p_N' \le p_N,$$
$$0.035p_M \le p_M' \le p_M. \tag{24}$$

Graphics of the collapse curves are projected in Fig. 5. As p_M/σ_Y increases from 0.035, the nonshakedown mode switches from the alternating plasticity collapse mode to the incremental plasticity one, at about the middle of the range; the incremental plasticity collapse curve $I = 1$ lies strictly below the plastic limit curve, the latter coincides with the proportional plastic limit one. The lower envelope of the incremental plasticity collapse $I = 1$ and alternating plasticity collapse $A = 1$ curves also agrees with the result $k_s = U = 1$ of direct application of Koiter's theorem, using FEM-DUAL method.

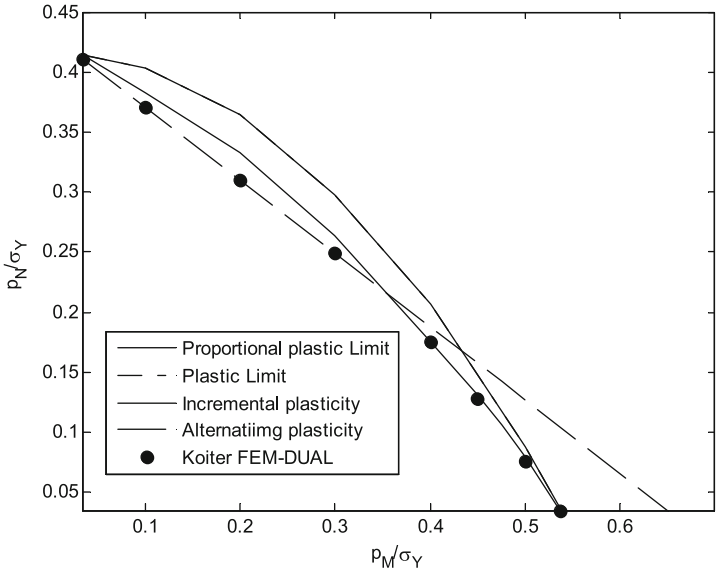

Fig. 5 The incremental plasticity collapse curve $I = 1$, alternating plasticity collapse curve $A = 1$, proportional plastic limit curve (coincides with the plastic limit one), and nonshakedown curve using FEM-DUAL method, for the grooved rectangular plate subjected to varying tension and bending

Initial Yield Stress

The initial yield stress σ_Y^i defining the cyclic or alternating plasticity collapse mode and the ultimate yield stress σ_Y^u determining the incremental collapse one are two basic plastic parameters for shakedown safety assessment of elastic plastic structures under variable and cyclic loads. Plastic deformation often starts from microscopic through mesoscopic to macroscopic scales without clear boundary. For high-cycle processes, σ_Y^i should be taken as small as the fatigue limit, since it defines that mode of collapse. For other ranges of cycles, σ_Y^i can be given higher values according to the respective fatigue curve. That fact is important for practical dynamic loading, where the number of loading cycles can be high (Pham 2007, 2008, 2010).

Cross-References

- ▸ Finite Element Methods
- ▸ Koiter, Warner Tjardus
- ▸ Limit Analysis of Plates

Acknowledgements Pham DC is supported by VAST Project NCVCC03.01/18-18 and NAFOSTED Project 107.02-2018.15.

References

Andersen KD, Christiansen E, Overton ML (2001) An efficient primal-dual interior-point method for minimizing a sum of Euclidean norms. SIAM J Sci Comput 22:243–262

Andersen ED, Roos C, Terlaky T (2003) On implementing a primal-dual interior-point method for conic quadratic programming. Math Prog 95:249–277

Belytschko T (1972) Plane stress shakedown analysis by finite elements. Int J Mech Sci 14:619–625

Bisbos CD, Makrodimopoulos A, Pardalos PM (2005) Second order cone programming approaches to static shakedown analysis in steel plasticity. Optim Meth Softw 20:25–52

Cheng D, Hu X, Martin C (2006) On the smallest enclosing balls. Commun Inf Syst 6:137–160

Garcea G, Armentano G, Petrolo S, Casciaro R (2005) Finite element shakedown analysis of two-dimensional structures. Int J Numer Method Eng 63:1174–1202

Gross-Weege J (1997) On the numerical assessment of the safety factor of elastic-plastic structures under variable loading. Inter J Mech Sci 39:417–433

Koiter WT (1963) General theorems for elastic-plastic solids. In: Sneddon IN, Hill R (eds) Progress in solids mechanics. North-Holland, Amsterdam, pp 165–221

König A (1987) Shakedown of elastic-plastic structures. Elsevier, Amsterdam

Le VC, Tran TD, Pham DC (2016) Rotating plasticity and nonshakedown collapse modes for elastic-plastic bodies under cyclic loads. Int J Mech Sci 111–112: 55–64

Makrodimopoulos A (2006) Computational formulation of shakedown analysis as a conic quadratic optimization problem. Mech Res Commun 33:72–83

Nam NM, An NT, Salinas J (2012) Applications of convex analysis to the smallest intersecting ball problem. J Convex Anal 19:497–518
Nguyen-Xuan H, Rabczuk T, Nguyen-Thoi T, Tran TN, Nguyen-Thanh N (2012) Computation of limit and shakedown loads using a node-based smoothed finite element method. Int J Numer Methods Eng 90: 287–310
Pham DC (2003) Shakedown theory for elastic-perfectly plastic bodies revisited. Int J Mech Sci 45:1011–1027
Pham DC (2007) Shakedown theory for elastic plastic kinematic hardening bodies. Int J Plast 23:1240–1259
Pham DC (2008) On shakedown theory for elastic-plastic materials and extensions. J Mech Phys Solids 56:1905–1915
Pham DC (2010) Shakedown working limits for circular shafts and helical springs subjected to dynamic fluctuating loads. J Mech Mater Struct 5: 447–458
Pham DC (2014) Reduced shakedown formulation in plane stress problems. Int J Comp Methods Sing 11:1343009
Pham DC (2017) Consistent limited kinematic hardening plasticity theory and path-independent shake-down theorems. Int J Mech Sci 130:11–18
Pham DC, Stumpf H (1994) Kinematical approach to shakedown analysis of some structures. Q Appl Math 52:707–719
Simon JW (2013) Direct evaluation of the limit states of engineering structures exhibiting limited, nonlinear kinematical hardening. Int J Plast 42: 141–167
Tran TD, Le CV, Pham DC, Nguyen-Xuan H (2014) Shakedown reduced kinematic formulation, separated collapse modes, and numerical implementation. Int J Solid Struct 51:2893–2899
Tran TN, Liu GR, Nguyen-Xuan H, Nguyen-Thoi T (2010) An edge-based smoothed finite element method for primal-dual shakedown analysis of structures. Int J Numer Methods Eng 82: 917–938
Vu DK, Yan AM, Nguyen DH (2004) A dual form for discretized kinematic formulation in shakedown analysis. Int J Solids Struct 41:267–277
Weichert D, Gross-Weege J (1988) The numerical assessment of elastic-plastic sheets under variable mechanical and thermal loads using a simplified two-surface yield condition. Int J Mech Sci 30: 757–767
Weichert D, Simon JW (2012) Shakedown analysis with multidimensional loading spaces. Comput Mech 49:477–485
Zhang T, Raad L (2002) An eigen-mode method in kinematic shakedown analysis. Int J Plast 18: 71–90
Zhang Z, Liu Y, Cen Z (2002) Boundary element methods for lower bound limit and shakedown analysis. Eng Anal Bound Elem 28:905–917

Shape Optimization for Direct and Inverse Problems in Electromagnetic Casting

Jean Rodolphe Roche
Université de Lorraine, CNRS, IECL, France

Synonyms

Direct an inverse problem in electromagnetic casting; Electromagnetic shaping of molten metals

Definition

Shape optimization is a mathematical and optimization method to solve optimal design problems where the unknown is the shape of the domain. Electromagnetic casting is a very useful techniques in metallurgical industry. Electromagnetic fields are used for contactless heating and shaping of hot melts. When the position, shape, and characteristics of inductors are known, the direct problem is to find the shape of the liquid metal mass. The inverse problem consists in finding the shape, the number, and the position of the inductors such that the electromagnetic force makes a given mass of molten metal acquire a target shape.

Introduction

Electromagnetic casting in metallurgical industry allows contactless heating and shaping of chemical aggressive hot molten metals.

The quasi-static model considered in this chapter concerns in the two dimensional case a vertical column of liquid metals falling down into an electromagnetic field induced by vertical conductors.

In the three-dimensional case, the model represents a bubble of liquid metal levitating in an electromagnetic field.

In both cases the equilibrium configurations of a prescribed mass of molten metal are the critical point of an energy involving a relation

between the electromagnetic, superficial, and gravity forces at the boundary of the liquid metal. From a practical point of view, the magnetic field must be created by inductors which are, each one, a set of bounded insulated strands.

The direct problem in electromagnetic casting considered in this chapter is very similar to those studied in Shercliff (1981), Sneyd and Moffatt (1982), Mestel (1982), Brancher and Séro-Guillaume (1985), Felici and Brancher (1991), Sero-Guillaume et al. (1992), and Coulaud (1998). In those papers the authors have proposed a physical analysis and simplifying assumptions that the mathematical model requires.

Shape sensitivity analysis and shape derivative methods are presented in the followings books: Sokołowski and Zolésio (1992), Henrot and Pierre (2005), and Allaire (2007).

Numerical computations of shapes in diverse situations and with different methods can be found in the following papers: Brancher et al. (1983), Gagnoud et al. (1986), Rappaz and Touzani (1991), Pierre and Roche (1991, 1993), Coulaud and Henrot (1994), Roche (1997), Novruzi and Roche (2000), and Eppler and Harbrecht (2012).

The inverse problem has been considered in a few number of papers; from the theoretical point of view, readers can consult in the two-dimensional case (Henrot and Pierre 1989; Felici and Brancher 1991) and in the three-dimensional case (Felici and Brancher 1991; Pierre and Rouy 1996). Numerical methods for the inverse problem concerning electromagnetic shaping can be found in Canelas et al. (2008, 2009a,b, 2011, 2014), Shin et al. (2012), and Canelas and Roche (2013).

The Model Problem

The Direct Problem

The model problem considered in this entry concerns in the two-dimensional case a vertical column of molten metal falling down into an electromagnetic field created by vertical inductors.

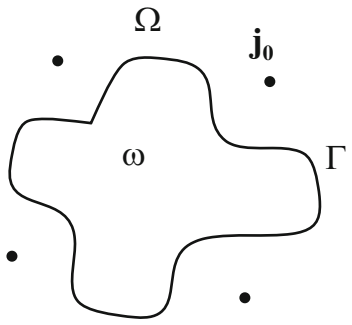

Fig. 1 Cross section of the vertical column of molten metal

The same model in the tridimensional case represents a bubble of liquid metal levitating in an electromagnetic fields.

In both cases it is assumed that the frequency of the imposed current is so high that the magnetic field does not penetrate into the metal, consequently the skin effect is neglected. Then the electromagnetic forces acting in the interface are reduced to the magnetic pressure.

Let $\omega \subset I\!R^d$, $d = 2, 3$ be the domain filled by the molten metal and Γ its boundary. Let denote Ω the exterior of the domain ω. The domain ω is assumed simply connected with a boundary sufficiently smooth.

In the three-dimensional case, the equilibrium surface is characterized by the following equations:

$$\begin{aligned} \nabla \times B &= \mu_0 \overline{j_0} \ \text{ in } \Omega \\ \nabla . B &= 0 \quad \text{in } \Omega \\ B.\nu &= 0 \quad \text{on } \partial\omega = \Gamma \\ ||B|| &\to 0 \text{ at } \infty \end{aligned} \tag{1}$$

$$\frac{\|B\|^2}{2\mu_0} + \sigma \mathscr{H} + \rho g \cdot x_3 = p_0 \text{ on } \Gamma \tag{2}$$

where $\overline{j_0}$ is the current density, B the magnetic field, μ_0 the magnetic permeability, ρ the density of the charge, g the gravitational acceleration, x_3 the height, $\mathscr{H}$ the mean curvature of Γ, σ the surface tension, and ν the unit normal directed toward ω. The constant p_0 is an unknown in the direct problem.

In the two-dimensional case, the most important difference is that the equilibrium term in Γ

does not depend on gravitational force:

$$\frac{\|B\|^2}{2\mu_0} + \sigma\mathscr{C} = p_0 \text{ on } \Gamma$$

where $\mathscr{C}$ is the curvature. The current density $\overline{j_0} = (0, 0, j_0)$ and $j_0 = I\sum_{p=1}^{m}\alpha_p\delta_{u_p}$. where I is the intensity of current, δ_{u_p}, with $1 \leq p \leq m$, are the Dirac masses at points u_p in the plane and α_p are dimensionless coefficients (Fig. 1).

The total energy of the system is given by Brancher et al. (1983) and Descloux (1991):

$$E(\omega) = -\frac{1}{2\mu_0}\int_{\Omega}||B||^2 dx + \sigma\int_{\Gamma} d\gamma + \int_{\Omega}\rho g x_3 dx \tag{3}$$

where B is the solution of system (1). In the two-dimensional case, we drop the last term in (3).

The variational formulation of the direct problem consists in considering the equilibrium domain ω as a stationary point for the total energy $E(\omega)$ under the constraint that measure of ω is given.

To compute the magnetic field B, we set $B = B^1 + \nabla\phi$ where B^1 is given by the Biot-Savart law and the scalar potential ϕ is the solution of the following problem:

$$\begin{aligned} -\Delta\phi &= 0 \quad \text{in } \Omega \\ \frac{\partial\phi}{\partial\nu} &= -B^1.\nu \quad \text{on } \Gamma \\ \phi(x) &= \circ(1) \text{ as } ||x|| \to \infty \end{aligned} \tag{4}$$

The solution of the exterior problem (4) can be represented using boundary integral operators, and an approximation can be computed using boundary elements.

The Inverse Problem

In this chapter is addressed the inverse problem in the two-dimensional case. The goal of the inverse problem is to find a configuration of inductors around the molten metal such that the solution of the system (1) and (2) gives a target shape.

In practice the magnetic field has to be created using a simple configuration of inductors, for example, in the present analysis, the electric current density j_0 will take the form:

$$j_0 = I\sum_{p=1}^{m}\alpha_p\delta_{u_p} \tag{5}$$

where I is the intensity of current, δ_{u_p}, with $1 \leq p \leq m$, are the Dirac masses at points u_p in the plane, and α_p are dimensionless coefficients.

In the two-dimensional case, to have existence results, (Henrot and Pierre 1989), it is necessary to assume that ω is simply connected, and the boundary Γ is only one Jordan curve. If $\overline{j}_0$ is compactly supported in Ω. and

$$p_0 \geq 2\mu_0\sigma\max_{x\in\Gamma}\mathscr{C}(x) \tag{6}$$

there exist B if and only if

1. Γ is an analytic curve.
2. If $p_0 = 2\mu_0\sigma\max_{x\in\Gamma}\mathscr{C}(x)$, this global maximum must be attained in an even number of points.

The magnetic field is well determined in a neighborhood of ω (local uniqueness).

Then if Γ is analytic and $\sigma \geq 0$ the shaping problem has a solution. We can always find a current distribution concentrated in a curve in Ω. But it is not always possible to have a current distribution j_0 given by adding of a finite number of Dirac masses.

In this paper, two different approaches to find a numerical solution of the two-dimensional inverse problem using classical shape optimization are considered. Let denote ω^* the target shape and V a regular vector field with compact support in an open neighborhood of ω^* and $\Gamma = (I+V)(\Gamma^*)$. Then the first formulation of the inverse problem is the following:

$$\min_{j_0}||V||^2_{L^2(\Gamma^*)} \tag{7}$$

with the constraints:

$$\int_{\Gamma}\left(\frac{1}{2\mu_0}||B||^2 + \sigma\mathscr{C}\right)Z.\nu d\gamma = \int_{\Gamma} p_0 Z.\nu d\Gamma \tag{8}$$

for all Z in $C^1(I\!R^2, I\!R^2)$, B is solution of system (1) and

$$\int_\omega dx = S_0 \tag{9}$$

An indirect approach of the inverse problem can be considered if we introduce a slack variable function $Q(x) : \Gamma^* \to I\!R$ in the equilibrium equation. Then we obtain the following second formulation of the problem:

$$\min_{j_0} ||Q||^2_{L^2(\Gamma^*)} \tag{10}$$

such that:

$$\int_{\Gamma^*} \left(\frac{1}{2\mu_0}||B||^2 + \sigma\mathscr{C} + Q\right) Z.\nu d\Gamma = \int_{\Gamma^*} p_0 Z.\nu d\Gamma \quad \forall\ Z \in C^1(I\!R^2, I\!R^2) \tag{11}$$

with B the solution of system (1). In this formulation the shape is no more an unknown of the problem.

Shape Derivatives

Assume that E is a real-valued function defined on the following set:

$$\mathscr{O} = \{\omega \subset I\!R^d;\ \omega \text{ a bounded and open set subset of class } \mathscr{C}^2\} \tag{12}$$

Following (Delfour and Zolésio 2001), let $V : [0, \tau] \times I\!R^d \to I\!R^d$ be a given velocity field for some fixed $\tau > 0$. Assume that :

$$\begin{cases} \forall x \in I\!R^d;\ V(.,x) \in \mathscr{C}^0([0,\tau];\ I\!R^d), \\ \exists c > 0, \forall x, y \in I\!R^d;\ ||V(.,y) - V(.,x)||_{\mathscr{C}^0([0,\tau];\ I\!R^d)} \le c||y - x|| \end{cases} \tag{13}$$

where $V(.,x)$ denotes the function $t \to V(t,x)$.. Associate to (13) the solution $x(t,X)$ of the ordinary equation:

$$\frac{dx}{dt}(t,X) = V(t,(x(t,X)); \quad t \in [0,\tau]; x(0,X) = X \in I\!R^d \tag{14}$$

and introduce the family of homeomorphisms

$$X \to T_t^V(X) = x(t,X) : I\!R^d \to I\!R^d \tag{15}$$

Definition 1 Let V verify the property (13). If the following limits exists:

$$\lim_{t \searrow 0} \frac{E(T_t^V(\omega)) - E(\omega)}{t} \tag{16}$$

we say that E has an Eulerian semi-derivative, and we denote it by $d(E(\omega); V)$
The shape functional E is said to be shape differentiable at ω if the Eulerian semi-derivative exists for all V and the map:$V \to d(E(\omega); V)$ is linear and continuous.

The shape derivative of the total energy has been obtained applying the given definition to the electromagnetic casting problem.

Theorem 1 *If $S(\omega)$ is the volume of ω. Under the hypotheses (13), the functions $\omega \to E(\omega)$, $S(\omega)$, are differentiable, for every Λ constant, we have:*

$$d(E(\omega) - \Lambda S(\omega); V) = \int_\Gamma \left(\frac{1}{2\mu_0}||B||^2 + \sigma\mathscr{H} + \rho g x_3 - \Lambda S(\omega)\right)(V.\nu)d\gamma \tag{17}$$

Then (B, ω) is the solution of the of the equilibrium system (1) and (2) if and only if there exists Λ such that for every direction V satisfying (13) we have:

$$d(E(\omega) - \Lambda S(\omega); V) = 0 \tag{18}$$

Consequently the numerical method to solve the direct problem compute a solution of Eq. (18), when B verify the system (1).

Numerical Method

Shape Discretization

We construct a sequence of $(\Gamma^k, B_{\omega^k}, Z^k)$ such that:

1. Γ^k is a piecewise linear closed surface approximation of Γ. The nodes of the surface Γ^k are denoted by $x^{i,k}$, $i = 1, \ldots, n$.
2. If ω^k is the domain of boundary Γ^k then B_{ω^k} is the numerical solution of the state PDE's equation (1).
3. Z^k is a continuous piecewise linear vector field from Γ^k in $\mathbb{R}^d$ such that:

$$Z^k(x) = \sum_{i=1}^{n} u_i Z^{i,k}(x)$$

and

$$Z^{i,k}(x^{j,k}) = \delta_{i,j}\hat{Z}^{i,k}$$

where $\hat{Z}^{i,k}$ is a vector associated to $x^{i,k}$.

The updated surface Γ^{k+1} is then given by:

$$\Gamma^{k+1} = \left\{ X = x + \sum_{i=1}^{n} u_i Z^{i,k}(x); \quad u_i \in \mathbb{R}, x \in \Gamma^k \right\}$$

where $\bar{u}^t = (u_1, \cdots .u_n) \in \mathbb{R}^n$ are the unknowns which determine the evolution of the surface Γ^k. Let denote $\omega(u) = (I + \sum_{i=1}^{n} u_i Z^i)\omega$.

The numerical approximation B_{ω^k} is computed using boundary finite element. Consequently the numerical solution of (1) is characterized by a vector denoted $q_h = \{q_i\}_{i=1,n}$. This vector is the solution of a linear system:

$$A(\bar{u})q_h = b(\bar{u}, u_p) \tag{19}$$

where the matrix $A(\bar{u})$ and the second term $b(\bar{u}, u_p)$ are a function of Γ.

Projection of the Equilibrium Equation

Let u_p be the vector of $x_p \in \mathbb{R}^2$; $p = 1, \ldots, m$ the position of the m inductors. If we project the equilibrium equation in finite dimension space generated by Z_i, $i = 1, \ldots n$, the discrete version of the shape derivative is now the following:

$$\begin{aligned} DE_i(u_p, u, q_h, p_0) = \frac{1}{2\mu_0}\int_{\Gamma} ||B_{\omega^k}||^2 (Z^i \cdot \overline{\nu})\, d\Gamma + \\ + \left(\frac{(x^i - x^{i-1})}{\|x^i - x^{i-1}\|} - \frac{(x^{i+1} - x^i)}{\|x^{i+1} - x^i\|} \right) \cdot \hat{Z}^i - p_0 \int_{\Gamma} (Z^i \cdot \overline{\nu})\, d\Gamma \end{aligned} \tag{20}$$

where $i = 1, \ldots n$.

Given u_p a numerical solution of direct problem is a solution of the system:

$$DE_i(u_p, u, q_h, p_0) = 0, i = 1, \ldots n \tag{21}$$

with the constraint that q_h is the solution of (19).

Numerical solution of problem (21) can be obtained using interior points optimization methods; see, for example, Herskovits (1998) and Arora and Wang (2005, 2004) or quasi-Newton methods; see Roche (1997) and Novruzi and Roche (2000).

First Inverse Problem Formulation

Let $L(u) = \int_{\omega(u)} dx$ and:

$$DE(u_p, u, q_h, p_0) = \{DE_i(u_p, u, q_h, p_0)\}_{i=1,\ldots n} \tag{22}$$

Then the numerical version of the first inverse problem formulation is the following:

$$\min_{u_p, u, q_h, p_0} ||V||^2_{L^2(\Gamma^*)} \tag{23}$$

with the constraint:

$$G(u_p, u, q_h, p_0) = \begin{pmatrix} A(u)q_h - b(u_p, u) \\ L(u) - S_0 \\ DE(u_p, u, q_h, p_0) \end{pmatrix} = 0 \tag{24}$$

This optimization problem with constraints can be solved using a quasi-Newton methods applied to Karush Kuhn Tucker necessary conditions; see, for example, Canelas et al. (2008, 2009a,b, 2011).

Second Inverse Problem Formulation

In order to obtain a numerical version of the second inverse problem formulation, a projection onto the piecewise linear polynomials of the slack function Q can be considered, and then the finite dimensional formulation is the following:

$$\min_{u_p, q_h, p_0} ||Q||^2_{L^2(\Gamma^*)} \tag{25}$$

with the constraint:

$$G(u_p, q_h, p_0, Q) = \begin{pmatrix} Aq_h - b(u_p) \\ DF(u_p, q_h, p_0, Q) \end{pmatrix} = 0 \tag{26}$$

where $DF(u_p, q_h, p_0, Q)$ is a vector such that:

$$DF_i(u_p, q_h, p_0, Q) = \frac{1}{2\mu_0} \int_{\Gamma^*} ||B_{\omega^k}||^2 (Z^i \cdot \overline{\nu})\, d\Gamma + \left(\frac{(x^i - x^{i-1})}{\|x^i - x^{i-1}\|} - \frac{(x^{i+1} - x^i)}{\|x^{i+1} - x^i\|} \right) \cdot \hat{Z}^i + \int_{\Gamma^*} Q_h (Z^i \cdot \overline{\nu})\, d\Gamma - p_0 \int_{\Gamma^*} (Z^i \cdot \overline{\nu})\, d\Gamma \tag{27}$$

$\forall\ i = 1, \ldots n.$

The numerical optimization problem associated to the second formulation of inverse problem can be solved using the same method implemented for the first formulation.

Numerical Results

The Direct Problem, Three-Dimensional Case

This section is devoted to present the numerical simulation of a three-dimensional electromagnetic shaping of a bubble where the magnetic field is created by 11 wires in an asymmetric configuration. The free boundary surface was discretized with 722 nodes and 1440 triangles.

The set of figures Figs. 2 and 3 show the evolution of the free boundary for this example. The initial iteration is not critical to achieve a good approximation of the free boundary surface. The obtained asymmetric equilibrium shape is the consequence of the opposite action of the magnetic pressure, the surface tension forces, and the gravity.

Numerical Results in the Case of the Two Dimensional Inverse Problem

In the example presented in this section, the goal is to obtain a distribution of a given number of inductors in order to build a bar with rectangular cross section. A number of inductor and the

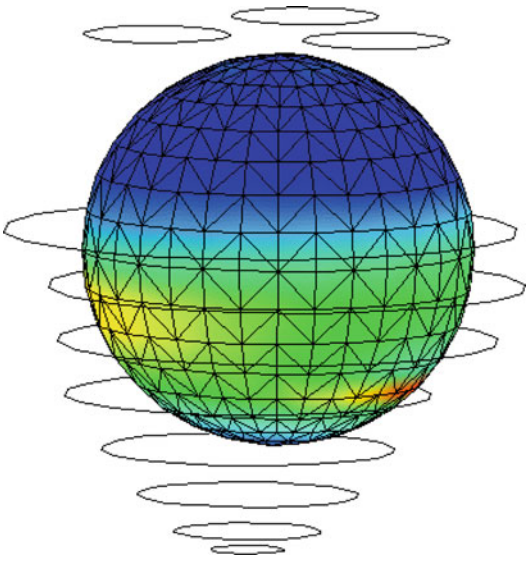

Fig. 2 Initial free surface

S

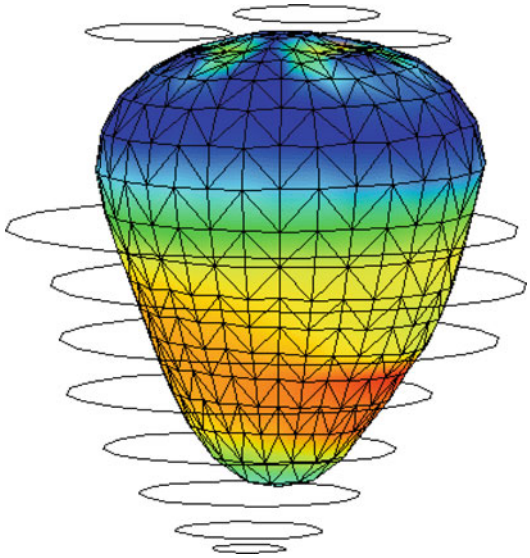

Fig. 3 Final shape (after 15 iterations)

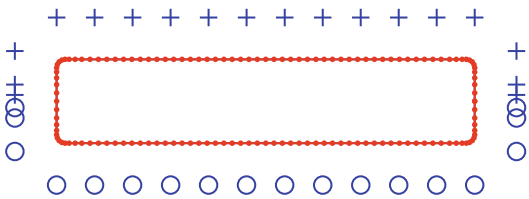

Fig. 4 Initial distribution of the inductors

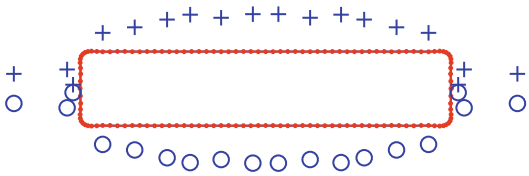

Fig. 5 Final distribution of the inductors and final shape in the case of formulation one

surface S are fixed. The intensity $I = 0.075$ and the surface tension $\sigma = 10^{-4}$. The coefficients $\alpha_p = \pm 1$, in Figs. 4, 5, and 6, + means $\alpha_p = 1$ and ∘ means $\alpha_p = 1$.

In Fig. 4 there are shown the initial position of the inductors and the target domain ω^*. The boundary is discretized with 132 nodes.

Figure 5 shows the final position of inductors after 400 iterations, in the case of the first formulation of the inverse problem.

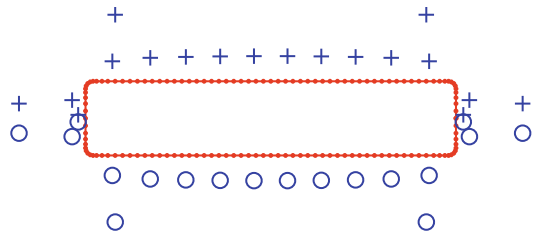

Fig. 6 Final distribution of the inductors and final shape in the case of formulation two

Figure 6 portrays the final position of the inductors after 192 iterations when the second formulation of the inverse problem is considered.

Conclusion

Classical shape optimization method to simulate electromagnetic casting is very useful in the case of the direct problem. These methods can manage free surface problems in two and three dimensions with symmetric or asymmetric shapes.

In the case of the inverse problem, classical shape optimization methods do not allow to modify the number of inductors. Topological shape optimization methods authorize the creation of new inductors. Consequently an algorithm combining classical and topological optimization can be useful to solve the inverse electromagnetic casting problem and many others similar problems.

Cross-References

▸ Boundary Element Methods

References

Allaire G (2007) Conception Optimale de Structures. Mathématiques and Applications, vol 58. Springer, Berlin

Arora JS, Wang Q (2004) Optimization of large-scale structural systems using sparse SAND formulations. Technical report, Optimal design Lab/CCAD, college of engineering/4110 SC, The University of Iowa, Iowa City, IA 52242

Arora JS, Wang Q (2005) Review of formulations for structural and mechanical system optimization. Struct Multidiscip Optim 30(4):251–272
Brancher JP, Séro-Guillaume OE (1985) Étude de la déformation d'un liquide magnétique. Arch Ration Mech Anal 90(1):57–85
Brancher JP, Etay J, Séro-Guillaume OE (1983) Formage d'une lame. J de Mécanique Théorique et Appliquée 2(6):976–989
Canelas A, Roche JR (2013) Topology optimization in electromagnetic casting via quadratic programming. Inverse Prob Sci Eng 22(3):419–435
Canelas A, Herskovits J, Telles JCF (2008) Shape optimization using the boundary element method and a SAND interior point algorithm for constrained optimization. Comput Struct 86(13–14):1517–1526. Structural optimization
Canelas A, Roche JR, Herskovits J (2009a) Inductor shape optimization for electromagnetic casting. Struct Multidiscip Optim 39(6):589–606
Canelas A, Roche JR, Herskovits J (2009b) The inverse electromagnetic shaping problem. Struct Multidiscip Optim 38(4):389–403
Canelas A, Novotny AA, Roche JR (2011) A new method for inverse electromagnetic casting problems based on the topological derivative. J Comput Phys 230(9):3570–3588
Canelas A, Novotny AA, Roche JR (2014) Topology design of inductors in electromagnetic casting using level-sets and second order topological derivatives. Struct Multidiscip Optim 50(6):1151–1163
Coulaud O (1998) Asymptotic analysis of magnetic induction with high frequency for solid conductors. RAIRO Modélisation Mathématique et Analyse Numérique 32(6):651–669
Coulaud O, Henrot A (1994) Numerical approximation of a free boundary problem arising in electromagnetic shaping. SIAM J Numer Anal 31(4):1109–1127
Delfour MC, Zolésio JP (2001) Shapes and geometries. Advances in design and control, vol 4. Society for Industrial and Applied Mathematics (SIAM), Philadelphia. Analysis, differential calculus, and optimization
Descloux J (1991) Stability of the solutions of the bidimensional magnetic shaping problem in absence of surface tension. Eur J Mech 10(5):513–526
Eppler K, Harbrecht H (2012) On a Kohn-Vogelius like formulation of free boundary problems. Comput Optim Appl 52(1):69–85
Felici TP, Brancher JP (1991) The inverse shaping problem. Eur J Mech B Fluids 10(5):501–512
Gagnoud A, Etay J, Garnier M (1986) Le problème de frontière libre en lévitation électromagnétique. Journal de Mécanique Théorique et Appliquée 5(6):911–934
Henrot A, Pierre M (1989) Un problème inverse en formage des métaux liquides. RAIRO Modélisation Mathématique et Analyse Numérique 23(1):155–177
Henrot A, Pierre M (2005) Variation et optimisation de formes. Mathematics and applications, vol 48. Springer, Berlin. Analysis, differential calculus, and optimization
Herskovits J (1998) Feasible direction interior-point technique for nonlinear optimization. J Optim Theory Appl 99(1):121–146
Mestel AJ (1982) Magnetic levitation of liquid metals. J Fluid Mech 117:27–43
Novruzi A, Roche JR (2000) Newton's method in shape optimisation: a three-dimensional case. BIT Numer Math 40(1):102–120
Pierre M, Roche JR (1991) Computation of free surfaces in the electromagnetic shaping of liquid metals by optimization algorithms. Eur J Mech B Fluids 10(5):489–500
Pierre M, Roche JR (1993) Numerical simulation of tridimensional electromagnetic shaping of liquid metals. Numer Math 65(1):203–217
Pierre M, Rouy E (1996) A tridimensional inverse shaping problem. Commun Partial Diff Equ 21(7–8):1279–1305
Rappaz J, Touzani R (1991) On a two-dimensional magnetohydrodynamic problem, I. Modelling and analysis. M^2AN 26(2):347–362
Roche JR (1997) Gradient of the discretized energy method and discretized continuous gradient in electromagnetic shaping simulation. Appl Math Comput Sci 7(3):545–565
Sero-Guillaume OE, Zouaoui D, Bernardin D, Brancher JP (1992) The shape of a magnetic liquid drop. J Fluid Mech 241:215–232
Shercliff JA (1981) Magnetic shaping of molten metal columns. Proc R Soc Lond Ser A Math Phys Sci 375(1763):455–473
Shin J, Spicer JP, Abell JA (2012) Inverse and direct magnetic shaping problems. Struct Multidiscip Optim 46(2):285–301
Sneyd AD, Moffatt HK (1982) Fluid dynamical aspects of the levitation-melting process. J Fluid Mech 117:45–70
Sokołowski J, Zolésio JP (1992) Introduction to shape optimization. Springer series in computational mathematics, vol 16. Springer, Berlin

Shape Sensitivity Analysis

▸ Relation Between Eshelbyan Mechanics and Topological Derivative Concept

Sharp Interface

▸ Chemical Affinity Tensor in Coupled Problems of Mechanochemistry

Shear Center

▸ Shear Web Theory

Shear Deformation Shell Theories

▸ Elastic Shells, Linear Shear-Deformable Theory

Shear Deformation Theories

▸ Anisotropic and Refined Plate Theories

Shear Web Assemblies

▸ Shear Web Theory

Shear Web Theory

Franz G. Rammerstorfer and
Isabella C. Skrna-Jakl
Institute of Lightweight Design and Structural Biomechanics, TU Wien, Vienna, Austria

Synonyms

Curved shear webs; Post-buckling; Rectangular shear webs; Shear center; Shear web assemblies; Shear webs; Tension field theory; Wagner's tension field; Web buckling

Definition

In lightweight design quite often structures are built of a combination of beams, e.g., forming frames or grids, and a skin, i.e., a typically thin web, which transfers shear loads and provides the required shear stiffness to the structure.

The shear web theory represents simplified methods for roughly calculating stresses in such components and for determining load-carrying capabilities even when local instabilities have appeared. This section provides an overview on the shear web theory as well as on the tension field theory. The descriptions are limited to rectangular webs; for more details and more general configurations, see, e.g., Magson (2013) and Peery (2011).

Introduction

The principal idea of the shear web theory is shown in Fig. 1 and becomes obvious when, as described now, substantial simplifications in the analysis of a girder with I-cross section, as typical in lightweight design, are applied.

Let us start with Bernoulli-Euler beam theory and successively simplify in order to eventually come to shear web theory. Here and in the following, it is assumed that all parts (webs, flanges, and struts) are made of one and the same isotropic linear elastic material.

$$J_y \approx \frac{t_w\, h^3}{12} + 2 t_f b \frac{h^2}{4} = 2 b t_f \left(\frac{h}{2}\right)^2 \left(1 + \frac{t_w\, h}{6 t_f b}\right)$$
$$= 2 b t_f \left(\frac{h}{2}\right)^2 \left(1 + \frac{A_w}{6\, A_f}\right),$$

$$\text{with } A_w \ll A_f \quad \Longrightarrow \quad \frac{A_w}{6\, A_f} \ll 1 \quad \Longrightarrow \quad J_y \approx 2\, A_f \left(\frac{h}{2}\right)^2,$$

$$\sigma_{\max} = \frac{M_y}{J_y}\frac{h}{2} \approx \frac{M_y}{A_f\, h}$$
$$\Longrightarrow \quad M_y \approx \sigma_{\max}\, A_f\, h = N_f h.$$

There, S_y, I_y, A_w, and A_f stand for the first and second moments of area with respect to axis y as well as for the cross-sectional areas of web and flanges, respectively.

The distribution of the shear stress σ_{xz}, caused by the shear force Q_z, reads $\sigma_{xz}{=}\tau(z)$

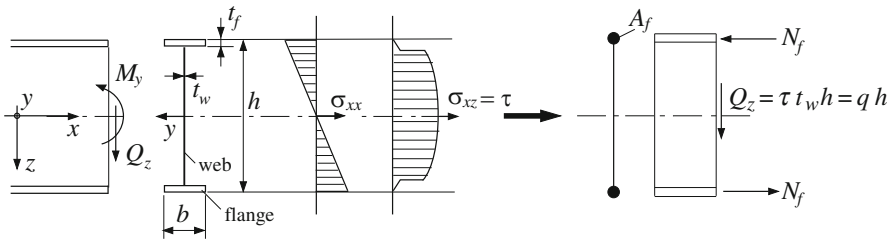

Fig. 1 I-girder simplified by applying shear web theory (Rammerstorfer 1992)

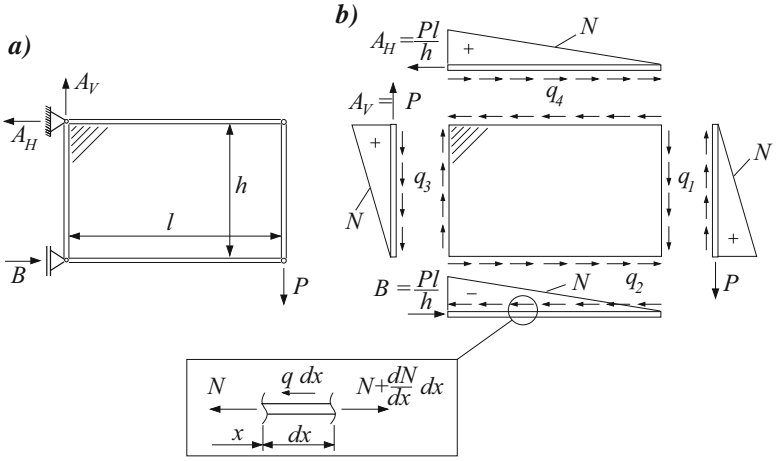

Fig. 2 (**a**) Simple shear web assembly; (**b**) stress resultants (Rammerstorfer 1992)

$= \frac{-Q_z\, S_y(z)}{J_y\, t(z)}$. For $A_w \ll A_f$, one gets $S_y(z) \approx A_f \frac{-h}{2} = \text{const}$. This leads to $\tau \approx \frac{Q_z\, A_f\, \frac{h}{2}}{2\, A_f \left(\frac{h}{2}\right)^2 t_w} = \frac{Q_z}{h\, t_w} = \text{const}$.

Eventually, we end up with the constant shear flow, $q = \tau t_w = \frac{Q_z}{h}$.

From the above derivations, one finds: If $t_w \ll h$ and $A_w \ll A_f$ (e.g., $t_w\, h \ll b\, t_f$), then the bending moment is (as approximation) transferred solely by normal forces in the flanges and the shear force (as approximation) solely by a constant shear flow in the web. The simple shear web theory neglects not only the contribution of the bending stresses σ_{xx} in the web to the bending moment but neglects these normal stresses at all and assumes that in the web only shear stresses σ_{xz} act.

The simple shear web theory for plane rectangular shear webs is based on the following rather rough assumptions (for non-rectangular webs, see, e.g., Magson 2013):

- The beam-like struts (flanges and stiffeners) are hinged together and transfer loading by normal forces only, provided that the load intensity is subcritical, i.e., no buckling appears.
- Bending moments are transferred only by normal forces in the struts and shear forces only by shear stresses in the web.
- External loads are applied to the hinges only, which connect the struts.

Plane Rectangular Shear Webs

A simplest shear web assembly is sketched in Fig. 2a. Applying the method of sectioning (see Fig. 2b) in combination with the equilibrium conditions to the individual sections (including $(dN/dx)dx = q\, dx$ as equilibrium condition for an infinitesimally small piece dx of a strut) leads to results as shown in Fig. 2b with $q_1 = q_2 = q_3 = q_4 = q = P/h$.

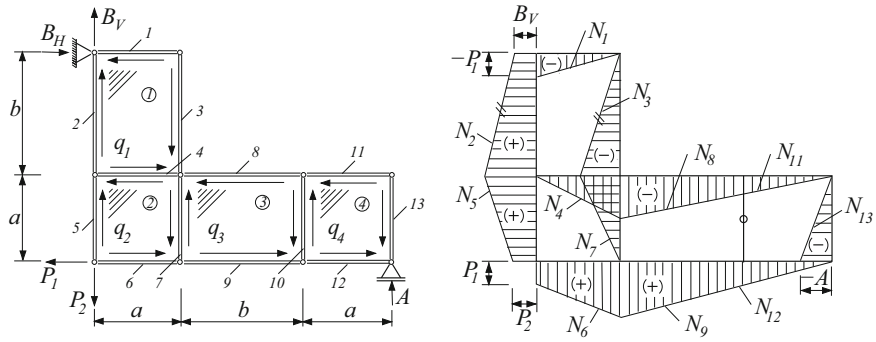

Fig. 3 Statically determinate shear web assembly; stress resultants: shear flows in the webs shown as acting on the struts; normal forces in the struts, + is tension; − is compression; compare (Rammerstorfer 1992)

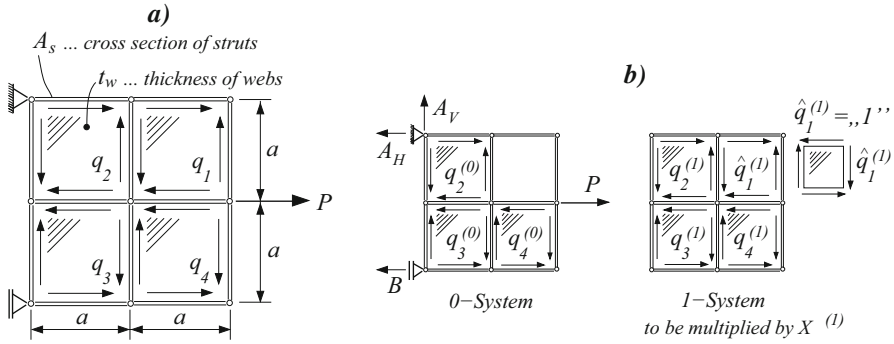

Fig. 4 (**a**) Statically indeterminate shear web assembly; (**b**) *(0)*- and *(1)-systems*, respectively; compare (Rammerstorfer 1992)

According to the abovementioned simplifying assumptions, in each shear web, a constant shear flow exists, which acts as loading at the struts. Equilibrium conditions applied to the struts render the linear normal force distributions in the struts. Provided that the shear web configuration is statically determinate, all shear flows in the webs and normal forces in the struts can be determined easily by the respective equilibrium conditions. A necessary condition for static determination of plane shear web assemblies is

$$s + b + f = 2\,k. \tag{1}$$

There, s is the number of struts, b is the number of webs, k is the number of nodes (treated as hinges), and f is the number of support reactions.

As an example, let us analyze the shear web assembly shown in Fig. 3.

Counting $s = 13,\ b = 4,\ k = 10$, and $f = 3$ shows that the assembly is statically determinate. Global equilibrium requires $A = P_1\,\frac{a+b}{2a+b}$, $B_H = P_1$, $B_V = P_2 - P_1\,\frac{a+b}{2a+b}$. For strut 1, equilibrium requires $B_H - q_1\,a = 0 \implies q_1 = \frac{B_H}{a} = \frac{P_1}{a}$ Analogously, for strut 13, $q_4\,a - A = 0 \Longrightarrow q_4 = \frac{P_1}{a}\,\frac{a+b}{2a+b}$, and for strut 10, $q_3\,a - q_4\,a = 0 \implies q_3 = q_4 = \frac{P_1}{a}\,\frac{a+b}{2a+b}$. Finally, q_2 results from the equilibrium of the cutout combination of struts 2 and 5: $q_1\,b + q_2\,a + B_V - P_2 = 0 \implies q_2 = \frac{P_1}{a}\left(\frac{a+b}{2a+b} - \frac{b}{a}\right)$

With $q_1, \ldots, q_4$, the distribution of the normal forces in the struts can be easily determined. From the right figure in Fig. 3, one sees that strut 10 is stress-free. Nevertheless, this strut is important for stability reasons, as will be shown later.

Application of Eq. 1 to the shear web assembly shown in Fig. 4 shows that this assembly is onefold statically indeterminate.

Such systems can be analyzed, for instance, by applying energy methods – see, e.g., Ziegler

(1995) – where the original system is replaced by the superposition of a statically determinate *(0)-system*, which is formed by cutting as much as necessary to come up with a statically determinate system, and to which all external loading is applied, and n individual *(k)-systems*, $k = 1, 2, \ldots, n$, to which the unknown, originally internal stress resultants at the cuts act as external forces of intensity $X^{(k)}$. There, n is the degree of the statical indetermination. The unknowns $X^{(k)}$ are calculated from the compatibility conditions – according to Menabrea's theorem – at the positions of the cuts:

$$\frac{\partial U^*}{\partial X^{(k)}} = 0 \quad \text{for} \quad k = 1, 2, \ldots, n\,, \qquad (2)$$

where U^* stands for the complementary energy of the loaded system.

In the following, the system given in Fig. 4 is treated by this procedure; there $n = 1$.

(i) Cut out one web (here web 1 is chosen) and get a statically determinate system, the *(0)-system*, to which the load is applied. There you can calculate all stress resultants of the *(0)-system*, $q_2^{(0)} = q_3^{(0)} = P/(2a)$, $q_4^{(0)} = 0$ as well as the normal force distributions in the struts, i.e., $N_j^{(0)}(x_j)$, $j = 1, \ldots, 12$. The coordinate x_j runs along the full length of the j-th strut.

(ii) The statically indeterminate quantity q_1 is the shear flow $X^{(1)} q_1^{(1)}$. The quantity $q_1^{(1)}$ results, like $q_2^{(1)}$, ..., $q_4^{(1)}$, from the *(1)-system*, on which $\hat{q}_1^{(1)}$ is applied as external loading at that web and that struts, where in step (i) the cut was made. The intensity of this loading is $\hat{q}_1^{(1)} =$ "1". This leads to $q_1^{(1)} = 1$, $q_2^{(1)} = q_3^{(1)} = -1$, $q_4^{(1)} = 1$ and to the corresponding normal force distributions in the struts, i.e., $N_j^{(1)}(x_j)$, $j = 1, \ldots, 12$.

Of course, eventually all quantities calculated in the *(1)-system* must be multiplied with the yet unknown factor $X^{(1)}$, which will be determined in the next step.

(iii) The unknown multiplier $X^{(1)}$ follows from the compatibility condition between the cutout web and the struts around it. Compatibility requires $\frac{\partial U^*}{\partial X^{(1)}} = 0$, with the complementary energy

$$U^* = \frac{1}{2\,EA} \sum_{i=1}^{12} \Big[\int_0^a \big(N_i(x_i)\big)^2 \, dx_i \Big] + \frac{1}{2\,G\,t} a^2 \sum_{j=1}^{4} q_j^2,$$

with

$$N_i(x_i) = N_i^{(0)}(x_i) + X^{(1)}\, N_i^{(1)}(x_i)\,,$$
$$q_j = q_j^{(0)} + X^{(1)}\, q_j^{(1)}.$$

The above compatibility condition leads to

$$X^{(1)} = P\, \frac{2EA + 5aGt}{8aEA + 16a^2Gt}$$

Finally, all stress resultants are determined. For instance, the shear flows are $q_1 = q_4 = X^{(1)}$, $q_2 = q_3 = \frac{P}{2a} - X^{(1)}$.

If the degree of statical indeterminate is $n > 1$, $X^{(k)}$ results from Eq. (2), and the stress resultants are, finally, $q_j^{(0)} + \sum_{k=1}^{n} X^{(k)}\, q_j^{(k)}$.

As will be shown later on, shear web assemblies exhibit substantial reserves in load-carrying capabilities even when the shear webs have buckled. However, due to their very low global torsional stiffness, such assemblies are prone to buckle sideways, i.e., by lateral-torsional buckling.

Curved Shear Webs

When the abovementioned simplifying assumptions of the shear web theory are accepted, the shear flow remains constant, even if the shear web is curved, and no torsion will appear if the line of action of the resultant shear force Q goes through the shear center M of the cross section; see Fig. 5.

For the sake of simplicity, symmetry of the cross section is assumed, and the shear force acts only in z-direction, i.e., $Q = Q_z$. From the static equivalence between the action of Q_z and the action of the shear flow q, it follows that

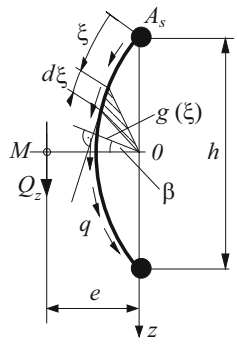

Fig. 5 Shear web assembly with curved web

$$Q_z = \int q \cos\beta(\xi)\, d\xi = \int_{-\frac{h}{2}}^{\frac{h}{2}} q\, dz = q\, h$$

$$\Longrightarrow \quad q = \frac{Q_z}{h}. \tag{3}$$

The position of M follows from

$$Q_z\, e = \int q\, g(\xi)\, d\xi = q \int g(\xi)\, d\xi = q\, 2\, A$$

$$\Longrightarrow \quad e = \frac{2A}{h}, \tag{4}$$

where A is the area enclosed by the web line and the line linking the upper with the lower girder.

Combined Shear Web Assemblies

Three-dimensional beam-like lightweight structures quite often consist of a composition of shear web assemblies. To each of such shear web assemblies, shear web theory may be applied, as shown for the example, sketched in Fig. 6.

In order to prevent the beam from twisting, the line of action of the shear force $Q = Q_z$ goes through the shear center M, the location of which is indicated by the distance e on the symmetry line.

According to the assumption that the bending moment M_y is transferred by normal forces in the stringers only, one gets from $M_y = (N_1 + N_2)h$ with $N_1/A_1 = N_2/A_2$ the normal forces in the stringers as $N_1 = \frac{M_y}{h}\frac{A_1}{A_1+A_2}$ and $N_2 = \frac{M_y}{h}\frac{A_2}{A_1+A_2}$.

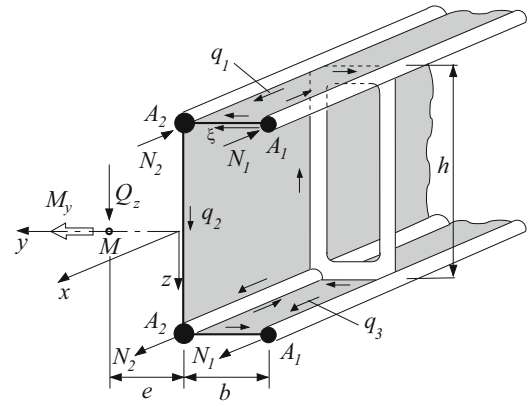

Fig. 6 Beam composed from shear web assemblies

The shear flows q_1, q_2, q_3 are determined from

$$q(\xi) = \frac{-\,Q_z\, S(\xi)}{J_y} \quad \text{with} \quad J_y \approx 2\,\frac{(A_1+A_2)h^2}{4}$$

and

$$S_1 = S_3 \approx -\,A_1\frac{h}{2}\,,\; S_2 \approx -\,(A_1 + A_2)\frac{h}{2}$$

There S_i stands for S_y in the ith portion of the cross section. This leads to

$$q_1 = q_3 = \frac{Q_z}{h}\frac{A_1}{A_1 + A_2}\,, \quad q_2 = \frac{Q_z}{h}.$$

The position of the shear center results from

$$q_2\, h\, e - q_1\, b\, \frac{h}{2} - q_3\, b\, \frac{h}{2}$$

$$= Q_z\, e - b\, h \left(\frac{Q_z}{h}\frac{A_1}{A_1 + A_2}\right) = 0$$

$$\text{as} \quad e = b\,\frac{A_1}{A_1 + A_2}.$$

From Shear Web Theory to Tension Field Theory

As mentioned above, shear web assemblies exhibit substantial reserves in load-carrying capabilities even when the shear webs have

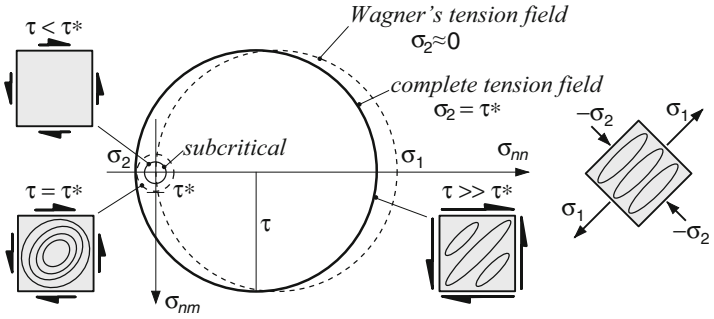

Fig. 7 Development of Mohr's circle in the deep post-buckling regime; compare (Rammerstorfer and Daxner 2009)

buckled. Critical in-plane loads of rectangular plates leading to buckling are calculated by

$$\sigma^* = kE\left(\frac{t}{b}\right)^2, \tag{5}$$

where the buckling factor k can be obtained from buckling factor diagrams in dependence of the plate's aspect ratio a/b – with a, b being the edge lengths of the plate – and the boundary conditions; see, e.g., Hertel (1986) and Wiedemann (2007).

This way, also that shear stress in the web, $\tau = q/t_w$, which leads to web buckling, i.e., τ^*, can be calculated by $\tau^* = k_w E\left(\frac{t_w}{b}\right)^2$. The buckling factor for web buckling, k_w, depends on the way the web is connected to the struts and how the stiffness of the struts contributes to clamping conditions. It is somewhere between the buckling factor for hinged and for clamped boundaries, respectively; see Hertel (1986).

With the approximating, conservative assumption that after buckling the web's incremental membrane stiffness in the direction of the principal compression stress vanishes, this principal stress will not grow anymore with increased loading. Hence, Mohr's circle moves to the right, when the shear stress $\tau > \tau^*$ grows; see Fig. 7.

If the ratios τ/τ^* are very large, i.e., the tension fields are well developed, the comparatively small principal compressive stress $|\sigma_2| \ll \sigma_1$ is neglected, Mohr's circle according to the classical *Wagner's tension field*, see Wagner (1929), is reached. Further approximations are characteristic for this simplifying model: The buckling folds are approximately inclined by 45°, and from Mohr's circle it follows that

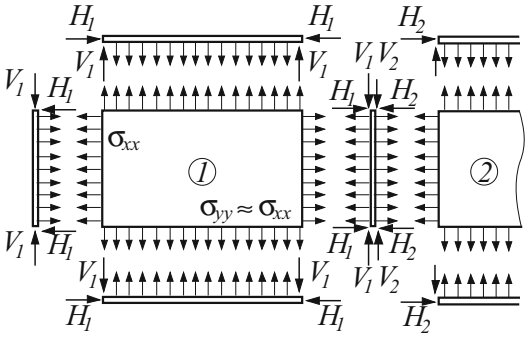

Fig. 8 Effects at interfaces and in the struts caused by the tension field in addition to shear due to shear web loading. Only these additional sectional forces are shown

$$\sigma_1 = 2\,\tau\,, \quad \sigma_{xx} = \sigma_{yy} = \tau. \tag{6}$$

Equation (6) reveals that the buckled web leads to *tensile* normal stresses between webs and struts; both σ_{xx} and σ_{yy} are always positive, regardless in which direction the external shear load acts! As shown in Fig. 8, these normal stresses lead to extra loading of the interfaces between webs and struts as well as to additional normal forces in the struts, i.e., loadings in addition to those resulting from the shear flows and normal forces according to shear web theory. Thus, pullout failure at the interfaces as well as bending and buckling of the struts must be considered with care when the ultimate load-carrying capacity should be determined.

Final collapse is eventually due to either one of the following failure modes or combinations of some of them: local plastic deformations, tensile cracking of the web (cracks running approximately perpendicularly to the folds), global instability due to buckling of the struts, failure of the connections between web and struts (due to

Fig. 9 Complete failure of a shear web assembly; compare (Rammerstorfer and Daxner 2009)

combined tension and shear), local buckling of the flanges of the struts, and overall instability by sideways buckling of the whole assembly, just to mention some of the typical modes.

Figure 9 shows, as an example, a shear web assembly, which because of substantial load increase after web buckling has failed by pulling out the web from the struts and by plastic buckling of the inner vertical strut.

Cross-References

- ▸ Analytical Stability Considerations in Lightweight Design
- ▸ Static and Dynamic Bifurcations
- ▸ Pure Torsion of Thin-Walled Cross Sections

References

Hertel H (1986) Leichtbau. Springer, Berlin
Magson THG (2013) Aircraft structures for engineering students. Elsevier, Oxford
Peery DJ (2011) Aircraft structures. Dover, Mineola
Rammerstorfer F (1992) Repetitorium Leichtbau, Oldenbourg. Copyright Walter de Gruyter GmbH. (Figures partially reproduced with permission.)
Rammerstorfer F, Daxner T (2009) Berechnungs- und Design-Konzepte für den Leichtbau. In: Degischer H, Lüftl (ed) Leichtbau: Prinzipien, Werkstoffauswahl und Fertigungsverfahren Wiley-VHC, Weinheim, p 29 & 30. Copyright Wiley-VCH Verlag GmbH & Co. KGaA. (Figures partially reproduced with permission.)
Wagner H (1929) Ebene Blechwandträger mit sehr dünnem Stegblech. Zeitschrift fur Flugtechnik und Motorluftschiffahrt 20(8):200–207; 20(9):227–231
Wiedemann J (2007) Leichtbau. Springer, Berlin/Heidelberg/New York
Ziegler F (1995) Mechanics of solids and fluids. Springer, New York

Shear Webs

▸ Shear Web Theory

Shell Branchings and Intersections

▸ Junctions in Irregular Shell Structures

Shell Thermomechanics, Resultant Nonlinear Theory

Wojciech Pietraszkiewicz
Faculty of Civil and Environmental Engineering, Department of Mechanics of Materials and Structures, Gdańsk University of Technology, Gdańsk, Poland

Synonyms

Dynamically and thermally exact shell theory; Rational thermomechanics of shells

Definition

Shell thermomechanics is the study of effects of heat upon mechanical properties of a thin solid body. The resultant shell theory is based on the set of two-dimensional balance laws of mass, linear and angular momenta, and energy as well as the entropy inequality which are formulated on the shell base surface as exact resultant implications of corresponding laws of three-dimensional rational continuum thermomechanics. The only approximations enter this shell model through

constitutive equations, which are experimental laws anyway.

Introduction

Nonlinear thermomechanic two-dimensional (2D) models of shells are usually developed using two main approaches: (1) the so-called *direct* formulation and (2) the *derived* or *deductive* formulation from three-dimensional (3D) continuum thermomechanics. But the final 2D relations of shell thermomechanics and physical interpretation of their ingredients vary substantially throughout the literature.

The resultant shell thermomechanics proposed by Simmonds (1984, 2012) seems to be the most promising way to formulate shell thermomechanics. All 2D relations were formulated on the shell base surface by exact through-the-thickness integration of appropriate 3D fields of rational continuum thermomechanics. The only approximations were made in the resultant balance of energy when expressed through the 2D stress and strain fields alone. The approximations were then transferred onto the resultant entropy inequality and the 2D constitutive equations, which are experimental laws anyway. The mechanical part of such resultant shell theory, originally proposed by Reissner (1974), gained considerable attention in the literature, and many results obtained in the field are now partly summarized in the books by Libai and Simmonds (1998) and Chróścielewski et al. (2004).

In this entry the extended resultant thermomechanics of shells proposed by Pietraszkiewicz (2011) is briefly presented. The local, resultant 2D balance laws of mass, linear and angular momentum, and energy as well as the entropy inequality for shells are constructed as the *exact resultant implications* of corresponding 3D laws of rational continuum thermodynamics. As compared with the results by Simmonds (1984, 2012), the following refinements are introduced:

- The resultant laws are formulated on the shell base surface which is taken to be the material surface during the entire shell motion.
- An additional stress power, called an interstitial working, is introduced on the 2D level, which completes the initially approximate resultant 2D balance of energy expressed through the 2D stress and strain measures alone.
- The extra surface heat and entropy supplies, following from nonuniform distribution of temperature across the thickness, are accommodated by three extra surface fields.

The kinematic structure of the resultant shell theory is that of the Cosserat surface with the translation vector and rotation tensor fields as the only kinematic field variables (Pietraszkiewicz 2018). The structure of the extended resultant 2D thermomechanical laws for shells reminds somewhat that of corresponding 3D laws of extended thermodynamics; see, for example, Müller and Ruggeri (1998).

Basic Principles

Within 3D continuum thermodynamics, one assumes that all material bodies possess mass, sustain forces and torques, and convert energy, and basic laws of thermodynamics are valid for any part $\mathcal{P}$ of the body $\mathcal{B}$.

To describe the mechanical behavior of $\mathcal{P}$ at any time $t \in T$, one assumes the following primitive quantities to be meaningful: the mass $\mathsf{M}(\mathcal{P}, t)$, the mass production $\mathsf{C}(\mathcal{P}, t)$, the linear momentum vector $\mathbf{L}(\mathcal{P}, t)$, the total force vector $\mathbf{F}(\mathcal{P}, t)$, the angular momentum vector $\mathbf{A}_{\mathrm{o}}(\mathcal{P}, t)$, and the total torque vector $\mathbf{T}_{\mathrm{o}}(\mathcal{P}, t)$. The latter two quantities are defined in an inertial frame $(\mathrm{o},\mathbf{e}_i)$ relative to a point o of the three-dimensional (3D) physical space $\mathcal{E}$ with V as its translation 3D vector space and where $\mathbf{e}_i \in \mathrm{V}$, $i = 1,2,3$, are orthonormal vectors. The primitive quantities are assumed to satisfy three balance laws of continuum mechanics: balances of mass, of linear momentum, and of angular momentum (Truesdell and Toupin 1960; Truesdell and Noll 1965). When written in the most general, global integral-impulse form, these laws are

$$\begin{aligned} \mathsf{M}|_{t_1}^{t_2} &= \int_{t_1}^{t_2} \mathsf{C}dt, \\ \mathbf{L}|_{t_1}^{t_2} &= \int_{t_1}^{t_2} \mathbf{F}dt, \\ \mathbf{A}_{\mathrm{o}}|_{t_1}^{t_2} &= \int_{t_1}^{t_2} \mathbf{T}_{\mathrm{o}}dt. \end{aligned} \tag{1}$$

When the theory is designed to account for thermal effects, one assumes additional primitive quantities to be meaningful: the total energy $\mathsf{U}(\mathcal{P}, t)$, the heating $\mathsf{Q}(\mathcal{P}, t)$, the entropy $\mathsf{H}(\mathcal{P}, t)$, and the entropy flux $\mathsf{J}(\mathcal{P}, t)$. It is generally accepted that these quantities have to satisfy no more than two laws of continuum thermodynamics. However, while the form of energy balance is universally accepted, there is no general agreement which specific form should take the 2nd law. One may consult reviews (Muschik et al. 2001; Muschik 2008) and books (Müller 2007; Badur 2009), where many references to historic papers and books on various formulations of continuum thermodynamics are given.

Within rational thermodynamics developed by Truesdell and Toupin (1960), Truesdell and Noll (1965), and Truesdell (1984), which is used here, the two laws of thermodynamics are the balance of energy (also called the 1st law) and the entropy inequality (also called the 2nd law) given by

$$\mathsf{U}|_{t_1}^{t_2} = \int_{t_1}^{t_2} (\mathsf{P} + \mathsf{Q})\, dt, \quad \mathsf{H}|_{t_1}^{t_2} \geq \int_{t_1}^{t_2} \mathsf{J}dt, \tag{2}$$

where $\mathsf{P}(\mathcal{P}, t)$ means the mechanical power, and $\mathsf{J}(\mathcal{P}, t)$ is taken in the Clausius–Duhem form; see below.

In continuum mechanics each placement $\chi(\mathcal{P}, t)$ of $\mathcal{P} \in \mathcal{B}$ at time t becomes a part $\mathrm{P}(t)$ of the region $\mathrm{B}(t) = \chi(\mathcal{B}, t)$ of $\mathcal{E}$. By $\mathrm{y} \in \mathrm{P(t)}$ one denotes the actual place of material particle and by $\mathbf{y} = \mathrm{y} - \mathrm{o}$ its position vector in the inertial frame $(\mathrm{o},\mathbf{e}_i)$. Then $\mathrm{P} \subset \mathrm{B}$ is the region of $\mathcal{E}$ occupied by $\mathcal{P}$ in the reference placement $\kappa(\mathcal{P})$ associated here with $t = 0$, while $\mathrm{x} \in \mathrm{B}$ is the reference place of material particle and $\mathbf{x} = \mathrm{x} - \mathrm{o}$ its position vector in the same inertial frame $(\mathrm{o},\mathbf{e}_i)$.

In the shell-like body, the boundary surface $\partial\mathrm{B}$ of the reference region B consists of three separable parts: the upper M^+ and the lower M^- shell faces and the lateral boundary surface $\partial\mathrm{B}^*$ such that $\partial\mathrm{B} = M^+ \cup M^- \cup \partial\mathrm{B}^*, M^+ \cap M^- = \varnothing$. Relative to the origin $\mathrm{o} \in \mathcal{E}$ of the inertial frame, the position vectors $\mathbf{x}$ and $\mathbf{y}$ are usually represented by

$$\begin{aligned} \mathbf{x}(x, \xi) &= \boldsymbol{x}(x) + \xi \boldsymbol{n}(x), \\ \mathbf{y}(x, \xi, t) &= \boldsymbol{y}(x, t) + \mathbf{z}(x, \xi, t), \\ \mathbf{z}(x, 0, t) &= \mathbf{0}. \end{aligned} \tag{3}$$

Here $\boldsymbol{x}(x) = \mathbf{x}(x, 0)$ is the position vector of corresponding point of some reference shell base surface $M \subset \mathcal{E}$, $\boldsymbol{n}(x)$ is the unit normal vector orienting M, $\xi \in [-h^-(x), h^+(x)]$ is the distance along $\boldsymbol{n}$ from M to x with $h = h^- + h^+$ the initial shell thickness, $\boldsymbol{y}(x,t)$ is the position vector of the actual shell base surface $M(t)$, and $\mathbf{z}(x, \xi, t)$ is a deviation of $\mathrm{y} \in \mathrm{B}(t)$ from $M(t)$.

Each placement $P(t)$ of the moving shell-like body can be represented through a part $\Pi(t)$ of the shell base surface $M(t) \subset \mathcal{E}$ taken here to be the material surface, i.e., consisting of the same material particles during the shell motion. By $y \in \Pi(t)$ one denotes a point of $\Pi(t)$ and by $\boldsymbol{y} = y - \mathrm{o}$ its position vector in the inertial frame. Then $\Pi \subset M$ represents a part of M, while $x \in \Pi$ is the point of Π and $\boldsymbol{x} = x - \mathrm{o}$ its position vector in the same inertial frame.

Under appropriate smoothness requirements, the mechanical primitive quantities can be expressed as the following volume and surface integrals of their densities, written here with respect to the reference placement:

$$\begin{aligned} \mathsf{M} &= \iiint_{\mathrm{P}} \rho_R \mathrm{dv}, \quad \mathsf{C} = \iiint_{\mathrm{P}} \mathrm{c}_R \mathrm{dv}, \\ \mathbf{L} &= \iiint_{\mathrm{P}} \rho_R \dot{\mathbf{y}}\, \mathrm{dv}, \quad \mathbf{A}_{\mathrm{o}} = \iiint_{\mathrm{P}} \mathbf{y} \times \rho_R \dot{\mathbf{y}} \mathrm{dv}, \end{aligned} \tag{4}$$

$$\begin{aligned} \mathbf{F} &= \iiint_{\mathrm{P}} \rho_R \mathbf{b}\, \mathrm{dv} + \iint_{\partial\mathrm{P}} \mathbf{t}_{\mathrm{n}} \mathrm{da}, \\ \mathbf{T}_{\mathrm{o}} &= \iiint_{\mathrm{P}} \mathbf{y} \times \rho_R \mathbf{b}\, \mathrm{dv} + \iint_{\partial\mathrm{P}} \mathbf{y} \times \mathbf{t}_{\mathrm{n}} \mathrm{da}. \end{aligned} \tag{5}$$

Here $\rho_R(\mathrm{x},t) > 0$ and $\mathrm{c}_R(\mathrm{x},t)$ are the referential mass and mass production (densities) per unit

volume of B, $\mathbf{b}(\mathrm{x},t)$ is the body force (density) per unit mass of B, $\dot{\mathbf{y}}(\mathrm{x},t)$ is the 3D velocity field, and $\mathbf{t}_{\mathrm{n}}(\mathrm{x},t)$ is the contact force (density) per unit area of ∂P with the unit normal vector $\mathbf{n}(\mathrm{x},t)$ orienting ∂P.

One can define the following resultant 2D surface fields:

$$\begin{aligned} \rho &= \int_{-}^{+} \rho_R \mu \mathrm{d}\xi, \quad c = \int_{-}^{+} \mathrm{c}_R \mu \mathrm{d}\xi, \\ \boldsymbol{l} &= \int_{-}^{+} \rho_R \dot{\mathbf{y}} \mu \mathrm{d}\xi, \quad \boldsymbol{k} = \int_{-}^{+} \mathbf{y} \times \rho_R \dot{\mathbf{y}} \mu \mathrm{d}\xi, \end{aligned} \tag{6}$$

$$\begin{aligned} \boldsymbol{n}_v &= \int_{-}^{+} \mathbf{t}_{\mathrm{n}} \mu \mathrm{d}\xi, \quad \boldsymbol{m}_v = \int_{-}^{+} \mathbf{z} \times \mathbf{t}_{\mathrm{n}} \mu \mathrm{d}\xi, \\ \int_{-}^{+} &\equiv \int_{-h^-}^{h^+}, \end{aligned} \tag{7}$$

$$\begin{aligned} \rho \boldsymbol{f} &= \int_{-}^{+} \rho_R \mathbf{b} \mu \mathrm{d}\xi + (\mathbf{t}_{\mathrm{n}} \alpha) \Big|_{-}^{+}, \\ \rho \boldsymbol{c} &= \int_{-}^{+} \mathbf{z} \times \rho_R \mathbf{b} \mu \mathrm{d}\xi + (\mathbf{z} \times \mathbf{t}_{\mathrm{n}} \alpha) \Big|_{-}^{+}, \end{aligned} \tag{8}$$

where $(\mathbf{x})\big|_{-}^{+} \equiv \mathbf{x}^{+} - \mathbf{x}^{-}$ and the geometric parameters $\mu, \alpha^{\pm}$ are given in Konopińska and Pietraszkiewicz (2007, A.15–A.17).

In (6), (7), and (8), $\rho(x,t) > 0$ and $c(x,t)$ are the referential surface mass and mass production (densities), $\boldsymbol{l}(x,t)$ and $\boldsymbol{k}(x,t)$ are the surface linear momentum and angular momentum vectors per unit area of M, while $\boldsymbol{f}(x,t)$ and $\boldsymbol{c}(x,t)$ are the surface force and couple vectors per unit mass of M, respectively. Additionally, $\boldsymbol{n}_v(x,t)$ and $\boldsymbol{m}_v(x,t)$ are the surface contact stress and couple-stress vectors describing internal mechanical interactions between the shell parts at the internal boundary $\partial\Pi\backslash\partial M_f$.

With the help of (6), (7), and (8), the mechanical primitive quantities can also be expressed through their resultant 2D representatives:

$$\mathsf{M} = \iint_{\Pi} \rho \, da, \quad \mathsf{C} = \iint_{\Pi} c \, da, \tag{9}$$

$$\begin{aligned} \mathbf{L} &= \iint_{\Pi} \boldsymbol{l} da, \quad \mathbf{F} = \iint_{\Pi} \rho \boldsymbol{f} \, da \\ &+ \int_{\partial\Pi\backslash\partial M_f} \boldsymbol{n}_v \, ds + \int_{\partial\Pi\cap\partial M_f} \boldsymbol{n}^* \, ds, \end{aligned} \tag{10}$$

$$\begin{aligned} \mathbf{A}_{\mathrm{o}} &= \int_{\Pi} (\boldsymbol{k} + \boldsymbol{y} \times \boldsymbol{l}) \Big) da, \\ \mathbf{T}_{\mathrm{o}} &= \int_{\Pi} (\rho \boldsymbol{c} + \boldsymbol{y} \times \boldsymbol{f}) \, da \\ &+ \int_{\partial\Pi\backslash\partial M_f} (\boldsymbol{m}_v + \boldsymbol{y} \times \boldsymbol{n}_v) \, ds \\ &+ \int_{\partial\Pi\cap\partial M_f} \left(\boldsymbol{m}^* + \boldsymbol{y} \times \boldsymbol{n}^*\right) ds, \end{aligned} \tag{11}$$

where $\boldsymbol{n}^*$, $\boldsymbol{m}^*$ are just the external resultant boundary force and couple vectors assigned along a part $\partial M_f \subset \partial M$, which are statically equivalent to distribution of external tractions $\mathbf{t}^*$ applied on $\partial \mathrm{B}_{\mathrm{f}}^*$.

Similarly, the primitive quantities associated with the 1st and 2nd laws can be expressed with respect to the reference placement by the following integrals:

$$\begin{aligned} \mathsf{U} &= \iiint_{\mathrm{P}} \rho_R \mathrm{u} \, \mathrm{dv}, \quad \mathsf{P} = \iiint_{\mathrm{P}} \mathrm{p} \mathrm{dv} + \iint_{\partial \mathrm{P}} \mathrm{p}_{\mathrm{n}} \mathrm{da}, \\ \mathsf{H} &= \iiint_{\mathrm{P}} \rho_R \eta \mathrm{dv}, \end{aligned} \tag{12}$$

$$\begin{aligned} \mathsf{Q} &= \iiint_{P} \rho_R \mathrm{r} \, \mathrm{dv} - \iint_{\partial P} \mathrm{p}_{\mathrm{n}} \mathrm{da}, \\ \mathsf{J} &= \iiint_{\mathrm{P}} \rho_R \mathrm{k} \, \mathrm{dv} - \iint_{\partial \mathrm{P}} \mathrm{j}_{\mathrm{n}} \mathrm{da}. \end{aligned} \tag{13}$$

Here $\mathrm{u}(\mathrm{x},t)$, $\eta(\mathrm{x},t)$, $\mathrm{r}(\mathrm{x},t)$, and $\mathrm{k}(\mathrm{x},t)$ are the 3D (referential) total energy, entropy, heat supply, and entropy supply (densities), all per unit mass of B, $\mathrm{p}(\mathrm{x},t)$ is the 3D mechanical power per unit volume of B, while $\mathrm{p}_{\mathrm{n}}(\mathrm{x},t)$, $\mathrm{q}_{\mathrm{n}}(\mathrm{x},t)$, and $\mathrm{j}_{\mathrm{n}}(\mathrm{x},t)$ are the 3D contact power, heat, and entropy fluxes through the boundary ∂P, respectively.

One can again define the resultant surface fields:

$$\begin{aligned} \rho u &= \int_{-}^{+} \rho_R \mathrm{u} \mu \mathrm{d}\xi, \quad p = \int_{-}^{+} \mathrm{p} \mu \mathrm{d}\xi, \\ p_v &= \int_{-}^{+} \mathrm{p}_{\mathrm{n}} \mu \mathrm{d}\xi, \quad \rho\eta = \int_{-}^{+} \rho_R \eta \mu \mathrm{d}\xi, \end{aligned} \tag{14}$$

$$\begin{aligned} \rho r &= \int_{-}^{+} \rho_R \mathrm{r} \mu \mathrm{d}\xi - (\mathrm{q}_{\mathrm{n}} \alpha) \Big|_{-}^{+}, \\ q_v &= \int_{-}^{+} \mathrm{q}_{\mathrm{n}} \mu \mathrm{d}\xi, \end{aligned} \tag{15}$$

$$\rho k = \int_{-}^{+} \rho_R \mathrm{k}\mu \mathrm{d}\xi - (\mathrm{j_n}\alpha)\,\big|_{-}^{+}\,,$$
$$j_\nu = \int_{-}^{+} \mathrm{j_n}\mu \mathrm{d}\xi. \tag{16}$$

In (14), (15), and (16), $u(x,t)$, $\eta(x,t)$, $r(x,t)$, and $k(x,t)$ are the resultant total energy, entropy, heat supply, and entropy supply (densities), all per unit mass of M, $p(x,t)$ is the resultant mechanical power per unit area of M, while $p_\nu(x,t)$, $q_\nu(x,t)$, and $j_\nu(x,t)$ are the resultant contact mechanical power, heat, and entropy fluxes through the internal boundary $\partial\Pi$, respectively.

With the help of (14), (15), and (16), the quantities (12) and (13) can also be expressed through their 2D representatives:

$$\mathsf{U} = \iint_{\Pi} \rho u da,\ \mathsf{P} = \iint_{\Pi} p da + \int_{\partial\Pi\setminus\partial M_f} p_\nu ds + \int_{\partial\Pi\cap\partial M_f} p^* ds,$$
$$\mathsf{H} = \iint_{\Pi} \rho\eta da, \tag{17}$$

$$\mathsf{Q} = \iint_{\Pi} \rho r da - \int_{\partial\Pi\setminus\partial M_h} q_\nu ds - \int_{\partial\Pi\cap\partial M_h} q^* ds, \tag{18}$$

$$\mathsf{J} = \iint_{\Pi} \rho k da - \int_{\partial\Pi\setminus\partial M_h} j_\nu ds - \int_{\partial\Pi\cap\partial M_h} j^* ds, \tag{19}$$

where p^* is the external resultant boundary power flux assigned along ∂M_f, while q^* and j^* are the external resultant boundary heat and entropy fluxes given along a part $\partial M_h \subset \partial M$, which are thermally equivalent to distributions of 3D heat q* and entropy j* fluxes assigned on $\partial \mathrm{B}_h^* \subset \partial \mathrm{B}^*$.

By the Cauchy postulate extended to the 2D thermal fields, the contact surface quantities $\boldsymbol{n}_\nu$, $\boldsymbol{m}_\nu$, q_ν, and j_ν can be represented through the respective surface stress resultant $\boldsymbol{N}(x,t) \in V \otimes T_xM$ and stress couple $\boldsymbol{M}(x,t) \in V \otimes T_xM$ tensors of the first Piola–Kirchhoff type, as well as the respective referential heat $\boldsymbol{q}(x,t) \in T_xM$ and entropy $\boldsymbol{j}(x,t) \in T_xM$ flux vectors according to

$$\boldsymbol{n}_\nu = \boldsymbol{N}\boldsymbol{\nu},\quad \boldsymbol{m}_\nu = \boldsymbol{M}\boldsymbol{\nu},\quad p_\nu = \boldsymbol{p}\cdot\boldsymbol{\nu},$$
$$q_\nu = \boldsymbol{q}\cdot\boldsymbol{\nu},\quad j_\nu = \boldsymbol{j}\cdot\boldsymbol{\nu}. \tag{20}$$

In these relations $\boldsymbol{\nu} \in T_xM$ is the unit vector externally normal to $\partial\Pi$, and T_xM is the 2D vector space tangent to M at $x \in M$.

In what follows one assumes, as is usual in solid mechanics, that mass is not produced during the process, $\mathsf{C} \equiv 0$. Hence, the balance of mass $(1)_1$ is identically satisfied.

If time derivatives of the set functions $\mathsf{L}(\mathcal{P},t)$, $\mathbf{A}_\mathrm{o}(\mathcal{P},t)$, $\mathsf{U}(\mathcal{P},t)$, $\mathsf{P}(\mathcal{P},t)$, and $\mathsf{H}(\mathcal{P},t)$ exist for all $t \in T$, one can write

$$\mathsf{L}\,\big|_{t_1}^{t_2} = \int_{t_1}^{t_2} \dot{\mathsf{L}} dt,\quad \mathbf{A}_\mathrm{o}\,\big|_{t_1}^{t_2} = \int_{t_1}^{t_2} \dot{\mathbf{A}}_\mathrm{o} dt,$$
$$\mathsf{U}\,\big|_{t_1}^{t_2} = \int_{t_1}^{t_2} \dot{\mathsf{U}} dt,\quad \mathsf{P}\,\big|_{t_1}^{t_2} = \int_{t_1}^{t_2} \dot{\mathsf{P}} dt,$$
$$\mathsf{H}\,\big|_{t_1}^{t_2} = \int_{t_1}^{t_2} \dot{\mathsf{H}} dt. \tag{21}$$

Then using the 2D representations (9), (10), (11), (17), (18), and (19), one obtains

$$\frac{d}{dt}\iint_{\Pi} \boldsymbol{l} da = \iint_{\Pi} \dot{\boldsymbol{l}} da,\ \frac{d}{dt}\iint_{\Pi} (\rho\boldsymbol{k} + \boldsymbol{y}\times\boldsymbol{l}) da = \iint_{\Pi} \left(\rho\dot{\boldsymbol{k}} + \dot{\boldsymbol{y}}\times\boldsymbol{l} + \boldsymbol{y}\times\dot{\boldsymbol{l}}\right) da, \tag{22}$$

$$\frac{d}{dt}\iint_{\Pi} \rho u da = \iint_{\Pi} \rho\dot{u} da,\quad \frac{d}{dt}\iint_{\Pi} p da = \iint_{\Pi} \dot{p} da,\quad \frac{d}{dt}\iint_{\Pi} \rho\eta da = \iint_{\Pi} \rho\dot{\eta} da, \tag{23}$$

and the four remaining laws of mechanics and thermodynamics for the shell-like body become

$$\iint_{\Pi} \left(\rho\boldsymbol{f} - \dot{\boldsymbol{l}}\right) da + \int_{\partial\Pi\setminus\partial M_f} \boldsymbol{n}_\nu ds + \int_{\partial\Pi\setminus\partial M_f} \boldsymbol{n}^* ds = \boldsymbol{0}, \tag{24}$$

$$\iint_{\Pi}\{\rho\boldsymbol{c}-(\rho\dot{\boldsymbol{k}}+\dot{\boldsymbol{y}}\times\boldsymbol{l})+\boldsymbol{y}\times(\rho\boldsymbol{f}-\dot{\boldsymbol{l}})\}da + \int_{\partial\Pi\setminus\partial M_f}(\boldsymbol{m}_\nu+\boldsymbol{y}\times\boldsymbol{n}_\nu)\,ds + \int_{\partial\Pi\cap\partial M_f}(\boldsymbol{m}^*+\boldsymbol{y}\times\boldsymbol{n}^*)\,ds=\boldsymbol{0}, \tag{25}$$

$$\iint_{\Pi}(\rho\dot{u}-p)\,da-\int_{\partial\Pi\setminus\partial M_f}p_\nu ds - \int_{\partial\Pi\cap\partial M_h}p^* ds-\iint_{\Pi}\rho r da + \int_{\partial\Pi\setminus\partial M_h}q_\nu ds+\int_{\partial\Pi\cap\partial M_h}q^* ds=0, \tag{26}$$

$$\iint_{\Pi}\rho\dot{\eta}da-\iint_{\Pi}\rho k da + \int_{\partial\Pi\setminus\partial M_h}j_\nu ds+\int_{\partial\Pi\cap\partial M_h}j^* ds\geq 0. \tag{27}$$

In what follows one assumes that M be a regular geometric surface, so that any kinks, branchings, and self-intersections are excluded. One also assumes that all surface fields discussed here are smooth in Π.

To (24), (25), (26), and (27) with (20), one can apply the surface divergence theorems:

$$\int_{\partial\Pi}\boldsymbol{a}\cdot\boldsymbol{v}\,ds=\iint_{\Pi}Div\,\boldsymbol{a}\,da, \qquad \int_{\partial\Pi}\boldsymbol{S}\boldsymbol{v}\,ds=\iint_{\Pi}Div\,\boldsymbol{S}\,da, \tag{28}$$

$$\int_{\partial\Pi}\boldsymbol{a}\times\boldsymbol{S}\boldsymbol{v}\,ds=\iint_{\Pi}\Big\{\boldsymbol{a}\times Div\,\boldsymbol{S} + \mathrm{ax}\Big[\boldsymbol{S}(Grad\,\boldsymbol{a})^T-(Grad\,\boldsymbol{a})\,\boldsymbol{S}^T\Big]\Big\}da, \tag{29}$$

valid for any $\boldsymbol{a}(x,t)\in T_xM$ and $\boldsymbol{S}(x,t)\in V\otimes T_xM$, where the surface gradient and divergence operators with respect to $x\in M$ are defined as in Gurtin and Murdoch (1975), and $(\mathrm{ax}\,\mathbf{T})\in V$ means the axial vector of the skew tensor $\mathbf{T}\in V\otimes V$, $\mathbf{T}^T=-\mathbf{T}$, so that $\mathbf{T}=(\mathrm{ax}\,\mathbf{T})\times\mathbf{1}$, where $\mathbf{1}\in V\otimes V$ is the 3D identity tensor. Then, after some transformations one obtains the following four local laws of resultant shell thermomechanics in the Lagrangian description valid in any $\Pi\in M$:

$$Div\,\boldsymbol{N}+\rho\boldsymbol{f}=\dot{\boldsymbol{l}}, \qquad Div\,\boldsymbol{M}+\mathrm{ax}\left(\boldsymbol{N}\boldsymbol{F}^T-\boldsymbol{F}\boldsymbol{N}^T\right)+\rho\boldsymbol{c}=\dot{\boldsymbol{k}}+\dot{\boldsymbol{y}}\times\boldsymbol{l}, \tag{30}$$

$$\rho\dot{u}-(p+Div\,\boldsymbol{p})-(\rho r-Div\,\boldsymbol{q})=0, \tag{31}$$

$$\rho\dot{\eta}-(\rho k-Div\,\boldsymbol{j})\geq 0, \tag{32}$$

where $\boldsymbol{F}=Grad\,\boldsymbol{y}\in V\otimes T_xM$ is the surface deformation gradient.

The corresponding dynamic and thermal boundary conditions are

$$\boldsymbol{n}^*-\boldsymbol{N}\boldsymbol{v}=\boldsymbol{0}, \quad \boldsymbol{m}^*-\boldsymbol{M}\boldsymbol{v}=\boldsymbol{0}, \quad p^*-\boldsymbol{p}\cdot\boldsymbol{v}=0 \quad \text{along } \partial M_f, \tag{33}$$

$$q^*-\boldsymbol{q}\cdot\boldsymbol{v}=0, \quad j^*-\boldsymbol{j}\cdot\boldsymbol{v}=0 \quad \text{along } \partial M_h. \tag{34}$$

The relations (30), (31), (32), (33), and (34) are formally *exact implications* of the global laws of continuum thermodynamics (1) and (2), with (21) and 2D representations (9), (10), (11) and (17), (18), (19), for the shell-like body represented during motion by the material base surface $M(t)$, which in the reference placement is M.

Modified Resultant Energy Balance

It was noted in Pietraszkiewicz (2011) that during the through-the-thickness integration, some part of the 3D mechanical power following from the Piola stress tensor **P** acting on surfaces in B parallel to M as well as from self-equilibrated distributions across the shell cross section of **P**, body forces **b**, and boundary tractions $\mathbf{t}^*$ is not accounted for. In fact, Pietraszkiewicz et al. (2006) proved explicitly that the 3D stress power can be expressed through the resultant 2D stress power *plus* an additional stress power not expressible through $\boldsymbol{N}$, $\boldsymbol{M}$. As a result, one can write the resultant 2D balance of mechanical energy symbolically as $\mathsf{P}_e-\mathsf{S}_e=\mathsf{K}_e$, where

indices e mean that these quantities are *effective* quantities calculated using only the surface fields defined on the material base surface. In particular, if S and S_e are given through their 2D representatives, then

$$\mathsf{S} = \iint_{\Pi} \sigma da, \quad \mathsf{S}_e = \iint_{\Pi} \sigma_e da, \quad \sigma_e < \sigma. \tag{35}$$

In continuum mechanics, the total energy $\mathsf{U}(\mathcal{P}, t)$ is often decomposed into the kinetic energy $\mathsf{K}(\mathcal{P}, t)$ and the internal energy $\mathsf{E}(\mathcal{P}, t)$:

$$\mathsf{U} = \mathsf{K} + \mathsf{E}, \quad \mathsf{E} = \iiint_{\mathrm{P}} \rho_R \varepsilon \mathrm{dv} = \iint_{\Pi} \rho\varepsilon da,$$
$$\rho\varepsilon = \int_{-}^{+} \rho_R \varepsilon \mu \mathrm{d}\xi. \tag{36}$$

On the other hand, the mechanical power $\mathsf{P}(\mathcal{P}, t)$ can be related to K by $\mathsf{P} = \dot{\mathsf{K}} + \mathsf{S}$. Then the balance of energy $(2)_1$ can be stated in the alternative simpler form:

$$\dot{\mathsf{E}} = \mathsf{S} + \mathsf{Q}, \quad \text{or} \quad \mathsf{E}\big|_{t_1}^{t_2} = \int_{t_1}^{t_2} (\mathsf{S} + \mathsf{Q}) dt. \tag{37}$$

From (37) follows the simpler form of local, resultant balance of energy

$$\rho\dot{\varepsilon} - \sigma - (\rho r - Div\, \boldsymbol{q}) = 0. \tag{38}$$

Thanks to Libai and Simmonds (1983, 1998), Chróścielewski et al. (2004), and Pietraszkiewicz et al. (2006), the integrand of S_e can also be given in the following coordinate-free form:

$$\sigma_e = \boldsymbol{N} \cdot \boldsymbol{E}^{\mathrm{o}} + \boldsymbol{M} \cdot \boldsymbol{K}^{\mathrm{o}}, \tag{39}$$

$$\boldsymbol{E} = \boldsymbol{J}\mathbf{F} - \boldsymbol{Q}\boldsymbol{I}, \quad \boldsymbol{K} = \boldsymbol{C}\mathbf{F} - \boldsymbol{Q}\boldsymbol{B}, \tag{40}$$

$$\boldsymbol{E}^{\mathrm{o}} = \boldsymbol{Q}\frac{d}{dt}\left(\boldsymbol{Q}^T\boldsymbol{E}\right) = Grad\, \boldsymbol{v} - \boldsymbol{\Omega}\boldsymbol{F},$$
$$\boldsymbol{K}^{\mathrm{o}} = \boldsymbol{Q}\frac{d}{dt}\left(\boldsymbol{Q}^T\boldsymbol{K}\right) = Grad\, \boldsymbol{\omega}. \tag{41}$$

In definitions (40) of the natural surface stretch $\boldsymbol{E}(x,t)$ and bending $\boldsymbol{K}(x,t)$ tensors, $\boldsymbol{I} \in V \otimes T_xM$ and $\boldsymbol{J} \in V \otimes T_yM(t)$ are the inclusion operators at $x \in M$ and $y \in M(t)$ (see Gurtin and Murdoch 1975); $\boldsymbol{B} \in V \otimes T_xM$ and $\boldsymbol{C} \in V \otimes T_yM(t)$ are the structure tensors of the shell in the reference and actual placement, respectively; and $\mathbf{F} \in T_yM(t) \otimes T_xM$ is the tangential surface deformation gradient such that $dy = \mathbf{F}dx$, $\boldsymbol{F} = \boldsymbol{J}\mathbf{F}$. The co-rotational time derivative $(.)^{\mathrm{o}}$ is defined in (41) through the rotation tensor $\boldsymbol{Q} = \boldsymbol{d}_i \otimes \boldsymbol{t}_i$, $\boldsymbol{Q}^T = \boldsymbol{Q}^{-1}$, $\det \boldsymbol{Q} = +1$, where $\boldsymbol{d}_i(x,t)$ and $\boldsymbol{t}_i(x)$, $i = 1,2,3$, are the orthonormal base vectors (directors) in the actual and reference placement, respectively. Moreover, now

$$\boldsymbol{u} = \boldsymbol{y} - \boldsymbol{x}, \quad \boldsymbol{v} = \dot{\boldsymbol{y}} = \dot{\boldsymbol{u}},$$
$$\boldsymbol{\omega} = \mathrm{ax}\left(\dot{\boldsymbol{Q}}\boldsymbol{Q}^T\right), \quad \boldsymbol{\Omega} = \boldsymbol{\omega} \times \mathbf{1}, \tag{42}$$

where $\boldsymbol{u}(x,t)$ is the surface translation vector and $\boldsymbol{Q}(x,t)$ is the surface rotation tensor. The fields $\boldsymbol{y}$ (or $\boldsymbol{u}$) and $\boldsymbol{Q}$ are independent kinematic variables of the shell motion. Thus, the complementary to (33) displacement boundary conditions are

$$\boldsymbol{y}^* - \boldsymbol{y} = \mathbf{0}, \quad \boldsymbol{Q}^* - \boldsymbol{Q} = \mathbf{0} \text{ along } \partial M_d = \partial M \setminus \partial M_f. \tag{43}$$

In the resultant balance of energy (38), the resultant stress power σ is required, while only its effective part σ_e is available in (39). Use of σ_e in place of σ in (38) as in Simmonds (1984, 2012) introduces undefinable error into the resultant energy balance (38). To compensate this error, one can introduce an additional stress power $\mathsf{W}(\mathcal{P}, t)$ of the shell-like body, called here *the interstitial working* after Dunn and Serrin (1985), such that $\mathsf{S} = \mathsf{S}_e + \mathsf{W}$. For any $\Pi \subset M$ the interstitial working may be represented locally as

$$\mathsf{W} = \int_{\partial\Pi} w_v ds = \iint_{\Pi} Div\, \boldsymbol{w} da, \tag{44}$$

where $w_v(x,t)$ is the surface contact interstitial working (density) and $\boldsymbol{w}(x,t) \in T_xM$ is the corresponding surface interstitial working flux vector such that $w_v = \boldsymbol{w} \cdot \boldsymbol{v}$, so that now $\sigma = \sigma_e + Div\, \boldsymbol{w}$. Then the local, resultant balance of energy (38) is

modified into

$$\rho\dot{\varepsilon} - \left(\boldsymbol{N}\cdot\boldsymbol{E}^{\mathrm{o}} + \boldsymbol{M}\cdot\boldsymbol{K}^{\mathrm{o}} + Div\ \boldsymbol{w}\right) - (\rho r - Div\boldsymbol{q}) = 0. \tag{45}$$

The resultant equation (45) can now be regarded as an *exact implication* of the global 3D balance of energy (37).

Modified Resultant Entropy Inequality

The local resultant entropy inequality in the form (32) is entirely decoupled from other local resultant balance laws (30) and (45).

In continuum thermodynamics, coupling of the 2nd law $(2)_2$ with other balance laws $(1)_{2,3}$ and with $(2)_1$ is achieved by introducing the absolute 3D temperature field $\theta(\mathrm{x},t) > 0$, through which the fields $\mathrm{k}(\mathrm{x},t)$ and $\mathrm{j_n}(\mathrm{x},t)$ in $(13)_2$ are related to those $\mathrm{r}(\mathrm{x},t)$ and $\mathrm{q_n}(\mathrm{x},t)$ in $(13)_1$. In rational continuum thermomechanics, these relations are taken as $\mathrm{k} = \mathrm{r}/\theta$ and $\mathrm{j_n} = \mathbf{q}\cdot\mathbf{n}/\theta$. The 3D entropy inequality in the form

$$\iiint_{\mathrm{P}} \rho_R\dot{\eta}\mathrm{dv} \geq \iiint_{\mathrm{P}} \rho_R\frac{\mathrm{r}}{\theta}\mathrm{dv} - \iint_{\partial\mathrm{P}} \frac{\mathbf{q}\cdot\mathbf{n}}{\theta}\mathrm{da} \tag{46}$$

is usually called the Clausius–Duhem inequality; see Truesdell and Toupin (1960) and Truesdell (1984).

Three different 2D temperature fields appear naturally in shell thermodynamics: a reference temperature associated with the base surface M and two temperatures of the upper and lower shell faces M^+ and M^-. Postulating some reasonable relations between the three surface temperatures, one can reduce the number of independent 2D temperature fields to two or to one, whichever is appropriate. In particular, Murdoch (1976a) proposed to use only one common temperature field associated with M, and this approach has recently been used by Eremeyev and Pietraszkiewicz (2009). Temperatures of the upper and lower shell faces as independent fields were used by Zhilin (1976) and Eremeyev and Zubov (2008), Naghdi (1972) and Green and Naghdi (1979) used the thickness-averaged temperature and its derivative in the transverse normal direction evaluated on M as independent fields, while Simmonds (2012) used the maximal and minimal temperatures across the thickness and introduced their average and difference temperatures as independent variables. Recently Eremeyev and Pietraszkiewicz (2011) developed the resultant, thermomechanic, quasistatic model of phase transitions in shells, where the referential mean temperature and its deviation suggested by Murdoch (1976b) were used. Any such proposal leads to a slightly different structure of the thermodynamic initial-boundary value problem for shells. In particular, for two independent 2D temperature fields, one needs two independent 2D energy balance equations. Since the shell thermodynamic theories mentioned above are not entirely resultant ones, they introduce an indefinable error into the 2D energy balance and entropy inequality.

In this entry the surface mean referential temperature $\theta(x,t)$ is defined by

$$\frac{1}{\theta} = \frac{1}{2}\left(\frac{1}{\theta_+}+\frac{1}{\theta_-}\right),\quad \frac{1}{\theta_+}=\frac{1}{\theta}-\frac{1}{2}\left(\frac{1}{\theta_-}-\frac{1}{\theta_+}\right),\quad \frac{1}{\theta_-} = \frac{1}{\theta} + \frac{1}{2}\left(\frac{1}{\theta_-} - \frac{1}{\theta_+}\right), \tag{47}$$

where θ_+ and θ_- are values of temperature on the upper and lower shell faces M^+ and M^-, respectively. The use of so defined θ itself does not introduce any approximation. Then the through-the-thickness integration in (46) with (47) allows one to represent the Clausius–Duhem inequality in the resultant form:

$$\iint_{\Pi}\left\{\rho\dot{\eta} - \rho\left(\frac{r}{\theta}+s\right) + \frac{1}{\theta}\,Div\,\boldsymbol{q} - \frac{1}{\theta^2}\boldsymbol{q}\cdot\boldsymbol{g} + Div\,\boldsymbol{s}\right\}da + \int_{\partial\Pi\cap\partial M_h}\left\{\frac{q^*}{\theta^*}+s^* - \left(\frac{q_\nu}{\theta}+s_\nu\right)\right\}ds \geq 0, \tag{48}$$

where

$$\begin{aligned} \boldsymbol{g} &= Grad\,\theta \in T_x M, \\ \rho r &= \int_-^+ \rho_R \mathrm{r}\mu \mathrm{d}\xi - (\mathbf{q}\cdot\mathbf{n}\alpha)\,|_-^+ , \end{aligned} \tag{49}$$

$$\begin{aligned} \rho s = &\int_-^+ \left(\frac{1}{\theta} - \frac{1}{\theta}\right)\,\rho_R \mathrm{r}\mu \mathrm{d}\xi \\ &+ \frac{1}{2}\left(\frac{1}{\theta_-} - \frac{1}{\theta_+}\right)(\mathbf{q}\cdot\mathbf{n}\alpha)\,|_-^+ , \end{aligned} \tag{50}$$

$$\begin{aligned} q_\nu &= \boldsymbol{q}\cdot\boldsymbol{\nu} = \int_-^+ \mathbf{q}\cdot\mathbf{n}^*\,\mu\,\mathrm{d}\xi, \\ s_\nu &= \boldsymbol{s}\cdot\boldsymbol{\nu} = \int_-^+ \left(\frac{1}{\theta} - \frac{1}{\theta}\right)\,\mathbf{q}\cdot\mathbf{n}^*\mu\mathrm{d}\xi, \end{aligned} \tag{51}$$

$$\begin{aligned} q^* &= \boldsymbol{q}^*\cdot\boldsymbol{\nu} = \int_-^+ \mathbf{q}^*\cdot\mathbf{n}^*\,\mu\,\mathrm{d}\xi, \\ s^* &= \boldsymbol{s}^*\cdot\boldsymbol{\nu} = \int_-^+ \left(\frac{1}{\theta^*} - \frac{1}{\theta^*}\right)\,\mathbf{q}^*\cdot\mathbf{n}^*\mu\mathrm{d}\xi, \end{aligned} \tag{52}$$

and the geometric parameters μ, $\alpha^{\pm}$, $\mathbf{n}^{\pm}$, $\mathbf{n}^*$ are given by Konopińska and Pietraszkiewicz (2007, A.15–A.17).

With definitions (49), (50), (51), and (52), the relations between the resultant fields appearing in (31), (32), and (34) become

$$k = \frac{r}{\theta} + s, \quad \boldsymbol{j} = \frac{\boldsymbol{q}}{\theta} + \boldsymbol{s}, \quad \boldsymbol{j}^* = \frac{\boldsymbol{q}^*}{\theta} + \boldsymbol{s}^*. \tag{53}$$

The extra surface fields s, $\boldsymbol{s}$, $\boldsymbol{s}^*$ in (53) take into account the extra surface heat and entropy supplies following from nonuniform distribution across the shell thickness of the temperature field θ, which now enters (48) only through its value θ on the base surface M. Presence of the extra fields in (48) assures that the resultant form of Clausius–Duhem inequality (48) still remains an exact implication of the 3D principle (46).

With usual continuity assumptions, the local form of (48) is

$$\begin{aligned} &\rho\dot{\eta} - \frac{1}{\theta}\,(\rho r - Div\,\boldsymbol{q}) - \rho s + Div\,\boldsymbol{s} \\ &\quad - \frac{1}{\theta^2}\boldsymbol{q}\cdot\boldsymbol{g} \geq 0 \quad \text{in } \Pi \subset M, \end{aligned} \tag{54}$$

$$\frac{q^*}{\theta^*} + s^* - \left(\frac{\boldsymbol{q}}{\theta} + \boldsymbol{s}\right)\cdot\boldsymbol{\nu} \geq 0 \quad \text{along } \partial M_h. \tag{55}$$

One can solve the exact, resultant balance of energy (45) for $\rho r - Div\,\boldsymbol{q}$ and use the result in (54), which gives

$$\begin{aligned} &\theta\rho\dot{\eta} - \rho\dot{\varepsilon} + \left(\boldsymbol{N}\cdot\boldsymbol{E}^{\mathrm{o}} + \boldsymbol{M}\cdot\boldsymbol{K}^{o} + Div\,\boldsymbol{w}\right) - \theta\rho s \\ &\quad - \frac{1}{\theta}\boldsymbol{q}\cdot\boldsymbol{g} + \theta\,Div\,\boldsymbol{s} \geq 0 \quad \text{in } \Pi \subset M. \end{aligned} \tag{56}$$

Upon introducing the surface free energy (density) $\psi(x,t)$ by $\psi = \varepsilon - \theta\eta$, one has $\theta\dot{\eta} - \dot{\varepsilon} = -\dot{\psi} - \dot{\theta}\eta$, and (56) takes the final form

$$\begin{aligned} &-\rho\dot{\psi} - \dot{\theta}\rho\eta + \boldsymbol{N}\cdot\boldsymbol{E}^{\mathrm{o}} + \boldsymbol{M}\cdot\boldsymbol{K}^{\mathrm{o}} + Div\,\boldsymbol{w} - \theta\rho s \\ &- \frac{1}{\theta}\boldsymbol{q}\cdot\boldsymbol{g} + \theta\,Div\,\boldsymbol{s} \geq 0 \quad \text{in } \Pi \subset M. \end{aligned} \tag{57}$$

The local resultant 2D entropy inequality (57) can now be regarded as an *exact implication* of the global Clausius–Duhem inequality (46) as well.

Remarks on Constitutive Equations

The local resultant 2D balance laws (30) and (45) and the inequality (57) are expressed through 16 fields, which together form the *shell thermomechanic process* over the domain $M \times T$. Different groups of the fields play different roles in the process. The fields $\boldsymbol{y}$, $\boldsymbol{Q}$, θ constitute the basic thermo-kinematic independent field variables of the initial-boundary value problem of shell thermomechanics. That only seven scalar fields can be taken as independent field variables here follows from the fact that there are only seven scalar resultant field equations (30) and (45) to determine them. The fields $\boldsymbol{N}$, $\boldsymbol{M}$, $\boldsymbol{q}$, ε, η, $\boldsymbol{w}$, s, $\boldsymbol{s}$ have to be specified by appropriate material constitutive equations and the fields $\boldsymbol{l}$, $\boldsymbol{k}$ by appropriate kinetic constitutive equations. When all the fields above are settled, the fields $\boldsymbol{f}$, $\boldsymbol{c}$, r

are supposed to be adjusted so as to satisfy the 2D balance equations (30) and (45). Every such process is called an *admissible thermomechanic process*; it is completely determined by the evolution of deformation and temperature of the shell base surface.

In the resultant shell thermomechanics, specific forms of the constitutive equations can be established by two main approaches. The *direct* approach consists in developing, for a restricted class of shell-like bodies, a general structure of 2D constitutive equations satisfying some reasonable physical and mathematical requirements. Then one has to devise a suitable sets of experiments from which the appropriate material constants or functions entering the constitutive equations can be established. In the *derived* or *deductive* approach, one has to devise suitable mathematical methods allowing one to deduce the 2D constitutive equations for shells as an exact, asymptotic of otherwise rational consequence of a given set of corresponding 3D constitutive equations of the parent theory.

Due to the limited space of this entry, the interested reader should consult discussion given in Pietraszkiewicz (2011) on constitutive equations of the refined resultant 2D thermomechanics of shells. There one can find some general requirements which the shell material constitutive equations must obey. Several admissible forms of the response functionals, in which also the possibility of longer-range spatial interactions is accounted for, have been proposed for constitutive equations of viscous shells with heat conduction and of thermoelastic shells. The procedure of Coleman and Noll (1963) has been used to analyze restrictions imposed by our refined entropy inequality (57) on the 2D forms of constitutive equations. Finally, several novel forms of the 2D kinetic constitutive equations obtained with the help of heuristic arguments have been provided.

Cross-References

- ▸ Elastic Shells, Resultant Nonlinear Theory
- ▸ Junctions in Irregular Shell Structures
- ▸ Surface Geometry, Elements

References

Badur J (2009) Development of notion of energy (in Polish). Wydawnictwo IMP PAN, Gdańsk

Chróścielewski J, Makowski J, Pietraszkiewicz W (2004) Statics and dynamics of multi-shells: nonlinear theory and finite element method (in Polish). IFTR PASci Press, Warsaw

Coleman BD, Noll W (1963) The thermodynamics of elastic materials with heat conduction and viscosity. Arch Ration Mech Anal 13(1):167–178

Dunn JE, Serrin J (1985) On the thermodynamics of interstitial working. Arch Ration Mech Anal 85:95–133

Eremeyev VA, Pietraszkiewicz W (2009) Phase transitions in thermoelastic and thermoviscoelastic shells. Arch Mech 61(1):125–152

Eremeyev VA, Pietraszkiewicz W (2011) Thermomechanics of shells undergoing phase transitions. J Mech Phys Sol 59(7):1395–1412

Eremeyev VA, Zubov LM (2008) Mechanics of elastic shells (in Russian). Nauka, Moscow

Green AE, Naghdi PM (1979) On thermal effects in the theory of shells. Proc R Soc Lond A 365:161–190

Gurtin ME, Murdoch AI (1975) A continuum theory of elastic material surfaces. Arch Ration Mech Anal 57:291–323

Konopińska V, Pietraszkiewicz W (2007) Exact resultant equilibrium conditions in the non-linear theory of branching and self-intersecting shells. Int J Solids Struct 44:352–368

Libai A, Simmonds JG (1983) Nonlinear elastic shell theory. Adv Appl Mech 23:271–371. Academic Press, New York

Libai A, Simmonds JG (1998) The nonlinear theory of elastic shells, 2nd edn. Cambridge University Press, Cambridge, UK

Müller I (2007) A history of thermodynamics: the doctrine of energy and entropy. Springer, Berlin

Müller I, Ruggeri T (1998) Rational extended thermodynamics, 2nd edn. Springer, New York

Murdoch AI (1976a) A thermodynamical theory of elastic material interfaces. Q J Mech Appl Math 29:245–275

Murdoch AI (1976b) On entropy inequality for material interfaces. J Appl Math Phys (ZAMP) 27:599–605

Muschik W (2008) Survey of some branches of thermodynamics. J Non-Equilib Thermodyn 33(2):165–198

Muschik W, Papenfuss C, Ehrentraut H (2001) A sketch of continuum thermodynamics. J Non-Newtonian Fluid Mech 96(1-2):255–290

Naghdi PM (1972) The theory of plates and shells. In: Flügge S, Truesdell C (eds) Handbuch der Physik, vol VIa/2. Springer-Verlag, Berlin, pp 425–640

Pietraszkiewicz W (2011) Refined resultant thermomechanics of shells. Int J Eng Sci 49(10):1112–1124

Pietraszkiewicz W (2018) Elastic shells, resultant nonlinear theory. In: Altenbach H, Őchsner A (eds) Encyclopedia of continuum mechanics, section: shells. Springer-Verlag, Berlin. (in print)

Pietraszkiewicz W, Chróścielewski J, Makowski J (2006) On dynamically and kinematically exact theory of shells. In: Pietraszkiewicz W, Szymczak C (eds) Shell structures: theory and applications. Taylor & Francis Group, London, pp 163–167
Reissner E (1974) Linear and nonlinear theory of shells. In: Fung YC, Sechler EE (eds) Thin shell structures. Prentice-Hall, Englewood Cliffs, pp 29–44
Simmonds JG (1984) The nonlinear thermodynamical theory of shells: descent from 3-dimensions without thickness expansions. In: Axelrad EL, Emmerling FA (eds) Flexible shells, theory and applications. Springer-Verlag, Berlin, pp 1–11
Simmonds JG (2012) The 2011 Koiter lecture: the simple logic of classical nonlinear thermodynamic shell theory. J Appl Mech Trans ASME 79:041005-1
Truesdell C (1984) Rational thermodynamics, 2nd edn. Springer-Verlag, New York
Truesdell C, Noll W (1965) The non-linear field theories of mechanics. In: Flügge S (ed) Handbuch der Physik, vol III/3. Springer-Verlag, Berlin
Truesdell C, Toupin R (1960) The classical field theories. In: Flügge S (ed) Handbuch der Physik, vol III/1. Springer-Verlag, Berlin
Zhilin PA (1976) Mechanics of deformable directed surfaces. Int J Solids Struct 12(9–10):635–648

Shells

▸ Analytical Stability Considerations in Lightweight Design

Shock

▸ Impact on Ceramic Materials

Shock Response

▸ High Strain Rate Metal Plasticity

Shock Structures

▸ System of Symmetric Hyperbolic Equations, Extended Thermodynamics of Gases

Shock Waves Via Ray Expansions

Yury A. Rossikhin[1,2], Anatoliy A. Burenin[3], and Dmitrii A. Potianikhin[4]
[1]Research Center on Dynamics of Solids and Structures, Voronezh State Technical University, Voronezh, Russia
[2]Research Center for Wave Dynamics of Solids and Structures, Voronezh State Technical University, Voronezh, Russia
[3]Institute of Machinery and Metallurgy, Far-Eastern Branch of Russian Academy of Sciences, Komsomolsk-na-Amure, Russia
[4]Komsomolsk-na-Amure State University, Komsomolsk-na-Amare, Russia

Synonyms

Surfaces of strong discontinuity in one-dimensional nonlinearly elastic media

Definition

Ray expansions approach for studying the surfaces of strong and weak discontinuity propagating in nonlinear elastic media.

Introduction

A method for solving dynamic problems of continuous media in the form of power series with respect to time behind the moving wave fronts propagating in a medium was suggested in Achenbach and Reddy (1967). Subsequently this approach was called the ray method. For the same purpose, power series in terms of the ray coordinate was utilized, measured from the surface of discontinuities (Babicheva et al. 1973). The effectiveness of the ray method for investigating the features of boundary waves propagating in deformable media was later

Yury A. Rossikhin: deceased.

confirmed by a number of publications, a review of which is given in Rossikhin and Shitikova (1995a) and Podil'chuk and Rubtsov (1986). In the case, when the shock wave (surface of strain discontinuity) is the leading front of the boundary perturbations propagating in the medium, the approach proposed in Babicheva et al. (1973) turned out to be inapplicable. A corresponding generalization of the ray method to such a special case was proposed by Rossikhin (1991) and Burenin and Rossikhin (1991). The latter case will be considered in this entry.

In order to construct the solution, the properties of shock waves in the deformable medium, the features of their appearance and the laws of propagation are need to be formulated and determined. For the purpose of describing the essence of the ray method, the one-dimensional case of plane shock waves in the elastic medium will be considered, and for one-dimensional cylindrical surfaces of strain discontinuities certain qualitative features will be specified.

Plane Shock Waves in an Incompressible Elastic Medium

Let us consider the simplest case of plane one-dimensional waves appearing in an incompressible elastic isotropic medium under conditions of its shock loading. In the Euler's spatial variables x_i, the Almansi strain tensor components d_{ij} dependence of the stresses σ_{ij} is determined by the Murnaghan formula

$$\sigma_{ij} = -p\delta_{ij} + \frac{\partial W}{\partial d_{ik}}\left(\delta_{kj} - 2d_{kj}\right), \qquad (1)$$

where $d_{ij} = \frac{1}{2}\left(u_{i,j} + u_{j,i} - u_{k,i}u_{k,j}\right)$, $u_{i,j} = \partial u_i/\partial x_j$, u_i are the components of the displacement vector, $W\left(d_{ij}\right) = W\left(I_1, I_2\right) = (a-\mu)\, I_1 + aI_2 + bI_1^2 - \kappa I_1 I_2 - \theta I_1^3 + cI_1^4 + dI_2^2 + kI_1^2 I_2 + \ldots$, $I_1 = d_{ii}$, $I_2 = d_{jk}\, d_{kj}$, μ is the shear modulus, a, b, κ, θ, c, d, and k are the elastic constants of higher orders, p is an unknown function of the additional hydrostatic pressure, and δ_{kj} is the Kronecker's symbol. Since $I_1 \le 0$ and $I_2 \ge 0$ for the incompressible medium, the minus sign is chosen before some terms in the expansion of the elastic potential function $W(I_1, I_2)$ in the power series in order all the elastic constants to be positive.

Let us consider a half-space $x_1 > 0$ assuming that its deformations are homogeneous and one-dimensional. Then due to the incompressibility, from the displacement gradient tensor components $u_{i,j}$ only $u_{2,1}$ and $u_{3,1}$ are differ from zero. According to (1), in this case it follows

$$\sigma_{11} = -p - \sum_{k=1}^{\infty} \beta_k m^k,$$
$$\sigma_{i1} = u_{i,1} \sum_{k=0}^{\infty} \gamma_k m^k \quad (i = 2, 3), \qquad (2)$$

where $m = u_{2,1}^2 + u_{3,1}^2$, $\beta_1 = \mu + a$, $\ldots$, $\gamma_0 = \mu$, $\gamma_1 = a + b + d + \kappa$, $\ldots$

Let us define the conditions for the appearance of surfaces of discontinuities in strains under the action on the medium on its boundary plane $x_1 = 0$. For this purpose, the dynamic conditions of compatibility could be rewritten as

$$\left[\sigma_{ij}\right] \nu_j = \rho^+ \left(\upsilon_j \nu_j - G\right)\left[\upsilon_i\right], \; \upsilon_i = \frac{\partial u_i}{\partial t} + \upsilon_j u_{i,j}, \qquad (3)$$

where $[f] = f^+ - f^-$, square brackets denote the jump in the value on the surface of discontinuity, indices «+» and «–» denote that the values are calculated immediately ahead of and behind the surface of the discontinuity, respectively, ν_j are components of the unit vector normal to the surface of discontinuity, and G is the velocity of the discontinuity surface. In the case under consideration, the relations take more simple form:

$$[\sigma_{11}] = 0, \; [\sigma_{i1}] = -\rho G\left[\upsilon_i\right], \; \left[\upsilon_i\right] = -G\tau_i,$$
$$\tau_i = \left[u_{i,1}\right], \; [\upsilon_1] = 0,$$

where the index i takes on the magnitude either $i = 2$ or $i = 3$. The first relationship in (3) is used to calculate the discontinuity in the density $[\rho]$, while others with due account for (2) are reduced

to the set of two equations with respect to three unknowns, namely: τ_2, τ_3, and G:

$$\tau_i \sum_{k=0}^{\infty} \gamma_k m^k + \left(u_{i,1} - \tau_i\right)[m] \sum_{k=1}^{\infty} \gamma_k \sum_{n=1}^{k} (-1)^{n-1} \times C_k^n m^{k-n} [m]^{n-1} = \rho G^2 \tau_i. \tag{4}$$

The signs «+» at $u_{i,1}$ and m are omitted, since only the values of these variables calculated ahead the plane of discontinuities are further utilized. Multiplying the first equation in (4) at $i = 2$ by τ_3 and the second at $i = 3$ by τ_2, and then subtracting one from the other, the conditions for the solvability of (4) as the conditions for the existence of the corresponding planes of discontinuities are obtained

$$\left\{\tau_3 \left(u_{2,1} - \tau_2\right) - \tau_2 \left(u_{3,1} - \tau_3\right)\right\}[m] = 0. \tag{5}$$

At $[m] \neq 0$, from (5) it follows that

$$\frac{u_{3,1}}{u_{2,1}} = \frac{\tau_3}{\tau_2}. \tag{6}$$

Without loss of generality, it is assumed that $u_{2,1} \neq 0$ ahead of the plane of discontinuity, while $u_{3,1} = 0$. This is achieved by an appropriate choice of the Cartesian coordinate system. Then $\tau_2 \neq 0$ and $\tau_3 = 0$ on the plane of discontinuity, and behind the shock wave $u_{3,1}$ remains zero. The plane defined by the x_1- and x_2-coordinate axes turns out to be the plane of polarization of the shock wave. A plane-polarized shock wave, for which conditions (6) are valid, is called the load wave. For its velocity G from (4) it follows

$$G = G_1 = \left\{\rho^{-1} \sum_{k=0}^{\infty} \gamma_k m^k + (\rho\tau_2)^{-1} \left(u_{2,1} - \tau_2\right) \times [m] \sum_{k=0}^{\infty} \gamma_k \sum_{n=1}^{k} (-1)^n C_k^n m^{k-n} [m]^{n-1}\right\}^{1/2}. \tag{7}$$

In addition to the solvability condition of the set of equations in discontinuities mentioned above, another limitation on the existence of shock waves in an elastic medium is the thermodynamic compatibility condition for discontinuities. In gas dynamics it is known as the Zemplen theorem (Chernyii 1988), which prohibits the existence of shock waves of expansion. The thermodynamic compatibility condition for an elastic medium has the form (Burenin and Chernyshov 1978)

$$-\frac{1}{2}\rho \left(\upsilon_j \nu_i - G\right)[\upsilon_i][\upsilon_i] + \sigma_{ij}[\upsilon_i]\nu_j - \left(\upsilon_j \nu_j - G\right)[W] \geq 0.$$

The thermodynamic meaning of this inequality lies in the fact that the shock wave even in the elastic medium is an irreversible process, and the entropy on it must increase (the discontinuity in entropy is less than zero). In the case of the considered unloading shock wave, this inequality is reduced to the form

$$\sum_{k=2}^{\infty} \sum_{n=3}^{2k} \left(\frac{n}{3} - 1\right) \frac{2k!(-1)^n}{n!\,(2k-n)!} s^{2k-n} \tau^n \geq 0, \tag{8}$$

where $s = u_{2,1}$, $\tau = \tau_2 = [u_{2,1}]$, $\tau_3 = 0$, $u_{3,1} = 0$.

Inequality (8) is certainly fulfilled if the medium is not deformed ahead of the plane of discontinuity. When the strains exist ahead of the shock wave of loading ($s = u_{2,1} \neq 0$), then the sufficient condition for fulfilling the inequality (8) is $s \cdot \tau \leq 0$. This means that the loading shock wave necessarily increases the preliminary shear strain.

The condition for the existence of shock waves (5) represents another opportunity when $[m] = 0$. In this case, the intensity of the preliminary shear in the medium is not changed on the shock wave, and only the shear strain direction varies abruptly in accordance with the produced impact. Such a shock wave is called either a neutral wave or a shock wave of circular polarization (Kulikovskii and Sveshnikova 1982). The velocity of propagation of such a plane of discontinuity is found from (4)

$$G = G_2 = \sqrt{\rho^{-1}\sum_{k=0}^{\infty}\alpha_k m^k}, \qquad (9)$$
$$\alpha_1 = \frac{\mu}{2}, \quad \alpha_2 = \frac{\gamma}{4}, \ldots$$

According to (9) and (7), the velocity of the load wave is always lager than the velocity of the neutral shock wave. The neutral shock wave is isentropic, since the thermodynamic compatibility condition for discontinuities becomes the identity on this wave. On this plane of discontinuity, the discontinuity in the additional hydrostatic pressure is absent, i.e. $[p] = 0$, in contrast to the load discontinuity plane.

It is convenient to illustrate the mechanical properties of shock waves by solving the self-similar problem of impact loading of an elastic incompressible half-space $x_1 > 0$ subjected to prestrains. Let us suppose that the load acting on the boundary plane $x_1 = 0$ is constant, and only at the moment of time $t = 0$ its value changes jump-wise. This is equivalent to the fact that up to the moment of time $t = 0$ everywhere in the elastic incompressible body $u_{2,1} = s_{20} = \text{const}$, $u_{3,1} = s_{30} = \text{const}$, $p = p_0 = \text{const}$, and after that they are changed on the boundary $x_1 = 0$ to the values $u_{2,1} = s_{21} = \text{const}$, $u_{3,1} = s_{31} = \text{const}$, and $p = p_1 = \text{const}$. Let us trace the peculiarities of the propagation of the considered boundary perturbation. For this purpose let us introduce the variables ξ, $u(\xi), \upsilon(\xi)$:

$$\xi = \frac{x_1}{ct}, \quad u(\xi) = \frac{u_2}{ct},$$
$$\upsilon(\xi) = \frac{u_3}{ct}, \quad c^2 = \mu\rho^{-1}.$$

The equations of motion in terms of such variables are reduced to the set of two ordinary differential equations

$$\left(\rho c^2\xi^2 + h_0 + h_1\left(u'\right)^2\right)u'' + h_1 u'\upsilon'\upsilon'' = 0,$$
$$h_1 u'\upsilon' u'' + \left(-\rho c^2\xi^2 + h_0 + h_1\left(\upsilon'\right)^2\right)\upsilon'' = 0, \qquad (10)$$

where $h_0 = \sum_{k=0}^{\infty}\gamma_k m^k$, $h_1 = 2\sum_{k=1}^{\infty}k\gamma_k m^{k-1}$, $m = \left(u'\right)^2 + \left(\upsilon'\right)^2$.

The set of Eqs. (10) has a trivial solution $u' = s_2 = \text{const}$ and $\upsilon' = s_3 = \text{const}$ if its determinant is different from zero. A nontrivial solution is possible if the determinant of the system (10) is equal zero

$$\left(\rho c^2\xi^2 + h_0 + h_1\left(u'\right)^2\right)$$
$$\times\left(-\rho c^2\xi^2 + h_0 + h_1\left(\upsilon'\right)^2\right) - \left(h_1 u'\upsilon'\right)^2 = 0. \qquad (11)$$

Direct verification shows that (11) becomes an identity if ξ and m are related as

$$\xi^2 = 1 + \left(\rho c^2\right)^{-1}\sum_{k=1}^{\infty}\gamma_k\,(1+2k)\,m^k = 1 + f(m).$$

Substituting this relationship into (10) leads to the fact that within the area of the nontrivial solution the following relationship is valid:

$$\frac{\upsilon'}{u'} = \frac{u_{3,1}}{u_{2,1}}.$$

Therefore, in this area the direction of the preliminary shear is not changed. Otherwise, the area of the nontrivial solution (10) could be only a plane-polarized simple Riemann wave. The planes bounding the area of the centered wave are the planes of discontinuity in accelerations. Position of the head and back fronts of the simple wave are given by the constant values of the variable ξ: $\xi^+ = (1 + f(m_0))^{1/2}$, and $\xi^- = (1 + f(m_1))^{1/2}$, where m_0 is the magnitude of the shear strains ahead of the front of the centered wave, and m_1 is their value behind the rear front. Since $\xi^+ > \xi^-$, then the condition for the existence of the simple wave is the inequality $m_1 < m_0$. Therefore, the simple wave leads to the plane-polarized decrease in shear prestrains. When $m_1 > m_0$, this Riemann wave must be replaced by a shock loading wave, which varies jump-wisely the value of the shear strains from m_0 to m_1. This case is quite similar to that in

gas dynamics, with the only difference that here deformations of shape change propagate in the medium, while in the gas dynamics the volume deformations do.

Another difference from the gas dynamics is that Eq. (11) has one more root $\xi^2 = 1 + (\rho c^2)^{-1} h_0$. Its substitution into (10) leads to the necessity to consider that $m'(\xi) \equiv 0$, whence it follows a single value of the self-similar variable ξ. It corresponds to the position of the central shock wave (9). Unlike the shock wave of loading, the simple central wave does not correspond to a neutral shock wave. Consequently, a change in the direction of the preliminary shear in accordance with the impact loading could occur only jumpwisely on the neutral shock wave.

Now it is not difficult to construct a solution of the given problem. Depending on the edge effect, two cases could take place: when $m_0 = s_{20}^2 + s_{30}^2 < m_1 = s_{21}^2 + s_{31}^2$ and when this inequality has an opposite sign. In the first case, the front of perturbations propagating in the medium is the shock wave of loading. The strain discontinuities on it must satisfy the condition of plane-polarization of the given plane of discontinuity, i.e. $\tau_2 = [u_{2,1}] = s_{20} - s_2$ and $\tau_3 = [u_{3,1}] = s_{30} - s_3$ satisfy the condition (6), but since the intensity of the shear could not be changed further, then s_2 and s_3 are connected by the relationship $m_1 = s_{21}^2 + s_{31}^2 = s_2^2 + s_3^2$ ($s_2 \neq s_{21}$ and $s_3 \neq s_{31}$). On the neutral shock wave, $\tau_2 = s_2 - s_{21} \neq 0$ and $\tau_3 = s_3 - s_{31} \neq 0$, but $[m] = 0$. At $m_0 > m_1$, the only difference is that within the area of the simple polarized wave the values $u_{2,1}$ and $u_{3,1}$ vary continuously from their magnitudes s_{20} and s_{30} to new magnitudes s_2 and s_3. The neutral shock wave (the wave of circular polarization) unfolds the preliminary shear $m_1 = s_2^2 + s_3^2$ in accordance with the action produced, i.e. $s_2^2 + s_3^2 = s_{21}^2 + s_{31}^2$..

It should be noted that the mentioned above qualitative features for the plane one-dimensional waves are valid for one-dimensional cylindrical waves as well. If the components of the displacement vector of an incompressible elastic medium in the cylindrical system of coordinates r, φ, z are represented by the dependences

$$u_r = r - r\cos\psi\,(r,t)\,,\ u_\varphi = r\sin\psi\,(r,t)\,,$$
$$u_z = u\,(r,t)\,,$$

then the analogue of (6) for the shock loading wave is the proportion

$$\frac{r\psi_{,r}}{u_{,r}} = \frac{\tau_\psi}{\tau_z}, \quad \tau_\psi = \left[r\psi_{,r}\right], \qquad \tau_z = \left[u_{,r}\right], \quad \frac{\partial\psi}{\partial r} = \psi_{,r}. \tag{12}$$

Applying the dynamic compatibility conditions for the discontinuities, we can obtain expressions for the velocities of the shock loading wave and the neutral elastic wave, respectively, as

$$G_1 = \left(h - [h] + \frac{u_{,r}}{\tau_z}[h]\right)^{1/2}, \ G_2 = h^{1/2}, \tag{13}$$

where $h = c^2(1 + \chi m^2 + \ldots)$, $m = (r\psi_{,r})^2 + (u_{,r})^2$, $\chi = (b - \mu)/2\mu$, and multi dots denote non-written terms with higher powers of m.

Plane Shock Waves in a Compressible Elastic Medium

When an elastic medium is compressible, then along with the deformations of shape change as a result of the boundary impact action, the deformations of volume change will also propagate along the medium. The last ones were previously excluded for the simplicity due to the assumption of the incompressibility of the medium. Now let us indicate the main qualitative features in the propagation of boundary shock perturbations when the compressibility of the medium is taken into account. In this case, the elastic potential could be expanded in the following power series:

$$W = \frac{\lambda}{2}I_1^2 + \mu I_2 + lI_1I_2 + mI_1^3 + nI_3 + \xi I_2^2 + \eta I_1^2 I_2 + \kappa I_2 I_3 + \chi I_1^4 + \ldots, \tag{14}$$

where $I_1 = d_{ij}$, $I_2 = d_{jk}\,d_{kj}$, $I_3 = d_{ij}\,d_{jk}\,d_{ki}$.

In Eq. (14) $\lambda, \mu, l, m, n, \xi, \eta, \kappa, \chi$ are the adiabatic constants of the elastic medium, which are calculated under the conditions of constancy of entropy rather than temperature, as in the statics of the nonlinear theory of elasticity. Considering (14), the stress is calculated by the Murnaghan formula

$$\sigma_{ij} = \frac{\rho}{\rho_0} \frac{\partial W}{\partial d_{ik}} \left(\delta_{kj} - 2d_{kj}\right), \qquad (15)$$

where ρ_0 is the density of the medium in its free state, and ρ is the current density. In the simple case of plane one-dimensional shock waves, calculating the components of the stress tensor with the help of (14) and (15) and substituting them into the dynamic compatibility conditions for discontinuities (3), the previously obtained results could be easily generalized. It turns out that the ahead front of the boundary perturbations propagating into the medium is a quasi-longitudinal plane-polarized shock wave. Assuming that the system of coordinate axes is chosen so that the pre-strains are connected only with nonzero components $u_{1,1}$ and $u_{2,1}$ of the displacement gradient tensor, then for such a plane of discontinuities the following relationships are valid:

$$\begin{gathered}
\tau_1 = \left[u_{1,1}\right] \neq 0, \quad \tau_2 = \left[u_{2,1}\right] \neq 0, \quad \tau_3 = \left[u_{3,1}\right] = 0, \quad \tau_2 = \delta u_{2,1}\tau_1 + \ldots. \\
G = G_1 = c_1 \left\{1 + a_1 u_{1,1} + c_1^{-1}\dot{u}_1 + a_2\tau + \tfrac{1}{4}\left(\tfrac{6\theta}{\lambda+2\mu} - 2a_1 - 1\right)u_{1,1}^2\right. \\
- \tfrac{1}{2}\left(\tfrac{3\theta}{\lambda+2\mu} - 2a_1 + 2a_1a_2 - 1\right)u_{1,1}\tau + \tfrac{1}{2}\left(\tfrac{\theta}{\lambda+2\mu} + a_2 - \tfrac{a_2^2}{2} - \tfrac{1}{2}\right)\tau^2 \\
\left. + c_1^{-2}(\dot{u}_1)^2 + (a_2+1)\,c_1^{-1}\dot{u}_1\tau + \left(a_1 + \tfrac{3}{2}\right)c_1^{-1}\dot{u}_1u_{1,1} + \tfrac{1}{2}\,\tfrac{\varphi+2\beta\delta}{\lambda+2\mu}u_{2,1}^2 + \ldots\right\},
\end{gathered} \qquad (16)$$

where

$$\begin{aligned}
&\dot{u}_1 = \frac{\partial u_1}{\partial t}, \quad a_1 = \alpha(\lambda+2\mu)^{-1}, \\
&a_2 = -\frac{1}{2}(a_1 - 1), \quad \alpha = 3(l+m+n) \\
&\quad - \frac{7}{2}(\lambda+2\mu), \quad \beta = \frac{l}{2} + \frac{3}{4}\eta - \frac{\lambda}{2} - 2\mu, \\
&\delta = \frac{2\beta}{\lambda+2\mu}, \quad \varphi = 2\xi + \eta + \frac{3}{2}\kappa - \frac{11}{2}l - 3m \\
&\quad - \frac{27}{4}n + \frac{5}{2}\lambda + 6\mu, \quad \theta = 4(\chi + \xi + \eta + \kappa) \\
&\quad - 12(l+m+n) + \frac{9}{2}(\lambda+2\mu), \\
&c_1^2 = (\lambda+2\mu)\,\rho_0^{-1}.
\end{aligned}$$

Hence it follows that on such a plane of discontinuities the pre-shear decreases. Behind the given quasi-longitudinal plane-polarized wave (only $u_{2,1}$ is also nonzero behind the plane of discontinuity), it follows the analogue of the shock loading wave considered earlier. It is also plane-polarized wave, that is in this case on this wave $\tau_3 = 0$. This wave is called quasi-transverse, since $\tau_1 = \beta(\lambda+2\mu)^{-1}(\tau_2 - 2u_{2,1})$, i.e. the longitudinal discontinuity τ_1 is a small value in terms of the small components of the displacement gradient tensor in comparison with τ_2. The velocity of the given plane of discontinuities is written in the form

$$\begin{aligned}
G = G_2 = c_2 \left\{1 + b_1 u_{1,1} + c_2^{-1}\dot{u}_1\right. \\
+ \left(\frac{\varphi}{2\mu} + b_2 - \frac{b_2^2}{2} - \frac{1}{4}\right)u_{1,1}^2 \\
+ \left(\frac{\gamma}{2\mu} + 2b_2\right)u_{2,1}^2 - 3b_1u_{2,1}\tau_2 \\
+ b_1\tau_2^2 + (b_1+1)\,u_{1,1}c_2^{-1}\dot{u}_1 \\
\left. + c_2^{-2}(\dot{u}_1)^2 + \ldots\right\},
\end{aligned} \qquad (17)$$

where $\gamma = \xi - l - \frac{3}{2}n + \frac{\lambda}{2} + \mu$, $b_1 = \frac{\gamma}{2\mu} - \frac{\beta^2}{\mu(\lambda+\mu)}$, $b_2 = \beta\mu^{-1} + 1$, $c_2^2 = \mu\rho^{-1}$.

The change in the direction of the preliminary shear in accordance with the impact produced

on the half-space, as before, could occur only on a neutral shock wave. The existence of such a plane of discontinuities is also the corollary from the dynamic compatibility conditions for discontinuities (3). In this case, the neutral shock wave is the transverse wave, since on it $\tau_1 = 0$, $\tau_2 \neq 0$, and $\tau_3 \neq 0$, while $\left[u_{2,1}^2 + u_{3,1}^2\right] = 0$. The velocity of its propagation is calculated as

$$\begin{aligned} G = G_3 = c_2\Big\{1 + b_2 u_{1,1} + c_2^{-1}\dot{u}_1 \\ + \frac{1}{4}\left(\frac{2\varphi}{\mu} + 4b_2 - 2b_2^2 - 1\right)u_{1,1}^2 \\ + \frac{\gamma}{2\mu}u_{2,1}^2 + (b_1 + 1)\,u_{1,1}c_2^{-1}\dot{u}_1 \\ + c_2^{-2}(\dot{u}_1)^2 + \ldots\Big\}. \end{aligned} \tag{18}$$

It could be shown, as before, that the neutral shock wave is isentropic. For the quasi-longitudinal shock wave, the thermodynamic restriction on possible discontinuities is reduced to the following: the production of entropy on the quasi-longitudinal shock wave is independent of the preliminary deformed state, and the condition for the growth of entropy in the first approximation in terms of small $u_{1,1}$ and $u_{2,1}$ is reduced to the inequality

$$\left(l + m + n - \frac{3}{2}(\lambda + 2\mu)\right)\tau_1^3 \leq 0 \tag{19}$$

Constants l, m, n, as a rule (Lourier 1980), are negative. Then we have an analogue of the Zemplen theorem in gas dynamics about the existence of only compression shock waves. As follows from (19), the production of entropy on the quasi-longitudinal shock wave has a third order of smallness in deformations. On the quasi-transverse shock wave, this order increases up to the fourth order, therefore it is impossible to draw a definite conclusion due to the lack of qualitative information on fourth-order elastic moduli ξ, η, κ, and χ. The same reason makes it necessary, when solving specific boundary-value problems, to answer preliminary (in contrast to the case of an incompressible medium) a question about what is larger G_1 or G_2.

Ray Method in the Dynamics of Shock Waves

The peculiarities in the construction of approximate solutions of shock deformation problems with the help of the ray method could be considered for the simplest case of the oblique impact on an undeformed elastic half-space $x_1 = x > 0$. It is supposed that starting from the moment of time $t = 0$, as a result of the impact, the boundary plane moves according to the law

$$\begin{aligned} u_1|_{x=\sum\limits_{n=1}^{\infty}\frac{1}{n!}g_n t^n} &= \sum_{n=1}^{\infty}\frac{1}{n!}g_n t^n, \\ u_2|_{x=\sum\limits_{n=1}^{\infty}\frac{1}{n!}h_n t^n} &= \sum_{n=1}^{\infty}\frac{1}{n!}h_n t^n. \end{aligned} \tag{20}$$

Relationships (20) imply that $u_1(x,t)$ and $u_2(x,t)$ on the boundary could be represented in terms of power series with respect to the time t, wherein $g_1 > 0$ and $h_1 > 0$. The first of these relationships is connected with the fact that immediately at the instant $t = 0$ a shock wave Σ_1 is generated, which is the longitudinal wave due to the absence of preliminary strains. The requirement $h_1 > 0$ could be easy fulfilled by the appropriate choice of the system of coordinates, essential only the condition of $h_1 \neq 0$. The second relationship in (20) describes the propagation of a quasi-transverse shock wave Σ_2 from the boundary of the half-space, which is generated at the moment of time $t = 0$. In the area of deformation located between the planes of discontinuities Σ_1 and Σ_2, $u_2 \equiv 0$ owing to the fact that Σ_1 is the longitudinal shock wave. The equation of motion of the medium in this case is reduced to one equation

$$\begin{aligned} u_{1,11}\left(1 - \gamma_1 u_{1,1} + \gamma_2 u_{1,1}^2 + c_1^{-1}u_{1,(1)} + \ldots\right) \\ - c_1^{-2}\left[u_{1,(2)}\left(1 - 2u_{1,1} + u_{1,1}^2\right)\right. \\ \left. + 2u_{1,(1)}u_{1,1(1)}\left(1 - u_{1,1}\right)\right] = 0, \end{aligned} \tag{21}$$

where $u_{1,(1)} = \frac{\partial u_1}{\partial t}$, $u_{1,(2)} = \frac{\partial^2 u_1}{\partial t^2}$, $\gamma_1 = 2\left(\frac{\alpha}{\lambda+2\mu} - 1\right)$, $\gamma_2 = 3\frac{\theta}{\lambda+2\mu} - 4\frac{\alpha}{\lambda+2\mu} + 1$, $\gamma_k u_{1,1}^k$ $(k>2)$, and $\ldots$ indicates the terms $\gamma_k u_{1,1}^k$ $(k>2)$.

From hereafter the symbol $u_{1,(s)}$ denotes the s-order partial derivatives with respect to time. Calculating σ_{11} according to (14) and (15) and then substituting it in (3) yield

$$\xi_1 \left\{ G_1^{-1} \left(1 + \frac{1}{2}\gamma_1 G_1^{-1}\xi_1 + \frac{\theta-\alpha}{\lambda+2\mu} G_1^{-2}\xi_1^2 + \ldots \right) - c_1^{-2} \right\} = 0, \quad \xi_1 = \left[u_{1,(1)} \right]. \tag{22}$$

Hence, for the velocity propagation G_1 of the plane of discontinuity Σ_1, the following power series expansion depending on the intensity of the discontinuity ξ_1 could be written:

$$G_1 = c_1 \left(1 + \alpha_1 c_1^{-1}\xi_1 + \alpha_2 c_1^{-2}{\xi_1}^2 + \ldots \right), \tag{23}$$

where $\alpha_1 = \frac{1}{4}\gamma_1$, $\alpha_2 = \frac{1}{2}\left(\frac{\theta}{\lambda+2\mu} + \frac{3\alpha^2}{(\lambda+2\mu)^2} - \frac{11}{2}\frac{\alpha}{\lambda+2\mu} + \frac{15}{4}\right)$ $\ldots$

Differentiatingthe equation of motion (21) s times with respect to time and writing the obtained result in the form of discontinuities for Σ_1 lead to the equation in discontinuities

$$\left\{ G_1^{-2} \left(1 - \gamma_1 G_1^{-1}\xi_1 + \left(G_1^{-2}\gamma_2 + c_1^{-2} \right)\xi_1^2 + \ldots \right) - c_1^{-2} \left(1 - G_1^{-2}\xi_1^2 \right) \right\} \xi_{s+2} - \left\{ 2G_1^{-2} \left(1 + G_1^{-1}\gamma_1\xi_1 + \left(G_1^{-2}\gamma_2 + c_1^{-2} \right)\xi_1^2 + \ldots \right) - 2c_1^{-2}G_1^{-1}\xi_1 \left(1 - G_1^{-1}\xi_1 \right) \right\} \frac{\delta\xi_{s+1}}{\delta t} + \zeta_s = 0, \tag{24}$$

where $\xi_s = [u_{1,(s)}]$, and

$$\zeta_s = G_1^{-2} \left\{ G_1^{-1} \frac{\delta G_1}{\delta t} \left(\xi_{s+1} - \frac{\delta\xi_s}{\delta t} \right) - \frac{\delta^2\xi_s}{\delta t^2} \right\} \left(1 + \gamma_1 G_1^{-1}\xi_1 + \gamma_2 G^{-2}\xi_1^2 + c_1^{-2}\xi_1^2 + \ldots \right) + \gamma_1 G_1^{-3} \sum_{k=0}^{s-1} C_s^k \left\{ \xi_{k+2} - 2\frac{\delta\xi_{k+1}}{\delta t} + G_1^{-1}\frac{\delta G_1}{\delta t} \left(\xi_{k+1} + \frac{\delta\xi_k}{\delta t} \right) + \frac{\delta^2\xi_k}{\delta t^2} \right\} \left(\xi_{s-k+1} - \frac{\delta\xi_{s-k}}{\delta t} \right) + \ldots + c_1^{-2} \left\{ 2G_1^{-1} \sum_{k=0}^{s} C_s^k \xi_{k+2} \left(\xi_{s-k+1} - \frac{\delta\xi_{s-k}}{\delta t} \right) - 2G_1^{-1} \sum_{k=0}^{s} C_s^k \xi_{k+1} \left(\xi_{s-k+2} - \frac{\delta\xi_{s-k+1}}{\delta t} \right) + \ldots \right\}.$$

When writing the equation in discontinuities (24), the recursive geometric and kinematic compatibility conditions for discontinuities in derivatives of the first (Thomas 1964) and higher orders (Rossikhin 1991; Bykovtsev and Ivlev 1998) of a function that is discontinuous on Σ_1 have been utilized. The theory of such restrictions on possible discontinuities on a moving surface is developed in Rossikhin (1991), and Rossikhin and Shitikova (1994) for the case of rectangular Cartesian coordinates and generalized to the case of curvilinear coordinates in Rossikhin (1991) and Rossikhin and Shitikova (1995b). Note that in (24) the coefficients ahead of the discontinuity ξ_{s+2} and the delta-derivative of the discontinuity ξ_{s+1} do not change with the increase in s, and only ζ_s is recursively calculated with increasing in s. Assuming that s could take on the magnitude $s = -1$, Eqs. (22) and (24) could be rewritten as one equation

$$M_{s+2}\xi_{s+2} + N_{s+1}\frac{\delta\xi_{s+1}}{\delta t} + \zeta_s = 0. \tag{25}$$

At $s=-1$, relationship (25) represents the dynamic compatibility condition for

discontinuities, at $s = 0$ it provides the equation of motion written in the discontinuities on Σ_1, and further s denotes the number of differentiations of the equation of motion. It is obvious that $N_0 = 0$, $N_1 = N_2 = N_3 = \ldots$, $M_2 = M_3 = \ldots$, and $\zeta_0 = \zeta_1 = 0$, wherein the condition $M_1 \neq M_2 = M_3 = \ldots$ is the main difference between the shock wave and the weak wave (the plane of discontinuities in accelerations). Relationship $M_1 = 0$ could be utilized, as follows from (22), to calculate the velocity of motion G_1 of the discontinuity plane Σ_1, and the velocity of propagation of perturbations within the medium is calculated from the condition $M_2 = 0$. If G_1 were coincided with the sound speed, then the first term in (25) would not exist, and therefore the intensity of the discontinuity ξ_1, as well as $\xi_2, \xi_3 \ldots$, would be described by an ordinary differential equation (it is called the attenuation equation). Such a case was considered in Achenbach and Reddy (1967) and Babicheva et al. (1973) and in numerous publications reviewed in Rossikhin and Shitikova (1995a). Consequently, the problems when the ahead front of the boundary perturbations propagates through the medium in the form of a shock wave could not be solved using "the traditional ray method" (Achenbach and Reddy 1967; Babicheva et al. 1973). That is why in 1991 the so-called "nonlinear version" of the ray method was proposed and developed by Rossikhin (1991) and Burenin and Rossikhin (1991), and some examples will be considered below.

First of all note that from (24) and (25) it is possible to write recurrent dependences in the form

$$\begin{gathered} \frac{\delta^n \xi_1}{\delta t^n} = F_n\left(\xi_1, \xi_2, \ldots, \xi_s, \xi_{n+1}\right); \\ \xi_{n+1} = \mathrm{H}_n\left(\xi_1, \frac{\delta \xi_1}{\delta t}, \frac{\delta^2 \xi_1}{\delta t^2}, \ldots, \frac{\delta^n \xi_1}{\delta t^n}\right). \end{gathered} \tag{26}$$

An approximate solution in the area of dynamic deformation behind the plane of discontinuity Σ_1 could be found in the form of the ray expansion

$$u_1^{(1)} = -\sum_{n=1}^{\infty} \frac{1}{n!} \xi_n \Big|_{t=t^*} \left(t - t^*\right)^n, \; t^* = \int_0^{x_1} \frac{d\Theta}{G_1(\Theta)}. \tag{27}$$

The coefficients of the ray series (27), depending either on time or on the ray coordinate x_1, remain unknown, but the compatibility conditions for discontinuities are fulfilled for them. They also must comply with the loading conditions (20). Let us represent the intensity ξ_1 of the shock wave Σ_1 in terms of the power series

$$\xi_1 = \sum_{k=0}^{\infty} \frac{1}{k!} d_k t^k; \quad d_k = \frac{\delta^k \xi_1}{\delta t^k}\Big|_{t=0}. \tag{28}$$

Constants d_k should be defined by fulfilling the initial and boundary conditions of the problem. The loaded boundary does not belong to the deformation area between Σ_1 and Σ_2, therefore, its calculation could be considered after the analysis of another deformation area located between the plane Σ_2 and the loaded boundary. Within this area, along with $u_1(x,t)$, the displacement component $u_2(x,t)$ is also non-zero. The equation of motion in this area is written in the form

$$\begin{gathered} \left(1 + \gamma_1 u_{1,1} + \gamma_2 u_{1,1}^2 + \gamma_3 u_{2,1}^2 + \ldots\right) u_{1,11} + \left(\lambda_1 u_{2,1} + \lambda_2 u_{1,1} u_{2,1} + \ldots\right) u_{2,11} \\ - c_1^{-2} \left\{ u_{1,(2)} \left(1 - u_{1,1}\right)^2 + 2 u_{1,(1)} u_{1,1(1)} \left(1 - u_{1,1}\right) + u_{1,(1)}^2 u_{1,11} \right\} = 0, \\ \left(1 + \mu_1 u_{1,1} + \mu_2 u_{1,1}^2 + \mu_3 u_{2,1}^2 + \ldots\right) u_{2,11} + \left(\nu_1 u_{2,1} + \nu_2 u_{1,1} u_{2,1} + \ldots\right) u_{1,11} \\ - c_2^{-2} \left\{ u_{2,(2)} \left(1 - u_{1,1}\right)^3 + \left(2 + u_{1,(1)} u_{2,1(1)} + u_{2,1} u_{1,(2)}\right) \left(1 - u_{1,1}\right)^2 + u_{1,(1)}^2 u_{2,1} u_{1,11} \right. \\ \left. + 2 u_{2,1} u_{1,(1)} u_{1,1(1)} \left(1 - u_{1,1}\right) + u_{1,(1)}^2 u_{2,11} \left(1 - u_{1,1}\right) \right\} = 0, \end{gathered} \tag{29}$$

where

$$\gamma_3 = \frac{\varphi + 3n - 4\mu}{\lambda + 2\mu}, \quad \lambda_1 = \frac{2\beta}{\lambda + 2\mu},$$
$$\lambda_2 = 2(\gamma_3 - \lambda_1), \quad \mu_1 = \frac{2\beta}{\mu} - 1,$$
$$\mu_2 = \mu^{-1}\left(\varphi - l - \frac{3}{4}n + \lambda + 5\mu\right),$$
$$\mu_3 = 3\mu^{-1}\left(\xi - l - \frac{3}{2}n + \lambda\right),$$
$$\nu_1 = 2\beta\mu^{-1} + 1, \quad \nu_2 = 2\mu^{-1}\left(\varphi + \frac{3}{4}n\right) + 14.$$

Differentiating Eqs. (29) s times with respect to time and writing the resulting relationships in discontinuities on Σ_2 result in the analogue of (24). Using the recursive geometric and kinematic compatibility conditions for discontinuities (Thomas 1964) yields

$$\begin{aligned} &A_{s+2}\eta_{s+2} + B_{s+2}\omega_{s+2} + D_{s+1}\frac{\delta\,\eta_{s+1}}{\delta\,t} \\ &\quad + E_{s+1}\frac{\delta\,\omega_{s+1}}{\delta\,t} + F_s = 0, \\ &P_{s+2}\eta_{s+2} + Q_{s+2}\omega_{s+2} \\ &\quad + R_{s+1}\frac{\delta\,\eta_{s+1}}{\delta\,t} + S_{s+1}\frac{\delta\,\omega_{s+1}}{\delta\,t} + T_s = 0, \end{aligned} \tag{30}$$

where $\eta_s = \left[u_{1,(s)}\right]\big|_{\Sigma_2}$ and $\omega_s = \left[u_{2,(s)}\right]\big|_{\Sigma_2}$.

As in Eq. (25) it is assumed that in Eq. (30) s could take on the magnitudes -1, 0, 1, 2, ... At $s = -1$, the set of equations in discontinuities (30) gives the dynamic conditions for the compatibility of discontinuities (it is the corollary of (3)). Without writing down the expressions for the coefficients in (30), it could be noted that they do not change with the change of s at $s = 1$, 2, 3, ... Only free terms of the set of Eqs. (30) change recurrently under the growth of s, in so doing $F_0 = T_0 = 0$. Consequently, in the case when Σ_2 is a weak wave ($\eta_1 = \omega_1 = 0$), the set of Eqs. (30) at $s = 0$ is found to be homogeneous:

$$\begin{aligned} A_2\eta_2 + B_2\omega_2 = 0, \\ P_2\eta_2 + Q_2\omega_2 = 0. \end{aligned} \tag{31}$$

The condition of the equality to zero of the determinant of (31) makes it possible to calculate the velocity of the surface of accelerations discontinuities. The subsequent steps with $s = 1$, 2, 3 ... allows one to obtain ordinary differential equations for the coefficients of the ray series.

In the case when Σ_2 is the shock wave ($\eta_1 \neq 0$ and $\omega_1 \neq 0$), $A_1 \neq A_2 = A_3 = \ldots$, $B_1 \neq B_2 = B_3 = \ldots$, $P_1 \neq P_2 = P_3 = \ldots$, and $Q_1 \neq Q_2 = Q_3 = \ldots$ in Eq. (30), while the recurrence relations for F_s and T_s involve the discontinuities η_{s+1} and ω_{s+1} and the discontinuities in the lower orders derivatives, the δ-derivatives of these discontinuities on Σ_2, as well as the δ-derivatives of $u_{1,1}$ and $u_{1,(1)}$ calculated immediately ahead of the plane Σ_2.

The velocity of the discontinuity plane Σ_2 could be found using the dynamic compatibility conditions for the discontinuities as

$$\begin{aligned} G = G_2 = c_2\big(1 + \beta_1 u_{1,1} + u_{1,(1)} \\ \times \left(1 + u_{1,1}\right) + \beta_2 u_{1,1}^2 + \beta_3\omega_1^2 + \ldots\big), \\ \eta_1 = -G_1^{-1}\delta\omega_1^2 + \ldots. \end{aligned} \tag{32}$$

where

$$\delta = (\lambda + \mu)^{-1}\left(\frac{l}{2} + \frac{3}{4}n - \frac{\lambda}{2} - 2\mu\right),$$
$$\beta_1 = \frac{1}{2}\mu^{-1}\left(l + \frac{3}{2}n - \lambda - 2\mu\right),$$
$$\beta_2 = \frac{1}{2\mu}\left(2\xi + \eta + \frac{3}{2}\chi - 4l - 3m - \frac{15}{4}n + \frac{\lambda}{2}\right) + \frac{1}{8\mu^2}\left(l + \frac{3}{2}n - \lambda - 3\mu\right)^2 + \frac{13}{8},$$
$$\beta_3 = \frac{1}{2\mu}\left\{\xi - l - \frac{3}{2}n + \frac{\lambda}{2} - \delta\left(l + \frac{3}{2}n - \lambda - 3\mu\right)\right\} + \frac{\delta}{2}.$$

S

At the initial step of calculation, i.e. at $s = 0$ from Eq. (30) it follows

$$\begin{aligned}
\eta_2 &= \left(\lambda_1 \delta c_2^{-1} \omega_1 - \lambda_2 u_{1,1}\right) c_2^{-1} \omega_1 \omega_2 + \ldots; \\
\frac{\delta \omega_2}{\delta t} &= \frac{1}{2} (\delta + 2\mu_3) c_2^{-2} \omega_1^2 \omega_2 + \ldots; \\
\frac{\delta \eta_2}{\delta t} &= -2\delta c_2^{-1} \omega_1 \frac{\delta \omega_1}{\delta t} + \ldots.
\end{aligned} \tag{33}$$

Considering (33) and putting $s = 1, 2, 3 \ldots$ in (30) yield

$$\begin{aligned}
\eta_{s+1} &= \Psi_{s+1} (\omega_1, \omega_2, \ldots, \omega_{s+1}), \\
\frac{\delta \eta_s}{\delta t} &= \Phi_s (\omega_1, \omega_2, \ldots, \omega_s, \omega_{s+1}), \\
\frac{\delta \omega_s}{\delta t} &= \Theta_s (\omega_1, \omega_2, \ldots, \omega_s, \omega_{s+1}).
\end{aligned} \tag{34}$$

Relationships (33) represent Ψ_2, Φ_1 and Θ_1 at $s = 1$. It is important to note that in such a way the δ-derivatives of η_s and ω_s are connected with η_{s+1} and ω_{s+1}, what allows one to calculate recurrently η_s and ω_s in terms of the intensity of the discontinuity ω_1 on the moving plane Σ_2 and the δ-derivatives of a considered function given on Σ_2. The ray expansions for the solutions for the displacement components in the domain behind the plane of the strong discontinuity Σ_2 are written in the form

$$\begin{aligned}
u_1^{(2)} &= -\sum_{n=1}^{\infty} \frac{1}{n!} \xi_n \Big|_{t=t^*} \left(t - t^*\right)^n \\
&\quad -\sum_{n=1}^{\infty} \frac{1}{n!} \eta_n \Big|_{t=t_*} (t - t_*)^n, \\
u_2^{(2)} &= -\sum_{n=1}^{\infty} \frac{1}{n!} \omega_n \Big|_{t=t_*} (t - t_*)^n,
\end{aligned} \tag{35}$$

where

$$t^* = \int_0^{x_1} \frac{d\Theta}{G_1(\Theta)}, \quad t_* = \int_0^{x_1} \frac{d\Theta}{G_2(\Theta)}.$$

Supposing that ω_1 could be represented in the form of the power series

$$\omega_1 = \sum_{k=0}^{\infty} \frac{1}{k!} m_k t^k, \quad m_k = \frac{\delta^k \omega_1}{\delta t^k}\Big|_{t=0}, \tag{36}$$

the constants d_k and m_k in Eqs. (28) and (36) are determined according to impact loading conditions (20). However, it is impossible to do this directly, since the δ-derivatives of the functions ξ_k and ω_k with respect to time given on different moving planes of discontinuity Σ_1 and Σ_2 do not enter into conditions (20). Therefore, with such a substitution, they should be excluded from the series (35) and (36) with the help of the dependences (26) and (28). From (20) it follows that

$$\begin{aligned}
\xi_1|_{t=0} &= \xi_{10} = -\frac{g + \delta\, c_2^{-1} h_1^2 \left(1 - g_1 c_1^{-1}\right)^{-1}}{1 - g_1 c_1^{-1}} + \ldots, \\
\omega_1|_{t=0} &= \omega_{10} = -h_1 \left(1 - g_1 c_2^{-1}\right) + \ldots, \\
\xi_2|_{t=0} &= \xi_{20} = \frac{g_2 \left(1 - c_1^{-1} \xi_{10}\right)}{\left(1 - g_1 c_2^{-1}\right)^2} + \ldots, \\
\omega_2|_{t=0} &= \omega_{20} = -\frac{h_2 - c_2^{-1} \omega_{10} g_2 + 2\, c_2^{-2} g_1^2 \omega_{10} \left(\beta_1 c_1^{-1} + c_2^{-1}\right) g_2}{\left(1 - g_1 c_2^{-1}\right)^2} + \ldots.
\end{aligned} \tag{37}$$

The values of other functions at $t = 0$, including d_1, d_2, m_1 and m_2, are calculated with the help of the found relationships (37) by substituting the latter into relations valid for discontinuities at any moment of time

$$\eta_1 = -\delta\, c_2^{-1}\omega_1^2 + \ldots,$$
$$\eta_2 = \left(\lambda_1\delta\, c_2^{-1}\omega_1 - \lambda u_{1,1}\right) c_2^{-1}\omega_1\omega_2 + \ldots,$$

$$\frac{\delta\xi_1}{\delta\, t} = \frac{\alpha}{2\,(\lambda + 2\mu)} c_1^{-1}\xi_1\xi_2 + \ldots,$$
$$\frac{\delta\omega_1}{\delta\, t} = \frac{1}{2}\,(\delta + 2\mu_3)\, c_2^{-2}\omega_1^2\omega_2 + \ldots, \tag{38}$$
$$\frac{\delta\eta_1}{\delta\, t} = -2\delta c_2^{-1}\omega_1\frac{\delta\omega_1}{\delta\, t} + \ldots.$$

The final approximate solution with the accuracy up to the two outlined terms of the ray series takes the form

$$\begin{aligned}
u_1^{(1)} &= -\xi_{10}\left\{1 + Bc_1^{-1}\xi_{20}\,(t - y_1)\right\} y_1 - \frac{1}{2}\xi_{20}y_1^2 + \ldots,\\
u_1^{(2)} &= u_1^{(1)} + c_2^{-1}\omega_{10}\delta\left\{1 + (\delta + 2\mu_3)\;c_2^{-2}\omega_{10}\omega_{20}\,(t - t_2)\right\} y_2\\
&\quad - \frac{1}{2}\left\{\lambda_1\delta\, c_2^{-1}\omega_{10} + \lambda_2 c_1^{-1}\xi_{10} - \lambda_2\xi_{20}\left(c_2^{-1} - c_1^{-1}B\xi_{10}\right)(t - y_2)\right\} c_2^{-1}\omega_{10}\omega_{20}y_2^2 + \ldots,\\
u_2^{(2)} &= -\omega_{10}\left\{1 + \frac{1}{2}\,(\delta + 2\mu_3)\;c_2^{-2}\omega_{10}\omega_{20}\,(t - y_2)\right\} y_2 - \frac{1}{2}\omega_{20}y_2^2 + \ldots,
\end{aligned} \tag{39}$$

where

$$y_1 = t - \frac{c_1^2\left(1 - c_1^{-1}g_1\right)}{B\alpha_1 g_1\xi_{20}}\ln\left(1 + \frac{B\alpha_1 g_1\xi_{20}}{c_1^3\left(1 + c_1^{-1}\alpha_1\xi_{10}\right)\left(1 - c_1^{-1}g_1\right)}x_1\right),$$
$$y_2 = t - \frac{1}{c_2 z_2}\ln\left(1 + \frac{z_2}{z_1}x_1\right), \quad z_1 = 1 + \beta_1 c_1^{-1}\xi_{10} - c_2^{-1}\xi_{10} + \beta_3 c_2^{-2}\omega_{10}^2,$$
$$z_2 = \left(\beta_1 c_1^{-1} + c_2^{-1} + c_1^{-1}\left(\beta_1\left(2c_1^{-1} - c_2^{-1}\right) - c_2^{-1}\right)B\xi_{10}\right)\, c_2^{-1}\xi_{20},$$
$$B = \beta_1 c_1 g_1^{-1} + \beta_2 c_1 (1 - z_1)^{-1} g_1.$$

Obviously, such cumbersome but recurrent procedure could be continued, and it is possible to obtain an approximate solution within the required accuracy.

Ray Method in the Case of One-Dimensional Cylindrical Waves

Let us consider one more example of the ray expansion construction for the solution of the dynamic problem of impact loading, when the surfaces of discontinuities are cylindrical. Consider an incompressible elastic medium the properties of which are given by the elastic potential $W = W(I_1, I_2)$ in the form (Lourier 1980):

$$W = W\,(I_1, I_2) = -2\mu I_1 + bI_1^2 - \mu I_2 - aI_1^3 - (\mu - b)\, I_1 I_2 + \ldots, \tag{40}$$

where μ is the shear modulus, and a and b are the elastic constants of higher order.

Assuming that the medium is located between rigid cylindrical surfaces $r = r_0$ and $r = R\,(R > r_0)$

and that the conditions of rigid adhesion are fulfilled on the boundary surfaces, while there is no displacement on the surface $r = R$ until the moment of time $t = 0$, and a displacement field $u_z = u(r, 0)$ is imported to the medium by the surface $r = r_0$, such that $u(r_0, 0) = u_0 = const$. Otherwise, until the time $t = 0$, the elastic medium is in an antiplane deformed state. Let the rigid shaft ($r \le r_0$) rotate from the instant $t = 0$ according to the law

$$\psi\,(r_0, t) = \psi_1 t + \psi_2 t^2 + \ldots, \quad u\,(r_0, 0) = u_0. \tag{41}$$

For the displacement vector components u_r, u_φ, u_z in the cylindrical coordinate system (r, φ, z), in the particular case of motion of a continuous medium is hold

$$u_r = r\,(1 - \cos\psi\,(r, t))\,, \quad u_\varphi = r \sin\psi\,(r, t)\,,$$
$$u_z = u\,(r, t)\,. \tag{42}$$

The equations of motion of the incompressible elastic medium could then be written in the form

$$\begin{aligned} &p_{,r} + r^{-1}\left(\mu\, r^2\psi_{,r}^2 + \theta_3 u_{,r}^2\right) \\ &\quad + \omega\,(\theta_1 + 2\theta_2 m) + \cdots = r\psi_{,t}^2, \\ &\left(1 + \chi_1 m^2\right)\left(\psi_{,rr} + 3\, r^{-1}\psi_{,r}\right) \\ &\quad + 2\chi_1 \omega m \psi_{,r} + \cdots = c_2^{-2}\psi_{,tt}, \\ &\left(1 + \chi_1 m^2\right)\left(u_{,rr} + r^{-1}u_{,r}\right) \\ &\quad + 2\chi_1 \omega m u_{,r} + \cdots = c_2^{-2}u_{,tt}, \end{aligned} \tag{43}$$

where indices after comma denote the partial derivatives with respect to the corresponding space coordinates and time t, $\omega = 2(u_{,rr}u_{,r} + r^2\psi_{,rr}\psi_{,r} + r\psi_{,r}^2)$, $m = (r\psi_{,r})^2 + (u_{,r})^2$, $h = c_2^2\left(1 + \chi_1 m^2 + \ldots\right),.$

$\theta_1 = \frac{1}{2}\,(\mu + b)\,,\ \theta_2 = \frac{3}{4}\,(\mu + a - b)\,,\ \theta_3 = \frac{1}{2}\,(b - \mu)\,,$ and $\chi_1 = \frac{\theta_2}{\mu}$.

The first equation in (43) is utilized to define the additional hydrostatic pressure $p(r, t)$ after solving the other equations for two functions $\psi(r, t)$ and $u(r, t)$. As before, the higher order terms of the deformations are denoted by multidots. The dynamic compatibility conditions for discontinuities make it possible to write the following set of equations in discontinuities:

$$\begin{aligned} &[\sigma_{rr}] = 0, \quad \left[\sigma_{r\varphi}\right] = -\rho G\left[\upsilon_\varphi\right], \\ &[\sigma_{rz}] = -\rho G\,[\upsilon_z]\,. \end{aligned} \tag{44}$$

This set of equations, after substituting the strain dependencies of stresses and Hadamard compatibility conditions for discontinuities (Thomas 1964), turns out to be a set of three equations in the unknown discontinuities $[p]$, $[\psi_{,r}]$, and $[u_{,r}]$. The velocity of propagation of a cylindrical shock wave remains also unknown. In this case, the first equation in (44) is utilized for calculation of $[p]$ with the help of the already calculated $[\psi_{,r}]$ and $[u_{,r}]$. For these values the last two equalities provide the set of equations

$$\begin{aligned} &h\left[r\psi_{,r}\right] + \left(r\psi_{,r} - \left[r\psi_{,r}\right]\right)[h] = G^2\left[r\psi_{,r}\right], \\ &h\left[u_{,r}\right] + \left(u_{,r} - \left[u_{,r}\right]\right)[h] = G^2\left[u_{,r}\right], \\ &\qquad h = G^2\,[m]\,\{\chi_1\,(m - 2\,[m]) + \ldots\}\,,. \end{aligned} \tag{45}$$

where, as before, the "+" signs of the values calculated ahead the surface of the discontinuities are omitted. Multiplying the first of equalities (45) by $[u_{,r}]$ and the second by $[r\psi_{,r}]$, and then subtracting the second such product from the first result in the condition for the existence of shock waves in the incompressible elastic medium

$$[h]\left(r\psi_{,r}\left[u_{,r}\right] - u_{,r}\left[r\psi_{,r}\right]\right) = 0. \tag{46}$$

Any cylindrical surface of discontinuities propagates through the medium only if (46) is fulfilled. This implies the existence of either the plane-polarized shock wave of loading Σ_1, for which

$$\frac{r\psi_{,r}}{u_{,r}} = \frac{\left[r\psi_{,r}\right]}{\left[u_{,r}\right]}, \quad G_1 = \left(h - [h] + \frac{u_{,r}}{\left[u_{,r}\right]}[h]\right)^{1/2}, \tag{47}$$

or the neutral shock wave Σ_2 under the conditions

$$[h] = [m] = 0, \quad G_2 = h^{1/2}. \tag{48}$$

It could be shown (Burenin et al. 2011) that $G_1 > G_2$. Thus, the elastic layer is divided by the surfaces Σ_1 and Σ_2 into three domains (Fig. 1). In the area I ($r_1(t) < r < R$) the medium is at rest at $u_z = u(r, 0)$, within the area II ($r_2(t) < r < r_1(t)$) the medium moves under the conditions $\psi = 0$ and $u_z = u(r, t)$, and in the area III $\psi = \psi(r, t)$ and $u_z = u(r, t)$. An approximate solution could be found in the form of the ray series:

$$u^{II}(r,t) = u^{I}(r) + \sum_{j=1}^{\infty} \kappa_j \frac{(t-t_1)^j}{j!},$$

$$\kappa_j = \left[\frac{\delta^j u}{\delta\, t^k}\right]\Big|_{t=t_1}, \quad t_1 = \int_{r_0}^{r} \frac{d\xi}{G_1(\xi)},$$

$$u^{III}(r,t) = u^{II}(r,t)|_{t=t_2} - \sum_{j=1}^{\infty} \omega_j \frac{(t-t_2)^j}{j!}, \tag{49}$$

$$\psi(r,t) = -\sum_{j=1}^{\infty} \eta_j \frac{(t-t_2)^j}{j!}, \quad \eta_j = \left[\frac{\delta^j \psi}{\delta\, t^j}\right]\Big|_{t=t_2},$$

$$\omega_j = \left[\frac{\delta^j u}{\delta\, t^j}\right]\Big|_{t=t_2}, \quad t_2 = \int_{r_0}^{r} \frac{d\xi}{G_2(\xi)}.$$

Since the intensities of the discontinuities η_1 and ω_1 on the neutral shock wave Σ_2 are connected by the relationship $[m] = 0$, then following the above discussed method for constructing the recurrence equations for the coefficients of the ray series, it is enough to consider

$$\kappa_1 = \sum_{k=0}^{\infty} \frac{1}{k!}\gamma_k t^k, \quad \eta_1 = \sum_{k=0}^{\infty} \frac{1}{k!}\beta_k t^k,$$
$$\beta_k = \frac{\delta^k \eta_1}{\delta\, t^k}\Big|_{t=0}, \quad \gamma_k = \frac{\delta^k \kappa_1}{\delta\, t^k}\Big|_{t=0}. \tag{50}$$

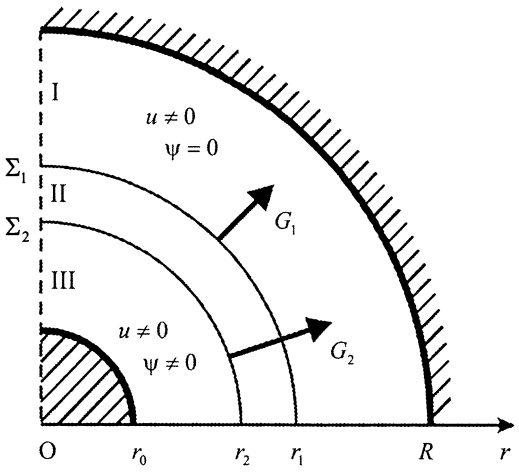

Fig. 1 Scheme of propagation of shock waves

For the propagation velocities of the cylindrical surfaces of discontinuities Σ_1 and Σ_2, it follows from (47) and (48) that

$$G_1 = c_2\left\{1 + \chi_1 u^I_{,r}\,(5 - 10\zeta + 10\zeta_2 - 5\zeta^3 + \zeta^4 + \ldots)\right\},$$
$$G_2 = c_2\left(1 + \chi_1 u^{II}_{,r} + \ldots\right). \tag{51}$$

Here one should bear in mind that $u^I_{,r}$ and $u^{II}_{,r}$ are calculated immediately ahead of Σ_1 and Σ_2 respectively. The coefficients of the power series (50) and, consequently, the coefficients of the ray series (49) should be determined according to the boundary conditions (41). It was discussed above that this cannot be done directly, for this purpose it is necessary to write recurrent relationships in the form

$$\frac{\delta \kappa_n}{\delta\, t_n} = b_n(\kappa_1, \kappa_2, \ldots, \kappa_{n+1}),$$
$$\frac{\delta \eta_n}{\delta\, t} = a_n(\eta_1, \eta_2, \ldots, \eta_{n+1}),$$
$$\kappa_{n+1} = f_n\left(\kappa_1, \frac{\delta \kappa_1}{\delta\, t}, \ldots, \frac{\delta^n \kappa_1}{\delta\, t^n}\right),$$
$$\eta_{n+1} = g_n\left(\eta_1, \frac{\delta \eta_1}{\delta\, t}, \ldots, \frac{\delta^n \eta_1}{\delta\, t^n}\right). \tag{52}$$

S

$$\frac{\delta\kappa_1}{\delta t} = \frac{5}{2}u_{,r}^4\kappa_2\chi_1 + \kappa_1\left(-\frac{c}{2r} - 10cu_{,r}^3u_{,rr}\chi_1 + \frac{10u_{,r}^3\kappa_2\chi_1}{c}\right) + \kappa_1^2\left(\frac{15u_{,r}^3\chi_1}{2r} - 15u_{,r}^2u_{,rr}\chi_1 + \frac{15u_{,r}^3\kappa_2\chi_1}{c^2}\right) + \ldots,$$

Restricting in Eq. (52) only by $n = 1, 2$ yields

$$\begin{aligned}\frac{\delta\eta_1}{\delta t} &= \frac{u_{,r}^4\eta_2\chi_1}{2} + \frac{2u_{,r}^3\eta_1\kappa_2\chi_1}{c} - \eta_1 c\left(\frac{3}{2r} + 2u_{,r}^3u_{,rr}\chi_1\right)\\ &+ \kappa_1\left\{\frac{2u_{,r}^3\eta_2\chi_1}{c} + \frac{6u_{,r}^2\eta_1\kappa_2\chi_1}{c^2} + 3\eta_1u_{,r}^2\chi_1\left(\frac{u_{,r}}{r} - 2u_{,rr}\right) + \frac{14r^2u_{,r}\chi_1}{5c^3}\eta_1^2\eta_2\left(u_{,r}^4\chi_1 - \frac{1}{2}\right)\right\}\\ &+ \kappa_1^2\left\{\frac{3u_{,r}^2\eta_2\chi_1}{c^2} + \frac{14r^2\chi_1}{5c^4}\eta_1^2\eta^2\left(6u_{,r}^4\chi_1 - 1\right) + \frac{3\eta_1\kappa_2u_{,r}\chi_1}{c^3}\left(2 - 79u_{,r}^4\chi_1\right)\right.\\ &\left. + \frac{3\eta_1\chi_1u_{,r}}{c}\left(\frac{u_{,r}}{r} + 2u_{,rr}\left(32u_{,r}^4\chi_1 - 1\right)\right)\right\} + \ldots\end{aligned} \tag{53}$$

The coefficients of the series (50) are then calculated in the form

$$\gamma_1 = \frac{1}{2}\frac{r_0^2\psi_1^2}{c_2u_{,r}(r_0)} + \ldots,$$
$$\gamma_2 = {c_2}^2u_{,rr}(r_0) + \ldots,$$
$$\beta_1 = -\psi_1, \quad \beta_2 = -\psi_2,$$

and thus the final approximate expansion of the solution could be within the accuracy of t^2.

Conclusion

The main difficulty in the numerical calculations of essentially nonstationary problems in continuum mechanics is connected with the generation and further propagation of surfaces of discontinuities in a medium. The governing features of motion of these surfaces are determined only from the solution of the corresponding boundary-value problem, and therefore the position of such surfaces, as well as the values of the discontinuities, must necessarily be considered at each time step of the algorithm. In the gas dynamics, such algorithms which are called discontinuity-assignment algorithms have been long and well known (Godunov et al. 1976; Belotserkovskii 1984). However, most of them cannot be applied directly in the dynamics of deformation. It is mainly connected with the fact that two processes are simultaneously presented in the deformed medium under dynamic loading conditions: the propagation of volume deformations (as in gas dynamics) and the propagation of deformation of the shape change. These processes are interrelated and interdependent, therefore discontinuities appear to be combined.

If it is necessary to directly assign discontinuities, for example, when waves interact with each other and with obstacles, the construction of numerical algorithms by the known methods of gas dynamics, as it was mentioned above, encounters great difficulties. That is why it has been proposed to include the forward-front ray

expansions of the solution (Rossikhin 1991; Burenin and Rossikhin 1991; Rossikhin and Shitikova 1996) in the numerical difference scheme for the purpose of algorithmic separation of discontinuities in numerical calculations (Burenin and Zinov'ev 2003). The procedure first applied to the process of plane shock waves propagation in the one-dimensional case (Burenin and Zinov'ev 2003) was further utilized to one-dimensional problems with axial symmetry (Gerasimenko and Zavertan 2008, 2009).

Cross-References

▸ Ray Expansion Theory

References

Achenbach J, Reddy D (1967) Note on wave propagation in linearly viscoelastic media. ZAMP 18(1):141–144

Babicheva LA, Bykovtsev GI, Verveiko ND (1973) Ray method of solving dynamic problems in elastic-viscoplastic media. J Appl Math Mech 37(1):132–141

Belotserkovskii OM (1984) Numerical modeling in mechanics of solids. Nauka, Moscow

Burenin AA, Chernyshov AD (1978) Shock waves in an isotropic elastic space. J Appl Math Mech 42(4): 758–765

Burenin AA, Rossikhin YA (1991) Ray method for solving one-dimensional problems of nonlinear dynamic theory of elasticity with plane surfaces of strong discontinuity. In: Applied problems of mechanics of deformable media. Dal'nauka, Vladivostok, pp 129–137

Burenin AA, Zinov'ev PV (2003) On the problem of extracting discontinuity surfaces in numerical methods for the dynamics of deformable media. In: Klimov DM (ed) Problems of mechanics. Devoted to the 90-th anniversary of Ishlinsky AYu. Physmathlit, Moscow, pp 146–155

Burenin AA, Dudko OV, Lapteva AA (2011) To the constitutive laws of deformation propagation. Siberian J Industr Math 4(4):14–23

Bykovtsev GI, Ivlev DD (1998) Theory of plasticity. Dal'nauka, Vladivostok

Chernyii GG (1988) Gas dynamics. Nauka, Moscow

Gerasimenko YA, Zavertan AV (2008) Calculations of the dynamics of an incompressible elastic medium with antiplane and twisting impact. Comput Mech Solid Media 1(3):46–56

Gerasimenko YA, Zavertan AV (2009) Ray expansions of solutions around fronts as a shock-fitting tool for shock loading simulation. Comput Math Math Phys 49(4):698–709

Godunov SK, Zabrodin AV, Ivanov MY, Prokopov GP (1976) Numerical solution of multidimensional gas dynamics problems. Nauka, Moscow

Kulikovskii AG, Sveshnikova EI (1982) Investigation of the shock adiabat of quasitransverse shock waves in a prestressed elastic medium. J Appl Math Mech 46(5):667–673

Lourier AI (1980) Nonlinear theory of elasticity. Nauka, Moscow

Podil'chuk YN, Rubtsov YK (1986) Application of the method of ray series to the investigation of axisymmetric nonstationary problems of the dynamical theory of elasticity. Sov Appl Mech 22(3):201–207

Rossikhin YA (1991) Perturbation methods in problems of wave dynamics of anisotropic bodies. DSci Dissertation, Cheboksary

Rossikhin YA, Shitikova MV (1994) A ray method of solving problems connected with a shock interaction. Acta Mech 102:103–121

Rossikhin YA, Shitikova MV (1995a) Ray method for solving dynamic problems connected with propagation of wave surfaces of strong and weak discontinuities. Appl Mech Rev 48(1):1–39

Rossikhin YA, Shitikova MV (1995b) The ray method for solving boundary problems of wave dynamics for bodies having curvilinear anisotropy. Acta Mech 109 (1–4):49–64

Rossikhin YA, Shitikova MV (1996) Methods for solving one-dimensional boundary-value problems in a nonlinear elastic medium. Acta Mech 114(1–4):51–69

Thomas T (1964) Plastic flow and fracture in solids. Academic Press, New York

Siebel, Erich

Holm Altenbach[1] and Otto T. Bruhns[2]
[1]Lehrstuhl Technische Mechanik, Institut für Mechanik, Fakultät für Maschinenbau, Otto-von-Guericke-Universität Magdeburg, Magdeburg, Germany
[2]Institute of Mechanics, Ruhr-University Bochum, Bochum, Germany

Erich Siebel (*May 17th, 1891 in Solingen, Germany; †October 17th, 1961 in Stuttgart, Germany) was an engineer and professor of materials science, testing, and strength of materials.

Erich Siebel

Education

Erich Siebel's father was Eduard Siebel, a manufacturer of leather goods. His mother was Theodora Müller. During 1912–1914 and after the war has ended in 1918, he was educated in mechanical engineering at the TH Berlin-Charlottenburg. He was awarded his doctorate there in 1922 with a thesis on calculation of power and performance requirements in forging and rolling ("Grundlagen zur Berechnung des Kraft- und Arbeitsbedarfs beim Schmieden und Walzen").

Professional Career

After a period as maintenance engineer in the steelworks industry in Dortmund and Krefeld, in 1925, he became head of department at the Kaiser Wilhelm Institute (KWI) for Steel Research in Düsseldorf with focus on metal forming ("Bildsame Formgebung"). Here Siebel conducted research on rolling and forging. In addition, he worked as a private lecturer at the Mining Academy in Clausthal. There he gave lectures on metal forming and theory of strength.

Moreover, Siebel carried out extensive investigations on boiler bottoms, which led to a new formula for calculating steam boilers. The revision of the material and construction codes for large boilers during this period is mainly due to his research. About his contributions to plasticity is reported in Bruhns (2019).

In 1931, Siebel was appointed full professor for materials science and testing, and strength of materials at the TH Stuttgart. During World War II in 1940, although he was not a member of the Nazi Party, he was appointed President of the Materials Testing Institute (Materialprüfanstalt – MPA) in Berlin-Dahlem (now BAM). At the same time, he was linked with a professorship at the TH Berlin. Siebel reorganized the MPA providing the basis for its continued existence after 1945. He remained president of the MPA even after the war had ended. In 1947, he returned to his former chair in Stuttgart and headed the Materials Testing Institute there until his retirement in 1957.

Scientific Achievements and Honors

In 1953, he founded a test field for metal forming, which investigated sheet metal forming processes and developed and tested models for these processes. Siebel has played a key role in numerous technical and scientific associations, as president of the German Standards Committee, among others. He was an honorary doctor of the TH Darmstadt and was an honorary member of several associations, including the European Research Association for Sheet Metal Processing.

Cross-References

▸ History of Plasticity

References

Bruhns OT (2019) The history of plasticity. Encyclopedia of Continuum Mechanics. Cham, Springer

Simple Mixtures

▸ Entropy Principle Exploited by Lagrange Multipliers

Simulation

▸ Metal Forming Simulation Based on Advanced Mechanical Model Strongly Coupled with Ductile Damage

Singular Solutions in Plane Strain Plasticity

Sergei Alexandrov
Ishlinsky Institute for Problems in Mechanics, Russian Academy of Sciences, Moscow, Russia

Synonyms

Asymptotic analysis; Double-shearing model; Infinite strain rate; Maximum friction law; Maximum friction surface; Rigid perfectly plastic model; Rigid plastic models; Strain rate intensity factor; Viscoplastic model

Definition

1. The maximum friction law demands that the friction stress is equal to the shear yield stress in the case of pressure-independent models considered,
2. The maximum friction law demands that the friction surface coincides with a stress characteristic or an envelope of stress characteristics in the case of the double-shearing model,
3. The maximum friction surface is a surface with maximum friction,
4. The strain rate intensity factor is the coefficient of the leading term in a series expansion of the quadratic invariant of the strain rate tensor in the vicinity of maximum friction surfaces.

The definition for the maximum friction law above applies at sliding.

Introduction

The successful mathematical modelling of the material behavior in the vicinity of frictional interfaces is a difficult problem. The maximum friction law is of special importance in this respect. The basic assumption of rigid plastic models is that elastic strains are neglected. For several rigid plastic models, the maximum friction law results in singular behavior of the velocity field in the vicinity of the friction surface. In particular, the quadratic invariant of the strain rate tensor approaches infinity near the surface. On the other hand, this invariant has a significant effect on the evolution of material properties in the course of deformation. Numerous experimental studies show that there is a very high gradient of material properties near frictional interfaces. Therefore, the singular behavior of the velocity field is in qualitative agreement with experiment.

Coordinate Systems

It is assumed that the flow is everywhere parallel to the (x, y) plane of a Cartesian coordinate system (x, y, z) and that the motion is independent of z. The friction surface is represented by a curve in the (x, y) plane (curve L in Fig. 1). The asymptotic analysis of solutions in the vicinity of the friction surface is facilitated by choice of a plane curvilinear orthogonal coordinate system (t, s) whose coordinate curve $s = 0$ coincides with L. The s – coordinate lines are straight and are orthogonal to L. The scale factor of s – lines is unity. The scale factor of t – lines is denoted as H. The s – axis is directed away from the rigid tool and toward the plastic material. Therefore, it is assumed that $s \geq 0$ in the asymptotic analysis presented below.

Fundamental Equations of Continuum Mechanics

In the case of the quasi-static flow of rigid plastic materials, the system of equations for any

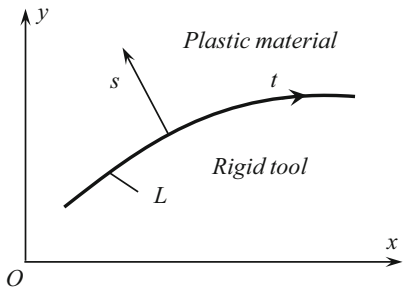

Fig. 1 Coordinate systems

model comprises the equations of equilibrium, yield criterion, flow rule, and, for some models, evolution equations for internal variables. The equations of equilibrium are independent of the constitutive equations and can be written in the (t, s) coordinate system as

$$\frac{\partial \sigma_{tt}}{\partial t} + H\frac{\partial \sigma_{ts}}{\partial s} + F_1 = 0 \quad \text{and} \quad H\frac{\partial \sigma_{ss}}{\partial s} + \frac{\partial \sigma_{ts}}{\partial t} + F_2 = 0. \tag{1}$$

Here σ_{tt}, σ_{ss} and σ_{ts} are the stress components referred to the (t, s) coordinate system. The terms F_1 and F_2 may depend on stress components and geometric parameters, but they are independent of stress derivatives. Let ξ_{tt}, ξ_{ss}, and ξ_{ts} be the components of the strain rate tensor and ω_{ts} is the only nonzero spin component. The relations between these quantities and the velocity components, u_t and u_s, are also independent of the constitutive equations. In the (t, s) coordinate system, these relations are

$$\xi_{tt} = \frac{1}{H}\frac{\partial u_t}{\partial t} + u_s G_1, \quad \xi_{ss} = \frac{\partial u_s}{\partial s}, \tag{2}$$
$$2\xi_{ts} = \frac{1}{H}\frac{\partial u_s}{\partial t} + \frac{\partial u_t}{\partial s} + u_t G_2,$$
$$2\omega_{ts} = \frac{\partial u_t}{\partial s} - \frac{1}{H}\frac{\partial u_s}{\partial t} - u_t G_2.$$

The terms G_1 and G_2 may depend on geometric parameters, but they are independent of velocity derivatives.

Constitutive Equations

Pressure-Independent Plasticity

Any isotropic pressure-independent plane strain yield criterion can be represented as (Hill 1950)

$$(\sigma_{tt} - \sigma_{ss})^2 + 4\sigma_{ts}^2 = 4k^2. \tag{3}$$

Here k is the shear yield stress. k is constant in the case of rigid perfectly plastic solids and is a monotonically increasing function of the quadratic invariant of the strain rate tensor in the case of viscoplastic solids. The flow rule associated with this yield criterion is

$$\xi_{tt} = \lambda\,(\sigma_{tt} - \sigma_{ss})\,, \quad \xi_{ss} = -\lambda\,(\sigma_{tt} - \sigma_{ss})\,,$$
$$\xi_{ts} = 2\lambda\sigma_{ts}. \tag{4}$$

Here λ is a nonnegative multiplier. This flow rule is usually called the normality rule. Eliminating λ between the equations in (4) gives

$$\xi_{tt} + \xi_{ss} = 0 \quad \text{and} \quad \frac{\xi_{tt} - \xi_{ss}}{\xi_{ts}} = \frac{\sigma_{tt} - \sigma_{ss}}{\sigma_{ts}}. \tag{5}$$

The quadratic invariant of the strain rate tensor is defined as

$$\xi_{eq} = \sqrt{\frac{2}{3}}\sqrt{\xi_{tt}^2 + \xi_{ss}^2 + 2\xi_{ts}^2}. \tag{6}$$

Pressure-Dependent Plasticity

Several models of pressure-dependent plasticity are available in the literature (see "▸ Planar Problems in Rigid-Plasticity for Granular Materials and Soils"). The present entry focuses on the double-shearing model based on the Mohr-Coulomb yield criterion (Spencer 1964). A widely used version of this model assumes that the material is incompressible. Under plane strain conditions, the Mohr-Coulomb yield criterion reads

$$(\sigma_{tt}+\sigma_{ss})\sin\phi + \sqrt{(\sigma_{tt}-\sigma_{ss})^2+4\sigma_{ts}^2} = 2c\cos\phi. \tag{7}$$

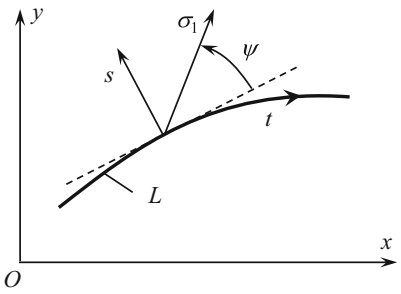

Fig. 2 Orientation of the algebraically greater principal stress

Here ϕ is the angle of internal friction and c is the coefficient of cohesion. The flow rule of the double-shearing model for incompressible materials yields

$$\xi_{tt} + \xi_{ss} = 0, \quad \sin 2\psi\,(\xi_{tt} - \xi_{ss}) - 2\cos 2\psi \xi_{ts} - 2\sin\phi\,(\omega_{ts} + d\psi/d\tau) = 0 \tag{8}$$

where ψ is the anticlockwise angular rotation of the direction of the algebraically greater principal stress σ_1 from the t – direction (Fig. 2) and $d/d\tau$ denotes the convected derivative.

Maximum Friction Law

In the case of rigid perfectly plastic materials, the shear yield stress is the maximum possible shear stress in the material. Therefore, it is natural to formulate the maximum friction law as

$$\sigma_{ts} = k \tag{9}$$

for $s = 0$. It has been assumed here, with no loss of generality, that the direction of flow dictates that $\sigma_{ts} > 0$. The friction law (9) is valid if the regime of sliding occurs. It is possible to propose an alternative formulation of the friction law (9). In particular, the system of equations comprising equations (1), (2), (3), and (5) is hyperbolic if k is constant. Equation (9) is satisfied on characteristic curves. Therefore, the alternative formulation of the maximum friction law is that the friction surface coincides with a characteristic curve or an envelope of characteristic curves.

The alternative formulation is useful in the case of other material models describable by hyperbolic systems. In particular, this formulation should be adopted for the double-shearing model.

In the case of viscoplastic materials, k depends on ξ_{eq}. The corresponding system of equations is not hyperbolic, and the maximum friction law given by Eq. (9) will be generalized on a class of viscoplastic models below.

Singularity in Solutions Near a Maximum Friction Surface

The analysis below is based on the assumptions that

(i) All stress and velocity components are bounded everywhere;
(ii) All derivatives with respect to t are bounded everywhere;
(iii) The solution is represented by Laurent series with respect to s near maximum friction surfaces.

Without a loss of generality, it is supposed that the tool is motionless (Fig. 1). Then,

$$u_s = 0 \tag{10}$$

for $s = 0$. Substituting (10) into the first equation in (2) gives

$$\xi_{tt} = \frac{1}{H}\frac{\partial u_t}{\partial t} \tag{11}$$

on the friction surface.

Rigid Perfectly Plastic Solids

The yield criterion (3) is satisfied by the standard substitution:

$$\sigma_{tt} = \sigma - k\sin 2\varphi, \quad \sigma_{ss} = \sigma + k\sin 2\varphi, \quad \sigma_{ts} = k\cos 2\varphi \tag{12}$$

where σ is the hydrostatic stress and φ is a new unknown. It follows from (4) and (9) that $0 \le \varphi \le \pi/2$ in some vicinity of the friction surface.

Substituting (12) into (5) yields

$$\xi_{tt} + \xi_{ss} = 0 \quad \text{and} \quad \xi_{tt} - \xi_{ss} = 2\xi_{ts} \tan 2\varphi. \tag{13}$$

With the substitution from the third equation in (12) the boundary condition (9) becomes:

$$\varphi = 0 \tag{14}$$

for $s = 0$.

Equations (13) and (14) combine to give $\xi_{tt} = \xi_{ss} = 0$ at the friction surface if $\xi_{ts} < \infty$. In this case, the friction surface coincides with a characteristic curve. This case results in a very special regime of flow. In particular, it follows from (11) that u_t is constant along the friction surface. Therefore, in what follows, it is assumed that

$$\xi_{ts} \to \infty \tag{15}$$

as $s \to 0$ and, using the first equation in (13), that

$$\xi_{tt} = -\xi_{ss} \neq 0 \tag{16}$$

at $s = 0$. In this case, the friction surface coincides with an envelope of characteristic curves. Assumption (ii) and Eq. (2) demand that the strain rate ξ_{tt} is bounded everywhere. Then, it follows from (16) that the strain rate ξ_{ss} is also bounded everywhere. This condition together with (2), (10), and (16) requires that

$$u_s = u_s^{(1)} s + o(s) \tag{17}$$

as $s \to 0$. Using assumption (iii) the velocity u_t is represented as

$$u_t = u_0 + u_t^{(1)} s^{\beta} + o\left(s^{\beta}\right) \tag{18}$$

as $s \to 0$. Assumption (ii) demands $\beta > 0$. Equation (15) together with (2) requires $\beta < 1$. Therefore,

$$0 < \beta < 1. \tag{19}$$

Using (2), (17) and (18) the shear strain rate can be represented as

$$2\xi_{ts} = u_t^{(1)} \beta s^{\beta - 1} + o\left(s^{\beta - 1}\right) \tag{20}$$

as $s \to 0$. Using (2), (16), and (17), the normal strain rates at $s = 0$ are determined as

$$\xi_{ss} = -\xi_{tt} = u_s^{(1)}. \tag{21}$$

Using this equation and taking into account that $\varphi \to 0$ as $s \to 0$, the second equation in (13) reduces to $-u_s^{(1)} = 2\xi_{ts}\varphi$ as $s \to 0$. Then, it follows from (20) that

$$\varphi = \varphi_0 s^{1-\beta} + o\left(s^{1-\beta}\right) \tag{22}$$

as $s \to 0$.

Expanding $\sin 2\varphi$ and $\cos 2\varphi$ in series, one can rewrite Eq. (12) as

$$\begin{aligned} \sigma_{tt} &= \sigma - [2k\varphi + o(\varphi)], \\ \sigma_{ss} &= \sigma + [2k\varphi + o(\varphi)], \\ \sigma_{ts} &= k\left[1 - 2\varphi^2 + o\left(\varphi^2\right)\right] \end{aligned} \tag{23}$$

as $\varphi \to 0$. Equations (22) and (23) combine to give

$$\begin{aligned} \sigma_{tt} &= \sigma - \left[2k\varphi_0 s^{1-\beta} + o\left(s^{1-\beta}\right)\right], \\ \sigma_{ss} &= \sigma + \left[2k\varphi_0 s^{1-\beta} + o\left(s^{1-\beta}\right)\right], \\ \sigma_{ts} &= k\left[1 - 2\varphi_0^2 s^{2(1-\beta)} + o\left(s^{2(1-\beta)}\right)\right] \end{aligned} \tag{24}$$

as $s \to 0$. Using (24) one can find the derivatives involved in (1) as

$$\begin{aligned} \frac{\partial \sigma_{tt}}{\partial t} &= \frac{\partial \sigma}{\partial t} - \left[\frac{2kd\varphi_0}{dt} s^{1-\beta} + o\left(s^{1-\beta}\right)\right], \\ \frac{\partial \sigma_{ss}}{\partial s} &= \frac{\partial \sigma}{\partial s} + \left[2k(1-\beta)\varphi_0 s^{-\beta} + o\left(s^{-\beta}\right)\right], \\ \frac{\partial \sigma_{ts}}{\partial t} &= -4k\varphi_0 \frac{d\varphi_0}{dt} s^{2(1-\beta)} + o\left[s^{2(1-\beta)}\right], \\ \frac{\partial \sigma_{ts}}{\partial s} &= -4k(1-\beta)\varphi_0^2 s^{(1-2\beta)} + o\left[s^{(1-2\beta)}\right] \end{aligned} \tag{25}$$

as $s \to 0$. Substituting (25) into (1) yields

$$\frac{\partial \sigma}{\partial t} - \left[\frac{2kd\varphi_0}{dt}s^{1-\beta} + o\left(s^{1-\beta}\right)\right] \tag{26}$$
$$-Hk\left[4\left(1-\beta\right)\varphi_0^2 s^{(1-2\beta)} + o\left(s^{(1-2\beta)}\right)\right] + F_1$$
$$= 0,\ H\frac{\partial \sigma}{\partial s} + H\left[2k\left(1-\beta\right)\varphi_0 s^{-\beta} + o\left(s^{-\beta}\right)\right]$$
$$-k\left[4\varphi_0\frac{d\varphi_0}{dt}s^{2(1-\beta)} + o\left(s^{2(1-\beta)}\right)\right] + F_2 = 0$$

as $s \to 0$. The presence of $s^{(1-2\beta)}$ in the first equation in (26) requires another term of this power of s. F_1 involves $\sigma_{tt} - \sigma_{ss}$ and σ_{ts}. Therefore, it cannot supply any term of the order $O\left[s^{(1-2\beta)}\right]$, as follows from (24). It is then necessary to examine two cases:

$$\beta = \frac{1}{2} \tag{27}$$

and

$$\sigma = \sigma_0 + \sigma^{(1)}s^{1-2\beta} + o\left(s^{1-2\beta}\right) \tag{28}$$

as $s \to 0$. Substituting (28) into the second equation in (26) shows that a term of the order $O\left(s^{-2\beta}\right)$ is present in the second equation in (26). No other term of this order is involved in this equation. Therefore, one is left with case (27). In this case, it is seen from (26) that

$$\sigma = \sigma_0 + \sigma^{(1)}\sqrt{s} + o\left(\sqrt{s}\right) \tag{29}$$

as $s \to 0$. Also, it follows from (18), (24), and (28) that

$$u_t = u_0 + u_t^{(1)}\sqrt{s} + o\left(\sqrt{s}\right),$$
$$\sigma_{tt} = \sigma_0 + \left(\sigma^{(1)} - 2k\varphi_0\right)\sqrt{s} + o\left(\sqrt{s}\right),$$
$$\sigma_{ss} = \sigma_0 + \left(\sigma^{(1)} + 2k\varphi_0\right)\sqrt{s} + o\left(\sqrt{s}\right),$$
$$\sigma_{ts} = k\left[1 - 2\varphi_0^2 s + o\left(s\right)\right] \tag{30}$$

as $s \to 0$. Substituting (29) into the second equation in (26) and collecting the terms of the order $O\left(1/\sqrt{s}\right)$ shows that $\sigma^{(1)} = -2k\varphi_0$. Therefore, (30) becomes

$$u_t = u_0 + u_t^{(1)}\sqrt{s} + o\left(\sqrt{s}\right),$$
$$\sigma_{tt} = \sigma_0 - 4k\varphi_0\sqrt{s} + o\left(\sqrt{s}\right),$$
$$\sigma_{ss} = \sigma_0 + o\left(\sqrt{s}\right),$$
$$\sigma_{ts} = k\left[1 - 2\varphi_0^2 s + o\left(s\right)\right] \tag{31}$$

Since the normal strain rates are bounded and $\xi_{ts} \to \infty$ as $s \to 0$, it is evident from (6), (20), and (27) that

$$\xi_{eq} = \frac{D}{\sqrt{s}} + o\left(\frac{1}{\sqrt{s}}\right) \tag{32}$$

as $s \to 0$. Here D is the strain rate intensity factor (Alexandrov and Richmond 2001). This factor controls the magnitude of the quadratic invariant of the strain rate tensor in the vicinity of maximum friction surfaces.

Summarizing, the solution is represented by (17) and (31) in the vicinity of a maximum friction surface if this surface is an envelope of characteristics.

Viscoplastic Solids

The qualitative behavior of viscoplastic solutions in the vicinity of maximum friction surfaces depends on the behavior of the function $k\left(\xi_{eq}\right)$ as $\xi_{eq} \to \infty$. If $k\left(\xi_{eq}\right) \to \infty$ as $\xi_{eq} \to \infty$, then it is always possible to find a solution satisfying the sticking condition. Such models are not considered in the present entry because the corresponding solutions are not singular. A distinguished feature of the models considered is $k\left(\xi_{eq}\right) \to k_s < \infty$ as $\xi_{eq} \to \infty$ where k_s is constant. Moreover, it is assumed that

$$k\left(\xi_{eq}\right) = k_s\left[1 - A\xi_{eq}^{-\alpha}\right] + o\left(\xi_{eq}^{-\alpha}\right) \tag{33}$$

as $\xi_{eq} \to \infty$. Here $A > 0$ and $\alpha > 0$ are constant. It is evident from (3) and (33) that k_s is the maximum possible shear stress. Therefore, the maximum friction law (9) should be replaced with

$$\sigma_{ts} = k_s \tag{34}$$

for $s = 0$. This law demands

$$\xi_{eq} \to \infty \tag{35}$$

as $s \to 0$.

Equation (12) satisfies the yield criterion (3). It is evident from (12) and (34) that the boundary condition (14) is valid. Equations (17), (18), (19), (20), (21), and (22) do not involve k. Therefore, these equations are also valid. In particular, it follows from (6), (20), and (21) that

$$\xi_{eq} = \xi_0 s^{\beta-1} + o\left(s^{\beta-1}\right) \tag{36}$$

as $s \to 0$.

Using (12), (22), (33) and (36) yields

$$\begin{aligned}
\sigma_{tt} &= \sigma - 2k_s\varphi_0 s^{1-\beta} + o\left(s^{1-\beta}\right), \\
\sigma_{ss} &= \sigma + 2k_s\varphi_0 s^{1-\beta} + o\left(s^{1-\beta}\right), \\
\sigma_{ts} &= k_s\left[1 - A\xi_0^{-1}s^{\alpha(1-\beta)} - 2\varphi_0^2 s^{2(1-\beta)}\right] + o\left(s^n\right)
\end{aligned} \tag{37}$$

as $s \to 0$. Here $n = 2(1-\beta)$ if $\alpha \geq 2$ and $n = \alpha(1-\beta)$ if $\alpha < 2$. This asymptotic expansion of the shear stress suggests that the cases $\alpha \geq 2$ and $\alpha < 2$ should be considered separately.

Consider the case $\alpha \geq 2$. In this case, Eq. (37) becomes

$$\begin{aligned}
\sigma_{tt} &= \sigma - 2k_s\varphi_0 s^{1-\beta} + o\left(s^{1-\beta}\right), \\
\sigma_{ss} &= \sigma + 2k_s\varphi_0 s^{1-\beta} + o\left(s^{1-\beta}\right), \\
\sigma_{ts} &= k_s\left[1 - Bs^{2(1-\beta)}\right] + o\left[s^{2(1-\beta)}\right]
\end{aligned} \tag{38}$$

The only difference between Eqs. (24) and (38) is that k and $2\varphi_0^2$ in (24) are replaced with k_s and B in (38). Therefore, Eq. (31) is replaced with

$$\begin{aligned}
u_t &= u_0 + u_t^{(1)}\sqrt{s} + o\left(\sqrt{s}\right), \\
\sigma_{tt} &= \sigma_0 - 4k_s\varphi_0\sqrt{s} + o\left(\sqrt{s}\right), \\
\sigma_{ss} &= \sigma_0 + o\left(\sqrt{s}\right), \\
\sigma_{ts} &= k_s\left[1 - Bs + o(s)\right]
\end{aligned} \tag{39}$$

as $s \to 0$. This equation supplies the asymptotic representation of solutions in the vicinity of maximum friction surfaces in the case under consideration.

Consider the case $\alpha < 2$. In this case, Eq. (37) becomes

$$\begin{aligned}
\sigma_{tt} &= \sigma - 2k_s\varphi_0 s^{1-\beta} + o\left(s^{1-\beta}\right), \\
\sigma_{ss} &= \sigma + 2k_s\varphi_0 s^{1-\beta} + o\left(s^{1-\beta}\right), \\
\sigma_{ts} &= k_s\left[1 - A\xi_0^{-1}s^{\alpha(1-\beta)}\right] + o\left[s^{\alpha(1-\beta)}\right]
\end{aligned} \tag{40}$$

as $s \to 0$. Using (40) one can find the derivatives involved in (1) as

$$\begin{aligned}
\frac{\partial\sigma_{tt}}{\partial t} &= \frac{\partial\sigma}{\partial t} - \left[\frac{2k_s d\varphi_0}{dt}s^{1-\beta} + o\left(s^{1-\beta}\right)\right], \\
\frac{\partial\sigma_{ss}}{\partial s} &= \frac{\partial\sigma}{\partial s} + \left[2k_s(1-\beta)\varphi_0 s^{-\beta} + o\left(s^{-\beta}\right)\right], \\
\frac{\partial\sigma_{ts}}{\partial t} &= -\frac{k_s A d\left(\xi_0^{-\alpha}\right)}{dt}s^{\alpha(1-\beta)} + o\left[s^{\alpha(1-\beta)}\right], \\
\frac{\partial\sigma_{ts}}{\partial s} &= -k_s A\xi_0^{-\alpha}\alpha(1-\beta)s^{\alpha(1-\beta)-1} + o\left[s^{\alpha(1-\beta)-1}\right]
\end{aligned} \tag{41}$$

as $s \to 0$. Substituting (41) into (1) gives

$$\begin{aligned}
&\frac{\partial\sigma}{\partial t} - \left[\frac{2k_s d\varphi_0}{dt}s^{1-\beta} + o\left(s^{1-\beta}\right)\right] \\
&\quad + H\left\{-k_s A\xi_0^{-\alpha}\alpha(1-\beta)s^{\alpha(1-\beta)-1} \right. \\
&\qquad \left. + o\left[s^{\alpha(1-\beta)-1}\right]\right\} + F_1 = 0, \\
&\quad H\left\{\frac{\partial\sigma}{\partial s} + \left[2k_s(1-\beta)\varphi_0 s^{-\beta} + o\left(s^{-\beta}\right)\right]\right\} \\
&- \left\{\frac{k_s A d\left(\xi_0^{-\alpha}\right)}{dt}s^{\alpha(1-\beta)} + o\left[s^{\alpha(1-\beta)}\right]\right\} + F_2 = 0.
\end{aligned} \tag{42}$$

as $s \to 0$. The second equation in (42) contains a term of the order $O\left(s^{-\beta}\right)$. Since $\alpha(1-\beta) > 0$, it follows from this equation that

$$\sigma = \sigma_0 + \sigma^{(1)}s^{1-\beta} + o\left(s^{1-\beta}\right) \tag{43}$$

as $s \to 0$. Moreover, $\sigma^{(1)} = -2k_s\varphi_0$. Then, Eq. (43) becomes

$$\sigma = \sigma_0 - 2k_s\varphi_0 s^{1-\beta} + o\left(s^{1-\beta}\right) \tag{44}$$

as $s \to 0$. The first equation in (42) contains a term of the order $O\left[s^{\alpha(1-\beta)-1}\right]$. It follows from (44) that the derivative $\partial\sigma/\partial t$ is of the order $O\left(s^{1-\beta}\right)$. Therefore, it is necessary to examine two cases:

$$\alpha\,(1-\beta) - 1 = 0 \tag{45}$$

and

$$\alpha\,(1-\beta) - 1 = 1 - \beta. \tag{46}$$

Using (19) one can find from (46) that $\alpha > 2$. This contradicts the assumption that $\alpha < 2$. Therefore, one is left with case (45). In this case,

$$\beta = 1 - \frac{1}{\alpha}. \tag{47}$$

This equation together with (19) shows that

$$1 < \alpha < 2. \tag{48}$$

Using (47) the asymptotic representation of solutions given in (18), (40), and (44) can be rewritten as

$$\begin{aligned} u_t &= u_0 + u_t^{(1)} s^{(\alpha-1)/\alpha} + o\left[s^{(\alpha-1)/\alpha}\right], \\ \sigma_{tt} &= \sigma_0 - 4k_s\varphi_0 s^{1/\alpha} + o\left(s^{1/\alpha}\right), \\ \sigma_{ss} &= \sigma_0 + o\left(s^{1/\alpha}\right), \\ \sigma_{ts} &= k_s\left(1 - A\xi_0^{-1}s\right) + o(s) \end{aligned} \tag{49}$$

as $s \to 0$.

Summarizing, in the vicinity of a maximum friction surface, the solution is represented by (17) and (39) if $\alpha \geq 2$ and by (17) and (49) if $1 < \alpha < 2$. No solution at sliding exists if $\alpha \leq 1$ (Alexandrov and Mishuris 2009).

Double-Shearing Model

In general, the equations of the double-shearing model are not hyperbolic. However, the stress equations comprising the yield criterion and the equilibrium equations are. The two characteristic directions make angle $\pi/4 + \phi/2$ with the direction of the major principal stress σ_1 (Fig. 3). The maximum friction law requires that the friction surface coincides with a characteristic curve or an envelope of characteristic curves. It is seen from the geometry of Fig. 3 that

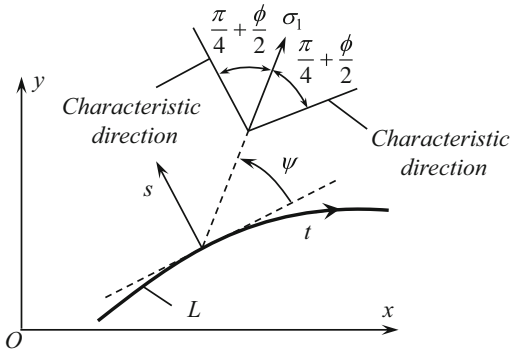

Fig. 3 Directions of stress characteristics

$$\psi = \frac{\pi}{4} + \frac{\phi}{2} \quad \text{or} \quad \psi = -\frac{\pi}{4} - \frac{\phi}{2} \tag{50}$$

for $s = 0$. In what follows, it is assumed that the first equation in (50) is satisfied. The other case can be treated in a similar manner.

The yield criterion (7) reduces to

$$\sigma \sin\phi + q = c\cos\phi \tag{51}$$

where

$$\sigma = \frac{1}{2}\left(\sigma_{tt} + \sigma_{ss}\right), \quad q = \frac{1}{2}\sqrt{(\sigma_{tt} - \sigma_{ss})^2 + 4\sigma_{ts}^2} \tag{52}$$

and

$$\begin{aligned} &\sigma_{tt} = \sigma + q\cos 2\psi, \\ &\sigma_{ss} = \sigma - q\cos 2\psi,\ \sigma_{ts} = q\sin 2\psi. \end{aligned} \tag{53}$$

It is convenient to introduce a new unknown variable γ as

$$\gamma = \frac{\pi}{4} + \frac{\phi}{2} - \psi. \tag{54}$$

Then, it follows from (50) that

$$\gamma = 0 \tag{55}$$

for $s = 0$. Using (54) Eq. (8) can be rewritten as

$$\begin{aligned} &\xi_{tt} + \xi_{ss} = 0, \\ &\cos(2\gamma - \phi)\,(\xi_{tt} - \xi_{ss}) - 2\sin(2\gamma - \phi) \\ &\xi_{ts} - 2\sin\phi\,(\omega_{ts} - d\gamma/d\tau) = 0. \end{aligned} \tag{56}$$

The strain rate ξ_{tt} in the second equation can be eliminated by means of the first equation. Then, one can use Eq. (2) to get

$$\begin{aligned} &2\cos(2\gamma - \phi)\frac{\partial u_s}{\partial s} + [\sin(2\gamma - \phi) + \sin\phi]\frac{\partial u_t}{\partial s} \\ &+ [\sin(2\gamma - \phi) - \sin\phi]\left(\frac{\partial u_s}{H\partial t} + u_t G_2\right) \\ &- 2\sin\phi\left(\frac{\partial \gamma}{\partial \tau} + \frac{u_t}{H}\frac{\partial \gamma}{\partial t} + u_s\frac{\partial \gamma}{\partial s}\right) = 0. \end{aligned} \tag{57}$$

The coefficient of the derivative $\partial u_t/\partial s$ vanishes at $\gamma = 0$ and, therefore, at $s = 0$. If $|\partial u_t/\partial s| < \infty$, then the solution is not singular. Therefore, in what follows it is assumed that

$$\frac{\partial u_t}{\partial s} \to \infty \tag{58}$$

as $s \to 0$. Then, the term $[\sin(2\gamma - \phi) + \sin\phi]\,\partial u_t/\partial s$ reduces to the expression $0 \cdot \infty$ at $s = 0$.

The solution for the rigid perfectly plastic model suggests that one seeks an asymptotic expansion in the form

$$\begin{aligned} &u_s = u_s^{(1)}s + o(s), \quad u_t = u_0 + u_t^{(1)}\sqrt{s} + o(\sqrt{s}), \\ &\gamma = \gamma_0\sqrt{s} + o(\sqrt{s}), \quad \sigma = \sigma_0 + \sigma^{(1)}\sqrt{s} + o(\sqrt{s}), \\ &q = q_0 + q^{(1)}\sqrt{s} + o(\sqrt{s}) \end{aligned} \tag{59}$$

as $s \to 0$. It is seen from (51) and (59) that

$$\sigma_0\sin\phi + q_0 = c\cos\phi. \tag{60}$$

Using (59) one can find that

$$\begin{aligned} &[\sin(2\gamma - \phi) + \sin\phi]\frac{\partial u_t}{\partial s} = \cos\phi\, u_t^{(1)}\gamma_0 + o(1), \\ &u_s\frac{\partial \gamma}{\partial s} = \frac{u_s^{(1)}\gamma_0}{2}\sqrt{s} + o\left(\sqrt{s}\right) \end{aligned} \tag{61}$$

as $s \to 0$. Then, collecting coefficients of like powers of s in (57), it is possible to confirm that this equation is satisfied. The first equation in (56) is consistent with the assumed expansion if $Hu_s^{(1)} + du_0/dt = 0$. It is understood here that H is calculated at $s = 0$.

Substituting (59) into (53) and taking into account (54), one gets

$$\begin{aligned} \sigma_{tt} &= \sigma_0 - q_0\sin\phi + \left(\sigma^{(1)} - q^{(1)}\sin\phi\right)\sqrt{s} \\ &\quad + o\left(\sqrt{s}\right), \\ \sigma_{ss} &= \sigma_0 + q_0\sin\phi + \left(\sigma^{(1)} + q^{(1)}\sin\phi\right)\sqrt{s} \\ &\quad + o\left(\sqrt{s}\right), \\ \sigma_{ts} &= q_0\cos\phi + \left(2q_0\gamma_0\sin\phi + q^{(1)}\cos\phi\right)\sqrt{s} \\ &\quad + o(s) \end{aligned} \tag{62}$$

as $s \to 0$. Substituting (62) into the first and second equations in (1) yields

$$\frac{H\left(2q_0\gamma_0\sin\phi + q^{(1)}\cos\phi\right)}{2\sqrt{s}} + o\left(\frac{1}{\sqrt{s}}\right) = 0 \tag{63}$$

and

$$\frac{H\left(\sigma^{(1)} + q^{(1)}\sin\phi\right)}{2\sqrt{s}} + o\left(\frac{1}{\sqrt{s}}\right) = 0 \tag{64}$$

as $s \to 0$, respectively. Therefore,

$$2q_0\gamma_0\sin\phi + q^{(1)}\cos\phi = 0, \;\; \sigma^{(1)} + q^{(1)}\sin\phi = 0. \tag{65}$$

Then, Eq. (62) becomes

$$\begin{aligned} \sigma_{tt} &= \sigma_0 - q_0\sin\phi + 2\sigma^{(1)}\sqrt{s} + o\left(\sqrt{s}\right), \\ \sigma_{ss} &= \sigma_0 + q_0\sin\phi + o\left(\sqrt{s}\right), \\ \sigma_{ts} &= q_0\cos\phi + o(s) \end{aligned} \tag{66}$$

as $s \to 0$.

Summarizing, in the vicinity of a maximum friction surface, the velocity field is represented by (59) and the stress field by (66).

Conclusions

Rigid plastic solutions are often describable by non-differentiable functions in the vicinity of maximum friction surfaces. This behavior of solutions is in qualitative agreement with the presence of narrow layers of severe plastic deformation in the vicinity of friction surfaces in machining and deformation processes (Griffiths 1987). Moreover, the presence of singular terms in exact solutions may cause difficulties with numerical solutions (Facchinetti and Miszuris 2016).

The existence of singular solutions has been demonstrated for some rigid plastic models not considered in the present entry (Alexandrov and Harris 2006; Alexandrov and Jeng 2013).

Cross-References

▸ Planar Problems in Rigid-Plasticity for Granular Materials and Soils

Acknowledgements This work was made possible by grant 17-01-00624 from RFBR (Russia).

References

Alexandrov S, Harris D (2006) Comparison of solution behaviour for three models of pressure-dependent plasticity: a simple analytical example. Int J Mech Sci 48(7):750–762

Alexandrov S, Jeng Y-R (2013) Singular rigid/plastic solutions in anisotropic plasticity under plane strain conditions. Cont Mech Therm 25(5):685–689

Alexandrov S, Mishuris G (2009) Qualitative behaviour of viscoplastic solutions in the vicinity of maximum-friction surfaces. J Eng Math 65(2):143–156

Alexandrov S, Richmond O (2001) Singular plastic flow fields near surfaces of maximum friction stress. Int J Non-Linear Mech 36(1):1–11

Facchinetti M, Miszuris W (2016) Analysis of the maximum friction condition for green body forming in an ANSYS environment. J Eur Cer Soc 36:2295–2302

Griffiths B (1987) Mechanisms of white layer generation with reference to machining and deformation processes. ASME J Trib 109(3):525–530

Hill R (1950) The mathematical theory of plasticity. Clarendon Press, Oxford

Spencer A (1964) A theory of the kinematics of ideal soils under plane strain conditions. J Mech Phys Solids 12:337–351

Singularity

▸ Static and Dynamic Bifurcations

Six-Field Theory of Shells

▸ Elastic Shells, Resultant Nonlinear Theory

Six-Parameter Shell Theory

▸ Elastic Shells, Resultant Nonlinear Theory

Sixth Degrees of Freedom

▸ On Treatment of Finite Rotations in FEM Analyses of Irregular Shell Structures

Size Dependence at the Nanoscale

▸ Size Effect in Nanomaterials

Size Effect in Nanomaterials

Victor A. Eremeyev
Faculty of Civil and Environmental Engineering, Gdańsk University of Technology, Gdańsk, Poland

Synonyms

Size dependence at the nanoscale

Definition

By size effect we mean a dependence of a material parameter such as Young's modulus on a specimen size which is used for the parameter determination.

Experimental Observation

In mechanics of materials at the macroscale, the size effect may appear in many cases as a result of influence of dislocations, microcracks, voids, grains, and subgrains (see, e.g., reviews Bažant 1999, 2000; Diebels and Steeb 2002). At the nanoscale the size effect may appear at the level of a single crystal, and it is mostly determined by surface-/interface-related phenomena. Indeed, a nanostructured material can be characterized by high ratio of material particles localized in the vicinity of a surface or interfaces to ones located in the bulk. A typical dependence of a material property P on a specimen of characteristic size L is shown in Fig. 1. Here P_∞ corresponds to the value of P at the macroscale, which formally corresponds to the limit $L \to \infty$. ℓ denotes a characteristic length, so the size effect is more pronounced when $L < \ell$. Various examples of similar to Fig. 1 behavior one can find in the literature (see, e.g., Cuenot et al. 2004; Jing et al. 2006; Chen et al. 2006).

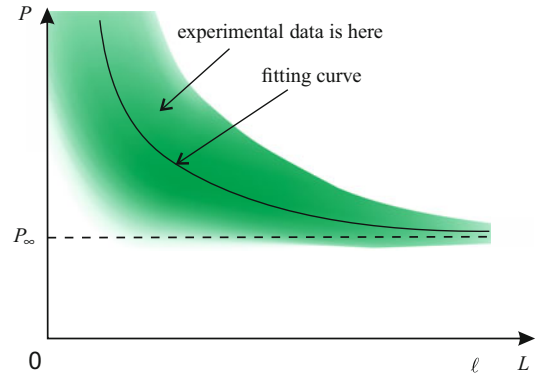

Fig. 1 Size effect: experimental data (green area), fitting curve (solid curve), and the value at the macroscale (dashed line)

Scaling Law

As a result of experimental observations, a scaling law was proposed by Wang et al. (2006), which has the following form:

$$P(L) = P_\infty \left[1 + \alpha \frac{\ell}{L} + o\left(\frac{\ell}{L}\right)\right], \qquad (1)$$

where α is a factor, ℓ is a characteristic length, and $o\left(\frac{\ell}{L}\right)$ denotes the remainder of higher order.

As an example of (1), one can consider a melting temperature of a spherical nanoparticle of radius R

$$T(R) = T_\infty \left[1 - 2\frac{\ell}{L}\right]; \qquad (2)$$

(see Wang et al. (2006) for more detail).

Concluding Remarks

Among the theories of continuum which can forecast size effect at the nanoscale, it is worth to mention the *surface elasticity* models proposed by Gurtin and Murdoch (1975, 1978) and by Steigmann and Ogden (1997, 1999), which found various applications in nanomechanics (see, e.g., Duan et al. (2008), Wang et al. (2011), Javili et al. (2012, 2013) and Eremeyev (2016) and

the references therein). Other models which have an intrinsic characteristic length are *stress-* and *strain-gradient elasticity* and *plasticity* (Fleck et al. 1994; Hutchinson and Fleck 1997; Eringen 2002; Forest et al. 2011; Aifantis 1999, 2016), *Cosserat* (*micropolar*), *couple stress*, and *micromorphic* media (Eringen 1999; Yang et al. 2002; Eremeyev et al. 2013; Liebold and Müller 2015). For these models one can expect an appearance of size effect.

Cross-References

- Cosserat Media
- Higher Gradient Theories and Their Foundations
- Micromorphic Approach to Materials with Internal Length
- Nonlocal Theories
- Strain Gradient Plasticity
- Surface Energy and Its Effects on Nanomaterials

References

Aifantis EC (1999) Gradient deformation models at nano, micro, and macro scales. J Eng Mater Technol 121(2):189–202

Aifantis E (2016) Chapter one – internal length gradient (ILG) material mechanics across scales and disciplines. Adv Appl Mech 49:1–110

Bažant ZP (1999) Size effect on structural strength: a review. Arch Appl Mech 69:703–725

Bažant ZP (2000) Size effect. Int J Solids Struct 37:69–80

Chen CQ, Shi Y, Zhang YS, Zhu J, Yan YJ (2006) Size dependence of young's modulus in ZnO nanowires. Phys Rev Lett 96(7):075505–4

Cuenot S, Frétigny C, Demoustier-Champagne S, Nysten B (2004) Surface tension effect on the mechanical properties of nanomaterials measured by atomic force microscopy. Phys Rev B 69(16):165410–5

Diebels S, Steeb H (2002) The size effect in foams and its theoretical and numerical investigation. Proc R Soc Lond A 458(3):2869–2883

Duan HL, Wang J, Karihaloo BL (2008) Theory of elasticity at the nanoscale. In: Advances in applied mechanic, vol 42. Elsevier, Amsterdam, pp 1–68

Eremeyev VA (2016) On effective properties of materials at the nano-and microscales considering surface effects. Acta Mech 227(1):29–42

Eremeyev VA, Lebedev LP, Altenbach H (2013) Foundations of micropolar mechanics. Springer-briefs in applied sciences and technologies. Springer, Heidelberg

Eringen AC (1999) Microcontinuum field theory. I. foundations and solids. Springer, New York

Eringen AC (2002) Nonlocal continuum field theories. Springer, New York

Fleck NA, Muller GM, Ashby MF, Hutchinson JW (1994) Strain gradient plasticity: theory and experiment. Acta Metall Mater 42(2):475–487

Forest S, Cordero NM, Busso EP (2011) First vs. second gradient of strain theory for capillarity effects in an elastic fluid at small length scales. Comput Mater Sci 50(4):1299–1304

Gurtin ME, Murdoch AI (1975) A continuum theory of elastic material surfaces. Arch Ration Mech Anal 57(4):291–323

Gurtin ME, Murdoch AI (1978) Surface stress in solids. Int J Solids Struct 14(6):431–440

Hutchinson J, Fleck N (1997) Strain gradient plasticity. In: Advances in applied mechanics, vol 33. Academic, New York, pp 295–361

Javili A, McBride A, Steinmann P (2012) Thermomechanics of solids with lower-dimensional energetics: on the importance of surface, interface, and curve structures at the nanoscale. A unifying review. Appl Mech Rev 65:010802-1-31

Javili A, dell'Isola F, Steinmann P (2013) Geometrically nonlinear higher-gradient elasticity with energetic boundaries. J Mech Phys Solids 61(12):2381–2401

Jing GY, Duan HL, Sun XM, Zhang ZS, Xu J, Li YD, Wang JX, Yu DP (2006) Surface effects on elastic properties of silver nanowires: contact atomic-force microscopy. Phys Rev B 73(23):235409-6

Liebold C, Müller WH (2015) Are microcontinuum field theories of elasticity amenable to experiments? A review of some recent results. In: Differential geometry and continuum mechanics. Springer, Cham, pp 255–278

Steigmann DJ, Ogden RW (1997) Plane deformations of elastic solids with intrinsic boundary elasticity. Proc R Soc A 453(1959):853–877

Steigmann DJ, Ogden RW (1999) Elastic surface-substrate interactions. Proc R Soc A 455(1982):437–474

Wang J, Duan HL, Huang ZP, Karihaloo BL (2006) A scaling law for properties of nano-structured materials. Proc R Soc Lond A 462(2069):1355–1363

Wang J, Huang Z, Duan H, Yu S, Feng X, Wang G, Zhang W, Wang T (2011) Surface stress effect in mechanics of nanostructured materials. Acta Mech Solida Sin 24:52–82

Yang FACM, Chong ACM, Lam DCC, Tong P (2002) Couple stress based strain gradient theory for elasticity. Int J Solids Struct 39(10):2731–2743

Size Effect Phenomenon

▸ Analysis of Cracks in Piezoelectric Solids with Consideration of Electric Field and Strain Gradients

Size-Dependent Plasticity Theory

▸ Strain Gradient Plasticity

Skeletal Muscle Modelling

Oliver Röhrle
Institute of Applied Mechanics (CE)/Continuum Biomechanics and Mechanobiology Research Group, Cluster of Excellence for Simulation Technology (SimTech), University of Stuttgart, Stuttgart, Germany

Synonyms

Active soft tissue modelling; Excitation-contraction coupling; Hill muscle modelling; Muscle mechanics; Neuromuscular modelling

Definition

Skeletal muscle modelling focuses on developing computer models capable of predicting the deformations and the exerted forces of a skeletal muscle that is activated through neural stimulation.

Background

In contrast to smooth or cardiac muscles, skeletal muscles have the capability to contract upon neural stimulation in a voluntary fashion. This characteristic together with the presence of joints and a rather rigid skeleton, to which skeletal muscles are typically attached via tendons, builds the basis for the voluntary and controlled motion of our body. Understanding and modelling the motion of the body is one of the oldest goals in the field of biomechanics. The key to understanding motion is to understand how muscles work – in particular how muscles generate force and how much force an individual muscle exerts upon stimulation. While research on muscle recruitment and control is a very active and very complex field of research by itself, the focus herein is on how to describe and model the mechanical behavior of skeletal muscle tissue, i.e., skeletal muscle modelling.

From an anatomical perspective, a skeletal muscle exhibits hierarchical structures composed of contractile elements (called sarcomeres) and connective tissue (mainly collagen). Within a continuum mechanical framework for modelling skeletal muscles, the sarcomeres are typically considered to be the smallest force-producing units within a muscle. Sarcomeres are connected in series to each other and form a myofibril. Multiple myofibrils in parallel form a muscle fiber. The muscle fiber itself is surrounded by a connective layer called endomysium. From an organizational point of view, muscle fibers are spatially grouped into parallel packets (fascicles) surrounded by a layer of connective tissue (perimysium). Multiple packets form the muscle belly, which is again surrounded by connective tissue (epimysium) and connected to bony structures through tendons. A schematic view is given in Fig. 1 (https://commons.wikimedia.org/wiki/File%3A1007_Muscle_Fibes_(large).jpg).

From a physiological, i.e., functional, point of view, two basic muscle fiber types are distinguished, i.e., Type I (slow twitch) and Type II (fast twitch) of which Type II muscle fibers are often further characterized into Type IIa, Type IIb, and Type IIx. The characterization is based on the isoform of a particular contractile protein called myosin. The different muscle fiber types differ in mechanical and metabolic properties. In contrast to Type II skeletal muscle fibers, Type I muscle fibers typically produce less force

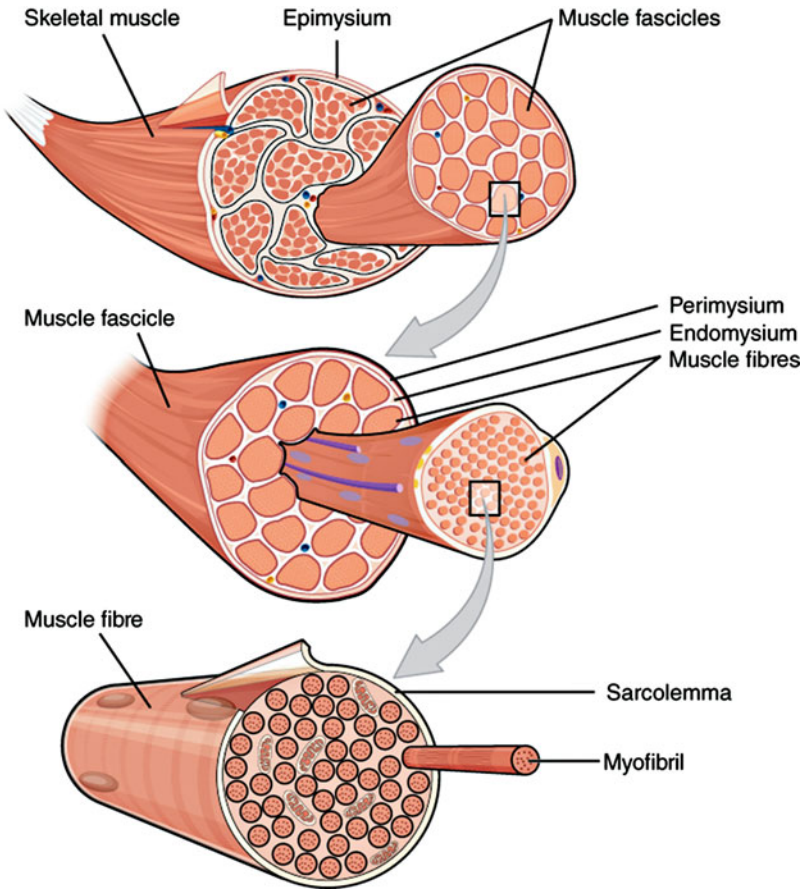

Fig. 1 Structure of a skeletal muscle. (Original image © by OpenStax Anatomy and Physiology)

but are more fatigue resistant. From a skeletal muscle recruitment point of view, several skeletal muscle fibers (of the same type) are controlled by the same lower motor neuron through nervous axons. The lower motor neuron, the axons and the respective fibers that are innervated by the axons, are called a motor unit, which is the smallest unit within a skeletal muscle to voluntarily contract. The lower motor neuron sends rate-coded impulses called action potentials. To each action potential corresponds under normal conditions a single instance of contraction (twitch) from all the fibers belonging to the same motor unit. During a voluntary contraction, motor units are activated in an orderly fashion, starting from the smallest ones, up until the biggest (recruitment size principle). In general, the recruitment of motor units for a given muscle is complete at a fraction (in some cases down to 60%) of the maximal voluntary contraction. The remaining force increment is attributed to an increase of motor units firing rate.

Taking into account all abovementioned structural and functional aspects within one computational model is currently nearly impossible. Too large are the differences in scales. One would have to consider small-scale aspects such as the chemo-electrical processes leading to contraction dynamics within a sarcomere, i.e., on the *ms* time scale or the *nm* length scale, as well as large-scale aspects such as muscle fatigue (several seconds), exercise training (weeks), or aging (years) or the entire musculoskeletal system (*m*). Hence, different modelling approaches have been developed over the years. On the largest scale (referring to the musculoskeletal scale and the several-seconds time scale), movement of the whole or of parts of the skeleton is typically modelled using *multi-body*-based modelling approaches. Within multi-body simulations, the mechanical behavior

of skeletal muscles are reduced to a point of mass, and the exerted skeletal muscle forces are applied to rigid bodies representing the bones of a skeleton as forces acting in the direction between the insertion and origin point of the respective muscles. Hence, they are often referred to 1-D models. The 1-D (skeletal muscle) line elements describe within multi-body simulations the muscle-tendon complex as a lumped material and enter the equations of motion (balance of momentum). These models are commonly referred as Hill-type muscle models, named after Archibald Vivian Hill, who did pioneering research on the production of heat and mechanical work in muscle (Hill 1938).

While 1-D formulations allow efficient simulations and some insights into movement, the reduction of the complex skeletal muscle's structure to a skeletal model consisting of a few lumped parameters is often an oversimplification. Hill-type models, for example, cannot take into account the heterogeneity of the tissue, e.g., fiber directions, varying collagen distributions, or account for the contact between the muscle and the surrounding tissues such as bones, other muscles, or the skin/fat layer. If one wants to include such properties, *continuum-mechanical-based* methods are indispensable. They can provide full volumetric resolution of the skeletal muscle tissue at the expense of (substantially) increased computational requirements.

Standard continuum-mechanical frameworks for modelling skeletal muscle mechanics include phenomenological descriptions of the material (the passive and active mechanical behavior of skeletal muscle tissue) on the macroscopic scale. In particular the activation dynamics is also reduced to a phenomenological quantity, e.g., a scalar parameter representing the level of activity. One of the first continuum-mechanical skeletal muscle models was proposed by Johansson et al. (2000). More recently, continuum-mechanical descriptions have been extended to incorporate more realistic activation dynamics and characteristics stemming from the fiber or sarcomere level, e.g., fiber type, motor units, and recruitment protocols. Such models typically include the biophysical processes originating within a sarcomere in order to compute the propagation of the action potentials and the force generation. They typically adopt systems biology approaches, e.g., Huxley-like models. The link from computing the level of activation or force generation of a single sarcomere or muscle fiber to the averaged level of activation on the whole muscle scale is due to upscaling (averaging). Such models that incorporate processes on the sarcomere level within continuum-mechanical principles on the muscle level are referred to multi-scale, multi-physics *chemo-electro-mechanical* skeletal muscle models, e.g., the chemo-electro-mechanical models originally proposed by Röhrle et al. (2008, 2012).

Kinematics and Governing Equations

During contractions, the change in length of a skeletal muscle can be 50% or more. Hence, modelling the mechanical behavior of skeletal muscle within a continuum-mechanical framework should appeal to finite deformation theory. Moreover, since skeletal muscle tissue is typically considered as a solid, one typically assumes a Lagrangian description. The key for modelling solid materials within a continuum-mechanical framework is to identify a stress-free configuration, the so-called reference configuration. However, since skeletal muscle tissue is, like all other biological tissue, naturally grown, it naturally exhibits residual stresses. Therefore, specifying the reference configuration is not easy and straightforward. The different ideas and methodologies for finding the reference configuration or applying suitable residual stresses to the reference configuration are omitted within this contribution.

Once the reference configuration is specified, a material point within the reference configuration is denoted by its position vector $\mathbf{X}$. If the tissue is subjected to a load or deformation, the movement of each material point is described by the motion or the placement function, $\chi(\mathbf{X}, t)$, and the respective position vector within the actual configuration is denoted by $\mathbf{x}(\mathbf{X}, t)$. Following the standard definitions of

continuum mechanics, the deformation gradient, $\mathbf{F}$, is a second-order tensor characterizing the local gradient of material point $\mathbf{X}$, i.e., the deformation of neighboring points, and is defined by $\mathbf{F} := \frac{\partial \chi(\mathbf{X},t)}{\partial \mathbf{X}}$.

Besides the reference and current configuration, specific modelling approaches might also require the introduction of a third, so-called intermediate, configuration. Details related to this configuration conform to the general modelling framework of inelasticity. In this framework, the deformation gradient is multiplicatively split into two parts, i.e., into an elastic deformation gradient $\mathbf{F}_e$ and a muscle-specific deformation gradient $\mathbf{F}_m$ describing, for example, growth or active behavior of skeletal muscle.

In skeletal muscle modelling, one typically aims to describe overall mechanical behavior of the skeletal muscle tissue. Hence, only the mechanical balance laws (balance of mass, balance of linear momentum, and balance of moment of momentum) are considered. The thermodynamical ones (energy and entropy) are often ignored, although temperature certainly plays a crucial role within the physiology of muscles. Ignoring the effects of temperature and focusing on its mechanical properties, the material behavior of the skeletal muscle tissue enters the balance equations through the balance of linear momentum, i.e.,

$$\rho\, \ddot{\mathbf{x}} = \operatorname{div}\left[J^{-1}\, \mathbf{P}\, \mathbf{F}^T\right] + \rho\, \mathbf{b}, \quad \text{on} \quad \Omega_M \qquad (1)$$

where ρ is the density of the skeletal muscle tissue, which can differ at each material point $\mathbf{X}$, $\ddot{\mathbf{x}}$ is the acceleration, J is the determinant of $\mathbf{F}$, $\mathbf{P}$ is the first Piola-Kirchhoff stress tensor describing the stress-strain relationship of skeletal muscle tissue, $\mathbf{b}$ denotes the body forces, and Ω_M describes the domain of the skeletal muscle tissue.

Most modelling approaches ignore body forces ($\mathbf{b} = \mathbf{0}$), which are caused by the effect of gravitation on the muscle body, and assume slow movements ($\ddot{\mathbf{x}} \approx \mathbf{0}$). In this case, the inertial effects described by the term $\rho\, \ddot{\mathbf{x}}$ can be neglected and a quasi-static setting can be assumed. Assuming quasi-static conditions is, however, for many scenarios involving the musculoskeletal system an oversimplification. This is particularly true if one aims to predict the mechanical behavior of skeletal muscles during impact, e.g., during running or during a car crash. Moreover, since relative soft skeletal muscle tissue is coupled to the rather rigid skeleton, muscles move relative to the bones and result in so-called wobbling masses. If one wants to capture such phenomena, one cannot ignore the inertia term. A fully dynamic simulation framework is needed.

Geometry

The mechanical behavior of a muscle strongly depends on its muscle architecture and its geometry. The ideal source for acquiring information on a skeletal muscle's geometry and its structural characteristics is (nondestructive) imaging. Such imaging techniques should also be capable of identifying the muscle fiber directions and distributions as the fiber direction plays a crucial role in skeletal muscle mechanics: Due to the arrangement of the sarcomeres and their functioning, skeletal muscles can only actively contract along the fibers. Currently, there exist two suitable state-of-the-art imaging techniques that are based on magnetic resonance tomography (MRI): (high-resolution) conventional MRI for determining, often in high resolution, the 3-D, geometrical extend of a skeletal muscle as well as its composition, e.g., fat inclusion or internal tendinous structures, and diffusion-tensor MRI (DT-MRI) for determining the fiber orientation within a muscle. The DT-MRI method can utilize in a biological tissue the diffusion sensitization in six directions and determine from that a diffusion tensor for each voxel of the image. Assuming that the diffusion sensitization is the largest along skeletal muscle fibers, the largest eigenvalue of the diffusion tensors and its associated Eigenvector provide, for each voxel, the principal direction of the averaged fiber direction within the respective voxel. Hence, DT-MRI is a methodology to define the fiber field of a muscle and, hence, a

way to intrinsically describe the local anisotropy of the tissue.

The collected images need to be segmented to extract the exact geometry of the muscles. Up till now, despite the development of automated methods such as deformable models that achieve a local optimal segmentation goal, manual segmentation is still the valid option for many clinical settings and researches in the field of skeletal muscle modelling. This is due to the fact that skeletal muscles lack distinguishing visual properties that permit applying simple automatic segmentation methods. This makes automatic segmentation a challenging topic for skeletal muscle image data, and the (long) process of manually segmenting images remains a bottle neck in this research field.

Moreover, the balance of momentum equations cannot be solved analytically – this even holds for simple geometries. Hence, a discretization scheme has to be employed in order to transform the continuous equation in a system of discrete (nonlinear) equations that can numerically be solved. A familiar method to discretize the segmented geometry is to utilize the finite element method. The details of discretization process including selecting the type of elements and the mesh fineness are direct results of the complexity of geometry (and the weak form of governing equations). The meshing and its associated challenges shall not be subject to this entry.

Constitutive Modelling

From a mechanical point of view, skeletal muscle tissue is a complex biological material consisting of different components that exhibit different phenomenons like elasticity, active deformation/force generation, or history-dependent material effects. Like most biological tissues, skeletal muscles are assumed to exhibit (visco-)elastic, transversely isotropic, inhomogeneous, and (nearly) incompressible behavior. Like in each continuum-mechanical framework, the constitutive equations describing the mechanical behavior of skeletal muscle tissue enter the framework through the balance of linear momentum, which are then discretized and solved to obtain the respective deformations and stresses and, hence, the predictions of the exerted muscle forces. Skeletal muscle constitutive modelling, however, differs from modelling classical solid materials by taking into account the ability to generate force, i.e., by taking into account its active behavior. The active force generation depends on many different aspects, i.e., on the current stretch of the skeletal muscle, on its contraction velocity, and its level of activation. As far as the passive material properties are concerned, one can choose a suitable phenomenological constitutive law, e.g., a Mooney-Rivlin-, Ogden-, or Fung-type law, and compute the respective material parameters by fitting the mechanical response of the computational model to experimental data. It should be noted that for skeletal muscle modelling, however, not all of these material properties are considered at all times. Depending on the application, different amounts of details can be reasonable, e.g., if slow movements are assumed, a force-velocity relationship might be omitted.

Additive Split of the Stress Tensor

The most common approach to model the mechanical behavior of skeletal muscle is to split the stress tensor additively into a passive and an active part. Each term accounts individually either for its passive or active properties. Hereby one assumes that the smeared overall behavior of the muscle tissue can be obtained by superposition, i.e.,

$$\mathbf{P} = \mathbf{P}_{\text{passive}} + \mathbf{P}_{\text{active}} , \tag{2}$$

where the active and passive contributions to the overall first Piola-Kirchhoff stress tensor, $\mathbf{P}$, are denoted with subscript “active” and “passive.” Based on its anatomical structure, skeletal muscle tissue is assumed to be transversal isotropic, i.e., muscle tissue has different mechanical properties in fiber direction than in cross-fiber direction. Anisotropic material properties are represented by structure tensors that can be derived from the fiber direction $\mathbf{a}_0$. In detail $\mathbf{M}_\text{f} = \mathbf{a}_0 \otimes \mathbf{a}_0$ accounts for specific material properties in fiber

direction, and $\mathbf{M}_{\mathrm{xf}} = \mathbf{I} - \mathbf{a}_0 \otimes \mathbf{a}_0$ accounts for specific material properties in cross-fiber direction.

It is known from experiments that passive skeletal muscle tissue shows viscoelastic behavior; consequently, the passive stress tensor, $\mathbf{P}_{\mathrm{passive}}$, depends on the fiber direction $\mathbf{a}_0$, the deformation gradient tensor $\mathbf{F}$, and the rate of deformation $\dot{\mathbf{F}}$, i.e., $\mathbf{P}_{\mathrm{passive}}(\mathbf{F}, \dot{\mathbf{F}}, \mathbf{a}_0)$. However, in continuum mechanical skeletal muscle models, viscous behavior is often neglected and passive skeletal muscle tissue is assumed to be hyperelastic, leading to $\mathbf{P}_{\mathrm{passive}} = \mathbf{P}_{\mathrm{passive}}(\mathbf{F}, \mathbf{a}_0)$.

Hyperelastic materials, also known as green elastic or conservative materials, behave elastically when subjected to large deformations. If thermal effects are neglected, the second Piola-Kirchhoff stress, $\mathbf{S}$, of hyperelastic materials is related to the instant Lagrangian Green strain, $\mathbf{E} = \frac{1}{2}(\mathbf{F}^T\mathbf{F} - \mathbf{I})$, by derivation of a scalar valued function $W(\mathbf{E})$, known as strain or elastic energy per unit volume, through the second Piola-Kirchhoff stress tensor $\mathbf{S} = \partial W(\mathbf{E})/\partial \mathbf{E}$ and $\mathbf{P} = \mathbf{FS}$. Unlike viscoelastic materials, the hyperelastic response of these types of materials is independent of its loading history. Moreover, due to its high content of water, skeletal muscle tissue is typically assumed to be incompressible. The incompressibility constraint, $\det \mathbf{F} = J = 1$, is included by incorporating the incompressible constraint within the stress tensor via the hydrostatic pressure, p, as a Lagrange multiplier.

The active force generation takes place at the sarcomeres, which consist of thin actin and thick myosin filaments. The molecular motor is based on the cyclic interaction of the myosin heads and the actin filaments (cross-bridge cycle) and is controlled by the intracellular calcium concentration, serving as a second messenger that is triggered by an electrophysiological stimulus (action potential). A continuum mechanical skeletal muscle does not consider individual sarcomeres. Rather a more abstract representation for the active tissue properties is chosen by introducing an average activation state in a representative elementary volume, i.e., stochastically distributed fluctuations of the microstructure state variables vanish. This can either be realized by purely phenomenological data fitting or detailed biophysical modelling. In order to obtain a universally valid material description, we introduce a generic internal state vector $\boldsymbol{\alpha}$, describing the averaged active properties of the muscle at a material point $\mathbf{X}$. Despite quite spatially heterogeneous activation of skeletal muscles, most continuum mechanical skeletal muscle models assume a constant value throughout the muscle. By convention, $\alpha = 0$ denotes a purely passive skeletal muscle, while $\alpha = 1$ defines the maximally stimulated skeletal muscle.

The amount of force that can be produced by the muscle is proportional to the overlap between the thin actin and the thick myosin filaments. This geometrical consideration on the microstructure configuration can be summarized in a material property known as the (active) force-length relation, which is depicted in Fig. 2.

Further, the active force that can be produced by the cross-bridges also depends on the contraction velocity. Consequently, the constitutive relation describing the active stress of the muscle tissue should depend on the fiber direction $\mathbf{a}_0$ and the generalized activation state vector $\boldsymbol{\alpha}$, which is a function of the deformation gradient tensor $\mathbf{F}$ and the rate of deformation $\dot{\mathbf{F}}$ and the fiber direction $\mathbf{a}_0$, i.e., $\mathbf{P}_{\mathrm{active}} = \mathbf{P}_{\mathrm{active}}(\boldsymbol{\alpha}, \mathbf{F}, \dot{\mathbf{F}}, \mathbf{a}_0)$.

Taking all abovementioned considerations into account, the general representation of the overall first Piola-Kirchhoff stress tensor, $\mathbf{P}$, for skeletal muscle tissue is given by

$$\mathbf{P} = \mathbf{P}_{\mathrm{passive}}(\mathbf{F}, \dot{\mathbf{F}}, \mathbf{a}_0) + \mathbf{P}_{\mathrm{active}}(\boldsymbol{\alpha}, \mathbf{F}, \dot{\mathbf{F}}, \mathbf{a}_0) - pJ\mathbf{F}^{T-1} \,. \tag{3}$$

Within this framework, additional properties, such as, for example, history-dependent muscle stiffness, can easily be incorporated by adding up an additional term to the total stress tensor.

Multiplicative Split

Besides the active stress modelling approach described above, there also exist active strain approaches to model the active behavior of skeletal muscle tissue. Within the active strain approach, the deformation gradient tensor, $\mathbf{F}$, is

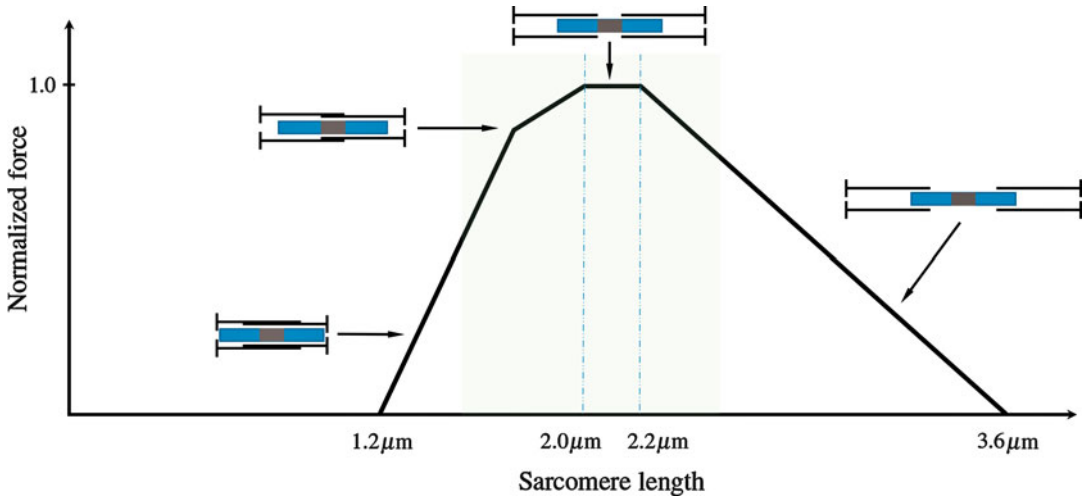

Fig. 2 Sketch of the force-length relationship motivated by actin-myosin overlap (actin, thin black structures; myosin, thick blue structures). In transparent green the typical working range of a skeletal muscle

multiplicatively decomposed into an elastic and an active part,

$$\mathbf{F} = \mathbf{F}_\mathrm{e}\,\mathbf{F}_\mathrm{a}\,, \tag{4}$$

where the active deformation gradient tensor $\mathbf{F}_\mathrm{a}$ accounts for the muscle's ability to actively generate force, while the elastic deformation gradient tensor $\mathbf{F}_\mathrm{e} = \mathbf{F}\mathbf{F}_\mathrm{a}^{-1}$ is a virtual measure for the mechanical distortion induced by the visible total deformation $\mathbf{F}$ and the microscopic active deformation $\mathbf{F}_\mathrm{a}$.

For simplicity, it is assumed that passive muscle tissue behaves in a hyperelastic sense. The active deformation gradient tensor $\mathbf{F}_\mathrm{a}$ depends on the same variables as introduced above, i.e., $\boldsymbol{\alpha}$, $\mathbf{F}$, $\dot{\mathbf{F}}$, and $\mathbf{a}_0$, and is given by

$$\mathbf{F}_\mathrm{a} = \mathbf{F}_\mathrm{a}(\boldsymbol{\alpha}, \mathbf{F}, \dot{\mathbf{F}}, \mathbf{a}_0)\,. \tag{5}$$

The first Piola-Kirchhoff stress tensor, $\mathbf{P}$, can be derived from the overall elastic energy stored in the body. The overall stored elastic energy can be derived from a potential $\Psi = \Psi(\mathbf{F}, \mathbf{F}_\mathrm{a}) = \Psi(\mathbf{F}_\mathrm{e})$. Consequently, the first Piola-Kirchhoff stress tensor, $\mathbf{P}$, can be directly derived from the potential Ψ:

$$\mathbf{P} = \frac{\partial \Psi(\mathbf{F}_\mathrm{e})}{\partial \mathbf{F}_\mathrm{e}} \mathbf{F}_\mathrm{a}^{T-1}\,. \tag{6}$$

The active stress approach (additive split) might be more intuitive as it might be easier and more straight forward to choose and fit appropriate constitutive equations to experimentally gained data. Moreover, it might be easier and more intuitive to include further mechanical properties. The active strain approach (multiplicative split), however, might be preferable from a mathematical point of view, as it is easier to guarantee convexity and therefore finding a stable solution.

Software Tools

In continuum mechanics, the balance of linear momentum equations is typically discretized using the finite element method (FEM). Using a biomechanically inspired constitutive law, a 3-D geometry and the FEM, to predict the mechanical behavior of skeletal muscles is not widespread. As such, no popular software package exists as a *go-to* tool to simulate skeletal muscle in three dimensions. This is not the case, for example, for simulation of muscle in multi-body dynamics, where skeletal muscles are typically modelled as

1-D elements, for which software packages such as the commercial software AnyBody (AnyBody Technology) or the open-source software package OpenSim (NCSRR) are widely used. Another issue in simulating skeletal muscle using FEM is that several software packages and codes are developed in-house to tackle specific problems and involve specialized work-flows that are either not immediately available and/or require in-depth knowledge to set up. In fact, there exist only a few software packages which provide the functionality to model (active) skeletal muscle within a generalized continuum-mechanical framework, for example, FEBiO (Musculoskeletal Research Lab Utah & Musculoskeletal Biomechanics Lab Columbia), LS-DYNA (LSTC), and OpenCMISS (Auckland Bioengineering Institute, Bradley et al. 2011). Further details are given in Table 1. These packages provide the ability to model an active (skeletal) muscle tissue in response to a stimulation.

While these packages provide perhaps the simplest way to simulate skeletal muscles, the use of more generalized FE packages is not precluded since they can usually be extended via user-defined material models, which describe (active) skeletal muscle properties. The implementation of user materials requires in-depth knowledge not only of muscle physiology but also about numerical aspects of the FE method and as such may not be a viable option for all use cases. However, prior to implementing user-defined skeletal muscle material models within FE packages, one should investigate the package's capabilities. To simulate fast movements or impact, inertial effects are essential. Further to couple electrophysiological principles to mechanics or to allow for complex recruitment principles, one needs to be able to include complex (electro-)physiological models, which are typically defined by means of ordinary differential equations. This, however, is not standard or easy to include and therefore still requires custom-build biomechanical software tools such as OpenCMISS. Some popular open-source and commercial packages are listed in Table 1.

The available contact formulation and its implementation might further influence the decision for a particular software is the contact formulation. This is particularly important at the musculoskeletal system level. In this case, commercial packages generally provide a more robust set of contact algorithms and are able to robustly deal with any nonlinearities which may arise due to contact between the muscle, tendon, and bone. Given the nature of muscle simulations, generally a large number of elements

Table 1 List of popular FE packages which can be used to simulate skeletal muscles

Software package	Provider	Muscle-model provided?	Dynamic
Abaqus unified FEA[a]	Dassault systèmes	No	Yes
ADINA[a]	ADINA R&D	No	Yes
ANSYS suite[a]	ANSYS	No	Yes
CHeart[b]	Kings college London	No	No
Code_Aster[c]	Électricité de France	No	Yes
COMSOL multiphysics[a]	COMSOL	No	Yes
FEAP[c]	U-California, Berkley	No	Yes
FEBiO[b]	U-Utah & U-Columbia	Yes	No
LS-DYNA[a]	LSTC	No	Yes
Marc[a]	MSC software	No	Yes
OpenCMISS[c]	U-Auckland	Yes	No
Z88Aurora[b]	U-Bayreuth	No	Yes

[a]Commercial
[b]Closed-source
[c]Open-source

and/or multi-physics are involved, and this may lead to excessively high computational times. In this case, the ability of the software package to efficiently solve the problem in parallel and on HPC (high performance computing) systems becomes a deciding factor.

Applications

The modelling of skeletal muscle provides insights into (neuro-)muscular function in vivo, which are either difficult or even impossible to obtain experimentally. For example, modelling allows the prediction of local stresses and strains within a muscle, muscle-bone contact pressures, overall force production due to changing motor control schemes, or effects of individual muscle perturbations, just to name a few. In silico experiments are vital in generating meaningful and nontrivial data to extend datasets that would be otherwise too small to reach an adequate statistical significance, for example, in case of rare diseases. The applications of skeletal muscle modelling can be grouped into three broad areas: (i) clinical applications, (ii) physical health and safety, and (iii) ergonomics and performance enhancement.

Clinical applications include diagnosis of neuromuscular diseases and evaluation of therapies. For example, detailed chemo-electromechanical models provide the basis to model diseases that specifically target the muscle tissue (either the muscle fibers directly or the surrounding connective tissues), the neuromuscular junction, the nerve, or the lower motor neurons. Musculoskeletal modelling allows the investigation of traumatic as well as degenerative alterations of the structures related to movement and motor control. The outcomes of surgical or therapy interventions can be forecast by simulating muscle forces, joint moments, and bone loads.

Beyond clinical applications, industrial applications of skeletal muscle simulations are useful in improving the physical health and safety of products and environments. In the automotive industry, crash simulation with passive dummies is an industry standard. More recently, simplified one-dimensional muscle models have been included to closer reflect real-life situations, accounting for muscle tension in preparation for impact. The use of three-dimensional muscle models would provide realistic geometry and mass distributions, which may have a large influence on crash results due to the extreme accelerations and decelerations involved. Furthermore, joint torques and resulting movements would also be more realistically represented by three-dimensional muscles.

In the area of ergonomics, the use of skeletal muscle simulations can be used to optimize products to, for example, reduce muscle fatigue, reduce short-duration muscle strain, or even optimize (reduce) the neuromuscular activity for a given task. This has implications in industries where physical labor constitutes a large part of the activity. Using the same principle as prosthetic or orthotic control design, exoskeletons could enhance range of motion and strength. In this case, due to the supramaximal loads involved, simulation of the underlying neuromuscular processes would be critical in providing safe, robust, and quick control algorithms.

Cross-References

▸ Coupled Problems in Biological Systems
▸ Finite Element Methods

References

Bradley CP, Bowery A, Britten R, Budelmann V, Camara O, Christie R, Cookson A, Frangi AF, Gamage T, Heidlauf T, Krittian S, Ladd D, Little C, Mithraratne K, Nash M, Nickerson D, Nielsen P, NordbøO, Omholt S, Pashaei A, Paterson D, Rajagopal V, Reeve A, Röhrle O, Safaei S, Sebastián R, Steghöfer M, Wu T, Yu T, Zhang H, Hunter PJ (2011) OpenCMISS: a multi-physics & multi-scale computational infrastructure for the VPH/Physiome project. Prog Biophys Mol Biol 107:32–47

Hill AV (1938) The heat of shortening and the dynamic constants of muscle. Proc R Soc Lond B Biol Sci 126(843):136–195

Johansson T, Meier P, Blickhan R (2000) A finite-element model for the mechanical analysis of skeletal muscles. J Theor Biol 206(1):131–149

Röhrle O, Davidson JB, Pullan AJ (2008) Bridging scales: a three-dimensional electromechanical finite element model of skeletal muscle. SIAM J Sci Comput 30(6):2882–2904
Röhrle O, Davidson J, Pullan A (2012) A physiologically based, multi-scale model of skeletal muscle structure and function. Front Physiol 3:358

Slip Avalanches

▸ Avalanches in Solids

Slips

▸ Avalanches in Solids

Small-Strain Thin Shell Theory

▸ Thin Elastic Shells, Lagrangian Geometrically Nonlinear Theory

Smart Structures

▸ Active Control of Sound, Applications of
▸ Adaptive Structures, Principles of

Snap-Through Buckling

▸ Numerical Treatment of Stability Problems in Lightweight Design

Sneddon, Ian Naismith

Raymond W. Ogden
School of Mathematics and Statistics, University of Glasgow, Glasgow, UK

Ian Naismith Sneddon (*December 8, 1919 in Renfrew, Scotland; †November 4, 2000 in Glasgow) was an applied mathematician whose main research interests were in the application of integral transforms to problems in the linear theory of elasticity, especially mixed boundary-value problems, an area in which he established a formidable international reputation. In addition to his research papers, he published an impressible number of influential books, most notably on integral transform methods.

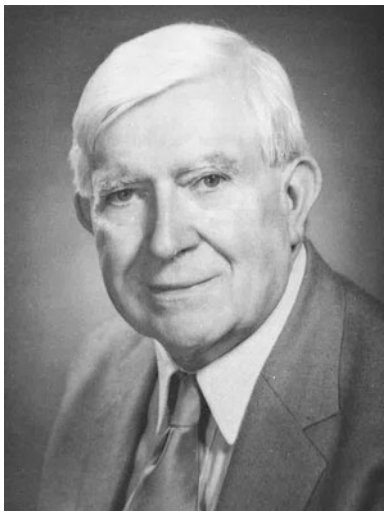

Ian Naismith Sneddon

Early Life and Education

Ian Naismith Sneddon was born in Renfrew (near Glasgow, Scotland), on December 8, 1919. Shortly after he was born, his family moved to Partick in the West End of Glasgow where Ian's father worked as a slater and plasterer. Ian attended Thornwood Primary School and

thereafter Hyndland Secondary School. He excelled at his studies, and his mathematical talent was recognized by the Principal Teacher of Mathematics, James Milroy, who provided Ian with much encouragement. At the early age of 15, he became Dux of the school (i.e., the top pupil), and at 16 in 1936, Ian enrolled at the University of Glasgow, where he studied both mathematics and physics (which was at that time referred to as natural philosophy). He graduated with a First Class Honours BSc in the combined subjects of mathematics and natural philosophy in 1940. He then moved to Cambridge University to continue his studies of mathematics and took Part II of the Mathematical Tripos, for which he was classified as a Wrangler, and in 1942 was qualified for a BA degree. At this point he was preparing to work in pure mathematics under the supervision of Professor G. H. Hardy, FRS, but war-related work called, and Ian was drafted to the Branch for Theoretical Research at the Armament Research Department at Fort Halstead in Kent, and this set the scene for a change in the direction of his interests.

Professional Life

It was in May 1944 that Ian moved to Fort Halstead, and he worked within the group superintended by the physicist N. F. Mott, FRS (later Sir Nevill and a Nobel Prize Laureate) in problems of solid mechanics. His work was closely associated with indentation problems and the fracture of steel used in tank armour plates, and this led to his solution of the problem of a "penny-shaped crack," in part based on methods applied in the Boussinesq problem. Ian rapidly became a leading international authority in the mathematical methods used for the solution of indentation and crack problems, developing expertise in the theory of integral transforms and mixed boundary value problems and applications within the context of linear elasticity.

After the war, in 1945, Mott returned to his position at Bristol University as Professor of Physics in the H.H. Wills Physical Laboratory and recruited Ian as a research fellow in theoretical physics. In the period until his departure from Bristol in 1946, Ian worked with Mott on the writing of the book *Wave Mechanics and Its Applications* (Mott and Sneddon 1948), and this was published in 1948. In 1946 Ian was appointed as a lecturer in Department of Natural Philosophy at his alma mater, the University of Glasgow, where he undertook research in both theoretical nuclear physics and elasticity theory and embarked on a teaching career. He was awarded the degree of DSc by the University of Glasgow in 1948, his submitted work for which was awarded the university's Kelvin Medal.

During this period in Glasgow, Ian was working on a major book that focused on Fourier, Laplace, Mellin, and Hankel transforms and their applications and was almost completed when he was appointed, in 1950, to the first chair of mathematics at the University College of North Staffordshire in Keele (subsequently named Keele University). At the age of 30, he was the youngest professor of mathematics in the UK. His book, entitled *Fourier Transforms* (Sneddon 1951), was published shortly after his arrival in Keele. It contained the dedication "To the University of Glasgow on the occasion of its fifth centenary 1451–1951."

At Keele Ian took on a heavy administrative responsibility and was involved in many university committees, but he managed to build up a small but strong group of mathematicians as well as to maintain his own research. This was in addition to the production of two undergraduate textbooks based on his teaching at both Glasgow and Keele: these widely used texts are entitled *Special Functions of Mathematical Physics and Chemistry* (Sneddon 1956) and *Elements of Partial Differential Equations* (Sneddon 1957).

After his 5 years at Keele, in 1956 Ian was invited to accept appointment as the newly established Simson Professor of Mathematics at the University of Glasgow, and he duly accepted and returned to Glasgow in 1957 where he remained until his retirement in 1985. In Glasgow Ian took on a heavy teaching load and introduced applied mathematics into the mathematics curriculum, which hitherto had been dominated by pure mathematics as applied

aspects of the subject were taught within the Department of Natural Philosophy. He had a long and distinguished career in Glasgow and played a major role in the life of the university, contributing substantially to many university committees, as well as serving as Head of the Department of Mathematics, Dean of the Faculty of Science, and member of the University Court (the University's governing body). He was elected as a Fellow of the Royal Society of Edinburgh (FRSE) in 1958 and awarded the Makdougall-Brisbane Prize of the RSE in the same year. He also served as a member of the Council of the RSE, including a total of 6 years as vice president.

In addition to his commitment to the University of Glasgow and the Royal Society of Edinburgh, Ian travelled extensively outside Scotland. In particular, he spent many periods in the USA, including as a Visiting Professor at North Carolina, Duke and Indiana Universities, and the State University of New York. He also had strong connections with Poland and was recognized there as a Foreign Member of the Polish Academy of Science (1968) and as a Commander of the Order of Polonia Restituta (1969). He was awarded the Copernicus Medal of Polish Academy of Sciences (1973) and received an Honorary Doctorate from Warsaw University (1973), while in 1979 he became a Commander of the Polish Order of Merit and, in the same year, was awarded the Eringen Medal of the Society of Engineering Science in the USA.

Ian devoted much time to service at the national level. For example, he spent various periods as a member of the Scientific Advisory Council of the Ministry of Defence and was Chairman of the Mathematics Committee of the then Science Research Council (SRC, now EPSRC) and as a member of the Universities Science and Technology Board. In recognition of this work, he was awarded the honour of an OBE (Order of the British Empire) in 1969.

In the UK his academic distinction was recognized by the conferring on him of honorary doctorates at Heriot-Watt University (1982), the University of Hull (1983), and the University of Strathclyde (1994). The finest accolade he received was his election as a Fellow of the Royal Society (FRS) in 1983 just 2 years prior to his retirement from the University of Glasgow.

Scientific Contributions

Ian's main contributions were to the application of integral transform methods in problems of the mechanics of solids, particularly mixed boundary value problems, with a focus on the linear theories of elastostatics, elastodynamics, and thermoelasticty. These are exemplified by contact and surface loading problems and crack problems highlighted in the books *Fourier Transforms* (Sneddon 1951); *Mixed Boundary Value Problems in Potential Theory* (Sneddon 1966); *Crack Problems in the Classical Theory of Elasticity* (Sneddon and Lowengrub 1969); *The Use of Integral Transforms* (Sneddon 1972), listed in chronological order of publication; as well as *The Linear Theory of Thermoelasticity* (Sneddon 1974), which was based on lectures given at the International Centre for Mechanical Sciences in Udine, Italy, and the set of notes *The Use of Operators of Fractional Integration in Applied Mathematics* (Sneddon 1979), published by the Polish Academy of Sciences.

He also published *An Introduction to the Mathematics of Medicine and Biology* (Defares and Sneddon 1960), presaging in 1960 what has become an important area of research in applied mathematics. In addition to his textbooks *Special Functions of Mathematical Physics and Chemistry* (Sneddon 1956) and *Elements of Partial Differential Equations* (Sneddon 1957) mentioned above, he published the textbook *Fourier Series* (Sneddon 1961).

Ian Sneddon's books have been widely influential in both research and undergraduate teaching and in total have attracted well over 10,000 citations in Google Scholar. Ian's research output has been prodigious, and many of his research papers have been groundbreaking and are highly cited: particular mention should be made of the papers *The relation between load and penetration in the axisymmetric Boussinesq problem for a punch of arbitrary profile* (Sneddon 1965),

On certain integrals of Lipschitz–Hankel type involving products of Bessel functions (Eason et al. 1955), and *The distribution of stress in the neighbourhood of a crack in an elastic solid* (Sneddon 1946), which, at the time of writing, have attracted, respectively, 3821, 2551, and 1454 citations, and these alone are indicative of his enormous influence.

Ian was an excellent advisor of PhD students, and 20 students graduated under his supervision, many of whom went on to become professors in various countries of the world, the most noted being A.J.M. Spencer, FRS, who was a professor at the University of Nottingham for many years.

Family and the Arts

In September 1943 Ian married Mary Campbell Macgregor, and Mary joined him in Cambridge until the move to Fort Halstead. Mary and Ian had three children, two sons and a daughter. In their home Ian and Mary offered warm and generous hospitality to many visitors, who remember such occasions with affection. Ian was renowned for the delightful fund of stories he recounted about famous mathematicians and scientists with whom he was acquainted.

Ian was an aficionado of the arts and in particular was heavily involved in the musical life of Scotland. He was a member of the Board of the Scottish National Orchestra, the Advisory Council of Scottish Opera, and was Chairman of the BBC Scottish Music Advisory Committee for several years. In addition, he was a member of the Board of the Citizens Theatre in Glasgow. Music also featured in his Polish connections during his many visits to Poland, and he was a strong supporter of the Scottish Polish Friendship Society.

Much more about Ian's life and work can be found in the excellent biographical memoir written by Professor Peter Chadwick, FRS (Chadwick 2002) for the Royal Society. His entry in the MacTutor History of Mathematics (O'Connor and Robertson 2003) is also a useful source of information, and, in particular, it contains links to obituaries in The Times and Scotsman newspapers and other links of interest.

Cross-References

- ▸ Dynamical Contact Problems of Fracture Mechanics
- ▸ Eringen, Ahmed Cemal
- ▸ Hill, Rodney
- ▸ Lee, Erastus Henry

References

Chadwick P (2002) Ian Naismith Sneddon, O.B.E. 8 December 1919 – 4 November 2000. Biograph Mem Fellows R Soc 48:417–437

Defares JG, Sneddon IN (1960) An introduction to the mathematics of medicine and biology. North Holland, Amsterdam

Eason G, Noble B, Sneddon IN (1955) On certain integrals of Lipschitz–Hankel type involving products of Bessel functions. Philos Trans R Soc Lond A 247:529–551

Mott NF, Sneddon IN (1948) Wave mechanics and its applications. Clarendon Press, Oxford

O'Connor JJ, Robertson EF (2003) Ian Naismith Sneddon. MacTutor history of mathematics. http://www-history.mcs.st-andrews.ac.uk/Biographies/Sneddon.html

Sneddon IN (1946) The distribution of stress in the neighbourhood of a crack in an elastic solid. Proc R Soc Lond A 187:229–260

Sneddon IN (1951) Fourier transforms. McGraw-Hill, New York

Sneddon IN (1956) Special functions of mathematical physics and chemistry. Oliver & Boyd, Edinburgh

Sneddon IN (1957) Elements of partial differential equations. McGraw-Hill, New York

Sneddon IN (1961) Fourier series. Routledge & Kegan Paul, London

Sneddon IN (1965) The relation between load and penetration in the axisymmetric Boussinesq problem for a punch of arbitrary profile. Int J Eng Sci 3:47–57

Sneddon IN (1966) Mixed boundary value problems in potential theory. North Holland, Amsterdam

Sneddon IN (1972) The use of integral transforms. McGraw-Hill, New York

Sneddon IN (1974) The linear theory of thermoelasticity. International Centre for Mechanical Sciences (CISM), Courses and Lectures no. 119. Springer, Vienna

Sneddon IN (1979) The use of operators of fractional integration in applied mathematics. Polish academy of sciences, applied mathematics series. Polish Scientific Editors, Warsaw/Poznan

Sneddon IN, Lowengrub M (1969) Crack problems in the classical theory of elasticity. Wiley, New York

SO(3)

▸ On Treatment of Finite Rotations in FEM Analyses of Irregular Shell Structures

Soft Body Impacts

▸ Soft Impact

Soft Impact

José Alfonso Artero-Guerrero, Jesús Pernas-Sánchez, David Varas, and Jorge López-Puente
Department of Continuum Mechanics and Structural Analysis, University Carlos III of Madrid, Madrid, Spain

Synonyms

Impact of soft projectiles; Low-strength projectile impact; Soft body impacts

Definition

Soft impact refers to high kinetic events in which a collision occurs between an object and a structure, being the mechanical properties of the first quite low compared with the later material. In a "soft impact event," the projectile is greatly deformed and even damaged during the interaction with the impacted structure, contrary to "rigid impact event" in which the projectile almost remains intact during the impact process. The typical examples of soft impacts are produced in the aerospace sector such as hail or ice impact, bird strike, and tire fragment impact.

Introduction

During its service life, structures can be subjected to a variety of loading cases. Restricted to dynamic loading, impact is one of the most concerning case due to its possible disastrous consequences. Impacts on structures can be produced by the accidental or the deliberate hit of an object into the structure that could be a civil infrastructure or transport structure. Regarding the differences between the material properties of projectile and structure, impacts can be divided in two main categories: rigid impacts and soft impacts. In the first, stiffness and strength of projectile are higher than the structure, and hence the damage is produced only in the structure, while the projectile almost remains unalterable. Soft impacts are those in which the mechanical properties of the projectile are significantly lower than the structure. In those both projectile and structure get deformed and damaged after the impact. If the properties of projectile and structure are similar, the case cannot be considered neither a rigid nor a soft impact event. Nevertheless the type of failures is similar to soft impactor cases, since damage occurred in both elements.

Concerning the relative velocity between projectile and structure, impacts can be divided in two categories: high velocity impact and low velocity. There are many definitions to clarify the border between these two categories, although it is commonly accepted that impacts above 40–50 m/s can be considered as high velocity impacts. The impact of a "rigid" projectile can be studied for low velocity impacts and high velocity impacts (González et al. 2011; Artero-Guerrero et al. 2015; López-Puente et al. 2002). However for soft impact, the study is only restricted to high velocity impacts since the low strength and stiffness of the material cannot affect importantly if the impact is at low velocity. The study of high velocity impact takes on particular importance in the aeronautic sector, and moreover, the impact of soft projectiles is not uncommon (Mines et al. 2007; Johnson et al. 2009). During certain maneuvers, such as takeoff and landing, the structural components can be hit by tire fragments; or during flight birds, hail or

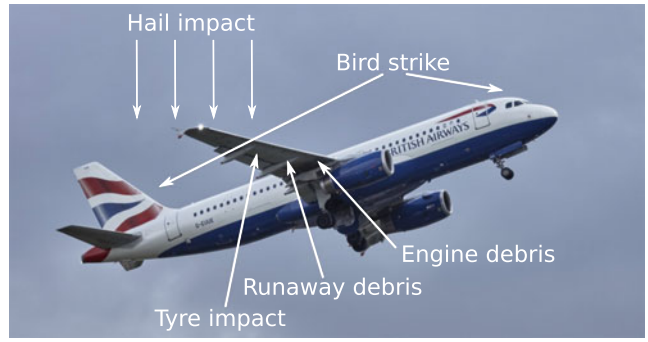

Fig. 1 Impact hazards in a commercial aircraft

ice can hit different parts of the aircraft as the fuselage, wings, stabilizers, radome, or nacelles. In Fig. 1 it can be seen the main impact hazards and the most probable impact location on an aircraft. Nevertheless, of all the different kinds of impacts, those involving hail and ice are the most dangerous due to their probability of occurrence as well as their potential consequences (Pernas-Sánchez et al. 2012). Other occasional debris could act as soft impactor such as foams in the case of the space shuttle accident (Melis et al. 2004; Fasanella et al. 2004; Carney et al. 2004) or other nonstructural parts but because of its low probability are less studied. The rain impact could be classified as a soft impact, considering the damage provoked by the repetitive impacts process (Abrate 2016).

Nowadays it has to be remarked that soft impactors have become even more important due to the use of composite material in aerospace structures. Composite materials are being used more and more in primary structures of aerospace structures because of its excellent specific properties which allow to achieve a reduction in the weight of the structure and hence a less fuel consumption. This main consequence has both economical and environmental advantages that have to be taken into account. Nevertheless it is well known the poor behavior of these types of materials when subjected to perpendicular dynamic loading (López-Puente et al. 2008). These types of impact could promote the delamination failure between each composite plies that could affect the bearing capacity of the structure and even the operability of the aircraft (Pernas-Sánchez et al. 2016a). So the soft impact event, mainly bird, ice, and tire fragment, on composite structures is certainly an area that worth the research. Therefore, vulnerability to impact has become an important issue from a regulatory perspective and aeronautical safety. Both the American and European regulatory certification requirements (FAR and JAR, respectively) include specific cases for preventing severe failure caused by an impact. This thread is also included by the European agency, literally from an EASA 2011 report "A critical safety issue for the design of primary aircraft structures is vulnerability and damage tolerance due to foreign object impact from bird strike, hail, tire rubber and metal fragments" (Toso and Johnson 2011), highlighting the impact threat as a key factor in the design of aircraft structures.

Bird strikes account for around 90% of all incident related to structural damage due to impact on aircraft (Meguid et al. 2008). Therefore the certification program gives a main importance to the bird impact resistance of aeronautical structures as radomes, wing leading edges, fuselage, tail wing, engines, or window frames. The cost and complexity of this test are very high; full-sized structures with real-like boundary condition should be tested raising the costs. Moreover, there exists an uncertainly in the behavior of the projectile due to the variability between bird species, and therefore it could promote different behaviors increasing the analysis complexity. Numerical methods are also very useful in these problems trying to reduce cost doing virtual testing campaign in which different designs are tried. A proper validation for the model with the experimental test is needed for the successful use of the numerical model. Also

the numerical model will help to understand the phenomena occurred in such a complex problem.

The threat of ice has become a subject of aircraft regulation for the aeronautical authorities (JAR-E 970), especially in aircraft with propellers or the ones with open rotor engines belonging to the new generation of aircraft used for medium-range routes (Pernas-Sánchez et al. 2012). Different studies, both experimentally and numerically, have analyzed the damage that this kind of impacts produces in aluminum (Chuzel 2009; Combescure et al. 2011) and CFRP structures (Kim et al. 2003; Johnson et al. 2006; Park and Kim 2010). It can be seen that in CFRP structures, these impacts are very concerned since delamination can be extended in all the structure(Pernas-Sánchez et al. 2016a). Researchers have also made an important effort in reproducing adequately its constitutive behavior since many different models can be found.

Regarding to tire fragment impact, these cases reached more importance after the accident of the supersonic Concorde aircraft in Paris (Authors 2000; Seddon et al. 2004). In that case, the impact of a tire fragment in the wings, where the fuel was allocated, generated some structural damage that added to the fire turned into the catastrophic failure of the aircraft. Moreover this accident ended with the era of the supersonic civil flights. The research effort has been focused also in the determination of constitutive models that reproduce adequately the force produced by the rubber in this impact and the damaged developed into the structure (Mines et al. 2007; Guégan et al. 2010; Neves et al. 2010).

Bird Strike

When a structure, in this case, an aerospace structure, is collided by one or more birds, the impact is known as bird strike. From the beginning of aeronautic history, bird strike has been a problem to concern; in fact it was already described by Wright brothers (MacKinnon 2004) in 1905, and the first fatal accident occurred in 1912 (Lewis 1995). Up to 2004, it has been reported 242 fatalities related to bird strike incidents (Stoll and Brockman 1997). Nevertheless there are many incident per year, some estimation reaches 30000 bird strike (ICAO, 2001, Proposed amendment to annex 14, unpublished), but the majority cause little or even no damage. This number can be increased due to the environmental awareness that has increased the bird population nowadays (Eschenfedler 2001). Moreover, the fact that airports are far away from cities and therefore closer to natural habitats of birds makes increase the possibility of bird strikes. The impacts are not restricted only to airports, because the possibility of finding a large flock of birds at high altitude is not negligible. In this case, the impact is even more dangerous since the aircraft velocity is higher. Some calculations provide a value of $USD 3 billion per year of economical losses for the aircraft companies (Short et al. 2000).

Bird Strike Experimental Tests

Due to the importance of the problem, both from a safety and economical point of view, bird strike tests have to be carried out to proof the viability of aircraft structure against this menace. Moreover, for certification purposes this impact is compulsory in certain aircraft components where the probability of bird strike is high (such as fuselage, windshield, or rotor blades). For example, Boeing 777 engines are required to produce at least 75% of full-rated thrust after the impact of four 1.125 kg birds (Lewis 1995). The structural parts are required to maintain its integrity once the impact has taken place. In order to perform the impact test, the bird has to be accelerated to the required velocity (50–200 m/s). Usually this is performed using a pneumatic launcher in which compressed air impels the projectile and accelerates it through the cannon barrel. To adapt the geometry of the bird to the inner diameter of the barrel, it is needed to use a sabot. The design requirement of this component is to maintain the bird integrity during the acceleration process so that the bird could completely impact the structure. In addition, the sabot should be light as well as be easily separated from the projectile once it exits the barrel, hence avoiding to alter the impact on the structural components. Due to the small time of the impact (milliseconds scale),

special instrumentation has to be used to register adequately the impact. High-speed cameras have to be used with an adequate frame rate (10–20 kfps), and dynamic sensors (usually piezoelectric) have to be used to register acceleration, forces, pressures, etc.

The literature regarding experimental bird strike against aerospace structure is scarce, because the majority of the research are centered on studying the impact on rigid plates to analyze the force produced and obtain data useful to validate its numerical models. Nevertheless it has to be remarked the work of Liu et al. (2017) in which a tail leading edge is impacted by a 3.6 kg bird. Experimental results are compared with numerical simulation obtaining a good correlation in terms of damage produced. Also in the work of Hu et al. (2016), experimental test is performed to analyze the impact resistance of a composite helicopter cockpit. A numerical simulation is used to improve the design of the cockpit. Aluminum plates impacted against bird are also analyzed in the work of Liu et al. (2014).

Certification tests require the use of real birds to perform the impact. Only the mass of the birds and the impact velocity are the variables defined in the certification program, varying for the different aircraft types. The variability of bird species or even between individuals from the same kind produces changes in the density and in the impactor geometry that could affect to the impact phenomenon and consequences. Therefore many companies use bird substitutes for the pre-certification tests in order to obtain more repeatable and confident results (Budgey 2000). The design of the bird substitute is focused on reproducing the pressure loading and not the biometric parameters of real birds. It has been tested different materials, such as meat, rubber, silicone, foam, wax, and emulsion, while the best results are obtained for gelatin (Wilbeck 1978; Nizampatnam 2007; Baughn and Graham 1988). Nevertheless it is important to follow the instructions for the gelatin preparation in order to achieve a correct pressure loading. Since the impactor geometry of the artificial bird is not defined, it has been done an intense work, both experimental and numerical, to determine the adequate one (McCallum and Constantinou 2005; Airoldi and Cacchione 2006; Zhu and Tong 2008). Typically, bird substitute has been simplified using cylinder, cylinder with hemispherical ends, ellipsoid, or even sphere. It can be concluded that best results are obtained with the use of cylinders with hemispherical ends. In these cases, the pressure pulse history predicted numerically correlated better with the experimental impacts performed. Apart from the shape of the substitute bird, it is necessary to determine the length/diameter ratio (L/D) of the impactor. Typically the better results are obtained with ($L/D = 2$). Recently, it has been tested more realistic artificial bird geometry, including the neck and even bones. In those tests, it can be seen that the impact of the neck, previously to the impact of the body, can prestress the structure and therefore modify the damage generated (McCallum and Constantinou 2005). Both experimental and numerical academic studies have appeared in recent years comparing the impact of real and substitute birds in different rigid targets (Allaeys et al. 2017) obtaining useful data that can be used in future research. Nevertheless, it is still needed more experimental test comparing real bird strike and artificial bird strike to define adequately the geometry of the bird substitute.

Numerical Modelling of Bird Strike

Due to the important cost, both on time and economical, that a bird strike carry, numerical modelling could be a useful tool to help study the impact on aircraft structures (Nizampatnam 2007). Usually an incremental step-by-step methodology is done for this purpose: testing experimentally one or two configurations of the bird strike into the structure, validate the numerical model, and then perform a virtual test campaign in which different impact conditions are studied and analyzed. Nowadays the confidence on numerical methods, and concretely finite element codes, has increased, and even it is discussed if the certification can be done using only numerical methods ("Certification by analysis"). However, the numerical model has to rely on material models that represent adequately the constitutive behavior of the

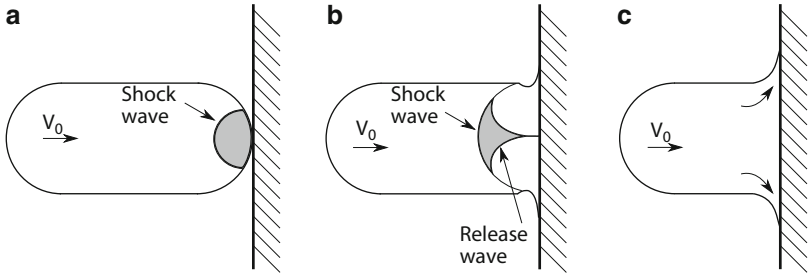

Fig. 2 Phases in a bird strike impact according to Wilbeck (1978). (**a**) Shock regime. (**b**) Release regime. (**c**) Steady flow regime

structure material and the bird material in such strain rate conditions.

Nevertheless, before the growth of the finite element codes, there were some more simplified models that predicted pressure contours of bird strike. Willbeck developed a theoretical model of the different stages that occur during an impact (Wilbeck 1978). The bird strike can be divided into three main stages: shock regime, release regime, and steady flow regime. These three stages can be seen in Fig. 2. During the first moment of the impact, a compressive shock wave is generated at the contact surface and transmitted through the projectile as the impact occurs. The pressure is very high and can be characterized by the Hugoniot relationship:

$$P_H = \rho_0 V_0 V_{\text{shock}} \tag{1}$$

where ρ_0 is the initial density, V_0 is the impact velocity, and V_{shock} is the velocity of the shock wave propagation. The model uses an empirical linear relation between the shock wave velocity and the impact velocity:

$$V_{\text{shock}} = c + kV_0 \tag{2}$$

where c is the sound velocity of the material and k the empirical constant. The second stage is the release regime in which a release pressure wave is generated in the projectile edges limiting the duration of the shock wave. The last stage is called steady flow regime. In this case the pressure and velocity can be considered constant during this phase. The pressure in the central axis of the projectile is called stagnation pressure, and it is obtained using the Bernoulli equation:

$$P_{\text{stg}} = \frac{1}{2}\rho_0 V_0^2 \tag{3}$$

As the point is far from the central axis, the pressure can be obtained using the following expression (Banks and Chandrasekhara 1963):

$$P(r) = P_{\text{stg}} \exp[-\frac{1}{2}\left(\frac{r}{a}\right)^2] \tag{4}$$

being r the distance from the impact point and a the radius of the projectile. During this phase it can be a radial expansion of the bird particles. In some cases, a phenomenon that can be considered also, is the force and therefore, possible damage on a structure, created by the subsequent impact of this mass diverted from the first impact. As it can be seen in Fig. 3, the characteristic curve shows the high pressure of the shock wave limited on time due to the release wave and the lasting of the steady flow pressure.

Since the use of finite element codes increases in the solid mechanics, bird strike has been a problem that has been tried to be solved using these codes. In order to rely on the model, it is crucial that material models reproduce accurately the behavior of the bird when subjected to impact. As it is known, birds are mostly composed of water, and in the range of the velocities at which the impact occurs, it can be considered that the bird behaves as a fluid. Therefore it is needed to determine the equation of state of the bird. Using the Hugoniot linear relation, Wilbeck (1978) obtained the following EOS:

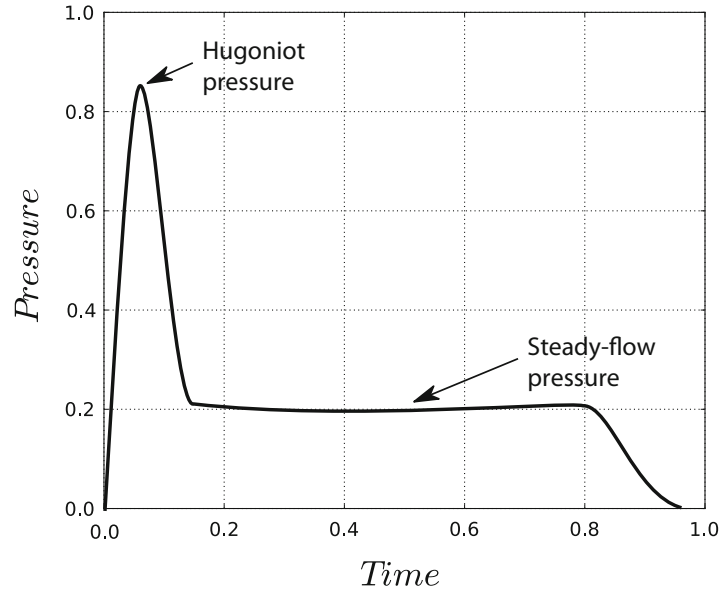

Fig. 3 Schematic representation of a pressure time history in a bird strike

$$P = \rho_0 c_0^2 \frac{\rho(\rho - \rho_0)}{((1-k)\rho + k\rho_0)^2} \tag{5}$$

Other EOS types as polynomial ones have been used showing that in the range of velocities considered for the bird strike ($V < 200$ m/s), the differences between the EOS are negligible. Usually the forces of bird strike impact on "rigid" structure are used to check the adequacy of the used EOS.

The bird strike problem is a highly nonlinear problem, and the numerical model has to be able to handle with large deformation, contact, and nonlinear behavior of materials. Therefore the most suitable codes correspond to those that are called "hydrocodes" based on explicit solvers. These solvers offer different discretization schemes that can be used: Lagrangian technique, Eulerian, Arbitrary Lagrangian Eulerian (ALE), or smooth particle hydrodynamics (SPH).

- Lagrangian technique. This approach is not appropriate in the cases in which it is expected large deformation of the impactor because it could lead to severe element distortion since the mesh is fixed to the material displacements. This problem could lead to some numerical instabilities (e.g., time integration instabilities) (Anghileri et al. 2005b; Pernas-Sánchez et al. 2012). Nevertheless there are several techniques that can handle this problem, as the element deletion (Stoll and Brockman 1997) or the use of a remeshing rule (Nizampatnam 2007). Element deletion helps to successfully terminates the simulation eroding from it the most deformed elements. However it causes inaccuracy due to the loss of momentum and energy that generates artificial oscillations in the contact force. Remeshing rules are based on modifying the mesh when deformations are high in order to alleviate them, but it increases importantly the computational cost associated with the simulation. There are several references that do not recommend the use of Lagrangian technique for bird strike (Georgiadis et al. 2008).
- Eulerian technique. Contrary to Lagrangian technique, in which the mesh is coupled with the material displacements, the Eulerian mesh is fixed to the space and the material flow across it. In the Eulerian technique, the solver first computes a Lagrangian step, then mesh moves back to the initial position, and the method introduces the material in its correct positions using an advection scheme. With this methodology element distortion is avoided, but computational cost increases

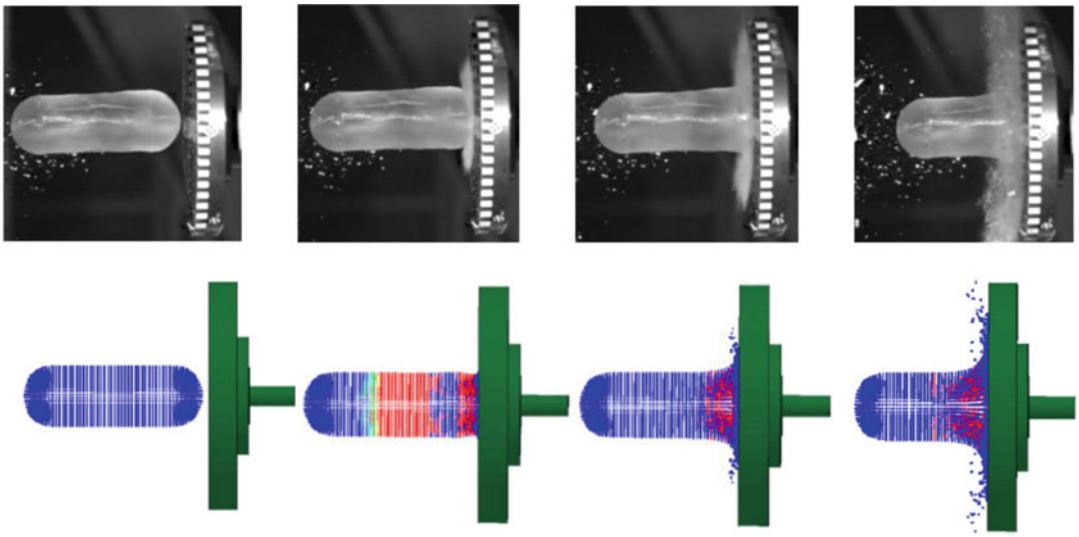

Fig. 4 Different time instants of a substitute bird impacting on a rigid plate in an experimental test and a numerical simulation using a SPH model

because of the advection step. In addition, boundaries are not well defined, and therefore a fine mesh has to be used. Eulerian technique can handle with accuracy high velocity fluid-structure interactions (FSI) (Varas et al. 2009, 2012; Artero-Guerrero et al. 2013, 2014) or fluid-like structure interaction as the bird strike.

- Arbitrary Lagrangian Eulerian technique. The ALE technique is a generalization of both previous ones, in such a way that the numerical mesh is not coupled to material deformation but has a particular velocity. There are several methods to define the movement of the mesh to be more efficient in avoiding severe element distortions (Hughes et al. 2013) and, consequently, better handle high deformations.
- Smooth particle hydrodynamics. The smooth particle hydrodynamics is a meshless method that discretizes the continuum into particles that interacts between them through a smoothing kernel definition. This method is suitable to model soft impact events since no mesh is presented, and therefore it could handle high deformations. This method was used previously giving good correlations with experimental results (Lacome 2004; Zammit et al. 2010; Anghileri et al. 2005a; Liu et al. 2008; Georgiadis et al. 2008; Wu et al. 2009; Salehi et al. 2010). In Fig. 4 it can be seen as an accurate modelling of the impact process of a bird substitute using the SPH model when comparing with the experimental results.

There is no clear conclusions about which is the best method in order to reproduce the problem; nevertheless the method has to handle appropriately the fluid-like behavior of the impactor during the impact in the most efficient way.

Ice Impact

Ice could impact against an aircraft during its flight. Due to the differences on the stiffness and strength between both materials, the impact can be considered as a soft impact. An example of this phenomenon is the hail impact that could be very dangerous when aircraft get into some hail storms. The size that could reach a hail (up to 50 mm) could be enough to create important damage on the structure. Not only hail impact has to be considered, because ice can grow in some parts of the aircraft and eventually it can flung from the component impacting into the structure. For example, nowadays the aerospace

industry is studying the possibility of introducing the open rotor engines in which several propellers are rotating at high velocity without a casing. It is known that this technology produces a decrease in the fuel consumption and therefore in CO2 emissions. However, in open rotor engines, ice can be accumulated in a propeller, and it can be released at very high velocity. That's why all the fuselage region near to the engine has to be ice impact resistant. In the space industry, also it has to be taken into consideration ice impacts since it can be accumulated also in fuel pipes and it can eventually hit the structure, in this case, at hypervelocity. Concerning other transport industries (car, naval, etc.) or oil and gas transportation industries, the ice impact could be an important threat to be studied. Nevertheless the range of velocities considered is much lower, and the impact cannot be considered as a soft impact. As it has been shown for bird impact, ice impact has been studied using experimental tests and also numerical models.

Ice Impact Experimental Tests

In order to perform ice impact tests, it is required the use of gas cannons that are able to accelerate the projectile at the impact velocity. The use of sabots is needed to adapt the geometry of the projectile to the inner diameter of the barrel. Moreover, in these cases, it has a second function which is to thermally insulate the ice in order to prevent the melting of the projectile. The brittle nature of the ice produces that frequently it can be broken during the acceleration because of the inertial forces or the vibrations experienced during it. The sabot has to help also to mitigate this undesirable effect because the ice has to reach the structure without losing its integrity. The manufacturing of ice projectile is also an aspect that has to be taken into consideration. Usually it is done following a two-step manufacturing process. In the first step, an ice block in which the air bubbles are concentrated in one side is manufactured; in the second step, the ice is melted into the desired shape by means of two pre-warmed metal blocks and a combination of gravity load and heat conduction. This melting process avoids to use any carving process which can produce cracks inside the ice projectile. It is worth to mention that the microstructure of the ice block obtained is columnar granular which is different from the hailstones formed in nature.

Concerning ice impact experimental test, there are several works in which ice is impacted against rigid plates to study the forces and pressures generated and others where the impact occurs against an aerospace structure in which also the damages produced in the structure are analyzed. Impact on rigid structures has been done using a "rigid" target supported in a system to measure the force, which could be a dynamic load cell or Hopkinson bars-based systems among others (Pernas-Sánchez et al. 2015; Pereira et al. 2006; Kim and Kedward 1999; Tippmann et al. 2013). In all the experimental results, it is shown that as the impact velocity raises, contact force increases as it can be seen in other soft impactors as birds. It has been detected also the effect of the different crystalline structure is negligible at high impact velocities. In the work of Pernas-Sánchez et al. (2015), it has been tested different ice sphere diameters, and it is concluded that the maximum contact force is only a function of the kinetic energy, and not the mass or velocity separately. Same trends have been observed in other works (Tippmann et al. 2013; Pereira et al. 2006; Kim and Kedward 1999). The aforementioned dependence on the projectile kinetic energy could be explained by attending to the ratio between the distortion energy density and the kinetic energy density. The first one (U_{dist}) is related to the energy needed to deform the material up to failure and in this case depends on the mechanical properties of the ice (which are very low). The second one (U_k) is the kinetic energy of the ice projectile per unit of mass. This ratio is very small:

$$\frac{U_{\text{dist}}}{U_k} = 10^{-3} \tag{6}$$

which means that the distortion energy density is negligible when compared to the kinetic energy density, and hence the impact is dominated by inertial effects. The impact process of a sphere into a rigid plate can be seen in Fig. 5. At the first instant of the impact, it can be seen a fragmentation front traveling into the ice sphere pro-

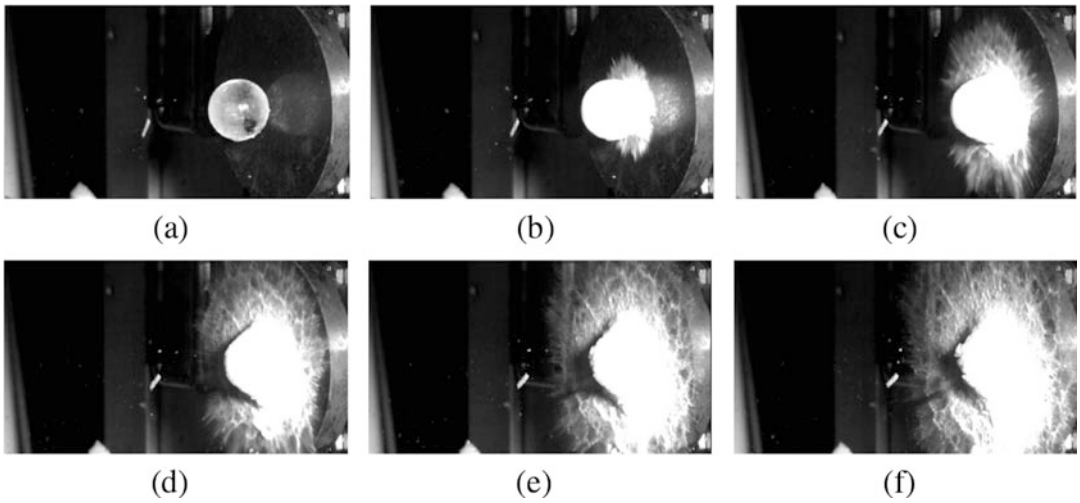

Fig. 5 Different instant point in an ice sphere impact on a rigid target (Pernas-Sánchez et al. 2015)

duced by the shock compressive wave produced in the impact and forming brittle cracks on the ice. It can be seen that the ice sphere becomes opaque after it. As the impact continues, the ice starts to deform radially which converts the ice into a set of small particles behaving as a fluid, similar to what happened on the bird strike. A phenomenon that can be considered also, as in the case of bird strike, is the force and, therefore, possible damage on a structure, created by the subsequent impact of the conglomeration of ice particles diverted from the first impact.

Ice projectile has been launched also against aerospace structural components to analyze the coupled response of the projectile and target. The behavior of the projectile does not differentiate to the one experienced on rigid target, exhibiting the brittle cracks and then the radial expansion. Different impactor geometries with different nose geometries have been used; nevertheless the sphere is the most used. It is shown that when an ice projectile with flat ends is launched normally, it produces the maximum deformations on aluminum plates (Anghileri et al. 2005c). This result can be predicted by the theory developed by Wilbeck (1978) for the impact of low strength projectiles. Ice impacts have been tested also into composite structure (Pernas-Sánchez et al. 2016a; Kim and Kedward 1999; Appleby-Thomas et al. 2011). As it is said before, one of the main drawbacks of composite materials is its poor impact performance, and therefore it is expected that ice impact consequence will be more catastrophic than on metal plates. Different composite plate thickness has been tested in the work of Pernas-Sánchez et al. (2016a). It has been observed that the main damage mode is composite delamination; however, fiber failure and debonding can be seen at higher kinetic energy. Contrary to solid projectile impact on composite plates where delamination increases gradually as the velocity increases before the penetration (Pernas-Sánchez et al. 2014), in ice impact delamination increases drastically from no damage to fully delamination in a small range of velocity. In cases where the composite laminates are thinner, penetration can be produced exhibiting a higher range of damages, as fiber failure or matrix cracking.

Experimental tests have been done also to characterize the ice behavior (Schulson 2001; Jones 1997; Fasanella and Boitnott 2006; Shazly et al. 2009). The majority of the tests have been carried out with $ice\ Ih$, the most common ice on earth. This kind of ice is formed when liquid water is cooled below 0 °C at ambient pressure. $Ice\ Ih$ possess a hexagonal crystal structure. Under low strain rate, it has been shown

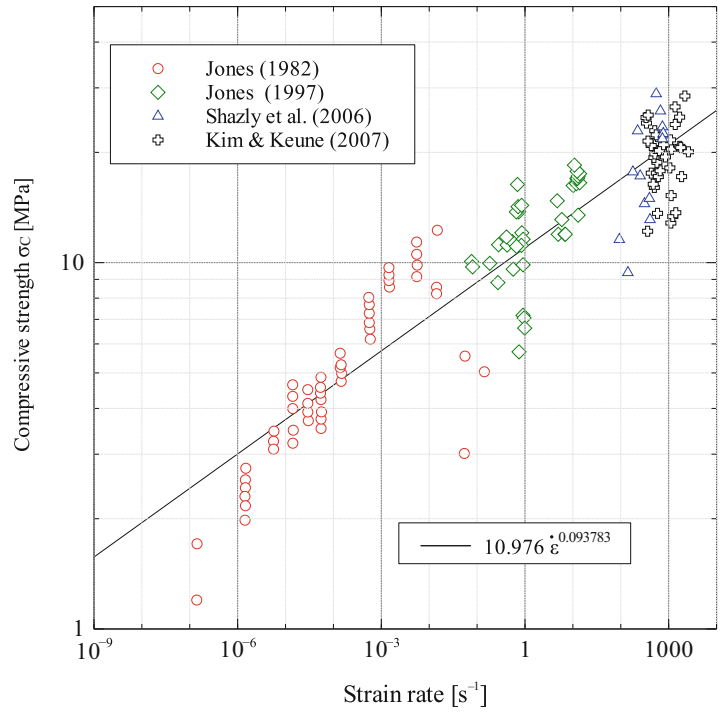

Fig. 6 Ice compressive strength as function of the strain rate (Pernas-Sánchez et al. 2012)

that the mechanical properties of ice depend on the condition of ice formation (single crystal, columnar or granular polycrystalline structure, presence of air bubbles, etc.). Young's modulus has been reported to be in the range of 9.7 to 11.2 GPa, and Poisson's ratio varies from 0.29 to 0.32. In tension, ice shows brittle behavior due to crack nucleation and cleavage. Tensile strength varies between 0.7 and 3.1 MPa and depends on the specimen volume, following a Weibull statistical distribution. On the other side, compression increases ductility and strength, like in other brittle materials, the mechanism usually hypothesized being intergranular friction. Compressive strength ranges between 5 and 25 MPa. This property is strongly affected by temperature as well, so experimental results are commonly provided for a given set of pre-defined temperatures (e.g., $-10\,^{\circ}\mathrm{C}$, $-20\,^{\circ}\mathrm{C}$, $-30\,^{\circ}\mathrm{C}$, $-40\,^{\circ}\mathrm{C}$). However, a change to brittle compressive failure appears at strain rates higher than 10^{-2} s^{-1}, that is, in the range of strain rates that could appear in a high velocity impact. Therefore it has to be analyzed the mechanical properties under these circumstances. It has been used high-speed universal testing machines ($\dot{\varepsilon} \sim 10\,s^{-1}$), drop-weight tower ($\dot{\varepsilon} \sim 10^2\,s^{-1}$), or split Hopkinson pressure bars ($\dot{\varepsilon} \sim 10^3\,s^{-1}$). In those tests it has been identified several common aspects: compressive strength increases with strain rates, and microstructure does not play an important role under high strain rates. In Fig. 6 it can be seen the relation between compressive strength and strain rate with data obtained in different works. Additionally, it has been reported that as the peak stress is reached in ice, the residual strength is not negligible during dynamic compression. All these tests have been used to characterize the mechanical behavior of ice.

Numerical Modelling of Ice Impact

Numerical modelling and specially FEM models of ice impact has been used to reproduce the consequences and damages on a structure, helping to understand the problem and also to design structures that could resist to this menace. The main effort on numerical modelling has been done on using an appropriate material model to reproduce

the behavior of ice under high velocity impacts and also in using the appropriate technique to reproduce the high deformation experienced on an ice impact.

Material models have been selected as function of the mechanical behavior observed on the characterization tests (Combescure et al. 2011; Tippmann et al. 2013; Carney et al. 2006; Anghileri et al. 2005c; Pernas-Sánchez et al. 2012). The first model appeared on the literature uses a Huber-Mises plastic flow model in combination with a failure criteria based on maximum plastic strain and hydrostatic stress. Once the onset of failure occurs, only hydrostatic pressure can be carried. Nevertheless this model does not take into account the pressure and strain rate dependence of material. These dependencies are firstly taken into account by Carney et al. (2006) who propose a modelling in which also various failure modes are considered: maximum plastic strain and pressure cutoff in compression and in tension. Drucker-Prager yield function has been used also to reproduce ice behavior (Pernas-Sánchez et al. 2012). In this work, also the strain rate dependence has been taken into consideration and the residual strength after the onset of failure. A power law strain rate sensitivity has been proposed. The model uses a nonassociated plastic flow rule in order to do not overestimate the volumetric part of the plastic strain. Finally the failures are defined by a compressive cutoff and a tensile cutoff. After the failure only compressive hydrostatic stress can be carried.

Ice material also exhibits high deformation during the impact process, and therefore it is required the use of an adequate technique to tackle this problem. Solutions are very similar to the ones used for bird strike impact: the use of a Lagrangian technique in combination with an appropriate erosion model, the Eulerian technique, the ALE, or the SPH meshless method. In the work of Pernas-Sánchez et al. (2012), there is an interesting comparison between these different methods. Although the Lagrangian technique is not able to reproduce the fluid-like behavior of the ice after the fracture process, in terms of pressure/load and computational cost, the Lagrangian technique is the most adequate. The previous

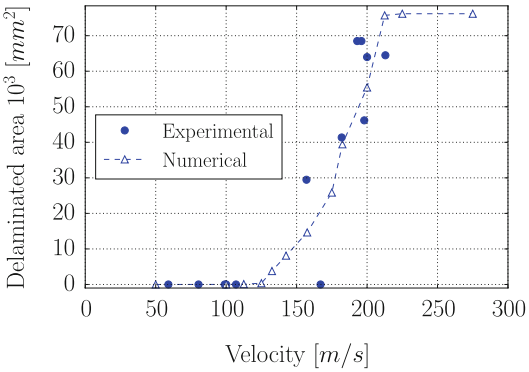

Fig. 7 Experimental and numerical delaminated area obtained in an ice sphere impact

model can be used also to analyze the damage of composite plates when subjected to high velocity ice sphere impact. It can be seen in Fig. 7 that the numerical model is able to reproduce accurately the delamination area generated in a plate in a velocity range from 50 to 275 m/s.

Tire Fragment Impact

The tire fragment impact has received less attention than the other two previous cases by the aeronautic industry. Nevertheless, since the accident of Concorde in Paris in the year 2000, some research has been done to analyze this problem. In this accident, a metal piece that was in the runaway produced the Concord tire explosion during the takeoff maneuver. Some tire fragments impacted into the aircraft wing where the fuel tanks are allocated. A high pressure wave was produced into the fuel tank that generated important damages on the structure leading to the catastrophic failure of the aircraft. One hundred and thirteen people were dead on the accident causing the end of the supersonic civil flights.

In this case of impact where the difference in stiffness between the impactor and the structure is high, as in the other soft impacts, an important part of the initial kinetic energy is wasted in the deformation of the projectile (Karagiozova and Mines 2007). In the case of the tire fragment, it is

not observed a massive fragmentation process as it can be seen in the ice or bird impact. Nevertheless the complexity of the process of tire impact (large deformation, nonlinear behavior, contact problems, inertial effects) means that experimental methods are needed both in terms of the mechanical characterization of materials in impact conditions and to validate the constitutive and simulation models developed.

Tire Impact Experimental Tests

In order to reproduce the experimental test of a tire fragment impact, it is required the use of an experimental setup similar to the one explained in the previous cases. The tire fragment has to be inserted in a sabot that is accelerated in a gas gun. As it has been said previously, the tire fragment impact is a problem less studied than other soft impact due to its low probability of occurrence. There are only very few experimental tests in which a tire fragment impact test is carried out (Mines et al. 2007; Guégan et al. 2010). It has to be remarked the work of Mines et al. (2007) in which it is analyzed cubic and parallelepiped tire fragment launched at different speeds (75–135 m/s) and angles (0°, 30°, 60°, and 90°) against aluminum plates. The results show that the high velocity normal impacts induce the higher deformations. However, the low velocity impact at an oblique angle produce important bending of the projectile, and a second impact can occur in the aircraft, producing even more damages in the structures than the high-speed case (Guégan et al. 2010).

In combination to the tire impact test, it has been carried out experimental tests to characterize the tire fragment material. Aircraft tires are designed to withstand high loads during short periods and to guarantee stability in adverse conditions such as high pressure gradients due to crosswinds, hydroplaning, as well as high temperatures and brake friction. To guarantee this, aircraft tires are made of a rubber matrix, usually natural rubber, with fabric reinforcements which tend to be nylon. It has been performed uniaxial quasistatic test both in tension and compression that have been useful to demonstrate the nonlinear behavior of tire rubber which experiences high deformation before failure (Mines et al. 2007). The presence of nylon fabric is responsible for the anisotropic behavior of the material. Moreover it is required dynamic experimental tests to fully characterize tire material under impact conditions. Drop-weight tower and gas gun test have been used to perform dynamic compression on the material (Mines et al. 2007). It has been concluded that the material has not shown a significant strain rate sensibility, despite contact force are higher on high velocity impact due to inertial effects.

Numerical Modelling of Tire Impact

As it was said previously, tire material is complex because it contains rubber and nylon fragment reinforcement. Therefore the material has to take into account the anisotropy and the nonlinear behavior. Characterization tests explained previously have been used to correlate the material models. The majority of the models used for the rubber are based on hyperelastic material model in which large deformations takes place without plastic deformations or any dissipation mechanisms (Treloar 1975; Ogden 1998; Johnson et al. 2009). In the case of incompressible material model, the constitutive model can be expressed on a strain energy function expressed through a power function of the principal stresses. If the material is compressible, the strain energy function can be expressed in terms of the porosity. In order to model the nylon reinforcement, one common technique is the introduction of one-dimensional bar element (Watanabe and Kaldjian 1985; Reese et al. 2001). The nodes of these elements are linked to those on the matrix, fulfilling the compatibility conditions.

There are very few simulations in which the impact of a tire fragment has been taken into consideration. In the work of Johnson et al. (2009), it has been analyzed the impacts of tire fragments on composite panels. The numerical results show that the composite failure is mainly delamination, while an important part of the kinetic energy of the impact is absorbed by the projectile deformation. In any case, the problem of impact caused by tire fragment is still an open field of research

both from the experimental and numerical point of view.

Other Soft Impacts

Soft impact event can referred also to the high velocity collision of water or another liquid against a structure (Abrate 2016). The most studied example is the impact of rain into aerospace structures. Certainly the erosion that can provoke the rain in the leading edges of turbine blades made of composite material is an issue that has to be taken into consideration. There are several works in which this problem has been investigated in composites aerospace structures (Matthewson and Gorham 1981; Hancox 1973). Another occasional debris that could act as soft impactor is the case of nonstructural parts that could detach and collide to the structure. An example of this was the Columbia space shuttle accident where the impact of foam generates some damage that has important consequences in the final accident of the structure (Melis et al. 2004; Fasanella et al. 2004; Carney et al. 2004). Nevertheless these cases are less studied because of their low probability of occurrence.

Finally, another impact that can be taken into consideration is the impact of composite debris against composites structures. This phenomenon raises its importance since the possible use of open rotor engines. In this case the engine has composite blades that are not enclosed by a casing, and one of them it could detach impacting to the surrounding structure. As it was said previously in these cases, the stiffness of the projectile and impacted structure is similar, and therefore it cannot be considered neither a soft nor a "rigid" impact event. Nevertheless it can be seen in the work of Mata-Díaz et al. (2017) that the behavior of a composite fragment when impacted to a rigid plate presents several similarities with a soft impact (highly deformation on the projectile, massive fragmentation process, etc.). Certainly this is a case in which it has to be done for further research.

Cross-References

▸ Numerical Methods and Modeling in Impulsive Dynamics

References

Abrate S (2016) Soft impacts on aerospace structures. Prog Aerosp Sci 81:1–17. Dynamic loading aspects of composite materials

Airoldi A, Cacchione B (2006) Modelling of impact forces and pressures in lagrangian bird strike analyses. Int J Impact Eng 32:1651–1677

Allaeys F, Luyckx G, Paepegem WV, Degrieck J (2017) Characterization of real and substitute birds through experimental and numerical analysis of momentum, average impact force and residual energy in bird strike on three rigid targets: a flat plate, a wedge and a splitter. Int J Impact Eng 99(Supplement C):1–13

Anghileri M, Castelletti L, Invernizzi F, Mascheroni M (2005a) Birdstrike onto the composite intake of a turbofan engine. In: 5th European LS-DYNA user's conference, Birmingham

Anghileri M, Castelletti L, Tirelli M (2005b) Fluid-structure interaction of water filled tanks during the impact with the ground. Int J Impact Eng 31(3): 235–254

Anghileri M, Invernizzi F, Mascheroni M (2005c) A survey of numerical models for hail impact analysis using explicit finite element codes. Int J Impact Eng 31:929–944

Appleby-Thomas GJ, Hazell PJ, Dahini G (2011) On the response of two commercially-important CFRP structures to multiple ice impacts. Compos Struct 93(10):2619–2627

Artero-Guerrero J, Pernas-Sánchez J, Varas D, López-Puente J (2013) Numerical analysis of CFRP fluid-filled tubes subjected to high-velocity impact. Compos Struct 96:286–297

Artero-Guerrero J, Pernas-Sánchez J, López-Puente J, Varas D (2014) On the influence of filling level in CFRP aircraft fuel tank subjected to high velocity impacts. Compos Struct 107:570–577

Artero-Guerrero J, Pernas-Sánchez J, López-Puente J, Varas D (2015) Experimental study of the impactor mass effect on the low velocity impact of carbon/epoxy woven laminates. Compos Struct 133(Supplement C):774–781

Authors V (2000) Accident on 25 July 2000 at la patte d'oie in gonesse to the concorde registered f-btsc by air France. Ministere de l'Équipement des transports et du logement Buereau d'enquetes et d'analyses pour la secourite de l'aviation civile

Banks R, Chandrasekhara D (1963) Experimental investigation of the penetration of a high-velocity gas jet through a liquid surface. J Fluid Mech 15:13–34

Baughn T, Graham L (1988) Simulation of a bird-strike impact on aircraft canopy material. J Aircr 25: 659–664

Budgey R (2000) The development of a substitute artificial bird by the international birdstrike research group for use in aircraft component testing. In: International bird strike committee ISBC25/WP-IE3, Amsterdam

Carney K, Melis M, Fasanella E, Lyle K, Gabrys J (2004) Material modeling of space shuttle leading edge and external tank materials for use in the Columbia accident investigation. NASA Report 20040070935

Carney K, Benson D, Dubois P, Lee R (2006) A phenomenological high strain rate model with failure for ice. Int J Solids Struct 43:7820–7839

Chuzel Y (2009) Caractérisation expérimentale et simulation numérique d'impacts de glace a haute vitesse. PhD thesis, INSA, Lyon

Combescure A, Chuzel-Marmot Y, Fabis J (2011) Experimental study of high-velocity impact and fracture of ice. Int J Solids Struct 48(20):2779–2790

Eschenfedler P (2001) Wildlife hazards to aviation. In: ICAO/ACI airports conference, Miami

Fasanella E, Boitnott R (2006) Dynamic crush characterization of ice. Technical report, NASA

Fasanella E, Lyle K, Gabrys J, Melis M, Carney K (2004) Test and analysis correlation of form impact onto space shuttle wing leading edge RCC panel 8. NASA Report 20040075041

Georgiadis S, Gunnion A, Thomson R, Cartwright B (2008) Bird-strike simulation for certification of the Boeing 787 composite moveable trailing edge. Compos Struct 86:258–268

González E, Maimí P, Camanho P, Lopes C, Blanco N (2011) Effects of ply clustering in laminated composite plates under low-velocity impact loading. Compos Sci Technol 71(6):805–817

Guégan P, Othman R, LeBreton D, Pasco F, Swiergiel N, Thevenet P (2010) Experimental investigation of rubber ball impacts on aluminium plates. Int J Crashworthiness 15:391–399

Hancox N (1973) The erosion of carbon fibre reinforced plastic by repeated liquid impact. Wear 23(1):71–81

Hu D, Song B, Wang D, Chen Z (2016) Experiment and numerical simulation of a full-scale helicopter composite cockpit structure subject to a bird strike. Compos Struct 149(Supplement C):385–397

Hughes K, Vignjevic R, Campbell J, Vuyst TD, Djordjevic N, Papagiannis L (2013) From aerospace to offshore: bridging the numerical simulation gaps-simulation advancements for fluid structure interaction problems. Int J Impact Eng 61:48–63

Johnson A, Holzapfel M, Kraft H, Reiter A (2006) Measurement of ice mechanical properties. Technical report IB 435 2006/55, DLR

Johnson A, Toso-Pentecôte N, Schwinn D (2009) Modelling damage in composite aircraft panels under tyre rubber impact. In: Proceeding of 17th international conference on composite materials

Jones S (1997) High strain-rate compression tests on ice. J Phys Chem B 101:6099–6101

Karagiozova D, Mines R (2007) Impact of aircraft rubber tyre fragments on aluminium alloy plates: II – numerical simulation using LS-DYNA. Int J Impact Eng 34:647–667

Kim H, Kedward K (1999) Experimental and numerical analysis correlation of hail ice impacting composite structures. Compos Struct 68:1–11

Kim H, Welch D, Kedward K (2003) Experimental investigation of high velocity ice impacts on woven carbon/epoxy composite panels. Compos Part A Appl Sci Manuf 34:25–41

Lacome J (2004) Smoothed particle hydrodynamics method in LS-DYNA. In: 3rd German LS-DYNA forum, Bamberg

Lewis C (1995) Engine bird ingestion. Airliner 1:17–19

Liu J, Li Y, Xu F (2008) The numerical simulation of a bird-impact on an aircraft windshield by using the SPH method. Adv Mater Res 33–37:851–856

Liu J, Li Y, Gao X (2014) Bird strike on a flat plate: experiments and numerical simulations. Int J Impact Eng 70(Supplement C):21–37

Liu J, Li Y, Yu X, Tang Z, Gao X, Lv J, Zhang Z (2017) A novel design for reinforcing the aircraft tail leading edge structure against bird strike. Int J Impact Eng 105(Supplement C):89–101. Design and analysis of protective structures 2015

López-Puente J, Zaera R, Navarro C (2002) The effect of low temperatures on the intermediate and high velocity impact response of CFRPs. Compos Part B Eng 33:559–566

López-Puente J, Zaera R, Navarro C (2008) Experimental and numerical analysis of normal and oblique ballistic impacts on thin carbon/epoxy woven laminates. Compos Part A Appl Sci Manuf 39:374–387

MacKinnon B (2004) Sharing the skies: an aviation industry guide to the management of wildlife hazards. Civil Aviation, Transport Canada

Mata-Díaz A, López-Puente J, Varas D, Pernas-Sánchez J, Artero-Guerrero J (2017) Experimental analysis of high velocity impacts of composite fragments. Int J Impact Eng 103(Supplement C):231–240

Matthewson MJ, Gorham DA (1981) An investigation of the liquid impact properties of a gfrp radome material. J Mater Sci 16(6):1616–1626

McCallum S, Constantinou C (2005) The influence of bird-shape in bird-strike analysis. In: 5th European LS-DYNA users conference, Birmingham

Meguid S, Mao R, Ng T (2008) FE analysis of geometry effects of an artificial bird striking an aeroengine fan blade. Int J Impact Eng 35:487–498

Melis M, Carney K, Gabrys J, Fasanella E, Lyle K (2004) A summary of the space shuttle Columbia tragedy and the use of ls dyna in the accident investigation and return to flight efforts. NASA Report 20040075041

Mines R, McKown S, Birch R (2007) Impact of aircraft rubber tyre fragments on aluminium alloy plates: I-experimental. Int J Impact Eng 34:627–646

Neves R, Micheli G, Alves M (2010) An experimental and numerical investigation on tyre impact. Int J Impact Eng 37:685–693

Nizampatnam L (2007) Models and methods for bird strike load predictions. PhD thesis, Wichita State University
Ogden R (1998) Nonlinear elastic deformations. Dover Publication Inc. Mineola, New York, USA
Park H, Kim H (2010) Damage resistance of single lap adhesive composite joints by transverse ice impact. Int J Impact Eng 37:177–184
Pereira J, Padula S, Revilock D, Melis M (2006) Forces generated by high velocity impact of ice on a rigid structure. Technical report TM-2066-214263, NASA
Pernas-Sánchez J, Pedroche D, Varas D, López-Puente J, Zaera R (2012) Numerical modeling of ice behavior under high velocity impacts. Int J Solids Struct 49(14):1919–1927
Pernas-Sánchez J, Artero-Guerrero JA, Varas D, López-Puente J (2014) Experimental analysis of normal and oblique high velocity impacts on carbon/epoxy tape laminates. Compos Part A Appl Sci Manuf 60(Supplement C):24–31
Pernas-Sánchez J, Artero-Guerrero JA, Varas D, López-Puente J (2015) Analysis of ice impact process at high velocity. Exp Mech 55(9):1669–1679
Pernas-Sánchez J, Artero-Guerrero J, Varas D, López-Puente J (2016a) Experimental analysis of ice sphere impacts on unidirectional carbon/epoxy laminates. Int J Impact Eng 96(Supplement C):1–10
Reese S, Raible T, Wriggers P (2001) Finite element modelling of orthotropic material behaviour in pneumatic members. Int J Solids Struct 38:9525–9544
Salehi H, Ziaei-Rad S, Vaziri-Zanjani M (2010) Bird impact effects on different types of aircraft bubble windows using numerical and experimental methods. Int J Crashworthiness 15:93–106
Schulson E (2001) Brittle failure of ice. Eng Fract Mech 68:1839–1887
Seddon CM, Moodie K, Thyer AM, Moatamedi M (2004) Preliminary analysis of fuel tank impact. Int J Crashworthiness 9(3):237–244
Shazly M, Prakash V, Lerch B (2009) High strain-rate behavior of ice under uniaxial compression. Int J Solids Struct 46:1499–1515
Short J, Kelley M, Speelman R, McCarty R (2000) Birdstrike prevention: applying aeroscience and bioscience. In: International bird strike committee, IBSC25/WP-RS4, Amsterdam
Stoll F, Brockman R (1997) Finite element simulation of high-speed soft-body impacts. In: Proceedings of the 38th AIAA/ASME/ASCE/AHS/ASC structures, structural dynamics & materials conference, Kissimmee, pp 334–344
Tippmann J, Kim H, Rhymer J (2013) Experimentally validated strain rate dependent material model for spherical ice impact simulation. Int J Impact Eng 57:43–54
Toso N, Johnson A (2011) LIBCOS-load upon impact behaviour of composite structure research project EASA.2009/3. Technical report, European Aviation Safety Agency
Treloar L (1975) The physics of rubber elasticity. Oxford Clarendon Press, Oxford, UK
Varas D, Zaera R, López-Puente J (2009) Numerical modelling of the hydrodynamic ram phenomenon. Int J Impact Eng 36(3):363–374
Varas D, Zaera R, López-Puente J (2012) Numerical modelling of partially filled aircraft fuel tanks submitted to Hydrodynamic Ram. Aerosp Sci Technol 16(1):19–28
Watanabe Y, Kaldjian M (1985) Modelling and analysis of bias-ply motorcycle tires. Math Model 6:80
Wilbeck J (1978) Impact behavior of low strength projectiles. Technical report AFML-TR-77-134, Air Force Materials Laboratory
Wu L, Guo Y, Li Y (2009) Bird strike simulation on sandwich composite structure of aircraft radome. Explosion Shock Waves 29:642–647
Zammit A, Kim M, Bayandor J (2010) Bird-strike damage tolerance analysis of composite turbofan engines. In: ICAS 2010, 27th international congress of the aeronautical sciences, Nice
Zhu S, Tong M (2008) Study on bird shape sensitivity to dynamic response of bird strike on aircraft windshield. J Nanjing Univ Aeron Astronaut 40:551–555

Softening

▸ Damage in Soft Biological Tissues

Softening and Fracture of the Arterial Wall

▸ Damage and Failure of the Vascular Wall

Solid Particles; Discrete Elements, Distinct Elements

▸ Discrete Element and Particle Methods

Solitons

▸ Nonlinear Waves in Continuous Media

Solution Techniques

▸ Nonlinear Computations

Spline Finite Element Methods

▸ Isogeometric Finite Element Analysis

Stability

▸ Static and Dynamic Bifurcations

Stability Behavior of Composite Plates and Shells

▸ Buckling and Postbuckling of Composite Plates and Shells

Stability Limit

▸ Analytical Stability Considerations in Lightweight Design

Stability of Structures

▸ Numerical Treatment of Stability Problems in Lightweight Design

State Space Formulation

▸ Principles of Material Modeling

Static and Dynamic Bifurcations

Alois Steindl
Institute for Mechanics and Mechatronics,
TU Wien, Vienna, Austria

Synonyms

Center manifold; Hopf bifurcation; Normal form; Singularity; Stability

Definition

Steady solutions of differential equations may lose their stability under parameter variations, and new solution types, e.g., periodic solutions, may emerge. To explore the dynamics close to the loss of stability, the originally high-dimensional system is reduced to a low-dimensional set of bifurcation equations by *center manifold theory*. The reduced system can be simplified further by *normal form theory*. These methods are demonstrated for the *Hopf bifurcation*, when a pair of complex eigenvalues crosses the imaginary axis and a family of periodic solutions branches off from the static equilibrium.

Introduction

We consider systems of ordinary differential equations (ODEs)

$$\dot{\boldsymbol{x}} = \boldsymbol{f}(t, \boldsymbol{x}; \boldsymbol{\lambda}), \tag{1}$$

where $\boldsymbol{x}(t) \in \mathbf{R}^n$ denotes the state vector, the time t is the independent variable, and $\boldsymbol{\lambda} \in \mathbf{R}^m$ contains the parameters. The right-hand side $\boldsymbol{f}(t, \boldsymbol{x}; \boldsymbol{\lambda})$ depends smoothly on its arguments.

In section "Lyapunov Stability", conditions for the stability of equilibria and periodic solutions of system (1) are given. If some parameter λ is varied, the equilibrium or periodic solution might become unstable at a critical value λ_c, and

new families of solutions could bifurcate from the original one. In order to study the behavior of the system close to the loss of stability, the influence of the noncritical variables on the system dynamics has to be taken care of by the application of center manifold theory, which allows to reduce the originally large system to a usually quite small system for the critical variables, as will be explained in section "Center Manifolds for Equilibria".

Using normal form theory, the reduced system can be simplified further and the unfolding of the critical equations can be derived, which allows to study the system dynamics in a small neighborhood of the critical parameter value λ_c.

Lyapunov Stability

Let $\boldsymbol{x}_0(t)$ be a solution of system (1) on the interval $t \in [0, \infty)$ for a fixed vector of parameter values $\boldsymbol{\lambda}$.

Definition 1 (Stability in the sense of Lyapunov) The solution $\boldsymbol{x}_0(t)$ is stable in the sense of Lyapunov, if for any $\varepsilon > 0$ there exists some $\delta > 0$, such that for all initial values $\boldsymbol{x}_1$ with $\|\boldsymbol{x}_1 - \boldsymbol{x}_0(0)\| < \delta$, the solution $\boldsymbol{x}(t)$ with $\boldsymbol{x}(0) = \boldsymbol{x}_1$ satisfies $\|\boldsymbol{x}(t) - \boldsymbol{x}_0(t)\| < \varepsilon$ for all $t > 0$.

If in addition $\lim_{t\to\infty} \|\boldsymbol{x}(t) - \boldsymbol{x}_0(t)\| = 0$, the solution $\boldsymbol{x}_0(t)$ is asymptotically stable.

This definition applies to all possible solutions of system (1), and it is in most cases impossible to give an analytical proof for arbitrary solutions. However, for equilibria and periodic solutions of autonomous or time-periodic systems, the establishment of stability is simple:

Let $\boldsymbol{x}_0$ be a steady solution of the autonomous ODE

$$\dot{\boldsymbol{x}} = \boldsymbol{f}(\boldsymbol{x}; \boldsymbol{\lambda}), \tag{2}$$

that is $\boldsymbol{f}(\boldsymbol{x}_0; \boldsymbol{\lambda}) = \boldsymbol{0}$, then the neighboring solutions are governed by the linearized ODE

$$\dot{\boldsymbol{y}} = \mathbf{A}(\boldsymbol{\lambda})\boldsymbol{y} \qquad \text{with } \mathbf{A}(\boldsymbol{\lambda}) = \left.\frac{\partial \boldsymbol{f}(\boldsymbol{x}; \boldsymbol{\lambda})}{\partial \boldsymbol{x}}\right|_{\boldsymbol{x}_0}, \tag{3}$$

and the eigenvalues σ_i of the Jacobian $\mathbf{A}(\boldsymbol{\lambda})$ determine the stability of $\boldsymbol{x}_0$ (Hartman 2002):

1. If $\Re(\sigma_i) < 0$ for all $i = 1, \ldots, n$, $\boldsymbol{x}_0$ is asymptotically stable.
2. If $\Re(\sigma_i) > 0$ for any $i \in \{1, \ldots, n\}$, $\boldsymbol{x}_0$ is unstable.
3. If $\Re(\sigma_i) = 0$ for some indices i and $\Re(\sigma_i) < 0$ for the remaining ones, the nonlinear terms of $\boldsymbol{f}(\boldsymbol{x}, \boldsymbol{\lambda})$ are needed to decide on stability.

   This situation is called the "critical case," and the corresponding values of $\boldsymbol{\lambda}$ are the "critical parameter values" $\boldsymbol{\lambda}_c$, which form the stability boundary in parameter space.

Similar results hold for periodic solutions: Let $\boldsymbol{x}_0(t)$ be a T-periodic solution of the T-periodic system (1) with $\boldsymbol{f}(t + T, \boldsymbol{x}; \boldsymbol{\lambda}) \equiv \boldsymbol{f}(t, \boldsymbol{x}; \boldsymbol{\lambda})$ for some period $T > 0$. Then also the Jacobian

$$\mathbf{A}(t; \boldsymbol{\lambda}) = \left.\frac{\partial \boldsymbol{f}(t, \boldsymbol{x}; \boldsymbol{\lambda})}{\partial \boldsymbol{x}}\right|_{\boldsymbol{x}_0(t)}$$

has period T in t and the eigenvalues μ_i (frequently called "Floquet multipliers") of the fundamental solution matrix (or "Floquet matrix") $\mathbf{Y}(T)$, which is obtained by solving the matrix valued initial value problem

$$\dot{\mathbf{Y}}(t) = \mathbf{A}(t; \boldsymbol{\lambda})\mathbf{Y}, \qquad \mathbf{Y}(0) = \mathbf{E}_n, \tag{4}$$

where $\mathbf{E}_n$ denotes the $n \times n$ unit matrix, determine the stability of $\boldsymbol{x}_0(t)$:

1. If $|\mu_i| < 1$ for all $i \in \{1, \ldots, n\}$, the periodic solution $\boldsymbol{x}_0(t)$ is asymptotically stable.
2. If $|\mu_i| > 1$ for any $i \in \{1, \ldots, n\}$, $\boldsymbol{x}_0(t)$ is unstable.
3. If $|\mu_i| = 1$ for some i and $|\mu_i| < 1$ for the remaining ones, again nonlinear terms are needed to decide on stability.

A similar situation occurs, if the T-periodic function $\boldsymbol{x}_0(t)$ is a solution of the autonomous system (2). Since in this case the phase of the solution is not determined by the explicit time dependence of $\boldsymbol{f}(t, \boldsymbol{x}; \boldsymbol{\lambda})$, any time-shifted solution $\boldsymbol{x}_0(t - t_1)$ is again a solution of (2) with period T. To

overcome this problem, one either introduces a Poincaré section or neglects the Floquet multiplier 1 related to the periodic eigenfunction $\boldsymbol{v}(t) = \dot{\boldsymbol{x}}_0(t)$. For the remaining multipliers, the same statements as above apply.

A powerful method to establish stability of a fixed point $\boldsymbol{x}_0$ is Lyapunov's direct method (Chicone 2006): Assume that there exists some scalar function $V(\boldsymbol{x})$ satisfying $V(\boldsymbol{x}_0) = 0$ and $V(\boldsymbol{x}) > 0$ for $\boldsymbol{x} \neq \boldsymbol{x}_0$. If

$$\dot{V}(\boldsymbol{x}) = \frac{\partial V}{\partial \boldsymbol{x}} \boldsymbol{f}(\boldsymbol{x}, \boldsymbol{\lambda}) < 0 \quad \text{for all } \boldsymbol{x} \text{ in a vicinity of } \boldsymbol{x}_0, \tag{5}$$

the fixed point $\boldsymbol{x}_0$ is asymptotically stable. If the inequality (5) is valid for a given choice of V and $\boldsymbol{f}$, it also holds for sufficiently small perturbations of $\boldsymbol{f}$, such that the stability persists for the perturbed system.

It is of course usually difficult to find a proper function V; in mechanical systems the total energy could serve as first guess.

Stability of Equilibria of Conservative Systems

In mechanical systems one frequently encounters equilibrium equations for a model loaded by conservative forces: Let $V(\boldsymbol{x}; \boldsymbol{\lambda})$ denote the potential energy of a mechanical model. The equilibrium equations are given by

$$\boldsymbol{0} = \boldsymbol{f}(\boldsymbol{x}; \boldsymbol{\lambda}) := \frac{\partial V}{\partial \boldsymbol{x}}. \tag{6}$$

Such an equilibrium $\boldsymbol{x}_0$ is stable, if the potential V is convex in the neighborhood of $\boldsymbol{x}_0$: $V(\boldsymbol{x}; \boldsymbol{\lambda}) > V(\boldsymbol{x}_0; \boldsymbol{\lambda})$ for $\boldsymbol{x} \neq \boldsymbol{x}_0$. To lowest order this condition can be checked by looking at the Hessian of V at the equilibrium point:

If the Hessian

$$H = \frac{\partial^2 V}{\partial \boldsymbol{x}^2}(\boldsymbol{x}_0, \boldsymbol{\lambda}), \quad \text{that is } H_{ij} = \frac{\partial^2 V}{\partial x_i \partial x_j}(\boldsymbol{x}_0, \boldsymbol{\lambda}) \tag{7}$$

is positive definite, the equilibrium $\boldsymbol{x}_0$ is stable. Positive definiteness can be checked by either calculating the eigenvalues of H – all eigenvalues of positive definite matrices are positive – or by Dirichlet's criterion, which states, that all principal minors have to be positive for stability. In the critical case, that is if some eigenvalues or principal minors vanish, higher-order derivatives have to be considered.

Center Manifolds for Equilibria

In this section the autonomous system (2) is transformed to Jordan Normal Form at the critical parameter value $\boldsymbol{\lambda}_c$. In order to correctly account for the contributions of the stable components to the dynamics of the critical variables, the *center manifold* is computed.

Let us assume that at the parameter value $\boldsymbol{\lambda}_c$, the Jacobian $\mathbf{A}(\boldsymbol{\lambda}_c)$ in (3) has n_c critical eigenvalues σ with $\Re(\sigma) = 0$ and the remaining $n_s = n - n_c$ stable eigenvalues lie in the left half plane. Arranging the (generalized) eigenvectors $\boldsymbol{v}_i$ of $\mathbf{A}(\boldsymbol{\lambda}_c)$ in the matrix

$$\mathbf{V} = [\mathbf{V}_c, \mathbf{V}_s] = [\boldsymbol{v}_1, \ldots, \boldsymbol{v}_{n_c}, \boldsymbol{v}_{n_c+1}, \ldots, \boldsymbol{v}_n], \tag{8}$$

starting with the eigenvectors corresponding to the critical eigenvalues, and introducing the change of coordinates

$$\boldsymbol{x} = \boldsymbol{x}_0 + \mathbf{V}\boldsymbol{y}, \text{ with } \boldsymbol{y} = (y_1, \ldots, y_{n_c}, y_{n_c+1}, \ldots, y_n)^T, \tag{9}$$

where $\boldsymbol{y}_c = (y_1, \ldots, y_{n_c})^T$ are called the "critical" variables, and $\boldsymbol{y}_s = (y_{n_c+1}, \ldots, y_n)^T$ the "stable" variables, system (1) is transformed to its Jordan normal form

$$\dot{\boldsymbol{y}} = \begin{pmatrix} \dot{\boldsymbol{y}}_c \\ \dot{\boldsymbol{y}}_s \end{pmatrix} = \begin{pmatrix} \mathbf{J}_c & \mathbf{0} \\ \mathbf{0} & \mathbf{J_s} \end{pmatrix} \begin{pmatrix} \boldsymbol{y}_c \\ \boldsymbol{y}_s \end{pmatrix} + \begin{pmatrix} \mathbf{g}_c(\boldsymbol{y}, \boldsymbol{\lambda}_c) \\ \mathbf{g}_s(\boldsymbol{y}, \boldsymbol{\lambda}_c) \end{pmatrix}, \tag{10}$$

where all eigenvalues of $\mathbf{J}_c$ lie on the imaginary axis and all eigenvalues of $\mathbf{J}_s$ are stable. The nonlinear part $\mathbf{g}(\boldsymbol{y}, \boldsymbol{\lambda}_c)$ is given by

$$\mathbf{g}(\boldsymbol{y}, \boldsymbol{\lambda}_c) = \mathbf{V}^{-1} \boldsymbol{f}_{\mathrm{NL}}(\mathbf{V}\boldsymbol{y}, \boldsymbol{\lambda}_c),$$

where

$$f_{\mathrm{NL}}(\Delta x, \lambda_c) = f(x_0 + \Delta x, \lambda_c) - \mathbf{A}(\lambda_c)\Delta x$$

contains the nonlinear expansion of f about the steady-state x_0.

Next we apply center manifold theory (Carr 1981), to reduce the n-dimensional system (10) to the essential dynamics governed by the n_c critical variables y_c. Whereas in the linear system the equations for the critical and stable variables decouple, the contribution of the stable variables y_s to the dynamics of y_c in the nonlinear equations has to be taken into account.

Definition 2 (Invariant Manifold) A set $S \subset \mathbf{R}^n$ is a *local invariant manifold* for (2) if for $x_0 \in S$, the solution $x(t)$ of (2) with $x(0) = x_0$ is in S for $|t| < T$ where $T > 0$. If we can always choose $T = \infty$, then we say that S is an *invariant manifold*.

If $y_s = h(y_c)$ is an invariant manifold for (10) and h is smooth, then it is called a *center manifold* if $h(\mathbf{0}) = \mathbf{0}$ and $h'(\mathbf{0}) = \mathbf{0}$, where h' denotes the Jacobian of h:

$$h'(y_0) = \frac{\partial h}{\partial y_c}(y_0).$$

The existence and the main properties of center manifolds are summarized in the following theorems (Carr 1981):

Theorem 1 *There exists a center manifold for* (10), $y_s = h(y_c)$, $|y_c| < \delta$, *where* h *is* C^2.

The dynamics on the center manifold is governed by the n_c*-dimensional system*

$$\dot{\mathbf{u}} = \mathbf{J}_c\mathbf{u} + \mathbf{g}_c(\mathbf{u}, h(\mathbf{u}), \lambda_c). \tag{11}$$

The next theorem shows that (11) correctly describes the asymptotic behavior of small solutions of (10):

Theorem 2 *Suppose that the zero solution of* (11) *is stable (asymptotically stable) [unstable]. Then the zero solution of* (10) *is stable (asymptotically stable) [unstable].*

Suppose that the zero solution of (11) *is stable. Let* $(y_c(t), y_s(t))$ *be a solution of* (10) *with* $(y_c(0), y_s(0))$ *sufficiently small. Then there exists a solution* $\mathbf{u}(t)$ *of* (11) *such that as* $t \to \infty$

$$y_c(t) = \mathbf{u}(t) + O(\exp(-\gamma t)), \tag{12}$$

$$y_s(t) = h(\mathbf{u}(t)) + O(\exp(-\gamma t)), \tag{13}$$

where $\gamma > 0$ *is some constant*

Equation (13) shows that the stable components $y_s(t)$ do not decay to zero exponentially fast, as one might conclude from the linearized system, but their long-time behavior is dominated by the critical variables $y_c(t)$. If for instance $y_c(t)$ converges to a periodic solution, then also $y_s(t)$ will approach a periodic function.

If we substitute $y_s = h(y_c)$ into the second equation of (10), we obtain the PDE

$$h'(y_c)(\mathbf{J}_c y_c + \mathbf{g}_c(y_c, h(y_c), \lambda_c)) = \mathbf{J}_s h(y_c) + \mathbf{g}_s(y_c, h(y_c), \lambda_c) \tag{14}$$

for $h(y_c)$, which together with the conditions $h(\mathbf{0}) = \mathbf{0}$, $h'(\mathbf{0}) = \mathbf{0}$ is the system to be solved for the center manifold. It is usually solved by a power series expansion. The next theorem (Carr 1981) shows that the center manifold can be approximated to any degree of accuracy.

For functions $\phi : \mathbf{R}^{n_c} \to \mathbf{R}^{n_s}$, which are C^1 in a neighborhood of the origin, define the nonlinear operator

$$(\mathbf{M}\phi)(y_c) = \phi'(y_c)(\mathbf{J}_c y_c + \mathbf{g}_c(y_c, \phi(y_c), \lambda_c)) - \mathbf{J}_s\phi(y_c) - \mathbf{g}_s(y_c, \phi(y_c), \lambda_c). \tag{15}$$

Note that by (14) $(\mathbf{M}h)(y_c) = \mathbf{0}$.

Theorem 3 *Let* ϕ *be a* C^1 *mapping of a neighborhood of the origin in* $\mathbf{R}^{n_c}$ *into* $\mathbf{R}^{n_s}$, *with* $\phi(\mathbf{0}) = \mathbf{0}$ *and* $\phi'(\mathbf{0}) = \mathbf{0}$. *Suppose that as* $y_c \to \mathbf{0}$, $(\mathbf{M}\phi)(y_c) = O(|y_c|^q)$, *where* $q > 1$. *Then, as* $y_c \to \mathbf{0}$, $|h(y_c) - \phi(y_c)| = O(|y_c|^q)$.

Example: Calculation of the Leading Center Manifold Expansion for a Hopf Bifurcation

Let us assume that the Jacobian $\mathbf{A}(\lambda_c)$ has a pair of purely imaginary eigenvalues $\sigma_{1,2} = \pm i\omega$ and that the remaining eigenvalues σ_k for $k > 2$ are simple and stable. We denote the critical variables

by z and $\bar{z}$ and the stable variables by y_k and search for the quadratic approximation of $y_k = h_k(z, \bar{z})$ using the ansatz

$$h_k(z, \bar{z}) = h_{k20} z^2 + h_{k11} z\bar{z} + h_{k02} \bar{z}^2. \quad (16)$$

Inserting (16) into (14), retaining only quadratic expressions in z and $\bar{z}$, and comparing the coefficients of z^2, $z\bar{z}$ and $\bar{z}^2$, respectively, we obtain the equations

$$\begin{aligned} 2h_{k20} i\omega &= \sigma_k h_{k20} + g_{k20}, \\ 0 &= \sigma_k h_{k11} + g_{k11}, \\ -2h_{k02} i\omega &= \sigma_k h_{k02} + g_{k02}, \end{aligned} \quad (17)$$

for the coefficients h_{kij}, where g_{kij} denotes the coefficient of $z^i \bar{z}^j$ in g_k. Since all coefficients on the left hand side of (17) lie on the imaginary axis, and $\Re(\sigma_k) < 0$, the equations are regular and yield the solutions

$$h_{k20} = \frac{g_{k20}}{2i\omega - \sigma_k}, \quad h_{k11} = \frac{g_{k11}}{-\sigma_k},$$
$$h_{k02} = \frac{g_{k02}}{-2i\omega - \sigma_k}.$$

Having obtained the quadratic approximation for y_k, we observe that the mixed terms $z y_k$ and $\bar{z} y_k$ introduce new cubic terms in the reduced equations: If we denote the coefficient of $z^i \bar{z}^j y_k$ in $g_1(\boldsymbol{y}_c, \boldsymbol{y}_s, \boldsymbol{\lambda}_c)$ by g_{1ijk}, we obtain the following coefficients for the reduced system $\mathbf{g}_r(\boldsymbol{y}_c) = \mathbf{g}_c(\boldsymbol{y}_c, \boldsymbol{h}(\boldsymbol{y}_c), \boldsymbol{\lambda}_c)$:

$$\begin{aligned} G_{130} &= g_{130} + \sum_{k=3}^{n} g_{110k} h_{k20}, \\ G_{121} &= g_{121} + \sum_{k=3}^{n} (g_{110k} h_{k11} + g_{101k} h_{k20}), \\ G_{112} &= g_{112} + \sum_{k=3}^{n} (g_{110k} h_{k02} + g_{101k} h_{k11}), \\ G_{103} &= g_{103} + \sum_{k=3}^{n} g_{101k} h_{k02}, \end{aligned} \quad (18)$$

where G_{1ij} denotes the coefficient of $z^i \bar{z}^j$ in the reduced equation for z.

If higher-order approximations for $\boldsymbol{h}$ are needed, this calculation also has to be applied to the coefficients in $\mathbf{g}_s$.

For demonstration purposes we also calculate the cubic expansion for the center manifold: Inserting

$$\begin{aligned} y_k = h_k(z, \bar{z}) &= h_{k20} z^2 + h_{k11} z\bar{z} + h_{k02} \bar{z}^2 \\ &+ h_{k30} z^3 + h_{k21} z^2 \bar{z} + h_{k12} z\bar{z}^2 + h_{k03} \bar{z}^3 \end{aligned}$$

into (14) and proceeding as before, we obtain the equations for the new coefficients:

$$\begin{aligned} 3h_{k30} i\omega + 2h_{k20} g_{120} + h_{k11} g_{220} &= \sigma_k h_{k30} + G_{k30}, \\ h_{k21} i\omega + 2h_{k20} g_{111} + h_{k11} g_{120} + h_{k11} g_{211} + 2h_{k02} g_{220} &= \sigma_k h_{k21} + G_{k21}, \\ -h_{k12} i\omega + 2h_{k20} g_{102} + h_{k11} g_{111} + h_{k11} g_{202} + 2h_{k02} g_{211} &= \sigma_k h_{k12} + G_{k12}, \\ -3h_{k03} i\omega + h_{k11} g_{102} + 2h_{k02} g_{202} &= \sigma_k h_{k30} + G_{k30}. \end{aligned}$$

The new entries on the left-hand side occur, because the term $\boldsymbol{h}'(\boldsymbol{y}_c)\mathbf{g}_c(\boldsymbol{y}_c, \boldsymbol{h}(\boldsymbol{y}_c))$ in (14) contributes cubic terms in $\boldsymbol{y}_c$, if both $\boldsymbol{h}$ and $\mathbf{g}$ contain quadratic terms. These cubic terms can be neglected, when calculating the quadratic terms in $\boldsymbol{h}$, but have to be taken into account, as soon as higher-order terms are needed. The coefficients G_{kij} in the right-hand side indicate that the original coefficients g_{kij} must be modified according to (18).

Inserting the cubic expansion of $\boldsymbol{h}$ into the reduced equations, we find that it leaves the quadratic and cubic terms unchanged but changes the terms of fourth and higher order. Therefore,

if only terms up to third order are required in the reduced system, the cubic terms in the center manifold expansion don't play any role and need not be calculated.

An inspection of (14) shows that if for a symmetric problem the nonlinearities start at third order, also the center manifold expansion starts at third order. For these systems it is in most cases not necessary to calculate the center manifold at all, unless fifth order terms are required.

Center Manifolds for Perturbed Parameter Values

In applications one is not only interested in the behavior of the system at the critical parameter value $\boldsymbol{\lambda}_c$ but also at nearby parameter values. There is a nice trick, to take this parameter dependency into account: First, we set $\boldsymbol{\lambda} = \boldsymbol{\lambda}_c + \boldsymbol{\varepsilon}$, such that the perturbation $\boldsymbol{\varepsilon}$ is a small parameter vector. Next, we regard this vector formally as additional state variables satisfying the trivial ODE

$$\dot{\boldsymbol{\varepsilon}} = 0.$$

The new critical state vector is now $\hat{\boldsymbol{y}}_c = (\boldsymbol{y}_c, \boldsymbol{\varepsilon})$, and the center manifold is written in the form

$$\boldsymbol{y}_s = \boldsymbol{h}(\boldsymbol{y}_c, \boldsymbol{\varepsilon}).$$

With this method it is possible to calculate the center manifold also for parameter values in the vicinity of the critical value $\boldsymbol{\lambda}_c$.

It should be noted that in general for varying $\boldsymbol{\lambda}$ also the steady state will change; therefore not only the linear and nonlinear part in the equations for $\boldsymbol{y}$ will depend on $\boldsymbol{\varepsilon}$, but for every component ε_i, there will also be a constant vector $\boldsymbol{b}_i$ proportional to ε_i, which is given by

$$\boldsymbol{b}_i = \varepsilon_i \mathbf{V}^{-1} \frac{\partial \boldsymbol{f}(\boldsymbol{x}, \boldsymbol{\lambda})}{\partial \lambda_i}(\boldsymbol{x}_0, \boldsymbol{\lambda}_c). \tag{19}$$

Since the matrix $\mathbf{J}_s$ is regular, the equilibrium equation

$$\mathbf{B} + \mathbf{J}\boldsymbol{y} + \boldsymbol{g}(\boldsymbol{y}, \boldsymbol{\varepsilon}) = \mathbf{0},$$

where $\mathbf{B} = [\boldsymbol{b}_1, \ldots, \boldsymbol{b}_m]$, can be solved for the stable components $\boldsymbol{y}_s$ of $\boldsymbol{y}$.

Normal Form Reduction of the Bifurcation Equations

After reducing the full system (10) to the n_c-dimensional system for the critical variables

$$\dot{\boldsymbol{y}}_c = \mathbf{J}_c \boldsymbol{y}_c + \mathbf{g}_r(\boldsymbol{y}_c), \qquad \text{where}$$
$$\mathbf{g}_r(\boldsymbol{y}_c) = \mathbf{g}_c(\boldsymbol{y}_c, \boldsymbol{h}(\boldsymbol{y}_c), \boldsymbol{\lambda}_c), \tag{20}$$

we apply a series of near-identity coordinate transformations to simplify it as much as possible (Arnold 1983; Wiggins 2003; Elphick et al. 1987). With the ansatz

$$\boldsymbol{y}_c = \boldsymbol{v} + \boldsymbol{h}(\boldsymbol{v}) \tag{21}$$

we try to determine the nonlinear function $\boldsymbol{h}(\boldsymbol{v})$ such that in the new variables, the bifurcation equations become

$$\dot{\boldsymbol{v}} = \mathbf{J}_c \boldsymbol{v} + \tilde{\mathbf{g}}_r(\boldsymbol{v}), \tag{22}$$

where $\tilde{\mathbf{g}}_r(\boldsymbol{v})$ is simpler than the original $\mathbf{g}_r(\boldsymbol{y}_c)$. Inserting (21) into (20) and using (22), we obtain the equation

$$(\mathbf{1} + \boldsymbol{h}'(\boldsymbol{v}))(\mathbf{J}_c \boldsymbol{v} + \tilde{\mathbf{g}}_r(\boldsymbol{v})) = \mathbf{J}_c(\boldsymbol{v} + \boldsymbol{h}(\boldsymbol{v}))$$
$$+\mathbf{g}_r(\boldsymbol{v} + \boldsymbol{h}(\boldsymbol{v})). \tag{23}$$

At lowest order we get

$$\boldsymbol{h}'(\boldsymbol{v})\mathbf{J}_c \boldsymbol{v} - \mathbf{J}_c \boldsymbol{h}(\boldsymbol{v}) + \tilde{\mathbf{g}}_r(\boldsymbol{v}) = \mathbf{g}_r(\boldsymbol{v}). \tag{24}$$

If the *homological operator* $(\mathsf{L}_{\mathbf{J}_c}\boldsymbol{h})(\boldsymbol{v}) = \boldsymbol{h}'(\boldsymbol{v})\mathbf{J}_c \boldsymbol{v} - \mathbf{J}_c \boldsymbol{h}(\boldsymbol{v})$ is regular, all entries in $\mathbf{g}_r(\boldsymbol{v})$ can be removed, and we obtain the trivial normal form $\tilde{\mathbf{g}}_r(\boldsymbol{v}) = \mathbf{0}$. Otherwise we have to choose a complementary subspace $\mathbf{L}^C$ to the range of L and project $\mathbf{g}_r(\boldsymbol{v})$ on $\mathbf{L}^C$ to obtain $\tilde{\mathbf{g}}_r(\boldsymbol{v})$.

For a diagonal matrix $\mathbf{J}_c = \mathbf{diag}(\sigma_1, \ldots, \sigma_{n_c})$, the operator $(\mathsf{L}_{\mathbf{J}_c}\boldsymbol{h})(\boldsymbol{v})$ acts diagonally on the monomials

$$h_i(\boldsymbol{v}) = \boldsymbol{v}^{\boldsymbol{m}} = v_1^{m_1} v_2^{m_2} \cdots v_{n_c}^{m_{n_c}},$$

with $m_i \geq 0$:

$$\mathsf{L}_{\mathbf{J}_c}\boldsymbol{v}^{\boldsymbol{m}} = (m_1\sigma_1 + m_2\sigma_2 + \cdots + m_{n_c}\sigma_{n_c} - \sigma_i)\boldsymbol{v}^{\boldsymbol{m}}. \tag{25}$$

If $\boldsymbol{m}\cdot\boldsymbol{\sigma} - \sigma_i \neq 0$, the term $g_{i,\boldsymbol{m}}\boldsymbol{v}^{\boldsymbol{m}}$ can therefore be removed from $g_i(\boldsymbol{v})$; otherwise it must be kept in the normal form.

Normal Form Calculation for the Hopf Bifurcation

In the previous section, we carried out the center manifold reduction for the case of purely imaginary eigenvalues and obtained the reduced equation

$$\dot{z} = i\omega z + G_{120}z^2 + G_{111}z\overline{z} + G_{102}\overline{z}^2 + G_{130}z^3 + G_{121}z^2\overline{z} + G_{112}z\overline{z}^2 + G_{103}\overline{z}^3. \tag{26}$$

The equation for $\overline{z}$ is just the complex conjugate of (26). Starting with the quadratic terms, we use the ansatz

$$\begin{aligned} z &= w + h_{20}w^2 + h_{11}w\overline{w} + h_{02}\overline{w}^2, \\ \overline{z} &= \overline{w} + \overline{h}_{20}\overline{w}^2 + \overline{h}_{11}\overline{w}w + \overline{h}_{02}w^2. \end{aligned} \tag{27}$$

With $\mathbf{J}_c = \mathbf{diag}(i\omega, -i\omega)$, we get

$$\mathsf{L}_{\mathbf{J}_c}w^k\overline{w}^l = (k-l-1)i\omega w^k\overline{w}^l \tag{28}$$

in the first row. For the quadratic terms $(k+l=2)$, we obtain the coefficients

$$h_{20} = \frac{G_{120}}{i\omega}, \quad h_{11} = \frac{G_{111}}{-i\omega}, \quad h_{02} = \frac{G_{102}}{-3i\omega} \tag{29}$$

and can eliminate all quadratic entries in $\mathbf{g}_r$. Before proceeding to the cubic terms, we have to take care of the induced changes of the higher-order coefficients: For the cubic terms, the product $\boldsymbol{h}'(\mathbf{w})\tilde{\mathbf{g}}_r(\mathbf{w})$ on the left-hand side of (23) doesn't contribute anything, because of the trivial quadratic terms in $\tilde{\mathbf{g}}_r(\mathbf{w})$, so we need only consider the cubic terms in the Taylor expansion of $\mathbf{g}_r(\mathbf{w} + \boldsymbol{h}(\mathbf{w}))$. For the new coefficient of $w^2\overline{w}$ we obtain the expression,

$$\tilde{G}_{121} = G_{121} + 2G_{120}h_{11} + G_{111}(\overline{h}_{11} + h_{20}) + 2G_{102}\overline{h}_{02}. \tag{30}$$

Next, we apply the method with a cubic ansatz for $\boldsymbol{h}$ to eliminate the cubic terms in $\tilde{\mathbf{g}}_r$ and obtain the equations

$$\begin{aligned} 2i\omega h_{30} &= \tilde{G}_{130}, & \tilde{\tilde{G}}_{130} &= 0, \\ 0\cdot h_{21} + \tilde{\tilde{G}}_{121} &= \tilde{G}_{121}, & & \\ -2i\omega h_{12} &= \tilde{G}_{112}, & \tilde{\tilde{G}}_{112} &= 0, \\ -4i\omega h_{03} &= \tilde{G}_{103}, & \tilde{\tilde{G}}_{103} &= 0. \end{aligned} \tag{31}$$

In this case we can eliminate all cubic terms except $\tilde{G}_{121}w^2\overline{w}$, which yields the single entry in the cubic normal form. Proceeding to higher-order nonlinearities, we observe that all terms $w^k\overline{w}^l$ can be eliminated, except those for which $k-l=1$. Therefore the normal form for the Hopf bifurcation has the general shape

$$\dot{z} = i\omega z + \sum_{l=1}^{\infty} G_{1,l+1,l}(z\overline{z})^l z = G(z\overline{z})z,$$

where $G(r^2)$ is an arbitrary smooth function. Since we are usually only interested in the lowest-order terms, the convergence problems for an infinite series of coordinate transforms do not matter in our case.

Unfolding of the Linear System Using Normal Forms

In order to investigate the influence of parameter variations on the bifurcation equations, we proceed as in the previous chapter (Arnold 1983). For simplicity we assume, that only the parameter λ_i is varied. Close to the bifurcation point, the linear part of the bifurcation equation reads

$$\dot{\boldsymbol{y}}_c = (\mathbf{J}_c + \varepsilon_i\mathbf{J}_1)\,\boldsymbol{y}_c, \tag{32}$$

where $\mathbf{J_1}$ is the leading $(n_c \times n_c)$-submatrix of the Jordan normal form perturbation

$$\mathbf{J}_p = \mathbf{V}^{-1}\frac{\partial\mathbf{A}(\boldsymbol{\lambda})}{\partial\lambda_i}\mathbf{V}.$$

Inserting the ansatz $\boldsymbol{y}_c = \boldsymbol{v} + \varepsilon_i \mathbf{H}\boldsymbol{v}$ into (32) and comparing the first-order terms in ε_i, we obtain the matrix equation

$$\mathbf{H}\mathbf{J}_c - \mathbf{J}_c\mathbf{H} + \tilde{\mathbf{J}}_1 = \mathbf{J}_1, \tag{33}$$

where $\tilde{\mathbf{J}}_1$ again denotes the linear perturbation matrix, which should become simpler than $\mathbf{J}_1$.

If $\mathbf{J}_c = \mathbf{diag}(\sigma_1, \ldots, \sigma_{n_c})$, then

$$(\mathbf{H}\mathbf{J}_c - \mathbf{J}_c\mathbf{H})_{kl} = (\sigma_k - \sigma_l)H_{kl}.$$

If all critical eigenvalues are different, all entries in $\mathbf{J}_1$ can be removed except the diagonal terms. If some eigenvalue occurs with (geometric) multiplicity p, a $p \times p$ block survives the normal form reduction.

Short Discussion of the Hopf Bifurcation

For simplicity we consider a scalar parameter λ, which becomes critical at λ_c:

$$\sigma_{1,2} = \pm i\omega, \qquad \Re(\sigma_k) < 0 \quad \text{for} k > 2.$$

After performing all preceding steps for the case of a pair of purely imaginary eigenvalues, we obtain the cubic complex differential equation

$$\dot{z} = (\alpha + i\beta + i\omega)z + \tilde{G}_{121} z^2 \bar{z}, \tag{34}$$

where $\alpha + i\beta = \varepsilon(\mathbf{J}_1)_{11}$ is the first entry in the perturbed Jacobian. The coefficient

$$\Re(\mathbf{J}_1)_{11} = \left.\frac{\partial \Re(\sigma_1)}{\partial \lambda}\right|_{\lambda=\lambda_c}$$

denotes the "speed," with which $\Re(\sigma_1)$ crosses the imaginary axis, if $\lambda = \lambda_c + \varepsilon$ passes the critical value. We assume that $\Re(\mathbf{J}_1)_{11} > 0$, such that the steady-state $\boldsymbol{x}_0$ becomes unstable for $\lambda > \lambda_c$ "with non-zero speed." In this case we can rescale ε, such that $\alpha = \varepsilon$.

Theorem 4 (Hopf bifurcation) *If the following conditions hold*

1. *The critical eigenvalue σ_1 crosses the imaginary axis with non-zero speed at $\lambda = \lambda_c$,*
2. *$\sigma_1(\lambda_c) = i\omega$, with $\omega > 0$,*
3. *$a_1 := \Re(\tilde{G}_{121}) \neq 0$,*

then a family of periodic solution bifurcates from the steady state at $\lambda = \lambda_c$. If $a_1 < 0$, the periodic solution exists for $\lambda > \lambda_c$ and is asymptotically stable.

Proof Rewriting (34) in polar coordinates $z = r\exp(i\varphi)$, we obtain the equations

$$\dot{r} = (\alpha + a_1 r^2)r, \tag{35}$$

$$\dot{\varphi} = \omega + \beta + \Im(\tilde{G}_{121})r^2. \tag{36}$$

Since we only consider small solutions, $\dot{\varphi} > 0$, so nontrivial steady solutions of (35) correspond to stationary rotations. The nontrivial steady solution of (35) is given by

$$r_0 = \sqrt{-\alpha/a_1},$$

so this solution exists, if α and a_1, the latter is also known as *first Lyapunov number*, have different signs.

The linearization of (35) at r_0 is given by

$$\dot{R} = (\alpha + 3a_1 r_0^2)R = 2a_1 r_0^2 R.$$

Since $r_0^2 > 0$, the sign of a_1 decides about stability. □

Let us finally discuss, what happens, if one of the conditions for the Hopf bifurcation is not fulfilled:

1. If $\Re((\mathbf{J}_1)_{11}) = 0$, the critical eigenvalue touches the imaginary axis. Depending on higher-order expansions of the eigenvalue behavior, it will either turn back into the stable half plane (for $\partial^2\sigma_1/\partial\lambda_1^2 < 0$) or cross the imaginary axis if $\partial^2\sigma_1/\partial\lambda_1^2 = 0$ and $\partial^3\sigma_1/\partial\lambda_1^3 > 0$. If a second parameter λ_2 is varied, we either obtain zero or two critical eigenvalues in the first case. The corresponding bifurcation is known as *Isola bifurcation* (Golubitsky et al. 1985). In the second case we need two further parameters to unfold the bifurcation.

2. If the frequency ω becomes zero, a *Takens-Bogdanov* bifurcation occurs, which is characterized by a pair of semi-simple zero eigenvalues. The bifurcation is studied in detail in Wiggins (2003) and Kuznetsov (1995).
3. If the *first Lyapunov number* $a_1 = 0$, a *Bautin bifurcation* (Kuznetsov 1995) occurs. One has to calculate the *second Lyapunov number* $a_2 = \Re(\tilde{g}_{132})$, which involves the treatment of terms up to order 5.

Cross-References

- ▸ Analytical Stability Considerations in Lightweight Design
- ▸ Buckling and Post-buckling of Plates
- ▸ Numerical Treatment of Stability Problems in Lightweight Design

References

Arnold VI (1983) Geometrical methods in the theory of ordinary differential equations. Springer, New York/Heidelberg/Berlin
Carr J (1981) Applications of centre manifold theory. Springer, New York
Chicone C (2006) Ordinary differential equations with applications. Springer, New York/Berlin
Elphick C, Tirapegui E, Brachet M, Coullet P (1987) A simple global characterization for normal forms of singular vector fields. Physica 29D:95–127
Golubitsky M, Stewart I, Schaeffer D (1985) Singularities and groups in bifurcation theory. Applied mathematics sciences, vols 1 and 2. Springer, New York/Heidelberg/Berlin
Hartman P (2002) Ordinary differential equations, 2nd edn. SIAM, Philadelphia
Kuznetsov YK (1995) Elements of applied bifurcation theory. Springer, New York
Wiggins S (2003) Introduction to applied nonlinear dynamical systems and chaos. Springer, New York

Stiffness and Strength of Anisotropic Heterogeneous Slender Structures

- ▸ Constitutive Modeling of Beams Using Mechanics of Structure Genome

Stochastic Continuum

- ▸ Continuum Mechanics with Spontaneous Violations of the Second Law of Thermodynamics

Stochastics

- ▸ Tensor Random Fields in Continuum Mechanics

Stokes, George Gabriel

Holm Altenbach
Lehrstuhl Technische Mechanik, Institut für Mechanik, Fakultät für Maschinenbau, Otto-von-Guericke-Universität Magdeburg, Magdeburg, Germany

Sir George Gabriel Stokes, 1st Baronet (August 13, 1819, in Skreen, County Sligo, Ireland; February 1, 1901, in Cambridge, England) was a physicist and mathematician with contributions to solid mechanics and physical optics. He popularized the Stokes' theorem in vector calculus and the theory of asymptotic expansions.

Early Years and Education

His father, Gabriel Stokes, was a reverend in Skreen (County Sligo) at the west coast of Ireland. His mother, Elizabeth Haughton, was the daughter of a priest. George Gabriel Stokes grew up in a religious surrounding as the youngest of six children. His father was a student of the Trinity College Dublin, and he educated George in Latin. In 1832 he moved to the school of Reverend R.H. Wall in Dublin.

In 1835 he attended the Bristol College in Bristol. Within 2 years Stokes was prepared for a study in Cambridge. The vice-chancellor, Dr. Jerrard, was an Irish, who was in the Cambridge University. Stokes showed his talent in mathematics, and he was awarded finally some prizes in mathematics.

George Gabriel Stokes

Professional Career and Scientific Achievements

Since 1837 Stokes studied in Pembroke College (University of Cambridge). In second year he was a student of William Hopkins, who prepared the best students for the best in the academic year (Senior Wrangler). In 1841 Stokes was graduated as a Senior Wrangler.

William Hopkins advertised Stokes to make his focus on hydrodynamics (Navier-Stokes equations). At the same time he got information on some papers of George Green. Stokes published in 1842 and 1843 papers on the motion of incompressible fluids. After that he observed that Jean Marie Constant Duhamel (1797–1872) got similar results. The same situation was when he investigated the inner friction in moving fluids. He introduced the proper equations, but similar equations were introduced by Claude Louis Navier (1785–1836), Siméon Denis Poisson (1781–1840), and Adhémar Jean Claude Barré de Saint-Venant (1797–1886). Finally he published his results in the United Kingdom, where the results from the continental Europe in that time where not well known.

The Stoke's theorem is some generalization of the fundamental theorem of calculus connecting n-dimensional volume integrals with $(n-1)$-dimensional surface integrals. The Gauß' theorem (or Gauß-Ostrogradsky theorem) is a special case.

In 1849 Stokes became the Lucasian Professor of Mathematics. This position was not well paid. So he was employed in addition as a professor of physics at the Government School of Mines in London (established in 1851).

Honors

From the Royal Society, of which he became a fellow in 1851, he received the Rumford Medal (1852, contribution to the wavelength of light) and later (1893) the Copley Medal. Since 1854 he was the secretary, and in between 1885 and 1890, he was the president. He was the first after Newton who combined the Lucasian Professor of Mathematics, the president of the Royal Society, and the member of the Parliament of the university. From 1883 to 1885, he was Burnett lecturer at Aberdeen, his lectures on light, which were published in 1884–1887, dealing with its nature, its use as a means of investigation, and its beneficial effects. On April 18, 1888, he was admitted as a Freeman of the City of London. On July 6, 1889, Queen Victoria created him the Baronet Stokes of Lensfield Cottage in the Baronetage of the United Kingdom; the title became extinct in 1916. In 1891, as Gifford lecturer, he published a volume on Natural Theology. He was a member of the Prussian Order Pour le Mérite. His academic distinctions included honorary degrees from many universities, including:

- Doctor mathematicae (honoris causa) from the Royal Frederick University on September 6, 1902, when they celebrated the centennial of the birth of mathematician Niels Henrik Abel.

The Stokes, a unit of kinematic viscosity, is named after him.

Cross-References

- ▸ Gauß, Johann Carl Friedrich
- ▸ Green, George
- ▸ de Saint-Venant, Adhémar-Jean-Claude Barré
- ▸ Poisson, Siméon Denis

Strain Gradient Plasticity

Lorenzo Bardella
Department of Civil, Environmental, Architectural Engineering and Mathematics, University of Brescia, Brescia, Italy

Synonyms

Plasticity theory at small scales; Size-dependent plasticity theory

Definition

Strain gradient plasticity (SGP) is a theory of continuum solid mechanics which aims at modeling the irreversible mechanical behavior of materials, with specific focus on metals and on their response at appropriately small size, typically on the order of micrometers or less. For such small metallic components, a variation in size leads to a peculiar effect, denoted as "smaller being stronger."

Background

The term plasticity refers to the irreversible mechanical behavior of materials, with particular reference to metals. This behavior occurs when the stress state is large enough for the material to *yield*, thus leading to a permanent deformation, denoted as plastic deformation. Such deformation can be observed, and the inherent plastic strain measured, after removing a suitable, monotonically applied load which enables yielding. In simple tests, such as uniaxial tension, the *yield stress* is experimentally recognized as the stress corresponding to the first abrupt change of slope in the stress-strain curve, limiting the elastic (i.e., reversible) regime. The slope of the stress-strain curve after yielding is proportional to the so-called *strain hardening*. The plastic deformation is mainly due to the nucleation, multiplication, and propagation of dislocations that are line defects within the metal crystal lattice.

SGP is a theory of continuum solid mechanics which aims at modeling the plasticity of metals at appropriately small scale. Specifically, SGP theory focuses on the size range between few tens of nanometers and few tens of micrometers, in which the peculiar "smaller being stronger" size effect has been experimentally measured. The torsion of thin wires (Fleck et al. 1994), the microindentation (Ma and Clarke 1995), and the microbending (Stölken and Evans 1998) are among the pioneering experimental observations of such size effect about two decades ago. However, much earlier, Hall (1951) and Petch (1953) discovered the size effect named after them, peculiar of the polycrystalline microstructure of common metals, consisting of many grains (each grain being a single crystal) with randomly distributed lattice orientation. On the basis of Hall and Petch experimental results on metals, such as mild steel and ingot iron, it has been established that the macroscopically observed yield stress increases, with respect to that characterizing the single grain, about proportionally to the inverse of the square root of the average grain size.

The size effect consisting of an increase of yield stress accompanied with diminishing size is referred to as *strengthening*. Experimental results also show a further size effect, that is, an increase in strain hardening with diminishing size. As demonstrated

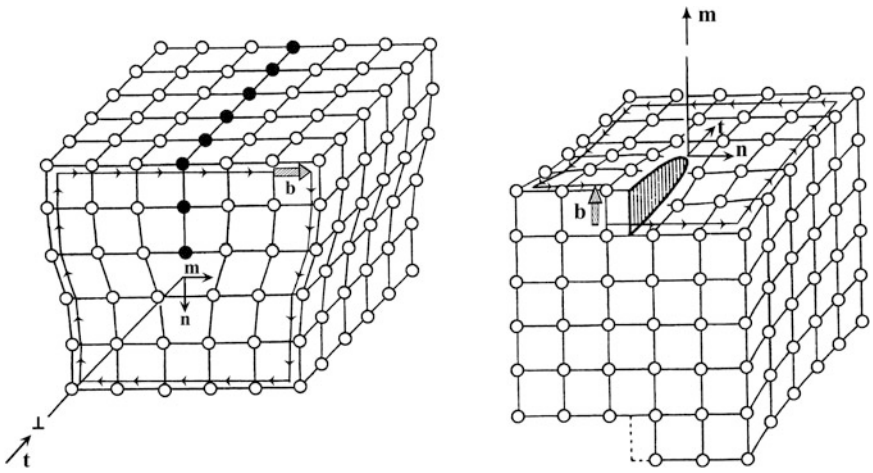

Fig. 1 Schematics for the atomistic characterization of edge (left) and screw (right) dislocations (Figure redrawn and modified from Hayden et al. 1965)

by Ashby (1970), geometrically necessary dislocations (GNDs) are the main responsible for such size-dependent behavior and, as illustrated in what follows, are related to the gradient of the plastic deformation.

GNDs are also denoted as excess or misfit dislocations in contrast to statistically stored dislocations (SSDs). In fact, in an appropriate average sense, SSDs annihilate each other. The propagation of the whole population of dislocations can be associated with the plastic strain magnitude (Hull and Bacon 2001). Any single (discrete) dislocation causes a lattice distortion, as illustrated in Fig. 1 for edge and screw dislocations in a cubic crystal. Figure 1 displays the Burgers circuits whose closure failure defines the Burgers vector **b**, characterizing each dislocation (Burgers 1939), along with the unit vectors **m**, **n**, and **t** defining the slip direction, the slip plane normal, and the direction orthogonal to **m** on the slip plane, respectively. The Burgers vector amplitude $|\mathbf{b}|$ is equal to an interatomic spacing. Edge dislocations represent half-planes of atoms (black circles in Fig. 1) in an otherwise regular crystal lattice. Hence, the slip direction is normal to the edge dislocation line, while in screw dislocations (Fig. 1 on the right) the slip direction coincides with the dislocation line. *Glide* is the most relevant component of dislocations' motion and occurs on a plane containing both the dislocation line and its Burgers vector.

The distortions represented in Fig. 1 are associated with internal stress fields that become very relevant when many dislocations are present, as in metal plasticity. Such stress fields sum up when due to GNDs (which, contrary to SSDs, do not annihilate each other), thus giving rise to long-range stress effects.

In polycrystalline metals subject to plastic deformation, dislocations, locally of the same sign, pile up against grain boundaries, thus forming regions of large GND density referred to as *boundary layers*.

The size of boundary layers depends on the crystallography and on the grain boundary strength (the larger the latter, the longer the maximum pileup length), while it is not much influenced by the grain size. As a result, the stiffening effect of boundary layers is inversely proportional to the grain size, thus leading to a size effect in the observed strain hardening. Moreover, in a polycrystal, with diminishing grain size, the dislocations' mean free path decreases along with the possibility of dislocations to enucleate and propagate.

Since nucleation and propagation of dislocations have to conspicuously occur at (macroscopic) yield, the above observation offers a qualitative interpretation of the Hall-Petch size effect.

Individual (discrete) dislocations cannot enter a *continuum* theory, which may instead account for the GND *density*, that is related to the incompatibility of the plastic distortion field, as shown in the next section.

A strain field is incompatible if it cannot be determined from the gradient of a suitably smooth vector field.

By building on the foregoing concepts, SGP theory extends the conventional plasticity theory (see, e.g., Fleck and Hutchinson 1997; Gurtin et al. 2010), in such a way that for size above $\approx$100 μm, SGP converges to conventional plasticity. At size below a few tens of nanometers, continuum theories may become inappropriate, and the mechanical behavior of metals is dominated by effects neglected by SGP, such as surface effects and dislocation core effects. SGP theory refers to absolute temperature lower than about half of the melting point and to strain rate lower than $\approx$10/s (Valdevit and Hutchinson 2012).

Notation

Lightface letters are employed for scalars, whereas boldface letters are used for first-, second-, third-, and fourth-order tensors, respectively represented by small Latin, small Greek, capital Latin, and capital blackboard letters, unless otherwise specified. When index notation is employed, it refers to an orthonormal system of coordinates. The symbol "$\cdot$" represents the inner product of vectors and tensors (e.g., $a = \mathbf{b} \cdot \mathbf{u} \equiv b_i u_i$, $b = \boldsymbol{\sigma} \cdot \boldsymbol{\varepsilon} \equiv \sigma_{ij}\varepsilon_{ij}$, $c = \mathbf{T} \cdot \mathbf{S} \equiv T_{ijk}S_{ijk}$). For any tensor, the modulus reads $|\boldsymbol{\rho}| \equiv \sqrt{\boldsymbol{\rho} \cdot \boldsymbol{\rho}}$. The symbol "$\otimes$" denotes the tensor product, e.g., $(\mathbf{m} \otimes \mathbf{n})_{ij} \equiv m_i n_j$. The symbol "$\times$" is adopted for the vector product: $(\mathbf{t})_i = (\mathbf{m} \times \mathbf{n})_i \equiv e_{ijk} m_j n_k = t_i$ and $(\boldsymbol{\zeta} \times \mathbf{n})_{ij} \equiv e_{jlk}\zeta_{il}n_k$, with $e_{ijk} = (i - j)(j - k)(k - i)/2$ denoting the Ricci-Curbastro tensor (or alternating symbol). For the composition of tensors of different orders, the lower-order tensor is on the right, and all its indices are saturated, e.g., $(\mathbf{t})_i = (\boldsymbol{\sigma}\mathbf{n})_i \equiv \sigma_{ij}n_j = t_i$, $(\mathbf{T}\mathbf{n})_{ij} \equiv T_{ijk}n_k$, and $(\boldsymbol{\sigma})_{ij} = (\mathbb{L}\boldsymbol{\varepsilon})_{ij} \equiv L_{ijkl}\varepsilon_{kl} = \sigma_{ij}$. $\mathrm{tr}\boldsymbol{\gamma} = \boldsymbol{\gamma} \cdot \boldsymbol{\delta} \equiv \gamma_{ii}$ is the trace of a second-order tensor, with $\boldsymbol{\delta}$ denoting the second-order identity tensor (or Kronecker symbol). $\mathrm{dev}\boldsymbol{\sigma} = \boldsymbol{\sigma} - \boldsymbol{\delta}\mathrm{tr}\boldsymbol{\sigma}/3$, $(\mathrm{sym}\boldsymbol{\gamma})_{ij} \equiv (\gamma_{ij} + \gamma_{ji})/2$, and $(\mathrm{skw}\boldsymbol{\gamma})_{ij} \equiv (\gamma_{ij} - \gamma_{ji})/2$ denote, respectively, the deviatoric, symmetric, and skew-symmetric parts of second-order tensors. By referring to a Cartesian system, $(\nabla\boldsymbol{\varepsilon})_{ijk} \equiv \partial\varepsilon_{ij}/\partial x_k \equiv \varepsilon_{ij,k}$, $(\mathrm{div}\mathbf{S})_{ij} \equiv S_{ijk,k}$, and $(\mathrm{curl}\boldsymbol{\gamma})_{ij} \equiv e_{jkl}\gamma_{il,k}$ designate, respectively, the gradient, the divergence, and the curl operators. $\dot{\boldsymbol{\varepsilon}}$ indicates the time derivative $\mathrm{d}\boldsymbol{\varepsilon}/\mathrm{d}t$, with t denoting the variable governing the loading history, not necessarily a physical time.

Theory

Kinematics

Attention is restricted to small strains and rotations. In this framework, the gradient of the displacement field $\mathbf{u}$ can be additively split into its elastic part, $(\nabla\mathbf{u})_{\mathrm{el}}$, and its plastic part, $\boldsymbol{\gamma}$, denoted as the plastic distortion:

$$\nabla\mathbf{u} = (\nabla\mathbf{u})_{\mathrm{el}} + \boldsymbol{\gamma} \tag{1}$$

The total strain, plastic strain, elastic strain, and plastic spin are, respectively, defined as

$$\boldsymbol{\varepsilon} = \mathrm{sym}\nabla\mathbf{u} \tag{2}$$

$$\boldsymbol{\varepsilon}^p = \mathrm{sym}\boldsymbol{\gamma} \tag{3}$$

$$\mathrm{sym}(\nabla\mathbf{u})_{\mathrm{el}} = \boldsymbol{\varepsilon} - \boldsymbol{\varepsilon}^p$$

$$\boldsymbol{\vartheta}^p = \mathrm{skw}\boldsymbol{\gamma}$$

There exist two main classes of conventional plasticity, that is, *crystal* plasticity and *phenomenological* plasticity. The former accounts for the crystal lattice, thus being more precise in the description of the plastic distortion,

associated with dislocations' motion. Instead, phenomenological plasticity neglects the crystal lattice and is mainly employed to model, in an appropriate average sense, the mechanical response of polycrystalline metals, for which the use of crystal plasticity is computationally much more expensive.

More specifically, in crystal plasticity, the plastic distortion is given by the following sum over the slip systems, whose orientation and number A depend on the crystallography (e.g., $A = 12$ in face-centered cubic metals, such as copper, silver, and gold):

$$\boldsymbol{\gamma} = \sum_{\beta=1}^{A} \gamma^{(\beta)} \mathbf{m}^{(\beta)} \otimes \mathbf{n}^{(\beta)} \tag{4}$$

in which $\gamma^{(\beta)}$, with $\beta = 1, \ldots, A$, are the plastic slips and $\mathbf{m}^{(\beta)}$ and $\mathbf{n}^{(\beta)}$ are the unit vectors defining, respectively, the slip direction and the slip plane normal for the slip system β. Definition (4) implies $\mathrm{tr}\boldsymbol{\gamma} = 0$, meaning that the plastic flow is isochoric. In crystal plasticity, the basic plastic variables are the plastic slips, while this is not the case in phenomenological plasticity, neglecting the crystallography along with Eq. (4).

While the compatibility of the displacement field implies

$$\mathrm{curl}(\nabla \mathbf{u}) = \mathbf{0}\,, \tag{5}$$

the incompatibility of $\boldsymbol{\gamma}$ results, in general, in the closure failure of its circuit C around any suitably smooth surface S within the continuum:

$$\mathbf{b}_{\mathrm{net}} = \oint_C \boldsymbol{\gamma}\, \mathrm{d}\mathbf{c} \tag{6}$$

in which $\mathbf{c}$ is the vectorial coordinate along C (having pointwise the direction of the tangent to C) and $\mathbf{b}_{\mathrm{net}}$ is the net Burgers vector, thus mimicking the characterization of a discrete dislocation in the crystal lattice (see Fig. 1). Given that, in general, the surface S is pierced by several dislocations, only dislocations whose Burgers vectors do not cancel out contribute to $\mathbf{b}_{\mathrm{net}}$. Hence, Eq. (6) is associated with the GND density.

By applying Stokes' theorem, Eq. (6) becomes

$$\mathbf{b}_{\mathrm{net}} = \int_S \mathrm{curl}\boldsymbol{\gamma}\ \mathbf{n}_S \mathrm{d}A \tag{7}$$

where $\mathbf{n}_S$ is the unit normal to the surface S, pointing according to the right-hand screw rule, given the positive sense of C.

Equation (7) suggests the definition of Nye's dislocation density tensor $\boldsymbol{\alpha}$ (Nye 1953; Kröner 1962; Fleck and Hutchinson 1997; Arsenlis and Parks 1999):

$$\boldsymbol{\alpha} = \mathrm{curl}\boldsymbol{\gamma} \tag{8}$$

such that

$$\mathbf{b}_{\mathrm{net}} = \int_S \boldsymbol{\alpha}\mathbf{n}_S \mathrm{d}A$$

from which one deduces that

> Nye's dislocation density tensor $\boldsymbol{\alpha}$ is a continuum representation of geometrically necessary dislocations such that α_{ij} is the i component of the net Burgers vector related to GNDs of line vector j.

From Eqs. (1), (5), and (8), one finds a link between $\boldsymbol{\alpha}$ and the elastic part of $\nabla \mathbf{u}$:

$$\boldsymbol{\alpha} = -\mathrm{curl}\ (\nabla \mathbf{u})_{\mathrm{el}} \tag{9}$$

In crystal plasticity, by substituting relation (4) into definition (8), and by making use of the identity $e_{ijk}e_{irs} = \delta_{jr}\delta_{ks} - \delta_{js}\delta_{kr}$, one obtains

$$\boldsymbol{\alpha} = \sum_{\beta=1}^{A} \mathbf{m}^{(\beta)} \otimes \left(\rho_{\perp}^{(\beta)} \mathbf{t}^{(\beta)} + \rho_{\odot}^{(\beta)} \mathbf{m}^{(\beta)}\right)$$

in which $\mathbf{t}^{(\beta)} = \mathbf{m}^{(\beta)} \times \mathbf{n}^{(\beta)}$ and $\rho_{\perp}^{(\beta)} = \nabla\gamma^{(\beta)} \cdot \mathbf{m}^{(\beta)}$ and $\rho_{\odot}^{(\beta)} = -\nabla\gamma^{(\beta)} \cdot \mathbf{t}^{(\beta)}$ are the projections of the plastic slip gradient onto the slip and transverse directions, respectively. Given the above emphasized property of $\boldsymbol{\alpha}$, by comparison with the schematics of Fig. 1, one can deduce that $\rho_{\perp}^{(\beta)}$ and $\rho_{\odot}^{(\beta)}$ represent, respectively, the densities of *pure* edge and screw GNDs for the slip system β (Arsenlis and Parks 1999). Here, the adjective "pure" refers to the fact that the characterization of Fig. 1 is ideal, whereby real

dislocations consist of loops, generally having, pointwise, both edge and screw components.

A Quite General Higher-Order Theoretical Framework

Many SGP theories have been developed in literature. While there exist gradient extensions of both phenomenological and crystal plasticity theories (see, e.g., Gurtin et al. 2010 and references therein), here attention is restricted to phenomenological SGP. Moreover, the focus is on the so-called *higher-order* theories.

> Higher-order (HO) theories postulate the existence of HO stresses (often referred to as microstresses) work-conjugate to appropriate combinations of the components of the plastic distortion gradient, $\nabla\boldsymbol{\gamma}$. Such combinations are then assumed as primal HO kinematic variables, and different choices of them lead to different SGP theories.

HO SGP theories are preferred because they involve HO boundary conditions.

> HO boundary conditions are unconventional boundary conditions governing, in the continuum sense, the behavior of dislocations at the boundary. They include the possibility of imposing that dislocations pile up at the boundary, thus forming boundary layers and triggering a nontrivial gradient response even in boundary value problems whose solution would be spatially homogeneous if predicted by a conventional theory.

HO SGP theories refer to the mechanical response of a body occupying a space region Ω, whose external surface $\partial\Omega$, of outward unit normal $\mathbf{n}_{\partial\Omega}$, consists of two couples of *complementary* parts, such that $\partial\Omega = \partial\Omega_s \cup \partial\Omega_u = \partial\Omega_f \cup \partial\Omega_h$. The conventional tractions $\mathbf{s}^0$ are known on $\partial\Omega_s$, while the displacement $\mathbf{u}^0$ is assigned on $\partial\Omega_u$. *Dislocations are free to exit the body* on $\partial\Omega_f$, while *dislocations are blocked and may pile up* on $\partial\Omega_h$.

Most commonly (Dillon and Kratochvíl 1970; Fleck and Hutchinson 1997, 2001; Huang et al. 2000; Forest and Sievert 2003; Gudmundson 2004; Gurtin 2004; Polizzotto 2009; Fleck and Willis 2009; Gurtin et al. 2010), HO theories are founded on postulating a *generalized Principle of Virtual Work* (PVW), which requires the *appropriate* definitions of the internal and external virtual works on any region Π of Ω. Several HO SGP theories may be derived by assuming that the internal virtual work, under the constraints given by relations (2) and (3), reads

$$\mathscr{W}_i(\Pi, \delta\mathbf{u}, \delta\boldsymbol{\gamma}) = \int_\Pi \Big(\boldsymbol{\sigma} \cdot (\delta\boldsymbol{\varepsilon} - \delta\boldsymbol{\varepsilon}^p) + \boldsymbol{\varsigma} \cdot \delta\boldsymbol{\gamma} + \mathbf{S} \cdot \nabla\delta\boldsymbol{\gamma}\Big) \mathrm{d}V \tag{10}$$

in which $\delta\varepsilon = \dot{\varepsilon}\delta t$ denotes a compatible variation of the kinematic field ε, $\boldsymbol{\sigma}$ is the conventional symmetric Cauchy stress, and the existence is then admitted of the unconventional stresses $\boldsymbol{\varsigma}$ and $\mathbf{S}$ work-conjugate to $\boldsymbol{\gamma}$ and $\nabla\boldsymbol{\gamma}$, respectively. Note that, because of the assumption of isochoric plastic flow, $\mathrm{tr}\boldsymbol{\varsigma} = S_{iij} = 0$.

The external virtual work is then provided by the contributions of the volume density of body forces $\mathbf{b}_\Pi$ and the contact actions on the boundary of Π, $\partial\Pi$, consisting of the two fields $\mathbf{s}$ and $\boldsymbol{\tau}$, conjugate to $\mathbf{u}$ and $\boldsymbol{\gamma}$, respectively:

$$\mathscr{W}_e(\Pi, \delta\mathbf{u}, \delta\boldsymbol{\gamma}) = \int_\Pi \mathbf{b}_\Pi \cdot \delta\mathbf{u}\, \mathrm{d}V + \int_{\partial\Pi} \Big(\mathbf{s} \cdot \delta\mathbf{u} + \boldsymbol{\tau} \cdot \delta\boldsymbol{\gamma}\Big) \mathrm{d}A \tag{11}$$

The generalized PVW equates $\mathscr{W}_i$ and $\mathscr{W}_e$, as defined in Eqs. (10) and (11). By integrating by parts, using the divergence theorem, and resorting to standard arguments of calculus of variations, one obtains the conventional balance equations:

$$\mathrm{div}\boldsymbol{\sigma} + \mathbf{b}_\Pi = \mathbf{0} \ \text{ in } \ \Pi \tag{12}$$

$$\boldsymbol{\sigma}\mathbf{n}_{\partial\Pi} = \mathbf{s} \ \text{ on } \ \partial\Pi \tag{13}$$

supplemented by

$$\mathrm{dev}\boldsymbol{\sigma} - \boldsymbol{\varsigma} + \mathrm{div}\mathbf{S} = \mathbf{0} \text{ in } \Pi \tag{14}$$

$$\mathbf{S}\mathbf{n}_{\partial\Pi} = \boldsymbol{\tau} \text{ on } \partial\Pi \tag{15}$$

These equations are referred to as higher-order balance equations.

An alternative approach to obtain the governing equations for *generalized continua* or, more specifically, for SGP theories has been proposed by Del Piero (2009). It consists of postulating the form of the external virtual work only and, then, resorting to indifference requirements and to the Cauchy tetrahedron theorem. Such a procedure allows one to highlight the different role of Eqs. (12) and (13) with respect to Eqs. (14) and (15), thus suggesting to denote the latter as pseudo-balance equations.

SGP theory can alternatively be founded on the so-called *insulation condition* in a *residual-based theory* (Polizzotto 2009), thus avoiding the generalized PVW at all.

Particularization to a Nye's Tensor-Based SGP and Introduction of Energetic and Dissipative HO Contributions

The following criteria discriminate among different HO SGP theories:

1. the choice of the primal HO kinematic variables (not necessarily the whole $\nabla\boldsymbol{\gamma}$);
2. whether the HO stress is associated with energetic (recoverable) or dissipative (unrecoverable) processes, *or both*.

Here, Nye's dislocation density tensor $\boldsymbol{\alpha}$ is adopted as a primal HO variable because of its physical meaning previously illustrated. However, SGP theories based on different primal HO variables, such as $\nabla\boldsymbol{\varepsilon}^p$ and $\nabla\dot{\boldsymbol{\varepsilon}}^p$, or even the gradient of the second invariant of $\dot{\boldsymbol{\varepsilon}}^p$ (in the effort to develop the simplest HO extension of von Mises plasticity), have been successfully proposed in literature (see, e.g., Aifantis 1984; Zbib and Aifantis 1992; Fleck and Hutchinson 2001; Gudmundson 2004; Fleck and Willis 2009; Fleck et al. 2015 and references therein). Such theories, with respect to that illustrated next (Gurtin 2004; Bardella 2010; Martínez-Pañeda et al. 2016), have the advantage of allowing a simpler implementation.

Here, it is assumed that $\mathbf{S}$ admits the decomposition

$$\mathbf{S} = \mathbf{S}^{(\mathrm{def})} + \mathbf{T}^{(\varepsilon)} \tag{16}$$

in which

$$S^{(\mathrm{def})}_{ijk} = e_{kjh}\zeta_{ih} - \frac{1}{3}\delta_{ij}e_{kph}\zeta_{ph} \tag{17}$$

$$T^{(\varepsilon)}_{ijk} = T^{(\varepsilon)}_{jik} \tag{18}$$

where $\boldsymbol{\zeta}$ is called the *defect stress* and definition (17) ensures that $\boldsymbol{\zeta}$ is work-conjugate to Nye's tensor, while $\mathbf{T}^{(\varepsilon)}$ is work-conjugate to the plastic strain gradient, because of property (18). Now, it is crucial to point out that there is no redundancy in the choice (16), (17), and (18) because $\boldsymbol{\zeta}$ is thought of to be constitutively dependent on the current (total) value of $\boldsymbol{\alpha}$, thus providing an energetic contribution, while $\mathbf{T}^{(\varepsilon)}$ has a dissipative nature, being thought of to be constitutively dependent on the plastic strain gradient *rate*, $\nabla\dot{\boldsymbol{\varepsilon}}^p$. In general, the energetic HO stress describes the long-range effect of GNDs at rest, while the dissipative HO stress aims at capturing the irreversibility inherent to GND motion. In order to generalize the conventional flow theory of plasticity, there must be an unconventional dissipative stress work-conjugate to the plastic strain. Here, $\boldsymbol{\varsigma}$ is totally unrecoverable, being constitutively dependent on $\dot{\boldsymbol{\gamma}}$, as specified later. Adding an energetic stress contribution dependent on $\boldsymbol{\varepsilon}^p$ (Gudmundson 2004) would introduce in the theory the conventional kinematic hardening, here neglected. However, the energetic HO stress leads to a "backstress" causing a HO kinematic hardening. Both dissipative and energetic HO contributions are employed because they can describe quite different size effects.

The dissipative HO contribution models the strengthening, in most cases. The size effect predicted by the energetic HO contribution strongly depends on the specific constitutive law adopted; it may consist of an increase in strain hardening with diminishing size, or strengthening, or a combination of both effects.

Hence, by substituting Eqs. (16), (17), and (18) into Eq. (10), the internal virtual work becomes

$$\mathscr{W}_i(\Pi) = \int_{\Pi} \Big(\underbrace{\boldsymbol{\sigma} \cdot (\delta\boldsymbol{\varepsilon} - \delta\boldsymbol{\varepsilon}^p) + \boldsymbol{\zeta} \cdot \delta\boldsymbol{\alpha}}_{\text{energetic}} + \underbrace{\boldsymbol{\varsigma} \cdot \delta\boldsymbol{\gamma} + \mathbf{T}^{(\varepsilon)} \cdot \delta\nabla\boldsymbol{\varepsilon}^p}_{\text{dissipative}} \Big) \mathrm{d}V$$

The balance equations along with all the boundary conditions *for the whole body* can be obtained by standard analytical manipulation on the generalized PVW.

In the absence of conventional body forces and under quasi-static loading, the conventional balance reads

$$\mathrm{div}\boldsymbol{\sigma} = \mathbf{0} \quad \text{in} \quad \Omega \tag{19}$$

$$\boldsymbol{\sigma}\mathbf{n}_{\partial\Omega} = \mathbf{s}^0 \text{ on } \partial\Omega_s \tag{20}$$

The HO balance equations are conveniently written by separating the symmetric and skew-symmetric parts of Eqs. (14) and (15). Accordingly, $\boldsymbol{\varsigma}$ is split as

$$\boldsymbol{\rho} = \mathrm{sym}\boldsymbol{\varsigma}$$

$$\boldsymbol{\omega} = \mathrm{skw}\boldsymbol{\varsigma}$$

thus obtaining

$$\mathrm{dev}\boldsymbol{\sigma} - \mathrm{sym}[\mathrm{dev}(\mathrm{curl}\boldsymbol{\zeta})] = \boldsymbol{\rho} - \mathrm{div}\mathbf{T}^{(\varepsilon)} \quad \text{in} \quad \Omega \tag{21}$$

$$\boldsymbol{\omega} + \mathrm{skw}(\mathrm{curl}\boldsymbol{\zeta}) = \mathbf{0} \quad \text{in} \quad \Omega \tag{22}$$

with static boundary conditions:

$$\mathbf{T}^{(\varepsilon)}\mathbf{n}_{\partial\Omega} + \mathrm{sym}[\mathrm{dev}(\boldsymbol{\zeta} \times \mathbf{n}_{\partial\Omega})] = \mathbf{0} \quad \text{on} \quad \partial\Omega_f$$

$$\mathrm{skw}(\boldsymbol{\zeta} \times \mathbf{n}_{\partial\Omega}) = \mathbf{0} \quad \text{on} \quad \partial\Omega_f$$

The static HO boundary conditions are homogeneous with the purpose to describe dislocations free to exit the body at $\partial\Omega_f$. They are referred to as *microfree* boundary conditions.

In rate form, the conventional kinematic boundary condition reads

$$\dot{\mathbf{u}} = \dot{\mathbf{u}}^0 \text{ on } \partial\Omega_u$$

Homogeneous HO kinematic boundary conditions are adopted. They are denoted as *microhard* and describe dislocations piling up at the boundary $\partial\Omega_h$.

In the SGP here considered, the form of the microhard conditions depends on whether the dissipative stress $\mathbf{T}^{(\varepsilon)}$ is accounted for or not (note that it can be easily neglected by setting to zero a specific material length scale parameter, as specified later). If $\mathbf{T}^{(\varepsilon)}$ enters the model, the microhard boundary conditions read

$$\dot{\boldsymbol{\varepsilon}}^p = \mathbf{0} \text{ and } \dot{\boldsymbol{\vartheta}}^p \times \mathbf{n}_{\partial\Omega} = \mathbf{0} \text{ on } \partial\Omega_h$$

Otherwise, if $\mathbf{T}^{(\varepsilon)}$ is neglected, one has

$$\dot{\boldsymbol{\gamma}} \times \mathbf{n}_{\partial\Omega} = \mathbf{0} \text{ on } \partial\Omega_h$$

Nonhomogeneous boundary conditions may be adopted to model the behavior of polycrystals' internal grain boundaries, which may become penetrable to (or emit) dislocations when many of them pile up, thus leading to a large internal stress. To this purpose, the jumps of the static and kinematic unconventional variables at the boundary can be constitutively related to the averages of their dual quantities (see, e.g., Gurtin and Needleman 2005; Fleck and Willis 2009; Poh and Peerlings 2016). Such use of the *phenomenological* SGP here concerned relies on findings on its suitability to provide also reasonable estimates of the behaviour of single crystals (Bardella 2009, 2010; Poh and Peerlings 2016).

After substituting the stresses with the kinematic variables through the constitutive laws (as specified next), the HO balance Eqs. (21) and (22) become second-order partial differential equations, representing the yield condition. In particular, in Eq. (21) energetic terms are on the left-hand side in such a way as to highlight the HO backstress contribution given by the defect stress, leading to an unconventional kinematic hardening.

Helmholtz Free Energy Density and Dissipation

The free energy density Ψ depends on both the elastic strain and Nye's tensor:

$$\Psi(\boldsymbol{\varepsilon}-\boldsymbol{\varepsilon}^p,\boldsymbol{\alpha})=\frac{1}{2}\mathbb{L}(\boldsymbol{\varepsilon}-\boldsymbol{\varepsilon}^p)\cdot(\boldsymbol{\varepsilon}-\boldsymbol{\varepsilon}^p)+\mathscr{D}(\boldsymbol{\alpha})$$

in which $\mathbb{L}$ is the elastic stiffness and $\mathscr{D}(\boldsymbol{\alpha})$ is the so-called *defect energy*. Hence, the Cauchy and defect stresses read, respectively

$$\boldsymbol{\sigma}=\mathbb{L}(\boldsymbol{\varepsilon}-\boldsymbol{\varepsilon}^p)$$
$$\boldsymbol{\zeta}=\frac{\partial\Psi}{\partial\boldsymbol{\alpha}}=\frac{\partial\mathscr{D}(\boldsymbol{\alpha})}{\partial\boldsymbol{\alpha}}$$

For dimensional consistency, $\mathscr{D}(\boldsymbol{\alpha})$ must involve at least one material length scale, henceforth referred to as "energetic length scale." The form of the defect energy is of crucial importance for the modeling.

A one-homogeneous defect energy, e.g., $\mathscr{D}(\boldsymbol{\alpha})\propto|\boldsymbol{\alpha}|$, models the strengthening only, while a defect energy quadratic in the whole Nye's tensor, that is, $\mathscr{D}(\boldsymbol{\alpha})\propto|\boldsymbol{\alpha}|^2$, models the increase in strain hardening with diminishing size only, with the energetic length scale governing the boundary layers' thickness.

The dissipation depends on the following phenomenological effective plastic flow rate extending the definition characterizing conventional von Mises plasticity:

$$\dot{E}^p=\sqrt{\frac{2}{3}|\dot{\boldsymbol{\varepsilon}}^p|^2+\chi|\dot{\boldsymbol{\vartheta}}^p|^2+\frac{2}{3}L^2|\nabla\dot{\boldsymbol{\varepsilon}}^p|^2} \quad (23)$$

in which χ is the material constant governing the dissipation due to the plastic spin and L is a "dissipative" material length scale parameter. $\dot{E}^p$ is work conjugate to the effective flow resistance

$$\Sigma=\sqrt{\frac{3}{2}|\boldsymbol{\rho}|^2+\frac{1}{\chi}|\boldsymbol{\omega}|^2+\frac{3}{2L^2}|\mathbf{T}^{(\varepsilon)}|^2} \quad (24)$$

under the following definitions for the unrecoverable stresses:

$$\boldsymbol{\rho}=\frac{2}{3}\frac{\Sigma}{\dot{E}^p}\dot{\boldsymbol{\varepsilon}}^p \quad (25)$$

$$\boldsymbol{\omega}=\chi\frac{\Sigma}{\dot{E}^p}\dot{\boldsymbol{\vartheta}}^p \quad (26)$$

$$\mathbf{T}^{(\varepsilon)}=\frac{2}{3}L^2\frac{\Sigma}{\dot{E}^p}\nabla\dot{\boldsymbol{\varepsilon}}^p \quad (27)$$

This ensures satisfaction of the second law of thermodynamics:

$$\boldsymbol{\rho}\cdot\dot{\boldsymbol{\varepsilon}}^p+\boldsymbol{\omega}\cdot\dot{\boldsymbol{\vartheta}}^p+\mathbf{T}^{(\varepsilon)}\cdot\nabla\dot{\boldsymbol{\varepsilon}}^p\equiv\Sigma\dot{E}^p>0\quad\forall\,\dot{\boldsymbol{\gamma}}\neq\mathbf{0} \quad (28)$$

The effective flow resistance is, in general, a function of both $\dot{E}^p$ and E^p, the latter dependence governing the isotropic hardening.

While the strengthening is physically related to the very small amount of plasticity occurring

at about the end of what is experimentally recognized as the elastic regime, mathematically, it has been demonstrated that, in the rate-independent case with $\chi = 0$ and in the absence of HO energetic contribution, the constitutive laws (24), (25), (26), and (27) lead to (dissipative) strengthening associated with the loss of stability of the purely elastic state (Chiricotto et al. 2016). Here a viscoplasticity framework is adopted, by properly specifying the dependence of Σ on $\dot{E}^p$. This allows plasticity to develop at any stress level such that there is no need to implement any yield criterion nor special treatment for the internal evolving boundaries between elastic and plastic regions, the latter being an issue in rate-independent formulations (see, e.g., Fleck and Willis 2009; Nielsen and Niordson 2014 and references therein). The effective flow stress is directly given in the form:

$$\Sigma(\dot{E}^p, E^p) = \sigma_Y(E^p) V(\dot{E}^p)$$

in which $\sigma_Y(E^p)$ is the isotropic hardening law. The following regularization of a unit step function, admitting convex potential, is adopted for $V(\dot{E}^p)$, as it allows one to obtain results that are substantially rate-independent, along with computational efficiency (Panteghini and Bardella 2016):

$$V(\dot{E}^p) = \begin{cases} \dfrac{\dot{E}^p}{2\dot{\varepsilon}_0} & \text{if } \dfrac{\dot{E}^p}{\dot{\varepsilon}_0} \le 1 \\ 1 - \dfrac{1}{2}\dfrac{\dot{\varepsilon}_0}{\dot{E}^p} & \text{if } \dfrac{\dot{E}^p}{\dot{\varepsilon}_0} > 1 \end{cases}$$

in which $\dot{\varepsilon}_0$ is a positive material parameter. Rate independence is obtained for $\dot{\varepsilon}_0 \to 0$; by suitably approaching this limit, an elastic domain can be numerically observed.

Minimum Principles

Under the assumption that the following dissipation potential exists and is convex in $\dot{E}^p$

$$\mathscr{V}(\dot{E}^p, E^p) = \int_0^{\dot{E}^p} \Sigma(e, E^p) \mathrm{d}e$$

along with a convex defect energy, the following minimum principles, useful for computational purposes, hold (Martínez-Pañeda et al. 2016). Under the kinematic constraints (3), (8), and (23), the field $\dot{\boldsymbol{\gamma}}$ minimizing the functional

$$\mathscr{H}(\dot{\boldsymbol{\gamma}}) = \int_\Omega \left[\mathscr{V}(\dot{E}^p, E^p) + \boldsymbol{\zeta} \cdot \dot{\boldsymbol{\alpha}} - \boldsymbol{\sigma} \cdot \dot{\boldsymbol{\varepsilon}}^p\right] \mathrm{d}V \tag{29}$$

satisfies the HO balance Eqs. (21) and (22).

Moreover, for a given $\dot{\boldsymbol{\varepsilon}}^p$, the conventional balance Eqs. (19) and (20) are satisfied by any kinematically admissible field $\dot{\mathbf{u}}$ minimizing the functional

$$\mathscr{J}(\dot{\mathbf{u}}) = \frac{1}{2}\int_\Omega \mathbb{L}\left(\mathrm{sym}\nabla\dot{\mathbf{u}} - \dot{\boldsymbol{\varepsilon}}^p\right) \cdot \left(\mathrm{sym}\nabla\dot{\mathbf{u}} - \dot{\boldsymbol{\varepsilon}}^p\right) \mathrm{d}V - \int_{\partial\Omega_s} \dot{\mathbf{s}}^0 \cdot \dot{\mathbf{u}} \, \mathrm{d}A \tag{30}$$

Minimum principles (29) and (30) extend to the present theory those developed by Fleck and Willis (2009) for a SGP theory adopting the plastic strain gradient as HO primal variable for both the energetic and dissipative contributions.

Example of Application: The Torsion of Thin Metal Wires

The torsion of thin metal wires is an emblematic benchmark for the behavior that SGP aims at modeling. Here, the experimental results of Fleck et al. (1994) are considered.

The wires are constituted by polycrystalline copper and are modeled as homogeneous and isotropic cylinders with circular cross section of radius a. Hence, in cylindrical coordinates, with r, θ, and z denoting, respectively, the radial coordinate, the circumferential coordinate, and the axis of torsion, the displacement field must read

$$u_\theta = \kappa z r$$
$$u_r = u_z = 0$$

where κ is the applied twist. $\sigma_{\theta z}$ is the sole nonvanishing Cauchy stress component, providing the torque T through

$$T = 2\pi \int_0^a \sigma_{\theta z}\, r^2 \mathrm{d}r$$

The sole nonvanishing components of $\boldsymbol{\gamma}$ and $\boldsymbol{\alpha}$ are $\varepsilon^p_{\theta z}(r)$, $\vartheta^p_{\theta z}(r) = -\vartheta^p_{z\theta}(r)$, and

$$\alpha_{rr} = -\frac{\varepsilon^p_{\theta z} + \vartheta^p_{\theta z}}{r}$$
$$\alpha_{\theta\theta} = -\frac{\mathrm{d}\varepsilon^p_{\theta z}}{\mathrm{d}r} - \frac{\mathrm{d}\vartheta^p_{\theta z}}{\mathrm{d}r}$$
$$\alpha_{zz} = \frac{\varepsilon^p_{\theta z} - \vartheta^p_{\theta z}}{r} + \frac{\mathrm{d}\varepsilon^p_{\theta z}}{\mathrm{d}r} - \frac{\mathrm{d}\vartheta^p_{\theta z}}{\mathrm{d}r}$$

All these components represent densities of pure screw dislocations and suggest to include in the defect energy a dependence on the invariant $\mathrm{tr}\boldsymbol{\alpha}$, which is a function of the plastic spin only, along with the essential dependence on $|\mathrm{dev}\boldsymbol{\alpha}|$.

The following regularization of the defect energy proposed by Forest and Guéninchault (2013) is considered (see also Groma et al. 2007; Svendsen and Bargmann 2010):

$$\mathscr{D}(\boldsymbol{\alpha}) = \mu\ell_1|\mathrm{tr}\boldsymbol{\alpha}| \ln\left(\frac{\ell_1|\mathrm{tr}\boldsymbol{\alpha}|}{\alpha_1} + 1\right) + \mu\ell_2|\mathrm{dev}\boldsymbol{\alpha}| \ln\left(\frac{\ell_2|\mathrm{dev}\boldsymbol{\alpha}|}{\alpha_2} + 1\right) \quad (31)$$

with ℓ_1 and ℓ_2 denoting independent energetic material length scales and α_1 and α_2 further positive material parameters.

A power law is adopted for the isotropic hardening:

$$\sigma_Y(E^p) = \sigma_0 + H(E^p)^{N_h}$$

in which σ_0 is the initial yield stress and H and N_h are nonnegative material parameters.

In the torsion problem, dislocations pile up at the wire center, where $\varepsilon^p_{\theta z}(0) = \vartheta^p_{\theta z}(0) = 0$, while they are free to exit the wire at $r = a$, where microfree conditions are imposed. The results reported next have been obtained by Bardella and Panteghini (2015) by an ad hoc implicit finite element implementation of this problem.

Figure 2 shows the comparison between the experimental results and the theoretical predictions, in terms of the normalized torque T/a^3 as a function of the nondimensional twist κa, that is, the maximum deformation experienced by the wire for a given κ. If there were no size effects, the theoretical curves in Fig. 2 would superimpose exactly, as well as the experimental ones in the absence of uncertainty and fluctuations. Even by neglecting the HO dissipation (i.e., by setting $L = 0$) and without resorting to any specific identification procedure, the following material parameters lead to a quite good prediction of the experimentally observed size effect: shear modulus $\mu = 45\,\mathrm{GPa}$, $\sigma_0 = 68\,\mathrm{MPa}$, $H = 150\,\mathrm{MPa}$, $N_h = 0.37$, $\dot{\varepsilon}_0 = 1.\mathrm{E}\text{-}5\,\mathrm{s}^{-1}$, $\ell_1 = 2.1\mathrm{E}\text{-}4\,\mu\mathrm{m}$, $\ell_2 = 2.1\mathrm{E}\text{-}3\,\mu\mathrm{m}$, $\alpha_1 \approx 2.8571\mathrm{E}\text{-}4$, and $\alpha_2 \approx 5.7143\mathrm{E}\text{-}3$, $\chi = 2/3$. Note that a finite deformation framework would be more appropriate in order to predict the experimental results reported in Fig. 2.

Open Problems

Predictions Under Nonproportional Loading in the Presence of HO Dissipative Contributions

The SGP here considered is of the *non-incremental* type, in the terminology of Fleck et al. (2014), referring to the constitutive laws governing the dissipation. In fact, in non-incremental theories, a *finite* HO stress is constitutively related to the *rate* of the chosen primal HO kinematic variable. In this case, rate-independent SGP may lead to an incremental purely elastic response, referred to as "elastic gap," when changing the loading direction after having conspicuously developed plasticity under proportional loading (Fleck et al. 2014, 2015; Bardella and Panteghini 2015; Fleck and Willis 2015; Carstensen et al. 2017). Whether this is a physical behavior or not should be discerned by suitable experiments. Non-incremental SGP theories are employed because their framework makes it easy to satisfy the second law of thermodynamics, as in Eq. (28).

In *incremental* SGP theories (see, e.g., Fleck and Hutchinson 2001), instead, the *rate* of the HO

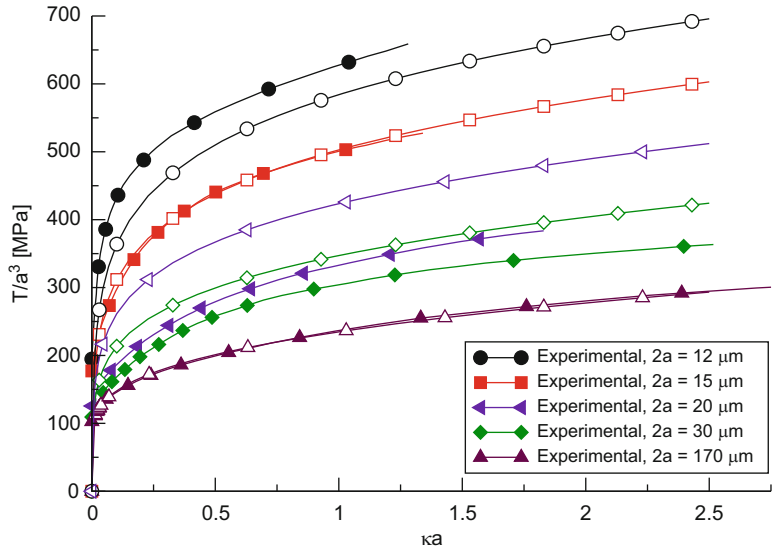

Fig. 2 Comparison with the experimental results of Fleck et al. (1994); void symbols represent the theoretical results (Figure adapted from Bardella and Panteghini 2015)

dissipative stress is constitutively related to the chosen primal HO kinematic variable. This class of theories is, on the one hand, free from "elastic gap" under nonproportional loading (Fleck et al. 2014). On the other hand, in such theories, it is difficult to ensure the satisfaction of the second law of thermodynamics for arbitrary loading history (Gudmundson 2004; Gurtin and Anand 2009; Fleck et al. 2015).

Cyclic Behavior Utilizing a Defect Energy that Predicts Strengthening

By referring to $\boldsymbol{\alpha}$ as primal HO variable, a defect energy allowing the prediction of conspicuous (energetic) strengthening has to be such that at very low $|\boldsymbol{\alpha}|$ a small increase of $|\boldsymbol{\alpha}|$ provides a large increase of $|\boldsymbol{\zeta}|$ and, then, a much slower increase of $|\boldsymbol{\zeta}|$ with $|\boldsymbol{\alpha}|$ for larger values of $|\boldsymbol{\alpha}|$. This is the case of the logarithmic form (31) or, at the largest extent, of the one-homogeneous form $\mathscr{D} = \ell\mu|\boldsymbol{\alpha}|$. Under cyclic loading, this turns out in a stress-strain curve that becomes concave at a certain point after inverting the load. This has been explained by resorting to the observation that the last dislocation piling up is the first leaving the pileup when inverting the load. Even though this explanation is perfectly appropriate for strain gradient crystal plasticity under single slip (Wulfinghoff et al. 2015), there is the need of further investigations in multislip and, most of all, in polycrystalline plasticity.

Cross-References

- Dislocations and Cracks in Generalized Continua
- Micromorphic Approach to Materials with Internal Length
- Nonlocal Theories

References

Aifantis EC (1984) On the microstructural origin of certain inelastic models. J Eng Mater Tech-T ASME 106:326–330

Arsenlis A, Parks DM (1999) Crystallographic aspects of geometrically-necessary and statistically-stored dislocation density. Acta Mater 47:1597–1611

Ashby MF (1970) The deformation of plastically non-homogeneous materials. Philos Mag 21:399–424

Bardella L (2009) A comparison between crystal and isotropic strain gradient plasticity theories with accent on the role of the plastic spin. Eur J Mech A-Solid 28:638–646

Bardella L (2010) Size effects in phenomenological strain gradient plasticity constitutively involving the plastic spin. Int J Eng Sci 48:550–568

Bardella L, Panteghini A (2015) Modelling the torsion of thin metal wires by distortion gradient plasticity. J Mech Phys Solids 78:467–492

Burgers JM (1939) Some considerations of the field of stress connected with dislocations in a regular crystal lattice. K Ned Akad Van Wet 42:293–325 (Part 1), 378–399 (Part 2)

Carstensen C, Ebobisse F, McBride AT, Reddy BD, Steinmann P (2017) Some properties of the dissipative model of strain-gradient plasticity. Philos Mag 97: 693–717

Chiricotto M, Giacometti L, Tomassetti G (2016) Dissipative scale effects in strain-gradient plasticity: the case of simple shear. SIAM J Appl Math 76: 688–704

Del Piero G (2009) On the method of virtual power in continuum mechanics. J Mech Mater Struct 4:281–292

Dillon OW J, Kratochvíl J (1970) A strain gradient theory of plasticity. Int J Solids Struct 6:1513–1533

Fleck NA, Hutchinson JW (1997) Strain gradient plasticity. Adv Appl Mech 33:295–361

Fleck NA, Hutchinson JW (2001) A reformulation of strain gradient plasticity. J Mech Phys Solids 49:2245–2271

Fleck NA, Willis JR (2009) A mathematical basis for strain-gradient plasticity theory. Part II: tensorial plastic multiplier. J Mech Phys Solids 57:1045–1057

Fleck NA, Willis JR (2015) Strain gradient plasticity: energetic or dissipative? Acta Mech Sinica 31: 465–472

Fleck NA, Muller GM, Ashby MF, Hutchinson JW (1994) Strain gradient plasticity: theory and experiments. Acta Metall Mater 42:475–487

Fleck NA, Hutchinson JW, Willis JR (2014) Strain gradient plasticity under non-proportional loading. Proc R Soc Lond A 470:20140267

Fleck NA, Hutchinson JW, Willis JR (2015) Guidelines for constructing strain gradient plasticity theories. J Appl Mech-T ASME 82:1–10

Forest S, Guéninchault N (2013) Inspection of free energy functions in gradient crystal plasticity. Acta Mech Sinica 29:763–772

Forest S, Sievert R (2003) Elastoviscoplastic constitutive frameworks for generalized continua. Acta Mech 160:71–111

Groma I, Györgyi G, Kocsis B (2007) Dynamics of coarse grained dislocation densities from an effective free energy. Philos Mag 87:1185–1199

Gudmundson P (2004) A unified treatment of strain gradient plasticity. J Mech Phys Solids 52:1379–1406

Gurtin ME (2004) A gradient theory of small-deformation isotropic plasticity that accounts for the Burgers vector and for dissipation due to plastic spin. J Mech Phys Solids 52:2545–2568

Gurtin ME, Anand L (2009) Thermodynamics applied to gradient theories involving the accumulated plastic strain: the theories of Aifantis and Fleck & Hutchinson and their generalization. J Mech Phys Solids 57: 405–421

Gurtin ME, Needleman A (2005) Boundary conditions in small-deformation, single-crystal plasticity that account for the Burgers vector. J Mech Phys Solids 53: 1–31

Gurtin ME, Fried E, Anand L (2010) The mechanics and thermodynamics of continua. Cambridge University Press, Cambridge

Hall EO (1951) The deformation and ageing of mild steel: III discussion of results. Proc Phys Soc B 64: 747–753

Hayden W, Moffatt WG, Wulff J (1965) The structure and properties of materials: vol III, mechanical behavior. Wiley, New York

Huang Y, Gao H, Nix WD, Hutchinson JW (2000) Mechanism-based strain gradient plasticity – II. Analysis. J Mech Phys Solids 48:99–128

Hull D, Bacon DJ (2001) Introduction to dislocations, 4th edn. Butterworth-Heinemann, Oxford

Kröner E (1962) Dislocations and continuum mechanics. Appl Mech Rev 15:599–606

Ma Q, Clarke DR (1995) Size dependent hardness in silver single crystals. J Mater Res 10:853–863

Martínez-Pañeda E, Niordson CF, Bardella L (2016) A finite element framework for distortion gradient plasticity with applications to bending of thin foils. Int J Solids Struct 96:288–299

Nielsen KL, Niordson CF (2014) A numerical basis for strain-gradient plasticity theory: rate-independent and rate-dependent formulations. J Mech Phys Solids 63:113–127

Nye JF (1953) Some geometrical relations in dislocated crystals. Acta Metall 1:153–162

Panteghini A, Bardella L (2016) On the finite element implementation of higher-order gradient plasticity, with focus on theories based on plastic distortion incompatibility. Comput Method Appl M 310: 840–865

Petch NJ (1953) The cleavage strength of polycrystals. J Iron Steel Inst 174:25–28

Poh LH, Peerlings RHJ (2016) The plastic rotation effect in an isotropic gradient plasticity model for applications at the meso scale. Int J Solids Struct 78–79: 57–69

Polizzotto C (2009) A link between the residual-based gradient plasticity theory and the analogous theories based on the virtual work principle. Int J Plasticity 25:2169–2180

Stölken JS, Evans AG (1998) A microbend test method for measuring the plasticity length scale. Acta Mater 46:5109–5115

Svendsen B, Bargmann S (2010) On the continuum thermodynamic rate variational formulation of models for extended crystal plasticity at large deformation. J Mech Phys Solids 58:1253–1271

Valdevit L, Hutchinson JW (2012) Plasticity theory at small scales. In: Bhushan B (ed) Encyclopedia of nanotechnology. Springer, Dordrecht, pp 3319–3327

Wulfinghoff S, Forest S, Böhlke T (2015) Strain gradient plasticity modelling of the cyclic behaviour of laminate microstructures. J Mech Phys Solids 79: 1–20

Zbib HM, Aifantis EC (1992) On the gradient-dependent theory of plasticity and shear banding. Acta Mech 92:209–225

Strain Gradient Theory

▸ Coleman-Noll Procedure for Classical and Generalized Continuum Theories

Strain Rate Intensity Factor

▸ Singular Solutions in Plane Strain Plasticity

Strains

▸ Kinematics

Stress

▸ Planar Problems in Rigid-Plasticity for Granular Materials and Soils

Stress Constraint

▸ Stress-Constrained Topology Optimization for Lattice Materials

Stress Intensity Factor

▸ Dynamical Contact Problems of Fracture Mechanics
▸ Fracture Mechanics of Composites

Stress Power

▸ Principles of Material Modeling

Stress Relaxation = Stress Release = Total or Partial Restoration of Unstressed State

▸ Nanomechanics of Stress Relaxation in Composite Low-Dimensional Structures

Stress Shielding

▸ Modeling of Bone Adaption Processes

Stress Tensor

▸ Continuous-Molecular Approach to Modeling of Nanostructures

Stress Tensor in Compressible Flows

▸ Kinetic Theory and Thermodynamics, Non-equilibrium Reacting Gas Flows

Stress-Constrained Topology Optimization for Lattice Materials

Damiano Pasini, Ahmed Moussa, and Amirmohammad Rahimizadeh
Department of Mechanical Engineering, McGill University, Montreal, QC, Canada

Synonyms

Cellular materials; Homogenization; Stress constraint; Topology optimization

Definition

In the context of architected materials, *cellular solids* indicate porous materials with cells that fill the space in either two or three dimensions, such as in foams. A lattice material is a subclass of them, where order governs cell arrangement and solid struts form a reticulated framework of cells, such as in a truss-system. *Homogenization* is a mathematical theory for materials with periodic or quasi-periodic microstructures, made of two or more constituent solids, such as in a composite, or by a single material with voids, such as in a cellular solid. Homogenization treats a periodic material as homogenized medium with effective properties calculated from a limited portion of it, the Representative Volume Element. *Topology optimization* is a structural optimization method that enables optimal material distribution within a given domain, subject to volume and possibly other constraints, under a prescribed set of loads and boundary conditions. Given topology optimization often leads to structures with high stress concentrations or even stress singularities, imposing stress-constraints is essential to delocalize stress peak and reduce the global stress level. This entry proposes a scheme to do so for lattice materials.

Introduction

Structural optimization has demonstrated remarkable success in creating lightweight structures that appeal the industry for their material saving (Cheng and Guo 1997; Holmberg et al. 2013). Structural optimization problems can be broken into four main categories: sizing, material, shape, and topology optimization. The differences between them mainly depend on the definition of the design variables, the parameters that can be changed during the optimization process (Bendsøe and Sigmund 2003; Sigmund 2000). In topology optimization, the main goal is to find the optimal material distribution in a given domain, subject to volume and possibly other constraints, under a given set of loads and boundary conditions (Bendsøe and Kikuchi 1988; Bendsøe and Sigmund 2003; Holmberg et al. 2013; Sigmund 2000). In other words, the goal is to find which elements are filled with material and which should be void, so as to minimize one or more objective function(s). In the traditional formulation of topology optimization ((Andreassen et al. 2011; Bendsøe and Sigmund 2003; Sigmund 2001) among others), one typical objective is structural compliance, which is typically minimized for a prescribed amount of volume fraction of material (Bendsøe and Sigmund 2003; Holmberg et al. 2013). This formulation has been adopted in a large range of benchmark problems, from the classical Messerschmidt–Bölkow–Blohm (MBB) beam, fixed beam, to others with more complex geometry commonly used, for example, in MEMS for compliant mechanism design (Andreassen et al. 2011; De Leon et al. 2015; Sigmund 1997, 2001).

Satisfying stress requirement is often paramount in topology optimization, and failing to do so often results in a material distribution with low durability and localized stress (Yang and Chen 1996). Including stress constraints into an optimization problem often requires to handle three issues (Bendsøe and Sigmund 2003). The first is associated with the problem singularity resulting from design variables approaching zero (Cheng and Jiang 1992; Cheng and Guo 1997; Le et al. 2010; Rozvany 2001), the second with the local nature of stress constraints (Le et al. 2010; Yang and Chen 1996), and the third with the highly nonlinear dependence of the stress on the design. While the second issue has direct impact onto the computational cost, the third often affects the convergence of the solution (Le et al. 2010; Yang and Chen 1996). Despite these challenges, the need to include stress constraints in topology optimization emerges from the seminal work of (Bendsøe and Kikuchi 1988), who in discussing their importance paved the way to subsequent methods handling local stress constraints (Cheng and Jiang 1992; Da Silva et al. 2018; De Leon et al. 2015; Duysinx and Bendsøe 1998; Holmberg et al. 2013; Le et al. 2010, Lee et al. 2012; Verbart et al. 2017;

Yang and Chen 1996). For example, Cheng et al. (Cheng and Guo 1997) proposed a relaxation technique to solve the singularity problem that appears with stress constraints. Duysinx and Bendsøe (1998) also presented two relevant stress criteria for porous composites to solve large-scale topology problems with local stress constraints. Their findings attest the relation between the number of local stress constraints and the computation cost; the higher the former, the larger the latter. Duysinx and Sigmund (1998) introduced a global stress measure that uses the well-known p-norm of the von Mises effective stress, where all stresses are grouped into one stress constraint, with the goal of reducing the computational time. While effective compared to the local constraint method (Holmberg et al. 2013), low control of the local stress was reported and in some cases the issue was prominent. To address this problem, stress clustering techniques were introduced to find a better tradeoff between the local stress control and the computational cost (Holmberg et al. 2013; Le et al. 2010; París et al. 2010). With these techniques, the elements are grouped into clusters and one stress constraint is applied to each cluster. The result is a reduction of the number of constraints as compared to a local constraint approach, with a retainment on the control of the stress behavior (Holmberg et al. 2013).

Besides solid materials, also cellular solids (Gibson and Ashby 1988) have been optimized via topology optimization. In this case, the need to handle stress constraints is even more acute because stress peaks typically accrue at the nodes where struts converge. For example, Seepersad et al. (2006) presented a robust approach to design cellular materials that account for imperfections at the connections between cells, as well as for wall thickness variations. Recently, Yingjun et al. (Wang et al. 2017) have proposed a multi-scale isogeometric topology optimization for 2D periodic lattice materials and compared its computational cost with the density-based topology optimization method. Both studies overlooked the influence of stress constraints on the material distributions and stress levels within the lattice domain. Generally, due to manufacturing errors in the connectivity among cells and wall thickness variations, lattice materials often feature abrupt changes in their structural geometry that lead to stress peaks, a detrimental issue not fully elucidated. These errors promote local failure of the lattice struts, which in turn might yield to catastrophic collapse of the macrostructure.

In topology optimization, the inclusion of stress constraints has not been tackled for lattice materials with alternative cell topologies. This chapter presents a scheme for handling stress constraints in density-based topology optimization of 2D graded lattices. The methodology is applied to two well-known benchmark problems in topology optimization: the MBB-beam and the fixed-beam, with the objective function of minimizing compliance. The structure is assumed as porous with a periodic tessellation of the unit cell, here selected a priori from a set of two candidate topologies. Asymptotic homogenization (Wang et al. 2017) is used to computationally characterize the mechanical properties of the representative volume element (RVE) as a function of its relative density. The clustering technique is used to segregate the stresses of all unit cells into groups using the modified p-norm. To address the effect of considering stress constraints and cell topology on the final design, the stress constrained formulation is then compared with the classical formulation with unconstrained stress. In the next section of this chapter, the methodology to calculate the effective properties of the lattice unit cells is presented, and the problem formulation is given for both stress constrained and classical topology optimization. In addition, the filtering method used, stress constraints handling, and sensitivity calculations are presented. The results are given for the optimized relative density and von Mises stress distributions, and a comparison is put forward for both stress constrained and classical formulations.

Methodology

This work studies the effect of including stress constraints in the problem formulation

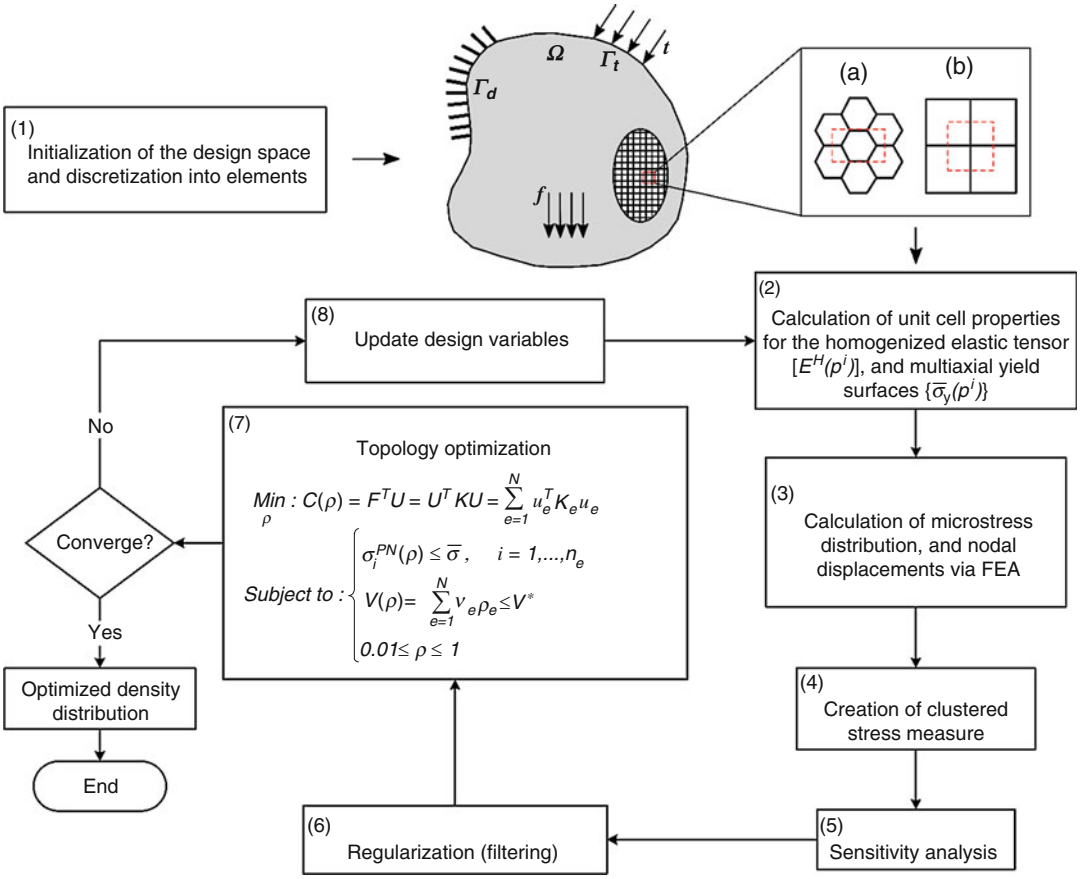

Fig. 1 Flow chart illustrating the design scheme used to optimally grade a cellular domain with predefined cell topologies under stress-constraints

of topology optimization for lattice materials. Figure 1 briefly depicts the scheme here presented, where the key steps rely on combining multiscale mechanics of lattice materials and stress-constrained density-based topology optimization, as summarized below:

- *Initialization of the design space.* The design domain Ω is constructed and discretized into mesh elements. Each element represents a unit cell that makes up the lattice domain.
- *Characterization of unit cell topology*. Two unit cells are selected a priori with topology of prescribed symmetry (Fig. 1a, b): The hexagon yielding isotropic in plane properties, and the square with orthogonal-isotropy. Asymptotic homogenization (AH) (Arabnejad and Pasini 2013; Wang et al. 2017) is used to calculate their effective elastic and yield properties (see Fig. 2), as a function of relative density ρ. The design variable is initially uniformly distributed within the porous domain.
- *Finite element model.* Finite element analysis (FEA) is used to solve the boundary value problem under given loads and boundary conditions (Fig. 1), a traction t at the traction boundary Γ_t, a displacement d at the displacement boundary Γ_d, and a body force f.
- *Topology optimization with clustered stress constraints*. A density-based topology optimization is implemented to find the optimized relative density distribution that minimizes compliance. The Method of Moving Asymptotes (MMA) updates the design variables ρ (Svanberg 1987), which

S

are then filtered by means of the density filter (Bruns and Tortorelli 2001). In addition to constraining the total amount of material relative density, the von Mises stress is restrained in the problem formulation and a clustering method is used for the purpose (see "Stress Constraints" section). The displacements at each node of a mesh element along with the homogenized properties of the unit cell are first retrieved to build the global stiffness tensor, followed by the calculation of the gradients of the objective function, through the partial derivative of the stiffness tensor with respect to its relative density (see section, "Appendix: Sensitivity Calculation of the Stiffness Tensor of the Lattice"), and constraints ("Sensitivity Analysis" section). The optimization process continues until convergence is reached, i.e., the attainment of the optimized relative density distribution that achieves the objective and satisfies the constraints.

Mechanical Properties of Lattice Materials

A fully detailed simulation of a porous domain requires the explicit modeling of all its microstructural features, a process that can be expensive and time-consuming (Arabnejad and Pasini 2013). Here instead, the porous structure is treated as a homogenized medium, whose effective elastic properties are obtained from the Representative Volume Element (RVE). In this study, two planar topologies are selected for the unit cell (see Fig. 1a, b), and AH (Hassani and Hinton 1998) is used to calculate their elastic properties as a function of relative density as described below.

RVE Elastic Properties

The basic assumption of AH theory is that each field quantity depends on two different scales: one at the macroscopic (global) level x and the other at the microscopic (local) level, $y = x/\eta$, with η being a magnification factor that scales the dimensions of the unit cell to the dimensions of the macroscopic domain. Field quantities, such as displacement, stress, and strain, are assumed to vary smoothly at the global level and are periodic at the microscale (Hassani and Hinton 1998). AH assumes that each physical field, such as the displacement field, u_i^η, in a porous elastic body, can be expanded into a power series with respect to η:

$$\begin{aligned} u_i^\eta(x_i, y_i) &= u_{0i}(x_i, y_i) + \eta u_{1i}(x_i, y_i) \\ &\quad + \eta^2 u_{2i}(x_i, y_i) + \ldots \qquad ; y_i = \frac{x_i}{\eta} \end{aligned} \tag{1}$$

where u_i^η is the exact value of the field variable and u_{0i} is the macroscopic (average) value of the field variable. u_{1i}, u_{2i} are perturbations in the field variables caused by the periodic arrangement of the units, x_i are the global level coordinates, and y_i are the micro level coordinates. With this approach, the effective stress tensor $\overline{\sigma}_{ij}$ of the unit cell can be written as a function of the average strain tensor $\overline{\varepsilon}_{kl}$ through the effective elastic tensor E^H_{ijkl} as:

$$\overline{\sigma}_{ij} = E^H_{ijkl}\overline{\varepsilon}_{kl} \tag{2}$$

Considering only first order terms in Eq. (1), the effective stiffness tensor of the building block E^H_{ijkl} can be obtained by solving a local problem formulated on the RVE with expression given by:

$$E^H_{ijkl} = \frac{1}{|Y|}\int_{Y_s} E_{ijpm} M_{pmkl} dY \tag{3}$$

where $|Y|$ is the total volume of the unit cell (including voids), Y_s is the solid part of the unit cell, and E_{ijpm} is the local elasticity tensor, which equals the elasticity tensor of the material in the solid domain of the cell and equals to zero for the void domain. In addition, the local structure tensor M_{ijkl} relating the macroscopic average strain $\overline{\varepsilon}_{kl}$ to the microscopic strain ε_{ij} is introduced as:

$$\begin{aligned} \varepsilon_{ij} &= M_{ijkl}\overline{\varepsilon}_{kl}, M_{ijkl} \\ &= \frac{1}{2}\left(\delta_{ik}\delta_{jl} + \delta_{il}\delta_{jk}\right) - \varepsilon^{*kl}_{ij} \end{aligned} \tag{4}$$

where δ_{ij} is the Kronecker delta, and ε_{ij}^{*kl} is the microscopic strain corresponding to the component kl of the macroscopic strain tensor $\overline{\varepsilon}_{kl}$. Under the assumption of small deformation and linear elasticity, the microstructural strain ε_{ij}^{*kl} is obtained by solving a local problem defined on the RVE (Guedes and Kikuchi 1990; Hollister and Kikuchi 1992):

$$\int_{Y_s} E_{ijpm}\varepsilon_{ij}^{1}(v)\varepsilon_{pm}^{*kl}(u)\,dY = \int_{Y_s} E_{ijkl}\varepsilon_{ij}^{1}(v)\overline{\varepsilon}_{kl}\,dY \tag{5}$$

where $\varepsilon_{ij}^{1}(v)$ is the virtual strain. In two dimensions, three arbitrary unit strains are required to construct the local structure tensor M_{ijkl}. Knowing that the periodicity of the strain field quantities at the microscale is ensured by applying periodic boundary conditions on the edges of the RVE, the nodal displacements on the opposite edges are equal (Hassani 1996; Hollister and Kikuchi 1992). Once the local structure tensor, M_{ijkl}, is obtained, the homogenized stiffness tensor, E_{ijkl}^{H}, of the unite cell is calculated by substituting the structure tensor into (3) (Arabnejad and Pasini 2012; Hollister and Kikuchi 1992). Since the planes of symmetry existing in a unit cell control the type of anisotropy of a lattice, this work examines two representative types of symmetry that yield isotropic (hexagon) and orthogonal-isotropic (square) properties. The detailed expressions of these terms can be found in the literature (Wang et al. 2017). The microscopic stress distribution can be defined by:

$$\sigma_{ij} = E_{ijkl}M_{klmn}\overline{\varepsilon}_{mn} \tag{6}$$

Using the microscopic stress tensor (6), and substituting $\overline{\varepsilon}_{kl}$ with the effective stress tensor $\overline{\sigma}_{ij}$ and the homogenized elastic tensor, E_{ijkl}^{H}, in (2) yields a simplified relationship between the microscopic stress distribution and the macroscopic stress tensor:

$$\sigma_{ij} = E_{ijkl}M_{klmn}\left(E_{rsmn}^{H}\right)^{-1}\overline{\sigma}_{rs} \tag{7}$$

wherein the $\overline{\sigma}_{rs}$ is the macroscopic stress distribution through the lattice unit cell. By considering the yield strength of the cell walls σ_{ys} and (7), the yield surface of the unit cell can be written as:

$$\overline{\sigma}_{ij}^{y} = \frac{\sigma_{ys}}{\max\left\{\sigma_{\mathrm{vM}}\left(\overline{\sigma}_{ij}\right)\right\}}\overline{\sigma}_{ij} \tag{8}$$

where the $\sigma_{\mathrm{vM}}\left(\overline{\sigma}_{ij}\right)$ is the von-Mises stress distribution within the unit cell domain corresponding to the macroscopic stress $\overline{\sigma}_{ij}$.

The procedure described above is applied to obtain the effective 2D elastic properties and yield strengths, with the assumption of beam/rod elements for the cell walls (Arabnejad and Pasini 2013), of the unit cell topologies examined in this work (Fig. 1a, b). Figure 2a, b shows their effective elastic moduli normalized with the bulk properties of the constituent solid (Young's modulus E_s, and Poisson's ratio υ_s) and expressed as a function of relative density ρ. Obtained via AH, E_{ii}, G_{ij}, and ν_{ij} are the 2D effective elastic moduli, shear moduli, and Poisson's ratios of a given lattice. As shown later in the "Numerical examples and discussion" section, the specific symmetry and set of elastic properties of a given unit cell has an impact on the optimized distribution of relative density. Figure 2c, d illustrates their predicted yield strengths, all normalized with the yield strength, σ_{ys}, of the solid material, and expressed as a function of relative density ρ. The yield strength for each unit cell is then used to constrain the stress in the optimization problem ("Stress Constraints" section).

Topology Optimization of Lattice Materials with Stress Constraints

A density-based topology optimization is here adopted to find the optimized material distribution within a given design domain subjected to prescribed boundary conditions and external forces, such as those shown in Fig. 3 (Bendsøe and Sigmund 2003). The design domain is cellular with unit cells having effective properties that can vary with relative density (Fig. 2). This section reports the problem formulation and

S

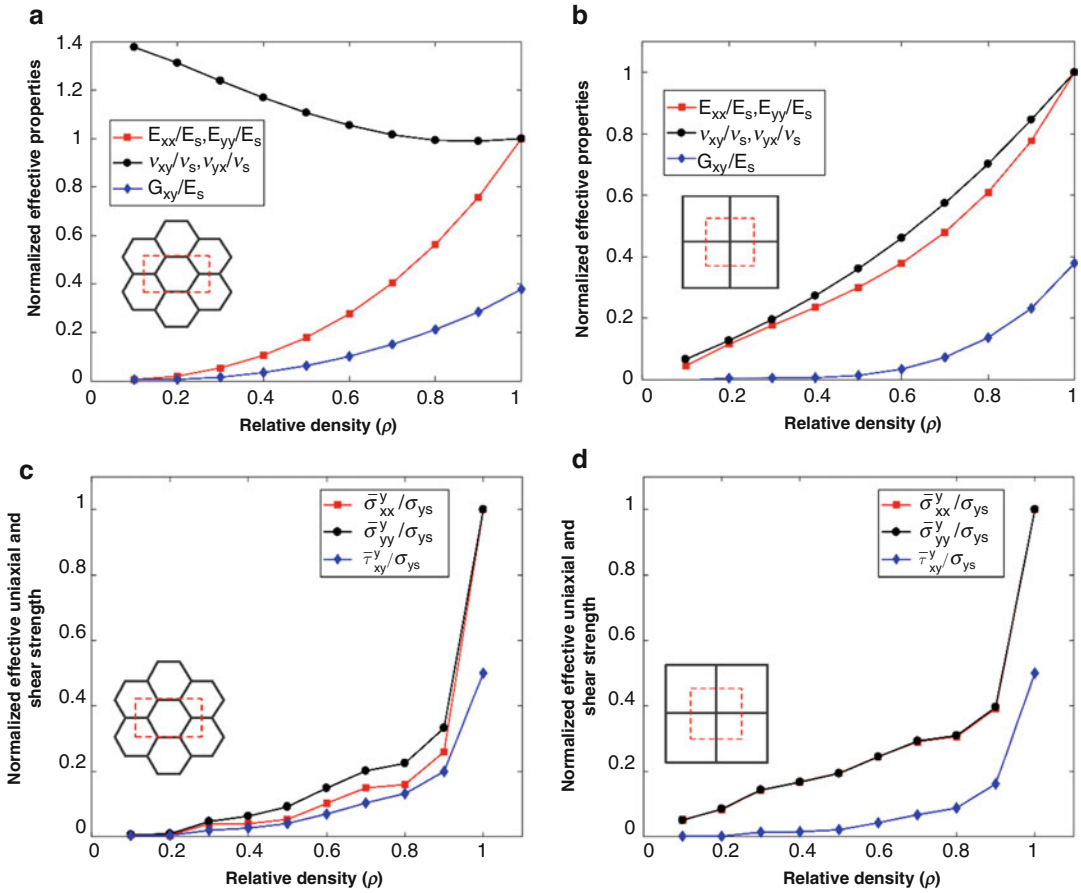

Fig. 2 Normalized effective mechanical properties and yield strengths as a function of relative density for hexagon, and square unit cells

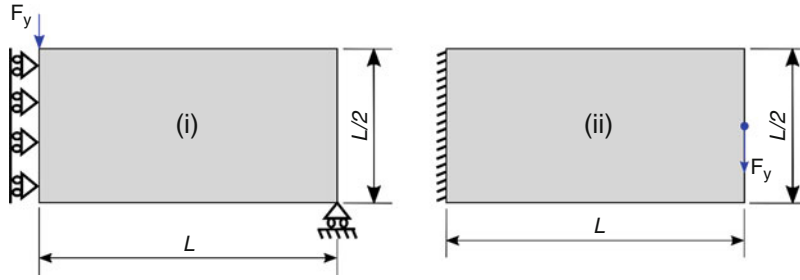

Fig. 3 The design domain, boundary conditions, and external loads for the optimization of (i) MBB-beam and (ii) fixed-beam

describes the filtering technique used. In addition, the stress constraints as well as the clustering technique are presented for each unit cell. The sensitivity analysis of both the objective function and the design constraints then follows.

Problem Formulation

The goal is to find the optimized material density distribution of a rectangular domain through the minimization of its compliance, under given support and loading conditions (Fig. 3). A set

of constraints is introduced in the optimization problem on both the total amount of material and the maximum stress level. The design domain is discretized into finite elements, where each element is assigned one design variable. The design variables ρ_i are then collected in a design vector. A final design is considered with a density distribution varying between a very small value of 0.01, to avoid stiffness matrix singularity, and 1. The mathematical formulation of the problem is expressed as:

$$\begin{aligned} &\underset{\rho}{Min} : C(\rho) = F^T U = U^T K U = \sum_{e=1}^{N} u_e^T K_e u_e \\ &Subject\ to : \begin{cases} \sigma_i^{PN}(\rho) \le \overline{\sigma}_i, & i = 1, \ldots, n_c \\ V(\rho) = \sum_{e=1}^{N} v_e \rho_e \le V^* \\ 0.01 \le \rho \le 1 \end{cases} \end{aligned} \tag{9}$$

wherein, ρ_e is the relative density of each element, V^* is the prescribed volume fraction of the solid material, and v_e is the volume of each element e; N is the total number of elements. The stress measure in topology optimization can be formulated in a number of ways (Duysinx and Bendsøe 1998; Duysinx and Sigmund 1998; Holmberg et al. 2013; Le et al. 2010; París et al. 2009). This work adopts a stress clustering technique explained later in this section (Holmberg et al. 2013; Le et al. 2010; París et al. 2010), where the stress measure is a modified p-norm based on the von Mises stress, which for cluster number i is denoted as $\sigma_i^{PN}(\rho)$ (Holmberg et al. 2013). The number of clusters, i.e., the number of stress constraints, is denoted n_c, and $\overline{\sigma}_i$ is the stress limit for the cluster number i.

For comparative purposes, we also report the traditional formulation in terms of minimum compliance, with a constraint only on the total amount of material expressed as volume fraction (Andreassen et al. 2011; Bendsøe and Sigmund 2003; Sigmund 2001). In a nested format, the problem is written by:

$$\begin{aligned} &\underset{\rho}{Min} : C(\rho) = F^T U = U^T K U = \sum_{e=1}^{N} u_e^T K_e u_e \\ &Subject\ to : \begin{cases} V(\rho) = \sum_{e=1}^{N} v_e \rho_e \le V^* \\ 0.01 \le \rho \le 1 \end{cases} \end{aligned} \tag{10}$$

Filtering of Design Variables

To avoid numerical instabilities, such as checkerboard patterns (Díaz and Sigmund 1995; Sigmund and Petersson 1998) and mesh dependency (Sigmund and Petersson 1998), the choice is to resort to a filtering method of either the sensitivities or the densities, an approach that can also serve to ensure manufacturability. Among several techniques available (Sigmund 2007), the density filter is implemented (Bruns and Tortorelli 2001), where each element density is redefined as a weighted average of the densities in a mesh-independent neighborhood of the element. The filter modifies the element density ρ_i to the filtered density $\tilde{\rho}_e$ as follows:

$$\tilde{\rho}_e = \frac{\sum_{i \in N_e} w(x_i)\, v_i \rho_i}{\sum_{i \in N_e} w(x_i)\, v_i} \tag{11}$$

where v_i is the volume of element i, N_e is the neighborhood of element e, and $w(x_i)$ is a weighting function that is given by the linearly decaying (cone-shape) function:

$$w(x_i) = R - \|x_i - x_e\| \tag{12}$$

where, R is the specified filter radius and, x_i and x_e contain the central coordinates of elements i and e respectively.

Stress Constraints

For each finite element that represents a unit cell in the structural domain, the stress vector at a stress evaluation point l, here located in the centroid of the element, can be written as a function of the filtered density $\tilde{\rho}$:

$$\sigma_l(\tilde{\rho}) = E^H(\tilde{\rho})\, B_l U(\tilde{\rho}) \tag{13}$$

where E^H is the homogenized elastic tensor of the lattice unite cell, and B_l is the strain-displacement matrix corresponding to stress evaluation point l. Since this work specifies the von Mises stress as a measure of stress at the stress evaluation point l, its expression as a function of the filtered density can be written in terms of the stress vector components as:

$$\sigma_l^{vM}(\tilde{\rho}) = \sqrt{\sigma_{lx}^2 + \sigma_{ly}^2 + \sigma_{lz}^2 - \sigma_{lx}^2\sigma_{ly}^2 - \sigma_{ly}^2\sigma_{lz}^2 - \sigma_{lz}^2\sigma_{lx}^2 + 3\tau_{lxy}^2 + 3\tau_{lyz}^2 + 3\tau_{lzx}^2} \tag{14}$$

where, σ_{lx}, σ_{ly}, and σ_{lz} are the normal stresses in x, y, and z directions, respectively; τ_{lxy}, τ_{lyz}, and τ_{lzx} are the shear stresses in xy, yz, and zx planes, respectively. Different approaches can be used to identify the stress constraints within the design domain, such as local and global approaches (Duysinx and Bendsøe 1998; Duysinx and Sigmund 1998) as well as clustered approaches (Holmberg et al. 2013; Le et al. 2010; París et al. 2010). Because the local approach is computationally expensive, and the global approach loses accuracy, we implement the stress clustering technique (Holmberg et al. 2013; Le et al. 2010; París et al. 2010), where the stress evaluation points are sorted into clusters, and only one stress constraint is applied to each cluster. This scheme allows to balance the control of the local stress and the computational cost (Holmberg et al. 2013). To create the clustered stress measures used in the problem formulation (9), stresses are clustered from several stress evaluation points and use them to calculate a single stress measure, $\sigma_i^{PN}(\tilde{\rho})$. This is done for each cluster through a modified p-norm. For each cluster of unit cells, the stress limit $\overline{\sigma}_i$ is set to the average distribution of the effective yield strength of the unit cells (Fig. 2), as a function of the filtered density. The stress measures are then normalized with the stress limits for each cluster. In addition to the volume fraction constraint, the stress measures are sorted in a column vector that feeds the MMA optimizer. The p-norm stress measure for the cluster i as a function of the filtered density, $\sigma_i^{PN}(\tilde{\rho})$, is expressed as:

$$\sigma_i^{PN}(\tilde{\rho}) = \left(\frac{1}{N_i} \sum_{l \in \Omega_i} \sigma_l^{vM}(\tilde{\rho})^p \right)^{\frac{1}{p}} \tag{15}$$

where p is the p-norm factor, the upper script PN stands for the p-norm, Ω_i is the set of stress evaluation points in cluster i, and N_i is the number of stress evaluation points in set Ω_i. The p-norm measure, $\sigma_i^{PN}(\tilde{\rho})$, underestimates the maximum local stress within each cluster (Duysinx and Sigmund 1998; Holmberg et al. 2013). The stress constraint in (9) can thus be re-written as a function of the filtered density:

$$\left(\sum_{l \in \Omega_i} \sigma_l^{vM}(\tilde{\rho})^p \right)^{\frac{1}{p}} \leq N_i^{\frac{1}{p}} \overline{\sigma}_i \tag{16}$$

Equation (16) sets the maximum local stress in the structure below $N_i^{\frac{1}{p}} \overline{\sigma}_i$. Increasing the value of the exponent p makes the p-norm value closer to the maximum stress in each cluster. However, numerical problems might emerge for too high values of p. On the other hand, $p = 1$ gives the mean stress for each cluster. Based on our testing and previous work in the literature (Duysinx and Sigmund 1998; Holmberg et al. 2013; Le et al. 2010), p is set to 8, a value that works well for the numerical problem examined in this work.

The local stress control is significantly affected by the number of clusters, n_c. Using $n_c = 1$ leads to the global approach with a rough estimate of the stress constraint; on the other hand, n_c equaling the total number of elements, N_e, yields to the local approach. In cluster i, the design domain might have evaluation points in the set Ω_i with either local high stresses that raise the p-norm value (9), or even relatively low stresses. Thus, the way in which the stress evaluation points are clustered together has an impact on the optimization problem (Holmberg

et al. 2013). Among the clustering techniques (Holmberg et al. 2013; Le et al. 2010; París et al. 2010), the stress level approach is here adopted as it provides the best design possible from the stress point of view (Holmberg et al. 2013). With this approach, stress evaluation points that have similar stress levels are clustered together. This method gives a large variation of the different $\sigma_i^{PN}(\tilde{\rho})$ values, but the stresses in the evaluation points within each cluster are as close to each other as possible. The p-norm measure then results in a good approximation of the local stresses of the unit cells within the cluster, which have a similar stress level, because this approaches one stress constraint value that represents each cluster (Holmberg et al. 2013).

The clustering scheme here used involves using the stress level to sort the stress evaluation points in a descending order such that

$$\underbrace{\sigma_1 \geq \sigma_2 \geq \sigma_3 \geq \cdots \geq \sigma_{\frac{n_e}{n_c}}}_{cluster\ 1} \geq \underbrace{\cdots \geq \sigma_{\frac{2n_e}{n_c}}}_{cluster\ 2} \geq \cdots \geq \sigma_{\frac{(n_c-1)n_e}{n_c}} \geq \underbrace{\cdots \geq \sigma_{n_e}}_{cluster\ n_c} \tag{17}$$

where the first n_e/n_c points create cluster 1, the next n_e/n_c points create cluster 2, and so on. All clusters in (17) have identical number of points except for the last cluster, which might contain fewer points.

Sensitivity Analysis

The Method of Moving Asymptotes (MMA), used to solve the optimization problem, requires first order sensitivity information from both the objective function and constraints (Svanberg 1987). At the macroscopic level, the mean compliance depends on the material properties of each element, which are a function of their relative density, ρ_e. The derivatives of the mean compliance with respect to the variation of ρ_e in the element e can be given by the chain rule as:

$$\frac{\partial C(\tilde{\rho})}{\partial \rho_e} = \sum_{i=1}^{N_e} \frac{\partial C(\tilde{\rho})}{\partial \tilde{\rho}_i} \frac{\partial \tilde{\rho}_i}{\partial \rho_e} \tag{18}$$

where the sensitivity of the filtered density $(\partial \tilde{\rho}_i / \partial \rho_e)$, with respect to the change in design variable ρ_e, is given by:

$$\frac{\partial \tilde{\rho}_i}{\partial \rho_e} = \frac{w(x_e)\, v_e}{\sum_{j \in N_i} w(x_j)\, v_j} \tag{19}$$

The sensitivity of the mean compliance with respect to the change in the filtered density $\tilde{\rho}_i$, $\partial C(\tilde{\rho}) / \partial \tilde{\rho}_i$, can be obtained from the expression of the objective function, which can be written in terms of the applied loads and the state variables as:

$$C(\tilde{\rho}) = F^T U(\tilde{\rho}) \tag{20}$$

where F is the global force vector, and U is the global vector of nodal displacements, which represents the state variables. The global force vector can be expressed by:

$$F = K(\tilde{\rho})\, U(\tilde{\rho}) \tag{21}$$

where K is the global stiffness matrix of the structure, which is the assembly of the elemental stiffness matrices of the design domain, as described in the Appendix. The sensitivity of the mean compliance with respect to the change in the filtered density $\tilde{\rho}_i$ is then defined as:

$$\frac{\partial C(\tilde{\rho})}{\partial \tilde{\rho}_i} = F^T \frac{\partial U(\tilde{\rho})}{\partial \tilde{\rho}_i} = U^T(\tilde{\rho})\, K(\tilde{\rho}) \frac{\partial U(\tilde{\rho})}{\partial \tilde{\rho}_i} \tag{22}$$

Taking the derivatives of the state Eq. (21) with respect to the element filtered densities $\tilde{\rho}_i$, and given F has a constant value, yields:

$$\frac{\partial K(\tilde{\rho})}{\partial \tilde{\rho}_i} U(\tilde{\rho}) + K(\tilde{\rho}) \frac{\partial U(\tilde{\rho})}{\partial \tilde{\rho}_i} = 0 \tag{23}$$

where, $\partial U(\tilde{\rho}) / \partial \tilde{\rho}_i$ can be expressed as:

$$\frac{\partial U(\tilde{\rho})}{\partial \tilde{\rho}_i} = -K^{-1}(\tilde{\rho}) \frac{\partial K(\tilde{\rho})}{\partial \tilde{\rho}_i} U(\tilde{\rho}) \tag{24}$$

Substituting (24) into (22) yields:

$$\frac{\partial C\left(\tilde{\rho}\right)}{\partial \tilde{\rho}_i} = -U^T\left(\tilde{\rho}\right)\frac{\partial K\left(\tilde{\rho}\right)}{\partial \tilde{\rho}_i}U\left(\tilde{\rho}\right) \tag{25}$$

The derivatives of the stiffness matrix of the domain microstructure $\partial K\left(\tilde{\rho}\right)/\partial\tilde{\rho}_i$, described by the porous unit cell, with respect to the filtered density are given in the Appendix. Once the stiffness matrix derivatives are calculated for each element/unit cell, the global stiffness derivatives can be assembled and used to calculate the sensitivity of the objective function with respect to the filtered density through Eq. (25). Substituting (25) into (18) yields to the final form of the sensitivity of the objective function with respect to the relative density ρ_e.

The sensitivity of the material volume V with respect to the element density ρ_e is thus expressed as:

$$\frac{\partial V\left(\tilde{\rho}\right)}{\partial \rho_e} = \sum_{i\in N_e}\frac{\partial V\left(\tilde{\rho}\right)}{\partial \tilde{\rho}_i}\frac{\partial \tilde{\rho}_i}{\partial \rho_e} \tag{26}$$

where,

$$\frac{\partial V\left(\tilde{\rho}\right)}{\partial \tilde{\rho}_i} = v_s \tag{27}$$

where v_s is the volume of the solid element, which in this study equals 1 as per the assumption that the element has a unit volume.

The stress constraints are the p-norm stresses in Eq. (15), and the gradients can be calculated by the chain rule:

$$\begin{aligned}\frac{\partial\sigma_i^{PN}(\tilde{\rho})}{\partial\rho_e} &= \sum_{l\in\Omega_i}\frac{\partial\sigma_i^{PN}(\tilde{\rho})}{\partial\sigma_l^{vM}}\frac{\partial\sigma_l^{vM}(\tilde{\rho})}{\partial\rho_e}\\ &= \sum_{l\in\Omega_i}\frac{\partial\sigma_i^{PN}(\tilde{\rho})}{\partial\sigma_l^{vM}}\left(\frac{\partial\sigma_l^{vM}(\tilde{\rho})}{\partial\sigma_l}\right)^T\frac{\partial\sigma_l(\tilde{\rho})}{\partial\rho_e}\end{aligned} \tag{28}$$

The term $\partial\sigma_i^{PN}\left(\tilde{\rho}\right)/\partial\sigma_l^{vM}$ in (28) is obtained by taking the derivative of (15) with respect to the von Mises stress calculated at the evaluation point l as follows:

$$\begin{aligned}\frac{\partial\sigma_i^{PN}\left(\tilde{\rho}\right)}{\partial\sigma_l^{vM}} &= \frac{1}{p}\left(\frac{1}{N_i}\sum_{l\in\Omega_i}\left(\sigma_l^{vM}\left(\tilde{\rho}\right)\right)^p\right)^{\left(\frac{1}{p}-1\right)}\\ &\quad\times\frac{1}{N_i}p\left(\sigma_l^{vM}\left(\tilde{\rho}\right)\right)^{p-1}\\ &= \left(\frac{1}{N_i}\sum_{l\in\Omega_i}\left(\sigma_l^{vM}\left(\tilde{\rho}\right)\right)^p\right)^{\left(\frac{1}{p}-1\right)}\\ &\quad\times\frac{1}{N_i}\left(\sigma_l^{vM}\left(\tilde{\rho}\right)\right)^{p-1}\end{aligned} \tag{29}$$

Moreover, the term $\partial\sigma_l^{vM}\left(\tilde{\rho}\right)/\partial\sigma_l$ in (28) represents the derivatives of the von Mises stress (14) with respect to the normal and shear stress components as:

$$\begin{aligned}\frac{\partial\sigma_l^{vM}(\tilde{\rho})}{\partial\sigma_{lx}} &= \frac{1}{2\sigma_l^{vM}(\tilde{\rho})}\left(2\sigma_{lx}\left(\tilde{\rho}\right)-\sigma_{ly}\left(\tilde{\rho}\right)-\sigma_{lz}\left(\tilde{\rho}\right)\right)\\ \frac{\partial\sigma_l^{vM}(\tilde{\rho})}{\partial\sigma_{ly}} &= \frac{1}{2\sigma_l^{vM}(\tilde{\rho})}\left(2\sigma_{ly}\left(\tilde{\rho}\right)-\sigma_{lx}\left(\tilde{\rho}\right)-\sigma_{lz}\left(\tilde{\rho}\right)\right)\\ \frac{\partial\sigma_l^{vM}(\tilde{\rho})}{\partial\sigma_{lz}} &= \frac{1}{2\sigma_l^{vM}(\tilde{\rho})}\left(2\sigma_{lz}\left(\tilde{\rho}\right)-\sigma_{lx}\left(\tilde{\rho}\right)-\sigma_{ly}\left(\tilde{\rho}\right)\right)\\ \frac{\partial\sigma_l^{vM}(\tilde{\rho})}{\partial\tau_{lxy}} &= \frac{3}{\sigma_l^{vM}(\tilde{\rho})}\tau_{lxy}\left(\tilde{\rho}\right)\\ \frac{\partial\sigma_l^{vM}(\tilde{\rho})}{\partial\tau_{lyz}} &= \frac{3}{\sigma_l^{vM}(\tilde{\rho})}\tau_{lyz}\left(\tilde{\rho}\right)\\ \frac{\partial\sigma_l^{vM}(\tilde{\rho})}{\partial\tau_{lzx}} &= \frac{3}{\sigma_l^{vM}(\tilde{\rho})}\tau_{lzx}\left(\tilde{\rho}\right)\end{aligned} \tag{30}$$

Finally, the term $\partial\sigma_l\left(\tilde{\rho}\right)/\partial\rho_e$ in (28) is the derivative of the stress vector in (13) with respect to design variable ρ_e and can be given by the chain rule:

$$\frac{\partial\sigma_l\left(\tilde{\rho}\right)}{\partial\rho_e} = \sum_{k=1}^{n_l}\frac{\partial\sigma_l\left(\tilde{\rho}\right)}{\partial\tilde{\rho}_k}\frac{\partial\tilde{\rho}_k}{\partial\rho_e} \tag{31}$$

where n_l is the number of stress evaluation points. $\partial\tilde{\rho}_k/\partial\rho_e$ is calculated using Eq. (19). Using (13), $\partial\sigma_l\left(\tilde{\rho}\right)/\partial\tilde{\rho}_k$ can be expanded and written as:

$$\frac{\partial\sigma_l\left(\tilde{\rho}\right)}{\partial\tilde{\rho}_k} = \frac{\partial E_k^H\left(\tilde{\rho}\right)}{\partial\tilde{\rho}_k}BU\left(\tilde{\rho}\right) + E_k^H\left(\tilde{\rho}\right)B\frac{\partial U\left(\tilde{\rho}\right)}{\partial\tilde{\rho}_k} \tag{32}$$

Using (24), Eq. (32) yields:

$$\frac{\partial \sigma_l(\tilde{\rho})}{\partial \tilde{\rho}_k} = \frac{\partial E_k^H(\tilde{\rho})}{\partial \tilde{\rho}_k} BU(\tilde{\rho}) - E_k^H(\tilde{\rho}) BK^{-1}(\tilde{\rho}) \frac{\partial K(\tilde{\rho})}{\partial \tilde{\rho}_k} U(\tilde{\rho}) \quad (33)$$

Substituting (33) into (31) yields to the final form $\partial \sigma_l(\tilde{\rho}) / \partial \rho_e$. Then, the final form of the gradients of the stress constraints is obtained by substituting (29), (30), and (33) into (28). After performing the sensitivity analysis that guides the search direction to the optimized solution, the MMA (Svanberg 1987) solves the optimization problem until convergence is achieved.

Numerical Examples and Discussion

This section studies the role of cell topology in the optimized distribution of relative density for the lattices shown in Fig. 1. The effect of including the stress constraint (formulation (9)) on the stress level distribution is also investigated, and we do so by comparing the optimized relative density and the von Mises (vM) stress distributions along the structural domains, with those obtained with the traditional compliance formulation in (10).

Two benchmark problems (Messerschmidt–Bölkow–Blohm (MBB) and fixed beams) are here examined for the minimum compliance of lattice materials. Figure 3 shows the rectangular design domains (length, $L = 100$ mm, and height $= L/2$, with an out-of-plane thickness of 1 mm), boundary conditions, and external loads (vertical point load $F_y = 1500$ N). Due to symmetry, the right half of the MBB-beam is modeled under the prescribed loading and conditions of symmetry imposed along the left edge and the lower right corner (Fig. 3(i)). The beams are assumed to be under plane stress. In both problems, the design domains are discretized into 5000 equal sized square elements with four nodes and 5151 nodes, where each element represents a unit cell of the cellular structure. Titanium alloy (Lin et al. 2004) (*Ti6Al4V*) is the base material of the lattices with Young's modulus $E_s = 120$ GPa, Poison's ratio $\upsilon_s = 0.3$, and yield limit $\sigma_{ys} = 900$ MPa.

For the stress evaluation, one point is used per element, which corresponds to the centroid of the four-node square element used here. The yield limit σ_{ys} is used to calculate the stress limit for each unit cell as a function of relative density (Fig. 2), which acts as a single stress constraint for each cluster. We consider ten clusters of unit cells that have similar von Mises stress levels, i.e., ten stress constraints. For each cluster, the stress measure should not exceed the stress limit, which is the average distribution of the effective yield strength for the cluster unit cells (Fig. 2). The design variable filter is applied with a filter radius, $R = 1.5$ times the element size. The optimization problem is solved until convergence is reached for a prescribed volume fraction V^* of 50% for the solid material.

Generally, for each stress constrained problem, no further change has been noticed in the objective after 100 iterations. Re-clustering frequency is applied at each iteration for the stress constrained formulation (9), while no re-clustering is performed for the traditional formulation (10). Figures 4 and 5 show the solutions for the MBB-beams (Fig. 3i) along with their convergence plots for both the formulations with and without stress constraints.

By comparing the results in Figs. 4 and 5, a range of insights can be gained into the inclusion of stress constraints (problem formulation (9) versus problem formulation (10)), as well as cell topology (square versus hexagon), the distribution of relative density, and the von Mises stress. The results are shown for square (orthogonal-isotropic), and hexagon (isotropic) unit cells used as building block of the cellular domain. The relative density varies between a low nonzero value to avoid singularity of the stiffness matrix, to 1, i.e., solid material. The von Mises stress varies between a very small value, which corresponds to a very low relative density, to 900 MPa for solid material.

Cell topology influences the optimized material distribution, and the inclusion of stress constraints plays a role too. First the unit cells have their own planes of symmetry,

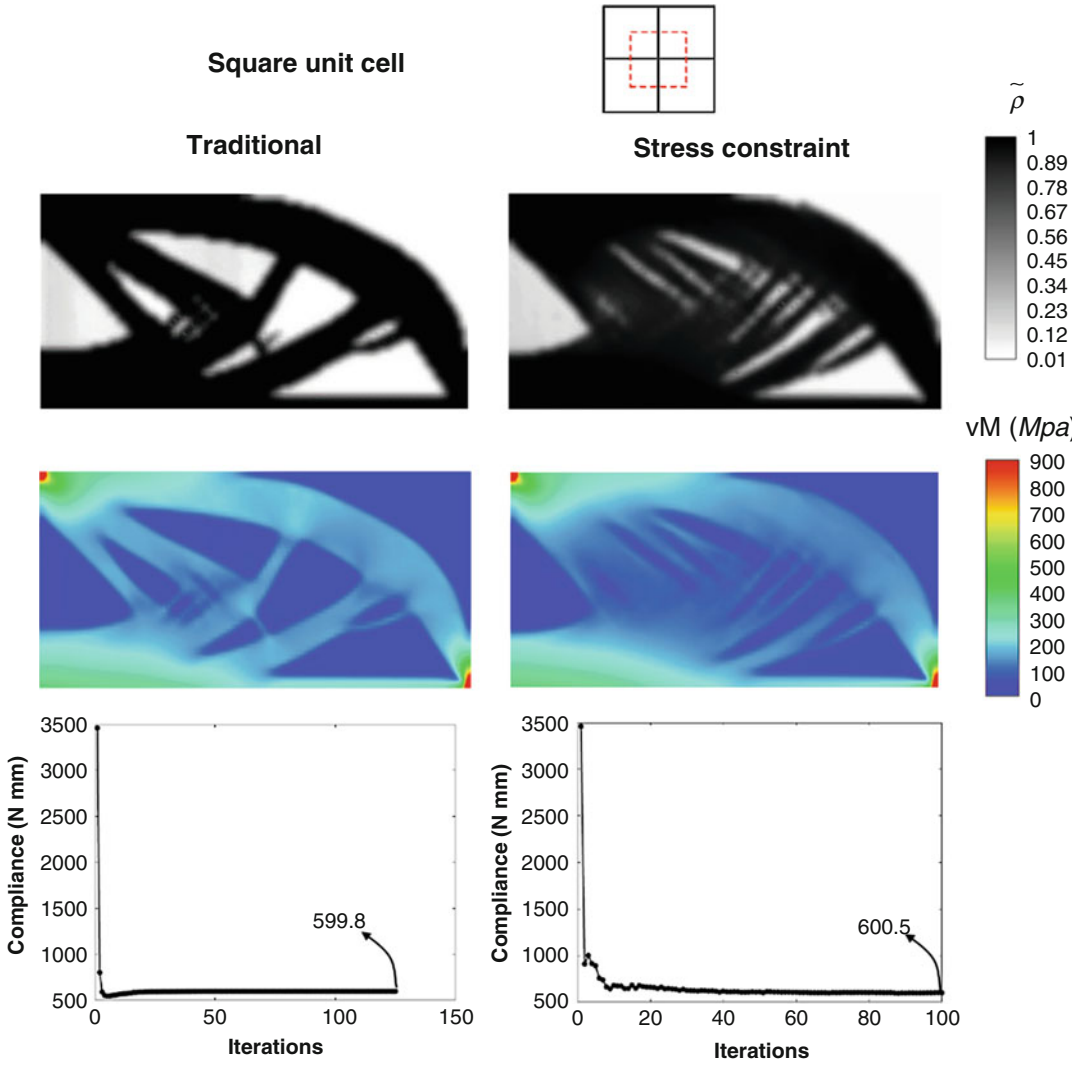

Fig. 4 Optimized relative density and von Mises stress distribution for the MBB-beam benchmark problem (square unit cell)

which control the type of anisotropy (the square unit is orthogonal-isotropic, and the hexagon is isotropic), hence affecting the material distribution within the design domain. In addition, the stress constraints have an impact on the stress distribution of the MBB-beam. From an inspection of the re-clustering frequency at every iteration, the stress-constrained formulation (9) enables average stress levels lower than those predicted with the traditional scheme (10). In addition, if any stress concentration is neglected at the load and support locations (shown in red), the stress distribution of the former is much more uniform and generally lower than the yield limit of the solid material. These observations point out the role of cell topology and stress constraints on the optimized density and stress distributions of a cellular domain. Moreover, small oscillations in the convergence plots of the compliance appear between iterations for the case of updated clusters, whereas the trends are relatively smooth when there is no re-clustering at all.

Similar to Figs. 4 and 5, Figs. 6 and 7 show the results for the fixed-beam example (Fig. 3 (ii)).

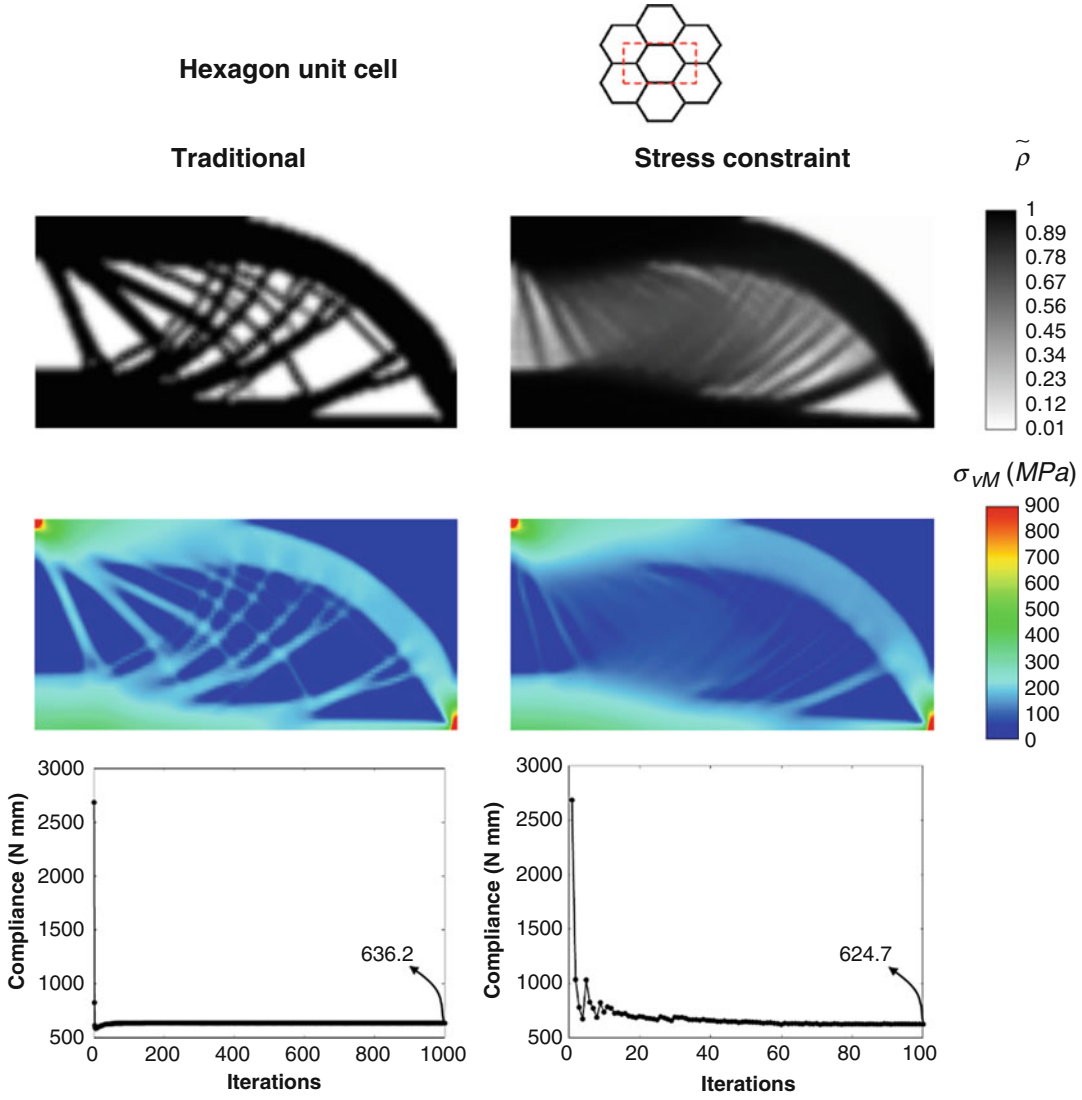

Fig. 5 Optimized relative density and von Mises stress distribution for the MBB-beam benchmark problem (hexagon unit cell)

The optimized relative density and von Mises stress distributions are illustrated for the traditional and constrained stress formulation with both square and hexagonal units. The results parallel those in Figs. 4 and 5 for the MBB beam. Cell topology plays a role as dictated by the planes of symmetry that each unit cell possesses. In addition for the stress-constraint problem, the average stress is lower with lower stress concentrations through the entire structure, and the stress distribution is much more even. Convergence plots for the updated clusters show small oscillations of the objective function, as opposed to those obtained without re-clustering. To further investigate the role of using the stress constrained approach on results, Fig. 8 shows the average von Mises stress distribution normalized with the yield strength, σ_{ys}, of the solid material over the domains of the MBB and fixed beams. Overall for the traditional and constrained stress formula-

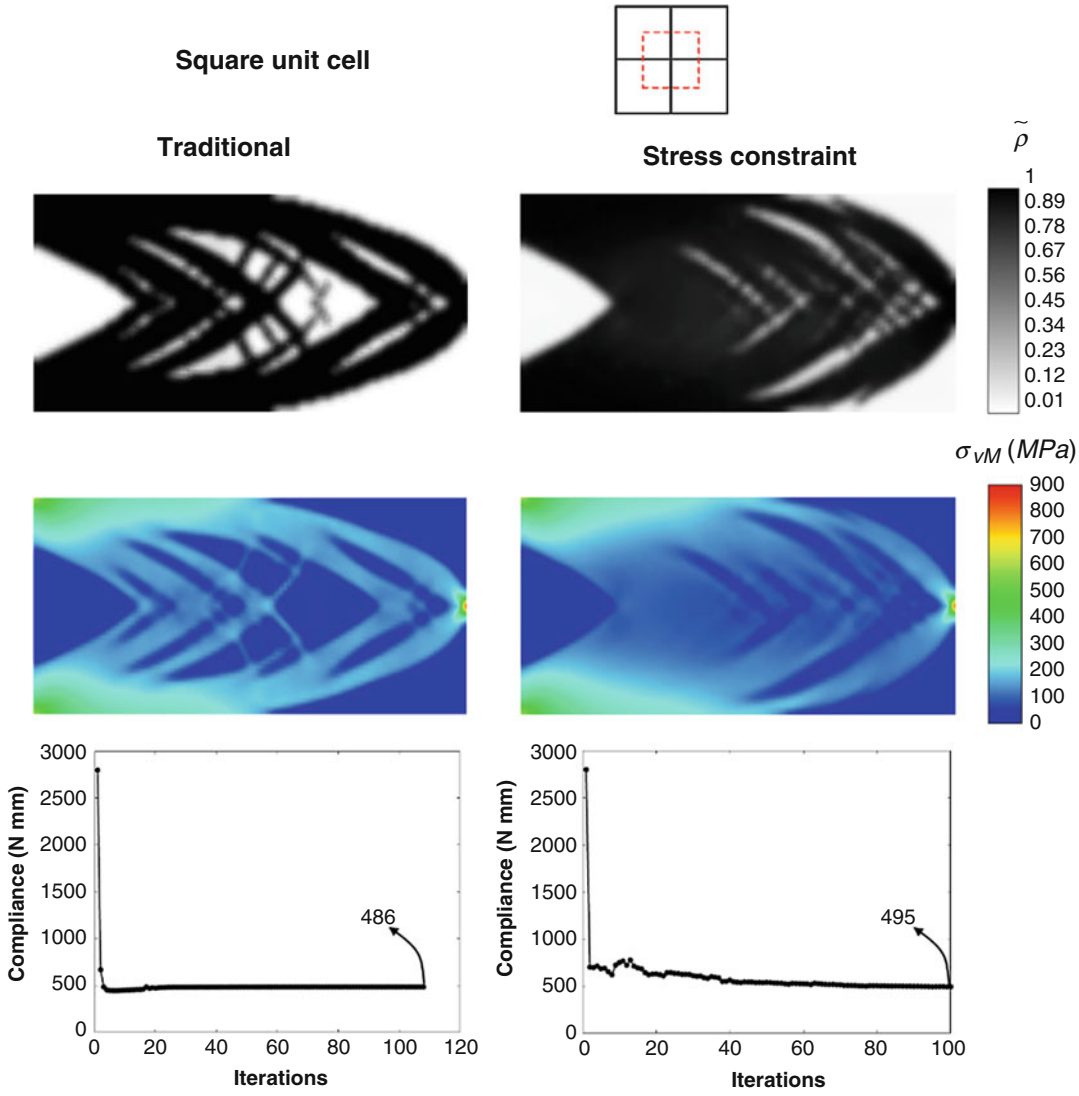

Fig. 6 Optimized relative density and von Mises stress distribution for the fixed-beam benchmark problem (square unit cell)

tions with both hexagonal and square unit cells, lower stress distribution is noticed for the latter than the former. In addition, as shown in Fig. 9 the average p-norm stress measure acknowledges the effective stress limit set for each cluster, except for the first cluster that has elements with local stress peaks in the case of MBB beam. Differences of about 7.4% and 22.8% are noticed for the hexagonal and square unit cells, respectively. As explained in the "Stress Constraints" section and in the literature (Holmberg et al. 2013; Zhou and Sigmund 2017), the p-norm factor might need to be adjusted to a value higher than 8 for the MBB beam benchmark problem, which lowers the elemental stresses to match the stress limit.

Conclusions

This chapter has presented a numerical investigation aiming at assessing the role of stress

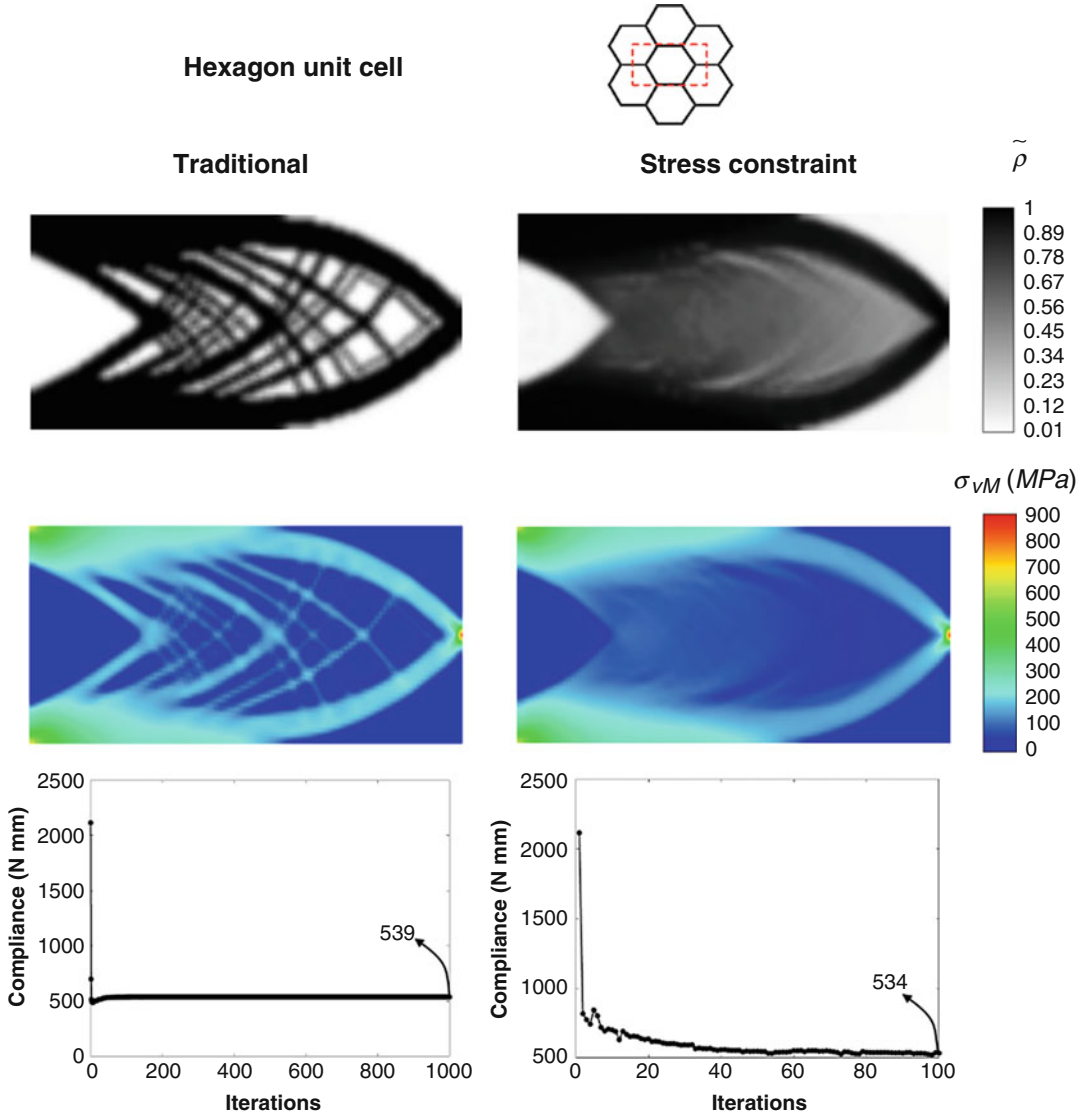

Fig. 7 Optimized relative density and von Mises stress distribution for the fixed-beam benchmark problem (hexagon unit cell)

constraints and cell topology in the topology optimization of 2D lattice materials. Cell topology and stress constraints are found to impact the optimized distribution of relative density and the stress levels throughout the cellular domain. Differences in the final designs obtained with both a traditional and a stress constraint formulation appear with the latter showing a lower average stress and a more uniform stress distribution.

Appendix: Sensitivity Calculation of the Stiffness Tensor of the Lattice

To compute the sensitivity of the structure compliance, the derivatives of the stiffness tensor are to be computed for the entire domain microstructure. This appendix presents the derivation of the stiffness tensor sensitivity of the domain with respect to the filtered density $\tilde{\rho}$. A four-node iso-

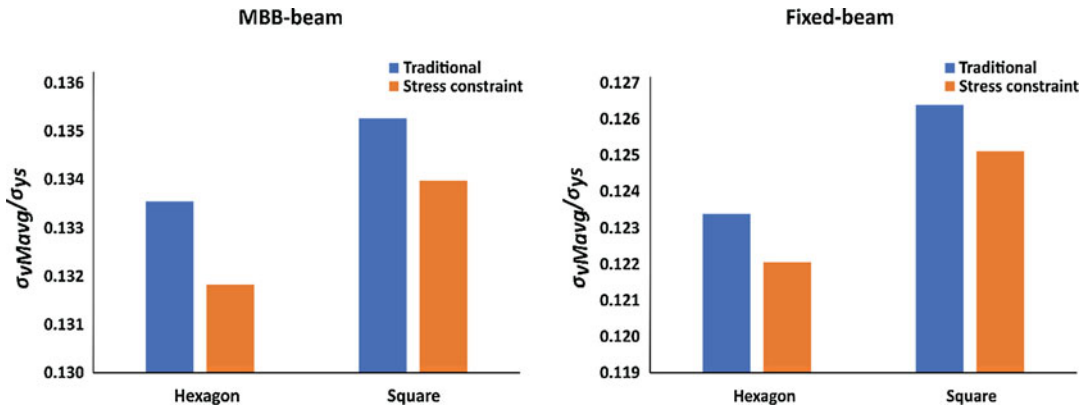

Fig. 8 Normalized average von Mises stress distribution within the design domains of the MBB and fixed beams using hexagon and square unit cells

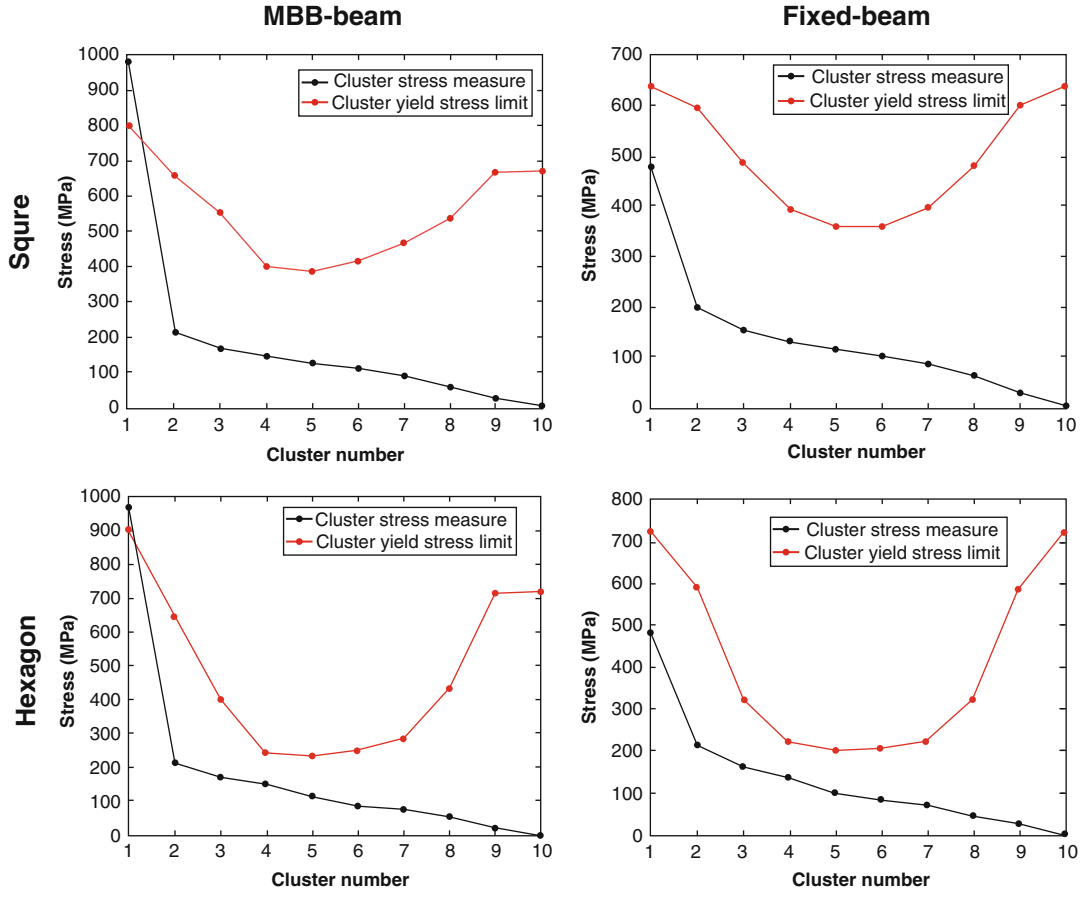

Fig. 9 Average p-norm stress measure compared to effective stress limit for each cluster, for the MBB and fixed beams using hexagon and square unit cells

parametric quadrilateral element (Hughes 1989) is used to discretize the finite domain.

The direct stiffness approach is used to find the global stiffness tensor K, where the structure domain is discretized into small elements with elemental stiffness matrix K_e, calculated before assembly, expressed as:

$$\begin{aligned} K_e\left(\tilde{\rho}\right) &= \int_{A^e} B^T E^H\left(\tilde{\rho}\right) B dA \\ &= \iint_{xy} B^T E^H\left(\tilde{\rho}\right) B \, dxdy \end{aligned} \tag{34}$$

where x and y are the global coordinates, B is the strain-displacement matrix, E^H is the homogenized elastic tensor of each element e described in the "Mechanical Properties of Lattice Materials" section, and A^e is the area of the element in the global coordinates. Since the strain-displacement matrix is independent of the design variables, the derivatives of the elemental stiffness matrix with respect to filtered density, $\tilde{\rho}$, can be expressed as follows:

$$\begin{aligned} \frac{\partial K_e\left(\tilde{\rho}\right)}{\partial \tilde{\rho}_e} &= \int_{A^e} B^T \frac{\partial E^H\left(\tilde{\rho}\right)}{\partial \tilde{\rho}_e} B dA \\ &= \iint_{xy} B^T \frac{\partial E^H\left(\tilde{\rho}\right)}{\partial \tilde{\rho}_e} B \, dxdy \end{aligned} \tag{35}$$

Here, the problem is assumed under plane stress conditions with a unit element thickness. Each mesh element corresponds to a rectangular unit cell. The elastic stiffness tensor E^H of a general orthotropic material can thus be expressed for each unit cell as a function of its filtered density, $\tilde{\rho}$, as:

$$\begin{aligned} &E^H\left(\tilde{\rho}\right) \\ &= \begin{bmatrix} \frac{E_{xx}(\tilde{\rho})}{1-\upsilon_{xy}(\tilde{\rho})\upsilon_{yx}(\tilde{\rho})} & \frac{\upsilon_{yx}(\tilde{\rho})E_{xx}(\tilde{\rho})}{1-\upsilon_{xy}(\tilde{\rho})\upsilon_{yx}(\tilde{\rho})} & 0 \\ \frac{\upsilon_{xy}(\tilde{\rho})E_{yy}(\tilde{\rho})}{1-\upsilon_{xy}(\tilde{\rho})\upsilon_{yx}(\tilde{\rho})} & \frac{E_{yy}(\tilde{\rho})}{1-\upsilon_{xy}(\tilde{\rho})\upsilon_{yx}(\tilde{\rho})} & 0 \\ 0 & 0 & G_{xy}\left(\tilde{\rho}\right) \end{bmatrix} \end{aligned} \tag{36}$$

Since asymptotic homogenization is used to calculate the elastic constants of the unit cell across a range of filtered density (Fig. 2), the elastic tensor of each element can be written as a function of the element filtered density and then used to evaluate the derivative of the elastic tensor with respect to the filtered density. For a four-node quadrilateral element with four Gauss points, the elemental stiffness tensor Eq. (34) and its derivatives (35) can be rewritten by using the Gauss quadrature rule for area integration as:

$$\begin{aligned} K_e\left(\tilde{\rho}\right) &= \int_{A^e} B^T E^H\left(\tilde{\rho}\right) B dA \\ &= \iint_{xy} B^T E^H\left(\tilde{\rho}\right) B \, dxdy \\ &= \iint_{st} B_{st}^T\left(s,t\right) E^H\left(\tilde{\rho}\right) B_{st}\left(s,t\right) \\ &\quad |J| \, dsdt = \sum_{i=1}^{2}\sum_{j=1}^{2} w_i w_j B_{st}^T\left(s_i,t_j\right) E^H \\ &\quad \left(\tilde{\rho}\right) B_{st}\left(s_i,t_j\right) \; |J| \end{aligned} \tag{37}$$

$$\begin{aligned} \frac{\partial K_e\left(\tilde{\rho}\right)}{\partial \tilde{\rho}} &= \int_{A^e} B^T \frac{\partial E^H\left(\tilde{\rho}\right)}{\partial \tilde{\rho}_e} B dA \\ &= \iint_{xy} B^T \frac{\partial E^H\left(\tilde{\rho}\right)}{\partial \tilde{\rho}_e} B \, dxdy \\ &= \iint_{st} B_{st}^T\left(s,t\right) \frac{\partial E^H\left(\tilde{\rho}\right)}{\partial \tilde{\rho}_e} \\ &\quad \times B_{st}\left(s,t\right) \; |J| \, dsdt \\ &= \sum_{i=1}^{2}\sum_{j=1}^{2} w_i w_j B_{st}^T\left(s_i,t_j\right) \frac{\partial E^H\left(\tilde{\rho}\right)}{\partial \tilde{\rho}_e} \\ &\quad \times B_{st}\left(s_i,t_j\right) \; |J| \end{aligned} \tag{38}$$

where s and t are the natural coordinates. Once the stiffness matrix derivatives are calculated for each element using (38), the global stiffness derivatives $\partial K\left(\tilde{\rho}\right)/\partial \tilde{\rho}_e$ can be assembled to calculate the compliance sensitivity vector

$\partial C\left(\tilde{\rho}\right)/\partial\tilde{\rho}_e$ for the whole cellular domain (Eq. 25). The sensitivity analysis is then implemented, under the optimization scheme described in the "Methodology" section, to seek the optimum relative density distribution that achieves the objective and satisfies the constraints.

References

Andreassen E, Clausen A, Schevenels M, Lazarov B, Sigmund O (2011) Efficient topology optimization in MATLAB using 88 lines of code. Struct Multidiscip Optim 43:1–16

Arabnejad S, Pasini D (2012) Multiscale design and multiobjective optimization of orthopedic hip implants with functionally graded cellular material. J Biomech Eng 134:031004–031010

Arabnejad S, Pasini D (2013) Mechanical properties of lattice materials via asymptotic homogenization and comparison with alternative homogenization methods. Int J Mech Sci 77:249–262

Bendsøe MP, Kikuchi N (1988) Generating optimal topologies in structural design using a homogenization method. Comput Methods Appl Mech Eng 71:197–224

Bendsøe MP, Sigmund O (2003) Topology optimization: theory, methods, and applications. Springer, Berlin/New York

Bruns TE, Tortorelli DA (2001) Topology optimization of non-linear elastic structures and compliant mechanisms. Comput Methods Appl Mech Eng 190:3443–3459

Cheng GD, Guo X (1997) ε-relaxed approach in structural topology optimization. Struct Optim 13:258–266

Cheng G, Jiang Z (1992) Study on topology optimization with stress constraints. Eng Optim 20:129–148

Da Silva GA, Beck AT, Cardoso EL (2018) Topology optimization of continuum structures with stress constraints and uncertainties in loading NME. Int J Numer Methods Eng 113:153–178

De Leon DM, Alexandersen J, Fonseca O, JS SO (2015) Stress-constrained topology optimization for compliant mechanism design. Struct Multidiscip Optim 52:929–943

Díaz A, Sigmund O (1995) Checkerboard patterns in layout optimization. Struct Optim 10:40–45

Duysinx P, Bendsøe MP (1998) Topology optimization of continuum structures with local stress constraints. Int J Numer Methods Eng 43:1453–1478

Duysinx P, Sigmund O (1998) New developments in handling stress constraints in optimal material distribution. In: 7th AIAA/USAF/NASA/ISSMO symposium on multidisciplinary analysis and optimization. Multidisciplinary analysis optimization conferences, American Institute of Aeronautics and Astronautics

Gibson LJ, Ashby MF (1988) Cellular solids: structure & properties. Pergamon Press, Oxford/New York

Guedes J, Kikuchi N (1990) Preprocessing and postprocessing for materials based on the homogenization method with adaptive finite element methods. Comput Methods Appl Mech Eng 83:143–198

Hassani BH (1996) A direct method to derive the boundary conditions of the homogenization equation for symmetric cells. Commun Numer Methods Eng 12:185–196

Hassani BH, Hinton E (1998) A review of homogenization and topology optimization I-homogenization theory for media with periodic structure

Hollister SJ, Kikuchi N (1992) A comparison of homogenization and standard mechanics analyses for periodic porous composites. Comput Mech 10:73–95

Holmberg E, Torstenfelt B, Klarbring A (2013) Stress constrained topology optimization. Struct Multidiscip Optim 48:33–47

Hughes TJR (1989) The finite element method: linear static and dynamic finite element analysis: Thomas J. R. Hughes. Comput Aided Civ Infrastruct Eng 4:245–246

Le C, Norato J, Bruns T, Ha C, Tortorelli D (2010) Stress-based topology optimization for continua. Struct Multidiscip Optim 41:605–620

Lee E, James KA, Martins JR (2012) Stress-constrained topology optimization with design-dependent loading. Struct Multidiscip Optim 46:647–661

Lin CY, Hsiao CC, Chen PQ, Hollister SJ (2004) Interbody fusion cage design using integrated global layout and local microstructure topology optimization. Spine (Phila Pa 1976) 29:1747–1754

París J, Navarrina F, Colominas I, Casteleiro M (2009) Topology optimization of continuum structures with local and global stress constraints. Struct Multidiscip Optim 39:419–437

París J, Navarrina F, Colominas I, Casteleiro M (2010) Block aggregation of stress constraints in topology optimization of structures. Adv Eng Softw 41:433–441

Rozvany GIN (2001) On design-dependent constraints and singular topologies. Struct Multidiscip Optim 21:164–172

Seepersad CC, Allen JK, McDowell DL, Mistree F (2006) Robust design of cellular materials with topological and dimensional imperfections. J Mech Des 128:1285–1297

Sigmund O (1997) On the design of compliant mechanisms using topology optimization. Mech Struct Mach 25:493–524

Sigmund O (2000) Topology optimization: a tool for the tailoring of structures and materials. Philos Trans Math Phys Eng Sci 358:211–227

Sigmund O (2001) A 99 line topology optimization code written in Matlab. Struct Multidiscip Optim 21:120–127

Sigmund O (2007) Morphology-based black and white filters for topology optimization. Struct Multidiscip Optim 33:401–424

Sigmund O, Petersson J (1998) Numerical instabilities in topology optimization: a survey on procedures dealing

with checkerboards, mesh-dependencies and local minima. Struct Optim 16:68–75
Svanberg K (1987) The method of moving asymptotes – a new method for structural optimization. Int J Numer Methods Eng 24:359–373
Verbart A, Langelaar M, Fv K (2017) A unified aggregation and relaxation approach for stress-constrained topology optimization. Struct Multidiscip Optim 55:663–679
Wang Y, Xu H, Pasini D (2017) Multiscale isogeometric topology optimization for lattice materials. Comput Methods Appl Mech Eng 316:568–585
Yang RJ, Chen CJ (1996) Stress-based topology optimization. Struct Optim 12:98–105
Zhou M, Sigmund O (2017) On fully stressed design and p-norm measures in structural optimization. Struct Multidiscip Optim 56:731–736

Stress-State Dependence

▸ Continuum Damage Model for Ductile Materials Based on Stress-State-Dependent Damage Functions

Structural Assessment of the Aneurysmatic Aorta

▸ Patient-Specific Simulation of Abdominal Aortic Aneurysms

Structural Control

▸ Adaptive Structures, Principles of

Structural Materials

▸ Methods to Determine the Mechanical Properties of Composite Materials with Continuous Fibers

Structural Safety

▸ Crashworthiness

Structure-Born Noise Reduction

▸ Active Control of Vibration, Applications of

Structured Materials

▸ Impact of Cellular Materials

Structure-Preserving Methods

▸ Computational Dynamics

Super-Quadrics; Shapes Resembling Ellipsoids or Other Quadrics

▸ Discrete Element and Particle Methods

Supraphysiological Loading

▸ Damage in Soft Biological Tissues

S

Surface Energy and Its Effects on Nanomaterials

Jianmin Qu[1] and Remi Dingreville[2]
[1]School of Engineering, Tufts University, Medford, MA, USA
[2]Center for Integrated Nanotechnologies, Sandia National Laboratories, Albuquerque, NM, USA

Synonyms

Effective modulus; Nanocomposites; Surface tension

Definition

Atoms at a free surface experience a different local environment than do atoms in the bulk of a material. As a result, the energy associated with these atoms will, in general, be different from that of the atoms in the bulk. The excess energy associated with surface atoms is called surface free energy. In traditional continuum mechanics, such surface free energy is typically neglected because it is associated with only a few layers of atoms near the surface and the ratio of the volume occupied by the surface atoms and the total volume of material of interest is extremely small. However, for nano-sized particles, wires, and films, the surface-to-volume ratio becomes significant and so does the effect of surface free energy. Consequently, the effective modulus of nano-sized structural elements should be considered, which by definition becomes size dependent.

Introduction

The elastic behavior of a material is characterized by its elastic modulus which defines the proportionality between the stress and strain when the material is subjected to external loads. Strictly speaking, modulus is an intensive property defined at each material point when the material is assumed to be a continuum. Therefore, it should be independent of the size of the material sample being considered. However, for inhomogeneous materials such as composites, it is often convenient for engineering design to define the overall (or effective) modulus of the material. Such effective modulus of a composite may depend on the properties of its constituents and the relative volume fraction of each constituent.

Atoms at or near a free surface experience a different local environment than do atoms in the bulk of a material. As a result, the equilibrium position and energy of these atoms will, in general, be different from their bulk positions and bulk energies. Thus, the surface region may have different moduli. In this sense, all structural elements (large or small) are not strictly homogeneous. However, the surface region is typically very thin, only a few atomic layers. It is thus perfectly acceptable to neglect the surface region and to use the bulk modulus of a structural element as its overall modulus, when the size of the element is in micrometers or larger. For nano-sized structural elements, however, the surface-to-volume ratio is much higher, and the surface region can no longer be neglected when considering the overall elastic behavior of nano-sized structural elements such as nanoparticles, nano-rods, nano-wires, nanotubes, nanobelts, nano-films, etc. Consequently, the effective modulus of nano-sized structural elements should be considered, which by definition becomes size dependent.

To include the surface region in modeling nano-sized structural elements inevitably involves discrete (or atomistic) analysis because the boundary region is only a few atomic layer thick. So, one of the fundamental issues that needs to be addressed in modeling the macroscopic mechanical behavior of nano-sized structural elements is the large difference in length scales. To establish a link between the atomistic structure of surfaces and macroscopic bulk elastic behavior, a two-step approach can be used. First, the surface atomistic structure and interactions should be captured and cast into surface free energy, a thermodynamic quantity of continuum. Then, this surface free energy will be included in the phenomenological description of strain energy density in modeling the macroscopic behavior of nano-sized structural elements.

Surface Free Energy and Surface Stress

Atoms at a free surface experience a different local environment than do atoms in the bulk of a material. As a result, the equilibrium position and energy of these atoms will, in general, be different from those of the atoms deep in the interior of the material. Properties of the material which

are sensitive to the atomic positions or energies will necessarily be affected at or near a surface. For conventional materials where the number of atoms near the free surface is much smaller compared to the total number of atoms in the sample of interest, such surface effects are insignificant and can be rightfully ignored. For nano-sized structural elements (such as nanoparticles, nanowires and nano-films), however, a substantial portion of atoms is located near the surface. Therefore, surface properties become significant in nano-sized elements. Consequently, the overall behavior of nano-sized elements is strongly influenced by the properties of the surface.

There are different ways in which the properties of the surface can be defined and introduced. For example, if one considers an "interface" separating two otherwise homogeneous phases, the interfacial property may be defined either in terms of an *interphase* or by introducing the concept of a *dividing surface*. In the first approach, the system is considered to be one in which there are three phases present – the two bulk phases and an interphase; the boundaries of the interphase are somewhat arbitrary and are usually chosen to be at locations at which the properties are no longer varying significantly with position. The interphase then has a finite volume and may be assigned thermodynamic properties in the normal way, e.g., Capolungo et al. (2006). In the second approach where a single dividing surface is used to separate the two homogeneous phases, the interface contribution to the thermodynamic properties is defined as the excess over the values that would obtain if the bulk phases retained their properties constant up to an imaginary surface (of zero thickness) separating the two phases. In this article, the second approach will be used.

The concept of a dividing surface was first introduced by Gibbs through the use of Gibbs surface free energy (also called surface tension in some literature). The Gibbs density of surface free energy, γ, is defined as the reversible work involved in creating a unit area of *new* surface at constant temperature, volume, and total number of moles. To further illustrate the concept of surface free energy density for a discrete system, consider a representative volume near the surface of a bulk crystal as shown in Fig. 1a. For simplicity, assume the surface is flat and homogeneous. Results derived under these assumptions remain valid for non-planar surfaces provided that the radius of curvature is significantly greater than the width of the transition region, which is typically a few atomic layer thick (Dingreville et al. 2005).

The surface free (excess) energy, w_n, of a near-surface atom is defined by the difference between its total energy and that of an atom deep in the interior of a large crystal. Clearly, w_n is a function of x_3 for the crystal shown in Fig. 1a, i.e., it reaches its maximum value on the surface and tends to zero deep into the crystal; see Fig. 1b. In addition, w_n is a function of the intrinsic crystal surface properties, as well as the relative surface

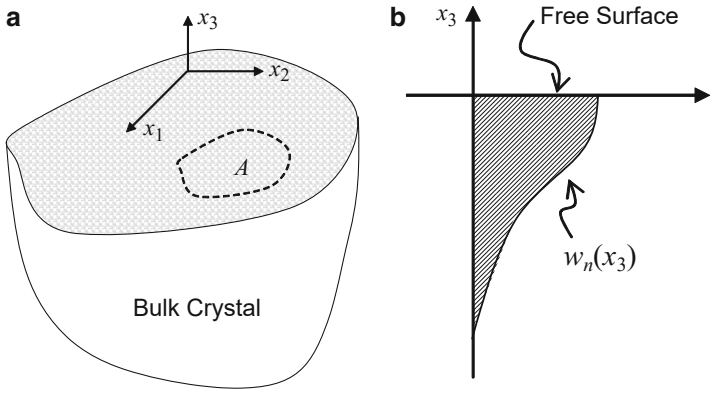

Fig. 1 (**a**) Free surface of a bulk crystal, (**b**) surface free energy as a function of the distance away from the surface

deformation. If there are N atoms underneath of an area A, see Fig. 1a, then the total surface free energy associated with area A is given by $\sum_{n=1}^{N} w_n$. Thus, the Gibbs surface free energy density is defined by

$$\gamma = \frac{1}{A}\sum_{n=1}^{N} w_n. \tag{1}$$

Note that the above definition is in the deformed configuration. It can be viewed as the Eulerian description of the surface free energy density. For solid crystal surfaces, the Lagrange description of the surface free energy density can be defined by

$$\Gamma = \frac{1}{A_0}\sum_{n=1}^{N} w_n, \tag{2}$$

where A_0 is the area originally occupied in the undeformed configuration by the same atoms that occupy the area A in the deformed configuration. It can be easily shown that the two areas are related through

$$A = A_0\left(1+\varepsilon^s_{\eta\eta}\right), \tag{3}$$

where $\varepsilon^s_{\alpha\beta}$ is the surface strain relative to the undeformed crystal lattice. Continuity of the strain field requires, for example, in the particular coordinate system shown in Fig. 1a,

$$\varepsilon^s_{\alpha\beta} = \varepsilon_{\alpha\beta}\big|_{x_3=0}, \alpha, \beta = 1, 2,$$

where ε_{ij} is the bulk strain of the crystal under a given external loading. In the above and the rest of this article, Roman indices range from 1 to 3 and Greek indices range from 1 to 2, unless indicated otherwise. For future references, Lagrangian strain measure will be used in this article.

It is clear from these two definitions that

$$\gamma A = \Gamma A_0. \tag{4}$$

Therefore, one has

$$\Gamma = \gamma\left(1+\varepsilon^s_{\eta\eta}\right). \tag{5}$$

Unfortunately, it is not always clear in the literature which of the two definitions of the surface free energy density is being used. This may be the cause of the wide range of values reported.

Having defined the surface free energy density, one can now introduce the concept of surface stress. Surface free energy corresponds to the work of creating a unit area of surface, whereas surface stress is involved in computing the work in deforming a surface. Specifically, the change in surface free energy should be equal to the work done by the surface stress as it deforms the surface area, i.e.,

$$d(\Gamma A_0) = A_0\Sigma^s_{\alpha\beta}d\varepsilon^s_{\alpha\beta}, \tag{6}$$

where $\Sigma^s_{\alpha\beta}$ is the Lagrangian surface stress tensor. Note that

$$d(\Gamma A_0) = \Gamma dA_0 + A_0 d\Gamma = A_0 d\Gamma. \tag{7}$$

Therefore, one has

$$\Sigma^s_{\alpha\beta} = \frac{d\Gamma}{d\varepsilon^s_{\alpha\beta}}. \tag{8}$$

This defines the surface stress tensor in terms of the Lagrange description of the surface free energy density. Substituting Eq. 5 into Eq. 8 yields the surface stress tensor in terms of the Eulerian surface free energy density:

$$\Sigma^s_{\alpha\beta} = \gamma\delta_{\alpha\beta} + \left(1+\varepsilon^s_{\eta\eta}\right)\frac{d\gamma}{d\varepsilon^s_{\alpha\beta}} \approx \gamma\delta_{\alpha\beta} + \frac{d\gamma}{d\varepsilon^s_{\alpha\beta}}, \tag{9}$$

where $\delta_{\alpha\beta}$ is the two-dimensional Kronecker delta, and the second equation is valid only for small strain deformation. The above is often referred to as the Shuttleworth relationship (Shuttleworth 1950; Sanfeld and Steinchen 2000).

As discussed by Nix and Gao (1998), the need to differentiate the Lagrange and Eulerian

descriptions of the surface stress even for infinitesimal deformation is necessitated by the fact that γ and $d\gamma/d\varepsilon^s_{\alpha\beta}$ can often be on the same order of magnitude.

In a liquid, where the atomic mobility is sufficiently high, atoms from the bulk will come to the surface when the surface is stretched. Such mass diffusion from the bulk to the surface ensures that the microscopic configuration of the surface is preserved following the deformation, i.e., the surface free energy density remains invariant to the surface strain (Shuttleworth 1950). Consequently, the second term in Eq. 9 vanishes, and the surface free energy is numerically equal to the surface stress. This is perhaps why historically surface free energy is also called surface tension. Adding to the confusion is perhaps the fact that both surface free energy density and surface stress have the same physical dimension of force per unit length.

For a solid, due to its long range correlation in atomic positions and low atomic mobility, it might not be possible, in any reasonable experimental time, to keep constant the local configuration around any particular atom in the surface region where the deformation of the surface area is performed. In other words, when a solid crystal deforms, its surface area may change. Such change of surface area is not accomplished by adding (or subtracting) mass to the surface. Instead, the change of surface area is accompanied by the change of surface free energy density. Consequently, the surface free energy density becomes a function of the surface strain in the solid. In this case, the second term in Eq. 9 is nonzero and surface stress is different from surface free energy density.

Just as in the case of surface free energy density, there is an alternative way of introducing the surface stress,

$$d(\gamma A) = A\sigma^s_{\alpha\beta} d\varepsilon^s_{\alpha\beta}, \tag{10}$$

where $\sigma^s_{\alpha\beta}$ may be called the Eulerian surface stress tensor. Note from Eq. 3 that $dA = A_0\delta_{\alpha\beta}d\varepsilon^s_{\alpha\beta}$. Thus,

$$A\sigma^s_{\alpha\beta} d\varepsilon^s_{\alpha\beta} = d(\gamma A) = \gamma A_0\delta_{\alpha\beta} d\varepsilon^s_{\alpha\beta} + Ad\gamma, \tag{11}$$

or

$$\sigma^s_{\alpha\beta} = \frac{\gamma}{1+\varepsilon^s_{\eta\eta}}\delta_{\alpha\beta} + \frac{d\gamma}{d\varepsilon^s_{\alpha\beta}} \approx \gamma\delta_{\alpha\beta} + \frac{d\gamma}{d\varepsilon^s_{\alpha\beta}}, \tag{12}$$

where the second equation is valid only for small strain deformation. This form of the Eulerian surface stress tensor appears to be new to the literature. Clearly,

$$\Sigma^s_{\alpha\beta} = \left(1+\varepsilon^s_{\eta\eta}\right)\sigma^s_{\alpha\beta}, \tag{13}$$

and for small deformation, the Eulerian and Lagrangian stress tensor become the same.

Now consider the total surface free energy of a given surface. Let S be the surface area after the deformation and S_0 be the corresponding area in the undeformed crystal lattice. It then follows from Eq. 6 that the total strain energy stored in the deformed surface is given by

$$U_{surface} = \int_{S_0}\left[\int_0^{\varepsilon^s_{\alpha\beta}} \Sigma^s_{\alpha\beta}\left(e_{\kappa\lambda}\right) de_{\alpha\beta}\right] dS_0, \tag{14}$$

where $\varepsilon^s_{\alpha\beta}$ is the surface strain in the final deformed configuration and $e_{\alpha\beta}$ is the integration variable representing the surface strain, and the fact that the surface stress is a function of the surface strain is explicitly indicated.

On the other hand, if the Eulerian definition of the surface stress Eq. 10 is used, one has

$$\begin{aligned} U_{surface} &= \int_S\left[\int_0^{\varepsilon^s_{\alpha\beta}} \sigma^s_{\alpha\beta}\left(e_{\kappa\lambda}\right) de_{\alpha\beta}\right] dS \\ &= \int_{S_0}\left[\int_0^{\varepsilon^s_{\alpha\beta}} \left(1+e_{\eta\eta}\right)\sigma^s_{\alpha\beta}\left(e_{\kappa\lambda}\right) de_{\alpha\beta}\right] dS_0, \end{aligned} \tag{15}$$

where the second equation follows from the fact that $dS = (1 + e_{\eta\eta})dS_0$. It then follows from Eq. 13 that the resultant total surface free energies from these two methods of calculation are the same. In this article, the Lagrange surface free energy density and surface stress tensor as defined by Eqs. 2 and 8, respectively, will be used.

Assuming the surface free energy density is a smooth function of the surface strain, one may expand the surface free energy density into power series of surface strain, $\varepsilon^s_{\alpha\beta}$,

$$\begin{aligned}\Gamma\left(\varepsilon^s_{\alpha\beta}\right) &= \Gamma_0 + \frac{\partial\Gamma}{\partial\varepsilon^s_{\alpha\beta}}\varepsilon^s_{\alpha\beta} + \frac{1}{2}\frac{\partial^2\Gamma}{\partial\varepsilon^s_{\alpha\beta}\partial\varepsilon^s_{\kappa\lambda}}\varepsilon^s_{\alpha\beta}\varepsilon^s_{\kappa\lambda} \\ &\quad + \frac{1}{6}\frac{\partial^3\Gamma}{\partial\varepsilon^s_{\alpha\beta}\partial\varepsilon^s_{\kappa\lambda}\partial\varepsilon^s_{\gamma\eta}}\varepsilon^s_{\alpha\beta}\varepsilon^s_{\kappa\lambda}\varepsilon^s_{\gamma\eta}\cdots \\ &= \Gamma_0 + \Gamma^{(1)}_{\alpha\beta}\varepsilon^s_{\alpha\beta} + \frac{1}{2}\Gamma^{(2)}_{\alpha\beta\kappa\lambda}\varepsilon^s_{\alpha\beta}\varepsilon^s_{\kappa\lambda} \\ &\quad + \frac{1}{6}\Gamma^{(3)}_{\alpha\beta\kappa\lambda\gamma\eta}\varepsilon^s_{\alpha\beta}\varepsilon^s_{\kappa\lambda}\varepsilon^s_{\gamma\eta}\cdots, \end{aligned} \tag{16}$$

where Γ_0 and $\Gamma^{(1)}_{\alpha\beta}\cdots$ are material and surface dependent. For a given material surface, they can be either measured experimentally or computed using atomistic simulations. Their values can be computed using molecular dynamic simulations (Dingreville et al. 2008; Dingreville and Qu 2007, 2009). Because of symmetry, one has $\Gamma^{(1)}_{\alpha\beta} = \Gamma^{(1)}_{\beta\alpha}$, $\Gamma^{(2)}_{\alpha\beta\kappa\lambda} = \Gamma^{(2)}_{\kappa\lambda\alpha\beta} = \Gamma^{(2)}_{\beta\alpha\kappa\lambda}$, and $\Gamma^{(3)}_{\alpha\beta\kappa\lambda\gamma\eta} = \Gamma^{(3)}_{\beta\alpha\kappa\lambda\gamma\eta} = \Gamma^{(3)}_{\kappa\lambda\alpha\beta\gamma\eta} = \Gamma^{(3)}_{\kappa\lambda\gamma\eta\alpha\beta}$. These conditions imply that there are at most 3 independent parameters in $\Gamma^{(1)}_{\alpha\beta}$, 6 in $\Gamma^{(2)}_{\alpha\beta\kappa\lambda}$, and 18 in $\Gamma^{(3)}_{\alpha\beta\kappa\lambda\gamma\eta}$.

Substitution of Eq. 16 into Eq. 8 yields

$$\Sigma^s_{\alpha\beta} = \Gamma^{(1)}_{\alpha\beta} + \Gamma^{(2)}_{\alpha\beta\kappa\lambda}\varepsilon^s_{\kappa\lambda} + \frac{1}{2}\Gamma^{(3)}_{\alpha\beta\kappa\lambda\gamma\eta}\varepsilon^s_{\kappa\lambda}\varepsilon^s_{\gamma\eta}. \tag{17}$$

Clearly, $\Gamma^{(1)}_{\alpha\beta} = \Gamma^{(1)}_{\beta\alpha}$ gives the internal stress of the surface. It represents the part of surface stress that exists even when the surface strain is absent (i.e., when the surface atoms remain in their positions as if they were deep inside a large crystal). The two-dimensional fourth-order tensor $\Gamma^{(2)}_{\alpha\beta\kappa\lambda} = \Gamma^{(2)}_{\kappa\lambda\alpha\beta} = \Gamma^{(2)}_{\beta\alpha\kappa\lambda} = \Gamma^{(2)}_{\alpha\beta\lambda\kappa}$ represents the surface elasticity tensor, while the two-dimensional sixth-order tensor $\Gamma^{(2)}_{\alpha\beta\kappa\lambda\gamma\eta}$ can be viewed as the tensor of the third-order elastic constants of the surface.

Another important comment that must be made here is that both surface free energy density and surface stress are macroscopic thermodynamic quantities. The basic idea of Gibbs surface energy is based on the concept of a dividing surface that separates the two adjacent phases. Under this assumption, the surface contributions to the thermodynamic quantities (e.g., surface free energy and surface stress) are defined as the excesses over the values that would obtain if the bulk phases retained their properties constant up to the dividing surface. In other words, the interface (not interphase) is a mathematical surface of zero thickness over which the thermodynamic properties change discontinuously from one bulk phase to the other. The excess amount is associated only with the dividing surface. Obviously, this is only an idealization of the realistic situation. In the case of a free surface, for example, the surface contributions to the surface free energy come from several layers of atoms near the surface. Molecular dynamic simulations show that free surface-induced lattice distortion extends about three layers of atoms into the bulk. So, strictly speaking, the surface free energy is defined not just on the surface but on a layer of mass near the surface. The idealization of the dividing surface is thus valid if and only if the bulk crystal is much larger than several atomic sizes. If the bulk crystal contains only a small number of atoms, the validity of macroscopic thermodynamic quantities such as surface free energy is questionable.

From the viewpoint of continuum mechanics, the dividing surface idealization means that there is an "excess" amount of deformation on the dividing surface due to surface stress. In other words, the matter in the dividing surface deforms differently from its neighboring matter in the bulk. This idealization justifies the requirement that the surface free energy $U_{surface}$ must be positive definite.

Effective Modulus of a Particle

Conventionally, elastic modulus of a material is an intensive property. It is defined as a pointwise quantity that relates the stresses and strains at each point in the material. When a material is not homogeneous, such as a composite material, its elastic modulus may vary from point to point. In this case, the concept of effective modulus can be introduced. For example, effective modulus is used to characterize the overall stiffness of a fiber-reinforced composite, where the fiber and matrix have different elastic moduli.

Now consider a particle made of a single phase material. On or near the particle surface, the atomistic structure is somewhat different from that of the bulk. Therefore, a particle of a single phase material, strictly speaking, is not a homogeneous body. The overall stiffness of the particle needs to be characterized by its effective modulus. However, when the particle size is large enough, the surface region is negligible in comparison to the particle volume. In this case, the surface region can be neglected and the particle can be considered as a homogenous body. Therefore, its elastic modulus is uniform and is the same as that of the material from which the particle is made. This is no longer the case when the particle size shrinks to the nanometer range, where the surface region becomes significant in comparison to the particle size. Consequently, the particle must be viewed as an inhomogeneous body, and the effective modulus of the particle needs to be used to characterize the stiffness of the particle. In this section, a formulation is developed to compute the effective modulus of a particle that incorporates the effect of its surface.

To this end, consider a perfect crystal of infinite extent. Within the infinite crystal, let Ω be an ellipsoidal region consisting of a certain number of atoms. Let the initial volume of Ω be V_0 and its surface area be S_0. Now imagine that Ω is removed from the infinite crystal to become a stand-alone particle, as shown in Fig. 2. The newly created surface of the particle gives rise to surface stresses. Consequently, the particle may deform. The self-equilibrium state of the particle will be discussed later in this section. For now, simply let $\hat{V}$ and $\hat{S}$ be the volume and surface area, respectively, of the particle in its self-equilibrium state.

To describe the deformation of the particle, let us introduce a uniform strain ε_{ij} in the bulk of the particle; ε_{ij} is measured from the perfect lattice of an undeformed crystal of infinite extent. For an ellipsoidal particle, see Fig. 3, the surface strain is related to the absolute bulk strain within the particle through a coordinate transformation

$$\varepsilon^s_{\alpha\beta} = t_{\alpha i} t_{\beta j} \varepsilon_{ij}\big|_S, \tag{18}$$

where the transformation tensor $t_{\alpha i}$ for the ellipsoidal surface is derived in Appendix A.

The total strain energy of the particle corresponding to ε_{ij} can then be written as

$$U = U_{bulk} + U_{surface}, \tag{19}$$

where U_{bulk} is the total strain energy in the bulk of the particle

$$\begin{aligned} U_{bulk} &= \int_{V_0} \int_0^{\varepsilon_{ij}} \frac{\partial \Phi}{\partial e_{ij}} de_{ij} dV_0 \\ &= \int_{V_0} \left[\Phi\left(\varepsilon_{ij}\right) - \Phi(0)\right] dV_0, \end{aligned} \tag{20}$$

where Φ is the bulk elastic potential, which can be expanded into a series of the bulk strain tensor

$$\Phi = \frac{1}{2} C_{ijkl} \varepsilon_{ij} \varepsilon_{kl} + \frac{1}{6} C^{(3)}_{ijklmn} \varepsilon_{ij} \varepsilon_{kl} \varepsilon_{mn} + \cdots, \tag{21}$$

where C_{ijkl} and $C^{(3)}_{ijklmn}$ are, respectively, the tensors of second- and third-order elastic constants of the perfect crystal lattice. Substituting Eq. 21 into Eq. 20 and neglecting higher order of strains lead to

$$U_{bulk} = V_0 \left[\frac{1}{2} C_{ijkl} \varepsilon_{ij} \varepsilon_{kl} + \frac{1}{6} C^{(3)}_{ijklmn} \varepsilon_{ij} \varepsilon_{kl} \varepsilon_{mn}\right]. \tag{22}$$

The total surface free energy on the entire particle surface follows from Eq. 14:

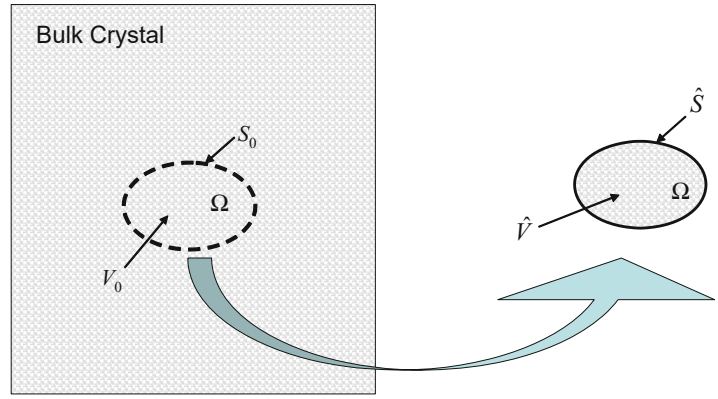

Fig. 2 A particle is created by removing it from a bulk crystal

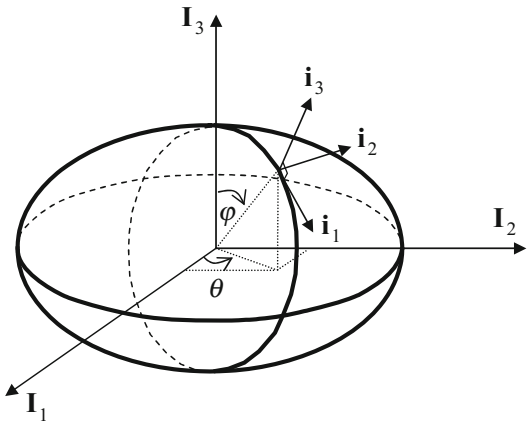

Fig. 3 An ellipsoidal particle

$$U_{surface} = \int_{S_0} \left[\int_0^{\varepsilon^s_{\alpha\beta}} \Sigma^s_{\alpha\beta}\left(e_{\kappa\lambda}\right) de_{\alpha\beta} \right] dS_0. \quad (23)$$

Substituting Eq. 8 into Eq. 23 yields

$$\begin{aligned} U_{surface} &= \int_{S_0} \left[\int_0^{\varepsilon^s_{\alpha\beta}} \frac{d\Gamma}{de_{\alpha\beta}} de_{\alpha\beta} \right] dS_0 \\ &= \int_{S_0} \left[\Gamma\left(\varepsilon^s_{\alpha\beta}\right) - \Gamma(0) \right] dS_0. \end{aligned} \quad (24)$$

Making use of the expansion (17) in Eq. 24, one has

$$\begin{aligned} U_{surface} = \int_{S_0} \Bigg[& \Gamma^{(1)}_{\alpha\beta} \varepsilon^s_{\alpha\beta} + \frac{1}{2} \Gamma^{(2)}_{\alpha\beta\kappa\lambda} \varepsilon^s_{\alpha\beta} \varepsilon^s_{\kappa\lambda} \\ & + \frac{1}{6} \Gamma^{(3)}_{\alpha\beta\kappa\lambda\gamma\eta} \varepsilon^s_{\alpha\beta} \varepsilon^s_{\kappa\lambda} \varepsilon^s_{\gamma\eta} \Bigg] dS_0, \end{aligned} \quad (25)$$

where the surface strain is related to the bulk strain within the particle through the coordinate transformation (Eq. 18). Substitution of Eq. 18 into Eq. 25 yields the strain energy stored in the surface of the ellipsoidal particle Ω when it is subjected to the bulk strain ε_{ij}:

$$\begin{aligned} U_{surface} = & \frac{V_0}{a} \tau_{ij} \varepsilon_{ij} + \frac{V_0}{2a} Q_{ijkl} \varepsilon_{ij} \varepsilon_{kl} \\ & + \frac{V_0}{6a} P_{ijklmn} \varepsilon_{ij} \varepsilon_{kl} \varepsilon_{mn}, \end{aligned} \quad (26)$$

where a is the smallest of the three semiaxes of the ellipsoid and

$$\begin{aligned} \tau_{ij} &= \frac{a}{V_0} \int_{S_0} \Gamma^{(1)}_{\alpha\beta} t_{\alpha i} t_{\beta j} dS_0, \\ Q_{ijkl} &= \frac{a}{V_0} \int_{S_0} \Gamma^{(2)}_{\alpha\beta\kappa\lambda} t_{\alpha i} t_{\beta j} t_{\kappa k} t_{\lambda l} dS_0, \end{aligned} \quad (27)$$

$$P_{ijklmn} = \frac{a}{V_0} \int_{S_0} \Gamma^{(3)}_{\alpha\beta\kappa\lambda\gamma\eta} t_{\alpha i} t_{\beta j} t_{\kappa k} t_{\lambda l} t_{\gamma m} t_{\eta n} dS_0. \quad (28)$$

The fourth-order tensor Q_{ijkl} can be viewed as the *surface rigidity tensor*. It represents the

combined effect of the surface stiffness, $\Gamma^{(2)}_{\alpha\beta\kappa\lambda}$, and the surface geometry. Note that the surface rigidity tensor has the dimension of force per unit length. It possesses the usual symmetry of stiffness tensors, $Q_{ijkl} = Q_{klij} = Q_{jikl} = Q_{ijlk}$. The integrals in Eqs. 27 and 28 can be further written as

$$\tau_{ij} = \frac{3}{4\pi}\int_0^{2\pi}\left[\int_0^{\pi}\Gamma^{(1)}_{\alpha\beta}t_{\alpha i}t_{\beta j}\rho d\phi\right]d\theta, \quad (29)$$

$$Q_{ijkl} = \frac{3}{4\pi}\int_0^{2\pi}\left[\int_0^{\pi}\Gamma^{(2)}_{\alpha\beta\kappa\lambda}t_{\alpha i}t_{\beta j}t_{\kappa k}t_{\lambda l}\rho d\phi\right]d\theta, \quad (30)$$

$$P_{ijklmn} = \frac{3}{4\pi}\int_0^{2\pi}\left[\int_0^{\pi}\Gamma^{(3)}_{\alpha\beta\kappa\lambda\gamma\eta}t_{\alpha i}t_{\beta j}t_{\kappa k}t_{\lambda l}t_{\gamma m}t_{\eta n}\rho d\phi\right]d\theta, \quad (31)$$

where

$$\rho = \sin\phi\sqrt{\sin^2\phi\cos^2\theta + \frac{a^2}{b^2}\sin^2\phi\sin^2\theta + \frac{a^2}{c^2}\cos^2\phi}. \quad (32)$$

It is important to observe that these tensors depend on the shape of the ellipsoid but not the size.

It then follows from substituting Eqs. 20 and 26 into Eq. 19 that

$$U = \frac{V_0}{a}\tau_{ij}\varepsilon_{ij} + \frac{V_0}{2}\left(C_{ijkl} + \frac{1}{a}Q_{ijkl}\right)\varepsilon_{ij}\varepsilon_{kl} + \frac{V_0}{6}\left(C^{(3)}_{ijklmn} + \frac{1}{a}P_{ijklmn}\right)\varepsilon_{ij}\varepsilon_{kl}\varepsilon_{mn}. \quad (33)$$

This gives the total strain energy of the particle when it deforms relative to the undeformed perfect crystal lattice of an infinite extent.

For the subsequent derivations, it is necessary at this point to make the following assumptions:

$$C_{ijkl} \gg \frac{1}{a}Q_{ijkl}, \quad C^{(3)}_{ijklmn} \gg \frac{1}{a}P_{ijklmn}. \quad (34)$$

As mentioned earlier, Q_{ijkl} and P_{ijklmn} are independent of the particle size a. Therefore, the above assumptions, for a given material, effectively place a lower limit on the particle size. Extensive numerical experiments have shown that Eq. 34 is valid for a as small as a few nanometers (Dingreville et al. 2005).

Because of surface stresses, the self-equilibrium state of the particle is different from the perfect crystal lattice of an infinite extent. The strain tensor, $\hat{\varepsilon}_{ij}$, that describes the deformation from the perfect crystal lattice to the self-equilibrium state of the particle can be found by minimizing the total strain energy. To this end, consider

$$\left.\frac{\partial U}{V_0\partial\varepsilon_{ij}}\right|_{\varepsilon_{ij}=\hat{\varepsilon}_{ij}} = \left(C_{ijkl} + \frac{1}{a}Q_{ijkl}\right)\hat{\varepsilon}_{ij} + \frac{1}{2}\left(C^{(3)}_{ijklmn} + \frac{1}{a}P_{ijklmn}\right)\hat{\varepsilon}_{kl}\hat{\varepsilon}_{mn} + \frac{1}{a}\tau_{ij} = 0. \quad (35)$$

This is a set of six quadratic equations for the six components of self-equilibrium strain tensor $\hat{\varepsilon}_{ij}$. It is difficult to solve such a system of nonlinear algebraic equations analytically. However, when the self-equilibrium strain is small, i.e., $\hat{\varepsilon}_{ij} \ll 1$, the quadratic term in Eq. 35 can be neglected. This, in conjunction with Eq. 34, yields the self-equilibrium strain

$$\hat{\varepsilon}_{ij} \approx -\frac{1}{a}\left(C_{ijkl} + \frac{1}{a}Q_{ijkl}\right)^{-1}\tau_{kl} \approx -\frac{1}{a}C^{-1}_{ijkl}\tau_{kl} = -\frac{1}{a}M_{ijkl}\tau_{kl}, \quad (36)$$

where $M_{ijkl} = C^{-1}_{ijkl}$ is the compliance tensor of the bulk crystal.

Now, the effective modulus tensor of the particle at the state of self-equilibrium can be defined as

$$\overline{C}_{ijkl} = \left.\frac{\partial^2}{\partial\varepsilon_{ij}\partial\varepsilon_{kl}}\left(\frac{U}{V_0}\right)\right|_{\boldsymbol{\varepsilon}=\hat{\boldsymbol{\varepsilon}}}. \quad (37)$$

Substitution of Eq. 36 into Eq. 37 gives

S

$$\overline{C}_{ijkl} = C_{ijkl} + \frac{1}{a} Q_{ijkl} + \left(C^{(3)}_{ijklmn} + \frac{1}{a} P_{ijklmn} \right) \hat{\varepsilon}_{mn}. \tag{38}$$

Further substitution of Eq. 36 into Eq. 38 leads to

$$\overline{C}_{ijkl} = C_{ijkl} + \frac{1}{a} Q_{ijkl} - \frac{1}{a} \left(C^{(3)}_{ijklmn} + \frac{1}{a} P_{ijklmn} \right) \left(C_{mnkl} + \frac{1}{a} Q_{mnkl} \right)^{-1} \tau_{kl}. \tag{39}$$

Finally, making use of Eq. 34 in Eq. 39 yields the effective modulus of the particle

$$\overline{C}_{ijkl} = C_{ijkl} + \frac{1}{a} \left(Q_{ijkl} - C^{(3)}_{ijklmn} M_{mnpq} \tau_{pq} \right). \tag{40}$$

It is seen that contribution of the surface energy to the effective modulus of the particle is inversely proportional to the particle size. It will be shown later numerically that the surface energy contribution is negligible unless the particle size approaches the nanometer range.

To close this section, it is worth mentioning that if the surface stiffness tensor is independent of the location, i.e., the surface is homogeneous, then the tensor Q_{ijkl} can be obtained analytically for spherical particles ($a = b = c$), wires, and fibers. Their expressions are given in Appendix C.

Thin Films

Consider a thin film made of a single crystal with cubic symmetry. Further, it is assumed that the top and bottom surfaces of the film are the planes of the cubic crystal (Baker et al. 1993). In the crystallographic coordinate system shown in Fig. 4, the second- and third-order elasticity tensors of the crystal are denoted by C_{ijkl} and $C^{(3)}_{ijklmn}$, respectively. Using the Voigt notations, the non-zero, independent components of these tensors are C_{11}, C_{12}, and C_{44} for C_{ijkl} and C_{111}, C_{112}, C_{123}, C_{144}, C_{155}, and C_{456} for $C^{(3)}_{ijklmn}$. The relationship between indices of the Voigt and tonsorial notations is given in Appendix B. For example, $11 \rightarrow 1$ and $23 \rightarrow 4$, thus, $C_{1123} = C_{14}$ and $C^{(3)}_{112323} = C_{144}$.

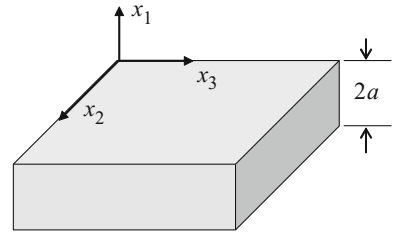

Fig. 4 A single crystal film

In this particular case, the integrals in Eq. 27 can be easily evaluated to yield the non-zero components of τ_{ij} and Q_{ijkl}

$$\tau_{22} = \tau_{33} = \Gamma_{11}, \tag{41}$$

$$Q_{2222} = Q_{3333} = K^s + \mu^s, \quad Q_{2233} = K^s - \mu^s, \; Q_{2323} = \mu^s \tag{42}$$

where Γ_{11}, K^s, and μ^s are related to $\Gamma^{(1)}_{\alpha\beta}$ and $\Gamma^{(2)}_{\alpha\beta\kappa\lambda}$ as indicated in Appendix B. Substituting the above into Eq. 40 yields the effective modulus tensor. Non-zero components of the effective modulus tensor for the thin film in terms of the Voigt notation are given in Appendix C.

It is seen from these expressions that the effective modulus tensor no longer has cubic symmetry. It becomes orthotropic. One quantity of interest is the in-plane unidirectional Young's modulus in the <100> direction

$$\overline{E}_{<100>} = \overline{E}_{22} = \overline{E}_{33} = \left(\overline{C}_{22} - \overline{C}_{23} \right) \left[1 + \frac{\overline{C}_{11}\overline{C}_{23} - \overline{C}^2_{12}}{\overline{C}_{11}\overline{C}_{22} - \overline{C}^2_{12}} \right]. \tag{43}$$

Substituting Eqs. C4, C5, C6, C7, C8, and C9 into Eq. 43 and keeping terms only up to $1/a$ yield

$$\overline{E}_{<100>} = E_{<100>} + \frac{1}{a}\left(K^s\kappa + \Gamma_{11}\chi\right), \quad (44)$$

where

$$E_{<100>} = C_{11} - \frac{2C_{12}^2}{C_{11}+C_{12}} \quad (45)$$

is the unidirectional Young's modulus of the bulk crystal in the <100> directions and

$$\kappa = \frac{\mu^s}{K^s}\left(\frac{C_{11}+2C_{12}}{C_{11}+C_{12}}\right)^2 + \left(\frac{C_{11}}{C_{11}+C_{12}}\right)^2, \quad (46)$$

$$\chi = \frac{\eta}{(C_{11}+C_{12})^2}\left[\left(\frac{2C_{12}^3-C_{11}^3-2C_{12}C_{11}^2-2C_{12}^2C_{11}}{C_{11}C_{12}}\right)C_{111} + \left(6C_{11} - \frac{C_{11}^2}{C_{12}} + \frac{4C_{12}^2}{C_{11}}\right)C_{112} + 2\left(C_{11} - 2C_{12} - \frac{2C_{12}^2}{C_{11}}\right)C_{123}\right]. \quad (47)$$

Clearly, κ and χ are due to surface stress and third-order elastic constants.

The in-plane biaxial Young's modulus is defined as

$$\overline{E}_b = \overline{C}_{22} + \overline{C}_{23} - \frac{2\overline{C}_{12}^2}{\overline{C}_{11}}. \quad (48)$$

Substituting Eqs. C4, C5, C6, C7, C8, and C9 into Eq. 48 and keeping terms only up to $1/a$ yield

$$\overline{E}_b = E_b + \frac{1}{a}\left(2K^s + \Gamma_{11}\chi\right), \quad (49)$$

where

$$E_b = \overline{C}_{11} + \overline{C}_{12} - \frac{2\overline{C}_{12}^2}{\overline{C}_{11}} \quad (50)$$

is the biaxial Young's modulus of the bulk crystal in the {100} planes and

$$\chi = \eta\left[\left(\frac{4C_{12}^2}{C_{11}^3} - \frac{1}{C_{12}}\right)C_{111} + 3\left(\frac{2}{C_{11}} - \frac{1}{C_{12}} - \frac{4C_{12}}{C_{11}^2}\right)C_{112} + \frac{6}{C_{11}}C_{123}\right]. \quad (51)$$

Clearly, χ is due to surface stress and third-order elastic constants.

Under the biaxial loading, $\sigma_{22} = \sigma_{33}$ and $\sigma_{11} = 0$, one can define an effective biaxial Poisson's ratio, $\overline{v}_b = -\varepsilon_{11}/\varepsilon$, where $\varepsilon = \varepsilon_{22} = \varepsilon_{33}$ because of the cubic symmetry in the x_2x_3-plane of the film. Making use of the above equations in conjunction with Eqs. C4, C5, C6, C7, C8, and C9, one arrives at

$$\overline{v}_b = \frac{2C_{12}}{C_{11}} + \frac{2\Gamma_{11}\eta}{aC_{11}C_{12}}\left[\left(\frac{4C_{12}}{C_{11}} - 1\right)C_{112} - \frac{2C_{12}^2}{C_{11}^2}C_{111} - C_{123}\right], \quad (52)$$

where the first term is the biaxial Poisson's ratio for a bulk crystal.

It is noted here that when $\overline{v}_b$ is assumed to be independent of the film thickness, i.e., neglecting the second term in Eq. 52, the effective biaxial Young's modulus Eq. 49 reduces to the effective biaxial modulus derived by Streitz et al. (1994a, b).

The self-equilibrium strain of the film follows directly from Eq. 36:

$$\hat{\boldsymbol{\varepsilon}} = \frac{\Gamma_{11}\eta}{a}\begin{bmatrix} 2/C_{11} & 0 & 0 \\ 0 & -1/C_{12} & 0 \\ 0 & 0 & -1/C_{12} \end{bmatrix}. \quad (53)$$

Clearly the sign of Γ_{11} determines whether there is a negative (contraction) or positive (dilatation) relaxation of the film in the plane directions. For $C_{12} > 0$, positive Γ_{11} would yield negative in-plane strain and positive transverse stain. The same result for the in-plane self-equilibrium $\hat{\varepsilon}_{22} = \hat{\varepsilon}_{33}$ has been obtained by Streitz et al. (1994a).

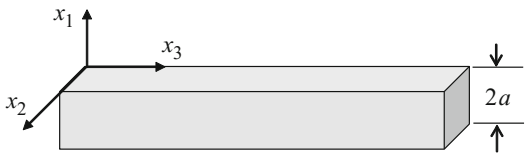

Fig. 5 A thin wire of square cross section

Thin Wire of Square Cross Section

Now, consider a thin wire of square cross section made of a single crystal with cubic symmetry as shown in Fig. 5. Again, assume that the surfaces of the wire are the {100} planes of the cubic crystal. The corresponding effective modulus tensor of the wire can be directly computed from the general formulas given by Eqs. 27, 28, 29, 30, 31, 32, 33, 34, 35, 36, 37, 38, 39, and 40. The nonzero components of the effective modulus tensor are given in Appendix C; see Eqs. C20, C21, C22, C23, C24, and C25.

It is seen from Eqs. C20, C21, C22, C23, C24, and C25 that, just like in the case of the film, the effective modulus tensor becomes orthotropic. The unidirectional Young's modulus in the axial direction is given by

$$\overline{E}_{<100>} = E_{<100>} + \frac{1}{a}\left(K^s\kappa + \Gamma_{11}\chi\right), \quad (54)$$

where

$$E_{<100>} = C_{11} - \frac{2C_{12}^2}{C_{11}+C_{12}} \quad (55)$$

is the unidirectional Young's modulus of the bulk crystal in the <100> directions and

$$\kappa = \frac{\mu^s}{K^s}\left(\frac{C_{11}+2C_{12}}{C_{11}+C_{12}}\right)^2 + \frac{C_{11}^2+4C_{12}^2}{(C_{11}+C_{12})^2}, \quad (56)$$

$$\chi = \frac{\eta}{(C_{11}+C_{12})^2}\left[3\left(2C_{11}-4C_{12}-\frac{C_{11}^2}{C_{12}}\right)C_{112} + \left(\frac{4C_{12}^2}{C_{11}}-\frac{C_{11}^2}{C_{12}}\right)C_{111}+6C_{11}C_{123}\right]. \quad (57)$$

The Poisson's ratio is given by

$$\overline{v}_{13} = \overline{v}_{23} = v_{13} + \frac{1}{a}\left(K^s\kappa + \Gamma_{11}\chi\right), \quad (58)$$

where

$$v_{13} = v_{23} = \frac{C_{12}}{C_{11}+C_{12}} \quad (59)$$

is the Poisson's ratio of the bulk crystal and

$$\kappa = \frac{C_{11}}{(C_{11}+C_{12})^2} - \frac{\mu^s}{K^s}\frac{C_{11}+2C_{12}}{(C_{11}+C_{12})^2} \quad (60)$$

$$\chi = \frac{\eta}{(C_{11}+C_{12})^2}\left[\left(1-2\frac{C_{12}}{C_{11}}\right)C_{111} + \left(4-\frac{3C_{11}}{C_{12}}-\frac{4C_{12}}{C_{11}}\right)C_{112} + \left(3-\frac{C_{11}}{C_{12}}+\frac{2C_{12}}{C_{11}}\right)C_{123}\right] \quad (61)$$

The self-equilibrium strain is given by

$$\hat{\boldsymbol{\varepsilon}} = \frac{-\Gamma_{11}\eta}{a}\begin{bmatrix} \frac{C_{11}-2C_{12}}{C_{11}C_{12}} & 0 & 0 \\ 0 & \frac{C_{11}-2C_{12}}{C_{11}C_{12}} & 0 \\ 0 & 0 & \frac{2}{C_{12}} \end{bmatrix} \quad (62)$$

Spherical Particles

Consider a spherical particle made of an isotropic elastic solid. Furthermore, assume that the particle's surface is homogeneous and isotropic. Clearly, this is an idealized case, for in reality a curved crystal surface inevitably involves different crystallographic surfaces and thus becomes nonhomogeneous and anisotropic. It is nevertheless interesting to study such an idealized case because of the simplicity of the solution.

Under such assumptions, the tensors Q_{ijkl} and $R_{ijkl} = C^{(3)}_{ijklmn}M_{mnpq}\tau_{pq}$ can be easily obtained analytically by setting $a = b = c$ in the equations derived earlier. Their expressions are given in Appendix C; see Eqs. C26, C27, and C28.

Making use of Eqs. C26, C27, and C28, one can easily find that the effective stiffness tensor is still isotropic for an isotropic spherical particle with isotropic surface. For such a particle of radius a, the effective bulk and shear moduli are

Table 1 Bulk and surface elastic constants for single crystal copper

C_{111} (GPa)	C_{112} (GPa)	C_{123} (GPa)	Γ_{11} (J/m^2)	K^s(J/m^2)	μ^s(J/m^2)
832.02	−621.92	15.29	1.3961	2.6755	−3.5524

$$\overline{K} = K + \frac{4}{3a}\left[K^s - \frac{\Gamma_1}{K}\left(\frac{3}{2}L + 3M + \frac{4}{3}N\right)\right], \tag{63}$$

$$\overline{\mu} = \mu + \frac{1}{a}\left[\frac{1}{5}\left(K^s + 6\mu^s\right) - \frac{2\Gamma_1}{3K}(3M + 4N)\right], \tag{64}$$

where K and μ are, respectively, the bulk and shear moduli of the bulk material and L, M, and N are the third-order elastic constants related to C_{ijk}; see Appendix B.

Making use of Eq. 36, one can compute the self-equilibrium strain of the spherical particle

$$\hat{\varepsilon}_{ij} = -\frac{1}{a}M_{ijkl}\tau_{kl} = -\frac{2\Gamma_{11}}{3aK}\delta_{ij}. \tag{65}$$

Clearly, a positive Γ_{11} would mean a contraction of the sphere due to surface stress.

Table 2 Bulk and surface elastic constants for polycrystal copper (isotropic)

K(GPa)	μ(GPa)	Γ_{11} (J/m^2)	K^s(J/m^2)	μ^s(J/m^2)
138.53	43.28	1.3961	2.6755	−3.5524

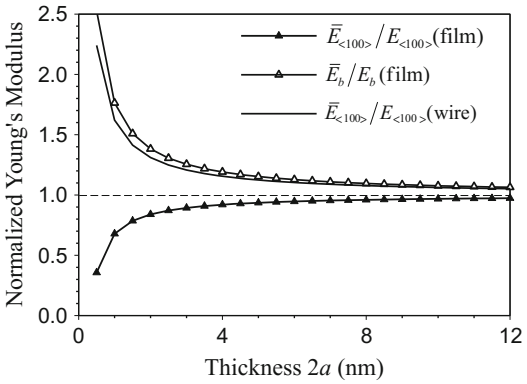

Fig. 6 Normalized effective Young's modulus of Cu films and wires of various sizes

Numerical Examples and Discussions

In this section, several numerical examples for the effective modulus and effective Poisson's ratio of copper spherical particles, wires of square cross section, and films are presented. For the films and wires, it is assumed that they are made of copper single crystals and that their crystallographic directions coincide with the surfaces of the films and wires as shown in Figs. 4 and 5. The cubic (second-order) elastic constants of the copper single crystals are $C_{11} = 167.38$ GPa and $C_{12} = 124.11$ GPa. The third-order elastic constants and the surface properties are given in Table 1. For the spherical particles, the isotropic elastic properties given in Table 2 are used.

The effective unidirectional and biaxial moduli for single crystal Cu films and wires of various thicknesses are plotted in Fig. 6. For the wires, the axial Young's modulus increases as the wire becomes thinner. For a Cu wire with diameter of 4 nm, the axial modulus is almost 20% more than its bulk value. A similar trend is seen for the biaxial modulus of Cu films. However, the uniaxial Young's modulus for the film shows the opposite trend, i.e., it decreases with film thickness. For a 2-nm-thick film, the uniaxial modulus is almost 20% less than its bulk value. Intuitively, one would think that the uniaxial Young's modulus for the film should behave more like the axial Young's modulus of the wire, because a film under uniaxial tension can be viewed as a row of many wires placed side by side under identical axial tension. This would be the case if the surface effect were not a factor. When the surface effect is significant, a row of wires placed side by side is no longer equivalent to a film because the surface area for the row of wires would be much larger.

The Poisson's ratio for the wire and the biaxial Poisson's ratio for the film are plotted in Fig. 7 for wires and films of various thicknesses. The dashed lines indicate the bulk

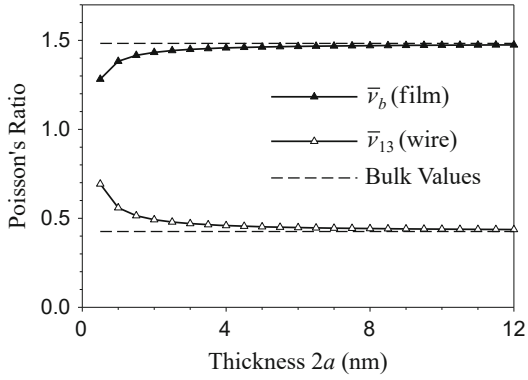

Fig. 7 Poisson's ratio for the films and the wires of various sizes

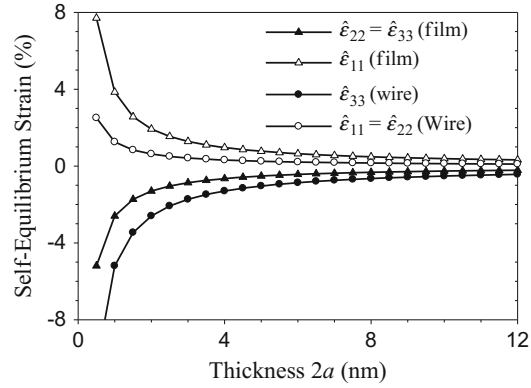

Fig. 8 Self-equilibrium strain for films and wires of various sizes

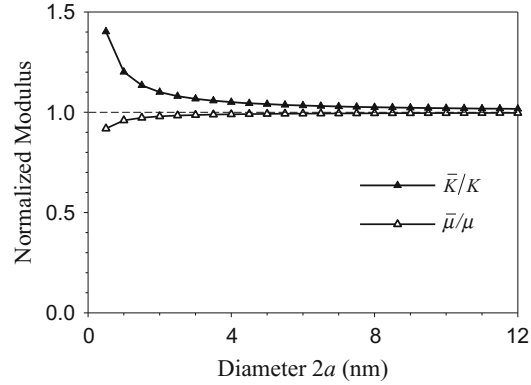

Fig. 9 Normalized effective modulus for spherical particles of various sizes

values without the effect of free surfaces. It is seen that the biaxial Poisson's ratio of the film decreases with decreasing film thickness, while the axial Poisson's ratio of the wire increases with decreasing wire thickness. In both cases, a sharp change occurs around thickness of 2 nm. It is interesting to note that molecular dynamic simulations by Diao et al. (2003) have shown that single crystal gold wires undergo a phase transformation from face-centered cubic symmetry to body-centered tetragonal symmetry when the wire diameter reduces to around 2 nm due to surface stress, giving rise to a significant increase in Poisson's ratio (Diao et al. 2004).

Plotted in Fig. 8 is the self-equilibrium strain for the films and wires. The in-plane strain for the film and the axial strain for the wire are both negative, indicating a reduction in size (area of the film or length of the wire). This is due to the tensile surface stress for Cu in the <100> direction. Accompanying the size reduction is the thickness increase indicated by the positive transverse strain for both film and wire. It is noted that the self-equilibrium strain is rather significant. For example, a film of 4 nm thickness could have an in-plane shrinkage of over 0.6% and transverse expansion of almost 1%.

Now, consider a spherical particle made of isotropic elastic material with elastic properties given in Table 2. The effective shear and bulk moduli of the particle are shown in Fig. 9. It is seen that the shear modulus is much less influenced by the surface energy. The self-equilibrium strain of the particle is shown in Fig. 10. Clearly, for a Cu particle, the surface tension tends to shrink the particle. For a particle of 2 nm in diameter, the radial strain is about 1%.

Finally, as a partial validation of the model presented here, the effective Young's modulus of thin films of various thicknesses was also computed using molecular static (MS) simulations (Dingreville et al. 2008). The agreement is excellent for a film as thin as 1 nm.

Summary

In this article, a framework is described to incorporate the surface free energy into the continuum theory of mechanics. Analytical

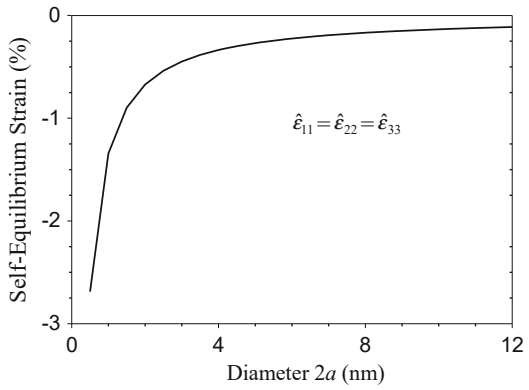

Fig. 10 Self-equilibrium strain for spherical Cu particles of various sizes

expressions were derived for the effective elastic modulus tensor of nano-sized structural elements that account for the effects of surface free energy. Explicit expressions of the effective elasticity tensors were obtained for thin films, wires, and spherical particles. The solutions so derived show that the overall elastic properties of structural elements (such as particles, wires, and films) are size dependent. Although such size dependency is negligible for conventional structural elements, it becomes significant when at least one of the dimensions of the structural element shrinks to nanometers. Numerical examples for copper were also presented in the article to quantitatively illustrate the effects of surface free energy on the elastic properties of nano-sized particles, wires, and films. It shows that the effect of surface energy on the elastic behavior becomes significant when one of the characteristic dimensions is below about 10 nm.

Cross-References

- Carbon Nanotubes
- Continuous-Molecular Approach to Modeling of Nanostructures
- Nanomechanics of Stress Relaxation in Composite Low-Dimensional Structures
- Size Effect in Nanomaterials

Appendix A: Coordinate Transformation

Consider the ellipsoid Ω shown in Fig. 3. When the ellipsoid is subjected to a uniform strain field, ε_{ij}, the surface of the ellipsoid deforms accordingly. Let the two-dimensional surface strain tensor, $\varepsilon^s_{\alpha\beta}$, be defined in a local coordinate system $(\mathbf{i}_1, \mathbf{i}_2, \mathbf{i}_3)$, where $\mathbf{i}_1$ and $\mathbf{i}_2$ are tangent to the surface and $\mathbf{i}_3$ is normal to the surface. Clearly, the choice of $\mathbf{i}_1$ and $\mathbf{i}_2$ is not unique. The following approach is taken to uniquely define the local coordinate system on the ellipsoidal surface.

In the spherical coordinate system,

$$x_1 = r\cos\theta\sin\phi,\ x_2 = r\sin\theta\sin\phi,\\ x_3 = r\cos\phi,\ 0 \le \theta \le 2\pi,\ 0 \le \phi \le \pi, \tag{A1}$$

a point on the surface of the ellipsoid can be represented by the vector

$$\mathbf{R}(\theta,\phi) = a\cos\theta\sin\phi\mathbf{I}_1 + b\sin\theta\sin\phi\mathbf{I}_2 + c\cos\phi\mathbf{I}_3 \tag{A2}$$

A local coordinate system at this point may be introduced by the following three unit vectors:

$$\mathbf{i}_3 = \frac{1}{d_1}\left(\cos\theta\sin\phi\mathbf{I}_1 + \frac{a}{b}\sin\theta\sin\phi\mathbf{I}_2 + \frac{a}{c}\cos\phi\mathbf{I}_3\right), \tag{A3}$$

$$\mathbf{i}_2 = \frac{\partial\mathbf{R}}{\partial\theta}\Big/\left\|\frac{\partial\mathbf{R}}{\partial\theta}\right\| = \frac{1}{d_2}\left(-\frac{a}{b}\sin\theta\mathbf{I}_1 + \cos\theta\mathbf{I}_2\right), \tag{A4}$$

$$\mathbf{i}_1 = \mathbf{i}_2\times\mathbf{i}_3 = \frac{a}{cd_1d_2}\cos\theta\cos\phi\mathbf{I}_1 + \frac{a^2}{bcd_1d_2}\sin\theta\cos\phi\mathbf{I}_2 - \frac{d_2}{d_1}\sin\phi\mathbf{I}_3, \tag{A5}$$

where

$$d_1=\sqrt{\cos^2\theta\sin^2\phi+\frac{a^2}{b^2}\sin^2\theta\sin^2\phi+\frac{a^2}{c^2}\cos^2\phi}, \tag{A6}$$

$$d_2=\sqrt{\frac{a^2}{b^2}\sin^2\theta+\cos^2\theta}, \tag{A7}$$

The transformation matrix between the global $(\mathbf{I}_1,\mathbf{I}_2,\mathbf{I}_3)$ and the local $(\mathbf{i}_1,\mathbf{i}_2,\mathbf{i}_3)$ coordinate systems is thus given by

$$[t_{ij}] = \begin{bmatrix} \frac{a}{cd_1d_2}\cos\theta\cos\phi & \frac{a^2}{bcd_1d_2}\sin\theta\cos\phi & -\frac{d_2}{d_1}\sin\phi \\ -\frac{a}{bd_2}\sin\theta & \frac{1}{d_2}\cos\theta & 0 \\ \frac{1}{d_1}\cos\theta\sin\phi & \frac{a}{bd_1}\sin\theta\sin\phi & \frac{a}{cd_1}\cos\phi \end{bmatrix}. \tag{A8}$$

Therefore, according to the tensor transformation rule, the surface strain in the local coordinate system can be written as

$$\varepsilon^s_{\alpha\beta}=t_{\alpha i}t_{\beta j}\varepsilon_{ij}. \tag{A9}$$

For a spherical particle ($a=b=c$), the transformation matrix reduces to

$$[t_{ij}] = \begin{bmatrix} \cos\theta\cos\phi & \sin\theta\cos\phi & -\sin\phi \\ -\sin\theta & \cos\theta & 0 \\ \sin\phi\cos\theta & \sin\phi\sin\theta & \cos\phi \end{bmatrix}. \tag{A10}$$

Bulk and Surface Elasticity Tensors

When subjected to a strain field ε_{ij}, the strain energy of an elastic body can be written as

$$\Phi=\frac{1}{2}C_{ijkl}\varepsilon_{ij}\varepsilon_{kl}+\frac{1}{6}C^{(3)}_{ijklmn}\varepsilon_{ij}\varepsilon_{kl}\varepsilon_{mn}+\cdots\cdots \tag{B1}$$

where C_{ijkl} is a fourth-order tensor consists of (second-order) elastic constants and $C^{(3)}_{ijkl}$ is a sixth-order tensor consisting of the third-order elastic constants of the solid. It can be easily shown that the following symmetry conditions must be met by these tensors:

$$C_{ijkl}=C_{jikl}=C_{klij}, \tag{B2}$$

$$\begin{aligned} C^{(3)}_{ijklmn}&=C^{(3)}_{jiklmn}=C^{(3)}_{klmnij}=C^{(3)}_{mnijkl}\\ &=C^{(3)}_{ijmnkl}=C^{(3)}_{mnklij}=C^{(3)}_{klijmn}. \end{aligned} \tag{B3}$$

Instead of the tensorial notation, it is convenient in certain cases to use the Voigt (contracted) notation for these tensors. For example, C_{11} is used for C_{1111}, C_{12} is used for C_{1122}, C_{123} is used for C_{112233}, etc. The general rules to contract the indices are (11) → (1), (22) → (2), (33) → (3), (12) → (6), (13) → (5), and (23) → (4). Of course, the symmetry properties of the elasticity tensor remain in their contracted form, e.g., $C_{12}=C_{21}$ and $C_{123}=C_{312}$.

For solids with cubic symmetry, there are three independent non-zero second-order elastic constants for C_{ijkl}:

$$\begin{aligned} &C_{11}=C_{22}=C_{33}, C_{12}=C_{13}=C_{23},\\ &C_{44}=C_{55}=C_{66} \end{aligned} \tag{B4}$$

and six independent non-zero third-order elastic constants for $C^{(3)}_{ijklmn}$:

$$C_{111}=C_{222}=C_{333}, C_{144}=C_{255}=C_{366}, \tag{B5}$$

$$C_{112}=C_{113}=C_{122}=C_{133}=C_{223}=C_{233}, \tag{B6}$$

$$C_{155}=C_{166}=C_{244}=C_{266}=C_{344}=C_{355}, \tag{B7}$$

$$C_{123}, C_{456}$$

For isotropic solids, the number of independent elastic constants is further reduced. For C_{ijkl}, there are only two independent ones. They are

$$\begin{aligned} &C_{11}=C_{22}=C_{33}=K+\frac{4\mu}{3},\\ &C_{12}=C_{13}=C_{23}=K-\frac{2\mu}{3}, \end{aligned} \tag{B8}$$

$$C_{44}=C_{55}=C_{66}=\mu, \tag{B9}$$

where K is called the bulk modulus and μ the shear modulus.

For isotropic solids, $C^{(3)}_{ijklmn}$ has three independent non-zero constants L, M, and N. They are related to C_{ijk} by

$$C_{111} = C_{222} = C_{333} = L + 6M + 8N, \quad \text{(B10)}$$

$$C_{144} = C_{255} = C_{366} = M, \quad \text{(B11)}$$

$$C_{112} = C_{113} = C_{122} = C_{133} = C_{223} = C_{233} = L + 2M, \quad \text{(B12)}$$

$$C_{155} = C_{166} = C_{244} = C_{266} = C_{344} = C_{355} = M + 2N, \quad \text{(B13)}$$

$$C_{123} = L, C_{456} = N. \quad \text{(B14)}$$

In terms of the Kronecker delta δ_{ij}, these elasticity tensors can be written conveniently as

$$C_{ijkl} = K\delta_{ij}\delta_{kl} + \mu\left(\delta_{ik}\delta_{jl} + \delta_{il}\delta_{jk} - \frac{2}{3}\delta_{ij}\delta_{kl}\right), \quad \text{(B15)}$$

$$\begin{aligned} C^{(3)}_{ijklmn} = {} & L\delta_{ij}\delta_{kl}\delta_{mn} \\ & + M\left(\delta_{ij}\delta_{km}\delta_{ln} + \delta_{ij}\delta_{kn}\delta_{lm}\right. \\ & + \delta_{im}\delta_{jn}\delta_{kl} + \delta_{in}\delta_{jm}\delta_{kl} \\ & \left.+\delta_{ik}\delta_{jl}\delta_{mn} + \delta_{il}\delta_{jk}\delta_{mn}\right) \\ & + N\left(\delta_{ik}\delta_{jm}\delta_{ln} + \delta_{im}\delta_{jk}\delta_{ln}\right. \\ & + \delta_{il}\delta_{jm}\delta_{kn} + \delta_{im}\delta_{jl}\delta_{kn} \\ & + \delta_{ik}\delta_{jn}\delta_{lm} + \delta_{in}\delta_{jk}\delta_{lm} \\ & \left.+\delta_{il}\delta_{jn}\delta_{km} + \delta_{in}\delta_{jl}\delta_{km}\right). \end{aligned} \quad \text{(B16)}$$

Next, consider the surface elasticity tensors $\Gamma^{(1)}_{\alpha\beta}$ and $\Gamma^{(2)}_{\alpha\beta\kappa\lambda}$. Again, it follows from the definition (16) that certain symmetry conditions must be met:

$$\Gamma^{(1)}_{\alpha\beta} = \Gamma^{(1)}_{\beta\alpha}, \Gamma^{(2)}_{\alpha\beta\kappa\lambda} = \Gamma^{(2)}_{\kappa\lambda\alpha\beta} = \Gamma^{(2)}_{\beta\alpha\kappa\lambda}. \quad \text{(B17)}$$

In general, $\Gamma^{(1)}_{\alpha\beta}$ and $\Gamma^{(2)}_{\alpha\beta\kappa\lambda}$ can be anisotropic in the surface (where they are defined). For isotropic surfaces, both $\Gamma^{(1)}_{\alpha\beta}$ and $\Gamma^{(2)}_{\alpha\beta\kappa\lambda}$ should be isotropic. It can be shown (Aris 1962) that $\Gamma^{(1)}_{\alpha\beta}$ is isotropic if and only $\Gamma^{(1)}_{12} = \Gamma^{(1)}_{21} = 0$ and $\Gamma^{(1)}_{11} = \Gamma^{(1)}_{22}$ and $\Gamma^{(2)}_{\alpha\beta\kappa\lambda}$ is isotropic if and only $\Gamma^{(2)}_{1112} = \Gamma^{(2)}_{1222} = 0$ and $\Gamma^{(2)}_{1111} = \Gamma^{(2)}_{2222} = \Gamma^{(2)}_{1122} + 2\Gamma^{(2)}_{1212}$. This is the case if the surface has a rotation axis of threefold or higher symmetry (Buerger 1963). Therefore, for a {111} surface, which has threefold symmetry, and for a {100} surface, which has fourfold symmetry, the surface stiffness tensors can be written as

$$\Gamma^{(1)}_{\alpha\beta} = \Gamma_{11}\delta_{\alpha\beta}, \Gamma^{(2)}_{\alpha\beta\kappa\lambda} = K^s\delta_{\alpha\beta}\delta_{\kappa\lambda} + \mu^s\left(\delta_{\alpha\kappa}\delta_{\beta\lambda} + \delta_{\alpha\lambda}\delta_{\beta\kappa} - \delta_{\alpha\beta}\delta_{\kappa\lambda}\right). \quad \text{(B18)}$$

Special Cases

Films

For the film shown in Fig. 4, the integrals in Eq. 27 can be written as integrals on the top and bottom surfaces of the film. On these surfaces, the integrands in both integrals are constants. Thus, they can be easily carried out to yields Eqs. 41 and 42. Consequently, the non-zero components of the fourth-order tensor $R_{ijkl} = C^{(3)}_{ijklmn}M_{mnpq}\tau_{pq}$ are obtained as

$$R_{1111} = 2\Gamma_{11}\eta\left(\frac{C_{112}}{C_{12}} - \frac{C_{111}}{C_{11}}\right),$$

$$R_{1122} = R_{1133} = \Gamma_{11}\eta\left(\frac{C_{123}+C_{112}}{C_{12}} - \frac{2C_{112}}{C_{11}}\right), \quad \text{(C1)}$$

$$R_{2222} = R_{3333} = \Gamma_{11}\eta\left(\frac{C_{111}+C_{112}}{C_{12}} - \frac{2C_{112}}{C_{11}}\right),$$

$$R_{2233} = 2\Gamma_{11}\eta\left(\frac{C_{112}}{C_{12}} - \frac{C_{123}}{C_{11}}\right), \quad \text{(C2)}$$

$$R_{2323} = 2\Gamma_{11}\eta\left(\frac{C_{155}}{C_{12}} - \frac{C_{144}}{C_{11}}\right),$$

$$R_{1313} = R_{1212} = \Gamma_{11}\eta\left(\frac{C_{144}+C_{155}}{C_{12}} - \frac{2C_{155}}{C_{11}}\right), \tag{C3}$$

where C_{ijk} are related to their third-order elastic constants as indicated in Appendix B and η is defined by Eq. C10. The non-zero components of the effective elasticity tensor for the thin film in terms of the Voigt notation can then be obtained from Eq. 40:

$$\overline{C}_{11} = C_{11} + \frac{2\Gamma_{11}\eta}{a}\left(\frac{C_{111}}{C_{11}} - \frac{C_{112}}{C_{12}}\right), \tag{C4}$$

$$\overline{C}_{12} = \overline{C}_{13} = C_{12} + \frac{\Gamma_{11}\eta}{a}\left(\frac{2C_{112}}{C_{11}} - \frac{C_{123}+C_{112}}{C_{12}}\right), \tag{C5}$$

$$\overline{C}_{22} = \overline{C}_{33} = C_{11} + \frac{1}{a}\Bigg[\left(K^s + \mu^s\right) + \Gamma_{11}\eta\left(\frac{2C_{112}}{C_{11}} - \frac{C_{111}+C_{112}}{C_{12}}\right)\Bigg], \tag{C6}$$

$$\overline{C}_{23} = C_{12} + \frac{1}{a}\Bigg[\left(K^s - \mu^s\right) + 2\Gamma_{11}\eta\left(\frac{C_{123}}{C_{11}} - \frac{C_{112}}{C_{12}}\right)\Bigg], \tag{C7}$$

$$\overline{C}_{44} = C_{44} + \frac{1}{a}\left[\mu^s + 2\Gamma_{11}\eta\left(\frac{C_{144}}{C_{11}} - \frac{C_{155}}{C_{12}}\right)\right], \tag{C8}$$

$$\overline{C}_{55} = \overline{C}_{66} = C_{44} + \frac{\Gamma_{11}\eta}{a}\left(\frac{2C_{155}}{C_{11}} - \frac{C_{144}+C_{155}}{C_{12}}\right), \tag{C9}$$

where η is a nondimensional constant given by

$$\eta = \frac{C_{11}C_{12}}{(C_{11}+2C_{12})(C_{11}-C_{12})}. \tag{C10}$$

Note that the positive definiteness of the strain energy density requires $C_{11} > |C_{12}|$. Thus, $\eta \geq 0$ if $C_{12} \geq 0$.

Wires

For the wire shown in Fig. 5, the integrals in Eq. 27 can be written as integrals on the lateral surfaces of the wire. On these surfaces, the integrands in both integrals are constants. Thus, they can be easily carried out to yield

$$\tau_{11} = \tau_{22} = \Gamma_{11}, \tau_{33} = 2\Gamma_{11}, \tag{C11}$$

$$Q_{1111} = Q_{2222} = K^s + \mu^s, Q_{3333} = 2\left(K^s + \mu^s\right), \tag{C12}$$

$$Q_{1133} = Q_{2233} = K^s - \mu^s, Q_{2323} = Q_{1313} = \mu^s. \tag{C13}$$

Consequently, the non-zero components of the forth-order tensor $R_{ijkl} = C^{(3)}_{ijklmn}M_{mnpq}\tau_{pq}$ are obtained as

$$R_{1111} = R_{2222} = \Gamma_{11}\eta\left(\frac{C_{111}+3C_{112}}{C_{12}} - \frac{2\left(C_{111}+C_{112}\right)}{C_{11}}\right), \tag{C14}$$

$$R_{3333} = 2\Gamma_{11}\eta\left(\frac{C_{111}+C_{112}}{C_{12}} - \frac{2C_{112}}{C_{11}}\right), \tag{C15}$$

$$R_{1122} = 2\Gamma_{11}\eta\left(\frac{C_{112}+C_{123}}{C_{12}} - \frac{2C_{112}}{C_{11}}\right), \tag{C16}$$

$$R_{1133} = R_{2233} = \Gamma_{11}\eta\left(\frac{C_{123}+3C_{112}}{C_{12}} - \frac{2\left(C_{112}+C_{123}\right)}{C_{11}}\right), \tag{C17}$$

$$R_{2323} = R_{1313} = \Gamma_{11}\eta\left(\frac{C_{144}+3C_{155}}{C_{12}} - \frac{2\left(C_{144}+C_{155}\right)}{C_{11}}\right), \tag{C18}$$

$$R_{1212} = 2\Gamma_{11}\eta\left(\frac{C_{144}+C_{155}}{C_{12}} - \frac{2C_{155}}{C_{11}}\right). \tag{C19}$$

The non-zero components of the corresponding effective elasticity tensor are thus given by

$$\overline{C}_{11} = \overline{C}_{22} = C_{11} + \frac{1}{a}\Bigg[\left(K^s+\mu^s\right) + \Gamma_{11}\eta\left(\frac{2\left(C_{111}+C_{112}\right)}{C_{11}} - \frac{C_{111}+3C_{112}}{C_{12}}\right)\Bigg], \tag{C20}$$

$$\overline{C}_{33} = C_{11} + \frac{1}{a}\Bigg[2\left(K^s+\mu^s\right) + 2\Gamma_{11}\eta\left(\frac{2C_{112}}{C_{11}} - \frac{C_{111}+C_{112}}{C_{12}}\right)\Bigg], \tag{C21}$$

$$\overline{C}_{12} = C_{12} + \frac{2\Gamma_{11}\eta}{a}\left(\frac{2C_{112}}{C_{11}} - \frac{C_{123}+C_{112}}{C_{12}}\right), \tag{C22}$$

$$\overline{C}_{13} = \overline{C}_{23} = C_{12} + \frac{1}{a}\Bigg[\left(K^s-\mu^s\right) + \Gamma_{11}\eta\left(\frac{2\left(C_{112}+C_{123}\right)}{C_{11}} - \frac{3C_{112}+C_{123}}{C_{12}}\right)\Bigg], \tag{C23}$$

$$\overline{C}_{44} = \overline{C}_{55} = C_{44} + \frac{1}{a}\Bigg[\mu^s + \Gamma_{11}\eta\left(\frac{2\left(C_{144}+C_{155}\right)}{C_{11}} - \frac{C_{144}+3C_{155}}{C_{12}}\right)\Bigg], \tag{C24}$$

$$\overline{C}_{66} = C_{44} + \frac{2\Gamma_{11}\eta}{a}\left(\frac{2C_{155}}{C_{11}} - \frac{C_{144}+C_{155}}{C_{12}}\right). \tag{C25}$$

Spherical Particles

$$Q_{ijkl} = \frac{4}{3}K^s\delta_{ij}\delta_{kl} + \frac{1}{5}\left(K^s+6\mu^s\right) \times \left(\delta_{ik}\delta_{jl} + \delta_{il}\delta_{jk} - \frac{2}{3}\delta_{ij}\delta_{kl}\right), \tag{C26}$$

$$\tau_{ij} = 2\Gamma_{11}\delta_{ij}, \tag{C27}$$

$$R_{ijkl} = \frac{2\Gamma_{11}}{3K}\left(3L+6M+\frac{8}{3}N\right)\delta_{ij}\delta_{kl} + \frac{2\Gamma_{11}}{3K}\left(3M+4N\right) \times \left(\delta_{ik}\delta_{jl} + \delta_{il}\delta_{jk} - \frac{2}{3}\delta_{ij}\delta_{kl}\right). \tag{C28}$$

References

Aris R (1962) Vectors, tensors, and the basic equations of fluid mechanics. Prentice Hall

Baker SP, Small MK, Vlassak JJ, Daniels BJ, Nix WD (1993) The search for the supermodulus effect. In: Mechanical properties and deformation behavior of materials having ultra-fine microstructures. Springer Netherlands

Buerger MJ et al. (1963) Elementary crystallography. Wiley

Capolungo L, Cherkaoui M, Qu J (2006) Homogenization method for strength and inelastic behavior of nanocrystalline materials. In: IUTAM symposium on size effects on material and structural behavior at micron- and nano-scales. Springer Netherlands

Diao J, Gall K, Dunn ML (2003) Surface-stress-induced phase transformation in metal nanowires. Nat Mater 2(10):656–660

Diao J, Gall K, Dunn ML (2004) Atomistic simulation of the structure and elastic properties of gold nanowires. J Mech Phys Solids 52(9):1935–1962

Dingreville R, Kulkarni AJ, Zhou M, Qu J (2008) A semi-analytical method for quantifying the size-dependent elasticity of nanostructures. Model Simul Mater Sci Eng 16(2):025002

Dingreville R, Qu J (2007) A semi-analytical method to compute surface elastic properties. Acta Mater 55(1):141–147

Dingreville R, Qu J (2009) A semi-analytical method to estimate interface elastic properties. Comput Mater Sci 46(1):83–91
Dingreville R, Qu J, Cherkaoui M (2005) Surface free energy and its effect on the elastic behavior of nano-sized particles, wires and films. J Mech Phys Solids 53(8):1827–1854
Nix WD, Gao H (1998) An atomistic interpretation of interface stress. Scr Mater 39(12):1653–1661
Sanfeld A, Steinchen A (2000) Surface energy, stress, capillary-elastic pressure and chemical equilibrium constant in nanoparticles. Surf Sci 463(3):157–173
Shuttleworth R (1950) The surface tension of solids. Proc Phys Soc Sect A 63(5):444–457
Streitz FH, Cammarata RC, Sieradzki K (1994a) Surface-stress effects on elastic properties. I. Thin metal films. Phys Rev B 49(15):10699–10706
Streitz FH, Cammarata RC, Sieradzki K (1994b) Surface-stress effects on elastic properties. II. Metallic multilayers. Phys Rev B 49(15):10707–10716

Surface Geometry, Elements

Wojciech Pietraszkiewicz
Faculty of Civil and Environmental Engineering, Department of Mechanics of Materials and Structures, Gdańsk University of Technology, Gdańsk, Poland

Synonyms

Differential geometry; Geometry of curves and surfaces

Definition

By geometry of a surface one usually means characterization of its metric and curvature properties in surface curvilinear coordinates. Due to a large variety of surface shapes, it is convenient to use the common tensor notation. In shell theory, the most useful concepts are the surface covariant differentiation, description of surface curves and surface divergence theorems of vector and tensor fields.

Introduction

Geometry of a surface embedded into the three-dimensional Euclidean point space was presented in many classical monographs, for example, by Eisenhart (1947) and do Carmo (1976). Within the needs of theoretical description required in shell structures, appropriate introductions were worked out as parts of the books by Green and Zerna (1954), Naghdi (1963), Chernykh (1964), Flügge (1972), Pietraszkiewicz (1977), Başar and Krätzig (2001), Ciarlet (2005), and Lebedev et al. (2010).

Here an elementary introduction to the surface differential geometry is given. The relations may be used as a common notation base for the geometric description of various shell models discussed in this section.

Geometry of a Surface

A surface $\mathcal{M}$ in the three-dimensional Euclidean point space $\mathcal{E}$ can locally be defined by the position vector $\mathbf{r} = \mathbf{r}(\theta^\alpha)$ as the function of two curvilinear coordinates θ^α, $\alpha = 1, 2$. Usually $\mathbf{r}$ is related to a reference frame $(O, \mathbf{i}_i)$, $i = 1, 2, 3$, in $\mathcal{E}$ with O a reference point and $\mathbf{i}_i$ some orthonormal vectors.

Two surface (covariant) vectors $\boldsymbol{a}_\alpha$ and the unit normal vector $\boldsymbol{n}$ defined by

$$\boldsymbol{a}_1 = \frac{\partial \mathbf{r}}{\partial \theta^1} \equiv \mathbf{r}_{,1}, \quad \boldsymbol{a}_2 = \frac{\partial \mathbf{r}}{\partial \theta^2} \equiv \mathbf{r}_{,2}, \quad \boldsymbol{n} = \frac{\boldsymbol{a}_1 \times \boldsymbol{a}_2}{|\,\boldsymbol{a}_1 \times \boldsymbol{a}_2\,|}, \tag{1}$$

form the fundamental triad of base vectors on $\mathcal{M}$. Two dual (contravariant) surface vectors are related to $\boldsymbol{a}_\alpha$ by

$$\boldsymbol{a}^\beta \cdot \boldsymbol{a}_\alpha = \delta^\beta_\alpha = \begin{cases} 1 \;\; if \;\; \alpha = \beta, \\ 0 \;\; if \;\; \alpha \neq \beta, \end{cases} \tag{2}$$

$$\boldsymbol{a}^1 = \frac{\boldsymbol{a}_2 \times \boldsymbol{n}}{(\boldsymbol{a}_1 \times \boldsymbol{a}_2) \cdot \boldsymbol{n}}, \quad \boldsymbol{a}^2 = \frac{\boldsymbol{n} \times \boldsymbol{a}_1}{(\boldsymbol{a}_1 \times \boldsymbol{a}_2) \cdot \boldsymbol{n}}. \tag{3}$$

The coefficients defined by

$$a_{\alpha\beta} = \boldsymbol{a}_\alpha \cdot \boldsymbol{a}_\beta, \quad a^{\alpha\beta} = \boldsymbol{a}^\alpha \cdot \boldsymbol{a}^\beta \tag{4}$$

are known as the covariant and contravariant components of the surface metric tensor. They allow one to calculate lengths of curves on $\mathcal{M}$, angles between them, and areas on $\mathcal{M}$.

The following relations are satisfied:

$$\boldsymbol{a}^\alpha = a^{\alpha\beta}\boldsymbol{a}_\beta, \quad \boldsymbol{a}_\alpha = a_{\alpha\beta}\boldsymbol{a}^\beta, \tag{5}$$

where the summation convention over the repeated Greek indices has been used. Similarly, the components $a^{\alpha\beta}$ and $a_{\alpha\beta}$ are used to raise or lower indices of components of the surface vectors and tensors.

In various geometric formulae, it is convenient to make use of components of the surface alternation tensor

$$\begin{aligned} &\varepsilon_{\alpha\beta} = \left(\boldsymbol{a}_\alpha \times \boldsymbol{a}_\beta\right) \cdot \boldsymbol{n}, \quad \varepsilon^{\alpha\beta} = \left(\boldsymbol{a}^\alpha \times \boldsymbol{a}^\beta\right) \cdot \boldsymbol{n}, \\ &[(\boldsymbol{a}_1 \times \boldsymbol{a}_2) \cdot \boldsymbol{n}]^2 = \det\left(a_{\alpha\beta}\right) = a > 0, \end{aligned} \tag{6}$$

which satisfy the relations

$$\begin{aligned} &\varepsilon_{12} = -\varepsilon_{21} = \sqrt{a}, \quad \varepsilon_{11} = \varepsilon_{22} = 0, \\ &\varepsilon^{12} = -\varepsilon^{21} = \frac{1}{\sqrt{a}}, \quad \varepsilon^{11} = \varepsilon^{22} = 0, \end{aligned} \tag{7}$$

$$\begin{aligned} &\varepsilon_{\alpha\beta}\varepsilon^{\lambda\mu} = \delta^\lambda_\alpha\delta^\mu_\beta - \delta^\lambda_\beta\delta^\mu_\alpha, \quad \varepsilon_{\alpha\beta}\varepsilon^{\lambda\beta} = \delta^\lambda_\alpha, \\ &\varepsilon_{\alpha\beta}\varepsilon^{\alpha\beta} = 2, \quad \varepsilon^{\alpha\lambda}\varepsilon^{\beta\mu}a_{\alpha\beta} = a^{\lambda\mu}, \\ &a^{\alpha\lambda}a^{\beta\mu}\varepsilon_{\alpha\beta} = \varepsilon^{\lambda\mu}, \end{aligned} \tag{8}$$

$$\begin{aligned} &\boldsymbol{a}_\alpha \times \boldsymbol{a}_\beta = \varepsilon_{\alpha\beta}\boldsymbol{n}, \quad \boldsymbol{a}^\alpha \times \boldsymbol{a}^\beta = \varepsilon^{\alpha\beta}\boldsymbol{n}, \\ &\boldsymbol{n} \times \boldsymbol{a}_\alpha = \varepsilon_{\alpha\beta}\boldsymbol{a}^\beta, \quad \boldsymbol{n} \times \boldsymbol{a}^\alpha = \varepsilon^{\alpha\beta}\boldsymbol{a}_\beta. \end{aligned} \tag{9}$$

Differentiation of the unit normal $\boldsymbol{n}$ with respect to the surface coordinates gives two vectors $\boldsymbol{n}_{,\alpha}$ tangent to $\mathcal{M}$. The coefficients

$$b_{\alpha\beta} = -\boldsymbol{n}_{,\alpha} \cdot \boldsymbol{a}_\beta = -\boldsymbol{n}_{,\beta} \cdot \boldsymbol{a}_\alpha = \boldsymbol{n} \cdot \boldsymbol{a}_{\alpha,\beta} \tag{10}$$

are known as the covariant components of the surface curvature tensor. Associated with $b_{\alpha\beta}$ two invariants

$$H = \frac{1}{2}a^{\alpha\beta}b_{\alpha\beta}, \quad K = \frac{1}{2}\varepsilon^{\alpha\lambda}\varepsilon^{\beta\mu}b_{\alpha\beta}b_{\lambda\mu} \tag{11}$$

are called the mean and the Gaussian curvatures of $\mathcal{M}$, respectively. The components of $b_{\alpha\beta}$ allow one to calculate curvatures and torsions of the surface curves.

Covariant Differentiation

Partial differentiation of the base vectors $\boldsymbol{a}_\alpha$ with respect to the surface coordinates leads to

$$\boldsymbol{a}_{\alpha,\beta} = \mathbf{r}_{,\alpha\beta} = \Gamma_{\lambda.\alpha\beta}\boldsymbol{a}^\lambda + b_{\alpha\beta}\boldsymbol{n}, \tag{12}$$

where

$$\begin{aligned} &\Gamma_{\lambda.\alpha\beta} = \boldsymbol{a}_\lambda \cdot \boldsymbol{a}_{\alpha,\beta} = \frac{1}{2}\left(a_{\lambda\alpha,\beta} + a_{\lambda\beta,\alpha} - a_{\alpha\beta,\lambda}\right), \\ &\Gamma^\mu_{\alpha\beta} = a^{\lambda\mu}\Gamma_{\lambda.\alpha\beta} = \boldsymbol{a}^\mu \cdot \boldsymbol{a}_{\alpha,\beta} = -\boldsymbol{a}^\mu{}_{,\alpha} \cdot \boldsymbol{a}_\beta \end{aligned} \tag{13}$$

are called the surface Christoffel symbols of the first and second kind, respectively.

Differentiation of the surface tangent field $\boldsymbol{v} = v^\alpha\boldsymbol{a}_\alpha = v_\alpha\boldsymbol{a}^\alpha$ gives

$$\begin{aligned} \boldsymbol{v}_{,\beta} = \left(v^\alpha\boldsymbol{a}_\alpha\right)_{,\beta} &= v^\alpha\big|_\beta\boldsymbol{a}_\alpha + b_{\alpha\beta}v^\alpha\boldsymbol{n} \\ &= v_{\alpha|\beta}\boldsymbol{a}^\alpha + b^\alpha_\beta v_\alpha\boldsymbol{n}, \end{aligned} \tag{14}$$

where the operation $(.)_{|\alpha}$ defined by

$$v^\alpha\big|_\beta = v^\alpha{}_{,\beta} + \Gamma^\alpha_{\lambda\beta}v^\lambda, \quad v_{\alpha|\beta} = v_{\alpha,\beta} - \Gamma^\lambda_{\alpha\beta}v_\lambda \tag{15}$$

is known as the covariant differentiation of the surface vector components.

Similarly, the covariant differentiation of the tangent surface tensor components is defined by

$$\begin{aligned} &T^{\alpha\beta}\big|_\lambda = T^{\alpha\beta}{}_{,\lambda} + \Gamma^\alpha_{\kappa\lambda}T^{\kappa\beta} + \Gamma^\beta_{\kappa\lambda}T^{\alpha\kappa}, \\ &T_{\alpha\beta|\lambda} = T_{\alpha\beta,\lambda} - \Gamma^\kappa_{\alpha\lambda}T_{\kappa\beta} - \Gamma^\kappa_{\beta\lambda}T_{\alpha\kappa}. \end{aligned} \tag{16}$$

In particular, one can prove that

$$a_{\alpha\beta|\lambda} = a^{\alpha\beta}\big|_\lambda = \varepsilon_{\alpha\beta|\lambda} = \varepsilon^{\alpha\beta}\big|_\lambda = 0. \tag{17}$$

In case of the spatial vector field $\boldsymbol{w}$ defined in the surface bases by

$$\boldsymbol{w} = w^\alpha \boldsymbol{a}_\alpha + w\boldsymbol{n} = w_\alpha \boldsymbol{a}^\alpha + w\boldsymbol{n}, \tag{18}$$

its differentiation on $\mathcal{M}$ leads to

$$\begin{aligned}\boldsymbol{w}_{,\beta} &= \left(w^\alpha\big|_\beta - b^\alpha_\beta w\right)\boldsymbol{a}_\alpha + \left(w_{,\beta} + b_{\alpha\beta}w^\alpha\right)\boldsymbol{n} \\ &= \left(w_{\alpha|\beta} - b_{\alpha\beta}w\right)\boldsymbol{a}^\alpha + \left(w_{,\beta} + b^\alpha_\beta w_\alpha\right)\boldsymbol{n}.\end{aligned} \tag{19}$$

Since $\boldsymbol{a}_{\beta|\lambda} = b_{\beta\lambda}\boldsymbol{n}$, $\boldsymbol{n}_{,\mu} = \boldsymbol{n}_{|\mu} = -b^\kappa_\mu \boldsymbol{a}_\kappa$, the repeated covariant differentiation of $\boldsymbol{a}_\beta$ gives the vector identity

$$\boldsymbol{a}_{\beta|\lambda\mu} - \boldsymbol{a}_{\beta|\mu\lambda} = R_{\alpha\beta\lambda\mu}\boldsymbol{a}^\alpha, \tag{20}$$

or three scalar identities

$$b_{\beta\lambda|\mu} = b_{\beta\mu|\lambda}, \quad b_{\alpha\lambda}b_{\beta\mu} - b_{\alpha\mu}b_{\beta\lambda} = R_{\alpha\beta\lambda\mu}, \tag{21}$$

where $R_{\alpha\beta\lambda\mu}$ are components of the surface Riemann-Christoffel tensor which are defined entirely through the metric components by

$$\begin{aligned}R_{\alpha\beta\lambda\mu} = \frac{1}{2}\left(a_{\alpha\mu,\beta\lambda} + a_{\beta\lambda,\alpha\mu} - a_{\alpha\lambda,\beta\mu} - a_{\beta\mu,\alpha\lambda}\right) \\ + \Gamma^\kappa_{\alpha\mu}\Gamma_{\kappa.\beta\lambda} - \Gamma^\kappa_{\alpha\lambda}\Gamma_{\kappa.\beta\mu}.\end{aligned} \tag{22}$$

The components $R_{\alpha\beta\lambda\mu}$ have the following symmetry conditions:

$$R_{\alpha\beta\lambda\mu} = -R_{\beta\alpha\lambda\mu} = -R_{\alpha\beta\mu\lambda} = R_{\lambda\mu\alpha\beta}, \tag{23}$$

so that, in fact, they are expressible in terms of only one independent component R_{1212}.

The relations (21) are known as the Codazzi-Gauss equations for the surface. Since $\mathcal{M}$ in the space $\mathcal{E}$ has been described by three spatial components of $\mathbf{r}$, the relations (21) express just three compatibility conditions which must be satisfied by six components of $a_{\alpha\beta}$ and $b_{\alpha\beta}$.

Surface Curves

Let $\theta^\alpha = \theta^\alpha(s)$ define a curve $\mathcal{C}$ on the surface $\mathcal{M}$, where s is the length coordinate along $\mathcal{C}$. A special case of $\mathcal{C}$ is the surface curve $\partial\mathcal{M}$ describing an edge of $\mathcal{M}$. With each point of $\mathcal{C}$ one can associate the orthonormal triad of vectors $\boldsymbol{\tau}, \boldsymbol{n}, \boldsymbol{\nu}$, where $\boldsymbol{\tau}$ is the unit vector tangent to $\mathcal{C}$ and $\boldsymbol{\nu}$ is the outward unit normal vector tangent to $\mathcal{M}$ defined by

$$\begin{aligned}&\boldsymbol{\tau} = \mathbf{r}_{,s} = \tau_\alpha \boldsymbol{a}^\alpha, \quad \boldsymbol{\nu} = \boldsymbol{\tau}\times\boldsymbol{n} = \nu_\alpha \boldsymbol{a}^\alpha, \\ &\boldsymbol{a}_\alpha = \nu_\alpha \boldsymbol{\nu} + \tau_\alpha \boldsymbol{\tau}, \quad \nu^\beta = \varepsilon^{\beta\alpha}\tau_\alpha, \quad \tau^\beta = \varepsilon^{\alpha\beta}\nu_\alpha.\end{aligned} \tag{24}$$

Differentiation of the triad $\boldsymbol{\nu}$, $\boldsymbol{\tau}$, $\boldsymbol{n}$ along $\mathcal{C}$ gives

$$\begin{aligned}\frac{d}{ds}\begin{bmatrix}\boldsymbol{\nu}\\ \boldsymbol{\tau}\\ \boldsymbol{n}\end{bmatrix} &= \boldsymbol{\omega}_\tau \times \begin{bmatrix}\boldsymbol{\nu}\\ \boldsymbol{\tau}\\ \boldsymbol{n}\end{bmatrix}, \\ \boldsymbol{\omega}_\tau &= \sigma_\tau \boldsymbol{\nu} + \tau_\tau \boldsymbol{\tau} + \rho_\tau \boldsymbol{n},\end{aligned} \tag{25}$$

where the normal curvature σ_τ, the geodesic torsion τ_τ, and the geodesic curvature ρ_τ of the surface curve $\mathcal{C}$ are defined by

$$\begin{aligned}&\sigma_\tau = b_{\alpha\beta}\tau^\alpha\tau^\beta, \quad \tau_\tau = -b_{\alpha\beta}\nu^\alpha\tau^\beta, \\ &\rho_\tau = \tau_\alpha \nu^\alpha\big|_\beta \tau^\beta.\end{aligned} \tag{26}$$

The value of σ_τ at each point $M \in \mathcal{M}$ depends on the direction $\boldsymbol{\tau}$ of $\mathcal{C}$. The principal directions are those for which $b_{\alpha\beta}\tau^\alpha\tau^\beta$ assume the extreme values under the condition $a_{\alpha\beta}\tau^\alpha\tau^\beta = 1$. The problem is equivalent to finding extremal values of the function

$$F\left(\tau^\alpha\right) = b_{\alpha\beta}\tau^\alpha\tau^\beta - \sigma_\tau\left(a_{\alpha\beta}\tau^\alpha\tau^\beta - 1\right). \tag{27}$$

Differentiation of (27) leads to the set of two homogeneous algebraic equations

$$\frac{1}{2}\frac{\partial F}{\partial \tau^\alpha} = \left(b_{\alpha\beta} - \sigma_\tau a_{\alpha\beta}\right)\tau^\beta = 0, \tag{28}$$

which nontrivial solutions exist provided that

$$\det\left(b_{\alpha\beta}-\sigma_\tau a_{\alpha\beta}\right)=0,\quad \sigma_\tau^2-2\sigma_\tau H+K=0. \tag{29}$$

The roots of $(29)_2$ are

$$\sigma_{1,2}=H\pm\sqrt{H^2-K} \tag{30}$$

and are called the surface principal normal curvatures at the point $M\in\mathcal{M}$.

The values σ_1 and σ_2 in (30) are always real, because

$$4\left(H^2-K\right)=\left(b_1^1+b_2^2\right)^2+4\left(b_2^1\right)^2\geq 0. \tag{31}$$

The equality in (31) takes place only if $b_1^1=b_2^2$ and $b_1^2=b_2^1$, under which the point of $\mathcal{M}$ is called spherical. If a point $M\in\mathcal{M}$ is not spherical, then σ_1 and σ_2 assume different values such that

$$\sigma_1\sigma_2=K,\quad \sigma_1+\sigma_2=2H. \tag{32}$$

The point $M\in\mathcal{M}$ is called elliptic when $K>0$, parabolic when $K=0$, and hyperbolic when $K<0$. The surface consisting entirely of one type of points mentioned above is called the surface of positive, zeroth, or negative Gaussian curvature, respectively.

The curve on a surface having tangent at each point along the principal direction is called the line of principal curvature. If $\tau^\alpha_{(1)}$ and $\tau^\alpha_{(2)}$ are two principal directions corresponding to σ_1 and σ_2, respectively, then multiplying (28) in succession by $\tau^\alpha_{(1)}$ and $\tau^\alpha_{(2)}$, and subtracting the results one obtains

$$(\sigma_2-\sigma_1)\,a_{\alpha\beta}\tau^\alpha_{(1)}\tau^\beta_{(2)}=(\sigma_2-\sigma_1)\,\boldsymbol{\tau}_{(1)}\cdot\boldsymbol{\tau}_{(2)}=0. \tag{33}$$

This means that, unless the point is spherical, the two principal directions are orthogonal. Moreover, multiplying the conditions (28) by ν^α one finds that in the principal directions $b_{\alpha\beta}\tau^\beta\nu^\alpha=0$, so that the geodesic torsion τ_τ vanishes identically along the principal line.

Various surfaces may conveniently be parameterized by different surface coordinate systems, which may neither be orthogonal nor coinciding with lines of principal curvatures, in general. But majority of surfaces are described and analyzed in orthogonal coordinates coinciding with lines of principal curvatures. In this case, it is convenient to introduce the unit surface base vectors $\boldsymbol{e}_1$ and $\boldsymbol{e}_2$ such that

$$\begin{aligned}&\boldsymbol{a}_1=A_1\boldsymbol{e}_1,\quad \boldsymbol{a}_2=A_2\boldsymbol{e}_2,\quad A_1=\sqrt{a_{11}},\\ &A_2=\sqrt{a_{22}},\quad a^{11}=\frac{1}{(A_1)^2},\quad a^{22}=\frac{1}{(A_2)^2},\\ &a^{12}=a_{12}=0,\quad a=(A_1A_2)^2.\end{aligned} \tag{34}$$

For orthogonal surface coordinates of principal curvatures, the nonzero Christoffel symbols of the second kind one finds from (13) to be

$$\begin{aligned}&\Gamma^1_{11}=\frac{1}{A_1}\frac{\partial A_1}{\partial\theta^1},\qquad \Gamma^1_{22}=-\frac{A_2}{(A_1)^2}\frac{\partial A_2}{\partial\theta^1},\\ &\Gamma^1_{12}=\frac{1}{A_1}\frac{\partial A_1}{\partial\theta^2},\qquad \Gamma^2_{22}=\frac{1}{A_2}\frac{\partial A_2}{\partial\theta^2},\\ &\Gamma^2_{11}=-\frac{A_1}{(A_2)^2}\frac{\partial A_1}{\partial\theta^2},\quad \Gamma^2_{12}=\frac{1}{A_2}\frac{\partial A_2}{\partial\theta^1}.\end{aligned} \tag{35}$$

The symbols (35) allow one to express covariant differentiation of vector and tensor components in terms of their partial differentiation.

With the help of (34) any vector $\boldsymbol{w}$ can be represented by its components as

$$\begin{aligned}&\boldsymbol{w}=w_{<1>}\boldsymbol{e}_1+w_{<2>}\boldsymbol{e}_2+w\boldsymbol{n},\\ &w_{<\alpha>}=A_\alpha w^\alpha=\frac{1}{A_\alpha}w_\alpha\ (\text{no sum over }\alpha).\end{aligned} \tag{36}$$

The components $w_{<\alpha>}$ are called the physical components of the vector $\boldsymbol{w}$.

Similarly, one can introduce the physical components of the surface tensor by

$$\begin{aligned}T_{<\alpha\beta>}&=\frac{1}{A_\alpha A_\beta}T_{\alpha\beta}=A_\alpha A_\beta T^{\alpha\beta}\\ &=\frac{A_\beta}{A_\alpha}T_\alpha^{\cdot\beta}\quad(\text{no sum over }\alpha,\beta).\end{aligned} \tag{37}$$

In particular, the physical components of the surface curvature tensor $b_{\alpha\beta}$ are defined by

$$b_{<11>} = \frac{b_{11}}{(A_1)^2} = -\frac{1}{R_1}, \qquad b_{<22>} = \frac{b_{22}}{(A_2)^2} = -\frac{1}{R_2}, \tag{38}$$

where R_1 and R_2 are the principal radii of curvatures of corresponding lines of principal curvatures.

Surface Divergence Theorem

Let the regular surface $\mathcal{M}$ be bounded by a closed smooth boundary $\partial\mathcal{M}$. The divergence of a tangential vector field $\boldsymbol{w} = w^\alpha \boldsymbol{a}_\alpha$ defined over $\mathcal{M}$ is the scalar field defined by $\mathrm{div}_s \boldsymbol{w} = \boldsymbol{w}_{,\alpha} \cdot \boldsymbol{a}^\alpha = w^\alpha|_\alpha$. For a mixed second-order tensor field on $\mathcal{M}$, $\boldsymbol{S} = \boldsymbol{S}^\alpha \otimes \boldsymbol{a}_\alpha$, $\boldsymbol{S}^\alpha = S^{i\alpha}\boldsymbol{c}_i$, where $\boldsymbol{c}_i$, $i = 1, 2, 3$, is any 3D vector base on $\mathcal{M}$ and $\otimes$ is the tensor product, the surface divergence is the vector field defined by $\mathrm{div}_s \boldsymbol{S} = \boldsymbol{S}^\alpha|_\alpha$.

The surface divergence theorem (also called the Green or Gauss theorem) relates integrals of the fields $\boldsymbol{w}$ and $\boldsymbol{S}$ along the boundary $\partial\mathcal{M}$ to their divergences over the surface $\mathcal{M}$ according to

$$\int_{\partial\mathcal{M}} w^\alpha \nu_\alpha ds = \iint_{\mathcal{M}} w^\alpha\Big|_\alpha da, \qquad \int_{\partial\mathcal{M}} \boldsymbol{S}^\alpha \nu_\alpha ds = \iint_{\mathcal{M}} \boldsymbol{S}^\alpha\Big|_\alpha da. \tag{39}$$

In shell theory these theorems are used to derive the Euler equations of some variational statements.

Cross-References

- Elastic Shells, Resultant Nonlinear Theory
- Junctions in Irregular Shell Structures
- Thin Elastic Shells, Lagrangian Geometrically Nonlinear Theory
- Thin Elastic Shells, Linear Theory

References

Başar Y, Krätzig WB (2001) Theory of shell structures, 2nd edn. VDI Verlag, Düsseldorf

Chernykh KF (1964) Linear theory of shells, part 2 (in Russian). University Press, Leningrad. English translation: NASA-TT-F-II 562, 1968

Ciarlet PG (2005) An introduction to differential geometry with application to elasticity. Springer, Berlin

Do Carmo MP (1976) Differential geometry of curves and surfaces. Prentice Hall, Upper Saddle River

Eisenhart LP (1947) An introduction to differential geometry with use of the tensor calculus. University Press, Princeton

Flügge W (1972) Tensor analysis and continuum mechanics. Springer, Berlin et al

Green AE, Zerna W (1954) Theoretical elasticity. Clarendon Press, Oxford

Lebedev LP, Cloud MJ, Eremeyev VA (2010) Tensor analysis with applications in mechanics. World Scientific, Singapore

Naghdi PM (1963) Foundations of elastic shell theory. In: Sneddon IN, Hill R (eds) Progress in solid mechanics IV. North-Holland, Amsterdam, pp 1–90

Pietraszkiewicz W (1977) Introduction to the non-linear theory of shells. Mitteilungen aus dem Institut für Mechanik 10. Ruhr-Universität, Bochum

Surface Tension

- Surface Energy and Its Effects on Nanomaterials

Surface Wave Propagation in 3D Medium

Yury A. Rossikhin[1,2] and Marina V. Shitikova[1,2]
Research Center on Dynamics of Solids and Structures, Voronezh State Technical University, Voronezh, Russia
Research Center for Wave Dynamics of Solids and Structures, Voronezh State Technical University, Voronezh, Russia

Synonyms

Transient surface waves of strong and weak discontinuity

Yury A. Rossikhin: deceased.

Definition

Transient surface wave is a line of strong or weak discontinuity (or a circumference for bodies of revolution) on which stressed-strained state characteristics of the medium possess jumps (discontinuities).

Preliminary Remarks

The majority of available studies on the surface wave propagation along surfaces of various 3D bodies deals with harmonic surface waves. Thus, for example, harmonic waves propagating along an isotropic cylinder free surface in the direction perpendicular to a generator have been described in detail by Viktorov (1966) and Brekhovskikh (1967). There are also similar waves with vertical and horizontal polarization on a surface of an anisotropic cylinder, which has the plane of transverse isotropy perpendicular to a cylinder axis (Viktorov 1974; Vaskova et al. 1975). The Rayleigh waves of the "diverging circles" type on an isotropic sphere surface under harmonic excitations were studied by Petrashen (1946).

The number of articles, wherein transient surface waves are investigated, is rather limited (Rossikhin 1986, 1992; Rossikhin and Shitikova 2000, 2004, 2014). One of the first studies in the field is the paper by Rossikhin (1986), who suggested the ray expansion method for analyzing the Rayleigh waves of the "diverging circles" type on an isotropic spherical surface. Moreover, it has been found that transient surface waves are very useful when studying dynamic surface instability of 3D bodies subjected to nonstationary excitation and pre-stressing (Bestuzheva et al. 1981; Rossikhin and Shitikova 2000, 2004).

In the present entry, horizontally and vertically polarized transient surface waves propagating along conic surfaces are considered by the ray expansion method.

Problem Formulation

A transient surface wave could be generated after the impulse exposure to a vertex of a cone with opening 2α, which is made of hexagonal crystal (Rossikhin 1992). The x_3-axis coincides with the axis of isotropy (Fig. 1), and it is a line of strong discontinuity (in the given case, it is a circumference), on which stressed-strained state characteristics of the medium have a break. The circle propagates with a constant normal velocity along the cone surface in the direction of its generators and is obtained as a result of the one real wave discontinuity surface (of the volume shear wave) intersection with the conic surface (the horizontally polarized surface wave is circle 1 on Fig. 1) or by the exit of the two intersecting (along this line complex wave discontinuity) surfaces (of quasi-transverse and quasi-longitudinal volume waves) onto the conic surface. The wave of the Rayleigh type is shown on Fig. 1 as circle 2.

Let us seek a solution to the problem

$$\sigma_{ij,j} = \rho \dot{v}_i, \tag{1}$$

$$\sigma_{ij} = \lambda_{ijkl} u_{k,l}, \tag{2}$$

satisfying the boundary conditions

$$\lambda_{ijkl} u_{k,l} N_j = 0, \tag{3}$$

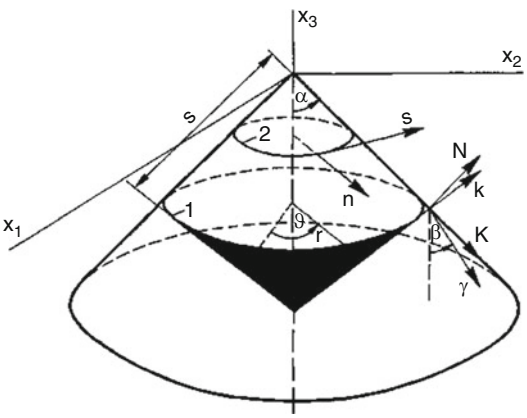

Fig. 1 Scheme of a surface wave front location on a conic surface

where σ_{ij} and λ_{ijkl} are components of the stress and elastic moduli tensors, respectively; u_i and v_i are components of the displacement and velocity vectors, respectively; ρ is the crystal density; N_j ($N_1 = \cos\alpha\cos\theta$, $N_2 = \cos\alpha\sin\theta$, $N_3 = \sin\alpha$) are components of the unit vector normal to the conic surface; θ is the angular cylindrical coordinate; a dot denotes differentiation with respect to time *t; and* differentiation with respect to x_k is denoted by $_k$.

Horizontally Polarized Surface Wave

To investigate the horizontally polarized surface wave using Cartesian coordinates (x_1, x_2, x_3), it is a need to introduce a conic wave surface with the help of the equation

$$x_i = \left(u^1 + G_s t\right)\ GG_s^{-1} v_i - u^1 K_i, \quad (4)$$

where v_i ($v_1 = \sin\beta\cos\theta$, $v_2 = \sin\beta \times \sin\theta$, $v_3 = -\cos\beta$) and K_i ($K_1 = \sin\alpha \times \cos\theta$, $K_2 = \sin\alpha\sin\theta$, $K_3 = -\cos\alpha$) are components of the unit vectors directed along the normal trajectory to the wave surface and along the generator of the crystal cone, respectively; $180^\circ - 2\beta$ is the opening of the wave cone where the angle β is undefined for the present; G and G_s $\left(GG_s^{-1} = \cos(\alpha - \beta)\right)$ are the wave surface velocities along its normal cone and along the generator of the crystal cone, respectively; and u^1 and $u^2 = \theta$ are orthogonal curvilinear coordinates on the wave surface retaining their values along the normal trajectories to this surface (the normal trajectory is the curve at every point of which the unit vector normal to the wave surface is directed tangentially to this curve). At $u^1 = -G_s t$, the wave surface (4) cuts the surface of the crystal cone.

Using (4) and taking into account $du^1/dt = du^2/dt = 0$, where d/dt is the derivative with respect to time along the normal trajectory to the wave surface, the known formulae from the theory of moving surfaces and lines could be obtained, namely, with $u^1 = \text{const}$, $dx_i/d(Gt) = v_i$, but with $u^1 = -G_s t$, $dx_i/d(G_s t) = K_i$. Also the geometrical characteristics of the wave surface could be found (Rossikhin 1992) which will be used below:

$$\begin{aligned}
x_{i,1} &= dx_i/du^1 = GG_s^{-1} v_i - K_i,\\
x_{i,2} &= dx_i/du^2 = r s_i,\\
r &= \left(u^1 + G_s t\right)\ GG_s^{-1}\ \sin\beta - u^1 \sin\alpha,\\
s_1 &= -\sin\theta, \quad s_2 = \cos\theta, \quad s_3 = 0\\
g_{11} &= x_{i,1} x_{1,\mathrm{i}} = 1 - G^2 G_s^{-2} = n^2,\\
g_{22} &= x_{i,2} x_{2,\mathrm{i}} = r^2, \quad g_{12} = 0,
\end{aligned} \quad (5)$$

where r is the polar radius, s_i are components of the unit vector directed tangentially to the surface wave, $g_{\alpha\beta}$ are covariant components of the wave surface metric tensor, and Greek suffixes take on the values 1, 2.

As with the transition through the wave surface (4) the components of the stress and strain tensors and the displacement velocity vector experience discontinuity, then writing Eq. (2) on the other sides of the wave surface, taking the difference of them, and applying the kinematic, geometric and dynamic conditions of compatibility (Thomas 1961; Rossikhin 1992)

$$\begin{aligned}
&[\dot{u}_i] = [v_i] = -G\lambda_i, \quad \left[u_{i,\mathrm{j}}\right] = \lambda_i v_j,\\
&\left[\sigma_{ij}\right] v_j = -\rho G\,[v_i],
\end{aligned} \quad (6)$$

yield

$$\left(\lambda_{ijkl} v_j v_t - \rho G^2 \delta_{ik}\right) \lambda_k = 0, \quad (7)$$

where δ_{ik} is Kronecker's symbol and the sign $[\ldots]$ denotes a difference of magnitudes of a certain value on the other sides of discontinuity surface (e.g., finite jump of this value).

Considering that $\lambda_i = \lambda_\tau s_i$ where λ_τ is the intensity of the volume shear wave and knowing the form of the elastic moduli matrix for the hexagonal crystal with the x_3-axis of isotropy, as a result it follows that

$$\rho G^2 = \mu \sin^2\beta + \lambda_{1313}\cos^2\beta, \quad (8)$$

where $\mu = \lambda_{1212}$.

In view of the conditions of compatibility (6), boundary conditions (3) are reduced to $\lambda_\tau(\mu \sin\beta \cos\alpha - \lambda_{1313}\cos\beta \sin\alpha) = 0$, and hence

$$\tan\beta = \lambda_{1313}\mu^{-1}\tan\alpha, \tag{9}$$

that is, the angles α and β do not equal each other and the volume shear wave is not perpendicular to the free surface of the crystal cone (Fig. 1).

Now let us consider the question about the character of the change in the intensity of the surface wave during its propagation. For that purpose, write Eq. (1) and the differentiated Eqs. (2) and (3) with respect to t on the other sides of the wave surface (4), take the difference of them, and apply the second-order condition of compatibility (Thomas 1961):

$$G\left[Z_{,j}\right] = -\left[\dot{Z}\right]\nu_j + \frac{d\,[Z]}{dt}\nu_j + Gg^{\alpha\beta}[Z]_{,\alpha}x_{j,\beta}, \tag{10}$$

where Z is a certain function and Greek letters after a point denote covariant differentiation with respect to the curvilinear surface coordinates u^α. As a result with due account for the geometrical characteristics of the wave surface (5) and relationships (6, 7, 8, and 9), it could be obtained

$$2\rho G^2\frac{d\lambda_\tau}{dt} + G\mu \sin\beta\frac{1}{r}\lambda_\tau + 2G\left(\mu\kappa\sin\beta - \lambda_{1313}\kappa_3\cos\beta\right)\frac{1}{n^2}\lambda_{\tau,1} = 0, \tag{11}$$

$$\left(\mu\kappa\cos\alpha + \lambda_{1313}\kappa_3\sin\alpha\right)\frac{1}{n^2}\lambda_{\tau,1} - \mu\frac{1}{r}\lambda_\tau\cos\alpha = 0, \tag{12}$$

where $\kappa = \cos(\alpha - \beta)\sin\beta - \sin\alpha$, $\kappa_3 = -\cos(\alpha - \beta)\cos\beta + \cos\alpha$, and $\lambda_{\tau,1} = \partial\lambda/\partial u^1$.

Eliminating the value $\lambda_{\tau,1}$ from (11) and (12) and considering that $d/ds = G_S^{-1}d/dt - \partial/\partial u^1$ and $r = s \sin\alpha$, where s is a distance measured from the vertex of the cone along its generator, in general case ($\alpha \neq \beta \neq 0 \neq 1/2\pi$) provide the equation

$$d\lambda_\tau/ds + \gamma s^{-1}\lambda_\tau = 0, \tag{13}$$

with

$$\gamma = \frac{\mu}{\rho G G_S}\left(\frac{1}{2}\frac{\sin\beta}{\sin\alpha} + \chi \cot\alpha\right),$$
$$\chi = \frac{\mu\kappa \sin\beta - \lambda_{1313}\kappa_3 \cos\beta + \rho G G_S n^2}{\mu\kappa\cos\alpha + \lambda_{1313}\kappa_3 \sin\alpha}, \tag{14}$$

the integration of which yields

$$\lambda_\tau = cs^{-\gamma}, \tag{15}$$

where c is a real arbitrary constant.

In the case of the isotropic cone $\lambda_{1313} = \mu$, and, as it follows from (3.5) and (3.6), $\rho G^2 = \mu$, $G = G_S$, and $\alpha = \beta$, i.e., the volume shear wave is perpendicular to the free surface of the isotropic cone (Fig. 1).

Using (14), it may be shown that when $|\alpha - \beta| = \Delta \ll 1$

$$\chi \cong \frac{(\mu - \lambda_{1313})\sin 2\beta}{2\left(\mu\cos^2\beta + \lambda_{1313}\sin^2\beta\right)} + 0(\Delta), \tag{16}$$

that is, in the isotropic case $\chi = 0$. Then from (13) it follows

$$\lambda_\tau = cs^{-1/2}. \tag{17}$$

At $\alpha = 1/2\pi$ (in this case β is also equal to $1/2\pi$), as it follows from (8) and (9), the value λ_τ changes due to the power law (17), i.e., during propagation of the surface shear wave of the "diverging circle" type along the plane $x_3 = 0$. This bounds the elastic anisotropic half-space $x_3 < 0$ with hexagonal symmetry; its intensity changes like an amplitude of the volume cylindrical wave propagating into the unbounded elastic isotropic space.

If the angle $\alpha \to 0$ (with that the angle β also tends to zero) and the value r remains constant and equal to R, then, as it follows from (11) and

(12), $\lambda_\tau = \text{const}$. In this case the horizontally polarized surface wave of the "diverging circle" type goes into the circle of discontinuity with the constant radius R moving along the x_3-axis of the crystal cylinder of the same radius.

Vertically Polarized Surface Wave

Now let us proceed to investigate the surface wave of the "diverging circle" type with vertical polarization (transient wave of the Rayleigh type). For this purpose, let us take into consideration complex conic wave surfaces of strong discontinuity (in the given problem, there are two: quasi-transverse and quasi-longitudinal):

$$\begin{aligned} x_1 &= r\cos\theta, \quad x_2 = r\sin\theta, \\ r &= \left[-n^2\left(u^1+gt\right)+gt\right]\sin\alpha \\ &\quad + Ggn\left(u^1+gt\right)\cos\alpha, \\ x_3 &= -\left[-n^2\left(u^1+gt\right)+gt\right]\cos\alpha \\ &\quad + Gg^{-1}n\left(u^1+gt\right)\sin\alpha, \end{aligned} \tag{18}$$

which at $u^{-1} = -gt$ intersect each other and emerge on the free surface of the crystal cone forming the circle with radius $gt\ \sin\alpha$, where g is the Rayleigh wave velocity along the generator of the crystal cone, so that

$$\begin{aligned} &r = s\sin\alpha, \quad x_3 = -s\cos\alpha, \\ &\mathrm{s} = \mathrm{gt}, \quad dx_i/d(gt) = K_i \end{aligned} \tag{19}$$

Such a representation of the transient Rayleigh wave generalizes immediately the "classic" Rayleigh wave, which is considered as the superposition of the longitudinal and transverse complex waves matched in such a way that there are no stresses on the surface of the half-space (Frank and Mises 1935). Similar generalizations of Rayleigh waves are met in Babich (1961) and Bestuzheva et al. (1981).

In terms of (18), the characteristics of the volume waves could be written as

$$\begin{aligned} &\nu_1 = \nu\cos\theta, \quad \nu_2 = \nu\sin\theta, \\ &\nu = Gg^{-1}\sin\alpha + n\ \cos\ \alpha, \\ &\nu_3 = -Gg^{-1}\cos\alpha + n\ \sin\ \alpha, \\ &k_1 = k\cos\theta, \quad k_2 = k\sin\theta, \\ &k = n\ \sin\ \alpha - Gg^{-1}\cos\alpha, \\ &k_3 = -n\cos\alpha - \ Gg^{-1}\sin\ \alpha, \\ &x_{i,1} = -nk_i, \quad x_{i,2} = rs_i, \\ &g_{11} = n^2, \quad g_{22} = r^2, \quad g_{12} = 0, \\ &\nu_{i,1} = 0, \quad \nu_{i,2} = -k_3 s_i, \quad n = \sqrt{1-G^2g^{-2}}, \end{aligned} \tag{20}$$

where ν_i are components of the unit normal vector to the wave surface and k_i are components of the unit vector directed along the generator of the conic wave surface, which have been already determined in (5).

Applying (20), it is easy to verify that the velocities G and g as the normal velocities of the emerging on the free surface volume wave and of the line of their intersection, respectively, are connected by the relations: $K_i\nu_i = Gg^{-1}$, $K_ik_i = n$, and $N_i\nu_i = n$.

Assuming that the complex waves are vertically polarized, i.e.:

$$\lambda_i = \lambda_r n_i + \lambda_3\delta_{3i}, \tag{21}$$

where λ_r and λ_3 are projections of the volume wave intensity vector on the r- and x_3-axes, respectively, and $n_i(\cos\theta, \sin\theta, 0)$ are components of the unit vector directed along the r-axis, from (7) it could be found

$$\begin{aligned} M(\lambda_r, \lambda_3) &= \left[(\lambda+2\mu)\nu^2 + \lambda_{1313}k^2 - \rho G^2\right]\lambda_r \\ &\quad + 2m\nu k\lambda_3 = 0, \\ N(\lambda_r, \lambda_3) &= m\nu k\lambda_r + \left(\lambda_{1313}\nu^2 + \lambda_{3333}k^2\right. \\ &\quad \left. -\rho G^2\right)\lambda_3 = 0, \end{aligned} \tag{22}$$

where $m = \lambda_{1133} + \lambda_{1313}$.

Equating the determinant of the system of homogeneous Eq. (22) to zero, the equation for determination of the complex volume wave velocities $G_{(\alpha)}$ (hereafter the indices 1 and 2 at the values refer to the quasi-transverse and quasi-longitudinal waves, respectively) could be obtained:

$$\left[(\lambda+2\mu)\,\nu^2+\lambda_{1313}k^2-\rho G^2\right] \times\left[\lambda_{1313}\nu^2+\lambda_{3333}k^2-\rho G^2\right]-m^2\nu^2k^2=0. \tag{23}$$

At $\alpha = 0$ and $\alpha = 1/2\pi$, Eq. (23) transforms to the biquadratic equation in G with real coefficients and determines the real velocities $G_{(\alpha)}$ of the complex waves. In general, when $0 < \alpha < 1/2\pi$, this equation possesses complex roots that conform to the complex velocities of the complex volume waves (the generalized volume waves).

Note that for the isotropic cone, in contrast to the anisotropic cone, the velocities $G_{(\alpha)}$ are real at every value of the angle α.

For analysis by the iterative method, it is convenient to rewrite Eq. (23) in view of (20) in the following form:

$$\left[(\lambda+2\mu)\,(\sin\alpha+\overline{n}\ \cos\alpha)^2 +\lambda_{1313}(\overline{n}\ \sin\alpha-\cos\alpha)^2-\rho g^2\right] \times\left[\lambda_{1313}(\sin\alpha+\overline{n}\cos\alpha)^2 +\lambda_{3333}(\overline{n}\sin\alpha-\cos\alpha)^2-\rho g^2\right] -m^2(\sin\alpha+\overline{n}\cos\alpha)^2(\overline{n}\sin\alpha-\cos\alpha)^2=0, \tag{24}$$

and consider it as the 4th-degree equation in the value $\overline{n} = \sqrt{g^2G^{-2}-1}$ with the parameter g (Farnell 1970).

As by virtue of the condition (23), Eq. (22) are linear-dependent; then by omitting one of them, for example, the second, from the first one, the connection between λ_r and λ_3 is found as

$$\lambda_3=-\chi\lambda_r,$$
$$\chi=(m\nu k)^{-1}\left[(\lambda+2\mu)\,\nu^2+\lambda_{1313}k^2-\rho G^2\right]. \tag{25}$$

To investigate the character of the Rayleigh wave intensity change during its propagation, one must use the procedure described above for the derivation of Eqs. (11) and (12). In doing so, it is necessary to remember that, as the Rayleigh wave is the line of intersection of the two volume complex waves, its intensity represents by itself the sum of intensities of these waves. Then from (1) and the differentiated Eq. (2) with respect to t, it follows that

$$M(L_r,L_3)=-2\rho G^3 d\lambda_r/dt +2G^2n^{-1}\lambda_{r,1}\,(\lambda+2\mu-\lambda_{1313})\,\nu k +G^2n^{-1}\lambda_{3,1}\left(k^2-\nu^2\right)m -G^2r^{-1}\nu\lambda_r\,(\lambda+2\mu), \tag{26}$$

$$N(L_r,L_3)=-2\rho G^3 d\lambda_3/dt +G^2n^{-1}\lambda_{r,1}\left(k^2-\nu^2\right)m -2G^2n^{-1}\lambda_{3,1}\,(\lambda_{3333}-\lambda_{1313})\,\nu k -G^2r^{-1}\nu\lambda_{1313}\lambda_3-G^2r^{-1}k\lambda_{1313}\lambda_r, \tag{27}$$

where L_r and L_3 are projections of finite discontinuity of the acceleration vector on the r- and x-axes, respectively, i.e.:

$$[\dot{v}_i]=L_rn_i+L_3\delta_{3i},\quad \lambda_{3,i}=\partial\lambda_3/\partial u^1,$$
$$\lambda_{r,1}=\partial\lambda_r/\partial u^1,\quad \lambda=\lambda_{1122}.$$

The left sides of Eqs. (26) and (27) are linear-dependent by virtue of the condition (23), and, as a consequence, the right sides of these equations are linear-dependent also. Linear combination of the right sides with due account of (25) leads to the relation

$$d\lambda_r/dt=G^2n^{-1}\psi\lambda_{r,1}-r^{-1}\varphi G^2\lambda_r, \tag{28}$$

S

with

$$\varphi = [bv(\lambda+2\mu) - mvk\lambda_{1313}(k - v\chi)] \times (b + mvk\chi)^{-1}\left(2\rho G^3\right)^{-1},$$

$$\psi = [2bvk(\lambda+2\mu-\lambda_{1313}) - m\left(k^2 - v^2\right)(mvk + \chi b) - 2mv^2k^2\chi(\lambda_{3333} - \lambda_{1313})] \times (b + mvk\chi)^{-1}\left(2\rho G^3\right)^{-1},$$

$$b = \lambda_{3333}k^2 + \lambda_{1313}v^2 - \rho G^2.$$

Moreover, from (26) the connection between the values L_3 and L_r could be obtained as

$$L_3 = -\chi L_r - 2\rho G^3(mvk)^{-1}d\lambda_r/dt + G^2(nmvk)^{-1}[2(\lambda+2\mu-\lambda_{1313})vk - \left(k^2 - v^2\right)\chi m]\lambda_{r,1} - G^2(rmk)^{-1}(\lambda+2\mu)\lambda_r. \tag{29}$$

From the boundary conditions (3) in view of (25), it yields

$$D^{(1)}\lambda_r^{(1)} + D^{(2)}\lambda_r^{(2)} = 0, \quad d^{(1)}\lambda_r^{(1)} + d^{(2)}\lambda_r^{(2)} = 0, \tag{30}$$

where

$$D = (\lambda+2\mu)v\cos\alpha + \lambda_{1313}k\sin\alpha - \chi(\lambda_{1133}k\cos\alpha + \lambda_{1313}v\sin\alpha),$$

$$d = \lambda_{1313}k\cos\alpha + \lambda_{1133}v\sin\alpha - \chi(\lambda_{1313}v\cos\alpha + \lambda_{3333}k\sin\alpha).$$

The condition of the existence of nontrivial solutions for the homogeneous system (30) gives the equation for determination of the Rayleigh wave velocity g:

$$D^{(1)}d^{(2)} - D^{(2)}d^{(1)} = 0. \tag{31}$$

Moreover, from (31) the connection between $\lambda_r^{(1)}$ and $\lambda_r^{(2)}$ is obtained:

$$\lambda_r^{(2)} = -\xi\lambda_r^{(1)}, \quad \xi = D^{(1)}D^{(2)-1}. \tag{32}$$

From the differentiated with respect to t boundary condition (2) with allowance for (29), it follows

$$D^{(1)}L_r{}^{(1)} - D^{(2)}L_r{}^{(2)} = \sum_{\alpha=1}^{2}\left[\left(-G_{(\alpha)}D^{(\alpha)} + 2\rho G_{(\alpha)}^3\overline{D}^{(2)}\right)d\lambda_r^{(\alpha)}/dt + G_{(\alpha)}^{(2)}n^{(\alpha)-1}Q^{(\alpha)}\lambda_{r,1}^{(\alpha)} + r^{-1}G_{(\alpha)}^2P^{(\alpha)}\lambda_r^{(\alpha)}\right], \tag{33}$$

$$d^{(1)}L_r{}^{(1)} + d^{(2)}L_r{}^{(2)} = \sum_{\alpha=1}^{2}\left[\left(-G_{(\alpha)}d^{(\alpha)} + 2\rho G_{(\alpha)}^3\overline{d}^{(2)}\right)d\lambda_r^{(\alpha)}/dt + G_{(\alpha)}^{(2)}n^{(\alpha)-1}q^{(\alpha)}\lambda_{r,1}^{(\alpha)} + r^{-1}G_{(\alpha)}^2p^{(\alpha)}\lambda_r^{(\alpha)}\right],$$

where

$$Q = (\lambda+2\mu)k\cos\alpha - \lambda_{1313}v\sin\alpha - \chi(\lambda_{1313}k\sin\alpha - \lambda_{1133}v\cos\alpha) - (\lambda_{1133}k\cos\alpha + \lambda_{1313}v\sin\alpha) \times [2(\lambda+2\mu-\lambda_{1313})vk - \left(k^2 - v^2\right)\chi m](mvk)^{-1},$$

$$P = -\lambda\cos\alpha + (\lambda_{1133}k\cos\alpha + \lambda_{1313}v\sin\alpha)(\lambda+2\mu)(mk)^{-1},$$

$$\overline{D} = (mvk)^{-1}(\lambda_{1133}k\cos\alpha + \lambda_{1313}v\sin\alpha),$$

$$q = \lambda_{1133}k\sin\alpha - \lambda_{1313}v\cos\alpha - \chi\lambda_{1313}k\cos\alpha - (\lambda_{1133}v\cos\alpha + \lambda_{3333}k\sin\alpha) \times [2(\lambda+2\mu-\lambda_{1313})vk - \left(k^2 - v^2\right)\chi m](mvk)^{-1},$$

$$p = -\lambda_{1133}\sin\alpha + (\lambda_{1313}\nu\cos\alpha + \lambda_{3333}k\sin\alpha)\,(\lambda + 2\mu)\,(mk)^{-1},$$
$$\overline{d} = (m\nu k)^{-1}\,(\lambda_{1313}\nu\cos\alpha + \lambda_{3333}k\sin\alpha)\,.$$

The left sides of Eq. (33) are linear-dependent by virtue of the condition (31), and, therefore, the right sides of these equations are linear-dependent also. Linear combination of the right sides allows one to obtain the equation for determination of the Rayleigh wave intensity:

$$d\lambda_r^{(1)}/ds + s^{-1}\gamma\lambda_r^{(1)} = 0, \tag{34}$$

where

$$\gamma = \left[-a^{(1)}\left(\beta_1 d^{(2)} - \beta_2 D^{(2)}\right) \times \left(\delta_1 d^{(2)} - \delta_2 D^{(2)}\right)^{-1} + g^{-1}\varphi^{(1)}G_{(1)}^2\right]\sin^{-1}\alpha,$$
$$\beta_1 = \beta_1\left(D^{(\alpha)}, \overline{D}^{(\alpha)}, Q^{(\alpha)}, P^{(\alpha)}\right) = -\varphi^{(1)}G_{(1)}^2\upsilon^{(1)} + G_{(1)}^2P^{(1)} - G_{(2)}^2P^{(2)}\xi + G_{(2)}^2n^{(2)-1}g^{-1}a^{(2)-1}\xi \times \left(G_{(2)}^2\varphi^{(2)} - G_{(1)}^2\varphi^{(1)}\right) \times \left(Q^{(2)} + \psi^{(2)}\upsilon^{(2)}\right) + G_{(2)}^2\varphi^{(2)}\upsilon^{(2)}\xi,$$
$$\delta_1 = \delta_1\left(D^{(\alpha)}, \overline{D}^{(\alpha)}, \mathrm{Q}^{(\alpha)}, \mathrm{P}^{(\alpha)}\right) = G_{(1)}^2n^{(1)-1}\upsilon^{(1)} - G_{(2)}^2n^{(2)-1}a^{(1)}a^{(2)-1}\xi \times \left(Q^{(2)} + \psi^{(2)}\upsilon^{(2)}\right) + G_{(1)}^2n^{(1)-1}Q^{(1)},$$
$$\upsilon^{(\alpha)} = -G_{(\alpha)}D^{(\alpha)} + 2\rho G_{(\alpha)}^3\overline{D}^{(\alpha)},$$
$$\beta_2 = \beta_1\left(d^{(\alpha)}, \overline{d}^{(\alpha)}, q^{(\alpha)}, p^{(\alpha)}\right),$$
$$\delta_2 = \delta_1\left(d^{(\alpha)}, \overline{d}^{(\alpha)}, q^{(\alpha)}, p^{(\alpha)}\right),$$
$$a^{(\alpha)} = 1 - G_{(\alpha)}^2n^{(\alpha)-1}\psi^{(\alpha)}g^{-1},$$
$$d/ds = g^{-1}d/dt - \partial/\partial u^1.$$

Integrating (34) yields

$$\lambda_r^{(1)} = cs^{\mathrm{Re}\,\gamma}\left[\cos\left(\mathrm{Im}\,\gamma\ \ln\ s\right) - i\ \sin\ \left(\mathrm{Im}\ \gamma\ \ln\ s\right)\right], \tag{35}$$

where $c = c' + ic''$ is a complex arbitrary constant.

Using the value $\lambda_r^{(1)}$ and relationships (25) and (32), one can calculate on the Rayleigh wave the discontinuities of displacement velocities along the normal to the crystal cone and along its generator:

$$[\upsilon_N] = \mathrm{Re}\sum_{\alpha=1}^{2}[\upsilon_i]^{(\alpha)}N_i = \mathrm{Re}\left\{\lambda_r^{(1)}\left[-G_{(1)}\left(\cos\alpha - \chi^{(1)}\sin\alpha\right) + G_{(2)}\xi\left(\cos\alpha - \chi^{(2)}\sin\alpha\right)\right]\right\},$$
$$[\upsilon_K] = \mathrm{Re}\sum_{\alpha=1}^{2}[\upsilon_i]^{(\alpha)}K_i = \mathrm{Re}\left\{\lambda_r^{(1)}\left[-G_{(1)}\left(\sin\alpha + \chi^{(1)}\cos\alpha\right) + G_{(2)}\xi\left(\sin\alpha + \chi^{(2)}\cos\alpha\right)\right]\right\}. \tag{36}$$

If the cone is isotropic, then the Rayleigh wave is formed as the line of the transverse and longitudinal complex wave intersection, on which it is convenient to specify the values $W_1 = [\upsilon_i]x_{i,1}$ and $\omega = [\upsilon_i]v_i$ instead of the values λ_r and λ_3. On the first wave (transverse), $W_1^{(1)} \neq 0$ and $\omega^{(1)} = 0$, but on the second wave (longitudinal), $W_1^{(2)} = 0$ and $\omega^{(2)} \neq 0$; therefore the equation for determination of the Rayleigh wave intensity could be obtained similar to (34):

$$d\omega^{(2)}/ds + r^{-1}\omega^{(2)}\,(1/2\ \sin\alpha - \mathrm{i}\overline{\gamma}\cos\alpha) = 0, \tag{37}$$

or

$$d\omega^{(2)}/ds + s^{-1}\omega^{(2)}\,(1/2 - \mathrm{i}\overline{\gamma}\cot\alpha) = 0 \tag{38}$$

where

S

$$\overline{\gamma} = \frac{n^{(2)2}\left[\left(1-2G_{(1)}^2 g^{-2}\right)\left(G_{(1)}\overline{n}^{(1)}+G_{(2)}\overline{n}^{(2)}\right)+2G_{(2)}\overline{n}^{(2)}\left(1-2n^{(1)2}G_{(1)}^2 G_{(2)}^{-2}\right)\right]}{2g\left[g^{-2}\left(G_{(2)}^2-G_{(1)}^2\right)\left(1-2G_{(1)}^2 g^{-2}\right)-2n^{(2)2}\right]} - \frac{G_{(2)}\overline{n}^{(2)}}{2g}.$$

Solving Eq. (38) yields

$$\omega^{(2)} = cs^{-1/2}\left[\cos\left(\overline{\gamma}\cot\alpha\ \ln s\right) + i\ \sin\left(\overline{\gamma}\cot\alpha\ \ln s\right)\right], \tag{39}$$

where $c = c' + ic''$ is a complex arbitrary constant.

Using the value $\omega^{(2)}$ and formula $W^{1(1)} = \xi\omega^{(2)}$, wherein $\xi = -\left(\lambda+2\mu n^{(2)2}\right)gG_{(2)}^{-1}\left(2\mu n^{(1)2}\right)^{-1}$, the displacement velocity discontinuities on the surface wave could be calculated:

$$[\upsilon_N] = bs^{-1/2}\left[c''\cos\left(\overline{\gamma}\cot\alpha\ \ln s\right) + c'\sin\left(\overline{\gamma}\cot\alpha\ \ln s\right)\right],$$
$$[\upsilon_K] = as^{-1/2}\left[c'\cos\left(\overline{\gamma}\cot\alpha\ \ln s\right) - c''\sin\left(\overline{\gamma}\cot\alpha\ \ln s\right)\right], \tag{40}$$

where

$$b = \sqrt{\frac{G_{(2)}^2}{g^2}-1}\left(2\frac{G_{(1)}^2}{g^2}-1\right), \quad a = \frac{G_{(2)}g}{2G_{(1)}^2}.$$

At $\alpha = 1/2\pi$, the conic surface becomes a plane, and relation (39) is reduced to the known relation:

$$\omega^{(2)} = cs^{-1/2}. \tag{41}$$

At $\alpha = 0$, the cone changes to a cylinder with radius R, and the surface wave of the "diverging circle" type goes into a circle with a constant radius moving along the x_3-axis with the velocity of the Rayleigh wave in the elastic isotropic medium. Then, instead of (37), the following equation is valid:

$$d\omega^{(2)}/dx_3 - iR^{-1}\overline{\gamma}\omega^{(2)} = 0. \tag{42}$$

Integrating (42) yields

$$\omega^{(2)} = c\left[\cos\left(\overline{\gamma}R^{-1}x_3\right) + i\ \sin\left(\overline{\gamma}R^{-1}x_3\right)\right]. \tag{43}$$

When $R \to \infty$, as it follows from (43), the displacement velocity discontinuities become constant, which conforms to the case of the straight line discontinuity propagation along the plane.

Numerical Example

As an example, consider the surface waves of the "diverging circle" type travelling along the surface of a cone made from a zinc oxide single crystal. The values of the elastic moduli for *ZnO* are taken from the handbook edited by Shaskolskaya (1982).

As the elastic moduli $\lambda_{1313} = 4.2449{\cdot}10^{11}$ dyn/cm^2 and $\lambda_{1212} = 4.4289{\cdot}10^{11}$ dyn/cm^2 for this monocrystal deviate slightly from each other, then $\alpha - \beta \ll 1$, and from (16) it could be found that χ is small. Thus, the value γ has the order of $O(1/2)$, and the horizontally polarized surface wave intensity attenuates as $s^{-1/2}$.

To calculate the velocity of the Rayleigh wave of the "diverging circle" type travelling along the free surface of the crystal cone made from a *ZnO* monocrystal, the procedure described in detail by Farnell (1970) may be used.

To eliminate the logarithmic singularity in the expression for the Rayleigh wave intensity, a truncated cone could be considered. Then in the expression for λ_r, the value $\ln s$ may be replaced by $\ln s^*$, where $s^* = sr^{*-1}\sin\alpha$ and r^* is the radius of the cone section.

Calculations show (Fig. 2) that as the angle α changes from 0 to $1/2\pi$ (the curves $1-3$ correspond to the following values of the opening of the cone: 0, $1/4\pi$, and $1/2\pi$), the value of the Rayleigh wave intensity $\lambda^* = \mathrm{Re}\,\lambda_r$ attenuates with oscillation when s^* increases from 1 to ∞, in such a way that attenuation is minimal (zero)

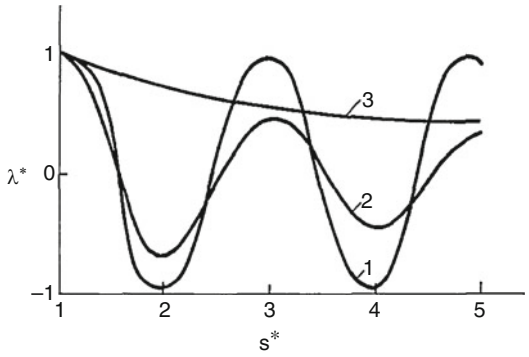

Fig. 2 Rayleigh wave intensity dependence on transmitted distance at various openings of a cone

at $\alpha = 0$ and maximal at $\alpha = 1/2\pi$. In the calculations it was assumed that $c' = c'' = 1$.

Closing Remarks

The procedure described in the present entry for horizontally and vertically polarized transient surface waves propagating along conic surfaces and treated by the ray expansion method could be utilized for 3D bodies of other geometries as well. It has been generalized for thermoelastic bodies of revolution (cone, sphere, cylinder, torus) in Rossikhin and Shitikova (2014), and its application for pre-stressed 3D bodies could be found in Bestuzheva et al. (1981) and Rossikhin and Shitikova (2000, 2004).

References

Babich VM (1961) About Rayleigh waves propagation along a surface of a homogeneous elastic solid of an arbitrary form. Dokl Akad Nauk SSSR 137: 1263–1266

Bestuzheva NP, Bukovtsev GI, Durova VN (1981) Study of transient surface waves in nonlinearly elastic media. Sov Appl Mech 17(12):1062–1067

Brekhovskikh LM (1967) About surface waves containing by boundary curvature in solid. Sov Phys Acoust 13:541–555

Farnell GW (1970) In: Mason WP, Thurston RN (eds) Physical acoustics, Academic Press, New York, vol 6. pp 139—202

Frank P, von Mises R (1935) Die Differential- und Integralgleichungen der Mechanik und Physik, Bd. II: Physikal. Teil. 2. Aufl. F. Vieweg & Sohn, Braunschweig

Petrashen GI (1946) Rayleigh problem for surface waves in sphere case. Dokl Akad Nauk SSSR 52:763–766

Rossikhin YA (1986) Impact of a rigid sphere onto an elastic half space. Sov Appl Mech 22:403–409

Rossikhin YA (1992) Non-stationary surface waves of "diverging circle" type in conic surfaces of hexagonal crystals. Acta Mech 92(1):183–192

Rossikhin YA, Shitikova MV (2000) Investigation of surface instability in an elastic anisotropic cone by the use of surface waves of weak discontinuity. Acta Mech 142(1–4):101–118

Rossikhin YA, Shitikova MV (2004) The influence of the initial stresses on the dynamic instability of an anisotropic cone. In: Goldstein RV, Maugin GA (eds) Surface waves in anisotropic and laminated bodies and defects detection. NATO science series II: mathematics, physics and chemistry, vol 163, pp 257–270. Kluwer

Rossikhin YA, Shitikova MV (2014) Transient thermoelastic Rayleigh waves on the surfaces of bodies of revolution. In: Hetnarski R (ed) Encyclopedia of thermal stresses, vol 11, pp 6225–6244. Springer

Shaskolskaya M (ed) (1982) Acoustic crystals. Handbook. Nauka, Moscow

Thomas TY (1961) Plastic flow and fracture in solids. Academic, Boston

Vaskova BI, Viktorov IA, Silvestrova IM, Talashev AA (1975) About Rayleigh waves on a cylindrical surface of cadmium sulphide crystal. Sov Phys Acoust 21: 466–467

Viktorov IA (1966) Physical foundations of Supersonic Rayleigh and Lamb waves application in technology. Nauka, Moscow

Viktorov IA (1974) Surface waves on a cylindrical surface of crystals. Sov Phys Acoust 20:199–206

Surface Waves

Peter G. Malischewsky
Institute of Geosciences, Friedrich-Schiller University Jena, Jena, Germany

Synonyms

Guided waves; Inhomogeneous waves; Interfacial waves; SAW (surface acoustic waves)

Definition

A surface wave is an inhomogeneous and self-sustaining wave at material surfaces or interfaces which propagates with a velocity being different from the velocities of elastic waves as a consequence of the fulfillment of boundary conditions. It can be considered as a solution of eigenvalue problems, which are met in literally all fields of physics and mathematics. Surface waves occur not only in continuum mechanics but also in fluid mechanics, electromagnetism and optics, solid-state physics, and quantum mechanics. In many cases, surface waves are a dispersive phenomenon, i.e., the phase velocity depends on frequency. Many phenomena of general wave theory like reflection, refraction, and scattering are also present in surface-wave theory and play an important role in the applications.

General Remarks

Special manifestations of elastic waves are such ones which propagate near the body surface without penetrating deeply into the body like body waves. These are surface waves, which are inhomogeneous waves, because their amplitude is varying on surfaces of constant phase. A schematic appearance of such waves propagating in direction x_1 and decaying in direction x_3 is presented in Fig. 1.

The following interfaces are possible candidates for these body surfaces:

(a) solid – vacuum (free surface)
(b) solid – solid
(c) solid – fluid.

All of them support the propagation of surface waves (SAW), but surface waves in the narrower sense occur on free surfaces. Note that, instead of surface waves, it is rather appropriate to speak of a broader category of guided waves, which propagate along the surface of a medium (case (a)), along internal discontinuities or other waveguides (cases (b) and (c)). In this manner, elastic waves can be roughly classified by the scheme in Fig. 2.

Waves of this type are different from the so-called evanescent waves at an interface, which are produced in the faster material by critical refraction and cling to the interface. They cannot exist without being continuously sustained by a wave from the interior. In contrast the surface waves that cling to a surface are self-sustaining, which is an essential feature of them. Generally speaking the surface-wave theory is a subsection of elastic-wave theory, but because of the special properties in propagating and in applying surface waves, the latter ones are usually treated separately.

At first it is assumed that the motion does not depend on one of the three space coordinates (let be x_2). A typical model for the demonstration of surface waves is in the simplest case a

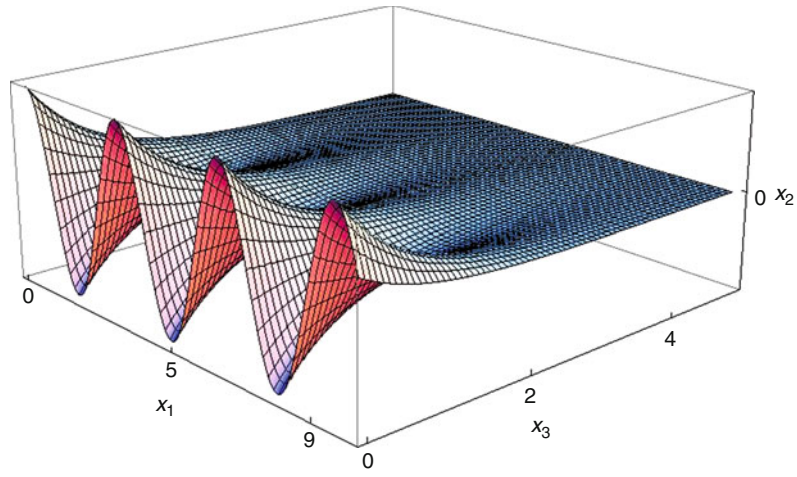

Fig. 1 Schematic appearance of a surface wave

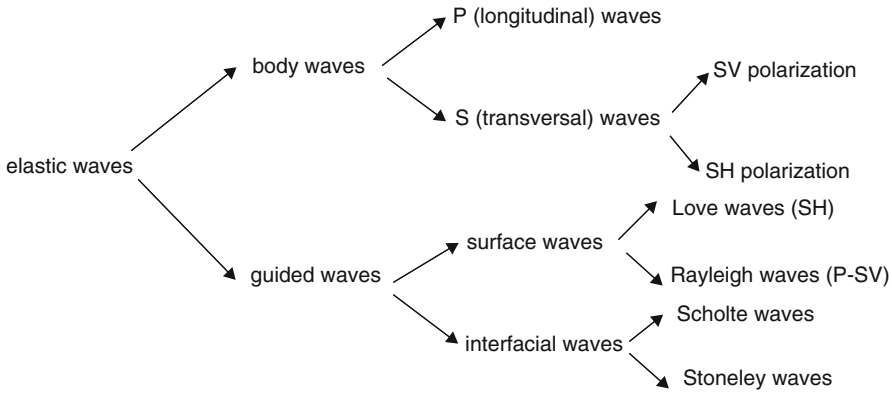

Fig. 2 Classification of elastic waves

homogeneous half-space possibly augmented by one or more layers on top of it. A Cartesian coordinate system is introduced so that $x_3 = 0$ is the free surface, the positive x_3-axis points into the half-space, and the waves are propagating into direction x_1. In this context, the x_1, x_3-plane is called the sagittal plane and the x_1, x_2-plane the transverse plane.

Separation of the Equation of Motion for Surface Waves

A natural starting point is as much as for body waves under the usual simplifying assumptions (see entry *Elastic Waves*) in absence of body forces the Navier equation in Cartesian coordinates

$$(\lambda + \mu)\, u_{j,\,j,\,i} + \mu\, u_{i,\,j,\,j} = \rho\, \ddot{u}_i \qquad (1)$$

or in vector notation

$$(\lambda + \mu)\ \mathrm{grad}\,\mathrm{div}\,\mathbf{u} + \mu\,\Delta\,\mathbf{u} = \rho\,\ddot{\mathbf{u}}. \qquad (2)$$

The following notations are used within these equations, u_i , Cartesian coordinates ($i = 1, 2, 3$) of the displacement vector $\mathbf{u}$; piecewise constant Lamé parameters λ and μ, and density ρ. The comma notation is used for partial derivatives (see, e.g., Eringen and Suhubi 1975), i.e.,

$$u_{i,j} \equiv \frac{\partial u_i}{\partial x_j}, \qquad (3)$$

and Einstein's summation convention is understood. The time derivation is denoted by a dot.

Cauchy's stress tensor components are given by (see Eringen and Suhubi 1975)

$$\sigma_{kl} = \lambda\,\delta_{kl}\,u_{r,r} + \mu\,(u_{k,l} + u_{l,k}), \qquad (4)$$

and the velocities of longitudinal P-waves $\alpha = \sqrt{(2\,\mu + \lambda)/\rho}$ and transversal S-waves $\beta = \sqrt{\mu/\rho}$ are needed later on.

Taking into account the model symmetry described above, the expressions for $u_{i,j,j}$ and $u_{j,j,i}$, respectively, are

$$\begin{aligned} u_{i,j,j} &= \frac{\partial^2 u_i}{\partial x_1^2} + \frac{\partial^2 u_i}{\partial x_3^2}, \\ u_{j,j,i} &= \delta_{i1}\left(\frac{\partial^2 u_1}{\partial x_1^2} + \frac{\partial^2 u_3}{\partial x_1\,\partial x_3}\right) \\ &\quad + \delta_{i3}\left(\frac{\partial^2 u_3}{\partial x_3^2} + \frac{\partial^2 u_1}{\partial x_1\,\partial x_3}\right), \end{aligned} \qquad (5)$$

where the Kronecker tensor δ_{ij} is used. A consequence of this structure is that (1) splits into a coupled system of partial differential equations for u_1 and u_3

$$\begin{aligned} &(2\mu + \lambda)\, u_{1,1,1} + \mu\, u_{1,3,3} + (\lambda + \mu)\, u_{3,1,3} \\ &\quad = \rho\, \ddot{u}_1, \\ &(2\mu + \lambda)\, u_{3,3,3} + \mu\, u_{3,1,1} + (\lambda + \mu)\, u_{1,1,3} \\ &\quad = \rho\, \ddot{u}_3, \end{aligned} \qquad (6)$$

S

and a single equation

$$\mu\ (u_{2,1,1} + u_{2,3,3}) = \rho\, \ddot{u}_2 \tag{7}$$

for u_2, i.e., the P-SV motion u_1, u_3 in the so-called sagittal plane is independent of the SH-motion u_2 in the transverse plane. This is still true when the assumption of piecewise constant material parameters is dropped. Then Eq. (7) adopts the form with the depth-dependent material parameters (see Malischewsky 1987) $\mu(x_3)$ and $\rho(x_3)$

$$\frac{\partial}{\partial x_1}\left[\mu(x_3)\ \frac{\partial u_2}{\partial x_1}\right] + \frac{\partial}{\partial x_3}\left[\mu(x_3)\ \frac{\partial u_2}{\partial x_3}\right] = \rho(x_3)\, \ddot{u}_2. \tag{8}$$

Surface Waves with SH-Polarization (Love Waves)

Homogeneous Half-Space

By using the separation ansatz for plane harmonic surface waves with SH-polarization in a half-space

$$u_2\,(x_1,\ x_3,\ t) = V(x_3)\ e^{\mathrm{i}\,(k\,x_1 - \omega\,t)} \tag{9}$$

with the amplitude-depth dependence $V(x_3)$, the wave number $k = \omega/c$, the circle frequency ω, and the phase velocity of surface waves c, the partial differential equation (7) becomes an ordinary differential equation for $V(x_3)$:

$$V'' - q^2\, V = 0 \text{ with } q^2 = k^2 - k_\beta^2 \text{ and } k_\beta = \omega/\beta. \tag{10}$$

When the surface $x_3 = 0$ is assumed stress-free, the boundary condition is $\sigma_{23} = 0$, and the character of surface waves requires at infinity $V(\infty) = 0$. These both conditions cannot be fulfilled simultaneously with the consequence that Love waves do not exist for a homogeneous half-space. However, by modifying the boundary condition $\sigma_{23}(0) = 0$ like a type of an impedance condition (Leontovich type) in the manner

$$\mu\, V'(0) + \varepsilon\, V(0) = 0, \tag{11}$$

the simplest elastic surface wave at all can propagate, and that is the reason for mentioning it. The impedance parameter ε has the dimension stress/length, and Eq. (10) together with the boundary conditions (11) for $x_3 = 0$ and $V(\infty) = 0$ for $x_3 = \infty$ defines an eigenvalue problem whose solution yields the eigenvalue k and the eigenfunction V:

$$k = \sqrt{k_\beta^2 + \varepsilon^2/\mu^2}\,, \quad V(x_3) = e^{-\frac{\varepsilon}{\mu}\,x_3}. \tag{12}$$

By defining a dimensionless phase velocity $C = c/\beta$ and a dimensionless "frequency" by $\bar{F} = \omega\,\mu/(\varepsilon\,\beta)$, it follows from (12)

$$C(\bar{F}) = \bar{F}/\sqrt{1 + \bar{F}^2}, \tag{13}$$

so that the phase velocity is frequency dependent, i.e., *dispersion* occurs, and $V(x_3)$ is the amplitude depth-dependence of this simple Love-kind surface wave.

Love Waves in a Model "Layer Over Half-Space" (LOH)

The top of the layer with thickness H is assumed stress-free, and continuity of the displacement and the corresponding stress is supposed on the interface $x_3 = H$:

$$\sigma_{23}^{(1)}(0) = 0,\ \ V^{(1)}(H) = V^{(2)}(H),$$
$$\sigma_{23}^{(1)}(H) = \sigma_{23}^{(2)}(H), \tag{14}$$

where layer parameters are labeled with 1 and half-space parameters with 2. There are two integration constants of (10) for the layer and one constant for the half-space. The nontrivial solution of the homogeneous system (14) requires a three-row determinant to vanish which yields after some algebra (see Kaufman and Levshin 2005) with the shear-velocity ratio $r_s = \beta_1/\beta_2$, the density ratio $r_d = \rho_1/\rho_2$, and the abbreviations $\gamma_1 = \sqrt{C^2 - 1}$, $\gamma_2 = \sqrt{1 - r_s^2 C^2}$, $C = c/\beta_1$, $F = H/\lambda_{\beta_1}$, and $\lambda_{\beta_1}$is shear wavelength of the layer,

$$2\pi F \frac{\gamma_1}{C} - \arctan\left[\frac{\gamma_2}{\gamma_1 r_d r_s}\right] - n\pi = 0. \quad (15)$$

The ambiguity was incorporated by the natural number n, which yields for $n=0$ the *fundamental Love mode* and for $n=1, 2, 3, \ldots$ the corresponding *higher modes*. All Love modes are d*ispersive*, i.e., their phase velocities are frequency-dependent: $C_n = C_n(F)$ and vary between 1 and r_s^{-1} : $1 \leq C_n \leq r_s^{-1}$. They have a lower limit frequency

$$F_n = \frac{n}{2\sqrt{1-r_s^2}}, \quad (16)$$

but the fundamental mode exists for all frequencies because $F_0 = 0$. The associated group velocity follows from the well-known formula for the dimensionless group velocity,

$$U(F) = \frac{C^2}{C - F\, dC/dF}, \quad (17)$$

which is representable for the simple model LOH also analytically. The phase and group velocities for the fundamental and first higher mode are given in Fig. 3. A characteristic of these curves is that phase and group velocities fall together at the low- and high-frequency ends. There is an infinite set of modes. However, for a fixed frequency, the number is limited.

The eigenfunctions $V(z)$, $z = x_3/H$, follow from (14) and (15) for the layer and the half-space, respectively:

$$V^{(1)}(z) = \cos(2\pi F z \gamma_1 / C),$$
$$V^{(2)}(z) = e^{-2\pi F(z-1)\gamma_2/C} \cos(2\pi F \gamma_1 / C) \quad (18)$$

and are presented with parameters of Fig. 3 in Fig. 4.

Rayleigh Waves in a Homogeneous Half-Space

By using the separation ansatz for plane harmonic surface waves in the sagittal plane (Rayleigh waves)

$$u_i(x_1, x_3, t) = U_i(x_3)\, e^{\mathrm{i}(k x_1 - \omega t)}, \quad i = 1, 3, \quad (19)$$

the system (6) becomes

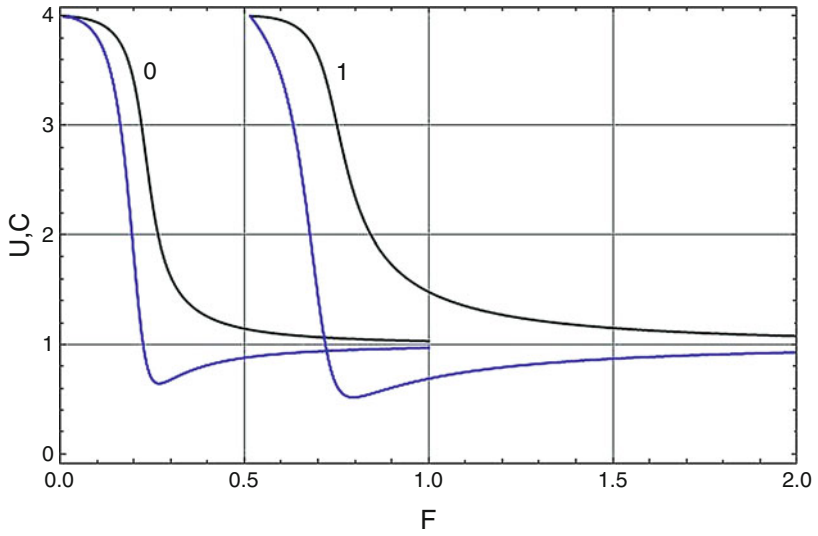

Fig. 3 Phase (black) and group (blue) velocities for the fundamental (0) and first higher (1) Love mode with $r_s = 0.25$ and $r_d = 1$

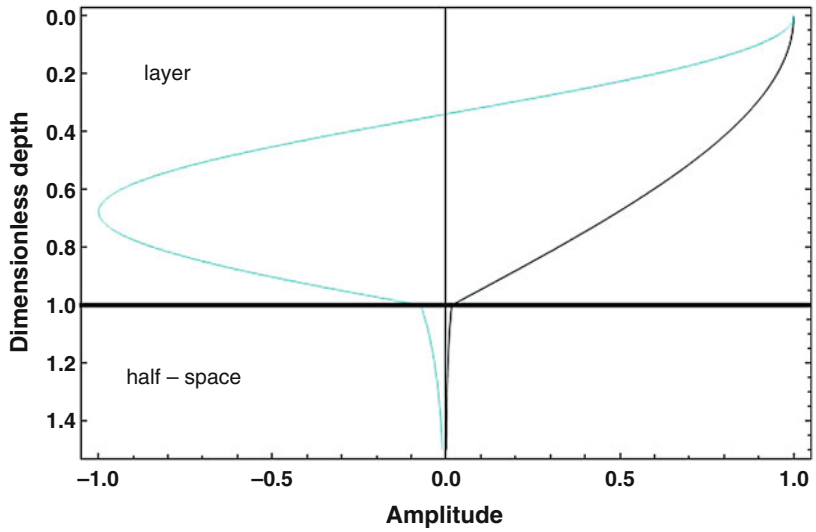

Fig. 4 Amplitude-depth dependences of the fundamental (black) and first higher (cyan) Love mode

$$\begin{aligned}\beta^2\, U_1'' + \mathrm{i}\, k\, (\alpha^2 - \beta^2)\, U_3' + (\omega^2 - k^2\, \alpha^2)\, U_1 = 0,\\ \alpha^2\, U_3'' + \mathrm{i}\, k\, (\alpha^2 - \beta^2)\, U_1' + (\omega^2 - k^2\, \beta^2)\, U_3 = 0.\end{aligned} \tag{20}$$

This system of ordinary differential equations can be solved by applying the well-known technique, and introducing the abbreviation $p^2 = k^2 - k_\alpha^2$, the solution is

$$\begin{aligned}U_1(x_3) &= c_1\, e^{-p\, x_3} + c_2\, e^{p\, x_3} + c_3\, e^{-q\, x_3} + c_4\, e^{q\, x_3},\\ U_3(x_3) &= \mathrm{i}\left[\tfrac{p}{k}\left(c_1\, e^{-p\, x_3} - c_2\, e^{p\, x_3}\right) + \tfrac{k}{q}\left(c_3\, e^{-q\, x_3} - c_4\, e^{q\, x_3}\right)\right].\end{aligned} \tag{21}$$

By denoting the x_3-dependent stress tensor components with $S_{i3}(x_3)$, the boundary conditions on the stress-free surface and in infinity, respectively, require:

$$\begin{aligned}S_{i3} = 0,\ \ i = 1,\ 3\ \ \text{for}\ x_3 = 0\ \text{and}\\ U_1(\infty) = U_3(\infty) = 0\ \text{or}\ c_2 = c_4 = 0.\end{aligned} \tag{22}$$

It should be noted that (20) together with (22) define a nonstandard eigenvalue problem because the eigenvalue k enters linearly and quadratically. Setting the determinant of the homogeneous system (22) for c_1 and c_3 to zero results in *Rayleigh's equation*

$$4\, p\, q - k^2\, (2 - C^2) = 0\,, \tag{23}$$

which can be transformed via γ to a cubic equation depending on Poisson's ratio ν:

$$\begin{aligned}x^3 - 8\, x^2 + 8\, x\, (3 - 2\gamma) - 16\, (1 - \gamma) = 0\,,\\ x = C^2\,,\ \ \gamma = \frac{\beta^2}{\alpha^2} = \frac{1\text{-}2\nu}{2(1\text{-}\nu)}\,,\ \ \text{and}\\ c_3 = -\frac{2pq}{2k^2 - k_\beta^2}\, c_1.\end{aligned} \tag{24}$$

By using the auxiliary functions

$$h(\gamma) = 17 - 45\,\gamma + 3\sqrt{33 - 186\gamma + 321\gamma^2 - 192\gamma^3} \text{ and}$$

$$\bar{h}(\gamma) = \sqrt[3]{h(\gamma)}, \tag{25}$$

where the main value of the cubic root is understood, the solution of (24) can be written analytically with Malischewsky's formula (Malischewsky 2004)

$$x(\gamma) = \frac{2}{3}\left[4 - \bar{h}(\gamma) + 2\,(1 - 6\,\gamma)/\bar{h}(\gamma)\right] \tag{26}$$

or is approximated excellently in the whole range of possible ν – values $-1 \le \nu \le 0.5$ by Malischewsky's approximation (Malischewsky 2005)

$$C = 0.874 + 0.196\,\nu - 0.043\,\nu^2 - 0.055\,\nu^3$$

or by the well-known Bergmann's approximation (Bergmann 1948) for positive Poisson's ratios (non-auxetic range):

$$C = \frac{0.87 + 1.12\,\nu}{1 + \nu}. \tag{27}$$

The phase velocity of Rayleigh waves in a homogeneous half-space is a slowly varying function of Poisson's ratio in the range $0.6889 \le C \le 0.9553$, but it does not depend on frequency, i.e., the Rayleigh waves are not dispersive. For $\nu = 1/4$ is $\gamma = 1/3$ and C becomes $C = \sqrt{2 - 2/\sqrt{3}} \approx 0.9194$, i.e., the velocity is a little bit less than the shear wave velocity. Once the phase velocity is determined, the particle motion for all depths is obtained by combining the amplitude-depth dependences (21) with the time dependence via (19). The occurrence of the imaginary unit **i** in (21) produces a phase shift of $\pi/2$, and the motion is rotational and elliptic, and the sense of motion depends on depth. The ellipticity $\chi(\nu)$ on the free surface is an important parameter and depends only on Poisson's ratio ν via C:

$$\chi(\nu) = \left|\frac{U_1(0)}{U_3(0)}\right| = 2\frac{\sqrt{1 - C^2}}{2 - C^2},$$

$$\text{e. g. } \chi\,(0.25) = \sqrt{2\sqrt{3} - 3} \approx 0.6813\,. \tag{28}$$

The behavior of the amplitude-depth functions U_1 and U_3 for Rayleigh waves together with the ellipticity is illustrated at Fig. 5. The particle motion is retrograde near the surface but

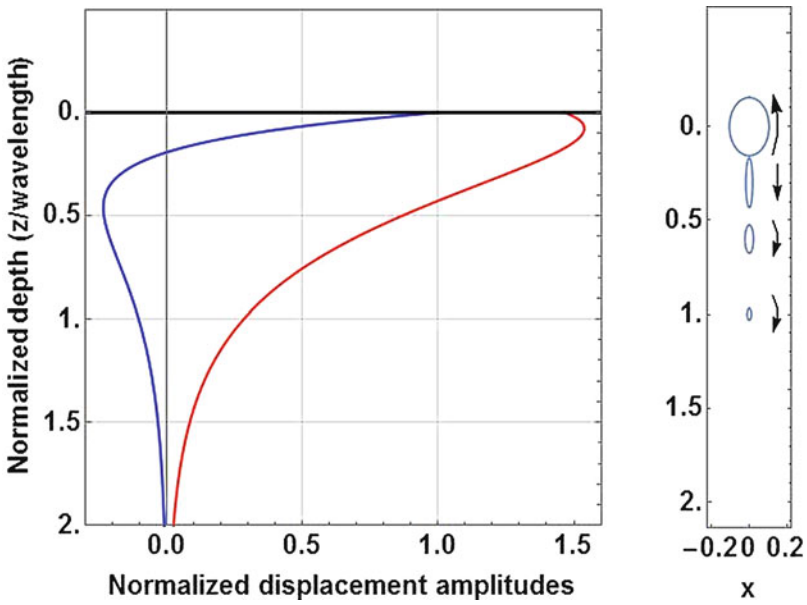

Fig. 5 Left: dependence of the horizontal (blue) and vertical (red) displacements of Rayleigh waves for $\nu = 0.25$ and $\omega = 1$ Hz; Right: elliptical particle motion in dependence on depth with indication of the sense of motion

S

reverses to prograde motion below the zero crossing of the horizontal displacement component. While the particle motion for a homogeneous half-space is always retrograde on the surface, the existence of a layer can change the sense of motion.

The existence of layers on top of the half-space (one layer is enough) makes the Rayleigh waves dispersive and produces an infinite set of modes, but for a fixed frequency, their number is limited with the consequence that the surface-wave modes do not form a complete set of eigenfunctions in the sense of functional analysis. The behavior of the phase and group velocities is usually more complex than for Love waves in the simple LOH model. One reason is the occurrence of so-called osculations, which means dispersion curves of different modes can come very near to each other (Foti et al. 2015).

Stoneley and Scholte Waves at a Solid-Solid and Solid-Fluid Interface, Resp.

Let the plane $x_3 = 0$ be the interface between two solids, and let the Stoneley waves propagate into direction x_1 and decay in direction of the positive and negative x_3-axis, respectively. These waves have U_1 and U_3 displacement components and are polarized in the sagittal plane as Rayleigh waves. Figure 6 reflects purely schematically this behavior. The analysis of these interfacial waves turns out to be not much different compared to that of the Rayleigh waves. The particle motion is elliptical as for Rayleigh waves, and these waves are also not dispersive. In the case of Stoneley waves for a solid-solid interface, there are two integration constants in the ansatzes in both media (1) and (2) for $U_j^{(\alpha)}$ $(j = 1, 3\,;\ \alpha = 1, 2)$, i.e., together four constants. The interfacial conditions at $x_3 = 0$ for perfectly bonded half-spaces with the continuity of $U_j^{(\alpha)}$ and $S_{j3}^{(\alpha)}$ yield an homogeneous system of four equations, the nontrivial solution of which requires a four-row determinant to vanish. This is a rather complicated equation, which determines the Stoneley-wave velocity c_S. It falls between the velocity of Rayleigh waves and that of shear waves in the slower medium. This secular equation can be found, e.g., at Kaufman and Levshin (2005). The existence of a real root, i.e., of Stoneley waves, appears to be a rather special phenomenon. They exist, when the corresponding velocities α and β of both media are rather near to each other. For the special case that $\alpha_1 = \alpha_2$ and $\beta_1 = \beta_2$ and only $\rho_1 \neq \rho_2$, a Stoneley wave always exists, and an analytical expression for c_S can be found. The secular equation is transformed into the one of Rayleigh waves (23) for $\rho_2 = 0$ and of Scholte waves when the second medium is fluid, i.e., $\beta_2 = 0$. Contrary to Stoneley waves, Scholte waves exist for all parameter combinations, and their velocity is smaller than the sound velocity in the liquid and smaller than the Rayleigh-wave velocity of the half-space.

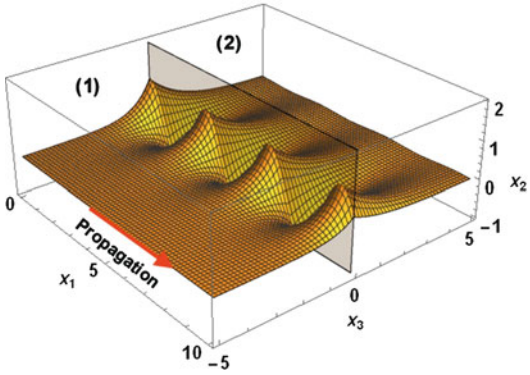

Fig. 6 Schematic illustration of Stoneley or Scholte waves; the interface $x_3 = 0$ is indicated by a semipermeable plane; (1) is solid and (2) is solid and fluid, respectively

Surface Waves, Eigenvalue Problems, and Some Extensions

By using the ansatz (9), an eigenvalue equation for Love waves may be obtained from (8) in the form

$$L\,V = \bar{\lambda}\,V \text{ with the operator}$$
$$L = \frac{1}{\mu}\left[\frac{d}{dx_3}\left(\mu\,\frac{d}{dx_3}\right) + \rho\,\omega^2\right]$$
$$\text{and the eigenvalue } \bar{\lambda} = k^2. \qquad (29)$$

It is an eigenvalue problem of the type Sturm-Liouville, i.e., it is well established in mathematics (see, e.g., Teschl 2012), and the eigenfunctions $V(x_3)$ of different Love modes satisfy a simple orthogonality relation. However, because of the infinite domain of definition (in the half-space), the operator L has a mixed spectrum consisting of discrete eigenvalues corresponding to the Love modes and a continuous part corresponding to the SH-waves. Such situations are usual in many fields of application, e.g., in the theory of optical waveguides or in quantum theory. It requires a careful consideration of the completeness of the used eigenfunction system. A similar situation occurs with Rayleigh waves, but it is a vector-eigenvalue problem and not a standard one as mentioned above. The corresponding orthogonality relation between the Rayleigh eigenfunctions is more complex than that of Love modes.

Sometimes, the assumption, that the wave motion does not depend on coordinate x_2, has to be dropped by using instead of (19) the more general ansatz

$$u_i(x_1,\, x_2,\, x_3,\, t) = U_i(x_3)\; e^{\mathrm{i}\,(k_1 x_1 + k_2 x_2 - \omega t)}\,, \quad i = 1,\, 2,\, 3, \tag{30}$$

which extends the corresponding eigenvalue problem and suggests the creation of a "supermode" system consisting of M Rayleigh modes and N Love modes. If a surface wave encounters a discontinuity under these assumptions, all Rayleigh and Love modes, which exist for a given frequency, are excited, i.e., such a supermode system has to be used instead of Rayleigh and Love waves alone.

Another extension is the consideration of curved wave fronts for surface waves. An usual phenomenon is the existence of cylindrical Rayleigh waves (Fig. 7).

It is interesting to note that the dispersion relation $c = c(\omega)$ for the latter waves is the same one as for plane surface waves (Kausel 2006).

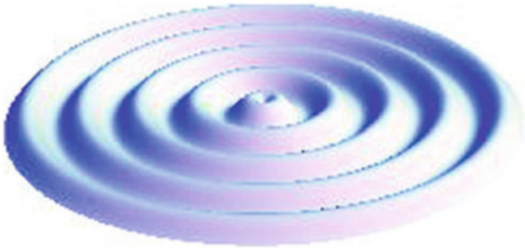

Fig. 7 Cylindrical Rayleigh waves (view from above)

Historical Remarks and Applications

Lord Rayleigh firstly introduced the waves, which bear his name, as a solution of the free vibration problem for an elastic half-space 1885. He anticipated the importance that such kind of wave could have in earthquake tremor transmission by considering the lower attenuation of these waves in comparison with body waves because of geometrical reasons. As a consequence the surface waves usually dominate seismograms of natural earthquakes in a certain distance from the source. Subsequently, the other surface waves beside Rayleigh waves were discovered, described, and applied (see Kaufman and Levshin 2005). The applications range from Spectral Analysis of Surface Waves (SAWS) in seismology and NDT up to the modern "lab-on-a-chip" conception, where the waves interact with media in physical contact with surface to mix, translate, and atomize fluids or to manipulate micro/nanoscale objects. Surface waves exist in an extremely wide frequency range over more than 10 orders of magnitude: ultra-long seismic surface waves have a frequency of 0.002 Hz, and the applications in a lab-on-a-chip extend up to 1 GHz and the world of surface phonons even up to 10 THz.

Cross-References

▸ Waves and Generalized Continua
▸ Waves in Continuous Media: Classical Theory

References

Bergmann L (1948) Ultrasonics and their scientific and technical applications. Wiley, New York
Eringen AC, Suhubi ES (1975) Elastodynamics. Academic Press, New York
Foti S, Lai CG, Rix GJ, Strobbia C (2015) Surface wave methods for near-surface site characterization. CRC Press, Boca Raton
Kaufman AA, Levshin AL (2005) Acoustic and elastic Wave fields in geophysics III. Elsevier, Amsterdam
Kausel E (2006) Fundamental solutions in elastodynamics. Cambridge University Press, Cambridge
Malischewsky P (1987) Surface waves and discontinuities. Elsevier, Amsterdam
Malischewsky P (2004) A note on Rayleigh-wave velocities as a function of the material parameters. Geofísica Internacional 43:507–509
Malischewsky P (2005) Comparison of approximated solutions for the phase velocity of Rayleigh waves. Nanotechnology 16:995
Rayleigh L (1885) On waves propagated along the plane surface of an elastic solid. Proc Lond Math Soc s1–17:4–11
Teschl G (2012) Ordinary differential equations and dynamical systems. American Mathematical Society, Providence

Surface/Interfacial Energy Theory of Solids

Xiang Gao[1,2] and Zhu-Ping Huang[1]
[1]Department of Mechanics and Engineering Science, Peking University, Beijing, China
[2]Department of Mechanical Engineering, Tufts University, Medford, MA, USA

Definition

Atoms at surfaces and interfaces experience a different local environment from atoms inside bulk materials, and the physical states and equilibrium positions of such atoms will, generally, differ from those of the interior atoms. This difference is the physical origin of the interfacial (or surface) energy and the interface (or surface) stress in solids and liquids, a topic which has been fully studied by many researchers (Cahn 2013; Cammarata 1994; Gibbs et al. 1906; Herring 1953; Orowan 1970; Povstenko 1993; Shuttleworth 1950; Streitz et al. 1994a, b). In the Gibbs treatment of the interfacial energy, the interface is regarded as a dividing surface between two different materials (or phases). The interfacial energy represents the excess free energy due to the existence of interface, and it is defined as the reversible work per unit area needed to create a new interface. When the interface of a solid is deformed, the interfacial energy will generally vary. The interface stress is associated with the reversible work per unit area needed to elastically stretch a pre-existing interface. Therefore, the interfacial energy and interface stress are essentially different concepts. For liquids, owing to the atomic mobility, the surface atoms increase during stretching since the interior atoms in the liquid can flow freely to the surface and consequently, the magnitudes of the surface energy and the surface stress (called surface tension sometimes) are the same. The atomic mobility in solids, by contrast, is very low, and the total amount of the surface atoms remains almost constant under elastic stretching. Hence, the surface stress of solids usually varies with surface deformation. The relationship between the surface stress and the surface strain is given by the famous Shuttleworth-Herring equation (Herring 1999; Shuttleworth 1950). As surfaces and interfaces have similar roles in continuum mechanics, we shall, for expediency, use the word "interface" to refer to both when describing general principles and when there is no need to differentiate them.

Deformation and Kinematics of Two-Dimensional Curved Surface

In this section, we will provide some preliminary definitions and notations that are necessary for describing the deformation of an interface. For more details, the author may refer to Huang and Wang (2013).

Consider a multiphase hyperelastic solid containing sharp interfaces between the phases. This configuration is referred to as the initial reference

configuration, denoted by κ_0, when no external load is applied. The interfaces are denoted collectively by A_0. A curvilinear coordinate system $\theta^\alpha(\alpha = 1, 2)$ will be used to describe the material point $\boldsymbol{Y}$ on the surface. The corresponding covariant base vectors at point $\boldsymbol{Y}$ in the reference configuration can be determined by $\boldsymbol{A}_\alpha = \boldsymbol{Y}_{,\alpha}$ with $\boldsymbol{A}_3$ being the unit normal vector. Here and in the following, the Greek indices take values in $\{1, 2\}$, and the Latin indices take values in $\{1, 2, 3\}$.

After deformation, the material point $\boldsymbol{Y}$ on the interface A_0 in the reference configuration will move to a point $\boldsymbol{y}$ on the interface A in the current configuration, denoted by κ. As shown in Fig. 1, the corresponding covariant base vectors at point $\boldsymbol{y}$ on the interface A can be written as $\boldsymbol{a}_\alpha = \boldsymbol{y}_{,\alpha} = \boldsymbol{Y}_{,\alpha} + \boldsymbol{u}_{,\alpha}$ with $\boldsymbol{a}_3$ being the unit normal vector, where $\boldsymbol{u}$ is the displacement. If the displacement $\boldsymbol{u}$ is decomposed into a sum of $\boldsymbol{u}_{0s} = u_0^\alpha \boldsymbol{A}_\alpha$ in the tangential direction and $\boldsymbol{u}_{0n} = u_0^n \boldsymbol{A}_3$ in the normal direction of the interface A_0, the base vector $\boldsymbol{a}_\alpha$ can be expressed in the reference configuration, which gives

$$\begin{aligned} \boldsymbol{a}_\alpha &= \boldsymbol{A}_\alpha + \left(u_0^\beta \boldsymbol{A}_\beta\right)_{,\alpha} + \left(u_0^n \boldsymbol{A}_3\right)_{,\alpha} \\ &= \boldsymbol{A}_\alpha + \left(u_0^\lambda\big|_\alpha - u_0^n B_\alpha^\lambda\right) \boldsymbol{A}_\lambda \\ &\quad + \left(u_0^\lambda B_{\lambda\alpha} + u_{0,\alpha}^n\right) \boldsymbol{A}_3 \end{aligned} \tag{1}$$

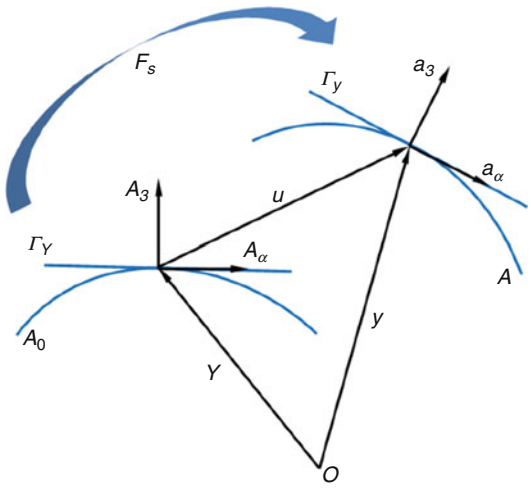

Fig. 1 Deformation of an elastic interface

where "|" denotes covariant derivative and $\boldsymbol{B} = B_{\lambda\alpha}\boldsymbol{A}^\lambda \otimes \boldsymbol{A}^\alpha$ is the curvature tensor of the surface A_0. Therefore, the interface deformation gradient can be written as

$$\boldsymbol{F}_s = \boldsymbol{a}_\alpha \otimes \boldsymbol{A}^\alpha = \boldsymbol{F}_s^{(in)} + \boldsymbol{F}_s^{(ou)} \tag{2}$$

where the in-plane term $\boldsymbol{F}_s^{(in)}$ and the out-of-plane term $\boldsymbol{F}_s^{(ou)}$ are

$$\begin{aligned} \boldsymbol{F}_s^{(in)} &= \boldsymbol{i}_0 + \boldsymbol{u}\nabla_{0s}, \\ \boldsymbol{F}_s^{(ou)} &= \boldsymbol{A}_3 \otimes \boldsymbol{D} \end{aligned} \tag{3}$$

In the above, $\boldsymbol{i}_0$ is the unit tensor on surface A_0, $\boldsymbol{u}\nabla_{0s} = \boldsymbol{u}_{0s}\nabla_{0s} - u_0^n \boldsymbol{B}$ is the surface displacement gradient, and $\boldsymbol{D} = \boldsymbol{u}_{0s} \cdot \boldsymbol{B} + u_0^n \nabla_{0s}$ in the reference configuration.

Similarly, the displacement $\boldsymbol{u}$ can also be decomposed as the sum of its tangential component $\boldsymbol{u}_s = u^\alpha \boldsymbol{a}_\alpha$ and normal component $\boldsymbol{u}_n = u^n \boldsymbol{a}_3$ on the interface A, and then the base vectors $\boldsymbol{A}_\alpha$ can be expressed in the current configuration, which gives

$$\begin{aligned} \boldsymbol{A}_\alpha &= \boldsymbol{a}_\alpha - \left(u^\beta \boldsymbol{a}_\beta\right)_{,\alpha} - \left(u^n \boldsymbol{a}_3\right)_{,\alpha} \\ &= \boldsymbol{a}_\alpha - \left(u^\lambda\big|_\alpha - u^n b_\alpha^\lambda\right) \boldsymbol{a}_\lambda \\ &\quad - \left(u^\lambda b_{\lambda\alpha} + u_{,\alpha}^n\right) \boldsymbol{a}_3 \end{aligned} \tag{4}$$

where $\boldsymbol{b} = b_{\lambda\alpha}\boldsymbol{a}^\lambda \otimes \boldsymbol{a}^\alpha$ is the curvature tensor of the interface A after deformation. Thus, the inverse of the interface deformation gradient is expressed as

$$\boldsymbol{F}_s^{-1} = \boldsymbol{A}_\alpha \otimes \boldsymbol{a}^\alpha = \boldsymbol{i} - \boldsymbol{u}\nabla_s - \boldsymbol{a}_3 \otimes \boldsymbol{d} \tag{5}$$

where $\boldsymbol{i}$ is the unit tensor on interface A, $\boldsymbol{u}\nabla_s = \boldsymbol{u}_s\nabla_s - u^n \boldsymbol{b}$ is the surface displacement gradient, and $\boldsymbol{d} = \boldsymbol{u}_s \cdot \boldsymbol{b} + u^n \nabla_s$ in the current configuration.

By using the polar decompositions of $\boldsymbol{F}_s$, the right and left Cauchy-Green tensors of the interface can be defined as $\boldsymbol{C}_s = \boldsymbol{U}_s^2 = \boldsymbol{F}_s^{\mathrm{T}} \cdot \boldsymbol{F}_s$ and $\boldsymbol{B}_s = \boldsymbol{V}_s^2 = \boldsymbol{F}_s \cdot \boldsymbol{F}_s^{\mathrm{T}}$, where $\boldsymbol{U}_s$ and $\mathbf{V}_\mathrm{s}$ are called the right and left stretch tensors of the interface, respectively.

Strain Measures of the Interface

Like the Seth strain measure (Seth 1961) for three-dimensional deformation, the two-dimensional strain tensor of interface can be formulated to characterize the stretching deformation. In the reference configuration, the Lagrangian strain tensor of the interface can be defined as

$$\begin{aligned} \boldsymbol{E}_s^{(m)} &= \frac{1}{2m}\left(\boldsymbol{U}_s^{2m} - \boldsymbol{i}_0\right), \quad m \neq 0 \\ \boldsymbol{E}_s^{(0)} &= \ln \boldsymbol{U}_s, \quad m = 0 \end{aligned} \tag{6}$$

where m is a real number. When $m = 1$, we obtain the Green strain tensor of the interface

$$\boldsymbol{E}_s^{(1)} = \frac{1}{2}\left(\boldsymbol{U}_s^2 - \boldsymbol{i}_0\right) = \frac{1}{2}\left(\boldsymbol{C}_s - \boldsymbol{i}_0\right) \tag{7}$$

which furnishes the change of the metric tensor of the interface and will be used in the following section.

Following Steigmann and Ogden (1999), the relative curvature $\boldsymbol{\kappa}$ of the interface can be defined by

$$\boldsymbol{\kappa} = -\boldsymbol{F}_s^{\mathrm{T}} \cdot \boldsymbol{b} \cdot \boldsymbol{F}_s \tag{8}$$

which is the pullback of the curvature tensor $\boldsymbol{b}$ from the current configuration to the reference configuration. Considering $\boldsymbol{b} = -\boldsymbol{a}_{3,\alpha} \otimes \boldsymbol{a}^{\alpha}$, Eq. (8) can be rewritten as

$$\boldsymbol{\kappa} = \boldsymbol{F}_s^{\mathrm{T}} \cdot \left(\boldsymbol{a}_{3,\alpha} \otimes \boldsymbol{A}^{\alpha}\right) = \boldsymbol{F}_s^{\mathrm{T}} \cdot \left(\boldsymbol{a}_3 \tilde{\nabla}_{0s}\right) \tag{9}$$

where $(\cdot)\,\tilde{\nabla}_{0s} = (\cdot)_{,\alpha} \otimes \boldsymbol{A}^{\alpha}$ that has the same meaning as the differential operator "∇" used by Gurtin et al. (1998). Similarly, the flexural deformation of an interface is usually characterized by the change of its curvature tensor (Langhaar 1974). Thus, the Lagrangian curvature strain of the interface can be defined as

$$\boldsymbol{\Lambda} = \left(b_{\alpha\beta} - B_{\alpha\beta}\right)\boldsymbol{A}^{\alpha} \otimes \boldsymbol{A}^{\beta} = -\boldsymbol{\kappa} - \boldsymbol{B} \tag{10}$$

Notably, the stretching and the flexural deformations of the interface are coupled with each other, and the shape of the interface is usually unknown after deformation, making the deformation of an interface quite complicated. Thus, the Lagrangian strain measures based on the initial reference configuration are preferable and more convenient for describing the deformation and kinematics of the interface.

Constitutive Relations of Elastic Interface

Let the excess free energy of interface per unit area of A in the current configuration be denoted by γ. This free energy depends not only on the particle coordinates (θ^1, θ^2) but also on the absolute temperature θ and the deformation of the interface, which can be described by the interface strain $\boldsymbol{E}_s^{(m)}$, and the curvature change of the interface. In order to simplify the discussion, the flexural resistance of the interface will not be considered, and the interface deformation process is assumed to be isothermal. Thus, the temperature and the curvature tensor of the interface will not be included in the expression of interfacial energy. Moreover, for the sake of notational simplicity, the dependence of γ on (θ^1, θ^2) will be suppressed in the following. The interface free energy per unit area of A_0 in the reference configuration can be written as $J_2\gamma$, where $J_2 = \det \boldsymbol{U}_s$ is the ratio between the area elements $\mathrm{d}A$ and $\mathrm{d}A_0$, i.e., $\mathrm{d}A = J_2\mathrm{d}A_0$. In the course of an isothermal deformation, the variation in the excess free energy of the interface on the area element $\mathrm{d}A$ can be written as $\delta(\gamma \mathrm{d}A) = \delta(J_2\gamma)\mathrm{d}A_0$, which is the reversible work needed to elastically stretch this pre-existing interface element:

$$\delta\left(J_2\gamma\right)\mathrm{d}A_0 = \left(\boldsymbol{T}_s^{(m)} : \delta\boldsymbol{E}_s^{(m)}\right)\mathrm{d}A_0 \tag{11}$$

where $\boldsymbol{T}_s^{(m)}$ is the interface stress conjugate to $\boldsymbol{E}_s^{(m)}$.

Then, in the sense of Green elastic material, the constitutive relation of the interface at finite deformation is

$$\boldsymbol{T}_s^{(m)} = \frac{\partial\,(J_2\gamma)}{\partial \boldsymbol{E}_s^{(m)}} \tag{12}$$

where the Lagrangian description has been used and $J_2\gamma$ is a potential function of the temperature and the Lagrangian strain of the interface. In particular, the first and second Piola-Kirchhoff interface stresses can be written as

$$\begin{aligned} \boldsymbol{S}_{\mathrm{s}} &= 2\boldsymbol{F}_{\mathrm{s}} \cdot \frac{\partial\,(J_2\gamma)}{\partial \boldsymbol{C}_s}, \\ \boldsymbol{T}_{\mathrm{s}}^{(1)} &= 2\frac{\partial\,(J_2\gamma)}{\partial \boldsymbol{C}_s} \end{aligned} \tag{13}$$

In the Eulerian description, the Cauchy stress of the interface is given by

$$\boldsymbol{\sigma}_{\mathrm{s}} = \frac{1}{J_2}\boldsymbol{F}_{\mathrm{s}} \cdot \boldsymbol{T}_{\mathrm{s}}^{(1)} \cdot \boldsymbol{F}_{\mathrm{s}}{}^{\mathrm{T}} \tag{14}$$

The above expressions are valid for anisotropic interfaces which depend on the crystallographic parameters of the interface. If the interface is isotropic relative to the reference configuration κ_0, the interfacial energy γ can be expressed as a function of the scalar invariants of right stretch tensor $\boldsymbol{U}_s$ (or left stretch tensor $\boldsymbol{V}_s$):

$$\gamma = \gamma\,(J_1, J_2) \tag{15}$$

where $J_1 = \mathrm{tr}\boldsymbol{U}_s = \mathrm{tr}\boldsymbol{V}_s$ and $J_2 = \det \boldsymbol{U}_s = \det \boldsymbol{V}_s$ are the first and second scalar invariants of $\boldsymbol{U}_s$ (or $\boldsymbol{V}_s$), respectively. Noting that

$$\begin{aligned} \frac{\partial J_1}{\partial \boldsymbol{C}_s} &= \frac{1}{2}\boldsymbol{U}_s^{-1}, \\ \frac{\partial J_2}{\partial \boldsymbol{C}_s} &= \frac{1}{2}J_2\boldsymbol{C}_s^{-1} \end{aligned} \tag{16}$$

we may obtain

$$\boldsymbol{T}_{\mathrm{s}}^{(1)} = J_2\left[\frac{\partial\gamma}{\partial J_1}\boldsymbol{U}_{\mathrm{s}}{}^{-1} + \left(J_2\frac{\partial\gamma}{\partial J_2} + \gamma\right)\boldsymbol{C}_{\mathrm{s}}{}^{-1}\right] \tag{17}$$

The engineering and the logarithmic stresses of the interface can be expressed by

$$\boldsymbol{T}_{\mathrm{s}}^{(1/2)} = J_2\left[\frac{\partial\gamma}{\partial J_1}\boldsymbol{i}_0 + \left(J_2\frac{\partial\gamma}{\partial J_2} + \gamma\right)\boldsymbol{U}_{\mathrm{s}}{}^{-1}\right] \tag{18}$$

$$\boldsymbol{T}_{\mathrm{s}}^{(0)} = J_2\left[\frac{\partial\gamma}{\partial J_1}\boldsymbol{U}_{\mathrm{s}} + \left(J_2\frac{\partial\gamma}{\partial J_2} + \gamma\right)\boldsymbol{i}_0\right] \tag{19}$$

The Cauchy stress of the interface is

$$\boldsymbol{\sigma}_s = \frac{\partial\gamma}{\partial J_1}\boldsymbol{V}_{\mathrm{s}} + \left(J_2\frac{\partial\gamma}{\partial J_2} + \gamma\right)\boldsymbol{i} \tag{20}$$

In the case that the current configuration κ and the reference configuration κ_0 coincide, the Cauchy stress of the interface in the reference configuration can be written as $\boldsymbol{\sigma}_s^* = \gamma_0^*\boldsymbol{i}_0$, where $\gamma_0^* = \gamma_0 + \gamma_1 + \gamma_2$ is the residual interface tension. $\gamma_1 = (\partial\gamma/\partial J_1)|_{J_1=2,J_2=1}$ and $\gamma_2 = (\partial\gamma/\partial J_2)|_{J_1=2,J_2=1}$ reflect the nature of solids, and $\gamma_0 = \gamma|_{J_1=2,J_2=1}$ reflects the nature of liquids. γ_0, γ_1, and γ_2 all together represent the intrinsic physical properties of the interface, and they are determined by the adjoining materials and their adhering condition at the interface.

Residual Stress Field Caused by the Interfacial Energy

As shown in the previous section, the residual interface stress is not zero in the reference configuration. Consequently, there exists a self-equilibrium stress field in the body of the materials due to residual interface stress, and the elastic strain energy of the body does not vanish even in the initial state (reference configuration). We will call this elastic field induced by the residual interface stress the "residual" elastic field. The elastic properties of a residually stressed body are fundamentally different from those of an initially stress-free body. The elastic tensors in the constitutive equations can depend explicitly on the residual stress, which are different from their counterparts in the classical theory.

To facilitate the description of the deformation induced by the interfacial energy in heterogeneous solids, one can hypothetically split the solid into homogenous pieces along its interfaces

and let them go back to their stress-free states. The above splitting operation is only a thought process. It cannot be realized in practice because it requires that the microscopic states of surface atoms to be the same as the bulk atoms inside. However, we can introduce a "fictious stress-free configuration" (denoted by κ_*) based on the above thought process and use it to describe and calculate the residual elastic field induced by residual interfacial stress.

Let $\boldsymbol{F}^*$ denote the deformation gradient from κ_* to κ_0 and $\boldsymbol{F}$ the deformation gradient from κ_0 to κ. From the above discussions, it is seen that the elastic stress field in the heterogeneous solid under external loads should depend on the deformation gradient $\boldsymbol{F}\cdot\boldsymbol{F}^*$. Hence the hyperelastic potential of the solid can be expressed as $\psi_0=\psi_0\left(\tilde{\boldsymbol{C}}\right)$, where $\tilde{\boldsymbol{C}}=\left(\boldsymbol{F}\cdot\boldsymbol{F}^*\right)^{\mathrm{T}}\cdot\left(\boldsymbol{F}\cdot\boldsymbol{F}^*\right)$ is the right Cauchy-Green tensor relative to κ_*. Therefore, the first Piola-Kirchhoff stress based on the reference configuration κ_0 is

$$\boldsymbol{S}^0=2\rho_0\boldsymbol{F}\cdot\boldsymbol{F}^*\cdot\frac{\partial\psi_0}{\partial\tilde{\boldsymbol{C}}}\cdot\boldsymbol{F}^{*\mathrm{T}} \tag{21}$$

and the Cauchy stress corresponding to the current configuration κ is

$$\boldsymbol{\sigma}=2\rho\boldsymbol{F}\cdot\boldsymbol{F}^*\cdot\frac{\partial\psi_0}{\partial\tilde{\boldsymbol{C}}}\cdot\boldsymbol{F}^{*\mathrm{T}}\cdot\boldsymbol{F}^{\mathrm{T}} \tag{22}$$

In the above expressions, ρ_0 and ρ denote the mass densities of the solid in the configurations κ_0 and κ, respectively, and conservation of mass yields $\rho_0/\rho=\det\boldsymbol{F}$.

The residual elastic stress field is the solution corresponding to the unloaded state when the current configuration coincides with the reference configuration. By setting $\boldsymbol{F}=\boldsymbol{I}$ in Eq. (22), the residual stress $\boldsymbol{\sigma}^*$ can be expressed as

$$\boldsymbol{\sigma}^*=2\rho_0\boldsymbol{F}^*\cdot\left(\left.\frac{\partial\psi_0}{\partial\tilde{\boldsymbol{C}}}\right|_{\boldsymbol{F}=\boldsymbol{I}}\right)\cdot\boldsymbol{F}^{*\mathrm{T}} \tag{23}$$

where $\boldsymbol{I}$ is the second-order identity tensor in the three-dimensional Euclidean space.

Equilibrium Equation of the Interface

Besides the constitutive relation of the interface, the second fundamental equation of the interface is the equilibrium equation, which describes the equilibrium relationship between the interface stress and the body stress at the interface. It is also called the generalize Young-Laplace equations of solid interface. The mathematical structure of this equation is very similar to that of the equilibrium equation of an elastic thin shell, but they have different physical meanings and application backgrounds. The generalized Young-Laplace equation reflects the effect of interface stress on the heterogeneous materials and is mainly applied to nanostructures. In the classical interface stress theory, this equation is usually used to explain the size effects of nanostructured materials.

In this section, the generalized Young-Laplace equation will be derived by the principle of minimum potential energy, which requires a new energy functional that accounts for the effect of interfacial energy in heterogeneous hyperelastic solids. This energy functional consists of three parts: first, the interfacial energy; second, the strain energy of the elastic body, which considers the residual elastic field induced by residual interface stress; and third, the potential of the external loads. It is written as

$$\begin{aligned}\prod(\boldsymbol{u})=&\int_{A_0}J_2\gamma\left(\boldsymbol{C}_s\right)\mathrm{d}A_0+\int_{v_0}\rho_0\psi_0\left(\tilde{\boldsymbol{C}}\right)\mathrm{d}v_0\\&-\int_{v_0}\rho_0\boldsymbol{f}\cdot\boldsymbol{u}\mathrm{d}v_0-\int_{\partial v_{0T}}\bar{\boldsymbol{t}}_0\cdot\boldsymbol{u}\mathrm{d}S_0\end{aligned} \tag{24}$$

where $\boldsymbol{u}$ is the displacement from the reference configuration to the current configuration, $\boldsymbol{f}$ is the body force per unit mass, and $\bar{\boldsymbol{t}}_0$ is the traction on the boundary. As discussed before, this energy functional does not vanish even in the reference state κ_0 when there is no displacement or external load.

Based on the energy principles in theory of elasticity, we have the following proposition: For any admissible displacement field $\boldsymbol{u}$ that satis-

fies the prescribed $\overline{\boldsymbol{u}}_0$ on the boundary ∂v_{0u}, the energy functional Eq. (24) takes a stationary value when $\boldsymbol{u}$ is a solution of the equilibrium state of the system, which is subjected to a body force $\boldsymbol{f}$ in v_0 and a traction $\overline{\boldsymbol{t}}_0$ on the boundary ∂v_{0T}. Thus, the $\delta\Pi(\boldsymbol{u}) = 0$ gives the governing equations of the system, including the equilibrium equation of the interface.

First, let us derive the variation of the first term (interfacial energy) in Eq. (24) and write the variation of the displacement as $\delta\boldsymbol{u}$:

$$\begin{aligned}\delta\left(J_2\gamma\right) &= \frac{\partial\left(J_2\gamma\right)}{\partial \boldsymbol{C}_s} : \delta\boldsymbol{C}_s \\ &= \frac{1}{2}\boldsymbol{T}_s^{(1)} : \left(\delta\boldsymbol{F}_s{}^{\mathrm{T}} \cdot \boldsymbol{F}_s + \boldsymbol{F}_s{}^{\mathrm{T}} \cdot \delta\boldsymbol{F}_s\right) \\ &= \left(\boldsymbol{F}_s \cdot \boldsymbol{T}_s^{(1)}\right) : \delta\boldsymbol{F}_s \\ &= \boldsymbol{S}_s : \delta\boldsymbol{F}_s \end{aligned} \tag{25}$$

Since the interface deformation gradient $\boldsymbol{F}_s$ is expressed as the sum of an "in-plane term" $\boldsymbol{F}_s^{(in)}$ and an "out-of-plane term" $\boldsymbol{F}_s^{(ou)}$, the first Piola-Kirchhoff interface stress $\boldsymbol{S}_s$ is also a "two-point" tensor in the two-dimensional space and can also be decomposed into the sum of an "in-plane term" $\boldsymbol{S}_s^{(in)} = \boldsymbol{F}_s^{(in)} \cdot \boldsymbol{T}_s^{(1)}$ and an "out-of-plane term" $\boldsymbol{S}_s^{(ou)} = \boldsymbol{F}_s^{(ou)} \cdot \boldsymbol{T}_s^{(1)}$. Then, with Eqs. (2) and (3), we may further get

$$\begin{aligned}&\boldsymbol{S}_s : \delta\boldsymbol{F}_s \\ &\quad= \boldsymbol{S}_s^{(in)} : \delta\boldsymbol{F}_s^{(in)} + \boldsymbol{S}_s^{(ou)} : \delta\boldsymbol{F}_s^{(ou)} \\ &\quad= \left(\delta\boldsymbol{u}_{0s} \cdot \boldsymbol{S}_s^{(in)}\right) \cdot \nabla_{0s} \\ &\qquad+ \left(\delta u_0^n \boldsymbol{A}_3 \cdot \boldsymbol{S}_s^{(ou)}\right) \cdot \nabla_{0s} \\ &\qquad- \delta\boldsymbol{u}_{0s} \cdot \left(\boldsymbol{S}_s^{(in)} \cdot \nabla_{0s} - \boldsymbol{A}_3 \cdot \boldsymbol{S}_s^{(ou)} \cdot \boldsymbol{B}\right) \\ &\qquad- \delta u_0^n \left(\boldsymbol{S}_s^{(in)} : \boldsymbol{B} + \left(\boldsymbol{A}_3 \cdot \boldsymbol{S}_s^{(ou)}\right) \cdot \nabla_{0s}\right). \end{aligned} \tag{26}$$

Now consider a region Ω_0 enclosed by an arbitrary closed smooth curve $\partial\Omega_0$ on the interface A_0 in the reference configuration. By using the Green-Stokes theorem, we have

$$\begin{aligned}&\int_{A_0} \left(\boldsymbol{S}_s : \delta\boldsymbol{F}_s\right) \mathrm{d}A_0 \\ &\quad= \int_{A_0} \delta\boldsymbol{u}_{0s} \cdot \Big[-\boldsymbol{S}_s{}^{(in)} \cdot \nabla_{0s} \\ &\qquad+ \boldsymbol{B} \cdot \left(\boldsymbol{A}_3 \cdot \boldsymbol{S}_s{}^{(ou)}\right)\Big] \mathrm{d}A_0 \\ &\qquad+ \int_{A_0} \delta u_0^n \Big[-\boldsymbol{S}_s{}^{(in)} : \boldsymbol{B} \\ &\qquad- \left(\boldsymbol{A}_3 \cdot \boldsymbol{S}_s{}^{(ou)}\right) \cdot \nabla_{0s}\Big] \mathrm{d}A_0 \\ &\qquad- \int_{\partial\Omega_0} \delta\boldsymbol{u}_{0s} \cdot \left[\!\left[\boldsymbol{S}_s{}^{(in)}\right]\!\right] \cdot \boldsymbol{n}_0 \mathrm{d}l_0 \\ &\qquad- \int_{\partial\Omega_0} \delta u_0^n \left[\!\left[\boldsymbol{A}_3 \cdot \boldsymbol{S}_s{}^{(ou)}\right]\!\right] \cdot \boldsymbol{n}_0 \mathrm{d}l_0 \end{aligned} \tag{27}$$

where $\mathrm{d}l_0$ is the differential element of the arc length on $\partial\Omega_0$, $\boldsymbol{n}_0 = \boldsymbol{l}_0 \times \boldsymbol{A}_3$ is the unit normal vector of the curve $\partial\Omega_0$ with $\boldsymbol{l}_0$ being the unit tangent vector of $\partial\Omega_0$, and $[\![\cdot]\!]$ represents the discontinuities across the curve $\partial\Omega_0$.

Under Eulerian description in the current configuration,

$$\delta\boldsymbol{F}_s = \delta\boldsymbol{a}_\alpha \otimes \boldsymbol{A}^\alpha = \left(\delta\boldsymbol{a}_\alpha \otimes \boldsymbol{a}^\alpha\right) \cdot \boldsymbol{F}_s \tag{28}$$

and the variation of interfacial energy can be expressed in the current configuration as

$$\begin{aligned}&\int_{A_0} \left(\boldsymbol{S}_s : \delta\boldsymbol{F}_s\right) \mathrm{d}A_0 \\ &\quad= \int_{A_0} \boldsymbol{S}_s : \left[\left(\delta\boldsymbol{a}_\alpha \otimes \boldsymbol{a}^\alpha\right) \cdot \boldsymbol{F}_s\right] \mathrm{d}A_0 \\ &\quad= \int_A \frac{1}{J_2}\left(\boldsymbol{S}_s \cdot \boldsymbol{F}_s^T\right) : \left(\delta\boldsymbol{a}_\alpha \otimes \boldsymbol{a}^\alpha\right) \mathrm{d}A \\ &\quad= \int_A \boldsymbol{\sigma}_s : \left(\delta\boldsymbol{u}\nabla_s\right) \mathrm{d}A \end{aligned} \tag{29}$$

Now consider a region Ω enclosed by a closed smooth curve $\partial\Omega$ on the interface A, and again, from the Green-Stokes theorem, we have

$$\int_A \boldsymbol{\sigma}_s : (\delta \boldsymbol{u} \nabla_s)\, \mathrm{d}A = -\int_A [\delta \boldsymbol{u}_s \cdot (\boldsymbol{\sigma}_s \cdot \nabla_s) + \delta u^n (\boldsymbol{\sigma}_s : \boldsymbol{b})]\, \mathrm{d}A - \int_{\partial\Omega} \delta \boldsymbol{u}_s \cdot [\![\boldsymbol{\sigma}_s]\!] \cdot \boldsymbol{n} \mathrm{d}l \tag{30}$$

where $\mathrm{d}l$ is the element of the arc length on $\partial\Omega$, $\boldsymbol{n} = \boldsymbol{l} \times \boldsymbol{a}_3$, with $\boldsymbol{l}$ being the unit tangent vector of $\partial\Omega$.

Next, let us discuss the variation of the strain energy of the elastic body. Considering that

$$\begin{aligned} \delta(\rho_0 \psi_0) &= \boldsymbol{S}^0 : (\delta \boldsymbol{u} \nabla_0) \\ &= (\det \boldsymbol{F})\, \boldsymbol{\sigma} : (\delta \boldsymbol{u} \nabla) \end{aligned} \tag{31}$$

and by the conservation of mass, we have

$$\int_{v_0} \delta(\rho_0 \psi_0)\, \mathrm{d}v_0 = \int_{\partial v_{0T}} \delta \boldsymbol{u} \cdot \left(\boldsymbol{S}^0 \cdot \boldsymbol{N}_0\right) \mathrm{d}S_0 - \int_{A_0} \delta \boldsymbol{u} \cdot [\![\boldsymbol{S}^0]\!] \cdot \boldsymbol{A}_3 \mathrm{d}A_0 - \int_{v_0} \delta \boldsymbol{u} \cdot \left(\boldsymbol{S}^0 \cdot \nabla_0\right) \mathrm{d}v_0 \tag{32}$$

where ∇_0 is the gradient operator in three-dimensional Euclidean space and $\boldsymbol{N}_0$ is the unit normal vector to the boundary in the reference configuration. $[\![\boldsymbol{S}^0]\!]$ represents the discontinuity of the first Piola-Kirchhoff stress across the interface A_0. In Eulerian description, Eq. (32) becomes

$$\begin{aligned} \int_{v_0} \delta(\rho_0 \psi_0)\, \mathrm{d}v_0 &= \int_v \boldsymbol{\sigma} : (\delta \boldsymbol{u} \nabla)\, \mathrm{d}v \\ &= \int_{\partial v_T} \delta \boldsymbol{u} \cdot (\boldsymbol{\sigma} \cdot \boldsymbol{N})\, \mathrm{d}S \\ &\quad - \int_A \delta \boldsymbol{u} \cdot [\![\boldsymbol{\sigma}]\!] \cdot \boldsymbol{a}_3 \mathrm{dA} \\ &\quad - \int_v \delta \boldsymbol{u} \cdot (\boldsymbol{\sigma} \cdot \nabla)\, \mathrm{d}v \end{aligned} \tag{33}$$

Finally, let us discuss the variation of the third and fourth terms (potential of external loads). In reference configuration, it is

$$-\int_{v_0} \rho_0 \boldsymbol{f} \cdot \delta \boldsymbol{u} \mathrm{d}v_0 - \int_{\partial v_{0T}} \bar{\boldsymbol{t}}_0 \cdot \delta \boldsymbol{u} \mathrm{d}S_0 \tag{34}$$

and in current configuration, it is

$$-\int_v \rho \boldsymbol{f} \cdot \delta \boldsymbol{u} \mathrm{d}v - \int_{\partial v_T} \bar{\boldsymbol{t}} \cdot \delta \boldsymbol{u} \mathrm{d}S \tag{35}$$

When the energy functional Eq. (24) takes stationary values, its variation should be zero. Considering the arbitrariness of displacement variation $\delta \boldsymbol{u}$, we obtain the governing equations of the hyperelastic solids with sharp interfaces. In Lagrangian description, they are as follows:

(i) The equilibrium equation of the body and the mechanical boundary condition

$$\begin{aligned} \boldsymbol{S}^0 \cdot \nabla_0 + \rho_0 \boldsymbol{f} = 0 \quad (\text{in } v_0) \\ \boldsymbol{S}^0 \cdot \boldsymbol{N}_0 = \bar{\boldsymbol{t}}_0 \quad (\text{on } \partial v_{0T}) \end{aligned} \tag{36}$$

(ii) The equilibrium equations of the interface

$$\begin{aligned} \boldsymbol{A}_3 \cdot [\![\boldsymbol{S}^0]\!] \cdot \boldsymbol{A}_3 &= -\boldsymbol{S}_s^{(in)} : \boldsymbol{B} \\ &\quad - \left(\boldsymbol{A}_3 \cdot \boldsymbol{S}_s^{(ou)}\right) \cdot \nabla_{0s} \quad (\text{on } A_0) \\ \boldsymbol{P}_0 \cdot [\![\boldsymbol{S}^0]\!] \cdot \boldsymbol{A}_3 &= -\boldsymbol{S}_s^{(in)} \cdot \nabla_{0s} \\ &\quad + \boldsymbol{B} \cdot \left(\boldsymbol{A}_3 \cdot \boldsymbol{S}_s^{(ou)}\right) \quad (\text{on } A_0) \end{aligned} \tag{37}$$

(iii) Continuity condition of interface stress

$$[\![\boldsymbol{S}_s]\!] \cdot \boldsymbol{A}_3 = 0 \quad (\text{across } \partial\Omega_0 \text{ on } A_0) \tag{38}$$

where $\boldsymbol{P}_0 = \boldsymbol{I} - \boldsymbol{A}_3 \otimes \boldsymbol{A}_3$ is the projection operator.

Similarly, the Eulerian description of the governing equation in the current configuration is

$$\begin{aligned} \boldsymbol{\sigma} \cdot \nabla + \rho \boldsymbol{f} = 0 \quad (\text{in } v) \\ \boldsymbol{\sigma} \cdot \boldsymbol{N} = \bar{\boldsymbol{t}} \quad (\text{on } \partial v_T) \end{aligned} \tag{39}$$

$$\begin{aligned} \boldsymbol{a}_3 \cdot [\![\boldsymbol{\sigma}]\!] \cdot \boldsymbol{a}_3 = -\boldsymbol{\sigma}_s : \boldsymbol{b} \quad (\text{on } A) \\ \boldsymbol{P} \cdot [\![\boldsymbol{\sigma}]\!] \cdot \boldsymbol{a}_3 = -\boldsymbol{\sigma}_s \cdot \nabla_s \quad (\text{on } A) \end{aligned} \tag{40}$$

$$[\![\boldsymbol{\sigma}_s]\!] \cdot \boldsymbol{a}_3 = 0 \qquad (\text{across } \partial\Omega \text{ on } A) \qquad (41)$$

Equations (37) and (40) are the equilibrium equations of the interface. Notably, the Lagrangian description is preferable when dealing with large elastic deformation of heterogeneous materials because, for such materials, the shapes of the deformed body and interfaces are generally unknown. Moreover, nanostructured materials are residually stressed at their initial state. Thus, it is advantageous to use the Lagrangian description of the fundamental equations of interface to study the influence of residual interface stress on the overall properties of nanostructures (Huang and Sun 2007; Sun et al. 2004).

The Effect of Curvature-Dependence of Interfacial Energy

In the previous sections, we developed the fundamental equations of the interface through interfacial energy using a standard continuum mechanics method. However, for simplicity in derivations, we don't consider the curvature-dependence of interfacial energy and assume that the interfacial energy is only a function of the strain tensor. The curvature-dependence of interfacial energy captures the intrinsic flexural resistance of solid interfaces and is responsible for the size dependence of surface stress of nanoparticles. In this section, we will give a brief introduction to the interface stress theory based on a curvature-dependence of interfacial energy.

Consider the curvature-dependence of interfacial energy, i.e., $\gamma = \gamma\left(\boldsymbol{E}_s^{(m)}, \boldsymbol{\kappa}\right)$; we have

$$\delta\left(J_2\gamma\right) \mathrm{d}A_0 = \left(\boldsymbol{T}_s^{(m)} : \delta\boldsymbol{E}_s^{(m)} + \boldsymbol{M}_s : \delta\boldsymbol{\kappa}\right) \mathrm{d}A_0, \qquad (42)$$

where $\boldsymbol{T}_s^{(m)}$ is the same as before while $\boldsymbol{M}_s$ is the interface bending moment conjugating to the relative curvature $\boldsymbol{\kappa}$. The interface stress driving force for the in-plane stretching deformation of the interface and the interface bending moment is pertinent to the out-of-plane flexural deformation of the interface. Then, the constitutive relations of the interface are

$$\boldsymbol{T}_s^{(m)} = \frac{\partial\left(J_2\gamma\right)}{\partial\boldsymbol{E}_s^{(m)}}, \quad \boldsymbol{M}_s = \frac{\partial\left(J_2\gamma\right)}{\partial\boldsymbol{\kappa}} \qquad (43)$$

The first and second Piola-Kirchhoff stresses and Cauchy stress of the interface are the same as before. Here, we mainly focus on the difference. The Eulerian bending moment of the interface is defined as

$$\boldsymbol{m}_s = \frac{1}{J_2}\boldsymbol{F}_s \cdot \boldsymbol{M}_s \cdot \boldsymbol{F}_s^{\mathrm{T}} = \boldsymbol{F}_s \cdot \frac{\partial\gamma}{\partial\boldsymbol{\kappa}} \cdot \boldsymbol{F}_s^{\mathrm{T}} \qquad (44)$$

It is noted that the above expressions are valid for anisotropic interfaces as well.

A detailed analysis of the material symmetry of the interface (Steigmann 2001) indicates that the interfacial energy $J_2\gamma$ is generally not an isotropic scalar-valued tensor function relative to the reference configuration. Since the interfacial energy $J_2\gamma$ is a rather complicated function of $\boldsymbol{C}_s$ and $\boldsymbol{\kappa}$, its explicit expression should be determined by the physical properties of the real material interfaces. In order to simplify this problem while still capturing the main physical features of the constitutive relation, it can be assumed that the material interface is hemitropic relative to the reference configuration. Hence, the interfacial energy $J_2\gamma$ can be expressed as a function of the six invariants of the right Cauchy-Green tensor $\boldsymbol{C}_s$ and relative curvature $\boldsymbol{\kappa}$ (Zheng 1993):

$$J_2\gamma\left(\boldsymbol{C}_s, \boldsymbol{\kappa}\right) = J_2\gamma\left(I_1, I_2, I_3, I_4, I_5, I_6\right) \qquad (45)$$

The six scalar invariants are defined as

$$I_1 = \mathrm{tr}\boldsymbol{C}_s, \quad I_2 = \det\boldsymbol{C}_s, \quad I_3 = \mathrm{tr}\boldsymbol{\kappa}, \quad I_4 = \det\boldsymbol{\kappa},$$
$$I_5 = \mathrm{tr}\left(\boldsymbol{C}_s \cdot \boldsymbol{\kappa}\right), \quad I_6 = \mathrm{tr}\left(\boldsymbol{C}_s \cdot \boldsymbol{\kappa} \cdot \boldsymbol{\varepsilon}\right). \qquad (46)$$

where $\boldsymbol{\varepsilon}$ denotes the permutation tensor on the surface A_0. Noting that

$$\begin{aligned}
&\frac{\partial I_1}{\partial \boldsymbol{C}_s} = \boldsymbol{i}_0, \quad \frac{\partial I_2}{\partial \boldsymbol{C}_s} = I_2 \boldsymbol{C}_s{}^{-1}, \\
&\frac{\partial I_3}{\partial \boldsymbol{\kappa}} = \boldsymbol{i}_0, \quad \frac{\partial I_4}{\partial \boldsymbol{\kappa}} = I_4 \boldsymbol{\kappa}^{-1}, \\
&\frac{\partial J_2}{\partial \boldsymbol{C}_s} = \frac{1}{2} J_2 \boldsymbol{C}_s^{-1}, \quad \frac{\partial I_5}{\partial \boldsymbol{C}_s} = \boldsymbol{\kappa}, \\
&\frac{\partial I_5}{\partial \boldsymbol{\kappa}} = \boldsymbol{C}_s, \quad \frac{\partial I_6}{\partial \boldsymbol{C}_s} = \boldsymbol{\varepsilon}^{\mathrm{T}} \cdot \boldsymbol{\kappa} = -\boldsymbol{\varepsilon} \cdot \boldsymbol{\kappa}, \\
&\frac{\partial I_6}{\partial \boldsymbol{\kappa}} = \boldsymbol{C}_s \cdot \boldsymbol{\varepsilon}^{\mathrm{T}} = -\boldsymbol{C}_s \cdot \boldsymbol{\varepsilon}
\end{aligned} \tag{47}$$

we obtain

$$\begin{aligned}
\boldsymbol{T}_s^{(1)} = 2J_2 \Bigg[&\frac{\partial \gamma}{\partial I_1} \boldsymbol{i}_0 + \left(I_2 \frac{\partial \gamma}{\partial I_2} + \frac{\gamma}{2} \right) \boldsymbol{C}_s^{-1} \\
&+ \frac{\partial \gamma}{\partial I_2} \boldsymbol{\kappa} + \frac{1}{2} \frac{\partial \gamma}{I_6} (\boldsymbol{\kappa} \cdot \boldsymbol{\varepsilon} - \boldsymbol{\varepsilon} \cdot \boldsymbol{\kappa}) \Bigg]
\end{aligned} \tag{48}$$

$$\begin{aligned}
\boldsymbol{M}_s = J_2 \Bigg[&\frac{\partial \gamma}{\partial I_3} \boldsymbol{i}_0 + I_4 \frac{\partial \gamma}{\partial I_4} \boldsymbol{\kappa}^{-1} + \frac{\partial \gamma}{\partial I_5} \boldsymbol{C}_s \\
&+ \frac{1}{2} \frac{\partial \gamma}{\partial I_6} (\boldsymbol{\varepsilon} \cdot \boldsymbol{C}_s - \boldsymbol{C}_s \cdot \boldsymbol{\varepsilon}) \Bigg]
\end{aligned} \tag{49}$$

where it should be pointed out that only the symmetric parts of the stress and bending moment are retained because their skew-symmetric parts do not contribute to the incremental interfacial energy presented in Eq. (42).

The Cauchy stress and Eulerian bending moment of the interface are

$$\begin{aligned}
\boldsymbol{\sigma}_s = 2 \Bigg[&\frac{\partial \gamma}{\partial I_1} \boldsymbol{B}_s + \left(I_2 \frac{\partial \gamma}{\partial I_2} + \frac{\gamma}{2} \right) \boldsymbol{i} \\
&- \frac{\partial \gamma}{\partial I_5} \boldsymbol{B}_s \cdot \boldsymbol{b} \cdot \boldsymbol{B}_s \\
&+ \frac{1}{2} \frac{\partial \gamma}{\partial I_6} J_2 (\boldsymbol{\mu} \cdot \boldsymbol{b} \cdot \boldsymbol{B}_s - \boldsymbol{B}_s \cdot \boldsymbol{b} \cdot \boldsymbol{\mu}) \Bigg]
\end{aligned} \tag{50}$$

$$\begin{aligned}
\boldsymbol{m}_s = &\frac{\partial \gamma}{\partial I_3} \boldsymbol{B}_s - I_4 \frac{\partial \gamma}{\partial I_4} \boldsymbol{b}^{-1} + \frac{\partial \gamma}{\partial I_5} \boldsymbol{B}_s^2 \\
&+ \frac{1}{2} \frac{\partial \gamma}{\partial I_6} J_2 (\boldsymbol{\mu} \cdot \boldsymbol{B}_s - \boldsymbol{B}_s \cdot \boldsymbol{\mu})
\end{aligned} \tag{51}$$

where $\boldsymbol{\mu}$ denotes the permutation tensor on the surface A. By using the Cayley-Hamilton theorem, Eq. (49) can be rewritten as

$$\begin{aligned}
\boldsymbol{M}_s = J_2 \Bigg[&\left(\frac{\partial \gamma}{\partial I_3} + I_3 \frac{\partial \gamma}{\partial I_4} \right) \boldsymbol{i}_0 - \frac{\partial \gamma}{\partial I_4} \boldsymbol{\kappa} \\
&+ \frac{\partial \gamma}{\partial I_5} \boldsymbol{C}_s + \frac{1}{2} \frac{\partial \gamma}{\partial I_6} (\boldsymbol{\varepsilon} \cdot \boldsymbol{C}_s - \boldsymbol{C}_s \cdot \boldsymbol{\varepsilon}) \Bigg]
\end{aligned} \tag{52}$$

The constitutive equation above clearly shows that there exists a stretching-bending coupling due to the curvature-dependent nature of the interfacial energy. Even when there is no in-plane stretching deformation, the residual interface stress may still depend on the flexural deformation. Furthermore, there exists an interface bending moment that characterizes the resistance to bending (flexural resistance) of the interface.

Unlike in the classical theory of elastic surfaces and shells, the constitutive equations above include the residual stress and the residual bending moment in the interface. In the reference configuration without any external load, the current and the reference configurations coincide, thus giving us $\boldsymbol{C}_s = \boldsymbol{i}_0 = \boldsymbol{i} = \boldsymbol{B}_s$, $\boldsymbol{B} = -\boldsymbol{\kappa} = \boldsymbol{b}$, and $\boldsymbol{\varepsilon} = \boldsymbol{\mu}$. The scalar invariants reduce to

$$\begin{aligned}
&J_2 = 1, \quad I_1 = 2, \quad I_2 = 1, \quad I_3 = -2H_0, \\
&I_4 = K_0, \quad I_5 = -2H_0, \quad I_6 = 0
\end{aligned} \tag{53}$$

where H_0 and K_0 are the mean and the Gaussian curvatures of the interface A_0, respectively. Hence, the residual interface stress and the residual interface bending moment can be written as

$$\begin{aligned}
\boldsymbol{\sigma}_s^* = &(\gamma_0 + 2\gamma_1 + 2\gamma_2) \boldsymbol{i}_0 - 2\gamma_5 \boldsymbol{B} \\
&+ \gamma_6 (\boldsymbol{\varepsilon} \cdot \boldsymbol{B} - \boldsymbol{B} \cdot \boldsymbol{\varepsilon})
\end{aligned} \tag{54}$$

$$\begin{aligned}
\boldsymbol{m}_s^* &= (\gamma_3 + \gamma_5) \boldsymbol{i}_0 - K_0 \gamma_4 \boldsymbol{B}^{-1} \\
&= (\gamma_3 + \gamma_5 - 2\gamma_4 H_0) \boldsymbol{i}_0 + \gamma_4 \boldsymbol{B}
\end{aligned} \tag{55}$$

where γ_0 is the initial interfacial excess free energy and $\gamma_i = \partial \gamma / \partial I_i$ ($i = 1 \sim 6$) reflect the natures of the solid interfaces. Notably, these two residual terms $\boldsymbol{\sigma}_s{}^*$ and $\boldsymbol{m}_s{}^*$ indicate that the interface has the inclination to stretch and

bend even though it cannot exist independently without the joining bulk materials. Here, the residual interface stress is not homogeneous at the interface because it is dependent on curvature.

To derive the equilibrium equations in this section, one need to replace the interfacial energy in energy functional Eq. (24) with the curvature-dependent interfacial energy $\gamma(\boldsymbol{C}_s, \boldsymbol{\kappa})$. The method is the same as before, but the derivation process is very tedious because of the complexity of the variation of the curvature tensor. For details, the reader may refer to Gao et al. (2014). Here, we only give the main results. When the curvature dependence of interfacial energy is considered, it changes the equilibrium equation of the interface, where the effects of interface bending moment should be considered. The Lagrangian description of the interface equilibrium equation is

$$\begin{aligned}
&\boldsymbol{A}_3 \cdot \left[\!\left[\boldsymbol{S}^0\right]\!\right] \cdot \boldsymbol{A}_3 = -\left(\boldsymbol{S}_s^{(in)} + \boldsymbol{S}_m^{(in)}\right) : \boldsymbol{B} \\
&\quad - \left[\boldsymbol{A}_3 \cdot \left(\boldsymbol{S}_s^{(ou)} + \boldsymbol{S}_m^{(ou)}\right)\right] \cdot \nabla_{0s} \quad (\text{on } A_0) \\
&\boldsymbol{P}_0 \cdot \left[\!\left[\boldsymbol{S}^0\right]\!\right] \cdot \boldsymbol{A}_3 = -\left(\boldsymbol{S}_s^{(in)} + \boldsymbol{S}_m^{(in)}\right) \cdot \nabla_{0s} \\
&\quad + \boldsymbol{B} \cdot \left[\boldsymbol{A}_3 \cdot \left(\boldsymbol{S}_s^{(ou)} + \boldsymbol{S}_m^{(ou)}\right)\right] \quad (\text{on } A_0)
\end{aligned} \tag{56}$$

where $\boldsymbol{S}_m^{(in)}$ and $\boldsymbol{S}_m^{(ou)}$ are the "in-plane" and "out-of-plane" components of the first Piola-Kirchhoff bending moment of the interface. The definition of the first Piola-Kirchhoff stress of the interface, $\boldsymbol{S}_s^{(in)}$ and $\boldsymbol{S}_s^{(ou)}$, remains the same. The expressions of $\boldsymbol{S}_m^{(in)}$ and $\boldsymbol{S}_m^{(ou)}$ are

$$\begin{aligned}
\boldsymbol{S}_m^{(in)} &= (\boldsymbol{a}_3 \nabla_{0s}) \cdot \boldsymbol{M}_s \\
&\quad + \frac{1}{J_2}\left[\mathrm{tr}\left(\boldsymbol{T}_1 \otimes \boldsymbol{D}\right)\boldsymbol{i}_0 - \left(\boldsymbol{T}_1 \otimes \boldsymbol{D}\right)^{\mathrm{T}}\right] \\
&\quad + \frac{(-\boldsymbol{Z} \cdot \boldsymbol{T}_1 + XT_2)}{J_2^3} \boldsymbol{F}_s{}^{(in)} \cdot (I_1 \boldsymbol{i}_0 - \boldsymbol{C}_s) \\
&\quad - \frac{T_2}{J_2}\left[\mathrm{tr}\left(\boldsymbol{F}_s^{(in)}\right)\boldsymbol{i}_0 - \left(\boldsymbol{F}_s^{(in)}\right)^{\mathrm{T}}\right],
\end{aligned} \tag{57}$$

$$\begin{aligned}
\boldsymbol{S}_m^{(ou)} &= \left(\boldsymbol{a}_3 \tilde{\nabla}_{0s} - \boldsymbol{a}_3 \nabla_{0s}\right) \cdot \boldsymbol{M}_s + \frac{1}{J_2}\left(\boldsymbol{A}_3 \otimes \boldsymbol{T}_1\right) \cdot \\
&\quad \left[\mathrm{tr}\left(\boldsymbol{F}_s{}^{(in)}\right)\boldsymbol{i}_0 - \left(\boldsymbol{F}_s{}^{(in)}\right)^{\mathrm{T}}\right] \\
&\quad + \frac{(-\boldsymbol{Z} \cdot \boldsymbol{T}_1 + XT_2)}{J_2^3} \boldsymbol{F}_s{}^{(ou)} \cdot (I_1 \boldsymbol{i}_0 - \boldsymbol{C}_s)
\end{aligned} \tag{58}$$

where

$$\begin{aligned}
\boldsymbol{a}_3 &= \frac{1}{J_2}\left(X\boldsymbol{A}_3 - \boldsymbol{Z}\right), \\
X &= \det \boldsymbol{F}_s^{(in)}, \\
\boldsymbol{Z} &= \boldsymbol{\varepsilon}^{\mathrm{T}} \cdot \boldsymbol{F}_s{}^{(in)} \cdot \boldsymbol{\varepsilon} \cdot \boldsymbol{D}
\end{aligned} \tag{59}$$

and

$$\begin{aligned}
\boldsymbol{T}_1 &= \boldsymbol{M}_s^{(in)} \cdot \nabla_{0s} - \boldsymbol{A}_3 \cdot \boldsymbol{M}_s^{(ou)} \cdot \boldsymbol{B}, \\
T_2 &= \boldsymbol{M}_s^{(in)} : \boldsymbol{B} + \left(\boldsymbol{A}_3 \cdot \boldsymbol{M}_s^{(ou)}\right) \cdot \nabla_{0s},
\end{aligned} \tag{60}$$

The Eulerian description of the equilibrium equations of the interface is much simpler, and it is

$$\begin{aligned}
&\boldsymbol{a}_3 \cdot [\![\boldsymbol{\sigma}]\!] \cdot \boldsymbol{a}_3 = -\left(\boldsymbol{\sigma}_s - \boldsymbol{b} \cdot \boldsymbol{m}_s\right) : \boldsymbol{b} \\
&\quad - \left(\boldsymbol{m}_s \cdot \nabla_s\right) \cdot \nabla_s \quad (\text{on } A) \\
&\boldsymbol{P} \cdot [\![\boldsymbol{\sigma}]\!] \cdot \boldsymbol{a}_3 = -\left(\boldsymbol{\sigma}_s - \boldsymbol{b} \cdot \boldsymbol{m}_s\right) \cdot \nabla_s \\
&\quad + \boldsymbol{b} \cdot \left(\boldsymbol{m}_s \cdot \nabla_s\right) \quad (\text{on } A)
\end{aligned} \tag{61}$$

It is interesting to note that Eq. (61) can also be written in a compact form:

$$[\![\boldsymbol{\sigma}]\!] \cdot \boldsymbol{a}_3 = -\boldsymbol{\Sigma}_s \cdot \tilde{\nabla}_s \tag{62}$$

where $\boldsymbol{\Sigma}_s = \boldsymbol{\sigma}_s - \boldsymbol{b} \cdot \boldsymbol{m}_s + \boldsymbol{a}_3 \otimes \left(\boldsymbol{m}_s \cdot \nabla_s\right)$ is a combination of the interface stress and interface bending moment.

Stress and Energy of Isotropic Interface Under Small Deformation Condition

Under small deformation, the equilibrium equation of the interface does not change, but the con-

S

stitutive relations of the interface can be greatly simplified, and they can be used to study the linear elastic properties of interface. The Green strain of the interface can be written as

$$\boldsymbol{E}_s = \boldsymbol{\varepsilon}_s + \boldsymbol{G}_s \tag{63}$$

where $\boldsymbol{\varepsilon}_s$ is the commonly used small-deformation strain

$$\begin{aligned}\boldsymbol{\varepsilon}_s &= \frac{1}{2}\left(\boldsymbol{u}\nabla_{0s} + \nabla_{0s}\boldsymbol{u}\right) \\ &= \frac{1}{2}\left(\boldsymbol{u}_{0s}\nabla_{0s} + \nabla_{0s}\boldsymbol{u}_{0s}\right) - u_0^n\boldsymbol{B}\end{aligned} \tag{64}$$

and $\boldsymbol{G}_s$ is the nonlinear (quadratic) part

$$\begin{aligned}&\boldsymbol{G}_s = \tfrac{1}{2}\left[\left(\nabla_{0s}\boldsymbol{u}\right)\cdot\left(\boldsymbol{u}\nabla_{0s}\right) + \boldsymbol{D}\otimes\boldsymbol{D}\right], \\ &\boldsymbol{D} = \boldsymbol{u}_{0s}\cdot\boldsymbol{B} + u_0^n\nabla_{0s}\end{aligned} \tag{65}$$

To start with, let us assume that the interface energy per unit area in the current configuration can be written as the following power series:

$$\begin{aligned}\gamma = {} & \gamma_0 + \gamma_1\left(J_1 - 2\right) + \gamma_2\left(J_2 - 1\right) \\ & + \frac{1}{2}\gamma_{11}(J_1 - 2)^2 + \gamma_{12}\left(J_1 - 2\right)\left(J_2 - 1\right) \\ & + \frac{1}{2}\gamma_{22}(J_2 - 1)^2 + \ldots\end{aligned} \tag{66}$$

where $\gamma_i = \left(\partial\gamma/\partial J_i\right)_{J_1=2,J_2=1}$ and $\gamma_{ij} = \left(\partial^2\gamma/\partial J_i\partial J_j\right)_{J_1=2,J_2=1}$. Under small deformation condition, the scalar invariants can be expressed as follows in terms of interface strain:

$$\begin{aligned}J_1 &= 2 + \mathrm{tr}\boldsymbol{E}_s + \det\boldsymbol{E}_s - \frac{1}{2}(\mathrm{tr}\boldsymbol{E}_s)^2, \\ J_2 &= 1 + \mathrm{tr}\boldsymbol{E}_s + 2\det\boldsymbol{E}_s - \frac{1}{2}(\mathrm{tr}\boldsymbol{E}_s)^2,\end{aligned} \tag{67}$$

Substitute Eqs. (66) and (67) into Eqs. (17) and (20), and leave out the high-order terms; one may get the linearized stress-strain relation for the second Piola-Kirchhoff stress and the Cauchy stress:

$$\begin{aligned}\boldsymbol{T}_s^{(1)} = {} & \gamma_0^*\boldsymbol{i}_0 + \left(\gamma_0^* + \gamma_1^*\right)\left(\mathrm{tr}\boldsymbol{\varepsilon}_s\right)\boldsymbol{i}_0 \\ & + \left(\gamma_1 - 2\gamma_0^*\right)\boldsymbol{\varepsilon}_s\end{aligned} \tag{68}$$

$$\boldsymbol{\sigma}_s = \gamma_0^*\boldsymbol{i} + \gamma_1^*\left(\mathrm{tr}\boldsymbol{\varepsilon}_s\right)\boldsymbol{i} + \gamma_1\boldsymbol{\varepsilon}_s \tag{69}$$

And the first Piola-Kirchhoff stress of the interface is

$$\begin{aligned}\boldsymbol{S}_s = {} & \gamma_0^*\boldsymbol{i}_0 + \left(\gamma_0^* + \gamma_1^*\right)\left(\mathrm{tr}\boldsymbol{\varepsilon}_s\right)\boldsymbol{i}_0 - \gamma_0^*\left(\nabla_{0s}\boldsymbol{u}\right) \\ & + \gamma_1\boldsymbol{\varepsilon}_s + \gamma_0^*\boldsymbol{F}_s^{(ou)}\end{aligned} \tag{70}$$

In the above expressions, $\gamma_0^* = \gamma_0 + \gamma_1 + \gamma_2$, and $\gamma_1^* = \gamma_1 + 2\gamma_2 + \gamma_{11} + 2\gamma_{12} + \gamma_{22}$. It is important to note that the above three kinds of interface stresses are different even under the small deformation condition. These three interface stresses become the same only when the residual interface stress γ_0^* vanishes. However, the influence of the residual interface stress γ_0^* may be quite important in the study of the effective properties of heterogeneous media with interface stress effects.

Through the integral of interface stress with their corresponding deformation measure, the interfacial energy formula in the reference configuration at small deformation can be obtained (Gao and Fang 2015):

$$\begin{aligned}J_2\gamma = {} & \int\boldsymbol{S}_s : \mathrm{d}\left(\tilde{\nabla}_s\boldsymbol{u}\right) = \gamma_0 + \sigma_0\left(J_2 - 1\right) \\ & + \frac{1}{2}\left(\lambda_s + 2\mu_s\right)\left(\mathrm{tr}\boldsymbol{\varepsilon}_s\right)^2 - 2\mu_s\det\boldsymbol{\varepsilon}_s\end{aligned} \tag{71}$$

where $(\sigma_0, \lambda_s, \mu_s)$ are the commonly used symbols of interface constants in the literature. They have the following relations with the previously defined interface constants: residual interface stress $\sigma_0 = \gamma_0^*$ and interface Lame constants, $\lambda_s = \gamma_1^*$ and $\mu_s = \frac{1}{2}\gamma_1$.

For curvature-dependent interfacial energy, one can still develop the related linear constitutive relation. For solid membrane, the following formula can be used to capture the intrinsic flexural stiffness of the interface:

$$\gamma^{cur} = \gamma\left(\boldsymbol{\kappa}\right) = \frac{1}{2}k_c(2H) = \frac{1}{2}k_c\left(\frac{-I_1I_3 + I_5}{I_2}\right)^2 \tag{72}$$

where H is the mean curvature of the interface and it can be expressed in terms of the scalar invariants in Eq. (46). With Eqs. (71) and (72), a linearized version of the interface stress theory based on the curvature-dependent interfacial energy can be developed. For details, the readers may refer to Gao et al. (2017).

Summary

The interfacial energy theory of solids is the study of the deformation and equilibrium of interface of elastic solids. In this entry, the fundamental equations of interface, including the constitutive relations and the equilibrium equations, are introduced, as well as the related methodologies to build them. When the characteristic length of materials and structures reduces to nanoscale, the surface-to-volume ratio is high, and the effect of interfacial energy (or surface energy) becomes significantly. The interface stress theory can be used to study the effect of interface stress on the effective properties of nanostructures (Altenbach and Eremeyev 2019; Altenbach et al. 2013a; Altenbach et al. 2013b) and nanocomposites (Duan et al. 2005a, b; Mogilevskaya et al. 2008; Sharma and Ganti 2004; Sharma et al. 2003; Sharma and Wheeler 2006). For some specific problems that are related to wrinkling, bending deformation, or large curvature change of the interfaces, one may need to consider the curvature dependence of the interfacial energy because it captures the intrinsic flexural rigidity of the interface (Chhapadia et al. 2011; Mohammadi and Sharma 2012; Zemlyanova and Walton 2012; Zemlyanova and Mogilevskaya 2018a, b).

Cross-References

- Micromechanics
- Nanomechanics of Stress Relaxation in Composite Low-Dimensional Structures
- Size Effect in Nanomaterials
- Surface Energy and Its Effects on Nanomaterials

References

Altenbach H, Eremeyev VA (2019) On nonlinear dynamic theory of thin plates with surface stresses. In: Altenbach H, Irschik H, Matveenko VP (eds) Contributions to advanced dynamics and continuum mechanics. Springer International Publishing, Cham, pp 19–26

Altenbach H, Eremeyev VA, Lebedev LP (2013a) Mathematical study of boundary-value problems of linear elasticity with surface stresses. In: Altenbach H, Morozov NF (eds) Surface effects in solid mechanics: models, simulations and applications. Springer, Berlin/Heidelberg, pp 1–19

Altenbach H, Eremeyev VA, Morozov NF (2013b) On the influence of residual surface stresses on the properties of structures at the nanoscale. In: Altenbach H, Morozov NF (eds) Surface effects in solid mechanics: models, simulations and applications. Springer, Berlin/Heidelberg, pp 21–32

Cahn JW (2013) Thermodynamics of solid and fluid surfaces. In: The selected works of John W. Cahn. Wiley, Hoboken, pp 379–399

Cammarata RC (1994) Surface and interface stress effects in thin films. Prog Surf Sci 46:1–38

Chhapadia P, Mohammadi P, Sharma P (2011) Curvature-dependent surface energy and implications for nanostructures. J Mech Phys Solids 59:2103–2115

Duan HL, Wang J, Huang ZP, Karihaloo BL (2005a) Eshelby formalism for nano-inhomogeneities. Proc R Soc Lond A 461:3335–3353

Duan HL, Wang J, Huang ZP, Karihaloo BL (2005b) Size-dependent effective elastic constants of solids containing nano-inhomogeneities with interface stress. J Mech Phys Solids 53:1574–1596

Gao X, Fang D (2015) Elastic energy of surfaces and residually stressed solids: an energy approach for the mechanics of nanostructures. J Appl Mech 82:011010–011019

Gao X, Huang Z, Qu J, Fang D (2014) A curvature-dependent interfacial energy-based interface stress theory and its applications to nano-structured materials: (I) general theory. J Mech Phys Solids 66:59–77

Gao X, Huang Z, Fang D (2017) Curvature-dependent interfacial energy and its effects on the elastic properties of nanomaterials. Int J Solids Struct 113–114:100–107

Gibbs, J.W., Bumstead, H.A., Van Name, R.G., 1906. Scientific papers of J. Willard Gibbs. Longmans, Green. London

Gurtin ME, Weissmüller J, Larché F (1998) A general theory of curved deformable interfaces in solids at equilibrium. Philos Mag A 78:1093–1109

Herring C (1953) The use of classical macroscopic concepts in surface energy problems. In: Structure and properties of solid surfaces. The University of Chicago Press, Chicago, p 5

Herring C (1999) Surface tension as a motivation for sintering. In: Fundamental contributions to the continuum

theory of evolving phase interfaces in solids. Springer, Berlin/Heidelberg, pp 33–69
Huang ZP, Sun L (2007) Size-dependent effective properties of a heterogeneous material with interface energy effect: from finite deformation theory to infinitesimal strain analysis. Acta Mech 190:151–163
Huang Z, Wang J (2013) Micromechanics of nanocomposites with interface energy effect. In: Handbook of micromechanics and nanomechanics. Pan Stanford Publishing
Langhaar HL (1974) Elastic surfaces and theories of shells. Acta Mech 19:109–128
Mogilevskaya SG, Crouch SL, Stolarski HK (2008) Multiple interacting circular nano-inhomogeneities with surface/interface effects. J Mech Phys Solids 56:2298–2327
Mohammadi P, Sharma P (2012) Atomistic elucidation of the effect of surface roughness on curvature-dependent surface energy, surface stress, and elasticity. Appl Phys Lett 100:133110
Orowan E (1970) Surface energy and surface tension in solids and liquids. Proc R Soc Lond A 316:473–491
Povstenko YZ (1993) Theoretical investigation of phenomena caused by heterogeneous surface tension in solids. J Mech Phys Solids 41:1499–1514
Seth, B.R., 1961. Generalized strain measure with applications to physical problems
Sharma P, Ganti S (2004) Size-dependent Eshelby's tensor for embedded nano-inclusions incorporating surface/interface energies. J Appl Mech 71:663–671
Sharma P, Wheeler LT (2006) Size-dependent elastic state of ellipsoidal nano-inclusions incorporating surface/interface tension. J Appl Mech 74:447–454
Sharma P, Ganti S, Bhate N (2003) Effect of surfaces on the size-dependent elastic state of nano-inhomogeneities. Appl Phys Lett 82:535–537
Shuttleworth R (1950) The surface tension of solids. Proc R Soc Lond A 63:444–457
Steigmann DJ (2001) Elements of the theory of elastic surfaces. In: Ogden RW, Fu YB (eds) Nonlinear elasticity: theory and applications. Cambridge University Press, Cambridge, pp 268–304
Steigmann DJ, Ogden RW (1999) Elastic surface – substrate interactions. Proc R Soc Lond A 455:437–474
Streitz FH, Cammarata RC, Sieradzki K (1994a) Surface-stress effects on elastic properties. I. Thin metal films. Phys Rev B 49:10699–10706
Streitz FH, Cammarata RC, Sieradzki K (1994b) Surface-stress effects on elastic properties. II. Metallic multilayers. Phys Rev B 49:10707–10716
Sun L, Wu Y, Huang Z, Wang J (2004) Interface effect on the effective bulk modulus of a particle-reinforced composite. Acta Mech Sinica 20:676–679
Zemlyanova AY, Mogilevskaya SG (2018a) Circular inhomogeneity with Steigmann–Ogden interface: local fields, neutrality, and Maxwell's type approximation formula. Int J Solids Struct 135:85–98
Zemlyanova AY, Mogilevskaya SG (2018b) On spherical inhomogeneity with Steigmann–Ogden interface. J Appl Mech 85:121009–121010
Zemlyanova A, Walton J (2012) Modeling of a curvilinear planar crack with a curvature-dependent surface tension. SIAM J Appl Math 72:1474–1492
Zheng Qs (1993) Two-dimensional tensor function representation for all kinds of material symmetry. Proc R Soc Lond A 443:127–138

Surfaces of Strong Discontinuity in One-Dimensional Nonlinearly Elastic Media

▸ Shock Waves Via Ray Expansions

Symmetric Hyperbolicity

▸ System of Symmetric Hyperbolic Equations, Extended Thermodynamics of Gases

System of Symmetric Hyperbolic Equations, Extended Thermodynamics of Gases

Ingo Müller
Technical University Berlin, Berlin, Germany

Synonyms

Entropy principle; Growth and decay of acceleration waves; Lagrange multipliers; Light scattering; Shock structures; Symmetric hyperbolicity

Definition

An ideal gas – simple as it may seem – has a considerable internal structure which is revealed by the moment equations of the kinetic theory

of gases. The internal structure makes itself felt in processes with steep gradients and rapid rates of change such as wave propagation and light scattering.

Extended thermodynamics writes all field equations as quasilinear first-order differential equations, and the entropy principle reduces those to symmetric hyperbolic equations which imply favorable physical and mathematical properties.

Introduction

Extended thermodynamics is an improved version of thermodynamics of irreversible processes which is based on equations of balance for all thermodynamic fields and on the entropy principle. The latter guarantees that the field equations of extended thermodynamics are symmetric hyperbolic if written in the proper variables, namely, the Lagrange multipliers needed for the exploitation of the entropy principle.

The moments of the kinetic theory of gases provide an instructive paradigm of extended thermodynamics. And the synthesis of the two theories permits a deep insight into the properties of gases such as • wave speeds, • shock structures, • light scattering, and • inertial effects.

Detailed reports on extended thermodynamics may be found in the book (Müller and Ruggeri 1998) by Müller and Ruggeri, in the review article (Müller and Weiss 2012) by Müller and Weiss, and in the dissertation (Reitebuch 2005) by Reitebuch.

Formal Structure of Extended Thermodynamics

Field Equations, Equilibrium, and Entropy Principle

The objective of extended thermodynamics is the determination of v fields $F_\alpha(x_i, t)(\alpha = 0, 1, 2, \ldots v\text{-}1)$ which are densities of v additive quantities. Thus they obey equations of balance of the form

$$\frac{\partial F_\alpha}{\partial t} + \frac{\partial F_{i\alpha}}{\partial x_i} = i_\alpha + \Pi_\alpha \quad (\alpha = 0, 1, 2, \ldots v\text{-}1). \tag{1}$$

$F_{i\alpha}$ are the components of their fluxes and Π_α are their production densities. Both are constitutive quantities , i.e., they depend on the material of the body under consideration. i_α represents inertial effects; its form will be made specific later for gases. Effects of gravitation and electromagnetism are ignored here.

In extended thermodynamics, the constitutive relations are local and instantaneous so that $F_{i\alpha}$ and Π_α at one point and time depend on the densities F_α at that point and time only

$$F_{i\alpha} = \hat{F}_{i\alpha}(F_\beta) \quad \text{and} \quad \Pi_\alpha = \hat{\Pi}_\alpha(F_\beta). \tag{2}$$

In particular, no gradients or rates of change occur among the independent variables.

Invariably the first five of the equations of balance are the conservation laws of mass, momentum, and energy for which the productions Π_α vanish. Equilibrium is defined as a process for which all other productions $\Pi_\alpha(\alpha = 5, 6, \ldots v\text{-}1)$ vanish as well.

If the constitutive functions $\hat{F}_{i\alpha}$ and $\hat{\Pi}_\alpha$ are known explicitly, one may eliminate $F_{i\alpha}$ and Π_α between (1) and (2) and arrive at an explicit set of field equations. Every solution of those is called a *thermodynamic process*.

In reality, however, the constitutive functions are unknown, and we must attempt to determine them, or at least to restrict their generality, and, perhaps, to reduce them to a few coefficients which may then be measured. This is the task of the constitutive theory whose most important tool is the entropy principle stated here in two parts:

(i) the entropy inequality

$$\frac{\partial h}{\partial t} + \frac{\partial h_i}{\partial x_i} = \sigma \geq 0 \tag{3}$$

must hold for all thermodynamic processes. h is the entropy density, h_i is the entropy flux, and σ is the density of the entropy production; all three are constitutive quantities, so that in extended thermodynamics,

they depend on the fields in a local and instantaneous manner, i.e.,

$$h = \hat{h}(F_\beta), \quad h_i = \hat{h}_i(F_\beta), \quad \sigma = \hat{\sigma}(F_\beta) \quad . \tag{4}$$

(ii) the entropy density is required to be a concave function of F_α, i.e.,

$$\frac{\partial^2 h}{\partial F_\alpha \partial F_\beta} - \text{negative definite.} \tag{5}$$

This property allows the entropy to reach a maximum in equilibrium.

Exploitation of the Entropy Principle: Symmetric Hyperbolic Systems

The key to the exploitation of the entropy inequality (1) is the observation that the inequality must hold for all thermodynamic processes, i.e., solutions of the field equations. Thus in a manner of speaking, the field equations provide constraints on the fields for which the inequality must hold. Lagrange multipliers may serve to get rid of such constraints. Indeed, by Liu (1972a, b), the new inequality

$$\frac{\partial h}{\partial t} + \frac{\partial h_i}{\partial x_i} - \Lambda_\alpha \left(\frac{\partial F_\alpha}{\partial t} + \frac{\partial F_{i\alpha}}{\partial x_i} - \Pi_\alpha \right) \geq 0 \tag{6}$$

must hold for all fields $F_\alpha(x_i, t)$. (Inertial terms are ignored in the exploitation of the entropy inequality.) The quantities Λ_α – the Lagrange multipliers – are themselves constitutive quantities so that, in extended thermodynamics, they may be functions of all densities F_β.

Insertion of the constitutive relations for h, h_i, and $F_{i\alpha}$ provides

$$\left(\frac{\partial h}{\partial F_\alpha} - \Lambda_\alpha \right) \frac{\partial F_\alpha}{\partial t} + \left(\frac{\partial h_i}{\partial F_\beta} - \Lambda_\alpha \frac{\partial F_{i\alpha}}{\partial F_\beta} \right) \frac{\partial F_\beta}{\partial x_i} + \Lambda_\alpha \Pi_\alpha \geq 0. \tag{7}$$

The left-hand side of this inequality is thus linear in the derivatives of the densities, and, since the inequality must hold for all fields, it must hold in particular for arbitrary values of the derivatives $\frac{\partial F_\alpha}{\partial t}$ and $\frac{\partial F_\alpha}{\partial x_i}$ at one point and time. Hence follows

$$dh = \Lambda_\alpha dF_\alpha, \quad dh_i = \Lambda_\alpha dF_{i\alpha}, \quad \text{and} \quad \sigma = \Lambda_\alpha \Pi_\alpha \geq 0 \tag{8}$$

lest the inequality be violated.

These are the results of the entropy inequality, and all of them contain the Lagrange multipliers which are auxiliary quantities. Even the entropic quantities h and h_i are auxiliary quantities in a manner of speaking because, after all, the constitutive theory has set out to find restrictions on the constitutive functions in (2), and h and h_i are supposed to help in that effort. Really useful results for our purpose should not contain the auxiliary quantities. But still, let us continue, because there will be some definite results without a specific characterization of the densities and without the knowledge of the Lagrange multipliers.

By $(8)_1$ differentiation of $\frac{\partial h}{\partial F_\alpha} = \Lambda_\alpha$ with respect to F_β shows that $\frac{\partial \Lambda_\alpha}{\partial F_\beta}$ is negative definite because of the required concavity of the entropy density. Therefore the Lagrange multipliers Λ_α form a set of fields which is equivalent to the densities F_α. If we introduce the scalar potential $h' = \Lambda_\alpha F_\alpha - h$ as the Legendre transform of h associated with the map $F_\alpha \Leftrightarrow \Lambda_\alpha$, and the vector potential $h'_i = \Lambda_\alpha F_{i\alpha} - h_i$, we obtain from (8)

$$dh' = F_\alpha d\Lambda_\alpha, \quad dh'_i = F_{i\alpha} d\Lambda_\alpha, \quad \text{and} \quad \sigma = \Lambda_\alpha \Pi_\alpha \geq 0 \text{ as before.} \tag{9}$$

Thus the densities and fluxes are seen to be derivatives of the potentials with respect to Λ_α. Note that h' is concave in the Lagrange multipliers since h is concave in the densities, because a Legendre transformation does not affect the concavity.

By (9), we may rewrite the system of field equations for F_α as a system of field equations for Λ_α, viz.,

$$\frac{\partial^2 h'}{\partial \Lambda_\alpha \partial \Lambda_\beta} \frac{\partial \Lambda_\beta}{\partial t} + \frac{\partial^2 h'_i}{\partial \Lambda_\alpha \partial \Lambda_\beta} \frac{\partial \Lambda_\beta}{\partial x_i} = \Pi_\alpha. \tag{10}$$

The advantage of this form lies in the observation that the system – with symmetric coefficient matrices and a negative definite coefficient matrix

of $\frac{\partial \Lambda_\beta}{\partial t}$ – is a symmetric hyperbolic system. We conclude that the entropy principle guarantees the symmetric hyperbolic character of extended thermodynamics for the Lagrange multipliers as fields.

Therefore Boillat (1974) has called the Λ_α's *privileged fields.* It is true that Boillat in 1974 did not know about the Lagrange multipliers. However, he found the privileged fields and later Ruggeri and Strumia (1981) identified those fields with the Lagrange multipliers of extended thermodynamics. Thus the mathematical theory of symmetric hyperbolic systems was joined to thermodynamics and vice versa.

The fields Λ_α are called *privileged,* because symmetric hyperbolic systems have convenient and desirable properties, namely, the well-posedness of initial value problems, i.e., existence and uniqueness of solutions, and continuous dependence of solutions on the data, e.g., see Godunov (1961) and Fisher and Marsden (1972). Also symmetric hyperbolic systems imply finite speeds.

The ingredients of the formal structure of extended thermodynamics are not only mathematically desirable, they also please the physicist. The attractive features include • field equations of balance type, • local and instantaneous constitutive equations, • existence of a nonequilibrium entropy density, • general constitutive entropy flux, • thermodynamic stability, • well-posedness of initial value problems, and • finite speeds.

If we wish that thermodynamics eventually should represent an integral part of mathematical physics, the foregoing analysis represents a large step forward: *the entropy principle has led to symmetric hyperbolic field equations*. We are tempted to postulate that all valid thermodynamic field theories ought to be of that type.

It remains to exploit the residual inequality $(9)_3$ for the entropy production σ, which is assumed nonnegative and is obviously minimal, namely, zero, in equilibrium, where all productions Π_α vanish. We may write (Normally the summation over the repeated index α is understood. But here we write the sum explicitly so as to indicate that it extends over $\alpha = 5, 6 \ldots$v-1 rather than over all α from 0 to v-1.)

$$\sigma = \sum_{\alpha=5}^{v-1} \Lambda_\alpha \Pi_\alpha, \tag{11}$$

since $\Pi_\alpha (\alpha = 0, 1, \ldots 4)$ are always zero, equilibrium or not. Thus of necessity we have

$$\left.\frac{\partial \sigma}{\partial \Pi_\alpha}\right|_E = \Lambda_\alpha|_E = 0 \quad (\alpha = 5, 6, \ldots v\text{-}1). \tag{12}$$

We conclude that the Lagrange multipliers $\Lambda_\alpha (\alpha = 5, 6, \ldots v\text{-}1)$ vanish in equilibrium. And if the productions Π_α are approximated as linear functions of $\Lambda_\alpha (\alpha = 5, 6, \ldots v\text{-}1)$, we may write

$$\Pi_\alpha = \sum_{\beta=5}^{v-1} L_{\alpha\beta} \Lambda_\beta (\alpha = 5, 6, \ldots v - 1). \tag{13}$$

Obviously, the matrix $L_{\alpha\beta}$ $(\alpha, \beta = 5, 6, \ldots v\text{-}1)$ must be positive definite, because of the inequality (8), but it is not necessarily symmetric. It *is* symmetric in extended thermodynamics of moments, described in the next section; see Müller and Weiss (2012).

Wave Speeds: Growth and Decay of Acceleration Waves

A wave is defined as a propagating surface, and mathematically it is represented by the equation $\phi(x_i, t) = 0$. Its normal n_i and normal speed V are given by

$$n_i = \frac{\frac{\partial \phi}{\partial x_i}}{|grad \phi|} \quad \text{and} \quad V = -\frac{\frac{\partial \phi}{\partial t}}{|grad \phi|}.$$

Here we are interested in weak waves, also called acceleration waves, surfaces across which the fields F_α or Λ_α are continuous although their gradients are not. Obviously the jump of the gradient of Λ_α must then point in the normal direction which we take to be the 1-direction. Therefore we have

$$\left[\frac{\partial \Lambda_\alpha}{\partial x_1}\right] = A_\alpha \quad \text{and} \quad \left[\frac{\partial \Lambda_\alpha}{\partial t}\right] = -V A_\alpha; \tag{14}$$

square brackets indicate differences between the two sides of the wave. Thus from the field Eq. (10), we obtain a linear homogeneous algebraic system for the A_α's, viz.,

$$\left(\frac{\partial^2 h_1'}{\partial\Lambda_\alpha\partial\Lambda_\beta} - \frac{\partial^2 h'}{\partial\Lambda_\alpha\partial\Lambda_\beta}V\right)A_\alpha = 0. \qquad (15)$$

It follows that the jumps of the gradients are proportional to the right eigenvalue d_α of the matrix in (15). We may thus write $A_\alpha = Ad_\alpha$ and call A the amplitude of the wave. Therefore the possible speeds – called characteristic speeds – are the roots of a v'th order homogeneous algebraic system, i.e., they result from setting the determinant of the system equal to zero:

$$\det\left(\frac{\partial^2 h_1'}{\partial\Lambda_\alpha\partial\Lambda_\beta} - \frac{\partial^2 h'}{\partial\Lambda_\alpha\partial\Lambda_\beta}V\right) = 0. \qquad (16)$$

There are v such speeds; in other words, we have v sounds. But of course, we cannot calculate any of them before knowing h and h_1' as functions of Λ_α. We only know that the V's following from (16) are real and finite; we know that from the symmetric hyperbolic character of the field equations.

The amplitude may decay, or it may grow depending on its initial value and on the size of the productions Π_α, which represent dissipation, and on the nonlinearity, i.e., the dependence of V on the fields. In the case of propagation into an undisturbed state of equilibrium, the governing equation for the rate of change of the amplitude A is a Bernoulli equation

$$\frac{\delta A}{\delta t} \underbrace{-\frac{\partial V}{\partial F_\beta}d_\beta}_{\alpha} A^2 \underbrace{-l_\alpha\frac{\partial \Pi_\alpha}{\partial F_\gamma}d_\gamma}_{\beta} A = 0 \qquad (17)$$

non linearity dissipation

with the solution

$$A(t) = \frac{A(0)\exp[-\beta t]}{1 - A(0)\frac{\alpha}{\beta}(\exp[-\beta t] - 1)}.$$

d_α and l_α are the right and left eigenvectors of the matrix in (15).

The first person to calculate the rate of change of the amplitude of an acceleration wave was Green (1964). The elegant form of the Bernoulli equation in (17) is due to Boillat (1965), the discoverer of the main field.

The nonlinearity in (17) occurs, if the wave velocity depends on the values of the fields F_α, as it does for a breaking water wave. Inspection of (17) shows that without the nonlinearity, i.e., for $\alpha = 0$, the amplitudes decay exponentially. On the other hand, if we have $\alpha \neq 0$ and if β is sufficiently small and the amplitude $A(0)$ is sufficiently large, there may be a blowup. Indeed at time

$$t_{cr} = \frac{1}{\beta}\ln\frac{1}{1 + \frac{\beta}{\alpha}\frac{1}{A(0)}} \qquad (18)$$

the amplitude of the acceleration wave becomes infinite and that means that the velocity has a jump; we may say that the acceleration wave has developed into a shock wave. We see from (18) that this can only happen for $|A(0)| > \frac{\beta}{\alpha}$, meaning that the initial amplitude is too big to be damped out in the course of time.

Extended Thermodynamics of Moments

Reminder of the Kinetic Theory of Gases

The kinetic theory of monatomic gases fits perfectly into the formal structure of extended thermodynamics described in section "Formal Structure of Extended Thermodynamics". And the results obtained in that section allow us to determine the form of the distribution function of atoms in a gas. In order to appreciate the analogies between the two theories, the reader should be familiar with the kinetic theory. If he is not, the following brief survey may serve.

The basic field to be determined by the kinetic theory is the distribution function $f(x_i, c_i, t)$, defined such that $f(x_i, c_i, t)d\bar{c}$ is the number density of atoms of mass μ at position x_i and time t with velocities between c_i and $c_i + dc_i$. The dis-

tribution function is governed by the Boltzmann equation

$$\frac{\partial f}{\partial t} + c_i \frac{\partial f}{\partial x_i} + i_i^c \frac{\partial f}{\partial c_i} = \int \left(f' f'^1 - f f^1 \right)' r V = \sin\Theta d\Theta d\varepsilon d\bar{c}^1, \quad (19)$$

where i_i^c is the inertial acceleration of an atom with velocity c_i. Thus

$$i_i^c = \underbrace{2W_{ik}(c_k - \dot{b}_k)}_{\text{Coriolis}} - \underbrace{W_{ik}^2(x_k - b_k)}_{\text{centrifugal}} + \underbrace{\dot{W}_{ik}(x_k - b_k)}_{\text{Euler}} + \underbrace{\ddot{b}_i}_{\text{translation}} . \quad (20)$$

W_{ik} is the matrix of angular velocity of the frame with respect to an inertial frame, and b_i is the distance vector between the origins of the two frames. The right-hand side of the Boltzmann equation represents the effect of collisions between atoms, and f, f', f^1, f'^1 are the values of the distribution function for the velocities $c_i, c_i', c_i^1, c_i'^1$ of two atoms before and after colliding. V is the relative speed of the colliding atoms, and r is the cross section for a collision with the parameters ε and Θ. (The form of the collision term on the right-hand side of the Boltzmann equation is universally known as the Stoßzahlansatz. The German word has defied translation and is therefore routinely used in English-language texts as well. For its derivation and interpretation, the reader may consult any book on the kinetic theory, e.g., Waldmann (1958) or Chapman and Cowling (1936/1961).)

Moments of the distribution function are defined as

$$F_{i_1 i_2 \ldots i_p} = \int \mu c_{i_1} c_{i_2} \ldots c_{i_p} f d\bar{c}; \quad (21)$$

they are symmetric tensors of rank p. In particular we have

$$F_0 = \rho - \text{ mass density and}$$
$$F_i = \rho v_i - \text{momentum density.} \quad (22)$$

By use of the velocity v_i of the gas, we may form the relative – or peculiar – velocity $C_i = c_i - v_i$ of an atom and thus define the internal moments

$$\rho_{i_1 i_2 \ldots i_p} = \int \mu C_{i_1} C_{i_2} \ldots C_{i_p} f d\bar{c}. \quad (23)$$

The first few moments F and ρ have a canonical notation and are named suggestively

$$\begin{aligned} F_{ij} &- \text{momentum flux} & -\rho_{ij} &= t_{ij} - \text{stress tensor} \\ \frac{1}{2}F_{ii} &= \rho e - \text{energy density} & \frac{1}{2}\rho_{ii} &= \rho\varepsilon - \text{internal energy density} \\ \frac{1}{2}F_{iij} &= J_j - \text{energy flux} & \frac{1}{2}\rho_{iij} &= q_j - \text{heat flux.} \end{aligned} \quad (24)$$

The specific internal energy may be replaced by the temperature because we have $\varepsilon = \frac{3}{2}\frac{k}{\mu}T$ in a monatomic gas. k is the Boltzmann constant. The internal energy ε and the pressure p are related by $\varepsilon = \frac{3}{2}\frac{p}{\rho}$. In general, i.e., for any tensorial rank, there is a one-to-one relation between the moments and the internal moments of the form

$$F_{i_1 i_2 \ldots i_p} = \sum_s^N \binom{N}{s} \rho_{(i_1 \ldots i_{N-s}} v_{i_{N-(s-1)}} \ldots v_{i_N)}. \quad (25)$$

The Boltzmann equation implies equations of balance for the moments, viz., (Round brackets enclosing indices denote symmetrization. Angular brackets will denote symmetrization and tracelessness.)

S

$$\frac{\partial F_{i_1 i_2 \ldots i_p}}{\partial t} + \frac{\partial F_{n i_1 i_2 \ldots i_p}}{\partial x_n} = \underbrace{p F_{(i_1 i_2 \ldots i_{p-1}} i^v_{i_p)} + p F_{n(i_1 i_2 \ldots i_{p-1}} 2W_{i_p)n}}_{\text{inertial} \quad \text{contribution}} + \Pi_{i_1 i_2 \ldots i_p}, \tag{26}$$

where i^v_i is given by (20) if c_k in that equation is replaced by the velocity v_k of the gas. $\Pi_{i_1 i_2 \ldots i_p}$ is the moment of the collision operator on the right-hand side of the Boltzmann equation

$$\Pi_{i_1 i_2 \ldots i_p} = \frac{1}{4} \int (c_{i_1} \ldots c_{i_p} + c^1_{i_1} \ldots c^1_{i_p} - c'_{i_1} \ldots c'_{i_p} - c'^1_{i_1} \ldots c'^1_{i_p})(f' f'^1 - f f^1) r V \sin\Theta d\Theta d\varepsilon dc^1 dc. \tag{27}$$

The Boltzmann equation also implies an inequality of the form

$$\frac{\partial h}{\partial t} + \frac{\partial h_i}{\partial x_i} = \underbrace{\frac{k}{4} \int \ln \frac{f' f'^1}{f f^1} (f' f'^1 - f f^1) r V \sin\Theta d\Theta d\varepsilon d\bar{c}^1 d\bar{c}}_{\text{entropy production density due to collisions}} \geq 0, \tag{28}$$

where

$$h = -k \int \left(\ln \frac{f}{y} - 1 \right) f d\bar{c} \quad \text{and}$$
$$h_i = -k \int c_i \left(\ln \frac{f}{y} - 1 \right) f d\bar{c}; \tag{29}$$

these are the kinetic theory definitions of the entropy density and the entropy flux. y is the smallest element $d\bar{x}d\bar{c}$ that can accommodate an atom, and it is related to the Planck constant, but we need not go into that here.

Analogies Between Extended Thermodynamics and Kinetic Theory

The analogy between the equations of balance (1) of extended thermodynamics and the moment equation (26) of the kinetic theory is now evident. It becomes even more evident when we introduce the multi-index $\alpha = i_1 i_2 \ldots i_p$ in (21) so that the moments read

$$F_\alpha = \mu \int c_\alpha f d\bar{c}, \text{ where } c_\alpha = 1 \text{ for } \alpha = 0 \text{ and } c_\alpha = \begin{pmatrix} c_{i_1} \\ c_{i_1} c_{i_2} \\ \bullet \\ \bullet \\ c_{i_1} c_{i_2} \ldots c_{i_N} \end{pmatrix} \text{ for } \alpha = 1, 2, \ldots \upsilon\text{-}1. \tag{30}$$

If we consider moments up to tensorial rank N, α runs from 0 to $\frac{1}{6}(N+1)(N+2)(N+3)$. Actually (26) represents a subclass of (1), because here the density F_α in one equation is equal to the flux in the previous equation. Thus only the "last fluxes" $F_{i i_1 i_2 \ldots i_N}$ and all production densities $\Pi_{i_1 i_2 \ldots i_p}$, except Π_0, Π_i, Π_{ii}, need to be considered as constitutive quantities. The five productions Π_0, Π_i, Π_{ii} vanish because of conservation of mass, momentum, and energy in an atomic collision; see (27).

Also evident is the analogy of the postulated entropy inequality (3) and the inequality (28) with (29) derived from the Boltzmann equation.

Obviously in the kinetic theory the densities, fluxes, and productions are all related to a single function, the distribution function $f(x_i, c_i, t)$ which is absent in extended thermodynamics. Given the observed analogies, we shall now proceed to show that the results of extended thermodynamics may serve to calculate $f(x_i, c_i, t)$ and thus determine the constitutive properties of a gas.

The Distribution Function and the Constitutive Relations for a Gas

We refer to $(9)_{1,2}$ and (30) and write

$$\begin{aligned} dh' = F_\alpha d\Lambda_\alpha &= \mu \int f d(\Lambda_\alpha c_\alpha) d\bar{c} \\ &= \mu \int dG(\Lambda_\alpha c_\alpha) d\bar{c} \\ &= d\left(\mu \int G(\Lambda_\alpha c_\alpha) d\bar{c}\right) \end{aligned}$$

$$\begin{aligned} dh'_i = F_{i_\alpha} d\Lambda_\alpha &= \mu \int c_i f d(\Lambda_\alpha c_\alpha) d\bar{c} \\ &= \mu \int c_i dG(\Lambda_\alpha c_\alpha) d\bar{c} \\ &= d\left(\mu \int c_i G(\Lambda_\alpha c_\alpha) d\bar{c}\right). \end{aligned} \tag{31}$$

Therefore $f(x_i, c_i, t)$ depends on the single variable $\chi = \Lambda_\alpha c_\alpha$ and so does G, the generator function of f; by $(31)_3$ we have $f = \frac{dG}{d\chi}$ and the potentials h' and h'_i thus read

$$h' = \mu \int G(\chi) d\bar{c} \quad \text{and} \quad h'_i = \mu \int c_i G(\chi) d\bar{c}. \tag{32}$$

Therefore the symmetric hyperbolic system (10) for a gas comes out as

$$\left(\mu \int c_\alpha c_\beta \frac{df}{d\chi} d\bar{c}\right) \frac{\partial \Lambda_\alpha}{\partial t} + \left(\mu \int c_i c_\alpha c_\beta \frac{df}{d\chi} d\bar{c}\right) \frac{\partial \Lambda_\alpha}{\partial x_i} = \Pi_\alpha. \tag{33}$$

From (32) we obtain for the entropy and its flux

$$h = \Lambda_\alpha F_\alpha - h' = \mu \int \left(\chi \frac{dG}{d\chi} - G\right) d\bar{c} \quad \text{and} \quad h_i = \Lambda_\alpha F_{i_\alpha} - h'_i = \mu \int c_i \left(\chi \frac{dG}{d\chi} - G\right) d\bar{c}, \tag{34}$$

so that, by comparison of (34) with (29), we have $\chi \frac{dG}{d\chi} - G = -\frac{\mu}{k}\left(\ln \frac{f}{y} - 1\right) f$ and hence, by differentiation with respect to χ

$$f = y \exp\left[-\frac{\Lambda_\alpha c_\alpha}{k/\mu}\right] \text{ and } f' = -\frac{1}{k/\mu} f. \tag{35}$$

The distribution function $f(x_i, c_i, t)$ has thus been identified in terms of the Lagrange multipliers $\Lambda_\alpha(x_i, c_i, t)$.

The constitutive relations follow as

$$F_{i\alpha} = \mu y \int c_i c_\alpha \exp\left[-\frac{\Lambda_\alpha c_\alpha}{k/\mu}\right] d\bar{c} \text{ for } \frac{1}{6}(N+1)(N+2)(N+3) < \alpha \leq \frac{1}{6}(N+2)(N+3)(N+4)$$

$$\Pi_\alpha = \frac{1}{4}\mu y^2 \int (c_\alpha + c^1_\alpha - c'_\alpha - c'^1_\alpha) \times \left(\exp\left[-\frac{\Lambda_\beta (c'_\beta + c'^1_\beta)}{k/\mu}\right] - \exp\left[-\frac{\Lambda_\beta (c_\beta + c^1_\beta)}{k/\mu}\right]\right) r V \sin\Theta d\Theta d\varepsilon d\bar{c}^1 d\bar{c} \tag{36}$$

So far, so good. However, there is a catch, because the independent variables here are the Lagrange multipliers Λ_α and not the densities F_α. It is true that, in principle, we may calculate the Λ_α's from the F_α's by (21), i.e.,

$$F_\alpha = \mu y \int c_\alpha \exp\left[-\frac{\Lambda_\alpha c_\alpha}{k/\mu}\right] d\bar{c} \text{ for}$$
$$\alpha \leq \frac{1}{6}(N+1)(N+2)(N+3) \tag{37}$$

by inversion. Unfortunately the inversion cannot be done analytically, or only in an approximate manner, except in equilibrium.

In *equilibrium* where all Λ_α's except $\Lambda_0, \Lambda_i, \Lambda_{ii}$ vanish, we can solve (37) and obtain

$$\Lambda_0|_E = -\frac{g|_E}{T} + \frac{v^2}{2T},$$
$$\Lambda_j\big|_E = -\frac{v_j}{T}, \text{ and}$$
$$\Lambda_{ii}|_E = \frac{3}{2T}, \tag{38}$$

where $g|_E = \varepsilon + \frac{p}{\rho} - T\frac{h|_E}{\rho}$ is the specific Gibbs free energy, often called chemical potential of the gas. Thus the equilibrium distribution function is given by

$$f|_E = y \exp\left[\frac{g|_E - \frac{1}{2}(c_i - v_i)^2}{k/\mu T}\right]$$
$$= \frac{\rho}{\mu}\frac{1}{\sqrt{2\pi\frac{k}{\mu}T}^3}\exp\left[-\frac{\frac{1}{2}(c_i - v_i)^2}{k/\mu T}\right]. \tag{39}$$

In *nonequilibrium* we may expand $f = y\exp[-\frac{\Lambda_\alpha c_\alpha}{k/\mu}]$ in (35) and break off after first order terms in the Λ's. Thus for $N = 3$ and $v = 20$, – the 20-moment theory – we obtain

$$f_{20} \approx f|_E\,(1 + (\Lambda_0 - \Lambda_0|_E)$$
$$+ (\Lambda_i - \Lambda_i|_E)c_i + \frac{1}{3}(\Lambda_{ii} - \Lambda_{ii}|_E)c^2$$
$$+ \Lambda_{<ij>}c_i c_j + \Lambda_{ijk}c_i c_j c_k), \tag{40}$$

and this allows us to determine the Λ's in terms of the F's. All that is needed in this case is the solution of integrals of the form $\int_{-\infty}^{\infty} x^n \exp x^2 dx$. We obtain after some calculation

$$f_{20} = f|_E\left(1 - \frac{1}{2}\frac{1}{\rho\left(\frac{k}{\mu}T\right)^2}\rho_{<ij>}C_iC_j - \frac{1}{2}\frac{1}{\rho\left(\frac{k}{\mu}T\right)^2}\rho_{ijj}C_i\left(1 - \frac{1}{5}\frac{C^2}{\frac{k}{\mu}T}\right) - \frac{1}{6}\frac{1}{\rho\left(\frac{k}{\mu}T\right)^3}\rho_{<ijk>}C_iC_jC_k\right) \tag{41}$$

Extended Thermodynamics of 20 Moments: Subsystems

The equations of balance for the first 20 moments $F_0 = \rho$, $F_i = \rho v_i$, F_{ij}, F_{ijk} may be written as

$$\frac{\partial\rho}{\partial t} + \frac{\partial\rho v_i}{\partial x_i} = 0$$
$$\frac{\partial\rho v_i}{\partial t} + \frac{\partial F_{in}}{\partial x_n} - \rho i_i^v - 2\rho v_k W_{ik} = 0$$
$$\frac{\partial F_{ij}}{\partial t} + \frac{\partial F_{ijn}}{\partial x_n} - 2\rho v_{(i}i_{j)}^v - 4F_{n(i}W_{j)n} = \Pi_{ij}$$
$$\frac{\partial F_{ijk}}{\partial t} + \frac{\partial F_{ijkn}}{\partial x_n} - 3F_{(ij}i_{k)}^v$$
$$- 6F_{n(ij}W_{k)n} = \Pi_{ijk}. \tag{42}$$

The system is closed by insertion of

$$\Pi_{ij} = -\frac{1}{\tau}\rho_{<ij>}$$
$$\Pi_{ijk} = -\frac{1}{\tau}\left(\frac{3}{2}\rho_{ijk} - \frac{1}{6}(\rho_{lli}\delta_{jk} + \rho_{llj}\delta_{ik} + \rho_{llk}\delta_{ij})\right.$$
$$+ v_i\rho_{<jk>} + v_j\rho_{<ik>}$$
$$\left.+ v_k\rho_{<ij>}\right), \tag{43}$$

which result from (27) for a particularly simple atomic interaction. (Atoms with a hypothetical repulsive power potential that falls off with an inverse fourth power. It is thought that such an

interaction, while not perfect, is not bad for rarefied monatomic gases.) Also for closure we set, according to (41)

$$\rho_{ijkl} = 6\frac{k}{\mu}T\rho_{(ij}\delta_{kl)} - 3\rho\left(\frac{k}{\mu}T\right)^2\delta_{(ij}\delta_{kl)}, \quad (44)$$

which, by (25), determines F_{ijkl} in $(42)_4$ in terms of ρ and ρ_{ij}.

Note that all equations, bar $(42)_1$ the mass balance, have inertial terms, not only the balance equations of momentum and energy. It is such terms by which the kinetic theory of gases contradicts the principle of material frame indifference; they lead to a frame dependence of the laws of Fourier and Navier-Stokes (see Müller 1972).

In order to appreciate the nature of the field equations for $N = 3$ better, we shall write them in linearized form, linearized about a homogeneous and constant state of rest – and without the inertial contributions. Figure 1 exhibits them in a panel, where they are repeated four times: upper left, upper right, lower left, and lower right. Also we have introduced the conventional notation: ρ for mass density, v_i for velocity, T for temperature, $t_{<ij>}$ for deviatoric stress, and q_i for heat flux. The traceless third-rank moment $\rho_{<ijk>}$ has no conventional name. We emphasize that the 20 equations are fully explicit, except for the single unknown parameter τ which we shall identify shortly.

The purpose of the panel with four parts lies in the black frames which differ between the parts. Those frames illustrate the nature of the extension in extended thermodynamics, and they exhibit the nature of conventional approximations like the theories of Fourier and Navier-Stokes.

Upper left: The frame embraces the Euler equations. These represent the conservation laws of mass, momentum, and energy in a gas free of dissipation; there is no irreversibility and ρ, v_i, and T are the only fields.

Upper right: The equations within the frame represent the Navier-Stokes-Fourier equations. The deviatoric stress is proportional to the deviatoric part of the velocity gradient, and the factor of proportionality, containing τ, is the viscosity; since the viscosity can be measured, τ is known. The heat flux is proportional to the gradient of temperature.

Lower right: The frame encloses Grad's 13-moment equations, a subcase of $N = 3$; see Grad (1949). They represent the prototypical equations of extended thermodynamics. Comparison of Grad's equations with the Navier-Stokes-Fourier equations shows that the latter ones ignore the rates of change and the gradients of $t_{<ij>}$ and q_i. Since rates of change are measured in terms of mean times of free flight and gradients in terms of mean free paths, we conclude that the Navier-Stokes-Fourier equations represent the behavior of dense gases in slow processes, while extended thermodynamics describes the gases in rapid processes and in rarefied gases.

Lower left: The frames enclose the equations of the Cattaneo theory, the earliest – and incomplete – version of extended thermodynamics; see Cattaneo (1948). It was invented in an ad hoc manner so as to resolve the *paradox of heat conduction*, by which disturbances in temperature propagate at an infinite speed. There is no such paradox according to Grad's equations, nor in any theory of extended thermodynamics, since it is based on symmetric hyperbolic equations.

The 20 equations of Fig. 1 are only here for illustration. It is possible to calculate the explicit full set of balance equations for moments for any N, and this has been done, although the result is too long to print out. So, in a manner of speaking, the full set for $N = 40$ (say) – where there are 12,341 equations – is only known to the computer. However, the computer can work with them; thus it can work out the speeds of propagation of acceleration waves implied by the system for any finite N.

Results

Characteristic Speeds

It follows from Eq. (16) that the characteristic wave speeds may be calculated as eigenvalues of a matrix. And, by (33) and (35), that equation reads

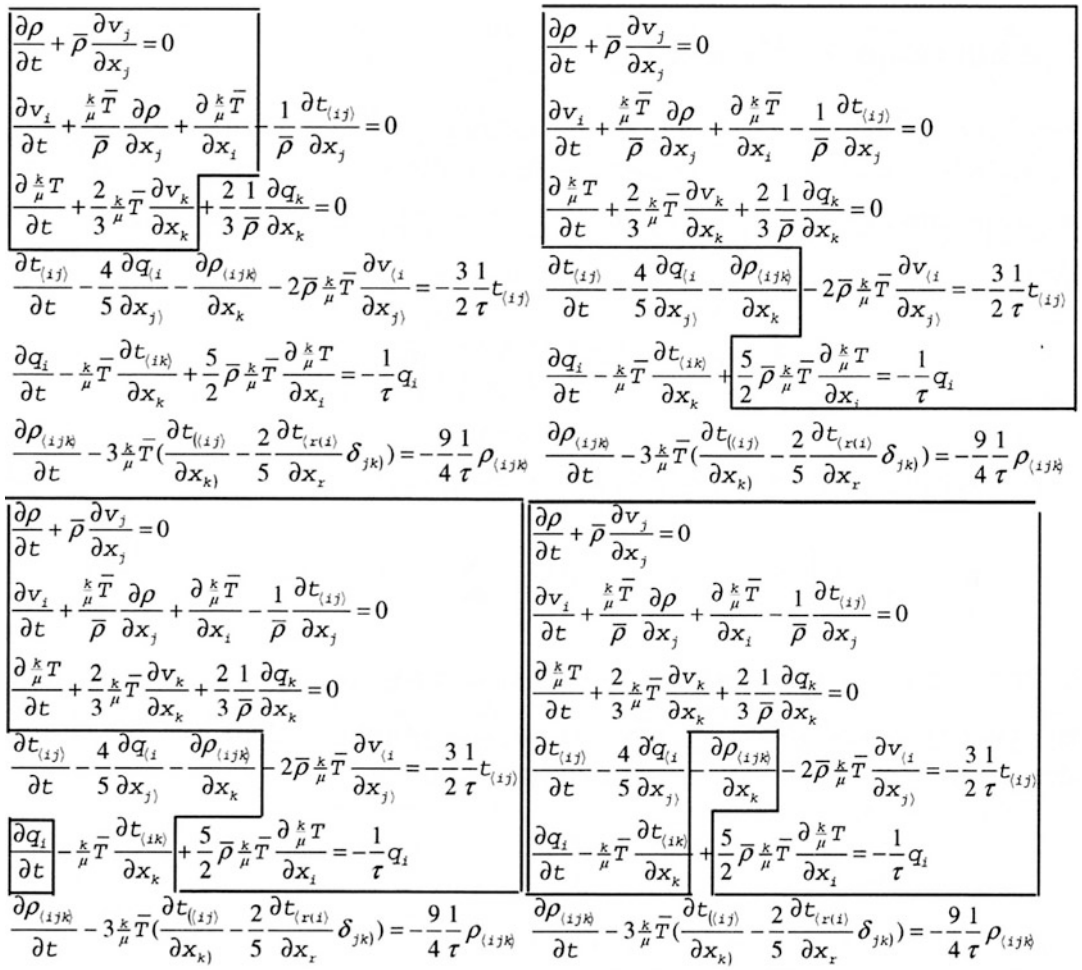

Fig. 1 The 20 equations of balance for $N = 3$. Upper left: Euler equations. Upper right: Navier-Stokes-Fourier equations. Lower left: Cattaneo equations. Lower right: Grad 13-moment equations

$$\det\left(\int c_i c_\alpha c_\beta f d\bar{c} - V\int c_\alpha c_\beta f d\bar{c}\right) = 0 \quad (45)$$

for a monatomic gas. If the wave propagates into a region of undisturbed equilibrium, the distribution function may be replaced by its equilibrium value (39) so that the integrals in (45) may be calculated explicitly. The matrix is a $v \times v$-matrix so that there are v speeds of propagation.

Naturally we are interested in the fastest one, which we shall call the pulse speed; see Fig. 2. The necessary calculations – though mathematically trivial – are cumbersome, and therefore they are best performed on the computer. We conclude from Fig. 2 that the pulse speeds are finite for all finite values of N – or v – and that they grow in value for growing N. Boillat and Ruggeri found a lower bound by which $\frac{V_{\max}}{\sqrt{\frac{5}{3}\frac{k}{\mu}T}} \geq \sqrt{\frac{6}{5}(N-\frac{1}{2})}$.

The obvious question is, of course, whether all these many sound speeds are ever seen or heard. The answer is obviously negative, and the reason for this lies in the fact that the waves are strongly damped before they reach our ears.

Shock Waves

Concerning the remark, made in above, about the formation of shocks from acceleration waves,

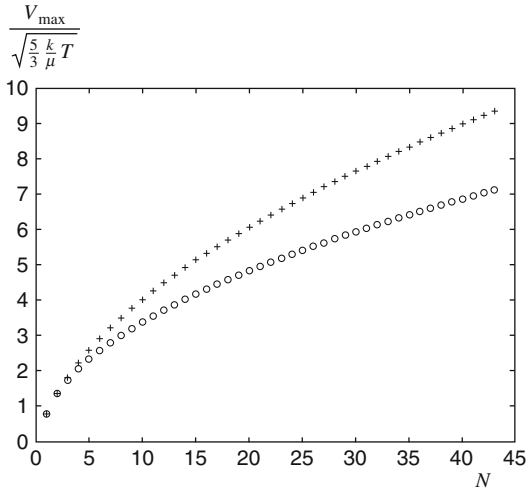

N	v	$\frac{V_{\max}}{\sqrt{\frac{5}{3}\frac{k}{\mu}T}}$
3	20	1.808
10	286	4.018
20	1771	6.080
30	5456	7.663
40	12341	8.996

Fig. 2 Pulse speeds referred to the normal sound speed. Crosses and table: Weiss (1990). Circles: Lower bound by Boillat and Ruggeri (1997)

there is a basic observation to be made. Indeed, shocks do not exist in nature as experiments have clearly shown: The microstructural nature of a gas prevents shocks. What does exist – and what may appear as a shock – is a *shock structure,* a smooth but steep transition between two relatively flat states of a gas; to be sure, the thickness of the shock structure is of the order of magnitude of a few mean free paths, but still it is smooth. Therefore, if a theory predicts a shock, or allows for a shock, it is not a valid theory, and it has to be improved. Extended thermodynamics shows how this has to be done because improvement of the classical theories is its *raison d'être*. Let us consider this:

First of all, the Navier-Stokes-Fourier theory does not allow for shocks. This would seem to recommend it as a good theory in view of the forgoing remarks. However, the shock structure which the theory permits us to calculate is wrong; see Fig. 3. (M_0 is the ratio of the speed of the fluid into the shock structure and the ordinary speed of sound.) Grad knew this when he first derived the 13-moment theory. He tried that theory out on shock structures, hoping, perhaps, to do better than Navier-Stokes-Fourier.

Unfortunately, however, his calculation came out worse – much worse! See Grad (1952). It is true that for $M_0 = 1.5$ Grad did calculate a smooth shock structure – see Fig. 4 – but for that low Mach number, there was only a minimal discrepancy anyhow between observation and the Navier-Stokes-Fourier theory according to Fig. 3. So that effort was not decisive. Therefore Grad proceeded with $M_0 = 2$ and he had a surprise: A subshock appeared (see Fig. 4_{right}), and certainly that was worse than the discrepancy of Fig. 3. Going up in Mach numbers, one can show that the subshock is first seen slightly above $M_0 = 1.65$ and then it grows in size. Grad did not appreciate the significance of this Mach number, or, at least, he does not comment on it. The significance is that $M_0 = 1.65$ is the pulse speed according to the 13-moment theory, and, if the gas rushes forward with more than that speed, its downstream region cannot move aside in time, and a shock must form or – in this case – a subshock. In a manner of speaking, it is for M_0>1.65 that we must speak of a truly supersonic flow in a 13-moment theory.

The recipe for avoiding this subshock is simple: We must abandon the 13-moment theory and adopt an extended theory with more equations and, therefore, a larger pulse speed: see the table of Fig 2. So, if we adopt a 286-moment theory, the appearance of the subshock is pushed upward to $M_0 = 4.018$, and if we adopt a 12,341-moment theory, the appearance of the subshock is

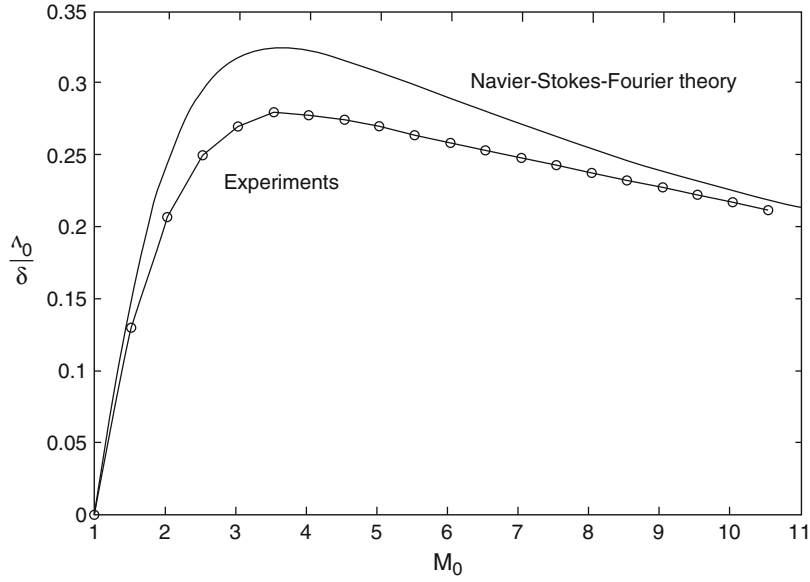

Fig. 3 Thickness δ of a shock structure according to the Navier-Stokes-Fourier theory as a function of the Mach number $M_0$of the structure. Λ_0 is the mean free path of the gas before the structure

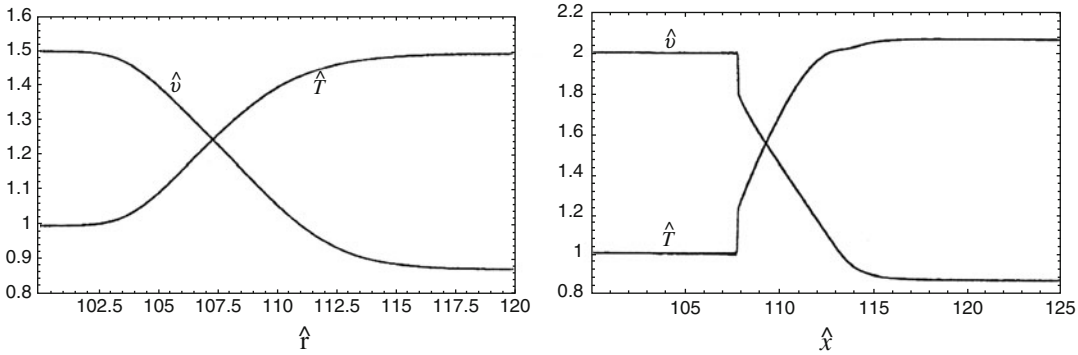

Fig. 4 Shock structures for Grad's 13-moment theory at $M_0 = 1.5$ (left) and at $M_0 = 2$ (right). The subshock of Fig. 4 right begins to develop at $M_0 = 1.65$, the pulse speed of the 13-moment theory

pushed to $M_0 = 8.996$. Eventually, if we prefer to have no subshock to appear, we need to go to a ∞-moment theory, because its pulse speed is infinite.

Light Scattering

The knowledge of the atomic microstructure of a gas makes all the above phenomena plausible, and there is no doubt that they exist: ■ *the frame dependence of stress and heat flux*, ■ *the multiple speeds*, ■ *the pulse speed*, and ■ *the shift of subshocks to high Mach numbers*. Yet, our experimental tools – thermal and caloric measurements – are too rough to detect such phenomena and to quantify them. More sensitive probes into the microstructure are needed. The measurement of light scattering spectra is such a probe.

Indeed, light scattering is a paradigm for the usefulness and practicality of extended thermodynamics. Let us consider this: Incoming laser light, i.e. light of a single frequency ω_i– most often green light with the wave length $\lambda_i \approx 0.4 \times 10^{-6}$ m – is scattered on the density fluctuations of a gas in equilibrium; see Fig. 5 top. While

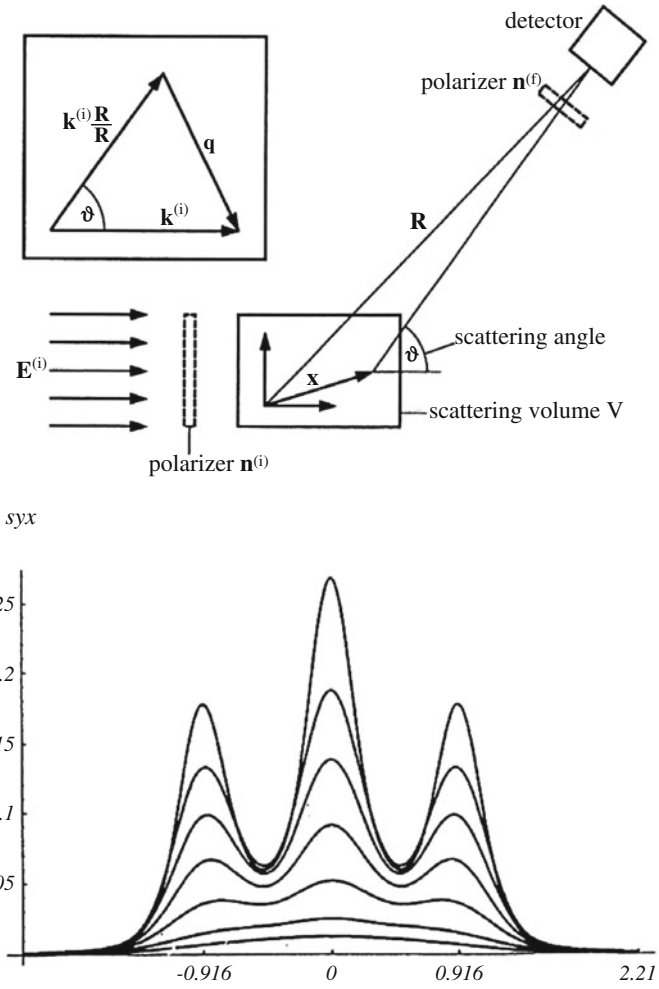

Fig. 5 Light scattering and scattering spectrum. Top: schematic experimental setup, Bottom: experimental curves for different pressures (see text)

most of the scattered light has the same frequency as the incoming light, the scattering spectrum also contains neighboring frequencies. For dense gases – typically a gas under the pressure of 4 bar or higher – the spectrum has three well-defined peaks, like the uppermost curve in Fig. 5 bottom. When the gas pressure is lowered, the peaks become less pronounced; they degenerate into shoulders, until eventually – for pressures less than 1 bar – there is a single bump in the center.

As long as there are peaks, i.e., for dense gases, the distance of the central and lateral peaks determines the sound speed of the gas or its temperature. From the half-width of the peaks and their relative heights, we may read off the viscosity and the thermal conductivity of the gas. That should come as a surprise to the reader! Indeed, he may well ask a question: How, if the scattering spectrum represents properties of density fluctuations in equilibrium, can it carry information about macroscopic transport coefficients like the viscosity?

The answer lies in the Onsager hypothesis according to which the mean regression of fluctuations follows the same laws as the macroscopic fields which – in our case – are the moments $F_{i1i2\ldots ip}$. We shall not go here into a discussion of that controversial hypothesis. Let it suffice to say that, without it, the interpretation of light scattering spectra in terms of the moments would be impossible. We accept the hypothesis, since it furnishes good results as we shall see.

If we compare the observed scattering spectra for a *dense* gas with the predictions of the

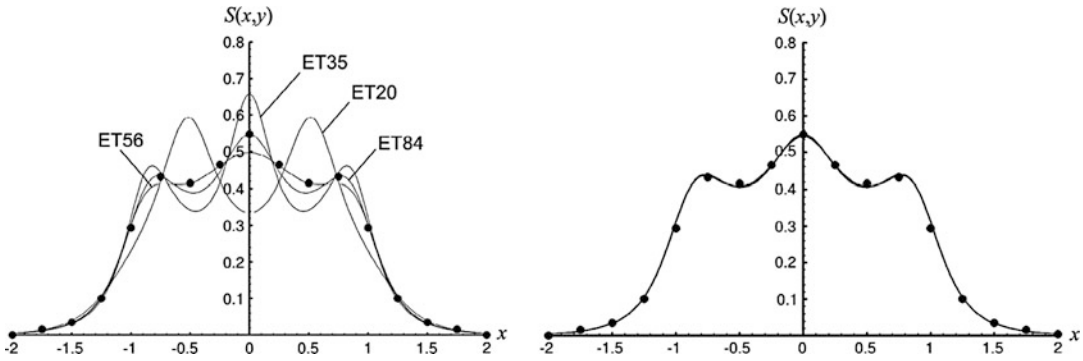

Fig. 6 Scattering spectra for xenon in extended thermodynamics for a low pressure. Dots represent measurements by Clark (1975). Left: spectra for 20, 35, 56, and 84 moments. Right: spectra for 120, 165, 220, and 286 moments

Navier-Stokes equations, we obtain an excellent agreement. Moreover the transport coefficients so determined agree well with their values obtained by more conventional means than light scattering, or those calculated from the kinetic theory of gases.

However, for a *rarefied* gas, the agreement is not good, if we still use the Navier-Stokes-Fourier equations. It is true that the expected gross features do appear: For a stronger degree of rarefaction, the three peaks of the spectrum degenerate into shoulders and, eventually, into a bump, even for Navier-Stokes. But the finer details are all wrong. We may well consider this as an opportunity to check out the validity of the equations of extended thermodynamics – and of the Onsager relations – both at the same time.

A prototypical case for the linearized equations is the 20-moment system shown in Fig. 1 and used there illustratively for the identification of various special cases. Equations like that for any specific number of moments are available, e.g., $v = 20, 35, 56, 84$, and their scattering spectra are shown in Fig. 6. Not two of them agree among themselves, and none of them agrees with the measured dots.

Ordinarily a situation like this calls for an adjustment of parameters, but that is impossible in the present case, because there are no free parameters, e.g., see Fig. 1. Indeed, extended thermodynamics of moments is a *theory of theories* with only *one* parameter: the number of equations. So, if we push up that number to $v = 120, 165, 220, 286$ and calculate the scattering spectra, we obtain convergence of results at $v = 120$ in the sense that more moments do not change the scattering spectrum and – what is more – they all agree with the measured values; see Fig. 6.

In other words, for a given pressure our *theory of theories* provides the possibility to determine its own range of validity, something that is usually said a theory cannot possibly do. Here, however, if we have two successive theories which provide the same results, the lower one is good enough: and *we can say that without conducting a single experiment.*

All of this is most satisfactory, but there is also disappointment. Indeed, we might have hoped that 13, or 14, or 20 moments might bring about a great improvement over the Navier-Stokes-Fourier solution and a good representation of experimental results. Instead we need hundreds of moments for even moderately rarefied gases. The microstructure of the gas is deeply hidden indeed.

Stationary Heat Conduction Between Coaxial Cylinders

All problems of extended thermodynamics discussed heretofore – wave speeds, shock structures, and light scattering – did not require boundary conditions or had trivial ones. On the other hand, even simple problems like heat

conduction between coaxial cylinders need that input.

Stationary heat conduction between coaxial cylinders has turned out to be a paradigmatic case for extended thermodynamics.

Boundary conditions present a problem in extended thermodynamics, because no moment beyond the heat flux can be prescribed and controlled on the boundary. Therefore it would seem that the 13-moment theory represents the ultimate useful extension for boundary value problems, and that might not be enough, according to the remarks on light scattering. Even that theory, however, provides an interesting modification of Fourier's law as was shown by Müller and Ruggeri (2004). The modified law reads for the radial heat flux q^1 in the gas between coaxial cylinders. (Of course, cylindrical coordinates are appropriate for this case, so that q^1 and $t^{<11>}$ are contravariant components of the heat flux and the stress. $t^{<11>}$ does *not* vanish in the 13-moment theory, although it does in the Navier-Stokes theory.)

$$q^1 = -\frac{5}{2}\frac{k}{\mu}p\tau\left(1 - \frac{7}{5}\frac{t^{<ij>}}{p}\right)\frac{dT}{dr}. \qquad (46)$$

The analysis shows that the modification becomes effective near the inner cylinder, where the temperature field is very steep. This is to be expected; see the comments concerning Fig. 1.

Beyond 13 moments the boundary values cannot be controlled; we must assume that the boundary values *adjust themselves,* in a manner of speaking. Barbera et al. (2004) have suggested that the boundary values in such cases fluctuate with the thermal motion and that the gas between the cylinders feels the most probable value determined by a maximum of entropy. There is not enough space to enter into that argument here.

The effects of inertial terms on the thermodynamic fields, put in evidence in (42), remain to be investigated systematically. Two results, however, have been established. First of all, the Fourier law is affected because the heat flux between coaxial rotating cylinders is no longer antiparallel to the temperature gradient; it acquires a frame-dependent component perpendicular to that gradient on account of the Coriolis force on the atomic motion; see Müller (1972). Secondly, it turns out that rigid rotation of the gas between the rotating coaxial cylinders is impossible, when heat conduction occurs between them; see Barbera and Müller (2006).

It is true that dissipation disguises the inertial effects. If dissipation could be reduced, or avoided altogether, it is suggested that the motion of the gas between rotating cylinders breaks up into vortices as happens in liquid helium. This remains to be proven.

References

Barbera E, Müller I, Reitebuch D, Zhao NR (2004) Determination of boundary conditions in extended thermodynamics. Cont Mech Thermodyn 16:411–425

Barbera E, Müller I (2006) Inherent frame dependence of thermodynamic fields in a gas. Acta Mech 184:205

Boillat G (1965) La propagation des ondes. Gauthier-Villars, Paris

Boillat G (1974) Sur l'existence et la recherche d'équations de conservation Supplémentaires pour les systèmes hyperboliques. C R Acad Sci Paris Sér A 278:909–912

Boillat G, Ruggeri T (1997) Moment equations in the kinetic theory of gases and wave velocities. Cont Mech Thermodyn 9:205–212

Cattaneo C (1948) Sulla conduzione del calore. Atti Sem Mat Fis Università Modena

Chapman SC, Cowling TG (1936/1961) The mathematical theory of non-uniform gases. Cambridge University Press, London

Clark NA (1975) Inelastic light scattering from density fluctuations in dilute gases. The kinetic-hydrodynamic transition in monatomic gases. Phys Rev A 12:232–244

Fisher A, Marsden PD (1972) The Einstein evolution equations as a first order quasi-linear symmetric hyperbolic system I. Commun Math Phys 28:1–38

Godunov SK (1961) An interesting class of quasi-linear systems. Dokl Akad Nauk 139:521–523; Soviet Math 2:947–949

Grad H (1949) On the kinetic theory of rarefied gases. Commun Pure Appl Math 2:331–407

Grad H (1952) The profile of a steady plane shock wave. Commun Pur Appl Math 5:257–300

Green WA (1964) The growth of plane discontinuities propagating into a homogeneous deformed material. Arch Ration Mech Anal 16:79–88

Liu I-S (1972a) On irreversible thermodynamics. Dissertation Johns Hopkins University

Liu I-S (1972b) Method of Lagrange multiopliers for the exploitation of the entropy inequality. Arch Ration Mech Anal 46:131–148

Müller I (1972) On the frame dependence of stress and heat flux. Arch Ration Mech Anal 45:241–250

Müller I, Ruggeri T (1998) Rational extended thermodynamics, 2nd edn. Springer, Heidelberg

Müller I, Ruggeri T (2004) Stationary heat conduction in radially symmetric situations. J Non-Newtonian Fluid Mech 119:139

Müller I, Weiss W (2012) Thermodynamics of irreversible processes – past and present. EPJ H. Historical perspectives on contemporary physics, vol 37. Springer, Heidelberg

Reitebuch D (2005) Konsistent geordnete erweiterte Thermodynamik. Dissertation TU, Berlin

Ruggeri T, Strumia A (1981) Main field and convex covariant density for quasi-linear hyperbolic systems. Relativistic fluid dynamics. Ann Inst H Poincaré 34A:65–84

Waldmann L (1958) Transporterscheinungen in Gasen von mittlerem Druck. In Handbuch der Physik, vol XII. Springer, Heidelberg

Weiss W (1990) Zur Hierarchie der erweiterten Thermodynamik. Dissertation TU Berlin